VOLCANIC GEOLOGY, MINERALOGY, AND PETROGENESIS OF THE DISCOVERY VOLCANIC SUBPROVINCE, SOUTHERN VICTORIA LAND, ANTARCTICA

Anne C. Wright-Grassham

Submitted in Partial Fulfillment
of the Requirements for the Degree of
Doctor of Philosophy in Geology

New Mexico Institute of Mining and Technology
Socorro, New Mexico

September, 1987

TABLE OF CONTENTS

LIST OF TABLES

APPENDICIES

LIST OF FIGURES

ABSTRACT

The Discovery volcanic subprovince (DVS) represents 19 m.y. of alkaline volcanic activity in the southern portion of the Erebus volcanic province, southern Victoria Land, Antarctica. Rocks older than 11 m.y. (Group I) are mildly undersaturated to saturated, mildly potassic, peralkaline trachytes, which form volcanic complexes at Mason Spur, and the Riviera and Gandalf Ridges. Less evolved rocks ar more common in the upper parts of the volcanic complexes, and follow mildly undersaturated, basanite to trachyte evolutionary trends. Rock younger than 11 m.y. (Group II) crop out over a much broader area, and form major volcanic centers at Mt Morning, Minna Bluff, Mt Discovery, Brown Peninsula, Black Island and White Island. Group II rocks usually exhibit strongly undersaturated, mildly potassic to sodic evolutionary trends, typically from basanite to phonolite. Grou II benmoreites and trachytes are less common, but occur in the lower sequences at Minna Bluff and Mt Discovery, and at Mason Spur. Ultrabasic and basic lavas are much more common in Group II than Group I.

Group I lavas are aphyric to weakly porphyritic. Feldspar is the most common phenocryst phase. Other phenocrysts include olivine and salite in ultrabasic and basic lavas, and ferrosalite to aegerine in the trachytes. Aenigmatite and arfvedsonite are usually present in th groundmass of the peralkaline trachytes. In contrast, Group II lavas are usually porphyritic to strongly porphyritic with phenocrysts of olivine, clinopyroxene, kaersutite, feldspar, and titanomagnetite.

Many DVS rock suites, each of which represents a mapped stratigraphic unit, exhibit well defined trends on major and trace element variation diagrams. All DVS rocks are light REE enriched, but Group I

samples are distinguished by increasing middle and heavy REE depletio with differentiation. Negative Eu anomalies characterize a few phonolites. In contrast, Group I rocks develop usually mild middle REE depletion, with pronounced negative Eu anomalies in the trachytes. DV rocks are divided into three petrological groups based on alkali enrichment trends (Group I, Group IIA and Group IIB). Group I rock suites exhibit trends of weak alkali and Al_2O_3 enrichment, and FeO* depletion. Alkali and early Al_2O_3 enrichment is followed by strong depletion in the trachytes. Group IIA rock suites exhibit the strongest trends of alkali and Al_2O_3 enrichment, and FeO* depletion. Trends exhibited by Group IIB rock suites usually lie between those of Group I and Group IIA.

The mineralogy and geochemistry of Group II rocks suggest they evolved from a basanite parent by fractional crystallization. Mass balance models support this hypothesis, and suggest that Group IIA rocks at Brown Peninsula (BP) are derived by fractionation of olivine clinopyroxene, titanomagnetite, kaersutite, feldspar and apatite to leave a 27 % residual liquid of tephriphonolite composition (Kyle et al., 1979). Mass balance models for Group IIB rocks at Minna Bluff (MB1) suggest they formed by fractionation of the same mineral phases as at Brown Peninsula, but in different proportions, to leave a 15 % residual liquid of trachyte composition. Mass balance models for Grou I rocks at Mason Spur (MS7) suggest that the tephrites may be derived by fractional crystallization from a basanite parent of similar composition to some Group II basanites, and that continued fractionation will produce the benmoreites. Fractionated phases include olivine, clinopyroxene, titanomagnetite, feldspar, nepheline, and apatite, but no kaersutite. Mass balance models for the derivation of

the trachytes from the benmoreites by fractional crystallization coul not be generated. However, models involving crustal melting or contam ination with crustal material were also unsuccessful. It is concluded that Group I trachytes may be derived from Group I benmoreites by fractional crystallization, but that other processes have also operated.

A model in which Group I, Group IIB, and Group IIA magmas are evolved by fractional crystallization of a parental basanite magma at different depths, is proposed to explain the geochemical and mineralogical variety of the Erebus volcanic province.

ACKNOWLEDGEMENTS

I thank Dr Philip R. Kyle for his advice, his help with XRF and INAA analysis and data reduction, and for his thorough editing of early drafts of this dissertation. I also thank the other members of r examining committee: Dr K. Condie, Dr A. Sanford, Dr A. Campbell, Dr S. Schery and Dr L. Werbelow. This work has benefited greatly from discussions with Dr J. Gamble, and fellow students Dr Ted Eggleston, Jim Moore, and Mike Knoper. I am particularly grateful to Mike for th use of his "Modulus" program used for trace element modelling of fractional crystallization and partial melting. I am also grateful to Kevin Cook for assistance with drafting figures.

Field work for this dissertation was supported by the Division o Polar Programs, National Science Foundation, with assistance from ITT Antarctic Services; the Naval Support Force, Antarctica; and the Roya New Zealand Air Force. I am particularly grateful to Bill McIntosh, Jim Moore, Kim Meeker, Pam Ellerman, and Ingrid Klich for their assistance and friendship in the field.

I thank Dr J. Gamble for permission to use the electron micro-probe at Victoria University of Wellington, New Zealand, and to him and K. Palmer for their assistance with making analyses; and Dr D. Johnson who assisted with photomicrographs.

Pat Mills, Annette Aguilar, Sarah Lazari, and Debbie Pettengill, of the Geoscience Department, provided willing assistance with word processing and use of equipment. I am most grateful also to Dr C. Yee and Ann Hewitt of the Humanities Department, where final printing of the dissertation took place.

To all my friends in Socorro, and to the Grassham family, a big thank you for your confidence and encouragement.

And last, but by no means least, I thank my husband, Phillip Grassham, for his unending support and understanding, which has been manifest in so many ways over the last three years.

This research was funded through National Science Foundation Gra DPP 8218493 to Dr Philip R. Kyle.

Chapter 1

INTRODUCTION

1.1 ALKALI VOLCANISM

Alkali volcanism typically occurs in an intraplate, continental or oceanic setting, and is commonly associated with hot spots or area of crustal extension (Williams and McBirney, 1979; McBirney, 1984). The marked similarity between alkali volcanic rocks from oceanic and continental areas can be accounted for if alkali magmas originate as partial melt in a mantle diapir, and do not interact with the overlying crust as they rise to the surface (Norry and Fitton, 1983; Fitton and Dunlop, 1985). Such an origin would also account for the association of alkaline provinces with hot spots and extensional tectonic regimes. Thus, alkaline volcanic rocks help delineate areas of crustal extension, also contribute valuable evidence for modelling mantle processes beneath regions of crustal attenuation. Alkaline rocks may also preserve a chronological record of changing stress regimes within the crust. For instance, intrusion of dyke swarms is commonly associated with renewed block faulting, while periods of tectonic quiescence may be characterized by more prolonged magma differentiation (Sorensen, 1974).

Within the rift environment strong structural control of vents i common. Individual vents may be aligned along axial or transverse faults, and major intrusions and volcanoes are commonly located at th intersection of major faults (e.g., Sorensen, 1970; Upton, 1974; Philpotts, 1974; Smith et al., 1978). In areas where the geology is poorly exposed alignment of volcanic centers may provide important clues about the location of unexposed, deeper structures.

Distinct zonal variation in mineralogy, geochemistry, and eruptive style is common in alkaline volcanic provinces, and individual eruptive centers commonly have their own petrological individuality (Carmichael et al., 1974). This variability reflects th diversity of conditions under which magma generation and evolution ha taken place. Over a span of a few million years these petrological characteristics can change, sometimes abruptly (Carmichael et al., 1974). Such changes often reflect changes in tectonic regime.

1.2 CENOZOIC ALKALI VOLCANISM IN ANTARCTICA

Mid to Late Cenozoic alkaline volcanism within the Antarctic continent is widespread (Figure 1.1), and has been subdivided into three principal geographic areas (Kyle, 1976): Antarctic Peninsula, Marie Byrd Land, and Victoria Land. The oldest outcrops are in Marie Byrd Land and are dated at about 30 Ma (Le Masurier and Wade, 1976), but volcanic sediments from the MSSTS-1 drillhole in McMurdo Sound, southern Victoria Land, are placed at >28 Ma (Harwood, 1986) on paleontological evidence and suggest that, despite the lack of outcrop, volcanic activity in this area probably started about the Late Oligocene also. Certainly, by Miocene times volcanic activity was wel established in all three areas, and has continued to Recent, with man volcanoes being presently active.

Sodic lavas predominate, with mildly and strongly undersaturated evolutionary trends seen in all areas. The inverse relationship between Na_2O/K_2O and crustal thickness documented in the Antarctic Peninsula (outcrops above the thickest crust (>30 km) are transitiona to a potassic series) has been attributed to different degrees of

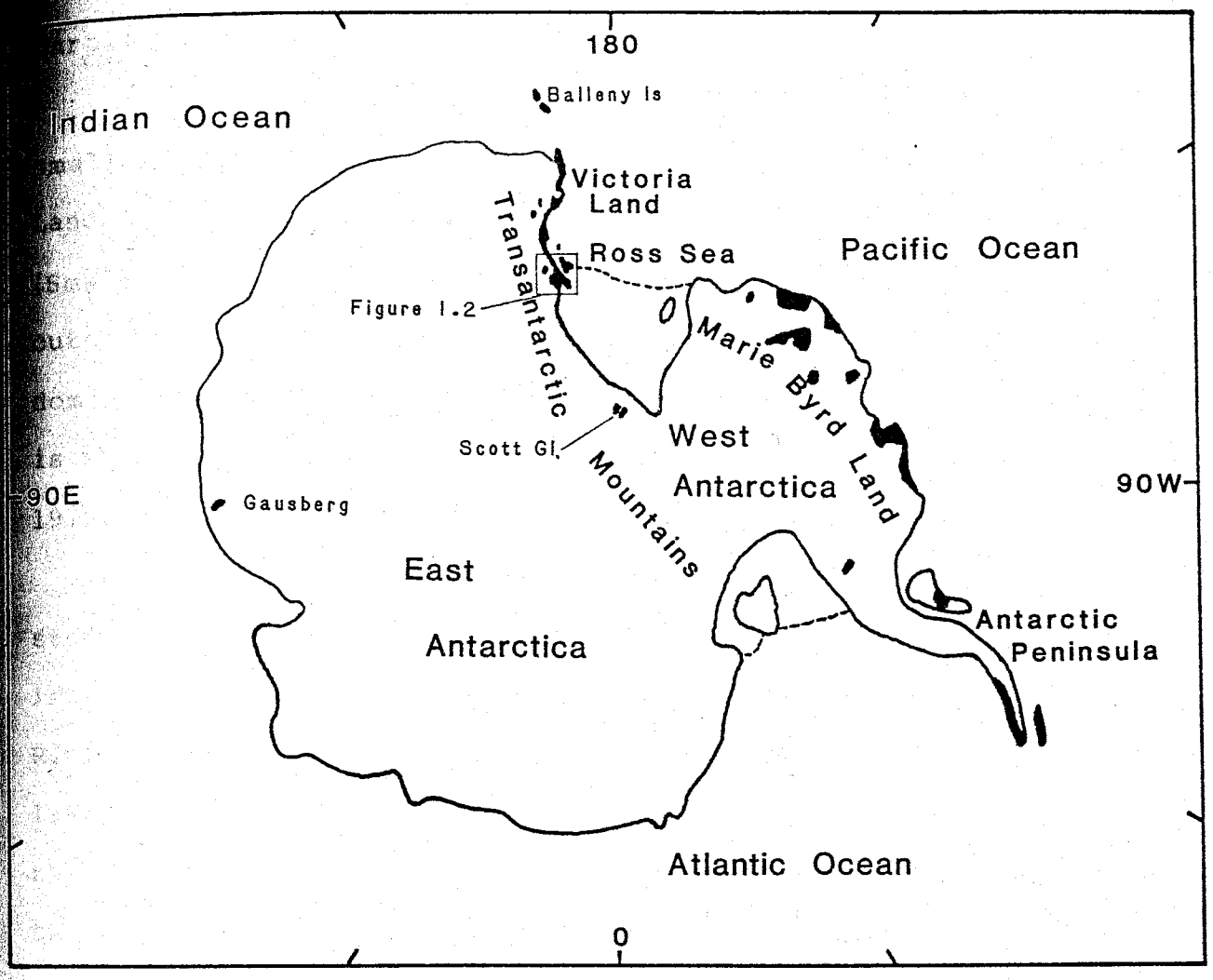

Figure 1.1 - Cenozoic alkaline volcanism in Antarctica (black), is divided into three main geographic areas: Antarctic Peninsula, Marie Byrd Land, and Victoria Land.

partial melting (Smellie, 1986).

Basaltic lavas are associated with shield volcanoes or numerous small cones. Hyaloclastites are an important rock type in Marie Byrd Land (Le Masurier and Wade, 1976) and the Antarctic Peninsula (Smellie, 1986), but form only a minor part of the Victoria Land outcrop. The evolved rock types may form small domes, but are predominantly associated with large stratovolcanoes. Outcrop distributio is strongly fault controlled (Smellie, 1986; Le Masurier and Wade, 1976; Kyle and Cole 1974).

The crustal structure of West Antarctica is still poorly understood, due in part to the extensive ice cover, but it is generally interpreted to be an area of diffuse continental crustal extension. Rift basins in the Ross Sea (Hayes and Davey, 1975; Vanney, et al., 1981; Davey, 1982; Cooper and Davey, 1985) are evidence of crustal thinning in this area, which is separated from the thickened crust of the Transantantarctic Mountains by a major crustal suture (McGinnis e al., 1985; Fitzgerald et al., 1986). The Cenozoic alkaline volcanism must be considered an integral part of this intraplate extensional tectonic setting.

Outcrops in the Victoria Land and Scott Glacier area are spread over a distance of 2000 km along the western margin of the Ross Embayment, and represent one of the most extensive alkaline volcanic provinces in the world (Kyle, 1974; Kyle, in press a). These rocks ar brought together collectively as the McMurdo Volcanic Group (MVG). Outcrops in the McMurdo Sound area being grouped into the Erebus volcanic province.

1.3 OBJECTIVES OF THIS STUDY

This dissertation investigates the petrologic evolution of Earl Miocene to Quaternary MVG rocks, that crop out in the southern McMur Sound area, southern Victoria Land, between the high scarp of Royal Society Range and the Ross Ice Shelf (Figure 1.2). This area specifi ally includes Mount Discovery, Mount Morning, the Foothills of Royal Society Range, Mason Spur, Minna Bluff, Brown Peninsula, Black Islan and White Island and is here defined as the Discovery volcanic sub-province (DVS), of the Erebus volcanic province. Prior to this study no comprehensive investigation of the DVS as a whole, or even many o the major volcanic centers within it, had been undertaken.

Specific objectives of this study were:

1. To examine the volcanic geology of the DVS, especially in areas not previously investigated, and establish a geologic history.
2. To examine petrographic, mineralogic, and geochemical evidence for magma evolution and to characterize any lava lineages found.
3. To qualitatively model the petrogenesis of defined lava lineages, and, where possible, to quantify these models.
4. To compare and contrast these models with models proposed fo lava lineages on Ross Island.
5. To integrate geologic, structural, chronologic, and petrologic data into a petrogenetic-tectonic model for the Erebus volcanic province.

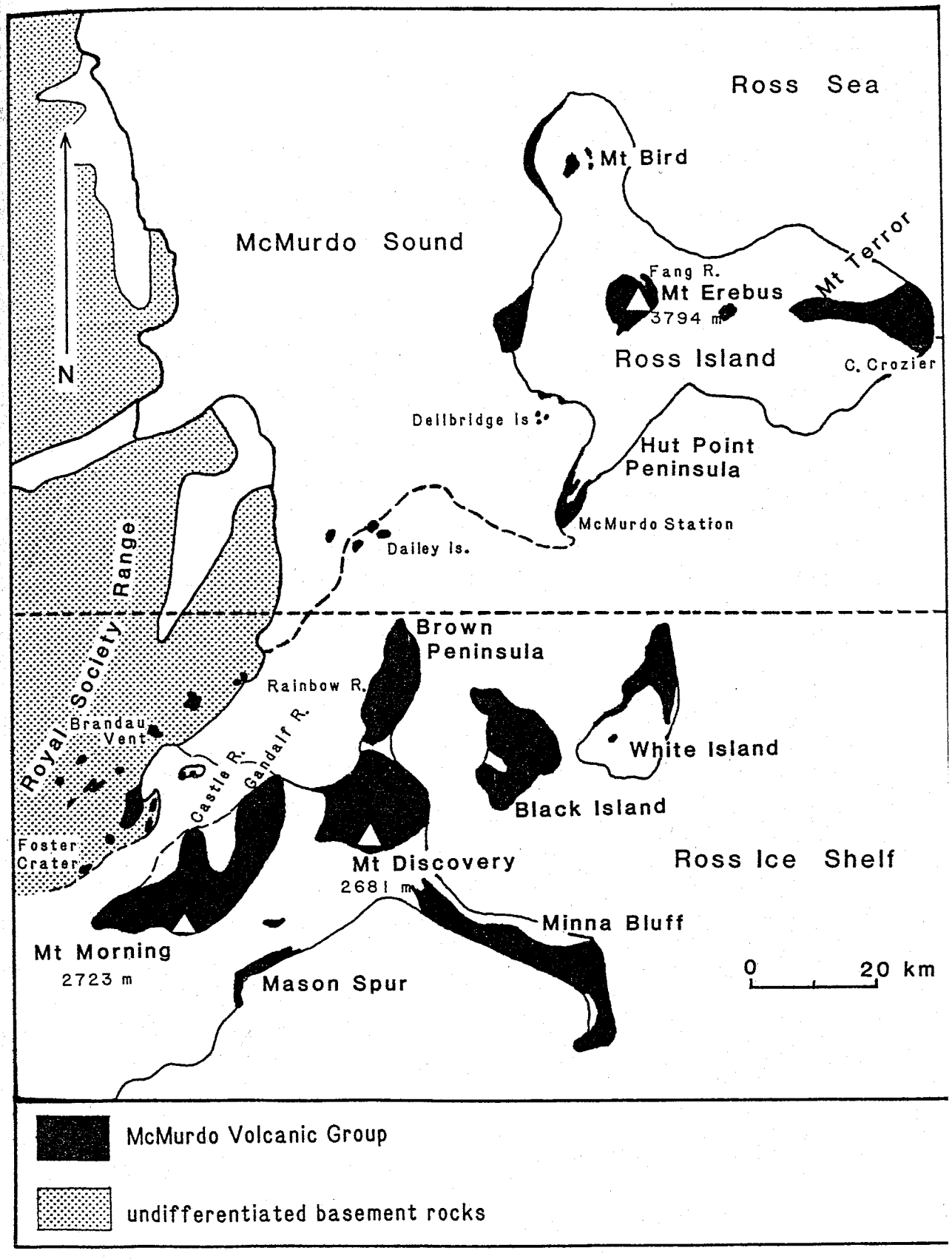

Figure 1.2 - Location of McMurdo Volcanic Group in the McMurdo Sou area. The DVS comprises those outcrops south of the dashed line.

1.4 PREVIOUS WORK

British geologists from the "heroic area" (1840 - 1916) made isolated observations of MVG rocks in the DVS (Prior, 1907; Ferrar, 1907; Debenham, 1923). Petrographic descriptions of samples collected during these early expeditions were made by Smith (1954). With the advent of improved logistic support following the establishment of permanent bases on Ross Island, field parties began making serious geological investigations of DVS, typically in conjunction with surveying and exploration (Harrington, 1959; Blank et al., 1963; Cole and Ewart, 1968; Cole et al., 1971). By the late 1960's interest in the DVS broadened (Treves, 1968; 1970) and the first detailed petrological study was made on inclusion-bearing basanites from Brandau Vent (McIver and Gevers, 1970). Since then detailed geological and petrological studies have been made at Rainbow Ridge (Kyle et al., 1979), Gandalf Ridge (Muncy, 1979), and Foster Crater (Kirsch, 1981; Kyle et al., 1987; Gamble and Kyle, 1987; Gamble et al., in prep.).

During the 1970's, rocks from the DVS were included in several geochemical and isotopic studies of the Erebus volcanic province (Jones and Walker, 1972; Goldich et al., 1975; Stuckless and Erickser 1976; Kyle, 1976). Kyle and Cole (1974) presented a model for the structural control of vents about Mt Discovery, in which crustal doming above a rising magma column would cause a three-pronged radial symmetry of subsidiary vents about the main central volcano. Many K-A age determinations have been made on DVS rocks, mostly for the purpos of interpreting glacial events (Armstrong, 1978; Kyle et al., 1979; Kyle, 1981a).

Reports of field observations and initial interpretations of the field work for this dissertation are published in Wright et al., 1983 1984; 1986).

1.5 FIELD WORK

A total of 85 days of field work was carried out during the 1982 83, 1983-84, and 1985-86 field seasons. Time spent in a particular area varied considerably (Table 1.1), and is an indication of the thoroughness of geological investigation there. During the 1977-78 field season the author also spent 13 weeks in the Foothills of Royal Society Range and made additional observations of the volcanic geolog (Wright, 1978; 1979a; b; c; 1980).

Table 1.1 - Summary of the time spent carring out field work in the various parts of the Discovery volcanic subprovince.

Area	Days of field work
Riviera Ridge	7
Gandalf Ridge	1
Mt Morning	5
Mason Spur	34
Helms Bluff	3
Mt Discovery	16
Minna Bluff	17
Foothills of Royal Society Range	2 days + prior observations

The general lack of formally accepted geographic place names in the DVS has necessitated the extensive use of informal place names. All formal and informal place names are located on accompany maps.

Chapter 2

REGIONAL GEOLOGY

2.1 REGIONAL GEOLOGY OF VICTORIA LAND

Victoria Land is underlain by a highly deformed basement complex of Late Precambrian to Early Paleozoic metamorphosed sedimentary, volcanic and intrusive rocks, intruded by slightly younger, granitoids, gabbros and lamprophyres (Grindley, 1981; Laird, 1981; Findlay et al., 1984; Borg et al., 1987). The basement complex is truncated by a major unconformity, which is overlain by Mid Paleozoic to Early Jurassic, terrestrial and shallow marine sedimentation of the Beacon Supergroup (Barrett et al., 1972). These sediments include coal and shale beds, but are principally composed of bedded and cross-bedded, well sorted sandstones. Major tholeiitic magmatism comprising the Ferrar Supergroup (Kyle et al., 1980) occurred in the Jurassic, and formed thick sills within the Beacon rocks. A second major break in the geologic record occurs between the Jurassic and the onset of alkaline volcanism by Early Miocene times. This volcanic activity has increased in intensity and extent to the present day, and represents the only major terrestrial deposition in Victoria Land since the Jurassic. However, an extensive record of marine sedimentation is found offshore (Cooper and Davey, 1985; Barrett and McKelvey, 1986).

2.2 TECTONIC SETTING OF VICTORIA LAND

The principal structural elements of Victoria Land are the Transantarctic Mountains, and the adjacent Victoria Land basin to the east (Figure 2.1). The Transantarctic Mountains have been variously described as a horst structure (David and Preistly, 1914), a block-

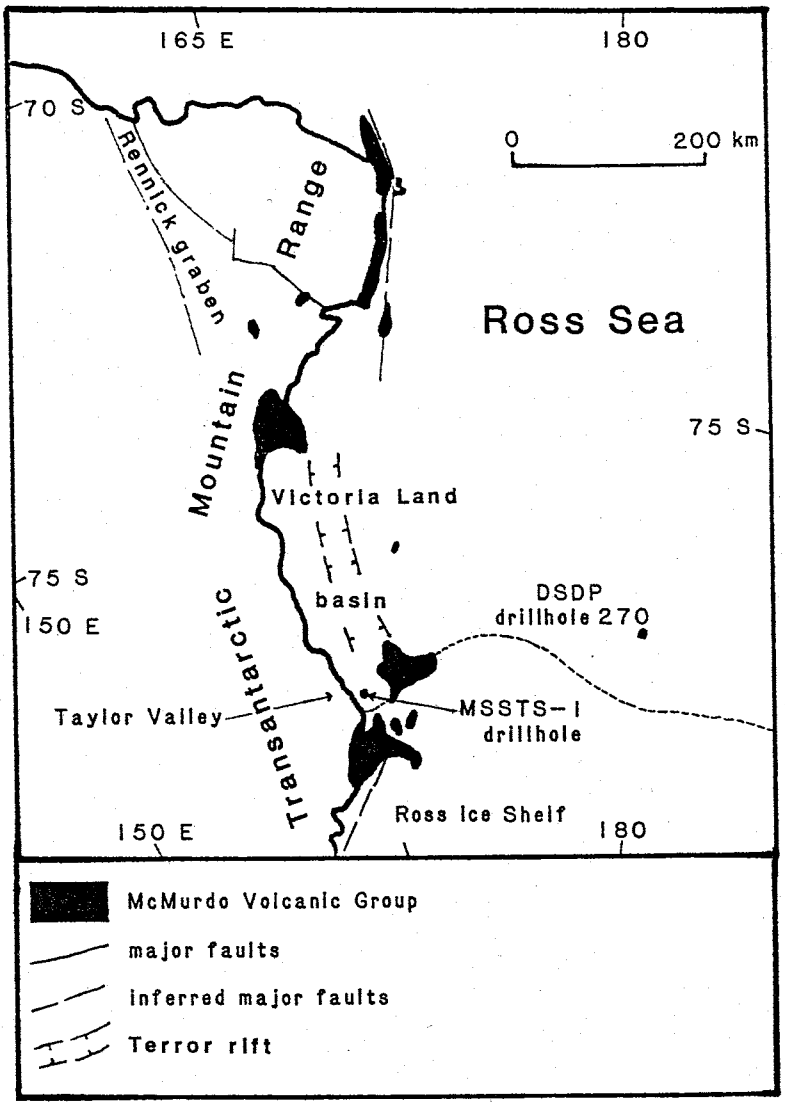

Figure 2.1 - Structural map of Victoria Land and the western Ross Sea, showing the location of the McMurdo Volcanic Group relative to major structural features as descibed in Kyle and Cole (1974), Davey (1982), Cooper and Davey (1985), and Deep Sea Drilling Project drillhole 270. Tne Rennick graben has also been referred to as the Bowers graben (Borg et al., 1987).

faulted and uplifted mountain range (Gunn and Warren, 1962), and a large tilt block (Fitzgerald et al., 1986; Gleadow and Fitzgerald, 1987). Some of the greatest uplift along the Transantarctic Mountain range occurs in southern Victoria Land where the axis of maximum uplift lies about 30 km inland. Major downstepping occurs along the eastern margin of the Transantarctic Mountains (Gleadow and Fitzgerald, 1987). Other studies suggest there is also left lateral strik slip along the range front (Barrett, 1965; Molnar et al., 1975; Hayes and Davey, 1975; Bennett and Sissons, 1984). The main range front fault zone generally lies offshore (Bennett and Sissons, 1984; McGinnis et al., 1983; 1985), but faults with major vertical offsets are exposed onshore, for instance, a major fault at the eastern margi of the Queen Maud Range has a minimum offset of 3 km (Barrett, 1965). Fission track study of apatites from southern Victoria Land indicate that the combined effect of step faulting in this area has produced a vertical offset of some 5 km (Gleadow and Fitzgerald, 1987) of which about 1000 m occurs on land.

Several major faults cut across the axial trend of the mountains (Craddock, 1971). Such faults are common within rift systems, where they may be associated with lateral offsets of, or changes in, the axial direction of the rift (Illies, 1969; 1978; Florensov, 1969; Eaton, 1979). A change in the axial trend of the Transantarctic Mountains from north-south to northwest-southeast in the vicinity of McMurdo Sound coincides with an area of major uplift and volcanism (Kyle, 1976). Major cross cutting faults are documented in the Ferrar and Taylor valleys, and extend off shore (Findlay et al., 1984; Bennett and Sissons, 1984).

Geophysical evidence from the McMurdo Sound region indicates that the crust thins from 40 - 45 km beneath the mountains to as little as 21 km beneath McMurdo Sound (Smithson, 1972; McGinnis et al., 1985). There is also a fundamental change in the nature of the crust across this area (Smithson, 1972; McGinnis et al., 1985). The boundary between the Transantarctic Mountains and the Ross Sea has been interpreted as an early Paleozoic, convergent plate margin, which created thicken crust beneath the Transantarctic Mountains (McGinnis et al., 1985; Gleadow and Fitzgerald, 1987). This area underwent a major thermal event with the intrusion of the Ferrar rocks in the Jurassic, followed by major uplift. Concommittent with Transantarctic Mountain uplift, the continental crust in the western Ross Sea has been thinned by low angle detachment faulting associated with crustal extension (Fitzgerald et al.,1986).

Stratigraphic and paleontological evidence (Priestly and David, 1912; Gunn and Warren, 1962; Miagkov, 1975; Brady and McKelvey, 1979; Webb, 1979) and fission-track dating of apatites (Gleadow and Fitzgerald 1984; 1987; Gleadow et al., 1984) are consistent with a tectonic history of initial gentle uplift of the mountains in southern Victoria Land during Jurassic to Early Tertiary times, followed by a more intensified rate of uplift since the Oligocene.

Considerable uplift of the Transantarctic Mountains must have taken place before the major valley systems were carved. These valley were in existence by the Early (Stump et al., 1980) and Late Miocene (Brady, 1979; Elston and Bressler, 1981) in the Scott Glacie and McMurdo Sound areas, respectively. At Gandalf Ridge (DVS) synvolcanic faulting and dyke intrusion of early MVG rocks along faults parallel to the axial trends of the Transantarctic Mountains are

further evidence that Transantarctic Mountain uplift was occurring in this area during Early to Mid Miocene times (Muncy, 1979; Kyle and Muncy, 1978, Kyle et al., in prep.).

In southern Victoria Land, there is fission-track evidence for 4.8 - 5.3 km of uplift during the last 50 m.y. with average uplift rates of 100 +/- 5 m/Ma along the axis of greatest uplift (Gleadow an Fitzgerald, 1987). Paleontological evidence from drillholes in Taylor Valley provide evidence for over 400 m of uplift during the Early Pliocene, requiring a minimum uplift rate of 80 m/Ma (Barrett and McKelvey, 1981; Webb and Wrenn, 1982; Wrenn and Webb, 1982). Elevated Middle Pliocene marine fossil beds in Wright Valley suggest average uplift rates of 40 - 70 m/Ma since that time (Webb, 1974), although Brady (1979) argues for an Early Pliocene age for the fauna, which would modify the inferred average rate of uplift to 38 - 59 m/Ma.

Multichannel seismic reflection profiles in the western Ross Sea define a 15 - 25 km wide central rift-depression (Terror rift) within the Victoria Land basin (Figure 2.1)(Davey, 1982; Cooper and Davey, 1985). The southern extension or termination of the rift basin has nc been delineated. Both margins of the rift are bounded by zones of north-south trending, predominantly normal faults. East-dipping listric faults have been identified along the western margin (McGinni et al., 1983; Cooper and Davey, 1985). Although the rift may have bee intermittently active since the Paleozoic, the latest downwarping is interpreted to have begun during Early to Mid Tertiary times. A more precise timing can be assigned in the McMurdo Sound area where cor-relation of drillhole data with seismic refraction profiles indicates that renewed subsidence followed a major erosional break lasting from

the Late Eocene to the Late Oligocene (Davey and Christoffel, 1984). The degree of lithification of sediments below the unconformity suggests that about 1 km has been lost to erosion, providing evidence fo considerable, though not necessarily dramatic uplift between the Late Jurassic and the Late Eocene. Although there are no drillholes within the Victoria Land basin, sedimentary horizons in the MSSTS-1 drillhol on the western shelf of McMurdo Sound have been traced laterally into the deeper parts of the basin using seismic refraction profiles (Dave and Christoffel, 1984). The profiles show onlapping sedimentary sequences, separated by several unconformities, that thicken consider ably into the basin. Further north sediments reach a maximum thicknes of 12 km; the upper 5 - 6 km of which are thought to be Late Oligocen and younger (Cooper and Davey, 1985). The older sequence probably includes Beacon rocks, which are found as xenoliths in lavas on Ross Island (Thomson, 1916).

Sediments in the Deep Sea Drilling Project hole 270, located on ridge to the east of the Victoria Land basin (Figure 2.1) indicate rapid downwarping from littoral conditions in the Late Oligocene to bathyal depths by the Early Miocene (Hayes and Frakes, 1975; Barrett 1975).

Thus, the onset of renewed subsidence in the Western Ross Sea, and the formation of the Victoria Land basin in particular, are coincident with a marked increase in Transantarctic Mountain uplift, and the onset of MVG volcanism during late Oligocene times. This tectonic regime has continued until present.

2.3 McMURDO VOLCANIC GROUP

2.3.1 Introduction

McMurdo Volcanic Group (MVG) comprises Late Cenozoic volcanic rocks cropping out along the western margin of the Ross Embayment (Ross Sea and Ross Ice Shelf) (Kyle, in press a) (Figure 2.2). Within this area three informal volcanic provinces are recognized on the grounds of geographic separation, structural setting and volcanic style (Kyle in press a):

Hallett volcanic province

Melbourne volcanic province

Erebus volcanic province.

The Balleny Islands were originally included as a fourth volcanic province in the MVG (Kyle and Cole, 1974), but are now excluded on geographic and tectonic grounds. Isolated MVG outcrops of tholeiite and alkali olivine basalt in the vicinity of Scott Glacier are not designated as a separate volcanic province. One outcrop (Sheridan Bluff) in this area is dated at 19.8 Ma (Stump et al., 1980), and is the oldest MVG outcrop.

2.3.2 Hallett Volcanic Province

The Hallett volcanic province comprises four elongate volcanic piles, each formed from two or three coalescing shield volcanoes erupted along north-south trending fissures (McIntosh and Kyle, in press). Lava flows, associated breccias, dykes, and subordinate pyroclastic deposits comprise the bulk of the four shield complexes, which are now considered to have been erupted under predominantly subaerial conditions (LeMasurier et al, 1983; McIntosh and Gamble, in press).

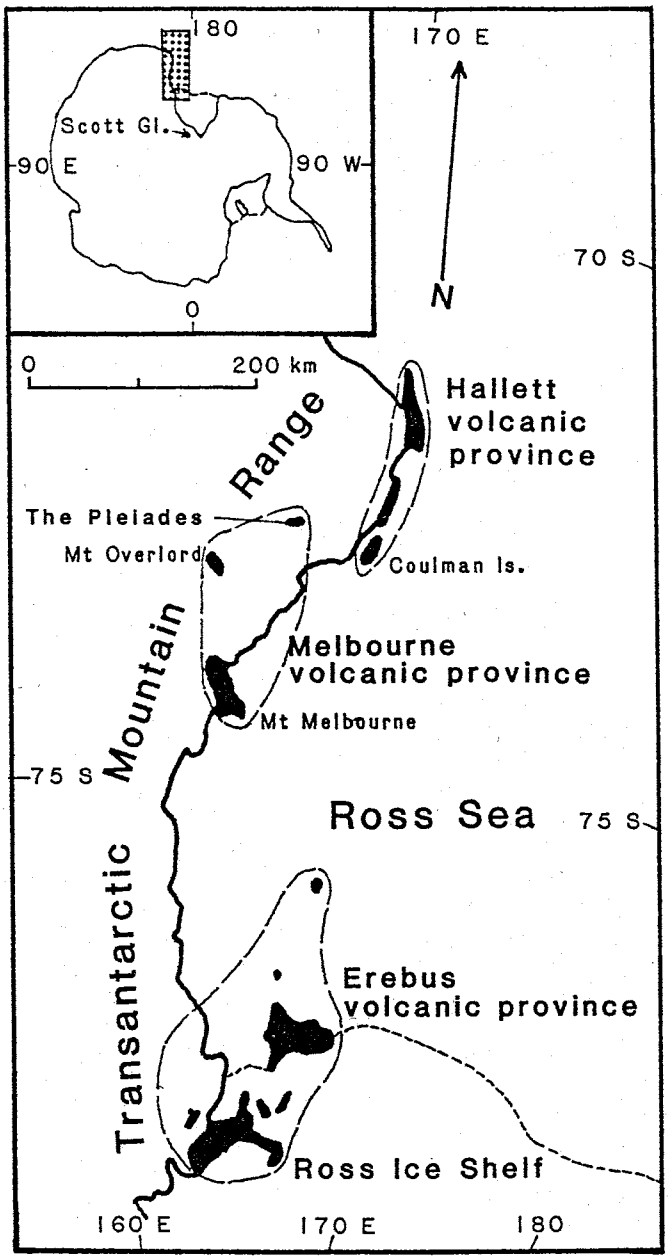

Figure 2.2 - Location of the three volcanic provinces of the McMurdo Volcanic Group (outcrops shown in black). This area is shaded on the inset map of Antarctica, which also shows the location of McMurdo Volcanic Group in the vicinity of Scott Glacier.

Volcanic centers are aligned along the proposed Hallett Fractur (Kyle and Cole, 1974). Large, vertical displacement along this fracture zone is likely, but only small displacements have been observed in outcrop (Jordan, 1981).

Basaltic lavas predominate, and whereas both mildly and strongly undersaturated evolutionary trends are seen, analysed samples sugges that the mildly undersaturated rocks are more common (McIntosh and Kyle, in press). All rocks are sodic.

Lavas as old as 13.24 Ma are known from the Adare Peninsula, and activity has continued until Holocene times (Stuivier and Braziunas, 1985).

2.3.3 Melbourne Volcanic Province

Melbourne volcanic province comprises an arcuate belt of alkalin volcanic rocks that stretch inland from Mt Melbourne and border the Hallett volcanic province in the north (Kyle, in press b). It include five large stratovolcanoes and numerous small basaltic vents. The location of individual vents is commonly associated with northwest-trending faults that parallel the Rennick Graben (Kyle and Cole, 1974). Unlike the Hallett and Erebus volcanic provinces, most centers in the Melbourne volcanic province are located within the Transantarctic Mountains rather than along the eastern range front.

Intermediate and trachytic rocks predominate and are associated with the large stratovolcanoes. Basaltic rocks form only a minor component of the stratovolcanoes where they crop out as small late stage parasitic cones. Magmas of a similar composition are the presumed parent for the more evolved lavas. Small isolated vents are

scattered throughout the province and include basanite, tephrite and alkali basalt lava flows and scoria cones.

There is no evidence that rock type and age are related. The oldest reliable age for the onset of volcanism in this area is 14.7 Ma (Kyle, in press b). Chronological control for the onset of major statovolcano formation is poor, but the oldest dated trachytes were erupted 7.2 Ma ago at Mt Overlord. The large stratovolcano of Mt Melbourne is presently active, with evidence of fumerolic activity at the summit and ash layers in ice (Nathan and Schulte, 1967; Keys et al., 1983; Worner and Viereck, 1986; Lyon, 1986).

2.3.4 Erebus Volcanic Province

The Erebus volcanic province comprises the major phonolite centers of Mt Erebus and Mt Discovery, and many smaller basanite shields and cones, and phonolite domes, which are scattered over the eastern flanks of the Transantarctic Mountains and form islands in McMurdo Sound and the southern Ross Sea. Evidence for an earlier period of major trachyte to peralkaline trachyte volcanism is seen in the southwestern portion of the area (DVS).

Erebus volcanic province straddles the crustal suture defined by McGinnis et al., 1985) at a point that coincides with a change in the axial trend of the Transantarctic Mountains. The concentration of volcanic activity in this area is presumably related to crustal weakness above an unstable zone in the mantle (Kyle, 1976; Moore, 1986).

The volcanic centers of Mt Erebus and Mt Discovery each consist of a large stratovolcano radially surrounded by subsidiary volcanic centers. It has been proposed that the three-fold radial configuratio

of the subsidiary vents around the main central volcano may be controlled by radial fractures in the crust caused by doming above a mantle plume (Kyle and Cole, 1974).

Dating of MVG rocks documents a history of volcanic activity spanning the period from about 19 m.y. to present (Muncy, 1979). However, drill core from the MSSTS-1 drillhole in McMurdo Sound contains volcanic sand correlated with MVG, that is paleontologically dated at >28 Ma (Harwood, 1986), and suggests that volcanism may have commenced much earlier than the dated terrestrial outcrops suggest (Barrett et al., 1986; Gamble et al., 1986). Major trachyte and peralkaline trachyte eruption occurred between 19 m.y. and about 14 - 12 m.y. ago, but then gave way to basanite - trachyte activity between 1 and 9 m.y. ago, before changing to the basanite - phonolite regime, which is still active.

Geologic and Petrologic Evolution of Ross Island

The volcanic edifice of Ross Island lies 50 km off the coast of southern Victoria Land at the northern edge of Ross Ice Shelf (Figure 1.2). Ross Island is sited within the Victoria Land basin, and comprises a centrally located, presently active, basanite to anorthoclas phonolite volcano of Mt Erebus (3794 m), which is predominantly composed of lava flows erupted both from the central vent, and from several parasitic domes (Moore and Kyle, in press). Present-day activity is associated with a summit agglutinate cone and lava lake (Kyl et al., 1982).

Three smaller volcanic centers (Mt Terror (3230 m), Mt Bird (176 m) and Hut Point Pensinsula) occupy radially symmetrical positions

about Mt Erebus. They generally represent older volcanic activity. These older volcanic centers are composed principally of basanite, with only minor kaersutite-bearing tephriphonolites and phonolites. Age K-Ar age dating (Forbes et al., 1974; Kyle and Treves, 1974; Armstrong, 1978) indicates that volcanic activity started at Ross Island with the growth of Mt Bird at least 3.8 - 4.6 m.y. ago. Younger, parasitic phonolite cones are dated at 3.23 Ma and 3.08 Ma. The age of Mt Terror remains undetermined, but late phase parasitic basanite and phonolite cones at Cape Crozier range in age from 1.35 Ma to 0.82 Ma, suggesting that Mt Terror probably formed 1.5 - 2.5 m.y. ago. Volcanic activity at Hut Point Peninsula began at least 1.3 m.y. ago and continued until 0.4 m.y. (Kyle, 1981b). Soon after the onset of volcanism at Hut Point Peninsula, the growth of the Erebus volcano was also initiated, almost 1 m.y. ago. By 0.7 Ma the older Erebus volcano, exposed at Fang Ridge, had formed, but was then largely buried by anorthoclase phonolite flows from the later Erebus volcano which is still active (Moore and Kyle, in press).

Despite very similar major element evolutionary trends for all lavas from Ross Island, two distinct lava lineages, with distinctive mineralogical and trace element characteristics, can be recognized. Lavas from the peripheral volcanic centers of Mt Bird, Mt Terror and Hut Point Peninsula are characterized by the presence of kaersutite, and belong to the DVDP lineage (Kyle, 1976; 1981c). In contrast, lavas from the Dellbridge Islands and Mt Erebus lack kaersutite, and belong to the Erebus lineage (Kyle, 1976; Moore, 1986).

A plausible model for the derivation of the DVDP lineage requires up to 74.9 % fractional crystallization of the parental basanite (Kyle, 1981c). Initial fractionating phases comprise olivine, clino-

pyroxene, kaersutite, Cr spinel, titanomagnetite, apatite, and plagi oclase. Later fractionating phases include clinopyroxene, kaersutite, magnetite, plagioclase, apatite, and either anorthoclase or sanidine

The most plausible model for the derivation of the Erebus linea fractionates up to 76.5 % of the parental basanite, with initial fractionating phases being olivine (Fo_{88}), clinopyroxene (En_{41}), Cr spinel (Usp_8), titanomagnetite (Usp_{52}), ilmenite, and apatite. Inter mediate fractionating phases include olivine (Fo_{66}), clinopyroxene (En_{40}), titanomagnetite (Usp_{73}), feldspar (An_{64}), and apatite; and final fractionating phases, olivine (Fo_{58}), clinopyroxene (En_{39}), titanomagnetite (Usp_{61}), feldspar (An_{44}), nepheline and apatite (Moore, 1986).

It is postulated that Ross Island sits above a mantle plume (Kyle, 1986) in which a parental basanite magma has been produced by low degrees of partial melting of garnet peridotite. The difference between the DVDP and Erebus lava lineages is attributed to crystal fractionation from a common basanitic parental magma under different physical and chemical conditions. The smaller volume and scattered distribution of evolved kaersutite-bearing lavas of the DVDP lineage derived from crystal fractionation at higher f_{H2O} and lower tempera- ture than the Erebus lineage lavas, in discrete, smaller magma cham- bers (Kyle, 1981c). In contrast, the large volume of evolved Erebus lineage lavas, lacking in kaersutite and eminating predominantly from a central vent area, are consistent with crystal fractionation in a large magma chamber beneath Mt Erebus (Moore, 1986). It is postulate (P.R. Kyle, pers. comm.) that the presence of a large volume of low density evolved magma beneath Mt Erebus has so far precluded the

uption of late-phase, less evolved lavas, that characterize the Mt
ird, Mt Terror, and Hut Point Peninsula volcanic centers.

Chapter 3

GEOLOGY OF THE DISCOVERY VOLCANIC SUBPROVINCE

3.1 INTRODUCTION

The DVS comprises alkaline volcanic rocks in the southern portion of the Erebus volcanic province (Figure 1.2). In the Foothills of Royal Society Range, the volcanic rocks overly a metamorphosed basement comprised of pre-Ordovician metasediments and intercalated orthogneiss (Koettlitz Group), Paleozoic granitoids, gabbros and lamprophyres (Granite Harbour Intrusive Group), and later alkaline plutons and dykes (Findlay et al., 1984). Basement rocks also crop out at a small locality at Gandalf Ridge, and are presumed to underlie the DVS. The Ferrar and Beacon Supergroups are exposed in the high scarp of Royal Society Range. Sandstone xenoliths in basanite at Mason Spur are most likely derived from the Beacon Supergroup, and suggest that Ferrar and Beacon rocks are probably present at depth beneath the southern portion of the DVS.

The principal basement structure is a series of high-angle, faults parallel to the scarp of Royal Society Range. The marked change in basement elevation from west to east across the DVS is attributed to downstepping along these faults. At Gandalf Ridge Early Miocene dykes intrude their own volcanic pile along the same north-south trend, and indicate that these zones of weakness were active by the early Miocene (Muncy, 1979).

The DVS outcrop is subdivided into nine geographic areas (Figure 3.1). Although the Riviera and Gandalf Ridges to the northeast, and the Mason Spur area to the southeast, could be geographically consid-

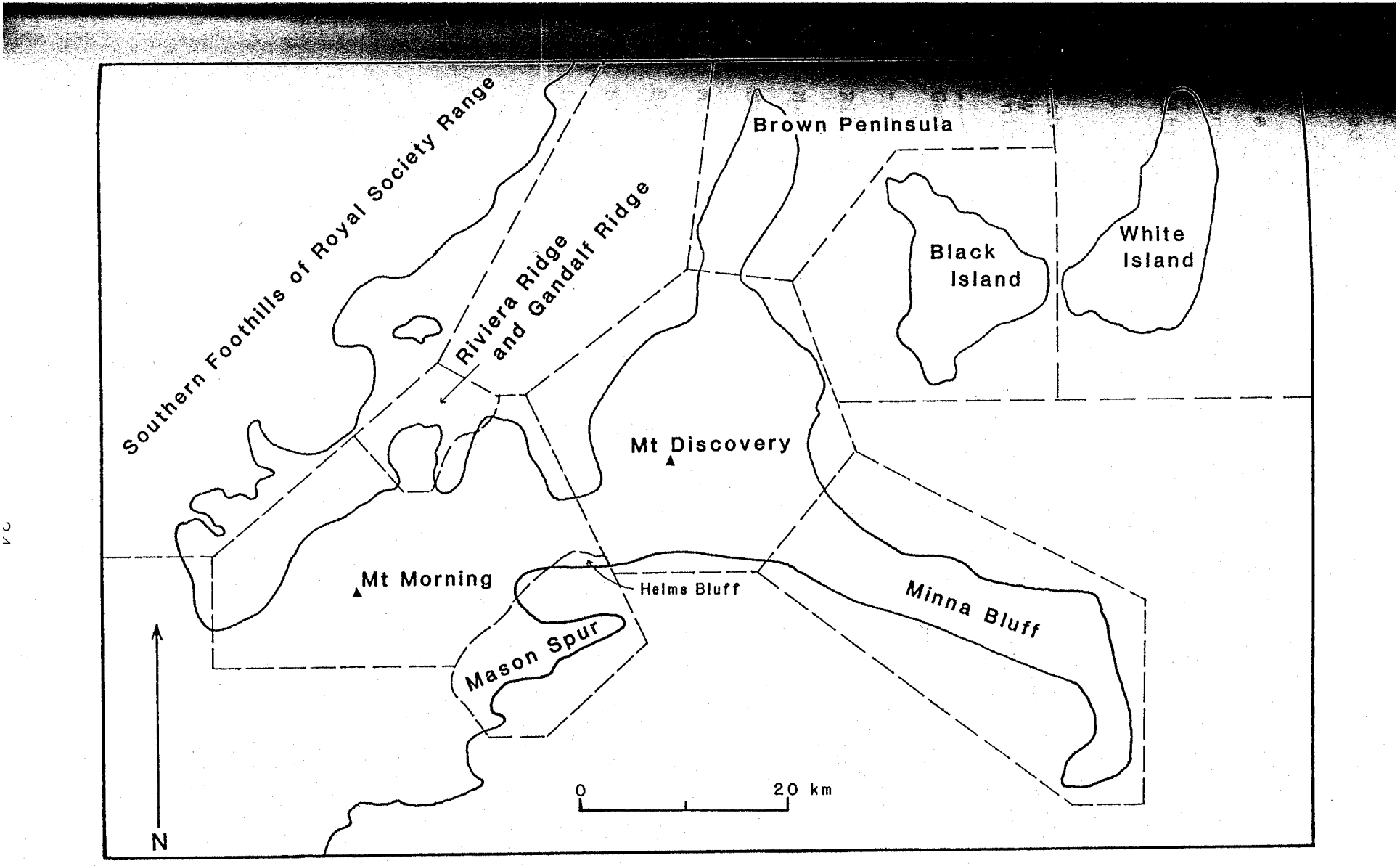

Figure 3.1 - Subdivision of the Discovery volcanic subprovince into the informal geographic areas used in this dissertation.

ced part of the Mt Morning area, they have been designated separately. This was done because Riviera Ridge, Gandalf Ridge and Mason Spur are the only outcrops of early DVS rocks, and were investigated in considerably more detail than Mt Morning. Within each area, informal lithostratigraphic units are recognized (Table 3.1).

Table 3.1 - Informal lithostratigraphic units of the DVS, listed by area. Lithostratigraphic units are prefixed by the area initials and are numbered from oldest to youngest within each area.

Geographic Area	Lithostratigraphic Unit
Riviera and Gandalf Ridges	RG1 - RG3
Mason Spur (including Helms Bluff)	MS1 - MS9
Minna Bluff	MB1 - MB2
Mt Discovery	MD1 - MD2
Brown Peninsula	BP
Black Island	BI1 - BI2
White Island	WI
Mt Morning	MM1 - MM2
Foothills of Royal Society Range	F

3.2 RIVIERA AND GANDALF RIDGES (RG)

3.2.1 Introduction

Extrusive and subvolcanic intrusive rocks of Miocene age crop out beneath younger basanites at Gandalf Ridge (Figure 3.2) and Riviera Ridge (Figures 3.3 and 3.4) on the northeastern side of Mount Morning. Although both areas are ice-free and of easy access, much of the geological detail is obscured by moraine, and colluvium.

The geology and petrology of Gandalf Ridge are described by Muncy (1979), and Kyle and Muncy (1978; in prep.).

3.2.2 Volcanic Geology

Two lithologically and stratigraphically distinct episodes of volcanism are recognized. The older rocks include a sequence of hawaiites, mugearites, trachytes, peralkaline trachytes and peralkaline rhyolites (RG1) overlain by a slightly younger basanite to trachyte suite (RG2) and are designated as the Gandalf volcanic complex (GVC). A later sequence of basanites and tephrites (RG3) unconformably overlies the older rocks, and is part of an extensive area of much younger basanite and trachyte volcanism.

RG1

At Gandalf Ridge hawaiite and mugearite flows rest unconformably on rocks of the Koettlitz Group, and are intruded by trachytes, peralkaline trachytes, peralkaline rhyolites and dacites (Muncy, 1979) (Figure 3.2). A later volcaniclastic diamictite unconformably overlies the volcanic rocks and has been interpreted as a lahar (Muncy 1979). At Castle Ridge a sequence of trachyte flows is overlain by a megabreccia containing clasts from a wide variety of volcanic lithologies

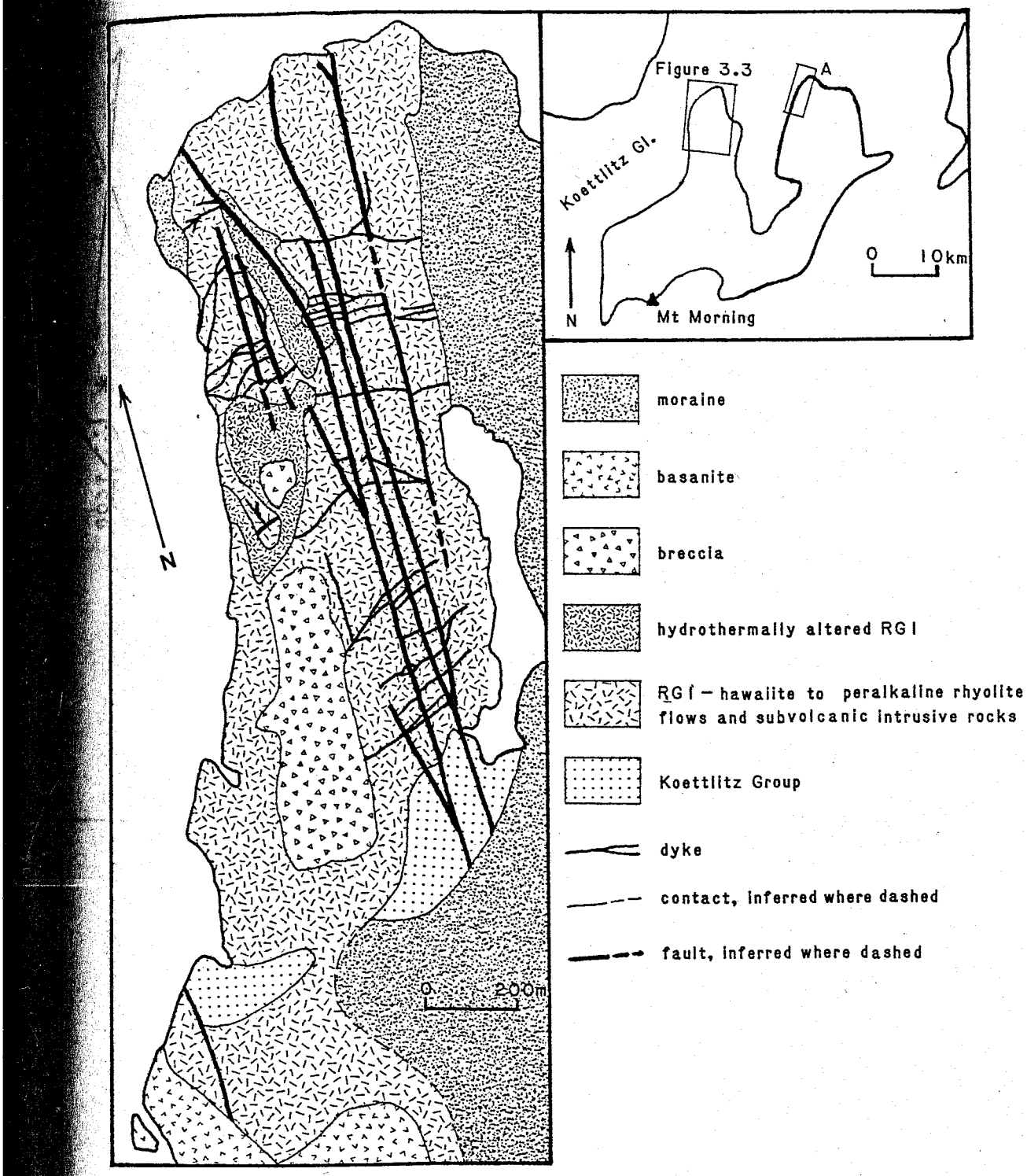

Figure 3.2 - Volcanic geology of Gandalf Ridge (after Muncy, 1979), Gandalf Ridge is shown as area A on the inset map.

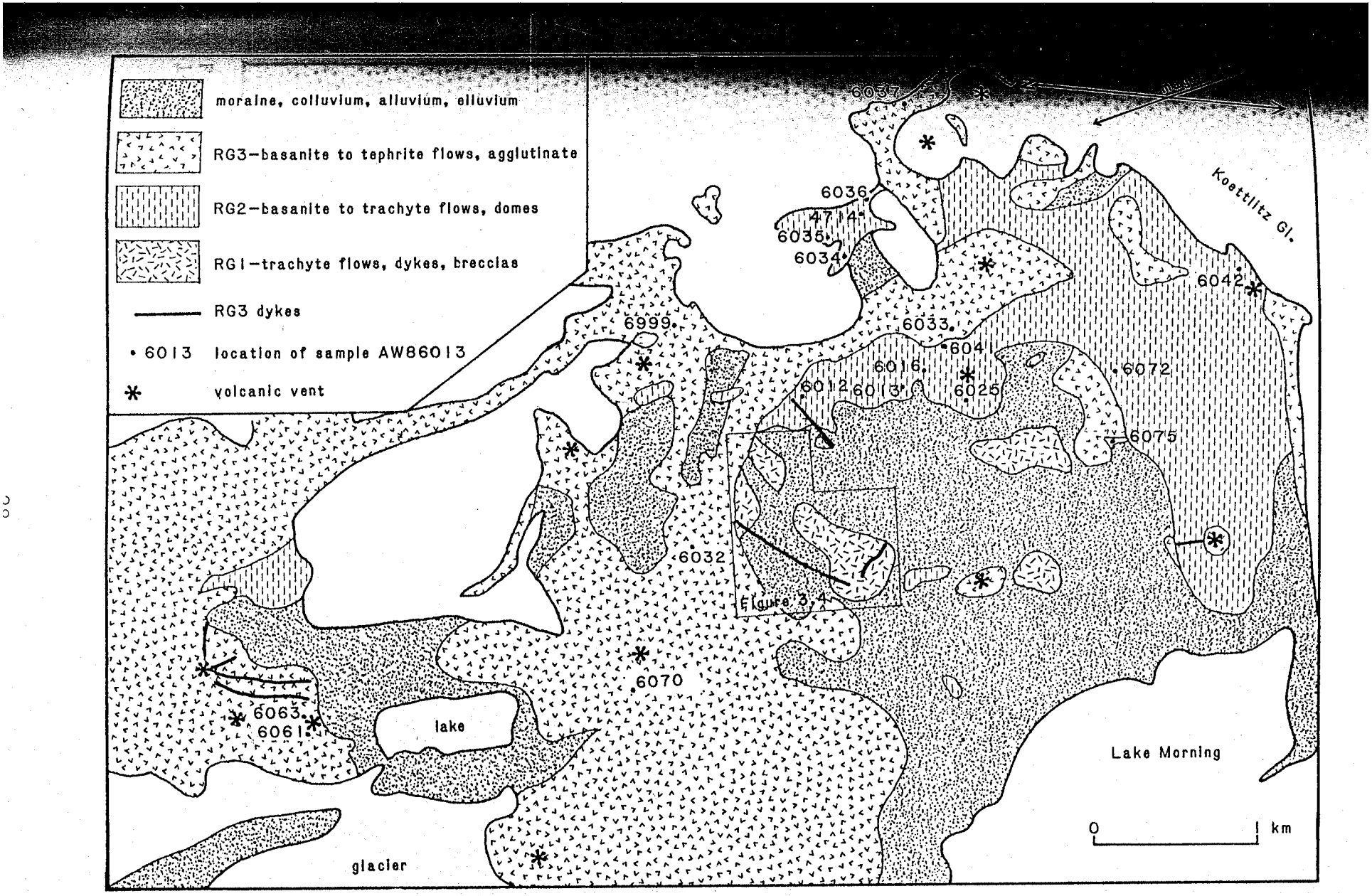

Figure 3.3 - Sketch map of the volcanic geology of Riviera Ridge. The location of this area is shown on the inset map accompanying Figure 3.2. An enlargement of the Castle Ridge area is given in Figure 3.4.

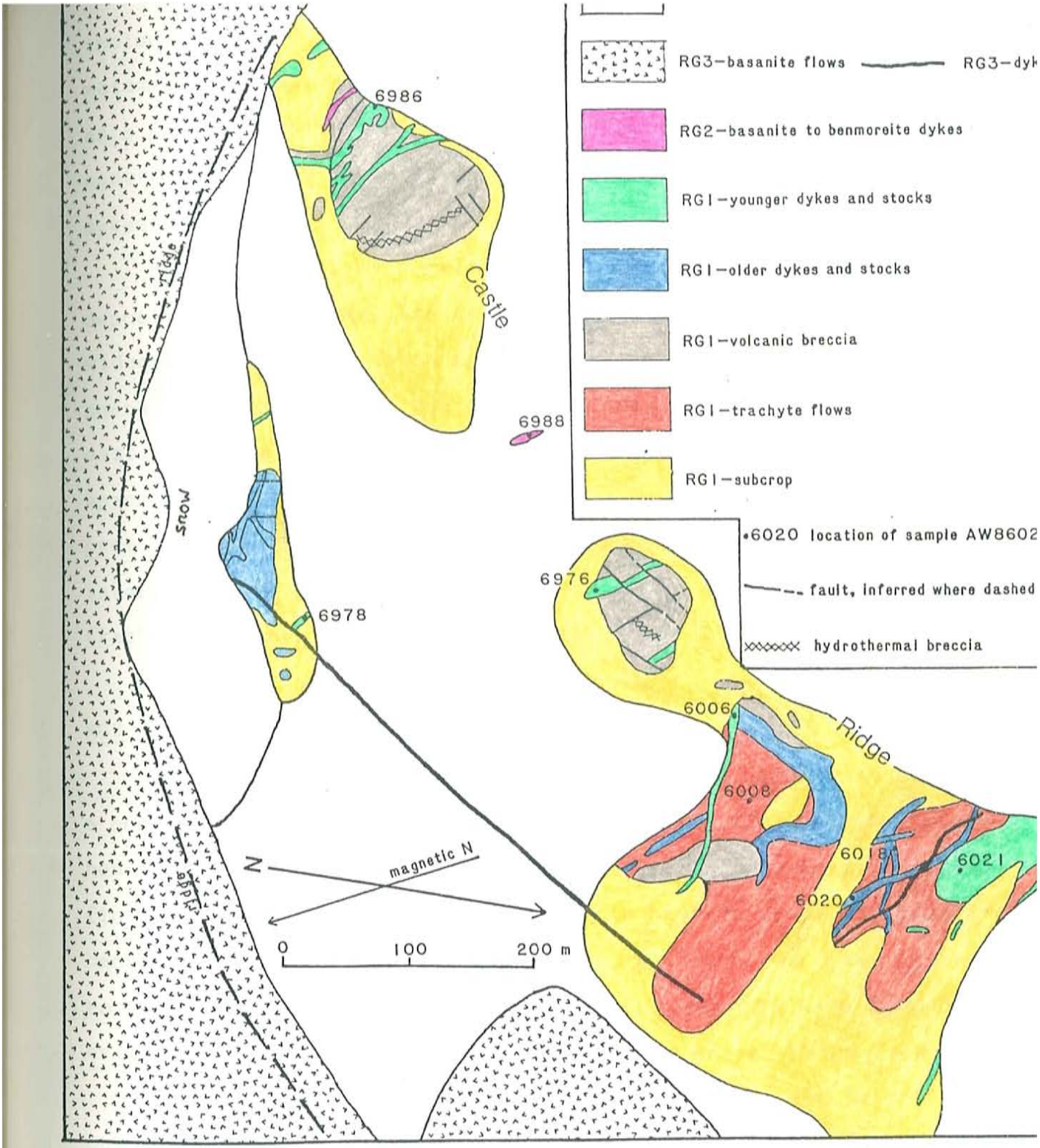

Figure 3.4 - Sketch map of the volcanic geology of Castle Ridge. The location of this area is shown on Figure 3.3.

including welded pyroclastic clasts, and a few accidental clasts of metamorphosed basement rocks (Figure 3.4). This breccia is interpreted as a possible cauldron-fill deposit. The sequence is intruded by numerous trachyte, peralkaline trachyte, and peralkaline rhyolite dykes and stocks.

At both locations numerous high-angle faults disrupt the volcanic deposits. Hydrothermal brecciation, alteration, and silicification is widespread. Dyke intrusion and faulting follow two main trends: one north to northwest, and the other approximately east-west to northeast. Dykes vary in width from 20 cm to 10 m and are irregularly spaced. Most are feldspar-phyric, but aphyric varieties are also present. A particularly dense dyke swarm at Gandalf Ridge has been interpreted as a high-level feeder system to a now eroded peralkaline trachyte volcano (Kyle and Muncy, 1978).

RG2

At Riviera Ridge a sequence of basanite to benmoreite lava flows a benmoreite dome and a phonolite dome overlie RG1. The lava flows are non-vesicular to weakly vesicular and occur in sequences of several flows (2 - 10 m thick) separated by thin breccia zones. No eruptive centers for these flows are identified, although two dykes belonging to RG2 are mapped (Figure 3.4). The domes appear to have formed by exogenous extrusion of lava which also feed short, thick flows.

RG2 is up to about 300 m thick. The lower contact is not seen in outcrop, but appears to have a subdued topography, and is marked by a overall change in rock type. RG2 outcrops have not been affected by the hydrothermal alteration that characterizes much of RG1.

RG3

RG3 comprises numerous young basanite and tephrite cinder and agglutinate cones, and associated tuff deposits and lava flows. The lava is vesicular to scoriaceous, except in the center of thick flows Individual vents comprise cones of cinder, bombs and agglutinate, with thin interbedded flows, that are 50 - 300 m high. Flows that extend beyond the cone usually spread out to form broad aa lava flows that may extend several kilometers from source. Two centers at Riviera Ridge have basal sequences of massive to bedded, palagonitized, lapilli and block tuff attributed to phreatomagmatic eruption. Dykes are exposed at several glacially eroded centers, including a spectacular radial dyke swarm at a cinder cone near the southern end of Riviera Ridge (Figure 3.3). RG3 dykes also intrude RG1 outcrops at Riviera Ridge (Figure 3.4).

3.2.3 Structural Geology

Structural trends in the GVC are difficult to correlate between the outcrops at Gandalf Ridge and Castle Ridge. At Gandalf Ridge two well developed trends are identified: a north-south zone of high angl faults, hydrothermal brecciation, and alteration, and an older northeast to east trending dyke swarm. The faults parallel faults associated with the high scarp of Royal Society Range, and suggest that Royal Society Range uplift was probably taking place at the same time as this early MVG volcanism (Muncy, 1979).

Trends are less well defined at Castle Ridge, perhaps because of the poorer control of the base map. Northnortheast trending faults offset younger GVC dykes, and have been intruded by two RG3 dykes (Figure 3.3). A northnorthwest to northwest trend is intruded by both

older and younger GVC dykes, a major zone of hydrothermal breccia ion, and a RG3 dyke.

3.3 MASON SPUR (MS)

3.3.1 Introduction

The 10 km long, southeast-facing scarp comprising Mason Spur rises as much as 1000 m above the Ross Ice Shelf and provides excellent, though not always accessible, exposures. These bluffs are attributed to a combination of marine and glacial erosion, and possibly tectonic downdropping. The area is largely ice-free. Colluvium, alluvium and moraine cover is significant, and facilitates access to adjoining outcrops.

Helms Bluff, located on the opposite side of Eady Glacier to Mason Spur, is included in the Mason Spur area, because of its similarity to the geology of Mason Spur.

3.3.2 Volcanic Geology

Two lithologically and stratigraphically distinct episodes of volcanism are identified at Mason Spur (Figures 3.5 to 3.9). The olde episode produced a mugearite - trachyte sequence (MS1 - MS5) of breccias, tuff deposits, flows and numerous stocks and dykes, overlain by a younger basanite - benmoreite sequence composed mostly of lava flow (MS7) . These units are collectively designated as the Mason volcanic complex (MVC). The younger episode included eruption of trachytes (MS8), including near vent pyroclastic deposits, a dome and flows, followed by basanite - tephrite cinder cones and lavas flows (MS9).

At Mason Spur the outcrop is cut by numerous faults on which the

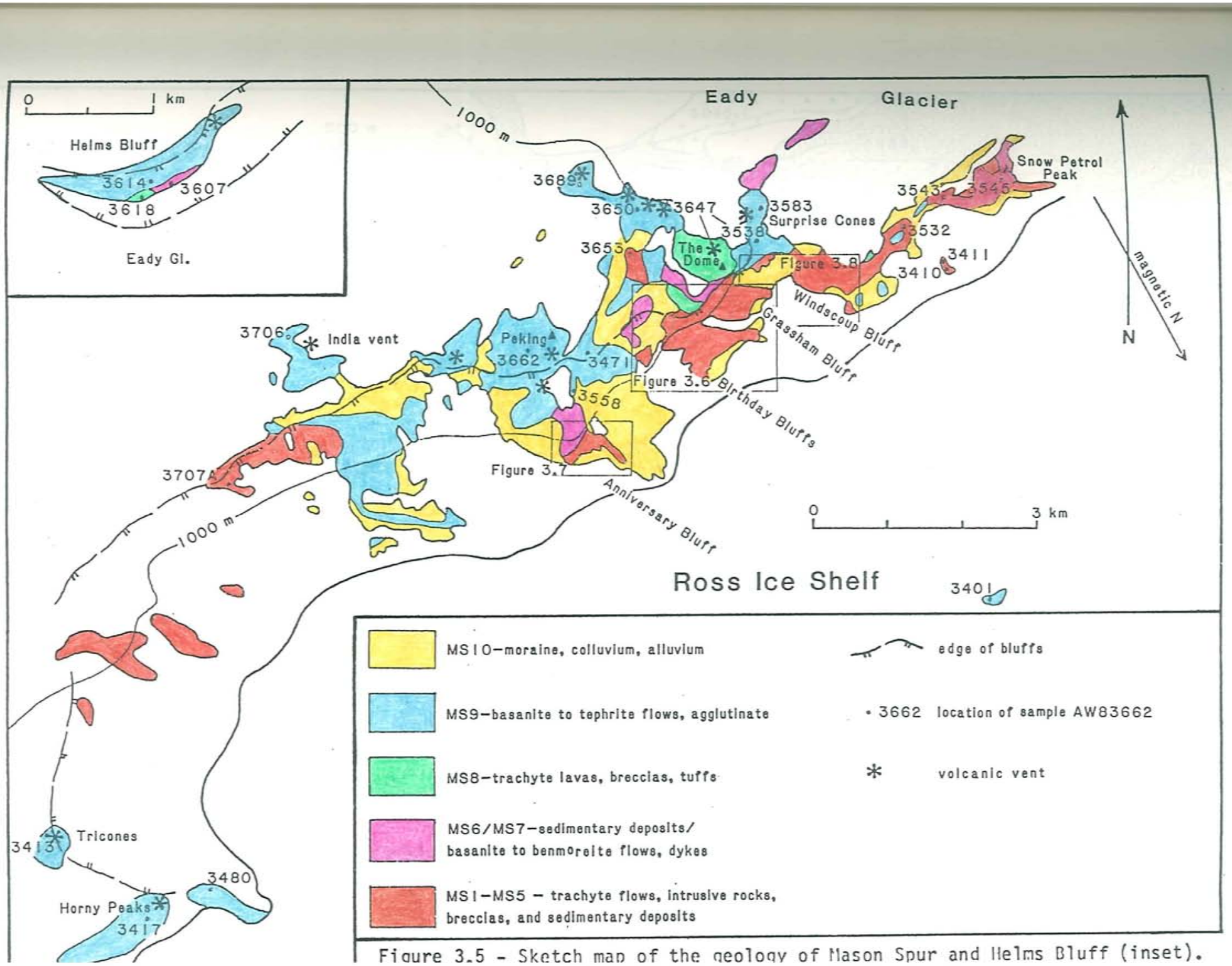

Figure 3.5 - Sketch map of the geology of Mason Spur and Helms Bluff (inset).

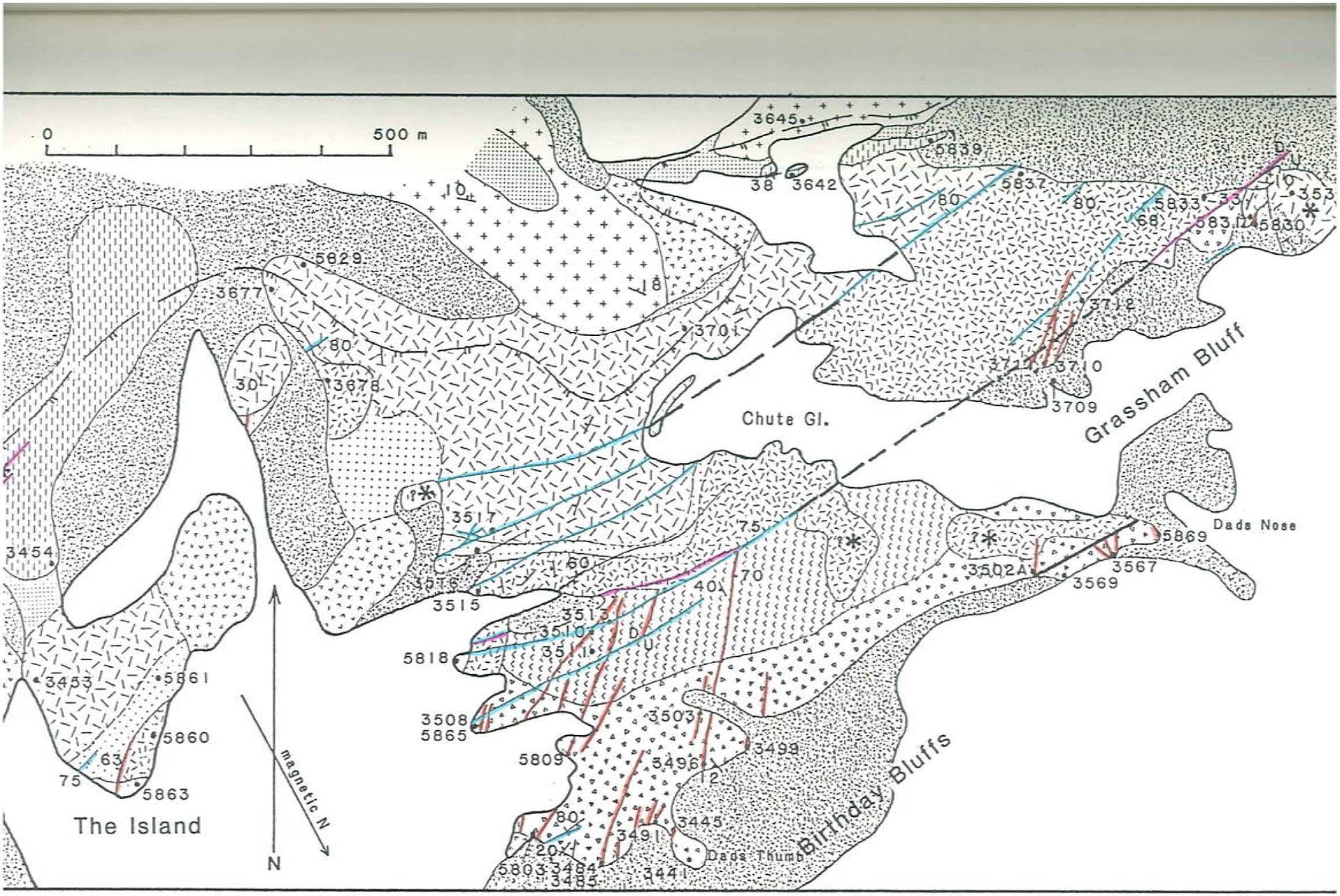
0
500 m
3645
5839
38
3642
5837
80
80
5833
33
68
5831
5830
353
10
D
U
5829
3677
80
30
3678
10
8
3701
3712
3711
3710
3709
Chute Gl.
Grassham Bluff
Dads Nose
5869
3567
3569
3502A
3517
75
60
3516
3515
40
70
3513
3510
3511
D
U
5818
3454
3453
5861
5860
63
75
5863
The Island
3508
5865
3503
3499
5809
3496
2
80
20
3445
3491
Dads Thumb
Birthday Bluffs
5803
3484
3485
3441
magnetic N
N

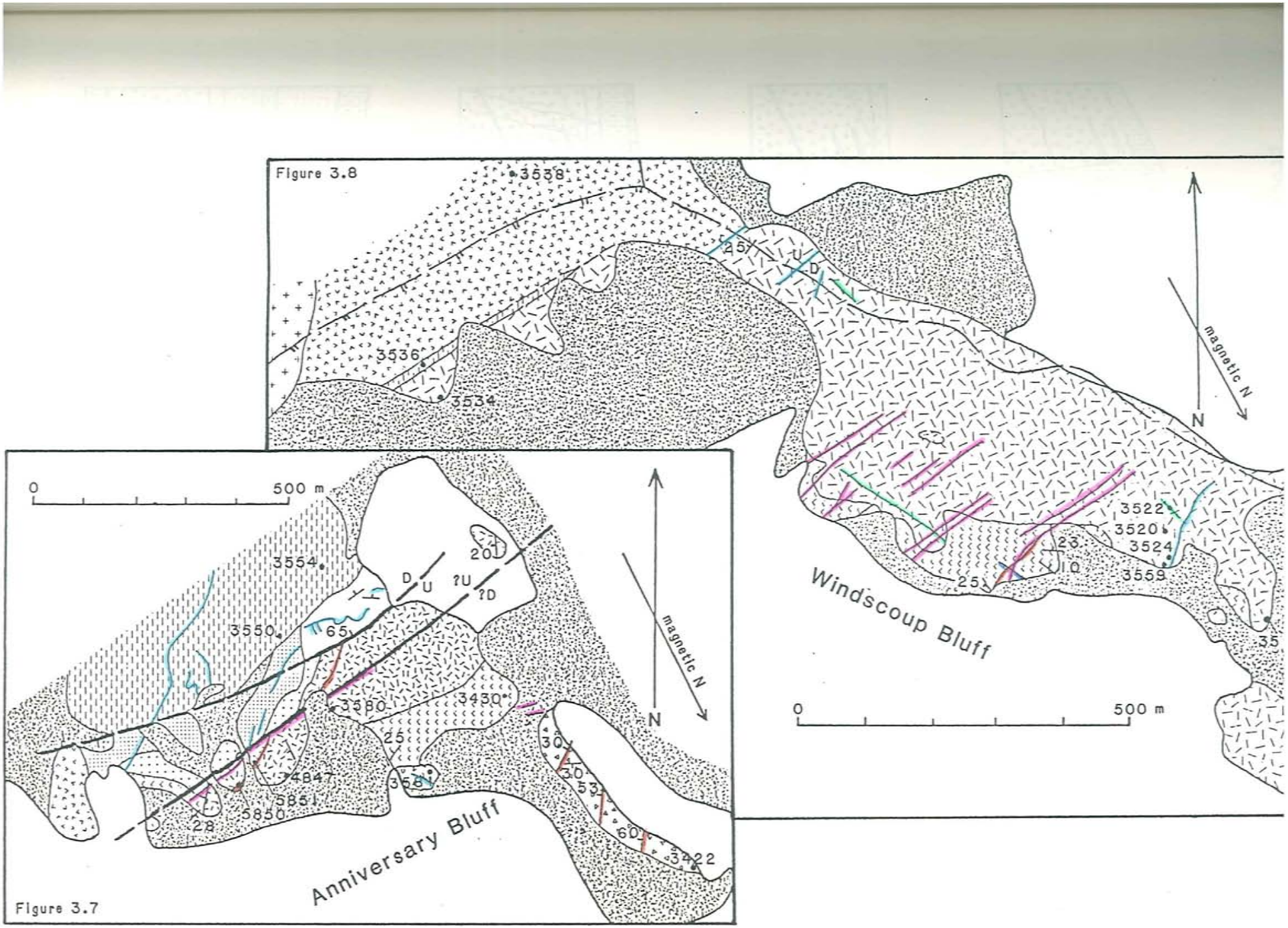
Figure 3.8
3538
3536
3534
25
U
D
magnetic N
N
S2
3522
3520
3524
3559
23
10
25
Windscoup Bluff
0
500 m
35
0
500 m
3554
20
D
U
?U
?D
65
3550
3580
3430
25
3585
4847
5851
5850
28
30
30
53
60
3422
magnetic N
N
Anniversary Bluff
Figure 3.7

progressive emplacement of units.

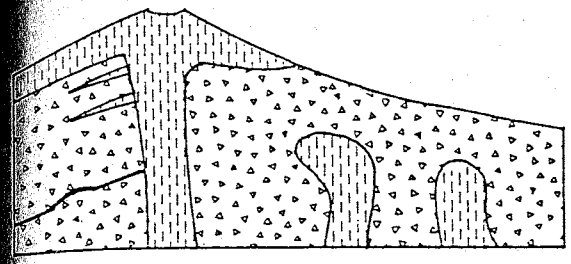

Eruption of peralkaline trachyte domes, flows, and volcanic breccias (MS1), with local unconformities.

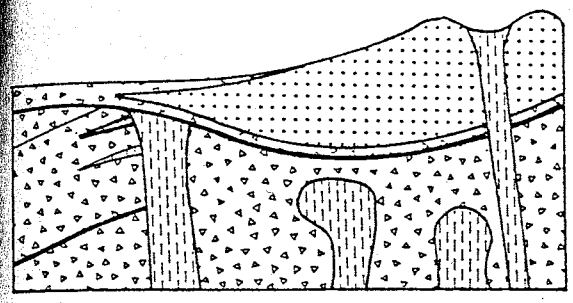

Deposition of diamictites (probably lahars) and eruption of mugearite and peralkaline trachyte tuff and agglutinate cones (MS2).

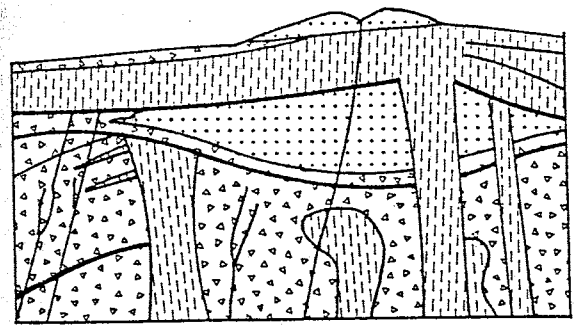

Eruption of thick peralkaline trachyte lava flows and minor interbedded breccias, tuffs, and agglutinate (MS3). Intrusion of a major north-northeast trending dyke swarm was emplaced during final MS3 activity.

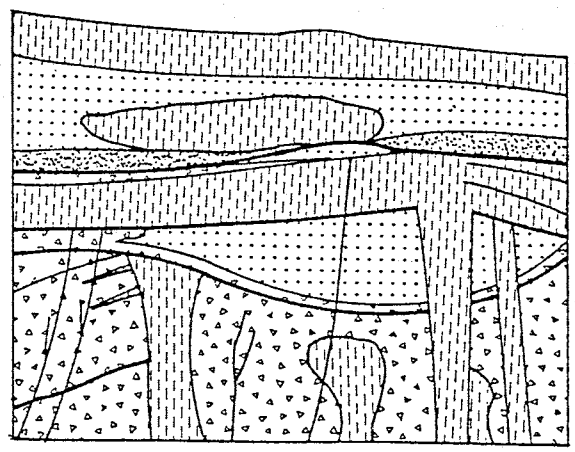

Deposition of sedimentary breccias (MS4), followed by eruption of thick trachyte and peralkaline trachyte lava flows, with interbedded bomb breccia and tuff (MS5). MS5 hyaloclastites occur locally.

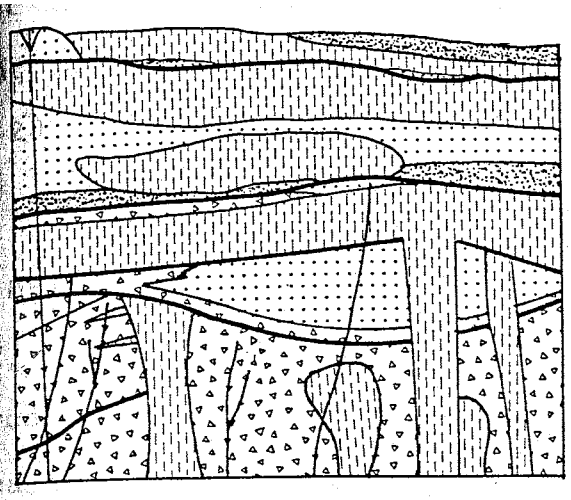

Deposition of sandstones, grits, and conglomerates (MS6) below and above thin basanite to benmorite flows (probably associated with shield volcanoes) and a tuff cone (MS7).

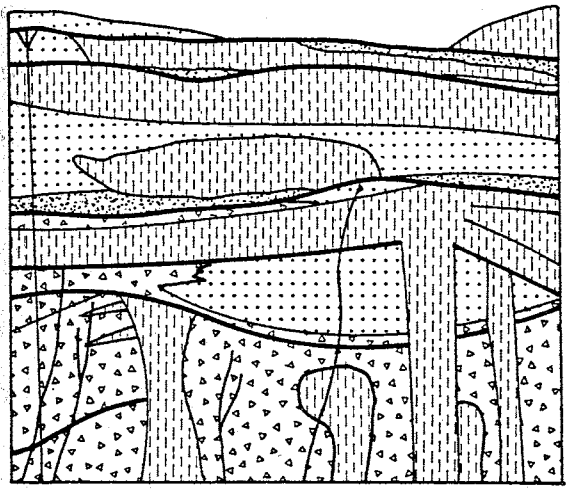

Eruption of trachyte tuff ring deposits, blocky lava flows, and a dome (MS8).

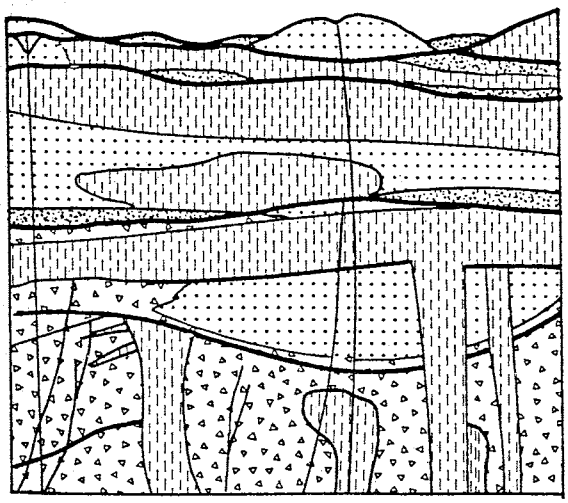

Eruption of basanite to tephrite cinder and agglutinate cones and thin lava flows, and emplacement of several dyk swarms (MS9).

Deposition of unconsolidated moraine, colluvium, and alluvium (MS10).

and direction of offset is measurable, the throws are less
20 m.

MS1 crops out at the base of Birthday Bluffs and Anniversary
ff, and is principally composed of massive volcanic breccias and
rcalated lava lobes and flows. The breccias are massive, unsorted
ically heterolithic, trachytic breccias which are clast and matrix
pported. Lithological variation is due mainly to differences in
enocryst content, vesicularity, and degree of crystallinity. Clasts
e usually 2 - 10 cm, but range up to 1 m in diameter. The less
mmon, clast supported breccias have subangular clasts in a grit and
iner matrix of lithologically similar fragments. With an increase in
e amount of matrix (up to 80 %), the matrix becomes finer, and
asts become increasingly rounded and smaller, commonly with altera-
ion rims. The principal cause of the variation in the nature and
mount of matrix is attributed to variable degrees of alteration.

These breccias grade laterally into brecciating lobes of trachyt
lava. At the southwestern end of Birthday Bluffs the breccias grade
upwards into a series of thin flow tongues and intercalated breccia,
which is overlain by a thick platy trachyte flow.

Because of the observed relationship between the breccias and adjacent brecciating lava lobes the principal origin of the breccias in this unit is inferred to have been dome and flow front collapse, probably associated with several overlapping domes. There may well be a lahar component that has gone unrecognized because of the considerable alteration that characterizes the breccias in this unit.

nced by discontinuous outcrops of colluvium, and small alluvial
bris flow and waterlain tuff deposits, which are exposed best along
e base of Birthday Bluffs.

The base of MS1 is not exposed. At Birthday Bluffs 200 m of this
it is exposed below an angular unconformity with MS2. This uncon-
mity is also exposed near the base of Grassham Bluff, but elsewhere
e upper contact of MS1 was not recognized in outcrop.

S2

MS2 is principally composed of near vent tuffs and agglomerates
f mugearite and trachyte composition erupted from vents at Windscoup
luff, Birthday Bluffs, The Island and Anniversary Bluff. It also
ncludes intercalated and more extensive diamictites which are inter-
preted as lahar deposits.

At Windscoup Bluff very altered, laminated and cross-laminated
uffs with antidune structures are overlain by massive bomb lapilli
uffs and agglutinate that dip away from a central feeder dyke.The
uff deposits are intensely altered by later dyke intrusion. A small
gglutinate outcrop of mugearite composition, at the base of Grassham
luff is correlated with the Windscoup Bluff vent.

A major peralkaline trachyte tuff and cinder cone vent, centered
in the vicinity of Dads Nose, deposited thinly bedded tuffs, welded
bomb lapilli tuff and agglutinate over a thin diamictite layer at
Birthday Bluffs.

Near vent airfall lapilli tuff deposits crop out at the base of
the Island, and conformably overlie a mugearite flow presumably
erupted from the same vent. The tuffs are conformably overlain by a

0-m-thick lahar.

At the western end of Anniversary Bluff thinly bedded, normally graded, airfall tuffs are interbedded with thin, laminated and cross-laminated tuff and lapilli beds with antidune structures which are attributed to deposition from base surge eruption associated with tuf ring formation. These are overlain by a massive, matrix-supported lapilli tuff, inferred to have formed as a tuff cone. Both the tuff cone and the older base surge deposits at Anniversary Bluff are intensely altered.

Massive, matrix-supported, hetrolithic conglomerates at Anniversary Bluff and Birthday Bluff are interpreted as lahars. These deposits are made up of irregular 5 - 10 m thick beds with reverse grading at the base. At Anniversary Bluff the lahars are interbedded with a 2.5-m- thick bed of well graded breccia tuff. Lahars underlie and overlie the tuff and cinder cone deposits at Birthday Bluffs, and hav been tectonically mixed with them prior to lithification and intrusio by the green dykes of MS3.

MS2 is truncated by an irregular unconformity which is well exposed at Anniversary Bluff and Windscoup Bluff. Where lower and upper contacts are exposed the unit varies in minimum apparent thickness between 120 m and 200 m.

MS3

Major outcrops of MS3 are exposed at Anniversary Bluff, Birthday Bluffs, and Grassham Bluff. The unit is made up of thick green, platy trachyte flows and intercalated diamictite and tuffs erupted from the vicinity of Dads Nose, and also from smaller parasitic pyroclastic

vents and domes in the vicinity of Birthday Bluffs and Grassham Bluffs. Two intrusive bodies of lava near Dads Nose may have fed the main MS3 vent, but these bodies were only viewed from a distance because of difficult access. At Windscoup Bluff windows expose trachyte lava flows and diamictite which are interpreted as belonging to MS3.

The two lowermost flows at Grassham Bluff are characterized by glassy lobes at their base, which are incursive into very altered, underlying diamictite. These features may represent pillows and hyaloclastite formed as lava encountered a thin layer of ice or water. Other flows in this unit have lower and upper autobrecciated, scoriaceous rubble layers, except where the flow top has been removed by erosion. An outcrop of massive, green, southwards-dipping trachyte lava exposed at the southwestern end of Birthday Bluffs is interpreted as a late stage parasitic dome.

Numerous green, platy trachyte dykes 0.5 - 8 m across cut through MS3 and older units, following a north-northeast trend. Several dykes exposed in Birthday Bluffs have brecciated centers and may have underlain pyroclastic vents, which have since been removed by erosion. At the southwestern end of Birthday Bluffs a broad, funnel-shaped, highly altered breccia outcrop parallels the dyke trend and is interpreted as a diatreme. A 100 m of thinly bedded lapilli tuff, bomb lapilli tuff, tuff with accretionary lapilli, and agglutinate, cut by local unconformities, near the top of the MS3 sequence at Grassham Bluff is evidence of a nearby pyroclastic peralkaline trachyte vent.

MS3 reaches a maximum thickness of 350 m at Grassham Bluff, and is truncated by an irregular unconformity. Weathering as deep as 1 m

thwestern end of Birthday Bluffs.

MS4 comprises bedded to massive trachytic breccias in matrix and last support, cropping out intermittently between Anniversary Bluff nd Windscoup Bluff. These deposits are interpreted as debris flow or ossibly glacial deposits, colluvium, and coarse fluviatile deposits. hey are truncated by an erosional surface, and vary in thickness fron to 50 m.

MS5 is made up of grey to green trachytic lava flows, small pyroclastic flows, tuffs and lapilli tuffs, and hyaloclastite, all of which are characterized by the presence of obsidian. The unit crops out from Anniversary Bluff to Windscoup Bluff, and was probably erupted from several vents. However, the feeder dykes at Windscoup Bluff are the only known vent locations (Figure 3.8).

Massive trachytic tuff containing obsidian bombs crops out at the base of MS5 at The Island and the southwest end of Birthday Bluffs. At Windscoup Bluff the basal deposit is a 10-m-thick, fiamme-bearing tuff. These deposits are interpreted as locally derived bomb tuff and a small pyroclastic flow, respectively. Deposits vary in thickness fr <1 to 50 m.

The pyroclastic deposits at Windscoup Bluff are overlain by a massive, matrix-rich, obsidian-bearing lapilli tuff containing lobes of trachytic lava, with spalling obsidian rinds. This deposit is interpreted as a trachytic hyaloclastite, which probably formed as th

ick trachyte dyke on the southwestern side of the bluff encountere
face ice or water.

The main component of MS5 is a series of medium to thick (30 -
00 m) trachytic lava flows separated by 1 - 50 m of thinly bedded
irfall tuffs and lapilli tuffs. The platy nature of these flows are
uggestive of both laminar and turbulent flow. A considerable thick-
ess of streaky, scoriaceous and glassy flow breccia is typical abov
nd below the platy central portion.

The tuffs are charcterized by obsidian clasts, and sometimes
ombs. Accretionary lapilli are also present in outcrops at Annivers-
ry and Birthday Bluffs. The tuffaceous matrix of the pyroclastic
ithologies in this unit are always very altered, probably because o
a high vitric component which was easily hydrated.

The overall thickness of MS5 varies from 150 m to almost 300 m.
The upper contact is an irregular unconformity commonly overlain by
sedimentary deposits of MS6.

MS6

MS6 crops out between Anniversary Bluff and Snow Petrol Peak. Th
unit comprises a wide variety of predominantly heterolithic, volcani-
clastic, sandstones, conglomerates, breccias, and diamictites, which
were deposited in a predominantly fluviatile environment. Minor depos
its in this unit include colluvium and diamictites. No specific evi-
dence of glacial deposition was observed.

This unit overlies an irregular unconformity on older rocks. It
underlies, interfingers with, and overlies MS7.

MS7

MS7 crops out between Anniversary Bluff and Snow Petrol Peak. It also forms the lowermost outcrop at Helms Bluff. Flows are usually non-vesicular to weakly vesicular, and aphyric or microporphyritic, basanites to benmoreites. Thickness varies between 2 m and 20 m. A few lavas are porphyritic, and these typically form the thicker flows. MS7 deposits are derived from several vents, which appear to have been fed by narrow, northeast trending dykes. The vents were usually subaerial and appear to have produced mainly lava flows. However, the vent cropping out above The Island includes pillow lavas and bedded surge and airfall deposits overlain by 100 m of massive matrix rich tuff, and probably formed when rising magma encountered surface water or ice.

At several localities the basal lava flows appear to have been emplaced over saturated sediments of MS6, and there is little doubt that MS7 was being erupted into an active sedimentary, predominantly fluviatile, environment. At Helms Bluff MS7 flows are truncated by a striated glacial unconformity, but this may be much younger than the MS7 volcanism.

MS8

MS8 crops out in the area above Birthday Bluffs and Grassham Bluff. The unit includes trachytic tuff ring deposits, with excellent exposures of base surge and airfall components, and an overlying sequence of blocky trachyte flows. A small trachyte intrusion at the southwest end of Birthday Bluff may be the feeder dyke for these deposits. A well preserved, exogenous, trachyte dome overlies the blocky flows. The small outcrop of trachyte lava at Helms Bluff is

comprising The Dome and is included in MS8.

MS8 varies in thickness up to 200 m.

MS9

MS9 comprises numerous basanitic vents throughout the area. Except for the subglacial, prograding hyaloclastite deposit at Helms Bluff, vents are subaerial and are characterized by agglutinate and cinder cones from 2 to 300 m high. Several cones may be associated with an eruptive center, for instance, the many overlapping vents at the Peking center. Another example is the many cones erupted along th fissure extending northwest from Surprise Cones. Thin lava flows may be interbedded with agglutinate within the cone, but larger flows hav typically flowed well beyond their source. In several cases these flows drape over the present-day scarp of Mason Spur and must post-dated formation of the bluffs.

Although the most recent MS9 deposits from the Surprise Cones fissure appear very young, sufficient time must have elapsed for the development of significant cirque erosion at Surprise Cones.

MS10

All unconsolidated sedimentary deposits are grouped into MS10. They are predominantly colluvium and alluvium associated with the Mason Spur scarp, and a thin blanket of moraine and colluvium coverin parts of the ridge.

Three main fault trends are seen at Mason Spur:

A north to northnortheast trend, extensively intruded by MS3 dykes, and later by dykes associated with the Peking center (MS9).

A northwest trend, intruded by the large MS5 feeder dykes at Windscoup Bluff, and later by the Surprise Cones fissure eruption (MS9).

A northeast trend followed by MS7 and MS9 dykes.

Evidence indicating the amount or direction of throw on the northeast trending faults is rare. No evidence of the direction or amount of movement on other fault sets was observed. In every case where a down/up determination could be made on northeast-trending faults from evidence seen in outcrop, the vertical displacement was relatively small (<20 m), and the downthrown side lay to the northwest. This is contrary to both local and regional topographic indications of probable downdropping to the southeast. Perhaps major faults are downthrown to the southeast, but the nature of the outcrop at Mason Spur is such that reference planes are less well exposed when offset is in this direction.

3.4 MINNA BLUFF (MB)

3.4.1 Introduction

The 50 km long peninsula of Minna Bluff has a ridge crest of 800 - 1000 m, and reaches a maximum elevation of 1060 m (Figure 3.10). It is composed of volcanic rocks, overlain by patchy and superficial moraine and colluvium. Although the area is largely ice-free, much of the volcanic geology is obscured by the moraine, which is attributed

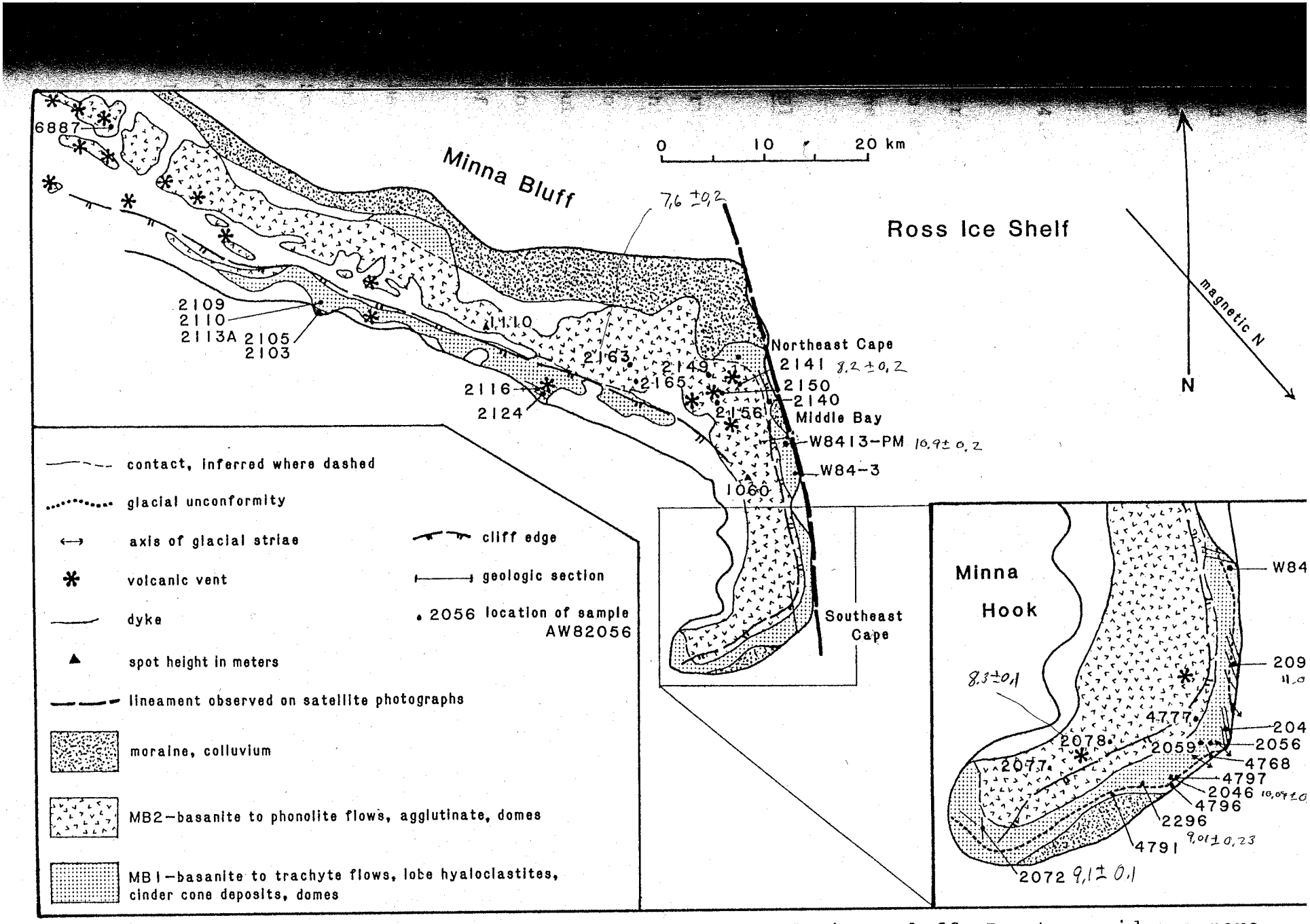

Figure 3.10 - Sketch map of the volcanic geology of Minna Bluff. Inset provides a more detailed enlargement of the Minna Hook area.

both local and Ross Ice Sheet glaciation (Stuiver et al., 1981). hundred to eight hundred meter high cliffs face southwest, sou east and were probably formed by combined tectonic downdropping glacial and marine erosion. The cliffs provide excellent geolog cal exposures, but access is usually difficult.

4.2 Volcanic Geology

Volcanic rocks at Minna Bluff are divided into two informal stratigraphic units (Figure 3.10) on the basis of lithology. There no evidence to suggest that a significant time break occurred betwee the eruption of these units.

MB1

The lower unit comprises a basanite to trachyte sequence that w erupted under subaerial, then subaqueous, then subaerial conditions. This unit is petrologically consistent despite variation in volcanic form due to a changing eruptive environment. Outcrops of the earlier subaerial deposits are limited to the base of the section along the south and east sides of Minna Hook, and include eroded domes and flo of phonotephrite to trachyte composition.

The overlying subaqueous flows and lobe hyaloclastites are of basanite to tephriphonolite composition and are associated with a widespread, striated, glacial unconformity (Figure 3.10 and 3.11). Sedimentary deposits associated with the unconformity include palagonitic, fluviatile sediments, debris flow deposits, and lenses of diamictite containing faceted clasts which are interpreted as tillit Local unconformities occur within the sedimentary horizons and separ-

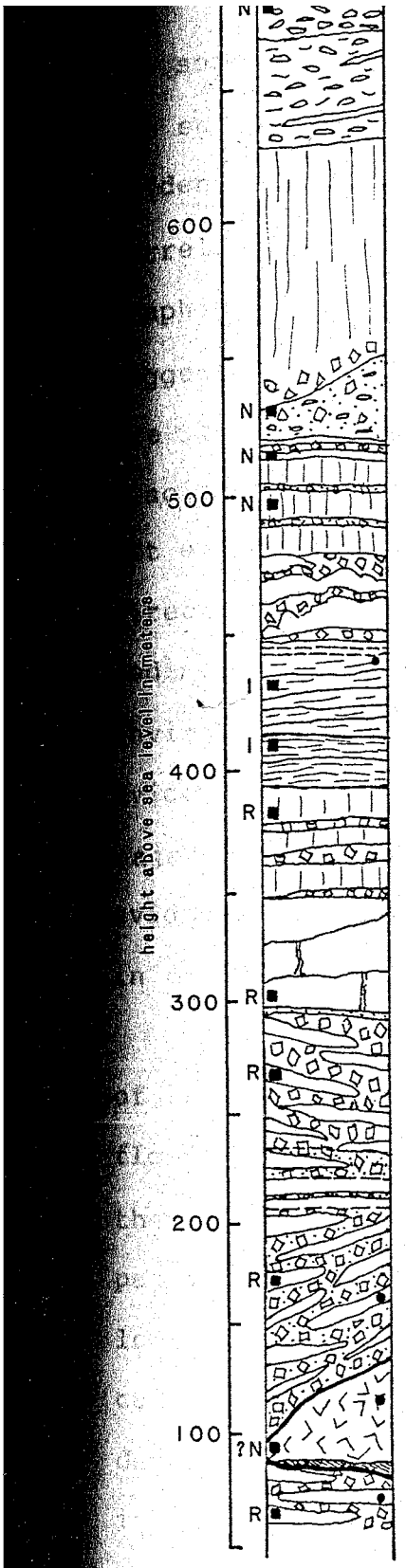

highly welded oxidized basanite cinder and bomb agglutinate

densely welded basanite agglutinate and thin intercalated flow

thick columnar jointed basanite flow

densely welded, partially oxidized basanite agglutinate

partially palogonitized poorly welded crystal-lithic tuff with occasional bombs

massive basanite flows and glassy flow breccia

massive to collumnar jointed basanite flows and oxidized flow breccia

glassy, lobate basanite flows separated by hyaloclasite

greenish-grey pahoehoe tephriphonolite flows and glassy to scoriaceous flow breccia (sample AW84777)

platy phonolite flows and yellow oxidized flow breccia

massive, collumnar-jointed basanite flows separated by oxidize flow breccia

glassy, pahoehoe basanite flows have common explosion pipes an lack a basal breccia

thin lahar overlain by strombolian airfall breccia and coarse laminated tuff

pahoehoe basanite flow tongues separated by scoriaceous brecci

pahoehoe basanite flow tongues separated by hyaloclasite

crudely bedded basanite hyaloclastite

pahoehoe basanite flows separated by hyaloclastite (sample AW82059)

massive to blocky, non-vesicular, benmorite dome or thick flow (sample AW82056)

undulating glacial unconformity overlain by bedded and cross-bedded palagonitized grits, sandstone and sedimentary breccia

phonotephrite flow tongues and scoriaceous oxidized breccia (sample AW84768)

Figure 3.11 - Measured geologic section at Southeast Cape. The location of samples fo geochemical analysis (•) and paleomagnetic determinations (■) are indicated. Norma reverse (R) and indeterminate (I) paleomagnetic determinations were made by W. McInt below the glacial unconformity strata are subhorizontal. Above the glacial unconformi strata strike 050 - 070 and dip 5^{0} - 25^{0} S.

some of the volcanic deposits. An unconformity near the base of section at Middle Bay (Figure 3.12) does not exhibit specific idence of glacial erosion (W.C. McIntosh, pers. comm.), but is rrelated with the glacial unconformity further south on strati-aphic grounds. Topography on the glacial unconformity is subdued, ggesting that the glaciation was either associated with a past Ros ce Shelf or with a local ice cap, and did not result from valley laciation. Glacial striae were observed at only three places, so ar not sufficient for a statistically significant analysis of ice flow direction. However, the striae do suggest a northwest flow axis. The sedimentary deposits are characteristic of a proglacial, fluvial environment (R. Powell, pers. comm.). Volcanic and sedimentological evidence suggests that the eruptive environment was adjacent to a major, subaerial, fluctuating ice front. However, the sedimentologica evidence is also consistent with a shallow marine environment just in front of an ice tongue (R. Powell, pers. comm.).

The subaqeous sequence grades upwards into a thick unit composed of discrete lava flow packages, each formed of many 1 - 5 m thick flows. The interfingering nature of these packages is well exposed in the southwest-facing cliffs and at Southeast Cape (Figure 3.11). Each package records successive outpourings from discrete vents, which are located along the length of Minna Bluff. The vents comprise cones composed of interbedded cinder, agglutinate, thin flows and minor tuf deposits. They supplied lavas of basanite to tephriphonolite composition. Interbedded benmoreite and trachyte lavas form flows up to 80 thick along the east-facing cliffs of Minna Hook.

Transition to MB2 is defined on the first appearance of phonolite, as opposed to benmoreite and trachyte lavas. For the most

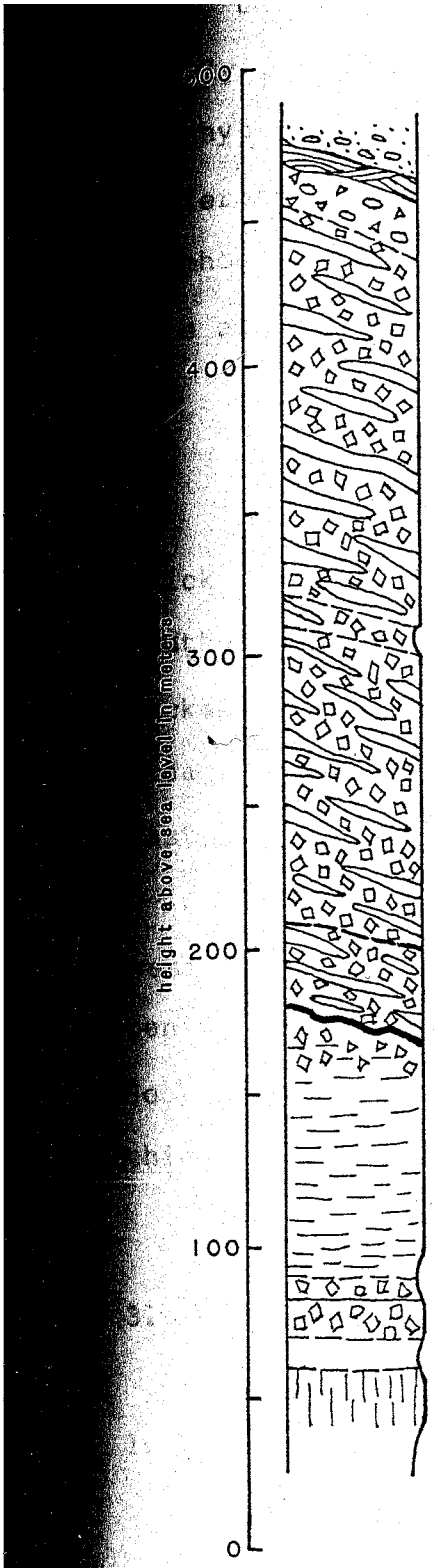

hydrothermally altered pyroclastic fall breccia

surge and airfall tuffs containing bombs and cinder

flow tongues separated by fine grained palagonitized and oxidized flow breccias

poorly exposed breccias and subordinate flow tongues

flow tongues and partially palagonitized flow breccia

? unconformity

flow tongues and partially palgonitized flow breccias

irregular erosion surface

thick platy trachyte flow and associated, weathered upper fl breccia

platy, autobrecciated green trachyte

angular autobrecciated black trachyte

vertically platy black trachyte (sample W8413-PM)

Figure 3.12 - Measured geologic section at Middle Bay, Minna Bluff. Observations and interpretations are those of W. McIntosh. The irregular erosion surface is correlated the glacial unconformity in Figures 3.10 and 3.11 on stratigraphic grounds, although evidence of glacial erosion of the unconformity at Middle Bay was not observed. The section below this unconformity is subhorizontal, whereas that above dips 020/25^{o} E.

weakly porphyritic or aphyric, green to glassy black benmoreites and trachytes can be recognized in the field. There is no lithological difference in lavas less evolved than tehriphonolite, so all basanite to phonotephrite rocks stratigraphically below the influx of phonolite are placed in MB1.

MB2

MB2 phonolites crop out as numerous small domes and associated thick flows in the north-south trending part of Minna Hook, whereas a Southeast Cape and along the southern cliffs they are preserved as a package of thin to medium thick flows (Figure 3.11). The main source area for the phonolites is the area between Northeast Cape and South east Cape.

Younger basanite to phonotephrite lavas were erupted from north west - southeast trending fissures along the northern half of the peninsula, and from two basanite centers at the southern end of Minna Hook. Deposits comprise cinder and agglutinate cones, and thin to thick lava flows.

3.4.3 Structural Geology

The main structural trends at Minna Bluff are:

1. A northwest-trending set of faults and associated dykes and fissures aligned along the main part of the peninsula. The rise of magma along these faults has not only controlled the location of individual vents, but is the most important factor controlling the location and shape of Minna Bluff, and suggests that this fault se

A north to northnorthwest dyke swarm exposed in the east-facing cliffs of Minna Hook which are associated with a MB2 basanite center in that vicinity.

3.5 MT DISCOVERY (MD)

3.5.1 Introduction

Mt Discovery is an undissected, symmetrical stratovolcano, about 25 km across at the base, that rises from below sea level to 2681 m. Shallow lower slopes on the mountain steepen above 1100 m to form the 30° slopes of the summit cone.

Mt Discovery is mostly ice-free, except for the southern slopes, which are completely ice covered. Glacial erosion has affected all deposits, with more severe glacial scouring and extensive moraine cover being ubiquitous below about 400 m elevation. Incipient cirque erosion on the northwestern and eastern flanks of the summit cone has steeped upper slopes to expose an earlier portion of the stratigraphic sequence. A small summit ice-cap, which probably infills a crater, spawns spectacular ice mushrooms. However, there are no ice towers, and no evidence of magma-ice interaction on Mt Discovery.

3.5.2 Volcanic Geology

The geology of Mt Discovery is divided into two units. MD1 comprises the lava flows and associated deposits that form the stratovolcano, whereas MD2 includes lavas from the many small local centers which postdate the formation of the stratovolcano (Figures 3.13, 3.14 and 3.15).

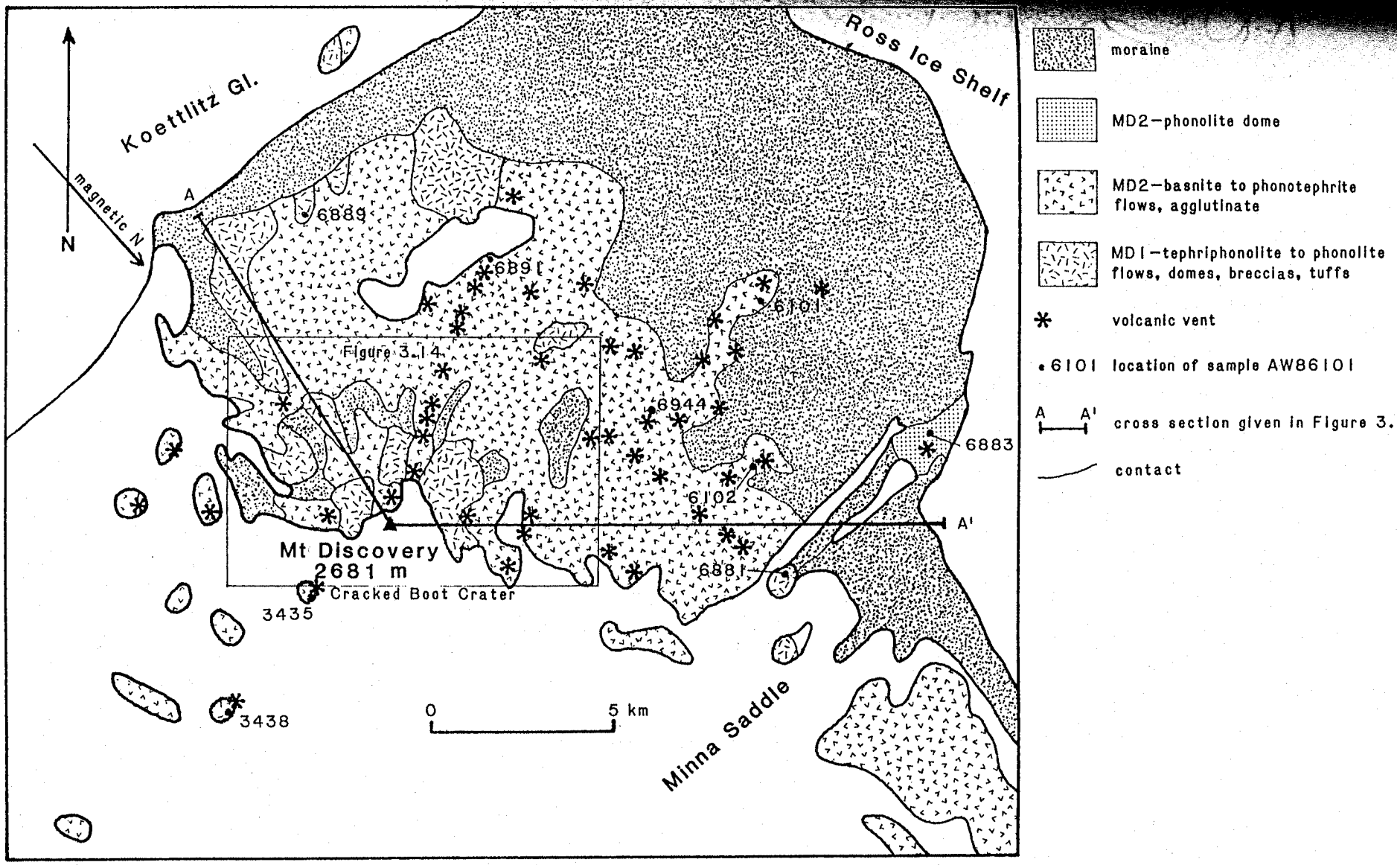

Figure 3.13 - Sketch map of the volcanic geology of Mt Discovery. A more detailed map of the geology of the upper slopes is given in Figure 3.14. Cross-section A-A' is given in Figure 3.15.

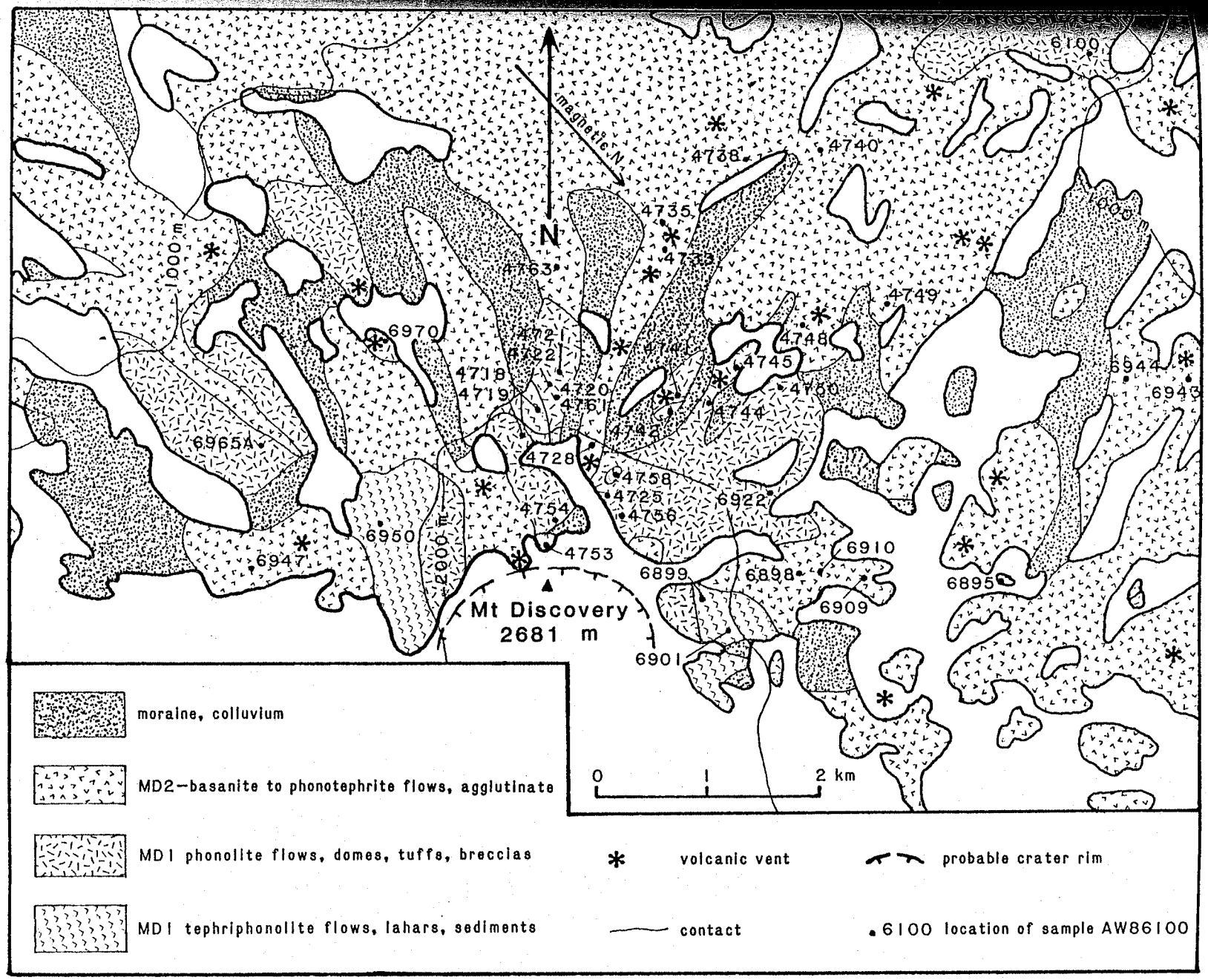

Figure 2.14 Sketch map of the volcanic geology of the upper slopes of Mt Discovery. The

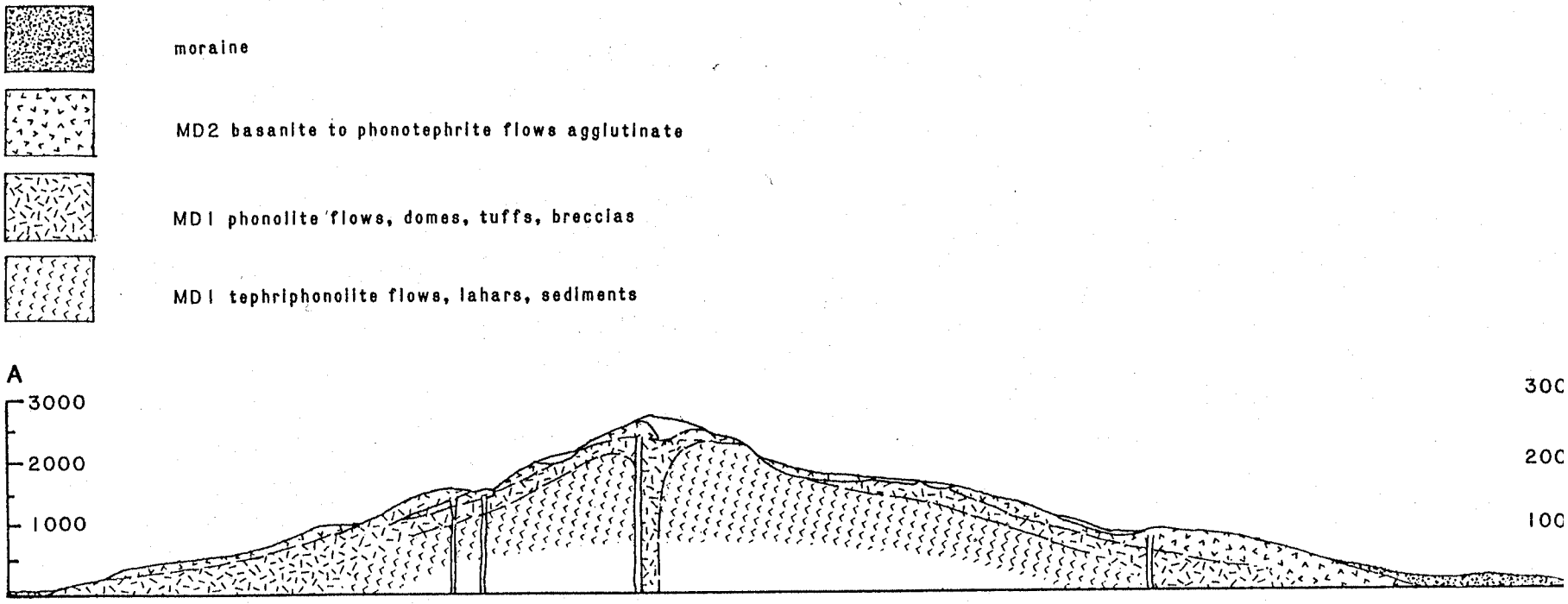

Figure 3.15 - Natural scale cross-section through Mt Discovery. The location of the cross-section is given in Figure 3.13. Vertical scale in meters.

MD1

The earliest exposed deposits form a core of steeply dipping (30° - 35°), plagioclase-phyric tephriphonolite flows (2 - 10 m thick) and a similar volume of interbedded lahar and volcaniclastic fluviatile sediment. This is capped by a series of phonolite flows (20 - 100 m thick) with occasional interbedded laharic lenses, which are conformable on the phonotephrite deposits. The phonolite flows were erupted both from a summit vent and also from small domes on the northern side of the mountain. They were extensive as evidenced by many exposures at lower elevations, especially on the northern side of the mountain. The uppermost 100 - 200 m of the phonolite sequence, is exposed on the northern side of the summit cone. It includes two thin (4 - 8 m thick) welded to densely welded units near the base, overlain by a poorly exposed unwelded pumice lapilli tuff.

MD2

After the phonolite volcanism ceased basanite to phonotephrite lavas began erupting from numerous small vents. In most cases the location of vents appears to have been controlled by a northnortheast trending fissure system running across Mt Discovery. Vent location is independent of altitude. A possible northwest alignment of vents is also seen on the eastern side of the mountain. MD2 vents are characterized by cones of cinder, bomb, agglutinate and thin flows that reach 50 - 300 m in height. Many are eroded to expose feeder dykes. Larger flows extend beyond the vent area and typically range in thickness from 3 to 10 m. They may extend for several kilometers from their source. A small, exogenous phonolite dome northeast from Minna Saddle is also included in MD2.

3.5.3 Structural Geology

The most obvious structure of the Mt Discovery area is the northeast alignment of MD2 cinder cones. These lineaments probably reflect underlying crustal structure. Despite the symmetrical shape of Mt Discovery radial structures were not observed.

3.6 BROWN PENINSULA, BLACK ISLAND AND WHITE ISLAND

3.6.1 Introduction

The volcanic complexes of Black Island and White Island protrude through Ross Ice Shelf and reach elevations of 1041 m and 762 m respectively (Figure 3.16). Brown Peninsula (816 m) is a similar volcanic complex which is connected to Mt Discovery by a low moraine covered saddle. White Island is largely shrouded by snow and ice, but Black Island and Brown Peninsula are essentially ice-free. However, much of the volcanic geology is obscured by moraine and talus.

The Brown Peninsula - Black Island - White Island area was not visited by this author. The following summary is taken from Cole and Ewart (1968), Cole et al. (1971) and Kyle et al. (1979). In the first two publications authors employed a simplified system of lithologic description. Outcrops were described as basaltic or trachytic. Analyse of these rocks indicate that the "basalts" are mostly basanites to phonotephrites, and the "trachytes" are tephriphonolites or phonolites. However, samples from outcrops on the northwestern part of Black Island include an alkali basalt.

3.6.2 Volcanic Geology

Brown Peninsula (BP)

Brown Peninsula consists of a series of coalescing north-south

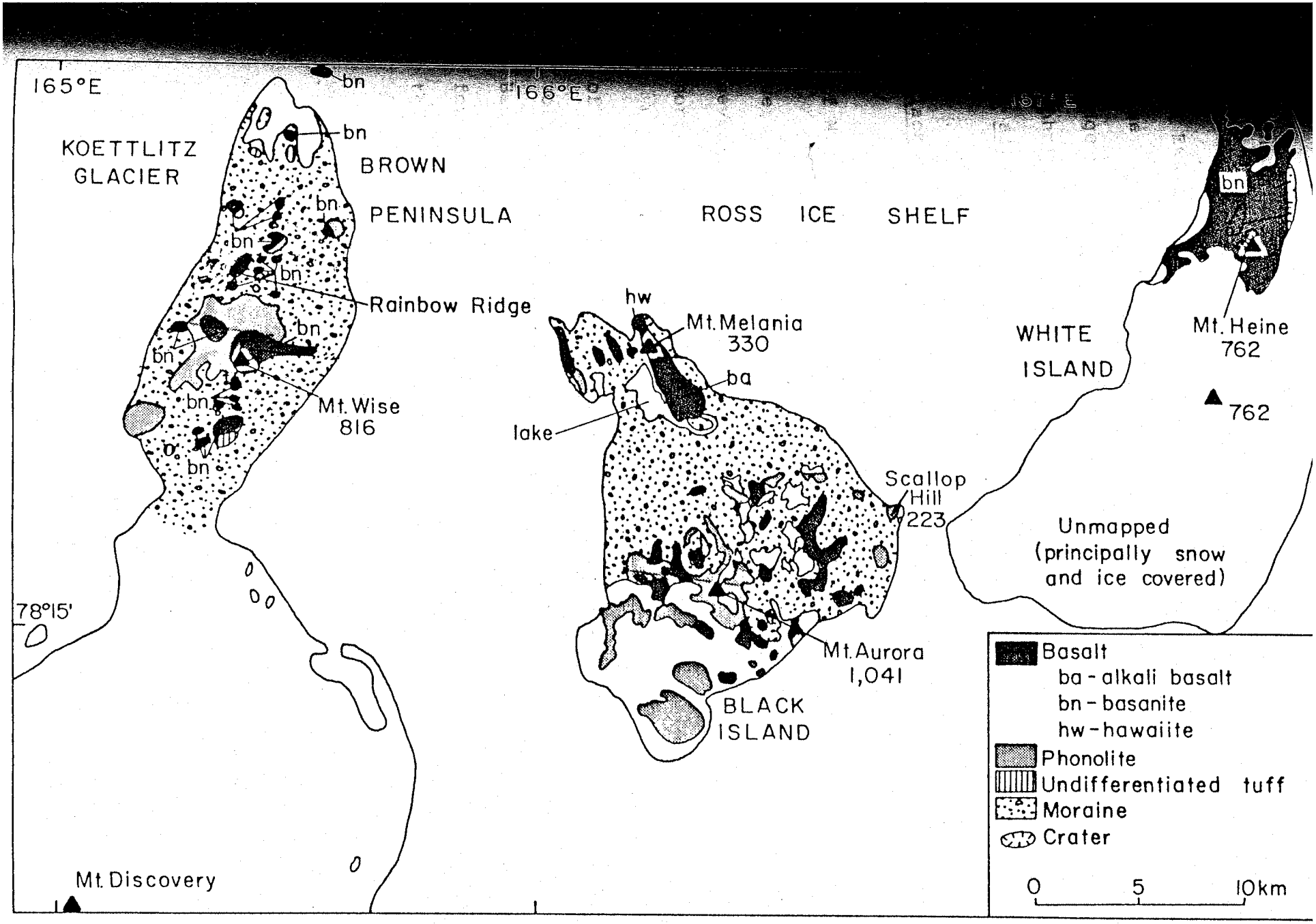

Figure 3.16 - Volcanic geology of Brown Peninsula, Black Island, and White Island (from Wright and Kyle, in press), compiled from data by Kyle et al. (1979), Cole and Ewart

aligned, basaltic to silicic volcanic centers (Kyle et al., 1979), most of which have been considerably modified by glacial erosion (Cole and Ewart, 1968). The youngest vents are located in the vicinity of Mt Wise and have not been significantly glaciated. Exposures at Rainbow Ridge provide a continuous stratigraphic sequence from basanite to tephriphonolite, which has been used for petrogenetic studies by Kyle et al. (1979).

Black Island (BI)

BI1 comprises alkali basalts and phonotephrites in the vicinity of Mt Melania on the northwest corner of Black Island. These deposits were erupted from a series of coalescing domes, which have been severely modified by glacial erosion. Outcrop patterns suggest a northwest alignment of vents (Cole and Ewart, 1968).

The younger deposits of BI2 comprise a relatively major sequence of "trachytic" flows, plugs and domes that form a large "trachyte" volcano (Aurora Trachyte Formation), isolated scoria cones (Nubian Basalt Formation), and a later phase of "trachyte" volcanism which formed small flows and two "trachyte" domes in the southern part of the island (Cole and Ewart, 1968).

White Island (WI)

Only the northern, relatively ice free portion of White Island has been geologically mapped (Cole et al., 1971). It comprises two overlapping "basalt" shields, surmounted by younger "basalt" cones.

6.3 Structural Geology

The predominant structural trend at Brown Peninsula and White Island is a northnortheast alignment of vents. On Black Island outcrop patterns in the Melania Basalt Formation suggest that BI1 vents were aligned along a northwest trend (Cole and Ewart, 1968). Vents in the Nubian Basalt Formation are described as having a crude westnorthwest alignment, but this is not evident from the map, which suggests a possible northnortheast alignment. The youngest trachyte domes at the southern end of Black Island are aligned on a northnortheast trend.

3.7 MT MORNING (MM)

3.7.1 Introduction

Mt Morning is a 2723-m-high, undissected shield volcano, 20 - 35 km across at its base, with average slopes of about 10°. The southern slopes are predominantly snow and ice covered, whereas the northern flanks provide good, but largely superficial exposures. There is a 2 km diameter, ice-filled, summit crater.

3.7.2 Volcanic Geology

The volcanic geology of Mt Morning is divided into two units (Figure 3.17). MM1 comprises the lava flows and associated minor deposits that form the main shield volcano, whereas MM2 includes later lavas erupted from many small local centers. There is no evidence for a significant time break separating the MM1 and MM2 deposition.

MM1

The earlier period of activity produced thick kaersutite-bearing phonotephrite to phonolite flows, which were erupted both from the

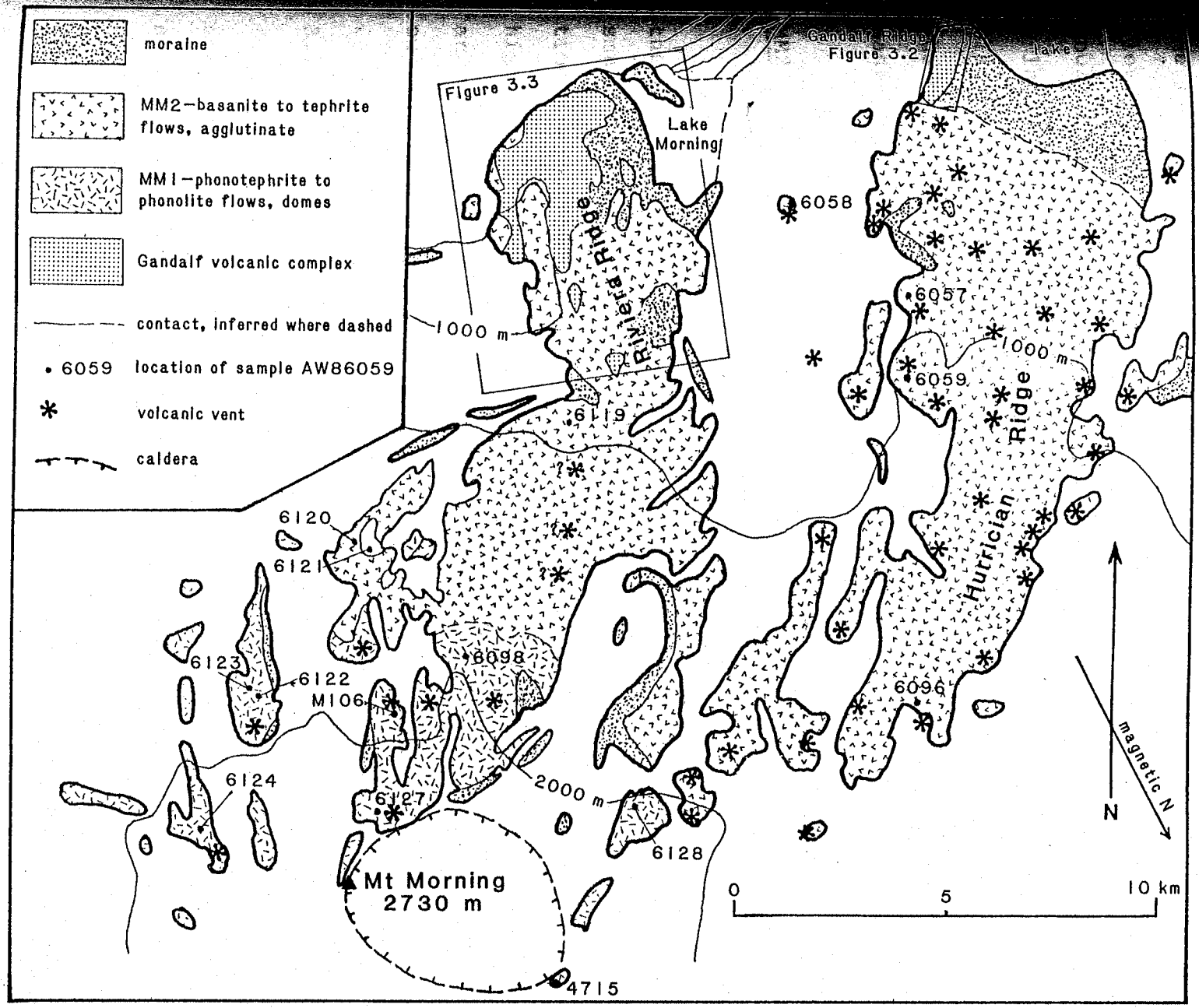

Figure 3.17 - Sketch map of the volcanic geology of Mt Morning. Location of Riviera Ridge (Figure 3.3) and Gandalf Ridge (Figure 3.2) is indicated.

summit area and from parasitic domes at between 2000 - 2600 m elevation on the northern side of the mountain (Figure 3.17). Because of the lack of associated tuffaceous deposits, eruption of the phonolite flows is inferred to have been a relatively quiet extrusive process. Boulders of a phonolite breccia in moraine (AW86129) are probably from a lahar, although lahars were not observed in outcrop. Unlike Mt Discovery, plagioclase-rich tephriphonolites were not found, although there is a single report of a "plagioclase-phyric hawaiite" from the eastern slopes of Mt Morning (P. Kyle, pers. comm.).

MM2

The second episode of volcanic activity at Mt Morning comprises the eruption of porphyritic basanite and tephrite lavas from numerous small vents. Individual vents comprise cones of cinder, bombs, agglutinate, and thin interbedded flows. Cones are typically 50 - 300 m high. Flows that have extended beyond the cone are rarely channelled and spread out to form broad aa lava flows 2 - 10 m thick, that may extend for up to 5 km from source.

3.7.3 Structural Geology

No radial structures were identified at Mt Morning. MM2 vents are concentrated along two north to northnortheast trending ridges on the northeast side of the mountain. This alignment of vents, especially on Hurricane Ridge, parallels similar alignments on Mt Discovery, and suggests that the rise of basanite and tephrite magma is controlled by a regional pattern of crustal fractures.

3.8 SOUTHERN FOOTHILLS OF ROYAL SOCIETY RANGE (F)

3.8.1 Introduction

The Southern Foothills of Royal Society Range (henceforth referred to as the Foothills area) comprise a mountainous area of pre-Ordovician basement rocks (Findlay et al., 1984) rising from sea level to 3000 m. The area is located immediately east of the prominent 1500 - 2000 m scarp of Royal Society Range (Figure 3.18), and is characterized by valley glaciers, which have fluctuated in height and extent during the period of Pliocene to Quaternary basanite volcanism. Glaciation has modified both the nature and form of certain volcanic deposits, and caused the erosion of others (Wright, 1980).

3.8.2 Volcanic Geology

Most of the over 50 vents within the Foothills area (Figure 3.18) were erupted subaerially and range in size from tiny scoria mounds to larger cones of intercalated scoria, agglutinate, bombs, and lava flows, that may reach as high as 300 m. The greatest concentration of vents is found in the Dromedary Platform - Roaring Valley area, where lavas crop out over an area of approximately 15 km^2 (Figure 3.19). Larger structures are commonly intruded by dykes, and in some cases there is evidence of a central plug (e.g., Foster Crater). However, many of these outcrops have been glacially eroded, and have commonly lost most, if not all, of the agglutinate and scoria deposits originally associated with them.

Lava flows within cinder cones are thin (30 cm - 1 m thick) whereas those that extend beyond the cone are typically 3 - 10 m thick. The vast majority of such flows are less than 4 km long and none would exceed 10 km in length. Due in part to the confining

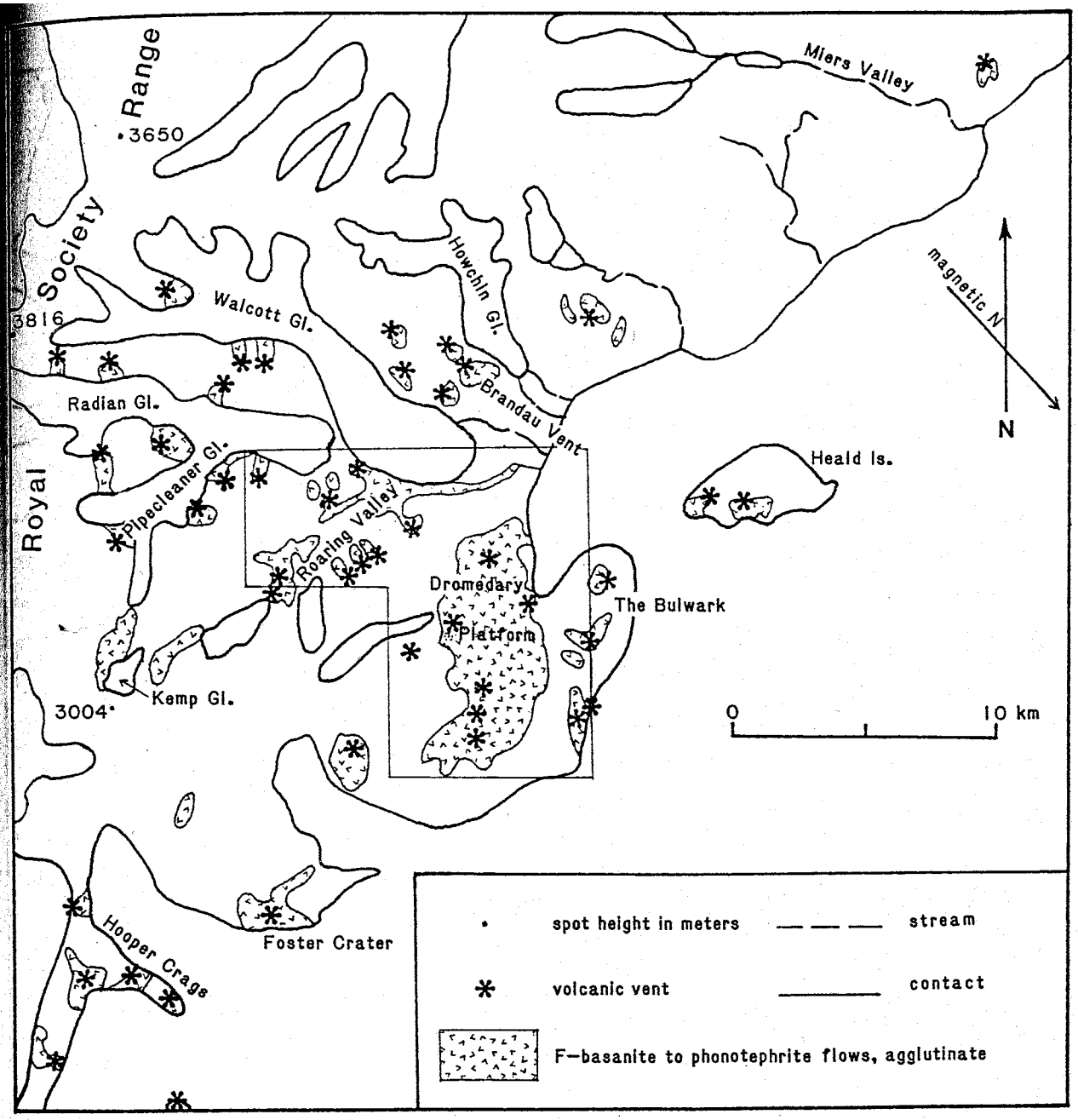

Figure 3.18 - Sketch map of the volcanic geology of the southern Foothills of Royal Society Range (after Wright, 1980). A more detaile enlargement of the Dromedary Platform - Roaring Valley area (outlined is given in Figure 3.19.

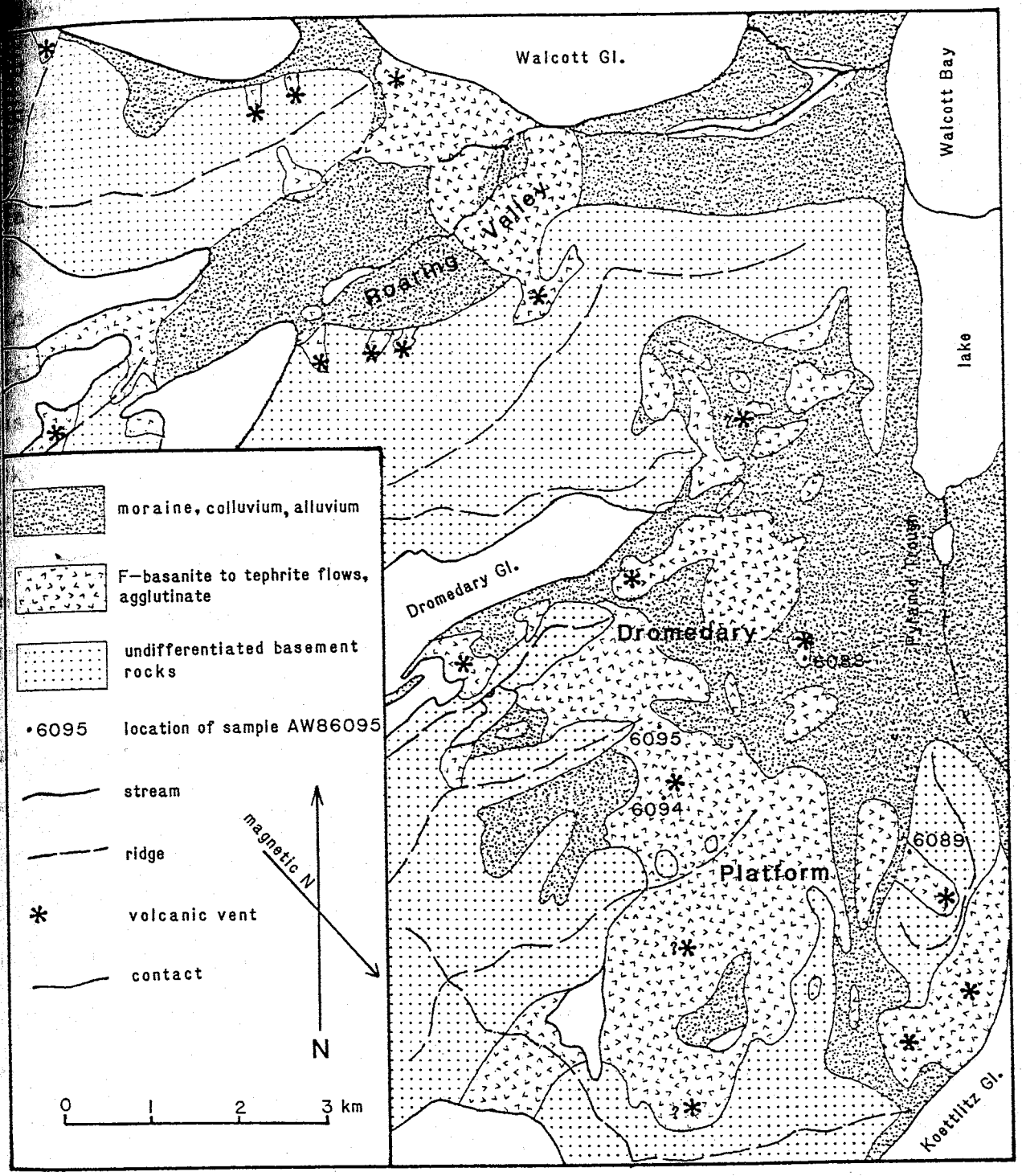

Figure 3.19 - Sketch map of the volcanic geology of the Dromedary Platform - Roaring Valley area, southern Foothills of Royal Society Range. The location of this area is shown in Figure 3.18.

effects of both topography and glacial damming, successive flows in the stream gully east of Walcott Glacier tongue expose a 30-m-thick sequence of at least five separate flows (Blank et al., 1963).

Subaqueous (presumably subglacial) eruption has produced hyaloclastites at vents in the Koettlitz Glacier neve (Figure 3.18) (Skinner et al., 1976) and at a small outcrop (AW86088) on the west side of Pyramid Trough (Figure 3.19). Minor pillow lava occurrences are associated with a flow from the Foster Crater vent, a vent to the east of Pipecleaner Glacier, and vents in the Hooper Crags area (Skinner et al., 1976). At The Bulwark there are excellent exposures of lava flows that flowed onto saturated phreatomagmatic deposits resulting in pillowed and incursive features (W. McIntosh, pers. comm.).

Reports of a kenyte flow (Blank et al., 1963), later reclassified as trachybasalt (Goldich et al., 1975) and Ne-hawaiite (Kyle, 1976), near the mouth of Miers Valley could not be substantiated. However, a diamictite containing trachytic-textured, plagioclase-phyric phonotephrite boulders was observed at approximately the same location. This lithology is unlike any known from the Foothills area, but is similar to lavas cropping out on Mounts Discovery and Erebus.

3.8.3 Structural Geology

A northeast alignment of vents is seen along the south wall of Roaring Valley and along the northern side of the Koettlitz Glacier, and a kilometer-long dyke on Heald Island follows a similar trend. A second north-south trend is seen locally, for instance, between the Pyramid and The Bulwark.

The northeast trend parallels an en echelon swarm of lamprophyre dykes that extend throughout the area, but which are particularly common in the vicinity of Walcott Glacier. This suggests that magmas in the Foothills area have mostly risen along old crustal fractures. The north-south trend is probably controlled by the fault zone associated with the Royal Society Range front.

Chapter 4

GEOCHRONOLOGY

4.1 INTRODUCTION

Prior to this study, geochronological data for the DVS was patchy, and did not provide adequate control of the stratigraphic sequences mapped at Mt Discovery, Minna Bluff, Riviera Ridge and Mason Spur. Further age dating was undertaken in order to place time constraints on the stratigraphy of these areas, and to allow correlation of the volcanic sequences between areas. Both aspects are crucial to the interpretation of the volcanic history of the DVS.

Conventional K-Ar ages were determined for 22 whole rock samples and one feldspar separate (Table 4.1). These samples are representative of the stratigraphic sequences at Mt Discovery and Minna Bluff, and the uppermost portions of the Gandalf and Mason volcanic complexes. K-Ar dating techniques are inappropriate for rocks from the lower part of the Mason volcanic complex, because alteration in parts of this sequence suggests that samples may not have remained closed with respect to Ar. Incremental $^{40}Ar/^{39}Ar$ determinations were made on three samples from the lower portion of the Mason volcanic complex (Table 4.2; Figure 4.1).

Analytical work for the K/Ar determinations was carried out under the supervision of K. Foland at the Department of Geology and Mineralogy, Ohio State University, Columbus; and F. McDowell of the Department of Geoscience, University of Texas at Austin. Samples were ground to between 180 and 250 microns (sieve size: 60 to 80 mesh). K was analysed by flame photometry using predigested samples. Ar determinations were made using isotope dilution methods. Details of sample

Table 4.1 - New K-Ar age determinations on whole rock and feldspar separate samples from the DVS. Two samples had minor, but significant groundmass alteration. These samples are indicated by an asterisk following the sample number, and the associated date is considered to be a minimum age only. Analyses were made at Ohio State University (O) and the University of Texas (T).

Sample (Unit)	Lab.	K (wt %)	Ave K (wt %)	40Ar* (mol/gx10^{-11})	40Ar* (%)	Age (Ma)	Ave Age (Ma)	Error (Ma)
Riviera Ridge and Gandalf Ridge								
AW86072 (RG2)	T	1.815 1.799	1.807 ± 0.011	2.670 2.684	65 66	13.9 14.2	14.1	± 0.3
AW86042 (RG2)	T	4.203 4.252	4.228 ± 0.035	4.859 4.807	71 74	13.2 13.0	13.1	± 0.3
AW86025 (RG2)	T	2.349 2.348	2.349 ± 0.001	2.670 2.684	51 52	13.0 13.1	13.0	± 0.3
Mason Spur								
AW83513 (MS7)	T	2.537 2.571	2.554 ± 0.024	2.706 2.688	60 67	12.1 12.0	12.1	± 0.2
AW85839 (MS7)	T	2.694 2.671	2.683 ± 0.016	2.813 2.684	72 68	12.0 11.5	11.7	± 0.4
AW83653* (MS7)	T	4.086 4.079	4.083 ± 0.005	4.063 4.066	74 73	11.4 11.4	11.4	± 0.2
AW83647 (MS8)	T	4.056 4.084	4.070 ± 0.020	2.245 2.109 2.174	77 72	6.33 5.95	6.13	± 0.20
AW83614 (MS9)	T	0.764 0.773	0.768 ± 0.006	0.296 0.285 0.324	14 16	4.42 4.26	4.51	± 0.31
Minna Bluff								
AW82097B Feldspar (MB1)	T	0.338		0.322 0.325	9 9	10.9 11.0	11.0	± 1.1
W8413-PM (MB1)	T	4.571 4.522	4.547 ± 0.035	4.372 4.272	70 73	11.0 10.8	10.9	± 0.2

Table 4.1 (continued)

Sample (Unit)	Lab.	K (wt %)	Ave K (wt %)	40Ar* (mol/gx10-11)	40Ar* (%)	Age (Ma)	Ave Age (Ma)	Error (Ma)
AW82097B* (MB1)	O	2.843 2.857 2.762 2.628	2.772 ± 0.105	4.866 4.657 4.729 4.583 4.602	66.98 61.75 65.97 69.70 67.93	10.09 9.662 9.811 9.508 9.549	9.73	± 0.46
AW82046 (MB1)	O	1.817 1.800	1.78 ± 0.025	3.118 3.097	41.33 40.72	10.10 10.03	10.04	± 0.20
AW82296 (MB1)	O	1.750 1.740 1.756 1.700 1.705 1.716	1.728 ± 0.024	2.744 2.673	28.13 26.97	9.134 8.899	9.01	± 0.23
AW82072 (MB1)	O	3.675 3.594 3.621 3.669	3.640 ± 0.039	5.750 5.711	67.37 74.77	9.086 9.025	9.06	± 0.12
AW82078 (MB2)	O	3.822 3.189 3.846	3.829 ± 0.007	5.537 5.568	85.07 80.03	8.319 8.366	8.34	± 0.10
AW82141 (MB2)	O	3.141 3.451	3.472 ± 0.029	4.850 5.096	32.88 50.72	8.038 8.445	8.25	± 0.18
AW82163 (MB2)	O	1.420 1.418 1.386 1.452 1.450 1.362 1.407	1.414 ± 0.033	1.774 1.793	49.02 39.46	7.221 7.298	7.26	± 0.22
Mt Discovery								
AW86950 (MD1)	T	2.965 3.029	2.997 ± 0.045	1.455 1.398	67 64	5.57 5.35	5.46	± 0.16
AW86970 (MD1)	T	3.572 3.532	3.552 ± 0.028	1.697 1.616	64 62	5.48 5.22	5.35	± 0.19

ble 4.1 (continued)

mple Unit)	Lab.	K (wt %)	Ave K (wt %)	40Ar* (mol/gx10^{-11})	40Ar* (%)	Age (Ma)	Ave Age (Ma)	Error (Ma)
W84720 (MD1)	T	4.223 4.257	4.240 ± 0.024	1.995 1.953	68 67	5.40 5.29	5.34	± 0.11
W86899 (MD1)	T	2.731 2.752	2.742 ± 0.015	1.278 1.246	62 64	5.33 5.21	5.27	± 0.10
W84753 (MD2)	T	1.827 1.835	1.831 ± 0.006	0.847 0.771 0.866	44 48	5.31 4.83	5.19	± 0.32
W86944 (MD2)	T	1.226 1.188 1.195	1.203 ± 0.020	0.480 0.436 0.485	21 28	4.58 4.16	4.45	± 0.26
W86883 (MD2)	T	3.985 3.992	3.989 ± 0.005	0.799 0.504 0.641	40 32	2.30 1.45	1.87	± 0.43

constants used: ^{40}K = 1.167 x 10^{-2} atom % of K
beta decay constant = 4.963 x 10^{-10}/y
K_e decay constant = 0.581 x 10^{-10}/y

Table 4.2 - Incremental $^{40}Ar/^{39}Ar$ determinations for three whole rock samples from the lower part of the Mason volcanic complex. Ages are given in Ma. Analyses were made by D.Lux at the University of Maine at Orono.

TEMP °C	40Ar/ 39Ar	37Ar/ 39Ar	36Ar/ 39Ar	MOLES 39Ar	39Ar %TOTAL	%40Ar RAD	K/Ca	APPARENT AGE Ma
AW83712							J = .005831	
800	4.02	0.0343	0.0092	94.8	12.9	31.6	14.2937	13.29 +/- 0.32
830	2.03	0.0197	0.0026	103.6	14.1	60.7	24.8475	12.91 +/- 0.34
840	1.67	0.0152	0.0015	67.9	9.3	71.2	32.3258	12.47 +/- 0.46
870	1.55	0.0135	0.0006	39.0	5.3	85.3	36.3768	13.88 +/- 0.23
910	1.76	0.0176	0.0017	41.4	5.6	69.5	27.9199	12.79 +/- 0.34
990	1.80	0.0382	0.0020	108.8	14.8	65.1	12.8336	12.29 +/- 0.38
1050	2.55	0.1056	0.0045	180.1	24.5	46.7	4.6398	12.49 +/- 0.29
fuse	3.97	0.0618	0.0084	98.4	13.4	36.5	7.9228	15.19 +/- 0.27
TOTAL				734.0	100.0			13.07
PLATEAU AGE (forced)								12.52 +/- 0.57

TEMP °C	40Ar/ 39Ar	37Ar/ 39Ar	36Ar/ 39Ar	MOLES 39Ar	39Ar %TOTAL	%40Ar RAD	K/Ca	APPARENT AGE Ma
AW83678							J = .005836	
800	2.95	0.0595	0.0056	63.7	7.1	42.9	8.2322	13.27 +/- 0.62
830	1.47	0.0390	0.0009	89.0	9.9	78.7	12.5737	12.14 +/- 0.50
840	1.18	0.0315	0.0001	115.4	12.9	94.7	15.5355	11.72 +/- 0.13
870	1.13	0.0287	0.0001	116.9	13.0	96.4	17.0669	11.46 +/- 0.12
900	1.13	0.0295	0.0001	162.3	18.1	96.4	16.6352	11.44 +/- 0.12
980	1.14	0.0393	0.0001	178.7	19.9	95.5	12.4551	11.47 +/- 0.18
1050	1.22	0.2734	0.0002	109.3	12.2	95.0	1.7919	12.12 +/- 0.16
FUSE	2.24	0.9663	0.0011	61.2	6.8	86.7	0.5067	20.31 +/- 0.28
TOTAL				896.6	100.0			12.37
PLATEAU AGE								11.46 +/- 0.09

TEMP °C	40Ar/ 39Ar	37Ar/ 39Ar	36Ar/ 39Ar	MOLES 39Ar	39Ar %TOTAL	%40Ar RAD	K/Ca	APPARENT AGE Ma
AW83569							J = .005718	
800	13.10	0.1757	0.0401	31.5	4.0	9.4	2.7890	12.63 +/- 0.61
850	2.60	0.0415	0.0045	216.1	27.5	47.4	11.8097	12.66 +/- 0.25
930	1.73	0.0154	0.0015	259.0	33.0	72.4	31.7765	12.87 +/- 0.16
975	1.80	0.0217	0.0017	109.7	14.0	70.3	22.5907	13.03 +/- 0.25
1010	1.98	0.0663	0.0019	55.2	7.0	69.3	7.3903	14.13 +/- 1.28
1050	1.98	0.0918	0.0017	61.0	7.8	72.6	5.3362	14.79 +/- 1.02
FUSE	2.63	0.0710	0.0022	52.3	6.7	74.2	6.8972	20.01 +/- 0.34
TOTAL				784.9	100.0			13.54
PLATEAU AGE								12.80 +/- 0.44

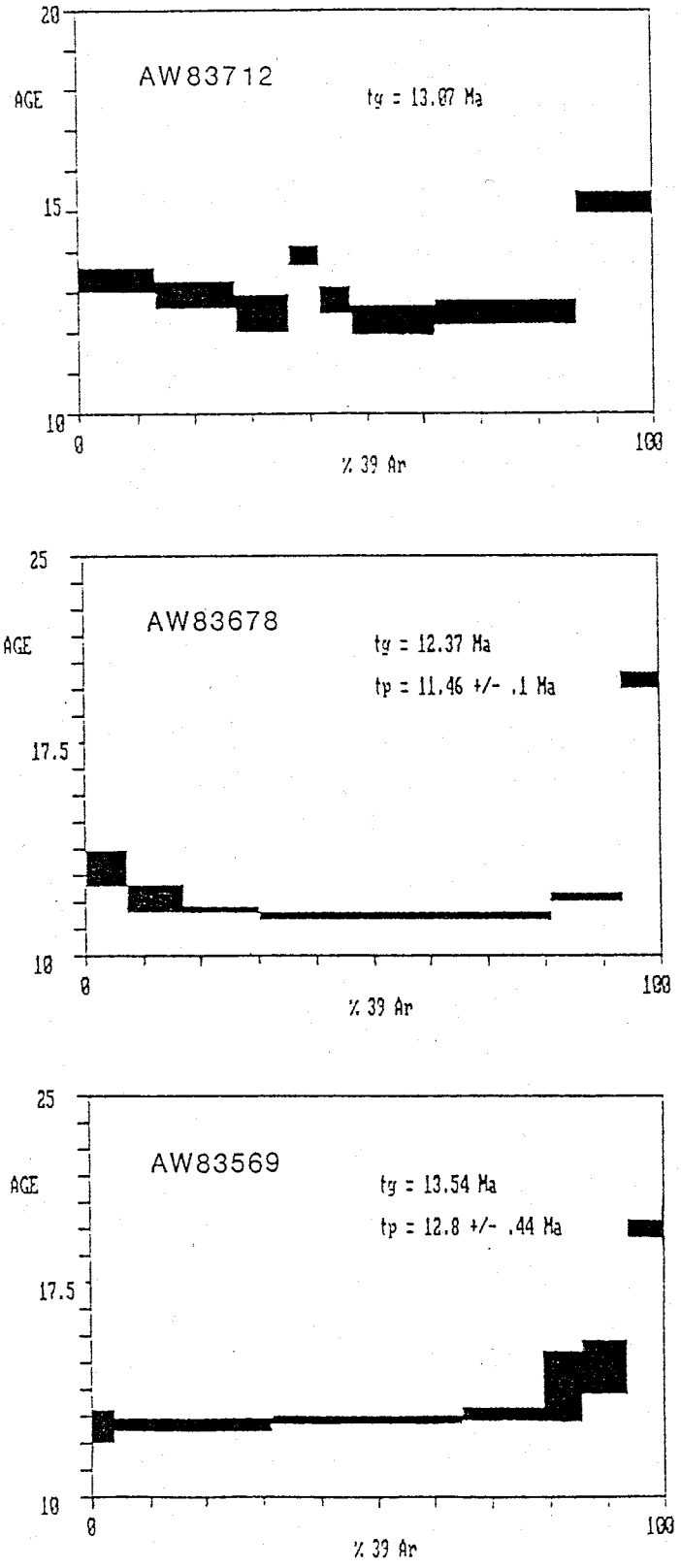

Figure 4.1 - Disturbed $^{40}Ar/^{39}Ar$ age spectra for samples from the lower part of the Mason volcanic complex. tg = total gas age, tp = plateau age.

paration, and analytical procedures are given in Appendix 2. Although the freshest available samples were chosen for K-Ar dating, W82097B and AW83653 contain minor secondary mineralization. Determinations on these samples are interpreted as minimum ages. Dating of feldspar separate from AW82097B indicates that the rock may be as much as 2 m.y. older than the whole rock minimum age determination.

Incremental $^{40}Ar/^{39}Ar$ determinations were made by D. Lux at the University of Maine at Orono.

4.2 RESULTS

The following assumptions are inherent to the determination and interpretation of these and previously determined K-Ar ages used in the discussion of DVS geochronology (Faure, 1977).

1. Rock samples are homogenous at the level sampled for individual K and Ar analyses, and aliquots used for analysis are representative of the lithology being dated.
2. All Ar escaped from the lava prior to final crystallization and there has been no subsequent addition of Ar to the sample other than by radioactive decay of ^{40}K, or adhesion of atmospheric Ar (i.e., there is no excess Ar).
3. All K and its decay products have remained in the sample since the time of crystallization (i.e., the sample has remained a closed system).
4. The decay constant for $^{40}K \rightarrow ^{40}Ar$ is accurately known and has remained constant over the last 20 m.y.. Previously published dates used in this discussion have been recalculated to the current IUGS recommendations (Steiger and Jager, 1977) using the method of

Dalrymple (1979).

5. The initial isotopic composition of K in the sample was normal at the time of eruption.

K analyses were made at least in duplicate, and agreed within experimentally determined limits. This not only assures an acceptable level of analytical precision, but also provides a check on sample homogeneity.

Ar analyses were also made at least in duplicate. The major source of error is atmospheric contamination, which varies between 15 and 91 %. Age determinations are consistent with stratigraphic position within the limits of uncertainty, and there is no evidence to suggest excess Ar contamination has affected any of the new K-Ar determinations. Excess Ar has probably contributed to significant error in a few determinations made by Armstrong (1978).

4.3 GEOCHRONOLOGY OF SPECIFIC AREAS

A Summary of new and published radiometric ages is given in Table 4.3.

4.3.1 Volcanic Detritus in the MSSTS-1 Drillhole

The MSSTS-1 drillhole, on the western shelf of McMurdo Sound, lies 25 km north of the DVS, but is pertinent to this discussion because volcanic sediments in the drillhole are partially if not totally derived from the DVS (Barrett et al., 1986). "Basaltic" detritus forms a significant part of the sand fraction in the drillhole from 0 to 60 m, and 200 m to the bottom of the hole at 227 m below the sea floor.

Volcanic detritus in the 0 - 60 m interval closely resembles the

Table 4.3 - Compilation of K-Ar age determinations inferred (from stratigraphic position) ages of stratigraphic units in the Discovery volcanic subprovince, listed by area.

Area	Unit	Age	Reference
Gandalf and Riviera Ridges	RG1	14.6 - 18.7	Muncy, 1979
	RG2	13.0 - 14.1	this study
	RG3	<13*	
Morning	MM1	1.0 - 1.2	Polyakov et al., 1976
		1.2	Armstrong, 1978
	MM2	2.2 - 2.4	Polyakov et al., 1976
Mason Spur	MS1 - MS5	>12.1**	
	MS7	11.7 - 12.1	this study
	MS8	6.1	this study
	MS9	<6.1***	
Minna Bluff	MB1	9.0 - 11.0	this study
	MB2	7.2 - 8.3	this study
Mt. Discovery	MD1	4.6	Polyakov et al., 1976
		5.3	Armstrong, 1978
		5.3 - 5.5	this study
	MD2	1.9 - 5.1	this study
Brown Peninsula	BP	2.2 - 2.8	Armstrong, 1978
Black Island	BI1	10.9	Armstrong, 1978
	BI2	3.4 - 3.9	Armstrong, 1978
		4.4	unpublished data by P. Webb; P. Kyle, pers. comm.
White Island	WI	0.2	Kyle, 1981a
Foothills	F1	13.6 - 14.2	Armstrong, 1978
	F2	0.1 - 3.0	Armstrong, 1978

* correlation with MM2 suggests age is <1 Ma.

** $^{40}Ar/^{39}Ar$ plateau ages range 11.46 - 12.8 Ma.

*** MS9 sample from Helms Bluff (AW83614) dated at 4.5 Ma, and youngest deposits geomorphically look to be <1 Ma.

lithologies exposed in DVS outcrops, and diatom assemblages suggest that it has been deposited over the last 21 m.y. (Harwood, 1986). This interpretation is broadly consistent with the age of DVS outcrops, although "basaltic" outcrops are not a significant part of the sequence in rocks older than 14 m.y.

Diatom assemblages in the lower interval suggest an age of about 30 m.y., but there are no exposures of alkaline volcanic rocks in the Erebus volcanic province that could have been a source for sediments of this age. A 6-cm-thick pebble layer at a depth of 213.3 m has provided basaltic clasts large enough to date, and a devitrified felsic clast with phenocrysts of quartz, alkali feldspar, plagioclase and aenigmatite (Gamble et al., 1986). K-Ar age determinations of 14 Ma and 24 Ma on samples from the pebble layer are considerably younger than the age suggested by the diatoms. The devitrified felsic clast is petrographically similar to highly evolved peralkaline lavas in the Gandalf volcanic complex, which are dated at 14.6 - 18.7 Ma (Armstrong, 1978; Muncy, 1979). Either volcanism in the McMurdo Sound area has been a much longer lived event than the present outcrop would suggest, or the diatom geochronology is in error.

4.3.2 Gandalf and Riviera Ridges, and Mt Morning

Whole rock K-Ar dating of rocks from Gandalf Ridge and Castle Ridge (Armstrong, 1978; Muncy 1979) indicates that early Gandalf volcanic complex volcanism is the oldest known in the Erebus volcanic province. The lower part of the sequence (RG1) is dominated by peralkaline trachytes, and spans a period of 18.7 to 14.6 m.y. These rocks probably record several periods of activity associated with discrete volcanic events, rather than continuous outpouring over the

entire >4 m.y. period. Never-the-less, these rocks represent an extended period during which eruption of evolved to highly evolved lavas predominated. The overlying sequence comprises basanite to trachyte lavas (RG2) which were erupted from numerous small vents between 13.0 and 14.1 m.y. These deposits represent a period in which smaller batches of more basic lava reached the surface. Overall, the Gandalf volcanic complex represents about 6 m.y. of volcanic activity.

The phonotephrite to phonolite volcanism associated with the growth of Mt Morning is much younger. K-Ar dates exhibit a particularly narrow age range from 1.0 - 1.2 Ma (Polyakov et al., 1976; Armstrong, 1978), suggesting that dated samples represent only the latest activity associated with the formation of the central volcano. This is consistent with the undissected nature of the outcrop. By analogy with other volcanoes of comparable size in the Erebus volcanic province (Kyle, 1976; Armstrong, 1978), Mt Morning probably formed over a 1 - 1.5 m.y. period from about 2.5 to 1.0 m.y ago. Several K-Ar determinations on "basalts" from "Mt Morning" (specific sample locations are unknown) gave ages of 2.2 - 2.4 Ma (Polyakov et al., 1976). Whereas these data are consistent with the expected age for earlier eruptions of basanite or tephrite lavas associated with the Mt Morning central volcano, this author found no evidence of older, more basic lavas being exposed. Mt Morning is overlain by numerous small basanite and tephrite vents (MM2, RG3), which appear to have commenced eruption shortly after phonolite eruptions ceased. This suggests the "basalts" dated by Polyakov et al. (1976) may be younger, inaccurately dated, MM2 lavas.

4.3.3 Mason Spur

Incremental $^{40}Ar/^{39}Ar$ determinations on three samples from the lower portion of the Mason volcanic complex exhibit disturbed spectra (Figure 4.1). Disturbed spectra may reflect the effects of geological processes (e.g., multiple degassing events, excess Ar, slow cooling), analytical artifacts (e.g., recoil, phase changes), and sample characteristics (e.g., grain size and shape characteristics, mixed mineral phases) (Harrison, 1983). Plateau ages (Fleck et al., 1977) of 11.5 M and 12.8 Ma are defined for samples AW83678 and AW83569, respectively A plateau age of 12.5 Ma was forced for AW83712. In each case the plateau age is less than the total gas age (equivalent to the K-Ar age) by 0.55 to 0.91 Ma. If the plateau ages are assumed to be a closer estimate of the real age, then K-Ar age determinations for other DVS rocks may be as much as a million years older than K-Ar dates suggest. Total gas ages are used in age comparisons and correlations of DVS rocks in order to be consistent with K-Ar age determinations.

The general shape of $^{40}Ar/^{39}Ar$ age spectra in Mason Spur samples resembles diffusion curves in which there has been >98% Ar loss (Faur 1977). However, this explanation for the disturbed spectra is not supported by the quality of the samples, in which alkali feldspar phenocrysts appear reasonably fresh.

Spectra for whole rock samples reflect the sum of the spectra fc individual minerals in the sample, and will consequently tend to be more complex than spectra determined on mineral separates. The sharp increase in Ar loss during final heating increments may be a product of Ar loss from a crystal lattice site that has retained Ar at lower temperatures. Ar retention is a documented problem in sanidines

(McDowell, 1983), which can retain some Ar even at fusion temperatures. The slightly greater amount of Ar lost during the initial heating step, as compared to the plateau, may be due to a small amount of excess Ar along grain boundaries (Harrison, 1983).

Basanite to benmoreite lavas in the upper part of the Mason volcanic complex (MS7) are K-Ar age dated at 11.7 Ma and 12.1 Ma. Like the upper part of the Gandalf volcanic complex, MS7 lavas represent a period in which more basic lavas were erupted from smaller vents. There is some 5 - 6 m.y. of volcanic quiescence between the cessation of Mason volcanic complex volcanism and the onset of younger basanite - trachyte activity (MS8 - MS9).

The younger trachyte volcanism at Mason Spur (MS8) is dated at 6.1 Ma, and marks the onset of the basanite - tephrite dominated activity. A MS9 basanite flow at Helms Bluff was dated at 4.3 Ma. This particular volcano was erupted subglacially, and is evidence that climatic conditions were more severe at that time. The undissected and unweathered appearance of young basanite agglutinate deposits northwest of Surprise cones suggests that MS9 volcanism has continued until very recently.

4.3.4 Minna Bluff

K-Ar age dates from Minna Bluff span a 4 m.y. period during which lava was erupted essentially continuously from medium to small, overlapping shields, domes, and cinder cones. The transition from the older basanite-trachyte sequence (MB1) to the younger basanite - phonolite sequence (MB2) occurred between 8.3 and 9.0 m.y. ago. It was accompanied by a decrease in the volume of lava erupted from individ-

centers, and an increase in the number of vents. Fissure eruptions occurred along the northern end of the peninsula.

The glacial unconformity near the base of MB1 probably formed between 10 and 11 m.y. ago. A minimum age of 9.7 +/- 0.5 Ma is given by the whole rock K-Ar determination on sample AW82097B, whereas the date determined on the feldspar separate from that sample was 11.0 +/- 1.1 Ma. It is uncertain whether the unconformity was cut by an expanded and grounded Ross Ice Shelf, or by a local ice cap. However, this unconformity does indicate that climatic conditions during latest Miocene times were such that a significant ice thickness existed at sea level in this area. This interpretation is consistent with evidence in the Upper Miocene - Lower Pliocene section of the MSSTS-1 drillcore (Barrett and McKelvey, 1986), which indicates that the depositional environment on the western shelf of McMurdo Sound fluctuated between floating and grounded ice conditions during this period.

4.3.5 Mt Discovery

New K-Ar age dates from Mt Discovery (MD1) cluster between 5.6 and 5.3 Ma. Whereas Armstrong's (1978) date of 5.3 Ma is consistent with this data, Polyakov et al.'s (1976) date of 4.6 Ma, which was determined on "trachyte", is unreasonably young for the MD1. The tephriphonolite core of Mt Discovery is only slightly older than the capping phonolite flows erupted from the summit crater. Parasitic phonolite domes on the northern side of the mountain are the same age as phonolites erupted from the summit crater. Most of this undissected volcano is unavailable for sampling, and these ages probably recor only the concluding phases of accumulation. By comparison with geo-

chronological investigations on Ross Island (Kyle, 1976; Armstrong, 1978), it is likely that the Mt Discovery stratovolcano was built up over a period of 1 to 1.5 m.y.

Between 5.1 and 5.3 m.y. ago phonolitic eruptions ceased. Basanitic to phonotephritic lavas (MD2) began erupting from small local vents, including a cone on the northern crater rim of the main stratovolcano dated at 5.1 Ma. A small phonolite dome on the lowermost southeastern slopes is dated at 2.2 Ma, and probably represents the youngest MD2 activity.

4.3.6 Brown Peninsula, Black Island, and White Island

K-Ar dates on four samples from Brown Peninsula (Armstrong, 1978) span a period of 0.6 m.y., and suggest that the entire volcanic pile at Brown Peninsula accumulated over a relatively short period of perhaps about 1 m.y. (Kyle et al., 1979). Although these lavas span just a few hundred thousand years, they exhibit a well documented sequence of magma evolution from basanite to benmoreite consistent with a model of fractional crystallization (Kyle et al., 1979).

The alkali basalt sample from the Mt Melania vicinity, Black Island (BI1), is dated at 10.9 Ma (Armstrong, 1978), and is similar in age to the basanite - trachyte sequence exposed at the base of Minna Bluff. There is a significant time break between the eruption of BI1 lavas, and the onset of phonolite activity about 4.4 m.y ago (unpublished data by P. Webb; P.R. Kyle, pers. comm.). The main phonolite volcano of Mt Aurora is dated at 3.9 Ma (Armstrong, 1978). Like the sequences at Mt Discovery and Mt Morning, slightly younger basanites mantle the Mt Aurora phonolite volcano, and are dated at 3.4 Ma

(Armstrong, 1978). The two phonolite domes at the southern end of the Island are probably younger still, but have not been dated.

A single sample from White Island has an age of 0.17 Ma (Kyle, 1981a). This is consistent with geomorphic evidence that suggests White Island is very young.

4.3.7 Foothills of Royal Society Range

The oldest K-Ar dates from the Foothills area are 13.6 Ma and 14.2 Ma (Armstrong, 1978). The 14.2 Ma date was determined on xenolith-bearing lavas (P.R. Kyle, pers. comm.) cropping out northeast of Howchin Glacier, and the date may reflect excess Ar. However, the 13.6 Ma age is not suspect. The sample is from an outcrop at the southern end of Pyramid Trough, and is correlated on the basis of age and location with outcrops at Riviera Ridge (RG2). These outcrops are separated by about 6 km, and lie on opposite sides of the Koettlitz Glacier.

There is no evidence of renewed volcanic activity in the Foothills area until about 3 Ma. The youngest dated sample is 0.08 Ma, but geomorphic evidence and the presence of tuff layers in glacier ice (Keys et al., 1977) suggest that this area should be considered volcanically dormant.

On the basis of age, the volcanic stratigraphy of the Foothills area is divided into older outcrops (F1), which are >13 m.y., and younger outcrops (F2), which are <3.0 m.y.

Chapter 5

GEOLOGIC HISTORY OF THE DISCOVERY VOLCANIC SUBPROVINCE

5.1 INTRODUCTION

Volcanic activity in the DVS has been essentially continuous over the last 19 m.y. (Figure 5.1). It is the most complete record of McMurdo Volcanic Group activity, and an excellent opportunity to study changes in eruptive style, tectonic style, and petrogenesis with time. This section summarizes data presented in chapters 2 to 4 in order to synthesize the tectonic and volcanic history of the DVS.

5.2 STRUCTURE AND TECTONIC HISTORY OF THE DVS

Extrapolation of crustal thickness determinations for the area to the north (Smithson, 1972; McGinnis et al. 1985), suggests that the western DVS is probably underlain by 40 - 45 km of continental crust. Crustal thickness decreases towards the east, and may be as little as 21 km beneath southern McMurdo Sound (Smithson, 1972; McGinnis et al. 1985). There is also a fundamental change in the nature of the crust beneath the Transantarctic Mountains and McMurdo Sound (Smithson, 1972; Berg, 1984; Berg et al., 1985; McGinnis et al., 1985).

Four structural trends are identified in the DVS (Figure 5.2). These have been active at different times in different areas. The trends are:

1. northnorthwest to north-south,
2. northwest,
3. northeast,
4. northnortheast.

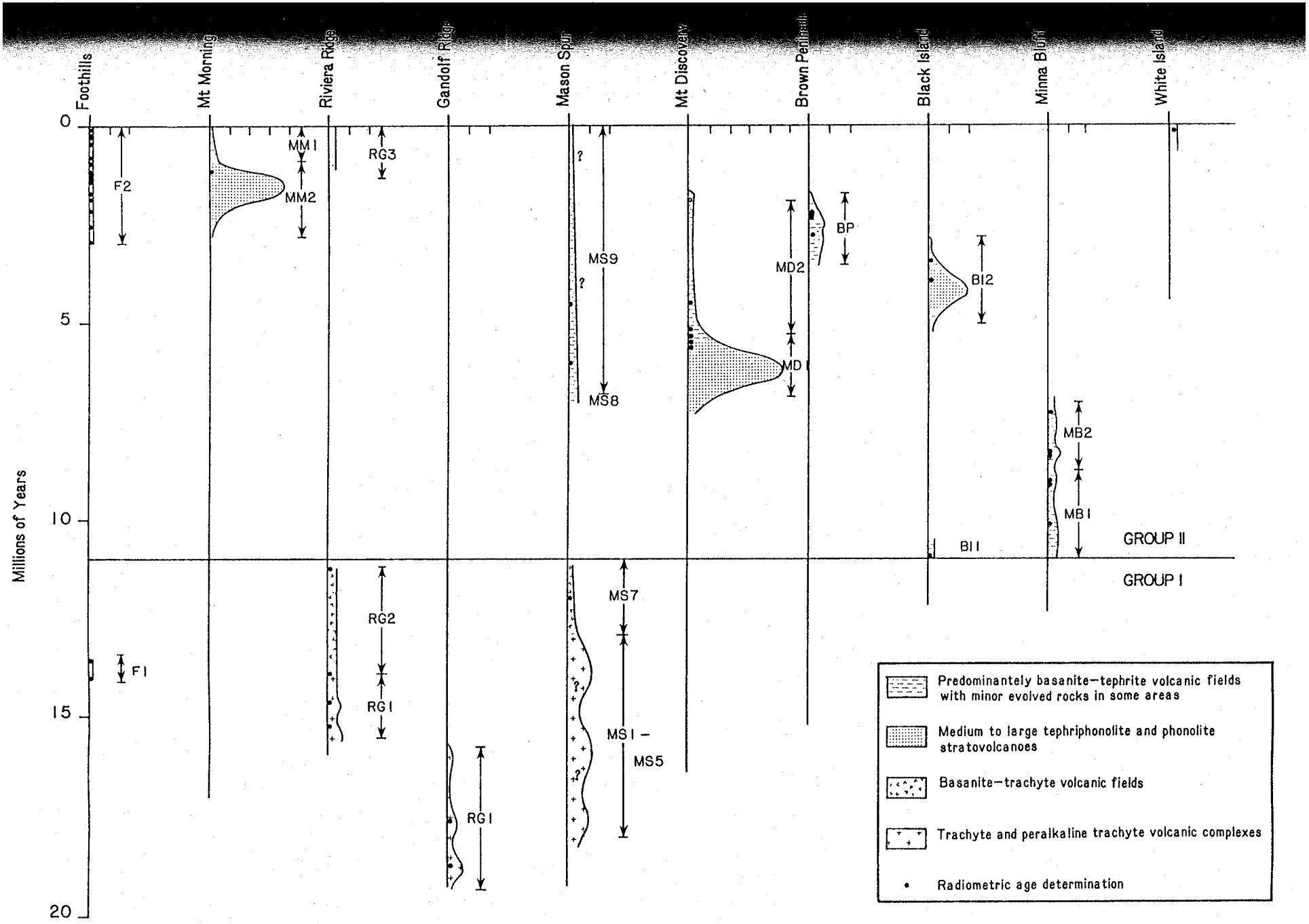

Figure 5.1 - Summary of the variation in rock type and stratigraphic thickness with time, for areas within the DVS. Tick marks along the horizontal axis represent 250 m intervals of stratigraphic accumulation per million

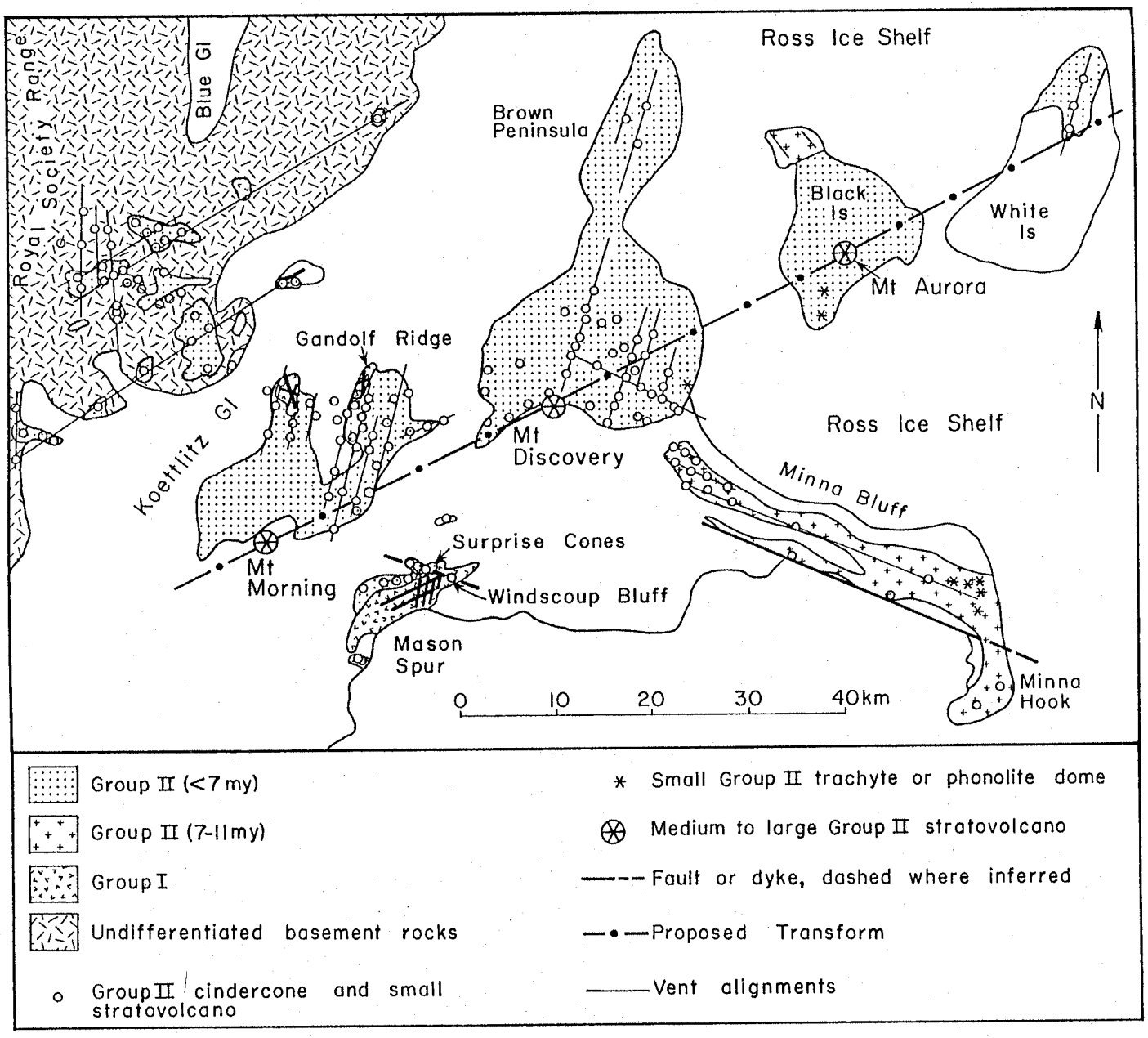

Figure 5.2 Structural aspects of the DVS. At Mason Spur, Riviera Ridge, and Gandalf

5.2.1 Northnorthwest to North-South Structures

The northnorthwest to north-south trend has never been a major control of volcanic activity, but is identified at Gandalf Ridge (Muncy, 1979) and in the Foothills of Royal Society Range, as zones of hydrothermal brecciation and alteration, dykes, and vent alignments. This trend parallels the north-south structural grain of the region, and is presumably caused by axial faults associated with the Victoria Land basin and the eastern margin of the Transantarctic Mountains. The identification of this trend in MVG rocks at Gandalf Ridge is evidence that east-west extension was active in the DVS as early as the Mid Miocene.

5.2.2 Northwest Structures

Northwest control of dykes and vent alignment occurs along the northwest-trending part of the Minna Bluff. A similar alignment is seen at Mason Spur, where MS5 dykes at Windscoup Bluff, and the most recent fissure eruptions extending northwest from Surprise Cones follow a similar trend. Less well defined northwest lineaments include the apparent northwest alignment of the oldest deposits on Black Island (BI1), and a possible northwest alignment of small basanite - tephrite vents on the eastern side of Mt Discovery.

These trends may be controlled by upper crustal weaknesses associated with northwest-trending F_2 fold axes, which are exposed in basement rocks cropping out between Heald Island and Garwood Valley (Findlay et al., 1984).

5.2.3 Northeast Structures

Northeast-trending faulting and dyke intrusion associated with emplacement of the upper Mason volcanic complex (MS7) occurred about

12 m.y. ago. This trend was not active during the emplacement of the lower Mason volcanic complex. A 16.8 - 17.6 m.y. old dyke swarm at Gandalf Ridge also has an east-west to northeast trend.

The alignment of the young phonolite stratovolcanoes of Mt Morning, Mt Discovery and Mt Aurora, suggests the presence of a major northeast-trending lineament through the DVS. Some small vents in the Foothills area are aligned along a parallel trend.

Locally exposed basement rocks do not exhibit northeast trending structures, although major northeast-trending faults are associated with the major valley systems to the north (Findlay et al., 1984; Bennett and Sissons, 1984). The alignment of three medium to large stratovolcanoes along this trend, and a change in the axial trend of the Transantarctic Mountains in the DVS, suggests that the stratovolcanoes may be aligned along a transform fault which dextrally offsets the crustal axis of extension. If so, this area probably marks the southern limit of the Victoria Land basin.

5.2.4 Northnortheast Structures

The northnortheast trend has provided channelways for ascending magma since early in the development of the Mason volcanic complex. I is also the pervasive control of basanite and tephrite vents on Mt Morning, Mt Discovery, Brown Peninsula, and possibly Black Island and White Island. This trend is not seen at Minna Bluff.

There is no clear northnortheast structural trend in local exposures of basement rocks. The pervasive northnortheast control of younger basanite and tephrite vents overlying the major stratovolcanoes suggests that a northnortheast-trending fracture system has been

active during the last 5 m.y. in the area south of the Koettlitz Glacier, and north of the proposed transform. The northnortheast trending lineaments intersect the proposed transform at an angle about 50o, which suggests that the northnortheast-trending struct may represent a conjugate fracture set.

5.2.5 Radial Symmetry at Mt Discovery

The radial distribution of major volcanic centers around Mt Discovery has been attributed to the rise of magma along zones of weakness generated by crustal doming above a rising magma column (and Cole, 1974). However, this hypothesis is not substantiated by current evidence. The age of the deposits forming each of the radi arranged volcanic centers ranges from 8.3 to 7.3 m.y. at Minna Blu 2.7 - 2.1 m.y. at Brown Peninsula, and probably ~2.5 - 1.0 m.y. at Morning. Mt Discovery is dated at between 5.1 and probably ~6.6 Ma Clearly these various centers are not cogenetic as the crustal dom model suggests. Any crustal doming associated with the emplacement magma beneath Mt Discovery occurred too late to influence the locat of volcanism at Minna Bluff. Furthermore, radial structures on Mt Discovery itself have not been observed.

5.3 VOLCANIC HISTORY OF THE DVS

Correlation of lithologies between areas results in a broad subdivision of the volcanic stratigraphy into two periods: 19 - 11 m.y. and 7 - 0 m.y (Figure 5.1). Outcrops at Minna Bluff and the ol deposits on Black Island occupy the intervening 4 m.y. period, from about 7 m.y. to 11 m.y., but are more similar in rock type and erup- tive style to the younger outcrops. In the following discussion, roc

older than 11 m.y. are collectively referred to as Group I: those younger than 11 m.y. comprise Group II.

A cartographic summary of the volcanologic history of the DVS is given in Figure 5.3.

5.3.1 Group I

Group I rocks crop out in the western part of the DVS, at Mason Spur, Riviera Ridge and Gandalf Ridge. Outcrops are predominantly composed of trachyte and peralkaline trachyte lavas that were erupted over a several million year period in which there was no significant change in rock type. A small volume of hawaiite and mugearite is interbedded with the trachytes at Mason Spur and Gandalf Ridge. Group I outcrops are deeply dissected, especially at Mason Spur where 800 m of Group I rocks is exposed. Although pyroclastic rocks are present, they are of volumetrically minor importance compared to lava flows. Older flows are intensely intruded by stocks and dyke swarms that are related to eruptions higher in the sequence. Hydrothermal alteration and brecciation is widespread and is associated with the intrusion. There are no ignimbrite deposits.

Volcanoes were small to medium in size, perhaps as much as 10 km across at the base and 700 m high. Individual volcanoes were probably built up over a relatively short period of time (~1 m.y.), because major unconformities are not present within stratigraphic units, whereas erosion, sedimentary deposition, and weathering are observed between units at Mason Spur. The absence of large volcanoes, on the scale of Mt Discovery for instance, suggests that individual volcanoe were feed either from small to medium sized magma chambers, or if a

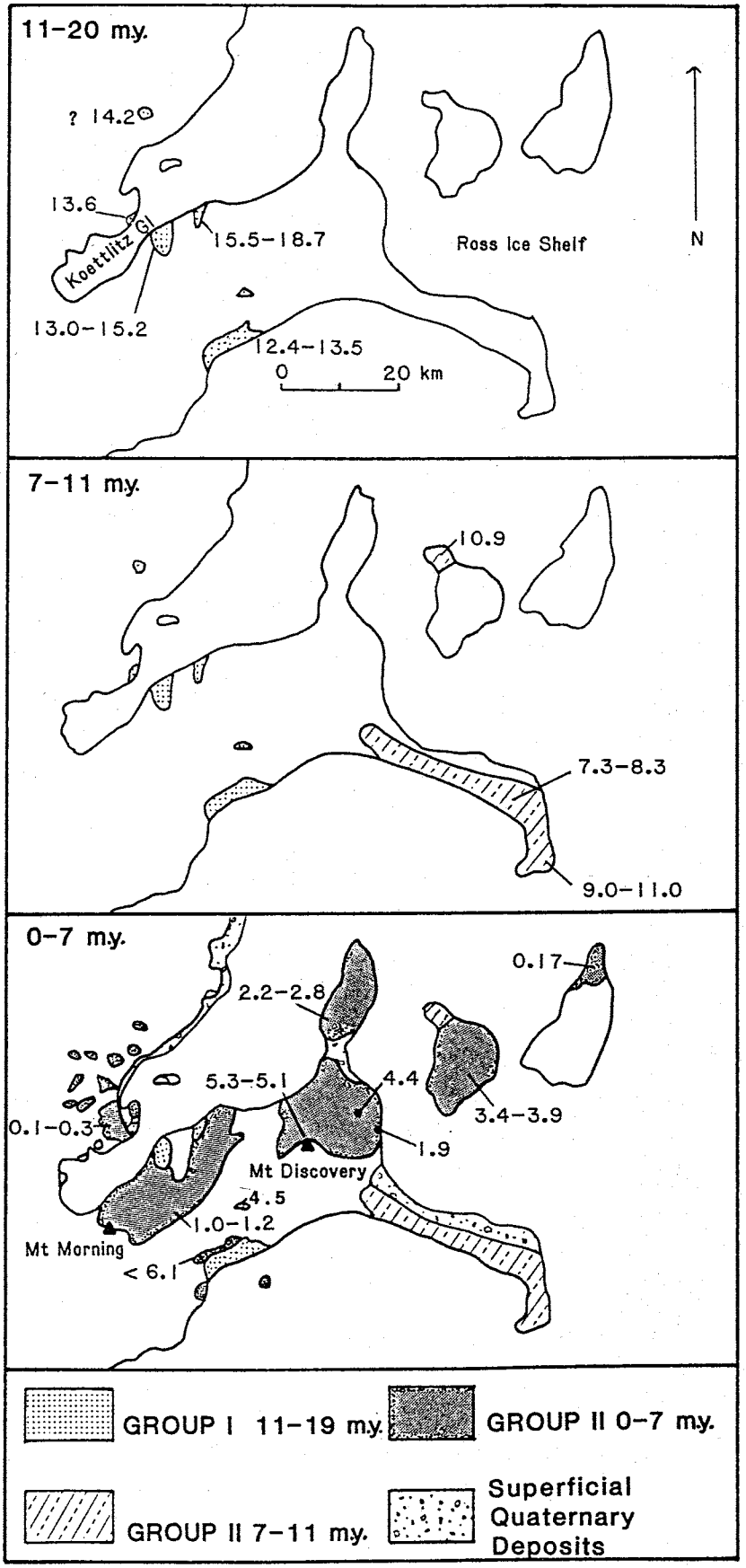

Figure 5.3 - Cartographic summary of the volcanic history of the DV
Ages for each outcrop area are given in million years and are a
combination of existing and new K-Ar determinations.

large magma chamber existed, from separate cupolas. At Mason Spur and Riviera Ridge the peralkaline trachyte sequence is capped by 100 - 200 m of basanite to minor benmoreite and trachyte lavas erupted from smaller vents.

Trachyte and peralkaline trachyte-dominated volcanism in the Gandalf volcanic complex lasted for at least 6 m.y. In contrast, peralkaline trachyte dominated activity in the Mason volcanic complex, may have taken place over a shorter 1 - 2 m.y. period. The conditions under which these highly evolved magmas were being generated, evolved and erupted, remained fairly constant from 19 to between 12 and 14 m.y. ago. The change to a regime in which more basic lavas were erupted from smaller volcanoes in the upper parts of the Gandalf and Mason volcanic complexes implies a change in the magmatic environment took place about 12 m.y. at Mason Spur, and about 14 m.y. ago at Riviera Ridge.

5.3.2 Group II

About 11 m.y. ago Group I volcanism ceased. The locus of activity shifted 50 km eastwards to the Minna Bluff - Black Island area. The volcanic record at Minna Bluff is essentially continuous from 11.0 to 7.0 m.y. and documents a period when volcanic activity elsewhere in the DVS was absent. The older deposits at Minna Bluff comprise thin to medium thick lava flows that built up broad shield volcanoes. Agglutinate and cinder deposits are comparatively minor. Lobe hyaloclastites are interbedded with palagonitized fluviatile sediments associated with a glacial unconformity, and were probably erupted subglacially. These outcrops suggest that eruption occurred during a fluctuating glacial and periglacial environment. However, the inter-

bedded nature of flows and palagonitized sediments is evidence that t glacial unconformity does not represent a break in volcanic activity. This conclusion is supported by K-Ar dating of the Minna Bluff sequence. The older outcrop on Black Island (BI1) exhibits similar characteristics to the lower Minna Bluff sequence.

There is no stratigraphic break separating the lower and upper portions of the Minna Bluff sequence. The distinction is based on a change from an older basanite - trachyte association, to a younger basanite - phonolite sequence. This change appears to be transitiona at about 8.3 to 9.0 m.y. ago. The change in rock type is coupled with a subtle reduction in the size of volcanoes, and an increase in the volume of agglutinate compared to the flows.

Deposits erupted during the period from 7 - 11 m.y. exhibit transitional charateristics. The lower Minna Bluff sequence (MB1) has similar volcano sizes and rock types to the uppermost deposits in the Gandalf and Mason volcanic complexes (RG2 and MS7). However, the MB1 lavas are generally more porphyritic and more vesicular than the Grou I lavas of similar composition. The volcanic geology and rock types found in the upper Minna Bluff sequence (MB2) are similar to younger Group II outcrops on Brown Peninsula and elsewhere.

Volcano size and rock type characteristics suggest that lavas forming the older sequence at Minna Bluff were generated and evolved under similar conditions to those which had existed in the Mason Spur - Riviera Ridge area for the preceding 3 m.y. The restricted areal extent of volcanism during this period suggests crustal extension was concentrated along the western margin of the southern Victoria Land basin.

The renewal of more widespread and voluminous volcanism began about 6 - 7 m.y. ago. This activity is characterized by a broad volcanic field comprising numerous small basanite to tephrite centers, large tephriphonolite and phonolite stratovolcanoes at Mt Discovery and Mt Morning, and a smaller one on Black Island. Small trachyte or phonolite domes occur at Mason Spur, Mt Discovery and Black Island. A Brown Peninsula a series of overlapping small to medium sized stratovolcanoes are built up of progressively more evolved lavas. At Mt Discovery, Mt Morning, Brown Peninsula and Black Island stratovolcanc formation is closely followed by the eruption of numerous small basar ite - tephrite centers. In the Foothills of Royal Society Range, at Mason Spur and on White Island basanite and tephrite volcanism has occurred without the prior formation of a stratovolcano.

Compared to the preceeding 12 m.y., the volume of less evolved magma erupted during the last 7 m.y. has increased greatly, and there is a much wider distribution of volcanic centers. In addition there has been the formation of the large stratovolcanoes of Mt Discovery and Mt Morning, which probably account for 120 km^3 and 150 km^3, resectively, of tephriphonolite and phonolite. By comparison, the basanite tephrite centers are small (<0.1 km^3).

The presence of mantle-derived xenoliths in basanites at several centers indicates that these lavas rose rapidly from mantle depths. The broad aeral distribution of centers suggests not only a broad zo of melting in the underlying mantle, but also a broad zone of crusta extension, and the development of deep crustal fractures in order to provide direct conduits from the mantle.

The changing nature of DVS volcanism may be accounted for by progressive thinning of the crust. This would have made it easier for less evolved magmas to reach the surface. Prior to 11 m.y ago volcanism was concentrated in the Riviera Ridge - Mason Spur area, and possibly further east in areas which are not currently exposed. About 11 m.y. extension was probably concentrated along the western margin of the southern Victoria Land Basin, and volcanic activity shifted to the Minna Bluff - Black Island area. The activation of a proposed northeast-trending transform through the DVS probably began 6 - 7 m.y. ago, and would account for the much broader distribution of Erebus volcanic province activity, of which the DVS is only a part. This regime has continued until present.

Chapter 6

PETROGRAPHY

6.1 INTRODUCTION

Two hundred and eight of the 210 analysed samples from the DVS were examined in thin section. Rock nomenclature follows Le Bas et al., (1986) (Figures 6.1 and 6.2) and is discussed further in Chapter 8.3. A petrographic summary of samples is given in Table 6.1. Detailed petrographic descriptions are given in Appendix 3.

Rock textures vary from dense to scoriaceous, and aphyric to strongly porphyritic, with glassy to medium grained groundmass. Glassy varieties are present typically as scoriaceous lavas or dense obsidia

Phenocrysts are defined as mineral grains whose maximum dimensio is greater than 1 mm. Microphenocrysts are less than 1 mm, but larger than groundmass minerals. Xenocrysts are present in some samples and are distinguished by rounded cores, alteration textures, and over-growths. They are particularly common in lavas that also contain xenoliths.

6.2 BASANITES AND ALKALI BASALTS

Group I basanites were only found in the upper Gandalf and Mason volcanic complexes, whereas Group II basanites occur throughout the DVS. A Group II alkali basalt was collected at Mason Spur (AW83662), and another occurrence has been reported at Black Island (Cole and Ewart, 1968).

The basanites are typically porphyritic to glomerophorphyritic and contain 5 - 25 % phenocrysts. Only 15% of basanite samples had less than 5% phenocrysts. The alkali basalt AW83662 is petrographical

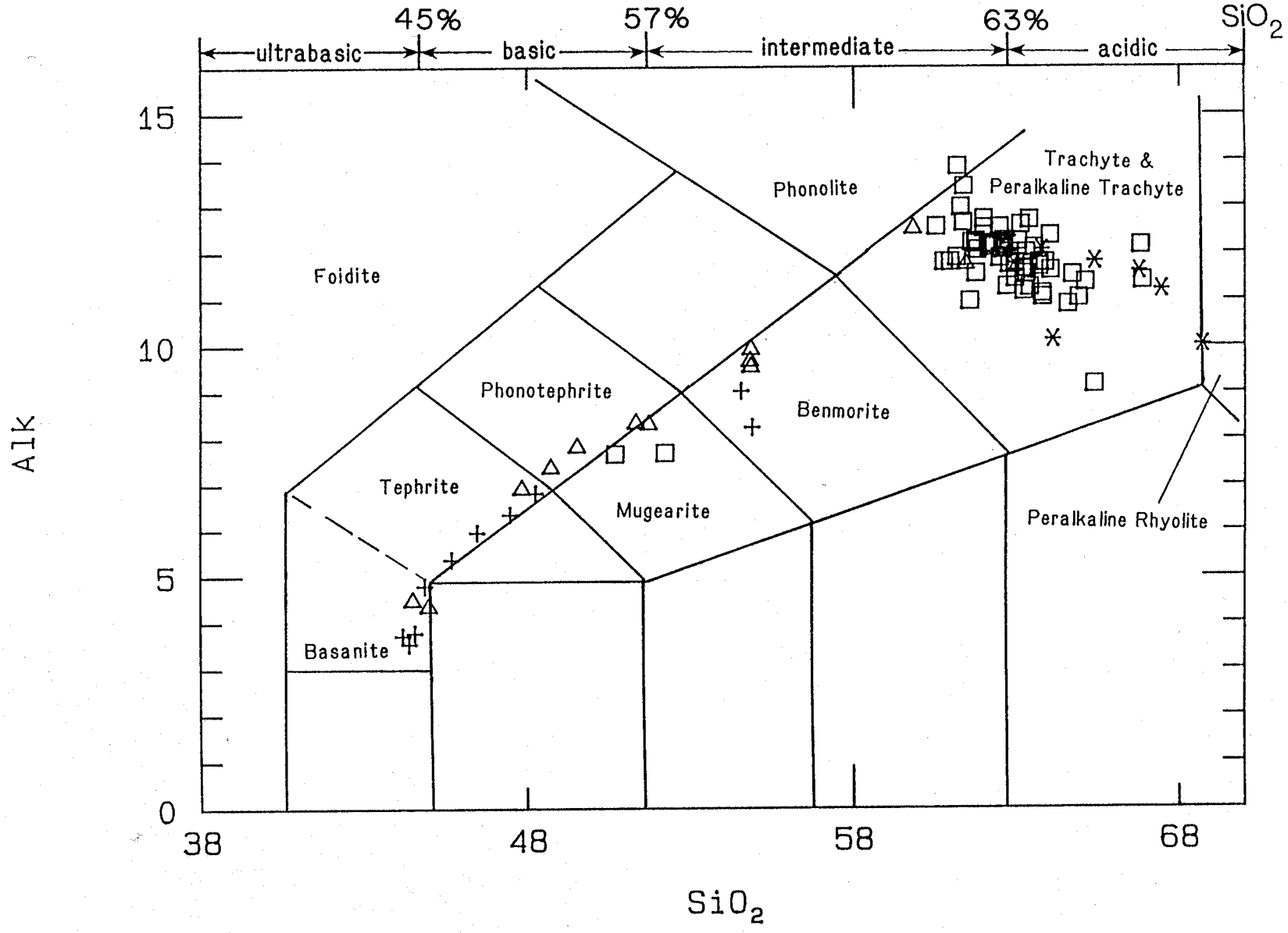

Figure 6.1 - New Group I analyses plotted on a total alkalis - SiO_2 (determinations plotted as oxide wt. %) diagram. Rock nomenclature is that of Le Bas et al. (1986). * lower Gandalf volcanic complex (RG1); ▵ upper Gandalf volcanic complex (RG2); □ lower [illegible] volcanic complex (MS1 - MS5); + upper Mason volcanic complex (MS7).

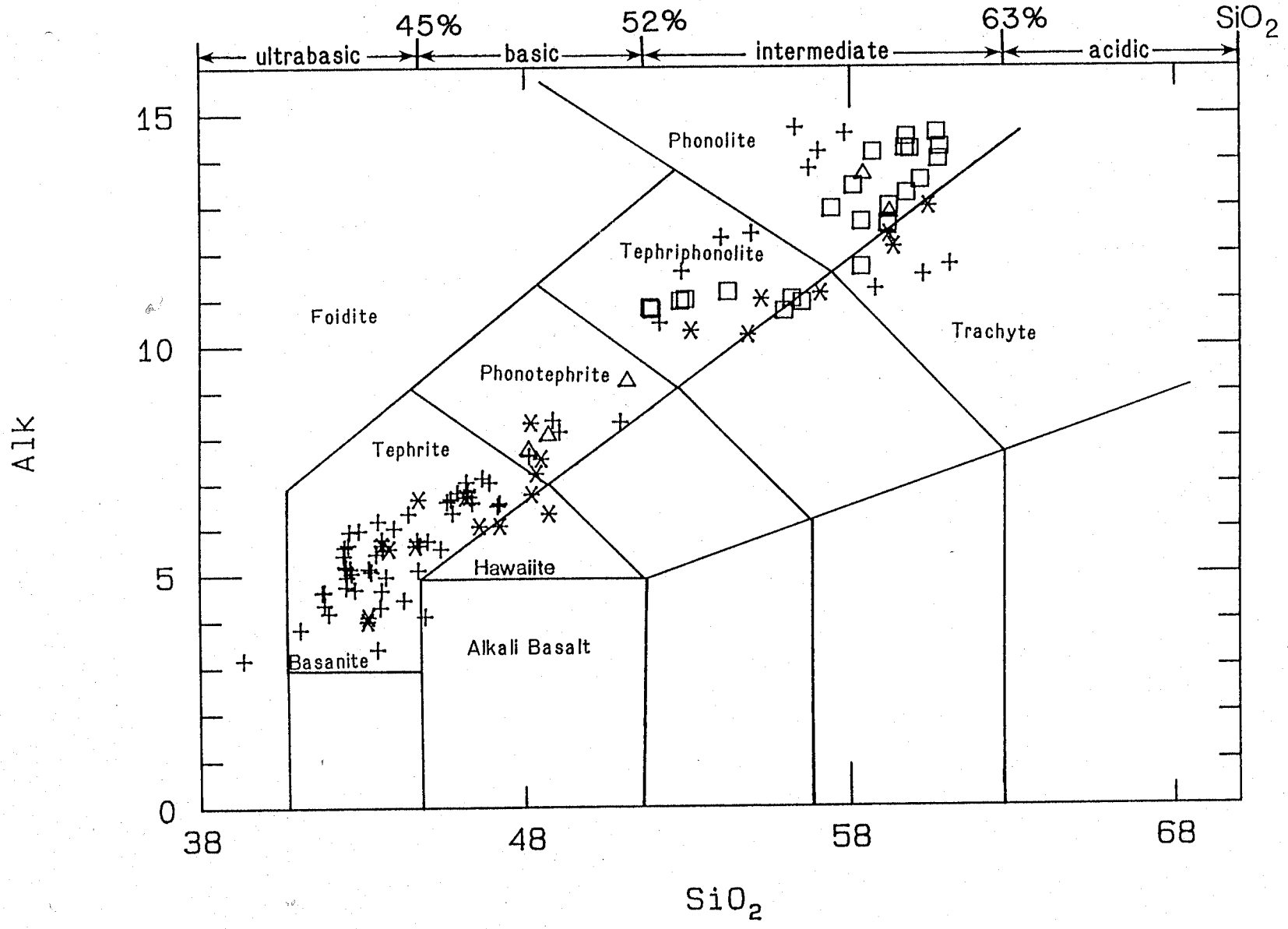

Figure 6.2 - New Group II analyses plotted on a total alkalis - SiO_2 (determinations plotted as oxide wt. %) diagram. Rock nomenclature is that of Le Bas et al. (1986). * lower Minna Bluff sequence (MB1); □ Mt Discovery (MD1); Δ Mt Morning (MM1); + other

Table 6.1 - Petrographic summary of samples collected from the DVS. Samples are listed by geographic area, and then by increasing SiO_2 content within each stratigraphic unit. A question mark preceding the sample number indicates uncertainty in its assignment to the stratigraphic unit. An asterisk after the sample number denotes a xenolith.

Sample Number	Rock Type	Texture	Mineralogy ol	cpx	Na-px	Na-am	kaers	bio	opq	aen	plag	feld	ne	ap	G'mass Texture	Second Minera
RIVIERA RIDGE AND GANDALF RIDGE																
RG1 (Group I)																
AW86021	ptr	a,v			g	g				g		g			g	
AW86978	tr	a,v			g			g				g			ig	o,z
AW86006	tr	a,v			g			g				g			t	z
AW86018	tr	p(<5),v			g	?g				g		p			t	o,z
AW86986	tr	p(<5),v			g			g				p			t	z,c
AW86020	ptr	p(5),v			g	g				g		p			t	o
AW86008	tr	p(10),v									r,x	p			c	o,z,c
AW86976	ptr	p(5)			g	g				r		p			i	o,c
RG2 (Group I)																
AW86035	b	a,v	g,pi	r				g		g		r,x			ig	z,c
AW86036	b	p(25),v	p,pi	r				r		p					ig	
AW86013	t	p(<5),v	g,pi	g				g		r		r		i	so	c
AW86012	pt	a	g,pi	g				g		g				i	ig	
AW86072	pt	a,v	g	g				g		g				i	ig	
AW86034	pt	a	g,pi	g				g		g					ig	
AW84714	m	a	g,pi	g				g		g				i	ig	
AW86988	bm	a	g,pi	g				g				g		g	t,ig	
AW86025	bm	mp(<5)	g,pi	g				g		r		g			g	
AW86041	bm	p(<5)	r	p				p		p		g		i	t	
AW86016	tr	a	g	g				g				g			f	
AW86075	tr	a,v		g				g				g			f	o,z

Table 6.1 (continued)

Sample Number	Rock Type	Texture	Mineralogy: ol	cpx	Na-px	Na-am	kaers	bio	opq	aen	plag	feld	ne	ap	G'mass Texture	Secondar Mineral
RG3 (Group II)																
AW86999*	f	cm		g			p			p			p		i,gl	o
AW86033	b	p(20),v	p	p				r		g					p	
AW86070	b	p(5)	p,px	g				g		g					p	
AW86061	b	p(5),v	p,px	g				g		g					g,c	
AW86037	t	mp(5),v	p	p				g		g		?g			ig	
AW86032	t	mp(5)	p	p			r,po	g		p					c	
AW86063	t	mp(<5),v	p,px	p			r,co	g		g		?g			ig	
AW86042	p	a		g				g				g			f	
MASON SPUR																
MS1 (Group I)																
AW83581	ptr	p(<5),v			g	g				g		p			t,c	o,z,c
AW83422	ptr	p(<5),v			g					r		p			t,c	o,z,c
?AW83441	ptr	p(5),v			g	g				g		p			t	o,z,c
AW83508	ptr	p(<5),v			r	g				r		p			t	o,z
AW85865	ptr	p(<5),v			r	g				r		p			t	o,z
AW85803	ptr	p(<5),v			g					g		p			t,c	o,z,c
AW83569	ptr	p(<5)			g	g				g		p			t	o,d
MS2 (Group I)																
AW85863	m	p(<5)			g			g			p	g			f	o,c
AW85831	m	a			g			g			g	g			t,c	o,c
AW83511	ptr	p(<5)			g					g		p			f	o
MS3 (Group I)																
AW83496	ptr	p(<5),v			g					g		p			f,c	o
AW83503	ptr	mp(<5)			r			r		g	r	p			f,c	
AW85851	tr	p(<5),v					?i,po			g		p			f	o,c
AW85850	tr	p(<5),v			g					r		p			t,c	o,c

Table 6.1 (continued)

Sample Number	Rock Type	Texture	Mineralogy ol	cpx	Na-px	Na-am	kaers	bio	opq	aen	plag	feld	ne	ap	G'mass Texture	Second Minera
MS3 (continued)																
?AW83711	ptr	mp(<5)			g	g		?g		r		g			t	o,d
AW83430	ptr	p(<5)			g	g			g			p,px			t	o,z
AW85818	ptr	p(5)			g	g		g				p			t,c	o,z
AW83445	ptr	a,v			g	?g			g			g			t,ig	o,z
AW83678	ptr	a			g	g		g				g			t,c	o
AW83499	ptr	a			g				g			g			f,c	o
AW83515	ptr	mp(<5),v			g				g			p			t,c	o,z
AW85847	ptr	p(5)			g	g			g	r		p			t	o
AW83484	tr	mp(<5),v			g	g			g			p			t	o,z
AW85809	ptr	a,v			g	?g			g			g			t	o,z
AW85837	ptr	a,v			g				g			g			f	
AW85860	ptr	mp(<5)			g	g			g	r		g			t	o,d
AW83491	ptr	a			g				g			g			f,c	o,c
AW83580	ptr	p(<5)			g	g			g			p			t	o
?AW83709	ptr	p(<5),v			r	?g		g				p			t	o,d
AW83710	ptr	p(<5)			r	?g			g			p			t	o
AW85833	ptr	a			g			g				g			f,c	o
?AW85830	ptr	p(5)			g		g		r			g			t,g	o,z,c
AW83502A	ptr	p(<5)			g		g		g			p			t	o
AW85869	ptr	a,v			g		g		g			g			t	o,z,c
AW83510	ptr	a,v										g			f,c	o,d
AW83567	ptr	a,v			g				g			g			t,c	o
AW83485	ptr	mp(<5)			g		?g		g			p			t,ig	o
AW83712	ptr	mp(<5),v			g				?g			g			f,c	o
AW83411	tr	p(<5)			g				g			p			f,c	o
MS5 (Group I)																
AW83701	tr	p(<5),v		g					g			p,px			f,c	o,d
AW85829	ptr	p(<5)			g	g			g			r			t,c	o,d

Table 6.1 (continued)

Sample Number	Rock Type	Texture	Mineralogy ol	cpx	Na-px	Na-am	kaers	bio	opq	aen	plag	feld	ne	ap	G'mass Texture	Seconda Minera
MS5 (continued)																
AW83532	ptr	mp(<5)			g	?g				g		r			f,c	o
AW83516	ptr	(obsidian - no thin section)														
AW83453	tr	mp(<5),v			g			p				g			t,c	d
?AW83707	ptr	a			g	?g				g		g			t,c	o
AW83522	tr	a,v			g					?g		g			t,c	d
?AW83533	ptr	p(<5)			g	g				g		p	g		t,c	o
AW83559	ptr	a,v			g	g				g		g			t,c	o
AW83520	ptr	p(5)			r					r		p			sp	o
AW83642	ptr	a,v			g	?g				g		g			c	o
AW83519	ptr	(obsidian - no thin section)														
AW83677	ptr	a,v			g					?g		g			t,c	d
AW83653	ptr	a,v			g					g		g			f,c	o
AW83524	ptr	p(<5),v			g	g				g		r			f	o
AW83517	ptr	mp(<5)			g	g				g		r			t	o
AW83534	ptr	mp(<5)			g	g				g		r			f,c	o
MS7 (Group I)																
AW83550	b	p(20),v	r,x	r,x				g			p,x	p,x			ig	c
AW83454	b	mp(<5),v	r	r				g			r				ig	c
?AW83545	b	mp(15)	p,px	p				g			p				i,c	o
AW83536	b	p(5),v	r,pi,x	p,x				g			r,x	r,x			ig	
AW83554	t	a,v	g,pi	g				g			g	g			ig	o,z,c
?AW83543	t	a	g	g				g			g				i,c	o
AW83410	t	a,v		g				g			g	g			i,c	o,z,c,
AW83607	t	p(<5),v	r,pi	g				g			g				ig	z,c
?AW83513	bm	mp(<5)		r				r			p	g			t,c	o,c
AW85839	bm	mp(<5)	g,ci	g			r,po	g			g				ig	o

Table 6.1 (continued)

Sample Number	Rock Type	Texture	Mineralogy											G'mass Texture	Secondar Minerals
			ol	cpx	Na-px	Na-am	kaers	bio	opq	aen	plag	feld	ne	ap	
MS8 (Group II)															
?AW83618	tr	mp(<5)	r		g			r			g				t,i	c,d
AW83645	tr	mp(<5)	p		r			r			p				f	
AW83647	tr	mp(<5),v	p,pi		r			r			p				f,c	o
MS9 (Group II)															
AW83471	b	p(5),v	p,px	r,x				g		g					i,c	o
AW83583	b	p(10),v	p	p				g		g					c	
AW83538	b	p(10),v	p	p				g		g					p,c	
AW83417	b	a,v	g,ci	g				g		g					p,ig	
AW83480	b	p(<5),v	r,pi	r				g		r					ig	o,z
AW83689	b	p(15),v	p,px	p,px			p	p		g					ig,c	o
AW83650	b	mp(15),v	p	p				g		g					ig	
AW83558	b	p(10),v	p	p,px				g		g					i,c	o
AW83401	b	p(5),v	p	p				g		g		r,x			gl	o
AW83706	b	mp(15),v	p	p				g		p					ig,c	
AW83614	b	p(10),v	p,px	p				p		p,x		r,x			ig	
AW83662	ab	p(10),v	p,px	p,gc,px				g		g					ig,c	o
?AW83413	t	p(10),v	p,px	p,gc			p,po	g		r,x		r,x			i,c	
MINNA BLUFF																
MB1 (Group II)																
AW82105	b	p(10),v	p,pi	p				g		g					ig	c
AW82124	b	p(10),v	p,ps	p				g		g					ig	z
AW82059	b	p(15)	p,pi	p,px			r	p		r,x				g	i	c
AW82113A	b	p(<5)	p,pi,px	p,gc				g		g		r,x			ig	
AW84797	t	p(20)	p,pi,px	p,gc			r,co	g		r,x		r,x			i	c

Table 6.1 (continued)

Sample Number	Rock Type	Texture	Mineralogy ol	cpx	Na-px	Na-am	kaers	bio	opq	aen	plag	feld	ne	ap	G'mass Texture	Secondary Minerals
MB1 (continued)																
AW82140	t	p(10),v	p,pi	p,gc				r			g				i	
AW82046	t	p(5),v	p,pi	p,gc			r,po	g			r,x				i	
AW82296	t	p(5),v	p,px,pi	p				g			g				i	c,z
AW82103	t	a,v	g,ci	g				g			g				p	c
AW82116	t	a	g,pi	g				g			g			g	p	c
AW82109	t	mp(5)	g,pi	r			r,po	g			g				p	c
AW82049	t	mp(<5),v	g,ci	g			r	g			g				p	c,z
AW82110	h	p(<5),v	g,ci	p			r,po	g			p			g	ig	c
AW84768	pt	p(10),v	g,ci	p,gc			p,po	r			p	?g		g	i	c
AW84796	pt	p(10)	g,pi	p			p,po	r			p,px				c	c
AW82097B	tp	p(20)		r			r	r			p			g	gl	c
W84-3	tp	p(5),v		r			p	p			p			g	tr	
AW82072	tp	mp(<5),v		r			p	g			p				ig	
AW82056	bm	p(<5),v		r			p,po	g	?g	p		r		r	i	c,z,o
W8413-PM	tr	mp(<5)		g			r,co		g			r			g	c
AW84791	tr	p(5)		g					g	r,x		p			t	c,o
W84-2	tr	p(5)		r				r	g			p			i	o
MB2 (Group II)																
AW82163	t	p(<5),v	p,px	r,px				r			r,x	?g			p	z
AW82077	t	p(5),v	g,pi	r			p,po	r			r,px	r,px		r	ig	
AW86887	pt	p(<5),v	g	g				g			r				ig	
AW82149	tp	p(5),v	r,x	r	r,x		p,po	r,x			r	p		r	i	o,c
AW82156	tp	p(<5)	r,pi	r,gc,px			p,po	g			p	g		r	t	o
AW84777	tp	p(<5)		g			p,po	p			p	p			f	o
AW82141	tp	p(<5),v		r,x	g		p,po	g			r	g			ig	o
AW82150	p	p(5)		r,x	r		p,co	r			r	p			ig	
AW82078	p	p(<5),v					r	g				p		r	i	
AW82165	p	mp(<5),v			g		p,co	g				g			i	

Table 6.1 (continued)

Sample Number	Rock Type	Texture	Mineralogy ol	cpx	Na-px	Na-am	kaers	bio	opq	aen	plag	feld	ne	ap	G'mass Texture	Secondar Minerals
MT DISCOVERY																
MD1 (Group II)																
AW84761*	pt	p(5),v	r	r			p,po		p		p	p		i	pk	
AW84758	tp	p(10),v	p	p			i		p		p	p		p	h	d
AW86899	tp	p(25),v	p	p			r		p		p	p		p	h	
AW86718	tp	p(25)	p	r			r		p		p	p		p	h,c	o
AW86950	tp	p(20),v	p	p					p		p	p		p	h	
AW86901	tp	p(25),v	p	p					p		p	p		p	gl	o
AW86895*	tp	p(5),v					p,po		r		p	p			pk,f	o
AW84756	tp	mp(5),v		r			p		p		p	r			h,c	
AW84722	tp	p(<5)			p,po				p			p			g	
AW84721	bm	mp(5),v			r		p,po		p		p	p		r	t	
AW84719	tr	p(<5),v		r			p		p		p	p			t	o
AW86922	p	p(5),v		r,x	r		p,po		p		p	p		i	t	o
AW84754	p	p(5),v			r		p		p		r	p			gl	d
AW84970	p	p(20),v			g				p			p			g	
AW83438	p	p(10),v			g		p,po		g		r	p		i	ig	
AW86889	p	a,v	r,x		g				g			g		i	ig	o,c
AW84720	p	p(<5)			g		r,po		g			r		r	t	o
AW84744	p	a,v			g				g			g			t,c	
AW84735	p	mp(<5),v			g				g			p			t,c	o
AW86965A	p	p(5),v			g				g			p			t	
AW84725	p	p(<5),v			r				p			p			t	o
AW84741	p	p(10)			r			p	p		p	p			t,c	o
AW84745	p	p(5),v							g		r	p			t	
AW86881	p	p(< ,v		r,x	p		p		g			p			t	
AW86100	p	p(<5),v					p,po		g		r	g			t	

Table 6.1

Sample Number	Rock Type	Texture	Mineralogy											G'mass Texture	Seconda Mineral
			ol	cpx	Na-px	Na-am	kaers	bio	opq	aen	plag	feld	ne	ap	
MD2 (Group II)															
AW86101	b	p(<5),v	p	r				r			g				ig	
AW84733	b	p(10),v	p	p,gc			r,po,x	r			p,x		?g		c	
AW86102	b	p(5),v	p	p,px,gc				r			g	r,x			ig	z
AW84738	b	p(5),v	p	p,gc				r			r,x				ig	
AW84740	b	p(5),v	p	p				g			g				c	o
AW84723	b	p(5),v	p,pi	r,gc				g			r,x				c	o
AW86944	b	mp(5),v	p	p				r			g				ig	
AW84728	t	p(5),v	p,px	p,gc				r			g				ig	
AW84750	t	p(10),v	p,px	p				p			g				ig	o
AW84763	t	p(5),v	p	r,gc				g			r,x		?g		ig	
AW84748	t	p(10),v	p,px	p,gc			r,po	p			r				ig,c	
AW86909	t	p(25),v	p,pi	p				p			p				p,ig	
AW86943	t	mp(<5)	r	r,gc	r,x		r,co	r			r,x				ig	
AW84749	t	mp(10),v	p	p				g			g				p	o
AW84742	t	p(<5),v	p	p				p			p,px				ig	
AW86891	t	mp(10)	p,px	p,gc			p,po	g			g				ig	
AW86910	t	p(15)	r	p				p			p,px				c	
AW86898	t	p(10),v	p	p,gc				p			p,px				g	
AW84753	pt	a,v	g	g				g			g				p,g	
AW86947	pt	p(5),v		p,gc			p,po	p			p,x	r,x			c	
AW83435	pt	a,v	g	g				g			g		?g		p,h	
AW86883	p	a,v			g		g,po	g				g			f	o
MT MORNING																
MM1 (Group II)																
AW86124	pt	p(5),v	r,x	r			p	r,x			p,x	r,x			t,c	
AW86122	pt	p(10)		p			p,po	g			p,x	p,x			ig	
AW86121	pt	p(5),v		r,px	g		p,po	g			p,x	r,x	?g	r	f	o
AW86123	p	p(5)	r,x	r	g		p,po,x	g			r,x	p,x			g	o
AW86127	p	p(<5),v		r	g		p,po	g				p			t,ig	o,z

Table 6.1 (continued)

Sample Number	Rock Type	Texture	Mineralogy										G'mass Texture	Secondar Minerals
			ol	cpx	Na-px	Na-am	kaers	bio	opq	aen	plag	feld	ne	ap		
MM2 (Group II)																
AW86057	b	p(15),v	p,px	p,px			i	p,px			p,px		?g		ig,c	
AW86119	b	p(20),v	p,px	p				g			g				ig	
AW86096	b	p(20),v	r	p,px				r			p,x	r,x			p,c	o
AW86058	b	mp(5),v	p	p				g			?g				ig,c	
AW86120	b	mp(<5),v	p	p				g			g				p,c	
AW84715	t	p(5),v	p,px	p,px	r,x		r,po	r			r	r,x			p,c	z
AW86098	t	P(<5),v		g				g			r		?g		ig	o
AW86128	p	p(<5),v			r							p			gl	d
FOOTHILLS OF ROYAL SOCIETY RANGE																
F2 (Group II)																
AW86094	b	p(10)	p	p				r			g		?g		ig	
AW86095	b	p(10),v	p	p				g			g				i,c	
AW86088	b	p(15)	p, px	r				p			p,px				i,c	
AW86089	t	mp(5)	p	g				p			p	g	?g		i,gl	

Abbreviations:

Rock type: b - basanite, ab - alkali basalt, t - tephrite, h - hawaiite, pt - phonotephrite, m - mugearite, tp - tephriphonolite, bm - benmoreite, p - phonolite, tr - trachyte, ptr - peralkaline trachyte, f - foidite.

Texture: p - porphyritic, mp - microporphyritic (percentage phenocrysts and microphenocrysts given to nearest 5 % in parentheses), a - aphyric, v - vesicular, cm - cumulate.

Mineralogy: ol - olivine, cpx - clinopyroxene, Na-px - sodic pyroxene, Na-am - sodic amphibole, kaers - kaersutite, bio - biotite, opq - opaque oxides, aen - aenigmatite, plag - plagioclase, feld - alkali feldspar, ne - nepheline, ap - apatite, p - present as phenocrysts (>1 %), r - rare as phenocrysts (<1 %), g - groundmass only, x - xenocrystic, px - partially xenocrystic, ci - completely iddingsitized, pi - partially iddingsitized, ps - partially serpentinized, co - completely oxidized, po - partially oxidized, gc - green cores observed, i - present as inclusions only.

Groundmass texture: i - interstitial, ig - intergranular, g - granular, c - cryptocrystalline, gl - glassy, h - hyalopilitic, p - pilotaxitic, so - subophitic, t - trachytic, f - felted, sp - spheriolitic, pk - poikilitic.

Secondary minerals: c - carbonates, o - oxides, z - zeolites, d - devitrified.

ly indistinguishable from the basanites.

Seriate colorless olivine is the most common phenocryst phase. Larger crystals are 1 - 2 mm across and may be subrounded or embayed. Smaller crystals are typically euhedral. Small chromian spinel or titanomagnetite inclusions are present in many crystals. Seriate, colorless to pale brown, euhedral to subhedral, augite phenocrysts are usually less than 2 mm across, and are subordinate to olivine. They may have a rounded core of pale green or olive green, often sieve-textured pyroxene. Small titanomagnetite inclusions are common, especially near crystal margins. Plagioclase and clinopyroxene xenocrysts may be present. Kaersutite xenocrysts are also present rarely in basanites from Group II. Anhedral clinopyroxene xenocrysts in AW86102 are characterized by trails of fluid inclusions, suggesting that the xenocrysts are derived from disintegration of a source that had undergone solid state deformation. Plagioclase, olivine, augite, opaque minerals and glass typically form a fine grained and vesicular, intergranular to interstitial, groundmass. The only difference between basanites from Groups I and II is that some Group I basanites contain plagioclase phenocrysts or microphenocrysts (e.g., AW83545, AW83454, AW86036).

6.3 TEPHRITES, HAWAIITES, PHONOTEPHRITES, AND MUGEARITES

Tephrites and phonotephrites are typical of Group I rocks from the upper Gandalf and Mason volcanic complexes. Hawaiites and mugearites occur in the lower parts of these complexes. Group II tephrites are found throughout the DVS, and a single hawaiite was collected fror the MBl. Group II phonotephrites were collected at Minna Bluff, Mt

Discovery and Mt Morning, and are reported from Brown Peninsula (Kyle et al., 1979). No mugearites are known from Group II.

Tephrites, hawaiites, phonotephrites and mugearites from Group I are aphyric to weakly porphyritic (</= 5% phenocrysts), and non-vesicular to weakly vesicular. Scattered phenocrysts or microphenocrysts of plagioclase are present in a few samples. Rare, olivine phenocrysts occur in tephrite AW83607. Kaersutite is not present. These samples usually have a medium grained, intergranular groundmass comprising plagioclase, partially iddingsitized olivine, augite, titanomagnetite, and apatite. Apatite commonly forms inclusions in the groundmass olivine.

Most tephrite, hawaiites, and phonotephrites from Group II have 5 - 25 % phenocrysts. About 10% of the samples were aphyric, and these came from the summit area of Mt Discovery and the lower sequence at Minna Bluff.

Olivine phenocrysts are similar to those in the basanites. Seriate, colorless to pale brown augite phenocrysts, some with rounded green cores, increase in abundance in tephrites and may be zoned to pinkish titanaugite at the rim. Small titanomagnetite inclusions are common. The abundance of both olivine and clinopyroxene phenocysts decreases beyond the ultrabasic-basic compositional boundary (Figure 6.2). Rounded titanomagnetite microphenocrysts, up to 0.5 mm across, are present in some samples. Plagioclase (up to 2 mm long) and pleochroic greenish-brown to dark brown kaersutite (up to 1 mm across) form phenocrysts in the tephrite field, and become increasingly abundant towards the phonotephrite boundary. Anhedral to subhedral kaersutite is the most abundant phenocryst in phonotephrite samples, and nearly always shows evidence of partial, late stage alteration to

titanomagnetite - clinopyroxene aggregates. In some samples kaersutite is preserved only as opaque pseudomorphs. Apatite inclusions are common in kaersutite and are preserved in the opaque pseudomorphs. Apatite may also form a microphenocryst phase. Tephrite and phonotephrite lavas usually have a vesicular, interstitial to cryptocrystalline, groundmass of plagioclase, clinopyroxene, olivine, opaque oxides, apatite, +/- interstitial ?nepheline, and interstitial cryptocrystalline material.

6.4 TEPHRIPHONOLITES

Tephriphonolites samples were collected at Minna Bluff and Mt Discovery. They are also reported from Brown Peninsula (Kyle et al., 1979). All are Group II rocks.

The tephriphonolites fall into two groups. Those forming the core of Mt Discovery are coarsely porphyritic with 10 - 25 % phenocrysts. Large plagioclase to anorthoclase glomerocrysts, 1 - 20 mm long predominate. Rounded olivine, augite, titanomagnetite and apatite microphenocrysts (<0.5 mm across) are scattered throughout. Kaersutite is present in AW86899 as a minor phenocryst phase, and in AW84758 as inclusions in plagioclase. The groundmass of these tephriphonolites is typically vesicular, and glassy.

The second group of tephriphonolites are associated with both the lower and upper sequences at Minna Bluff, and the later phonolite lavas of Mt Discovery. Except for AW82097B which has 20% phenocrysts, these samples are aphyric to weakly porphyritic. Seriate plagioclase phenocrysts and glomerocrysts are the most abundant. Euhedral to subhedral crystals are typically 0.5 to 2 mm long, and much smaller

than the feldspar phenocrysts in the tephriphonolites forming the core of Mt Discovery. Kaersutite is a common phenocryst or microphenocryst phase. Euhedral, pale brown, colorless or pale green clinopyroxene is common as microphenocrysts. Small relict olivines may be present. Rounded titanomagnetite and euhedral apatite microphenocrysts occur in some samples. Groundmass textures vary from glassy to intergranular to trachytic, and are comprised of feldspar microlites, pale green clinopyroxene, and opaque oxides, with accessory apatite in some samples.

6.5 BENMOREITES

Group I benmoreites are limited to the upper sequences in the Gandalf and Mason volcanic complexes. Two benmoreites were sampled from Group II. One is associated with the phonolite flows on Mt Discovery (AW84721) and the other came from the lower Minna Bluff sequence (AW82056). Only very small amounts of benmoreite were erupted in either Group. The benmoreites are aphyric to weakly porphyritic. Those from Group I are non-vesicular, whereas the two samples from Group II are vesicular.

Porphyritic Group I rocks contain plagioclase phenocrysts. Rare olivine phenocrysts are present in AW86041, and rare, partly altered kaersutite phenocrysts are present in AW85839. This is the only occurrence of kaersutite in Group I samples. The intergranular to trachytic groundmass comprises feldspar microlites, pale green clinopyroxene, opaque oxides, and sometimes olivine and apatite. The olivine is partially to completely iddingsitized.

Benmoreites in Group II contain plagioclase to anorthoclase phenocrysts, and partially altered kaersutite phenocrysts. Rare apatite and pale green clinopyroxene microphenocrysts are also present.

Titanomagnetite microphenocrysts are present in AW84721. Olivine is not present in Group II benmoreites. The intersitial or trachytic groundmass is comprised of feldspar microlites, pale green clinopyroxene, and opaque oxides.

6.6 PHONOLITES

Phonolites are limited to Group II samples, with the exception o AW83642, which is petrographically similar to other Group I trachytes Group II phonolites were sampled at Mt Morning, Mt Discovery, and the upper Minna Bluff sequence. Phonolites are also reported from Black Island (Cole and Ewart, 1968).

Most phonolites contain 5% or less phenocrysts, although samples with up to 20% phenocrysts were collected from Mt Discovery. Seriate, euhedral phenocrysts of plagioclase to anorthoclase feldspar, up to 2 mm long, are most common. Euhedral to anhedral kaersitite microphenocrysts in various stages of alteration, are present in many samples. AW84741 contains no kaersutite, but has microporhyritic flakes of dar brown biotite, most of which are preserved as inclusions in feldspar. Subhedral microporphyritic, pale green clinopyroxene is present in many samples, and may be packed with secondary opaque oxide inclusions. Microphenocrysts of titanomagnetite and rarely apatite, may also be present, but apatite is more commonly preserved as inclusions in kaersutite. Small, rounded and overgrown olivine and clinpyroxene xenocrysts are present rarely. The groundmass comprises alkali feldspar microlites, green clinopyroxene, and opaque oxides. In sample AW82078 kaersutite replaces pyroxene as a groundmass mineral, and in AW86881 clinopyroxene and kaersutite coexist in the groundmass.

Groundmass textures are typically trachytic to felted. Granular, interstitial and glassy varieties are less common.

6.7 TRACHYTES

Most trachyte samples occur in the lower Gandalf and Mason volcanic complexes; eighty percent are peralkaline. Trachyte samples from Group II include three from Minna Bluff (MB1), three from Mason Spur (MS8), and a single sample associated with the phonolite flows on Mt Discovery (MD1). None of the Group II trachytes are peralkaline.

Trachytes from Group I are aphyric to weakly porphyritic. About half are vesicular. Euhedral to subhedral anorthoclase is the dominant, and commonly the only phenocryst phase in porphyritic trachytes from Group II. Rare plagioclase phenocrysts are preserved in several samples, but are usually overgrown by alkali feldspar. Feldspar phenocrysts vary in size up to 5 mm in length, and may be glomeroporphyritic. Rare phenocrysts and microphenocrysts of green pyroxene and/or titanomagnetite are present in a few samples. The green pyroxene may be packed with opaque oxide inclusions. Trachytic to felted groundmass textures are typical. The groundmass of peralkaline trachytes comprises alkali feldspar and green clinopyroxene or sodic pyroxene, with interstital aenigmatite, and scattered sodic amphibole. Relict titanomagnetite grains are preserved in a few samples. The groundmass of non-peralkaline trachytes is similar, except that titanomagnetite grains are typically present and aenigmatite and alkali amphibole are generally absent. Nearly all these trachytes have suffered secondary alteration, including oxidation, zeolitization, and deposition of carbonates. Aenigmatite is usually altered to hydrated iron oxides.

Group II trachytes are mineralogically more varied than trachytes from Group I. Minna Bluff trachytes are similar to those in Group I, except for the presence of completely altered kaersutite phenocrysts in W8413-PM. Although samples are not peralkaline, aenigmatite rather than titanomagnetite occurs in the groundmass. It is not accompanied b sodic amphibole. Feldspar and rare green pyroxene phenocrysts, and titanomagnetite microphenocrysts are accompanied by kaersutite phenocrysts in the Mt Discovery trachyte. MS8 trachytes at Mason Spur are distinctive in that they contain euhedral microphenocrysts of olive green, fayalitic olivine, as well as green pyroxene, titanomagnetite, and alkali feldspar microphenocrysts.

6.8 RHYOLITES AND DACITES

Peralkaline rhyolites and dacites are reported from Gandalf Ridge (Muncy, 1979). These samples are petrographically similar to Group I peralkaline trachytes.

6.9 XENOLITHS IN BASANITES AND TEPHRITES

Ultramafic xenoliths are present in some basanites in the Foothills of Royal society Range, and include dunite, pyroxenite, wehrlite, websterite, lherzolite, amphibolite, glimmerite, and gabbro (McIver and Gevers, 1970; Kirsch, 1981; Kyle et al., 1987; Gamble and Kyle, 1987). Dunite, pyroxenite and amphibolite xenoliths also occur in basanites at Riviera Ridge and Hurricane Ridge. Amphibolite AW86999, from Riviera Ridge, was examined in thin section. It is comprised of intergrown kaersutite and subordinate plagioclase crystals, up to 1.4 mm across, in a granular matrix of anhedral kaersu-

tite, plagioclase, alkali feldspar, apatite and augite crystals, and vesicular, opaque glass; and exhibits an orthocumulate texture.

Crustal xenoliths occur in many basanites and tephrites throughout the DVS. Berg (1984; 1985) has examined xenoliths from several DV locations and has found considerable diversity, even in xenoliths fro the same location. Most are basic gneisses or granulites comprised principally of calcic plagioclase, orthopyroxene and clinopyroxene. Orthogneiss, quartzite and calc-silicate lithologies also occur.

6.10 XENOLITHS IN THE MT DISCOVERY PHONOLITES

Many phonolites at Mt Discovery carry numerous, pale grey, round ed vesicular xenoliths up to 5 cm across (e.g., AW84761, AW86895). These comprise scattered plagioclase and unaltered kaersutite phenocrysts, and rare clinopyroxene to pale green clinopyroxene microphenocrysts. The coarse-grained alkali feldspar matrix encloses partially altered kaersutite needles. These xenoliths do not exhibit cumulate textures.

6.11 PETROGRAPHIC COMPARISON OF GROUPS I AND II

A summary of the generalized crystallization histories of Group and II magmas is given in Table 6.2. The main petrographic differences between the Groups are:

1. the general degree of vesiculation and abundance of phenocrysts in Group II ultrabasic and basic lavas, as compared to Group I lavas of similar composition,
2. the variety and abundance of xenoliths and xenocrysts in Group II lavas, and the absence of "green cored" pyroxenes in Group I,
3. the usually finer grained and glassier groundmass texture of

Table 6.2 - Generalized paragenesis of Group I and II magmas. It is uncertain whether peralkaline trachytes are derived from non-peralkaline trachytes of whether they are generated directly from less evolved magmas.

GROUP I

Basanite	Tephrite/ Hawaiite	Phonotephrite/ Mugearite/ Benmoreite	Trachyte	Peralkaline Trachyte
olivine + pale brown clinopyroxene + titanomagnetite	plagioclase + olivine + pale brown clinopyroxene + titanomagnetite + apatite	plagioclase + olivine + pale green clinopyroxene + titanomagnetite + apatite	alkali feldspar + sodic pyroxene + titanomagnetite	alkali feldspar + sodic pyroxene + sodic amphibole + aenigmatite

GROUP II

Basanite	Basanite	Tephrite	Phonotephrite Tephriphonolite	Phonolite
olivine + Cr spinel	olivine + pale brown clinopyroxene + titanomagnetite	olivine + pale brown clinopyroxene + plagioclase + kaersutite + titanomagnetite + apatite	plagioclase + kaersutite + pale brown clinopyroxene + titanomagnetite + apatite	alkali feldspar + kaersutite + pale green clinopyroxene + titanomagnetite

Benmoreite	Trachyte
plagioclase + kaersutite + pale green clinopyroxene + titanomagnetite + apatite	alkali feldspar + kaersutite + pale green clinopyroxene + titanomagnetite

ultrabasic to intermediate Group II lavas relative to those of Group I,

4. the abundance of kaersutite in Group II lavas, and its general absence in lavas from Group I, and
5. the earlier crystallization of plagioclase in Group I lavas.

Kaersutite is not present in Group II trachytes at Mason Spur (MS8). It is less abundant in lavas associated with each of the large stratovolcanoes, and in the MB1 sequence at Minna Bluff, than in other Group II samples. Plagioclase is typically more abundant in these tephriphonolites, phonolites, benmoreites and trachytes with diminished kaersutite.

Chapter 7

MINERALOGY

7.1 INTRODUCTION

Phenocryst and groundmass minerals were analysed in 20 representative samples (Table 7.1; Figure 7.1) using the electron microprobe at Victoria University of Wellington, New Zealand. Analytical procedures and results are given in Appendix 4. Previous mineralogical investigations in the DVS are limited to the mineralogy of xenoliths and their basanite hosts at Foster Crater (Kirsch, 1981; Gamble and Kyle, 1987) and Brandau Vent (McIver and Gevers, 1970), in the Foothills of Royal Society Range.

The following discussion makes use of a magnesium index number (mg) which is defined as 100Mg/(Mg + Fe*), where Mg and total Fe (Fe* are in atomic percent. Mn is not included in the denominator or combined with estimates of Fe^{2+}, because while Mn readily substitutes fo Fe^{2+}, the effect of the Mn component in a solid solution can signifcantly affect mineral stability (Lindsley, 1980), and hence its occurrence.

7.2 OLIVINE

7.2.1 Introduction

Olivine was analysed in eight Group II samples (Figure 7.2), an ranges in composition from Fo88-20. Previous workers analysed olivines, of Fo_{93-88} composition, in basanites and xenoliths at Foste Crater and Brandau Vent (McIver and Gevers, 1970; Kirsch, 1981). Representative analyses are given in Table 7.2. Cation formula are calculated on the basis of four oxygens.

Table 7.1 - Rock samples used for microprobe analysis. Stratigraphic units are described in Chapter 3; the chronological division into Groups I and II in chapter 5.3; and rock nomenclature in Chapter 8.3.

Sample Number	Rock Type	Stratigraphic Unit	Group
MASON SPUR			
AW83502A	peralkaline trachyte	MS3	I
AW83503	peralkaline trachyte	MS3	I
AW83533	peralkaline trachyte	MS5	I
AW83513	benmoreite	MS7	I
AW83647	trachyte	MS8	II
MINNA BLUFF			
AW82105	basanite	MB1	II
AW84797	tephrite	MB1	II
AW82109	tephrite	MB1	II
AW84796	phonotephrite	MB1	II
AW82097B	tephriphonolite	MB1	II
AW82056	benmoreite	MB1	II
AW82078	phonolite	MB2	II
AW82150	phonolite	MB2	II
MT DISCOVERY			
AW84738	basanite	MD2	II
AW84750	tephrite	MD2	II
AW84742	tephrite	MD2	II
AW84761	phonotephrite xenolith in phonolite	MD1	II
AW84758	tephriphonolite	MD1	II
AW84721	benmoreite	MD1	II
AW84741	phonolite	MD1	II
AW84725	phonolite xenolith in tephrite	MD1	II

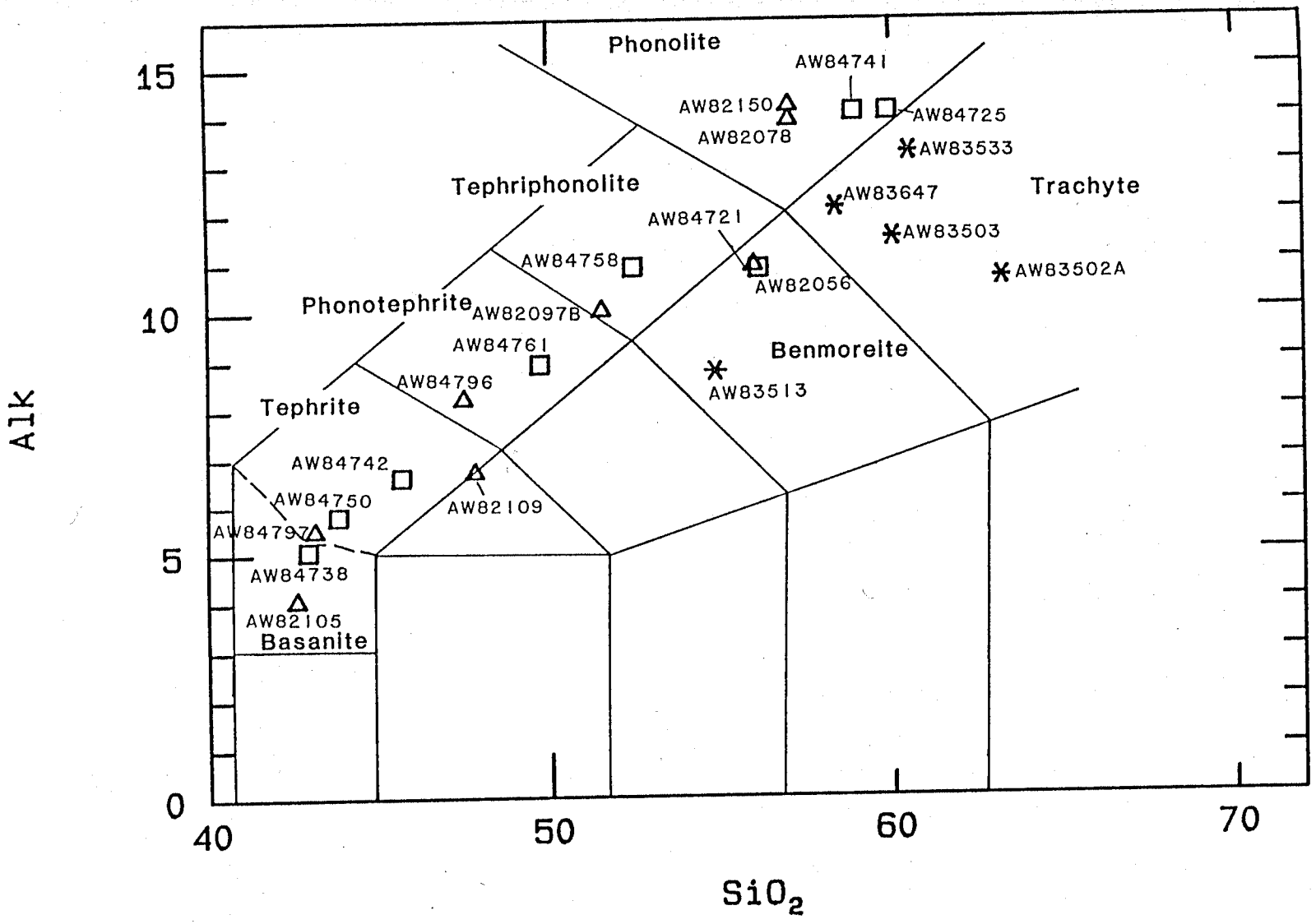

Figure 7.1 - Total alkalis (Alk) - silica diagram (determinations plotted as oxide wt. %) showing the composition and nomenclature (after Le Bas et al., 1986) of samples chosen for microprobe analysis of mineral phases. Δ Minna Bluff, □ Mt Discovery, * Mason Spur.

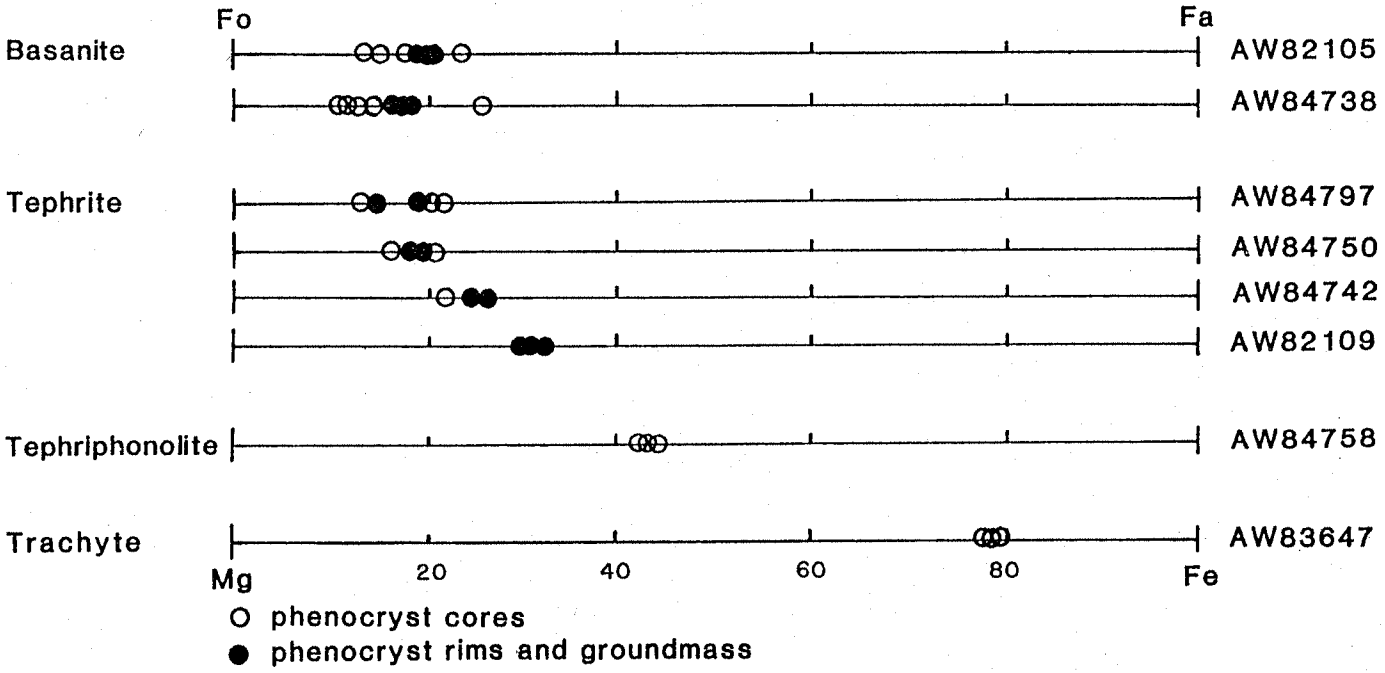

Figure 7.2 - Variation of Mg and Fe (expressed in atom %) for olivines analysed from DVS rocks. All analyses are of olivines from Group II samples.

Table 7.2 - Representative microprobe analyses of olivine from the Discovery volcanic subprovince. Total iron is given as FeO*. Percent forsterite (Fo) is also given. Cation formula are calculated on the basis of four oxygens.

	1	2	3	4	5	6
Analysis No.	P5.C	P1A.R	G1.C	G3.C	P1.C	S1.C
SiO2	40.28	39.17	37.90	36.31	35.55	31.75
TiO2	0.00	<0.10	0.22	<0.10	<1.10	0.00
Al2O3	0.06	0.04	0.04	<0.04	<0.06	0.00
FeO*	14.71	18.14	23.14	27.62	34.97	55.46
MnO	0.22	0.23	0.54	0.62	1.11	2.36
MgO	44.24	41.86	37.29	34.22	27.45	8.02
NiO	0.18	<0.14	<0.16	<0.15	<0.16	<0.14
CaO	0.27	0.32	0.31	0.41	0.43	0.85
Total	99.96	99.76	99.44	99.18	99.51	100.05
Si	1.100	1.000	0.998	0.980	0.997	1.018
Ti	0.000	0.000	0.004	0.000	0.000	0.000
Fe2+	0.310	0.390	0.501	0.630	0.820	1.487
Mn	0.020	0.000	0.012	0.010	0.026	0.064
Mg	1.650	1.590	1.464	1.380	1.146	0.383
Ca	0.010	0.010	0.009	0.010	0.013	0.029
Total	2.980	2.990	2.997	3.010	3.003	2.982
Fo(%)	84.2	80.3	73.7	68.7	57.5	20.5
mg	0.84	0.80	0.74	0.69	0.58	0.21

1. Phenocryst core in basanite AW82105, MB1, Minna Bluff.
2. Phenocryst rim in basanite AW82105, MB1, Minna Bluff.
3. Groundmass olivine in tephrite AW84742, Mt Discovery.
4. Groundmass olivine in tephrite AW82109, MB1, Minna Bluff.
5. Phenocryst core in tephriphonolite AW84758, Mt Discovery.
6. Microphenocryst core in trachyte AW83647, MS8, Mason Spur.

7.2.2 Occurrence

Mg-rich olivine ($Fo_{<50}$) is an important seriate phenocryst and groundmass phase in lavas of ultrabasic composition from both Groups I and II. Large, rounded and embayed phenocrysts are also present in many Group II ultrabasic and basic lavas. The abundance of olivine phenocrysts decreases gradually in Group I rocks as their composition changes from hawaiite to benmoreite. In contrast, once kaersutite begins to crystallize in Group II rocks, there is a sharp reduction in the abundance of olivine phenocrysts. Fe-rich olivine is present in Group II trachytes from MS8 at Mason Spur, but is not found in other Group I or II trachytes.

Olivine occurs as xenocrysts, and is a constituent of many ultramafic xenoliths in some basanites from the Foothills and Riviera Ridge areas. These olivines, and associated olivine xenocrysts may display deformation lamellae and oxidation (McIver and Gevers, 1970; Kirsch, 1981). Olivine also forms rare xenocrysts in some Group II phonolites Olivines in Group I rocks tend to be more iddingsitized than those from Group II.

7.2.3 Chemical Composition

Olivine in basanites and tephrites ranges from $Fo_{88.3}$ to $Fo_{68.7}$ Olivines in the tephriphonolite sample have a composition of $Fo_{57.7-56.0}$, and olivine microphenocrysts in trachyte AW83647 have compositions of $Fo_{19.9-20.5}$. A decrease in the mg value from core to rim is typical of most phenocrysts, which are usually rimmed by olivine of groundmass composition. Reverse compositional zoning was detected in some larger phenocrysts from AW82105, AW84797, and AW84738, and is consistent with the petrographic observation of rounding and embay-

ment. A progressive decrease in the mg value of phenocryst rims and groundmass olivine occurs from basanite to trachyte.

CaO and MnO are ubiquitous minor components in olivine, and increase with FeO* content (Figures 7.3 and 7.4). CaO/FeO* ratios are typical lower for the cores of reversely zoned phenocrysts, compared to other olivines analysed from the same sample. Trace amounts of NiO and Al_2O_3, were detected in about half the samples.

7.2.4 Discussion

The demise of olivine in Group II lavas is associated with the increasing abundance of kaersutite. This relationship has been noted elsewhere in the MVG (Kyle, 1976; 1981c; Moore, 1986), and is consistent with experimental studies in which kaersutite is stabilized at the expense of olivine and clinopyroxene (Crawthorn, 1976a). This stabilization of kaersutite is largely dependent on melt composition (Duke, 1976), especially the a_{Na2O} (Cawthorn, 1976a), although increasing f_O will also contribute to the destabilization of the fayalite component of olivine with falling temperature (Nitsan, 1974). The difference in the distribution of olivine between Groups I and II is unlikely to reflect differences in f_{O2}, because the variation in pyroxene composition suggests that most rocks from both Groups I and II crystallized under similar f_{O2} conditions (section 7.4.4).

The normal zoning exhibited by most olivine phenocrysts probably reflects changes in melt and coexisting mineral compositions, and possibly crystallization under conditions of falling temperature. The reverse-zoned olivine phenocrysts may have crystallized from the host at cooler temperatures. Alternatively, they could have crystallized

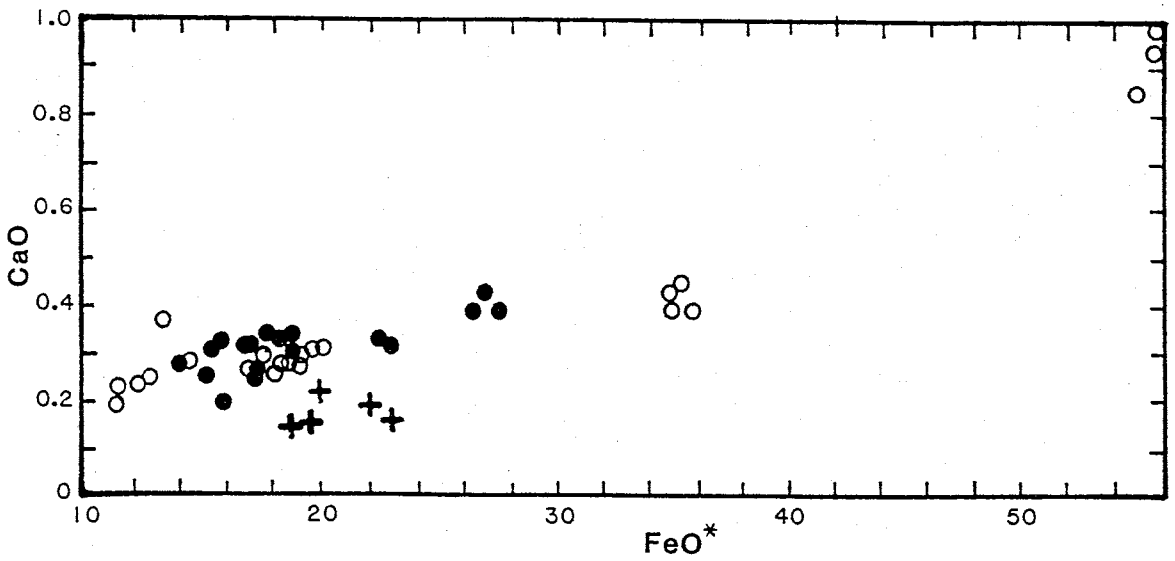

Figure 7.3 - Plot showing the variation of CaO (wt. %) with FeO* (wt. %) for olivines from Group II samples. ○ phenocryst cores, ● phenocryst rims and groundmass, + rounded and embayed cores.

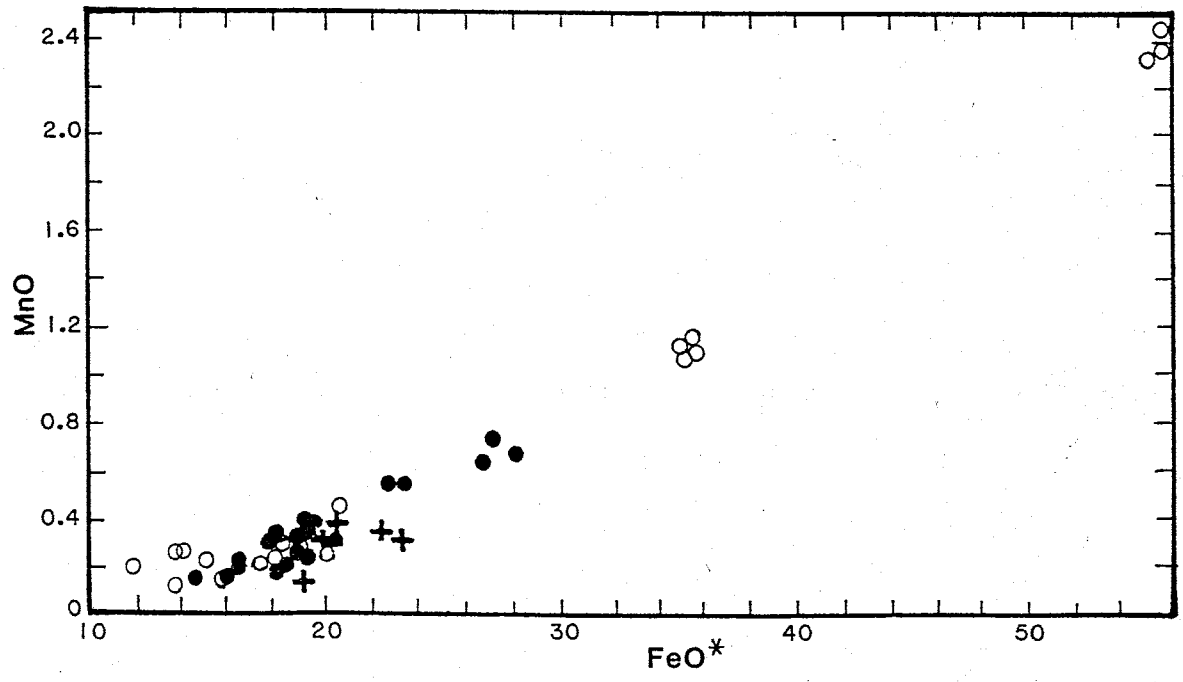

Figure 7.4 - Plot showing the variation of MnO (wt. %) with FeO* (wt. %) for olivines from Group II samples. ○ phenocryst cores, ● phenocryst rims and groundmass, + rounded and embayed cores.

from a slightly more silicic magma and become incorporated into the host later. Temperature increases in the host could have resulted from convection of the magma to a hotter part of the magma chamber, or from the influx of hotter magma into the magma chamber. If the cores of reverse-zoned olivines crystallized from a different melt, they may have become incorporated into their host by crystal settling, or by magma mixing.

The increasing Fe content of olivine is accompanied by an increase in MnO. MnO/FeO* ratios remain fairly constant for all DVS olivines (Figure 7.4). Comparison of the MnO/FeO* trends in olivines from Group II rocks with other olivines from the MVG (Figure 7.5), suggests that the olivines in Group II basanite to tephriphonolite hosts crystallized under similar conditions to olivines in DVDP lineage rocks on Ross Island. In contrast, olivines from the trachyte AW83647 lie on the trend defined by olivines from The Pleiades (Kyle, 1986). This suggests that the crystallization history of the MS8 trachytes may have been considerably different to that of other Group II rocks. Although partitioning of Mn between olivine and melt is strongly temperature dependent, the temperature effect decreases as the melt composition becomes more silicic (Watson, 1977). Whereas the initial divergence in MnO/FeO* trends is probably due to crystallization under different regimes of decreasing temperature, the steepenin of the curve for olivines from more silicic rocks probably reflects the increased effect of melt composition and the composition of co-existing mineral phases.

The CaO content of olivine increases with increasing a_{SiO2} in the melt, and decreases with pressure (Stormer, 1973). Temperature ha little effect on the distribution of Ca between olivine and the melt

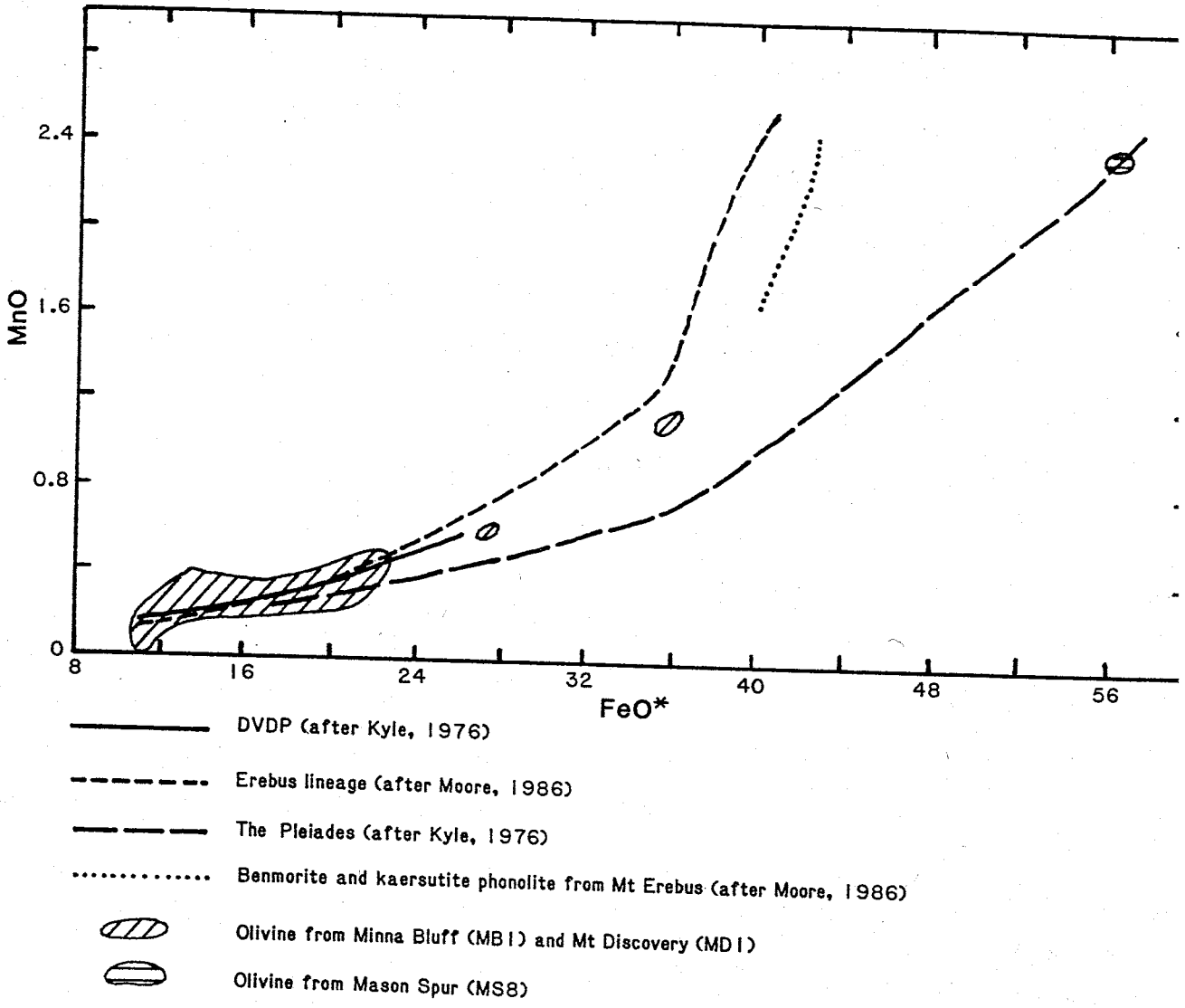

Figure 7.5 - Comparison of DVS olivines and olivines from elsewhere i the McMurdo Volcanic Group. Most olivines from Group II rocks lie on or extend the trend defined by olivines from DVDP lineage rocks, but the fayalitic olivines from the MS8 trachytes lie on the trend define by olivines from The Pleiades in the Melbourne Volcanic Province.

in ultrabasic and basic lavas (Leeman and Scheidegger, 1977). The positive correlation between FeO* and CaO in DVS olivines (Figure 7.3), probably reflects the changing bulk composition of the melt. Lower CaO/FeO* ratios characteristic of the rounded and embayed phenocrysts suggests that these crystals either formed at higher pressures than the seriate phenocrysts, or that they crystallized from less silicic melts than their host lavas.

There are three generations of olivine in ultrabasic and basic Group II lavas. Olivine with Fo_{88-93}, identified in xenoliths at Foster Crater and Brandau Vent, has an inferred mantle origin (McIver and Gevers, 1970; Kirsch, 1981). The other two generations of olivine are much more widespread, and have Fo contents that preclude equilibrium with mantle compositions (Frey and Printz, 1978). The normal zoning and seriate nature of most olivine phenocrysts is clear evidence of their cognate origin. The rounded and embayed phenocrysts with $Fo_{<80}$ are more enigmatic. Their mg values suggest they formed at lower temperatures or crystallized from a more silicic melt than the seriate phenocrysts. In contrast, their CaO content suggests they crystallized at higher pressures or from a less silcic melt than the seriate phenocrysts. The contradictory evidence provided by the mg values and CaO contents strongly suggests that the rounded and embayed phenocrysts did not crystallize from a separate magma. They may have crystallized from the host under conditions of lower temperature and higher pressure, perhaps as cooler magma was forced downwards by convection in a large magma chamber.

6.3 ORTHOPYROXENE

Orthopyroxene ($En_{89.9-57.4}$) is present in ultramafic xenoliths, and as xenocrysts at Brandau Vent and at Foster Crater (McIver and Gevers, 1970; Kirsch, 1981). The orthopyroxene may have exsolution lamellae of clinopyroxene, and kink-banding attributable to solid state deformation. In addition it may be rimmed by an irregular zone of fine grained olivine (McIver and Gevers, 1970) or opaque oxide (Kirsch, 1981). This orthopyroxene has an inferred mantle origin (McIver and Gevers, 1970; Kirsch, 1981). Orthopyroxene at Foster Crater also occurs as exsolution lamellae in clinopyroxene, and as discrete unstrained grains rimmed by opaque oxide.

7.4 CLINOPYROXENE

7.4.1 Introduction

Clinopyroxene was analysed in 19 samples (Figures 7.6 and 7.7), and ranges in composition from diopside to hedenbergite to aegerine. Previous workers analysed clinopyroxene of En_{57-33} composition in basanites and xenoliths at Brandau Vent and Foster Crater (McIver and Gevers, 1970; Kirsch, 1981). Representative analyses are given in Tables 7.3, 7.4, and 7.5.

Cation formula are calculated on the basis of four cations, and charge balanced to give an estimate of Fe^{3+} (Neumann, 1976). When Si Al > 2 this procedure produces identical results to recalculation on the basis of six oxygen followed by iterative charge balancing (Papik et al., 1974). For pyroxenes incorporating Ti into the Z site the results differ. The procedure used here produces more realistic results from a good analysis, but does not provide a test for poor analyses, because the cation total is forced to equal four.

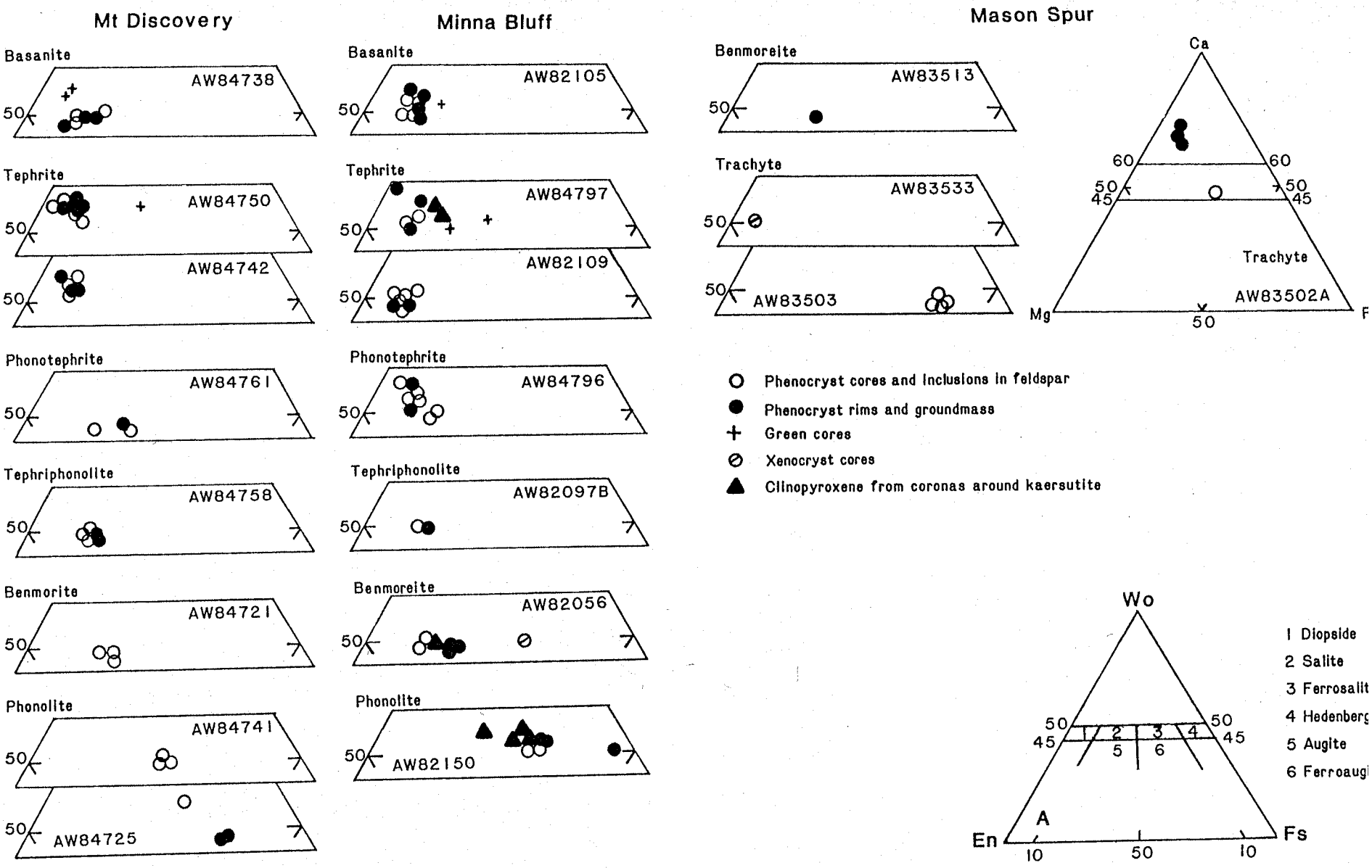

Figure 7.6 - Variation in the Ca-Mg-Fe^{2+} composition of clinopyroxenes from DVS rocks. Except for the sodic pyroxenes of AW83502A, clinopyroxene compositions are shown on an enlarged portion of the Ca-Mg-Fe^{2+} triangle as indicated by the shading. Clinopyroxene

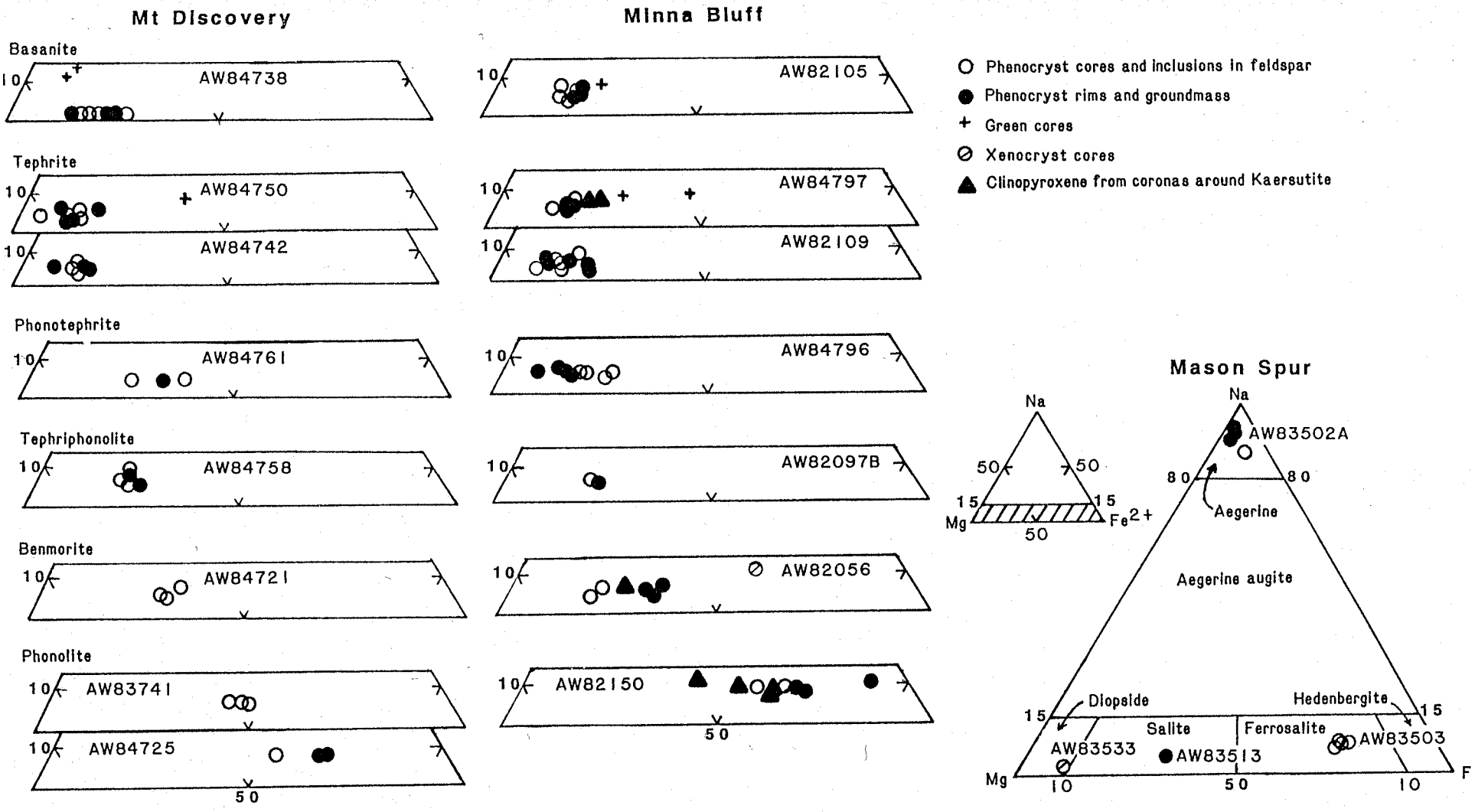

Figure 7.7 - Variation in the Na-Mg-Fe^{2+} composition of clinopyroxenes from DVS rocks. Clinopyroxenes from Mt Discovery and Minna Bluff are shown on an enlarged portion of the Na-Mg-Fe^{2+} triangle as indicated by shading. Pyroxenes from Mason Spur are shown on the full triangular diagram, along with pyroxene nomenclature (Deer et al., 1978).

Table 7.3 - Microprobe analyses of green cores in clinopyroxene from the DVS. Total iron was analysed as FeO*. Fe_2O_3 and FeO are calculated by chargebalancing. Cation formula are calculated on the basis of four cations.

Sample No.	AW84738		AW84750	AW82105	AW84797	
Analysis No.	P4.C	M1.C	P5B.C	P6.C	P8.C	P9.C
Pyroxene Type	F	F	F	F	A	A
SiO2	45.77	45.22	44.08	47.10	48.44	50.37
TiO2	3.37	2.44	3.77	2.65	1.50	1.29
Al2O3	9.73	7.46	7.79	8.56	4.12	3.66
Cr2O3	0.00	<0.13	0.00	<0.14	0.00	0.00
FeO*	7.60	9.64	13.03	8.81	14.92	10.17
MnO	0.15	0.20	0.51	<0.15	0.20	0.36
MgO	11.12	11.63	7.67	11.08	7.85	11.39
CaO	21.72	21.28	22.24	21.30	21.95	21.86
Na2O	1.57	1.24	1.00	0.99	0.93	0.91
K2O	<0.06	<0.06	<0.06	<0.06	<0.05	<0.06
Sum	101.03	99.11	100.09	100.49	100.22	100.01
Fe2O3	5.47	8.13	4.72	1.94	2.87	1.87
FeO	2.67	2.32	8.78	7.07	12.33	8.49
Total	101.57	99.92	100.56	100.69	100.50	100.20
Si	1.676	1.696	1.685	1.748	1.857	1.890
Ti	0.093	0.069	0.108	0.074	0.043	0.036
Al	0.421	0.330	0.351	0.374	0.186	0.161
Cr	0.000	0.000	0.000	0.000	0.000	0.000
Fe3+	0.151	0.230	0.136	0.054	0.093	0.053
Fe2+	0.082	0.073	0.281	0.219	0.395	0.267
Mn	0.005	0.006	0.017	0.000	0.007	0.011
Mg	0.608	0.650	0.437	0.613	0.449	0.637
Ca	0.853	0.855	0.911	0.847	0.901	0.879
Na	0.112	0.090	0.074	0.071	0.069	0.066
Ac	11.2	9.0	7.4	7.1	6.9	6.6
Ft	2.0	7.0	3.1	-	-	-
Tc	9.3	6.9	10.8	7.4	3.6	6.0
Ct	11.7	9.6	6.7	11.3	4.5	10.2
Wo	31.2	31.0	35.6	33.0	39.9	36.7
En	30.4	32.5	21.9	30.7	31.9	37.1
Fs	4.3	4.0	14.9	10.2	12.8	6.3
mg	71.5	72.3	51.2	69.2	48.4	66.6

AW84738 - basanite, MD2, Mt Discovery, AW84750 - tephrite, MD2, Mt Discovery, AW82105 - basanite, MB1, Minna Bluff, AW84797 - tephrite, MB1, Minna Bluff.
Pyroxene Type: F - fassaitic, A - acmitic (Duda and Schmincke, 1985).
Pyroxene Endmenbers: Ac - acmite, Ft - ferritschermak, Tc - Ca-Ti-tschermak, Ct - Ca tschermak, Wo - wollastonite, En - enstatite, Fs - ferrosilite.

Table 7.4 - Representative microprobe analyses of Al-clinopyroxene from the DVS. Total iron was analysed as FeO*. Fe_2O_3 and FeO are calculated by charge balancing. Cation formula are calculated on the basis of four cations.

Sample No.	AW84738	AW82105		AW84797
Analysis No.	P4.C	P2B.C	P2B.R	P1A.M
SiO2	44.61	48.98	46.94	48.88
TiO2	3.33	1.85	2.67	2.15
Al2O3	10.89	6.58	8.80	7.02
Cr2O3	<0.15	0.57	0.57	0.67
FeO*	7.71	5.84	6.06	5.14
MnO	<0.12	<0.13	<0.13	<0.14
MgO	10.86	13.64	12.48	13.46
CaO	22.01	21.99	22.68	22.66
Na2O	<1.29	0.61	0.51	0.50
K2O	<0.05	<0.06	<0.06	<0.06
Sum	99.41	100.06	100.10	100.48
Fe2O3	0.00	0.95	0.47	0.11
FeO	7.71	4.99	5.64	5.04
Total	99.41	100.16	100.15	100.49
Si	1.681	1.806	1.737	1.804
Ti	0.094	0.051	0.075	0.060
Al^{IV}	0.319	0.187	0.255	0.196
Al^{VI}	0.164	0.100	0.130	0.109
Cr	0.000	0.017	0.017	0.019
Fe3+	0.000	0.029	0.013	0.003
Fe2+	0.243	0.152	0.175	0.136
Mn	0.000	0.000	0.000	0.000
Mg	0.610	0.749	0.688	0.741
Ca	0.888	0.867	0.867	0.896
Na	0.000	0.044	0.037	0.036
K	0.000	0.000	0.000	0.000
Ac	-	4.4	3.7	3.6
Tc	9.4	5.1	7.5	6.0
Ct	14.7	10.1	12.6	10.2
Wo	32.3	36.0	33.9	36.7
En	30.5	37.6	34.6	37.1
Fs	12.1	7.0	7.6	6.3
mg	71.5	80.6	78.6	71.0
Al^{IV}/Al^{VI}	1.95	1.87	1.96	1.80

Sample Description: AW84738 - basanite, MD2, Mt Discovery, AW82105 - basanite, MB1, Minna Bluff, AW84797 - tephrite, MB1, Minna Bluff.
Pyroxene Endmembers: Ac - acmite, Tc - Ca-Ti-tschermak, Ct - Ca tschermak, Wo - wollastonite, En - enstatite, Fs - ferrosilite.

Table 7.5 - Representative microprobe analyses of titansalite, hedenbergite and aegerine from the DVS. Total iron was analysed as FeO*. Fe_2O_3 and FeO are calculated by charge balancing. Cation formula are calculated on the basis of four cations.

Analysis No.	P1B.C	G1.C	G3.C	M3.C	P2.R
SiO2	47.42	47.90	48.45	49.16	50.76
TiO2	2.39	3.14	0.86	0.90	0.50
Al2O3	7.79	4.83	2.48	0.89	0.45
Cr2O3	<0.14	0.00	<0.14	0.00	0.00
FeO*	7.37	8.54	19.79	22.81	28.62
MnO	0.24	0.21	1.10	0.94	0.24
MgO	12.46	11.93	4.95	3.73	0.59
CaO	21.32	22.87	21.08	20.03	5.40
Na2O	0.84	0.62	1.13	1.09	11.38
K2O	<0.06	<0.06	0.10	0.00	0.00
Sum	99.83	100.04	99.94	99.55	97.94
Fe2O3	2.15	2.33	3.92	1.67	31.49
FeO	5.44	6.44	16.23	21.30	0.28
Si	1.759	1.795	1.904	1.960	1.945
Ti	0.067	0.088	0.025	0.027	0.014
Al	0.341	0.213	0.115	0.042	0.018
Fe3+	0.068	0.066	0.117	0.051	0.907
Fe2+	0.161	0.202	0.533	0.721	0.009
Mn	0.008	0.007	0.037	0.032	0.007
Mg	0.689	0.666	0.290	0.223	0.035
Ca	0.848	0.918	0.888	0.859	0.221
Na	0.060	0.045	0.086	0.085	0.845
K	0.000	0.000	0.005	0.000	0.000
NT	-	-	-	-	1.0
Ac	6.0	4.5	9.1	8.1	83.5
Ft	0.4	1.0	1.3	-	-
Tc	6.7	8.8	2.5	2.6	3.6
Ct	10.4	1.8	3.2	0.8	-
Wo	33.7	40.1	40.9	40.5	8.8
En	34.5	33.3	14.5	10.6	1.8
Fs	8.4	10.4	28.5	37.4	0.6
mg	75.1	71.3	30.9	22.8	3.7

Sample Description:

P1B.C Titansalite phenocryst core from basanite AW82105, MB1, Minna Bluff.

G1.C Groundmass titansalite from tephrite AW82109, MB1, Minna Bluff.

G3.C Groundmass hedenbergite from phonolite AW82150, MB2, Minna Bluff.

M3.C Hedenbergite microphenocryst core from peralkaline trachyte, AW83503, MS3, Mason Spur.

P2.R Aegerine phenocryst core from peralkaline trachyte AW83502A, MS3, Mason Spur.

Pyroxene Endmembers: NT - Na-Ti-pyroxene ($NaTi_{0.5}(Fe^{2+},Mg)_{0.5}Si_2O_6$), Ac - acmite, Ft - ferritschermak, Tc - Ca-Ti-tschermak, Ct - Ca tschermak, Wo - wollastonite, En - enstatite, Fs - ferrosilite.

Pyroxene nomenclature used is that of Deer et al. (1978) (Figures 7.6 and 7.7). Use is made of the following qualifiers:

titan- TiO_2 > 2.00 wt. % (Yagi and Onuma, 1967)

chrome Cr_2O_3 > 0.60 wt. % (Duda and Schmincke, 1985)

Al- Al^{IV}/Al^{VI} between 1.0 and 3.2 (Wass, 1979a)

The solid solution series from diopside to hedenbergite are referred to as calcic clinopyroxene. Aegerine-augite and aegerine are sodic pyroxenes.

7.4.2 Occurrence

Clinopyroxene is present in all DVS lavas except the Group II phonolite AW82078 from MB2, and Group I obsidians AW83516 and AW83519 in MS5. Colorless to pale brown calcic clinopyroxene forms seriate phenocrysts and/or groundmass minerals in all ultrabasic and basic lavas. It also occurs as large (>2 mm across) phenocrysts in many lavas from Group II. Some clinopyroxene phenocrysts in Group II lavas, especially those with compositions near the basanite - tephrite boundary (Figure 7.1), have rounded pale green or olive green cores. The green cores are commonly packed with tiny opaque inclusions, or fluid inclusions, and are mantled by a zone of colorless pyroxene. Large phenocrysts may also exhibit colorless cores that grade outwards into pale brown salite. Clinopyroxene phenocrysts in many ultrabasic and basic lavas of Group II are rimmed by a pinkish brown titansalite similar to those in their groundmass. Calcic clinopyroxene is also a constituent of many ultramafic and mafic xenoliths in Group II basanites from the Foothills of Royal Society Range and the Riviera Ridge area.

There is a transition from pale pale brown salite to pale green

ferrosalite in lavas of intermediate composition. The ferrosalites occur as seriate microphenocrysts, and in the groundmass. Darker, emerald green aegerine-augite and aegerine may be present as microphencrysts and groundmass in peralkaline trachytes from Group I, and in group II trachytes from MB1 and MS8.

7.4.3 Chemical Composition

The mg index of clinopyroxenes from Group II basanites, tephrites, and phonotephrites are similar. A small decrease in the mg index occurs in clinopyroxenes from tephriphonolites, and a much greater decrease is exhibited by clinopyroxenes from phonolites. Most analyses of clinopyroxenes from Group II rocks plot above the diopside - hedenbergite join (Figure 7.7), which causes a significant Ca tschermak component in end member calculations. In contrast, clinopyroxenes from Group I plot below the diopside - hedenbergite join. A diopside in peralkaline trachyte AW83533 could not have crystallized from its silicic host and is interpreted as a small xenocryst. Reverse compositional zoning in a clinopyroxene from benmoreite AW82056 suggests that the core of this mineral is also a xenocryst.

The colorless to pale brown cores of large clinopyroxene phenocrysts from Group II rocks, including the mantles around the green cores, exhibit high Al_2O_3 contents (> 6.0 wt %) and are Al-clinopyroxenes. They have Al^{VI} contents similar to clinopyroxenes in lower crustal and mantle-derived xenoliths from other alkaline provinces (Aoki and Shiba, 1973; Wass, 1979a; Duda and Schmincke, 1985). Ti and Al decrease sharply in clinopyroxenes from Group II ultrabasic and basic hosts, as the SiO_2 content of the clinopyroxene and the host

lava increases, and the mg value of the clinopyroxene decreases (Figures 7.8 and 7.9). A contrasting trend of increasing Ti and Al from core to rim is exhibited by many clinopyroxene phenocrysts from Group II basabites and tephrites. This tendency for phenocryst rims and groundmass to be enriched in TiO_2 is consistent with titaniferrous rims observed in samples AW84738, AW84750, AW84797, and AW84796. The Ti and Al content of clinopyroxene from the coronas surrounding many kaersutite phenocrysts in Group II lavas may differ significantly from the composition of other clinopyroxene in the rock (Figures 7.6, 7.7, 7.8, and 7.9).

The increase in the Na content of clinopyroxenes from Group II basanites to phonolites is very small (Figure 7.7), and there is no tendency to develop a sodic pyroxene trend. Clinopyroxenes from Group I rocks exhibit a similar trend of minimal Na erichment in basanite to benmoreite hosts, and even some trachyte and peralkaline trachyte lavas. In contrast, the pyroxenes in other Group I peralkaline trachytes exhibit a pronounced enrichment in sodic pyroxene with the crystallization of aegerine ($Ac_{79.2-83.5}$) in sample AW83502A.

Cr_2O_3 was detected in some Group II calcic pyroxenes, but Cr distribution is variable. Cr tends to be highest in the cores of the colorless and pale brown phenocrysts.

Composition of the green pyroxene cores of some Group II clinopyroxenes varies considerably, especially between rock samples (Figures 7.6 and 7.7). In general, the green core is richer in Fe^{2+} and Mn and is depleted in Al, Ti, and Cr compared to the mantling pyroxene. In basanite AW84738 from Mt Discovery the green cores are significantly richer in Fe^{3+} and Na, but depleted in Fe^{2+}.

Pyroxenes in phonotephrite xenolith (AW84761) from phonolite on

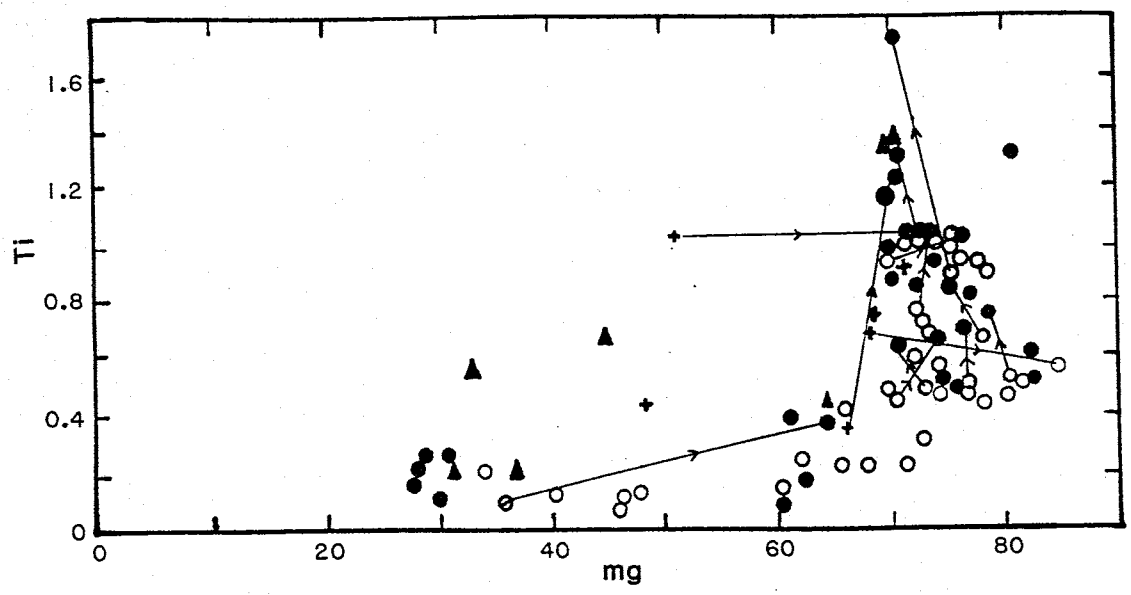

Figure 7.8 - Variation of Ti (atom %) with magnesium index (mg) for Group II rocks from Mt Discovery and Minna Bluff. + green cored pyroxene, ○ phenocryst core and inclusions in feldspar, ● phenocryst rim and groundmass, ⊘ xenocryst core, ▲ clinopyroxene from kaersutite corona. Tie-lines link analyses from the same crystal, with arrows indicating the direction from core to rim.

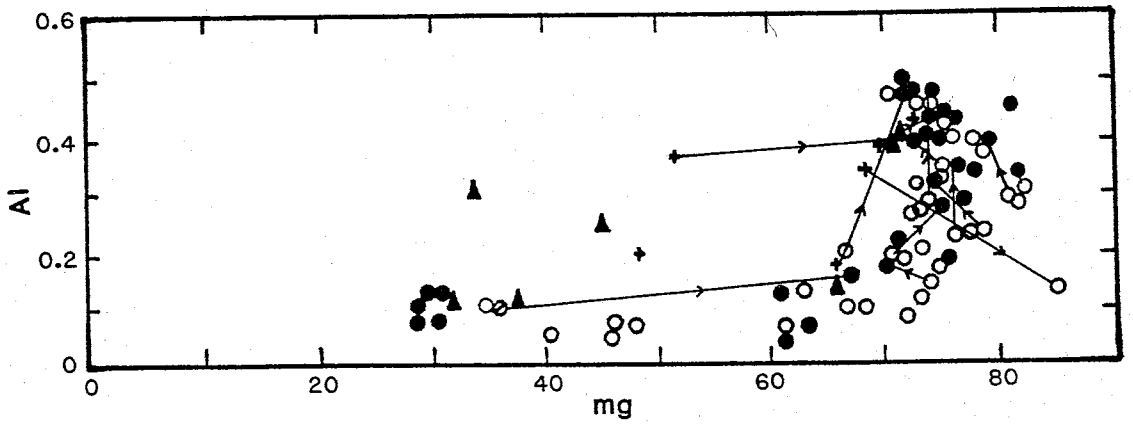

Figure 7.9 - Variation of Al (atom %) with magnesium index (mg) for Group II clinopyroxenes from Mt Discovery and Minna Bluff. + green cored pyroxene, ○ phenocryst core and inclusions in feldspar, ● phenocryst rim and groundmass, ⊘ xenocryst core, ▲ clinopyroxene from kaersutite corona. Tie-lines link analyses from the same crystal, with arrows indicating the direction from core to rim.

Mt Discovery are lower in Na than other Mt Discovery pyroxenes (Fi 7.7). Mg, Fe*, Al, and Ti concentrations are similar to clinopyro enes in hosts of similar composition.

7.4.4 Discussion

Calcic Pyroxene

The small variation in Fe^{2+}-Mg-Ca content of diopside, salit and titansalite phenocrysts over a broad range in host composition implies that Fe^{2+} in the melt was being buffered, probably by reac between olivine, magnetite and silica (Nash and Wilkinson, 1970; G 1973; Veiten 1980). The high Ca and usually low Cr content of calc pyroxenes probably reflects the concentration of these elements in melt. Such conditions could have been generated by the early fracti ation of olivine (Wilkinson, 1956) and chromian spinel, which are t earliest crystallizing phases in DVS lavas.

The high Al and Ti contents of clinopyroxene in ultrabasic and basic hosts (Table 7.5) are typical of pyroxenes in undersaturated lavas and have been attributed to low a_{SiO2} (Gibb, 1973). Decreasin trends for these elements with increasing SiO_2 in the host is relat directly to the increasing SiO_2 content of the melt (Campbell and Borley, 1974; Gupta et al., 1973). Trends of increasing Ti and Al, Al^{VI}/Al^{IV} between the phenocryst cores and rims in ultrabsaic and basic lavas is attributed to the effect of decreasing pressure as crystallization proceeded (Yagi and Onuma, 1967; Thompson, 1974; Wa 1979a), and suggests that the magma crystallized under variable pre sure conditions during its ascent.

Three generations of calcic pyroxene are recognized in samples

from the DVS: a pale green, or olive green resorbed core, a colorless to pale brown mantle, and a pinkish brown rim. Similar observations have been made in basanites from Ross Island (Kyle, 1976, 1981c), and in numerous alkaline provinces world wide (Brooks and Printzlau, 1978; Wass, 1979a; Duda and Schminke, 1985).

"Green cores" have been subdivided on textural and geochemical criteria into three types (Duda and Schmincke, 1985):

a) pleochroic grey-green to brownish cores (fassaitic)

b) pleochroic olive green to ochre cores (fassaitic)

c) predominantly non-pleochroic pale green to grass green cores (acmitic).

All three types are represented in the DVS, although type "b" cores were only observed in rocks from Mt Discovery. Type "a" cores are commonly sieve-textured with opaque fluid inclusions. Type "c" cores, which in the Massif Central area were limited to foidite hosts, are commonly found in basanite and tephrite hosts in the DVS. It is possible that some "c type" cores may be petrographically misidentified type "a" cores, because Duda and Schimincke (1985) noted difficulty in unambiguous petrographic identification. However, "c" type cores have been identified geochemically in basanite at Minna Bluff (Figure 7.10), and commonly contain numerous tiny opaque oxide inclusions.

DVS green cores are characterized by a high degree of compositional variation (Table 7.3). Most have elevated concentrations of Mn and Fe^{2+} and/or Na and Fe^{3+}, and low Cr, Al and/or Mg when compared to the mantling clinopyroxene composition. The fassaitic cores have significantly higher Ti and Al than the acmitic cores. Na contents are generally lower than for green cored pyroxenes from similar rocks on Ross Island (Kyle, 1981c). Mg index values fall in the range of 48.4

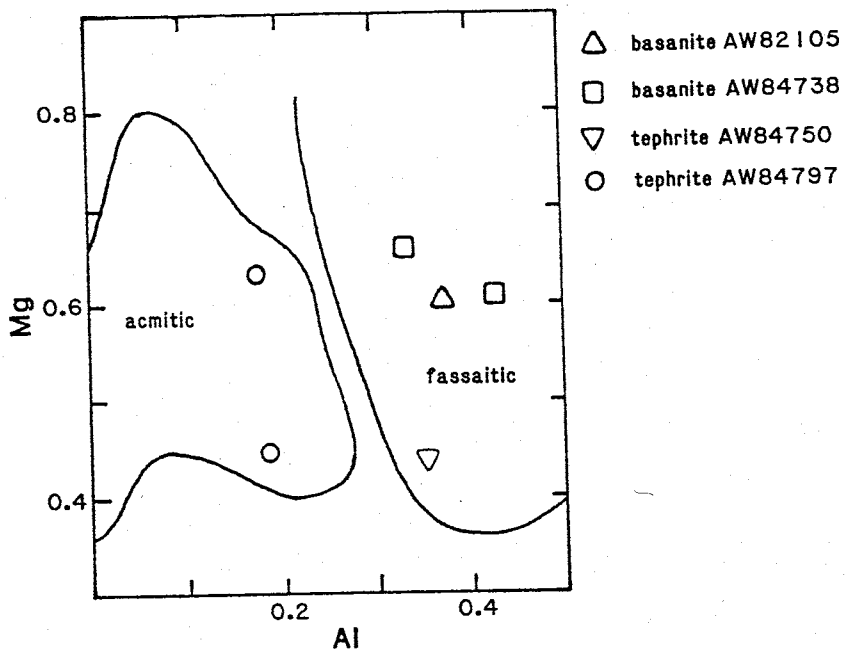

Figure 7.10 - Plot of Mg against Al (expressed in formula units calculated on the basis of four cations) of green cored pyroxenes from DVS rocks. Fields are those of Duda and Schmincke (1985), and enclose fields of acmitic and fassaitic green cored clinopyroxenes, from the Massif Central, France.

to 72.3. Duda and Schmincke (1985) used a plot of Mg/Al to geochemica ly separate fassaitic and acmitic cores (Figure 7.10). When this criterion is used to distinguish fassaitic from acmitic cores in DVS clinopyroxenes, the green cores with the least amount of Na_2O are designated as "acmitic", although their composition is far from that of acmite.

Models for the origin of green cored pyroxenes fall into three categories:

a) The green cores are cognate, with the reverse Mg-Fe zoning being caused by a change in the parameters controlling crystallizatio (e.g., an increase in f_{O2} due to resorption of kaersutite at lower pressures (Frisch and Schmincke, 1969), or sinking in a convecting magma chamber (Borley et al., 1971)). The green cores have also been attributed to high pressure crystallization (Wilkinson, 1975; Kyle, 1981c).

b) The green cores are xenocrysts precipitated from a more silicic melt, and have been subsequently entrained in the basic host, either in the upper mantle (Brookes and Printzlau, 1978; Wass, 1979a; Wass et al., 1980), or in the crust (Barton et al., 1982).

c) The green cores are xenocrysts of disintegrating and entraine upper mantle wall rock (McIver and Gever, 1970; Barton and Bergen, 1981; Lloyd, 1981).

Green cores from DVS rocks always occur as discrete crystals, no crystal aggregates, which suggests they are not derived from disintegrated solid. Model C is, therefore, an unlikely origin for DV green cores. There is insufficient evidence to make a clear choic between models a and b. The compositional variety, especially betwee

rock samples, suggests DVS green cores may have more than one origin.

Natural (Wilkinson, 1975; Wass, 1979b) and synthetic (Merrill and White, 1975) green pyroxenes, of broadly similar composition to the green cores, can crystallize from alkaline liquids at mantle pressures. Experimental studies of an alkali basalt with 2 wt. % H_2O have shown that the Na_2O content of clinopyroxene will almost double to about 1 wt. % with an increase in the pressure of crystallization from 13.5 to 18 kb (Green and Hibberson, 1970). However, there is no data on which molecular components Na, Ti, Fe^{2+}, Fe^{3+}, and Al are incorporated into. Since the Al^{VI} component of clinopyroxene also increases with pressure (Wass 1979a), perhaps the Na is incorporated into an omphacite (Kyle, 1976) or jadeite component. End member calculations usually combine Na with Fe^{3+} in an acmite molecule (Kyle, 1976; Duda and Schmincke, 1985), but estimates of Fe^{3+} for two analyses in this study are insufficient to account for all the Na. Alternative sites for Na are in jadeite or Na-Ti-pyroxene and the presence of these molecules in DVS green cores would have important implications for the pressure of crystallization. Jadeite is a high pressure mineral, whereas Na-Ti-pyroxene favors Fe^{2+}-rich varieties of pyroxene at crustal depths (Nielsen, 1974).

The optical continuity of the transition from Al-clinopyroxene to titansalite, and the presence of salite and titansalite as a groundmass phase, is clear evidence that these pyroxenes are cognate phases. Sr isotopic studies of titanaugite and host lava elsewhere in the MVG also supports a cognate origin for this generation of crystals (Stuckless and Ericksen, 1976). Detailed studies of basanites from the Massif Central, France, including geophysical evidence of crustal magma chambers, suggest that titanaugite rims form at crustal depths

(Duda and Schmincke, 1985).

A marked increase in Fe^{2+} content and the concomitant decrease of Mg in calcic pyroxenes from intermediate hosts are coupled with only slight increases in Na and decreases in Ca. The low acmite component does not mirror the increasing Na_2O content of the melt, and presumably reflects a low oxygen fugacity that favors the reduced form of iron. This suggests that oxygen fugacity, not a_{Na2O} or a_{SiO2} has controlled the crystallization of clinopyroxene, rather than sodic pyroxene, in lavas of intermediate composition, and that f_{O2} has been similar for Group II and most I magmas. The low and decreasing Ti and Al content of clinopyroxenes in intermediate hosts is attributed to low concentrations of these elements in the melt. This condition is probably caused by plagioclase, titanomagnetite and kaersutite fractionation from the basic magmas.

Sodic Pyroxene

Aegerine-augite and aegerine were analysed in a peralkaline trachyte (AW83502A) at Mason Spur (Table 7.5), and are evidence of th late stage development of sodic pyroxene microphenocrysts and groundmass in some peralkaline acid hosts from Group I.

Aegerine and acmite are compositionally identical and it is generally assumed that experimental studies on acmite are equally applicable to aegerine. Bailey (1969) determined that acmite will onl crystallize directly from a peralkaline melt. However, the presence o ferrosalite in peralkaline trachyte AW83503, suggests that it takes more than just a peralkaline bulk composition to crystallize aegerine

Unlike diopside, which is stable over a wide range of temperatur and pressure, hedenbergite and acmite are sensitive to small changes

in temperature and P_{O2}. At oxygen fugacities controlled by the hematite-magnetite buffer acmite is stabilized at higher temperatures (Bailey, 1963), and is more likely to crystallize. Yagi (1966) suggested that hedenbergite is destabilized by increasing P_{O2} according to the following reaction:

$$2CaFeSi_2O_6 + 1/2O_2 = 2CaSiO_3 + 2SiO_2 + Fe_2O_3$$

hedenbergite — wollast-onite — quartz — hematite

and that higher P_{O2} would stabilize acmite as follows:

$$Na_2SiO_3 + Fe^{2+}_2SiO_4 + 2SiO_2 + 1/2O_2 = 2NaFe^{3+}Si_2O_6$$

sodium metasilicate — fayalite — quartz — acmite

The presence of aegerine in some peralkaline trachytes at Mason Spur suggests that these lavas may have crystallized under higher f_{O2} conditions than other DVS magmas. However, the lack of sodic pyroxene in most DVS lavas is an indication that oxygen fugacities were well below that of the hematite-magnetite buffer (Bailey, 1963) in these magmas.

7.5 CALCIC AMPHIBOLE

7.5.1 Introduction

Calcic amphibole, of kaersutite to ferrokaersutite composition, was analysed in six Group II samples (Figure 7.11). Representative analyses are given in Table 7.6. Cation formula are calculated on the basis of 23 oxygen. No attempt was made to estimate Fe^{3+}, or to determine the nature of the volatile component. Amphibole nomenclatur is that of Leake (1978).

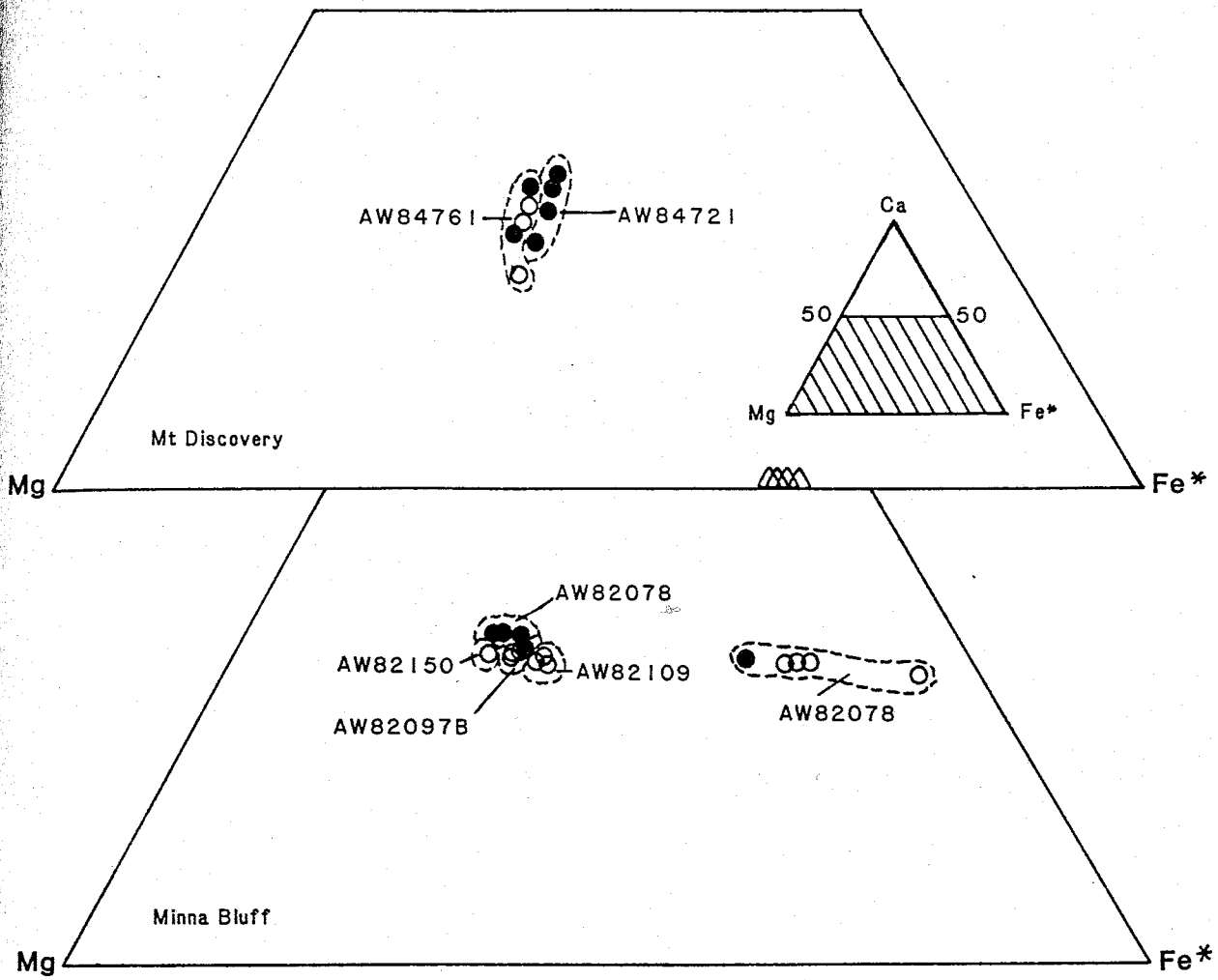

Figure 7.11 - Ca-Mg-Fe* (FeO* = total iron as FeO) composition of kaersutites and biotite from Mt Discovery and Minna Bluff.

Table 7.6 - Representative microprobe analyses of kaersutites and biotite from the DVS. Total iron was analysed as FeO*.

	P1.C	P5B.C	P4.C	P1.C	P8.C	G2.C	I5.C
SiO2	39.10	39.94	40.39	40.89	38.20	37.74	34.57
TiO2	5.80	7.50	6.21	6.08	4.86	7.29	5.48
Al2O3	13.35	12.30	11.73	10.67	11.71	14.59	13.24
FeO*	13.80	12.30	14.62	12.40	23.66	11.63	25.18
MnO	0.26	0.17	0.51	0.41	0.47	0.15	0.71
MgO	10.60	11.28	9.78	12.19	4.33	11.48	7.43
CaO	11.54	12.08	11.35	11.29	11.03	12.43	0.00
Na2O	2.77	2.61	3.19	2.95	2.64	2.52	1.06
K2O	1.07	1.18	1.03	0.97	1.42	1.16	8.70
Total	98.29	99.36	98.81	97.85	98.32	98.99	96.37
mg	57.3	61.7	53.5	62.9	24.2	63.5	33.8

P1.C Kaersutite phenocryst core from tephrite AW82109, MB1, Minna Bluff.

P5B.C Kaersutite phenocryst core from benmoreite AW82097B, MB1, Minna Bluff.

P4.C Kaersutite phenocryst core from tephriphonolite AW84721, MD1, Mt Discovery.

P1.C Kaersutite phenocryst core in inclusion AW84761 from phonolite MD1, Mt Discovery.

P8.C Ferrokaersutite, phenocryst core from phonolite AW82078, MB2, Minna Bluff.

G2.C Groundmass kaersutite from phonolite AW82078, MS2, Minna Bluff

I5.C Biotite inclusion in feldspar phenocryst, AW84741, MD1, Mt Discovery.

7.5.2 Occurrence

Strongly pleochroic, brown kaersutite or ferrokaersutite is a common phenocryst phase in basic and intermediate Group II lavas. It also occurs in some ultramafic tephrites from Group II. There is a general increase in the abundance of kaersutite in rocks of tephrite to phonotephrite or tephriphonolite composition. Kaersutite phenocrysts in phonolites are usually smaller, and the mineral is volumetrically less abundant. Kaersutite only forms a groundmass phase in phonolites AW82078 at Minna Bluff, and AW86881 at Mt Discovery. Kaersutite is present in ultramafic xenoliths, and forms xenocrysts and megacrysts in Group II basanites at Foster Crater (Kirsch, 1981), Riviera Ridge, and the southeast ridge of Mt Discovery. The only Group I occurrences of kaersutite are phenocrysts in benmoreite AW85839, and possibly the small, dark brown, pleochroic inclusions in feldspar phenocrysts from the trachyte AW885851.

Many kaersutites are partially or completely altered to titanomagnetite, or have fine-grained coronas of clinopyroxene + titanomagnetite +/- plagioclase +/- olivine. Nepheline was identified by microprobe analysis in a kaersutite corona in phonolite AW82150.

Apatite commonly forms inclusions in kaersutite, and its presence is useful in identifying primary opaque phenocrysts from those that are an alteration product of kaersutite.

7.5.3 Chemical Composition

Except for the ferrokaersutite cores in phenocrysts from phonolite AW82078 at Minna Bluff, the calcic amphiboles analysed in this study are kaersutites. They exhibit limited compositional variation with respect to CaO, MgO, FeO* (Figure 7.11), and TiO_2.

Geochemical trends can not be related to changes in the composition of the host lavas. Samples from Minna Bluff exhibit an almost constant CaO content, whereas those from Mt Discovery show a significant variation in CaO content within phenocrysts from the the same sample.

The ferrokaersutite cores in phenocrysts from phonolite AW82078 are distinctly richer in iron and contain less MgO and TiO_2 than other DVS kaersutites. AW82078 is also unusual in that it has crystallized groundmass kaersutite in the absence of pyroxene.

7.5.4 Discussion

Despite common evidence of late stage disequilibrium, kaersutite was crystallizing from most basic and intermediate Group II magmas at depth. The presence of groundmass kaersutite in AW82078 and AW86881 also indicates that kaersutite was probably in or near equilibrium with some Group II phonolites at eruptive temperatures and pressures.

Silica-undersaturated melts will stabilize kaersutite at higher temperatures (Aoki, 1970; Allen and Boettcher, 1973; Cawthorn, 1976b), and this may be one reason why kaersutite is typically found in the Group II lavas. The stabilizing effect of higher P_{H2O} on calcic amphibole is also an important consideration (Wilkinson, 1961; Le Maitre, 1969; Nishikawa *et al.*, 1971; Vinx and Jung, 1977), but is secondary to the effects of temperature at pressures below about 20 kb (Yagi *et al.*, 1975; Vinx and Jung, 1977). Holloway (1973) concluded from experimental work that calcic amphibole could be an important phase in igneous rocks, even at relatively low f_{H2O}, and at pressures corresponding to crustal depths. His work showed that calcic amphibole was stabilized at higher temperatures by higher total pressures. The

abundance of kaersutite phenocrysts in Group II lavas suggests these lavas may have crystallized at lower temperatures and/or higher pressures, though not necessarily higher P_{H2O} than those in Group I. The difference in Na_2O content between Group I and II melts may also have contributed to kaersutite stabilization in Group II lavas. Cawthorn's (1976b) experimental work emphasizes the importance of a_{Na2O} in stabilizing amphibole at crustal depths (5 kb).

The Al, Ti and Na content of igneous calcic amphiboles is sensitive to pressure (Best, 1974; Cawthorn, 1976a). These elements, therefore, provide important clues as to the depth of kaersutite crystallization. Comparison of Best's (1974) data with DVS calcic amphiboles suggests the Mt Discovery kaersutites and those from the tephriphonolite AW82097B at Minna Bluff crystallized at shallow crustal depths (Figure 7.12). Other kaersuites from Minna Bluff lie between Best's fields of shallow crustal- and mantle-derived kaersutites. The extreme Fe enrichment of the ferro kaersutite (Figure 7.11) suggests it may have crystallized from a magma that was richer in Fe than its host. Such a magma may have evolved at or near the base of the crust (Figure 7.12A), and become mixed with a less evolved melt prior to eruption. Calcic amphiboles from Ross Island and The Pleiades (Kyle, 1976; Kyle, 1986) fall between the mantle and crustal fields, which suggests that lower crustal magma chambers may be more common in these areas of the MVG.

7.6 ALKALI AMPHIBOLE

Alkali amphibole occurs as a subordinate groundmass phase in most aegerine or aegerine-augite bearing peralkaline trachytes from Group I. It is not found in Group II rocks. The alkali amphibole was identi

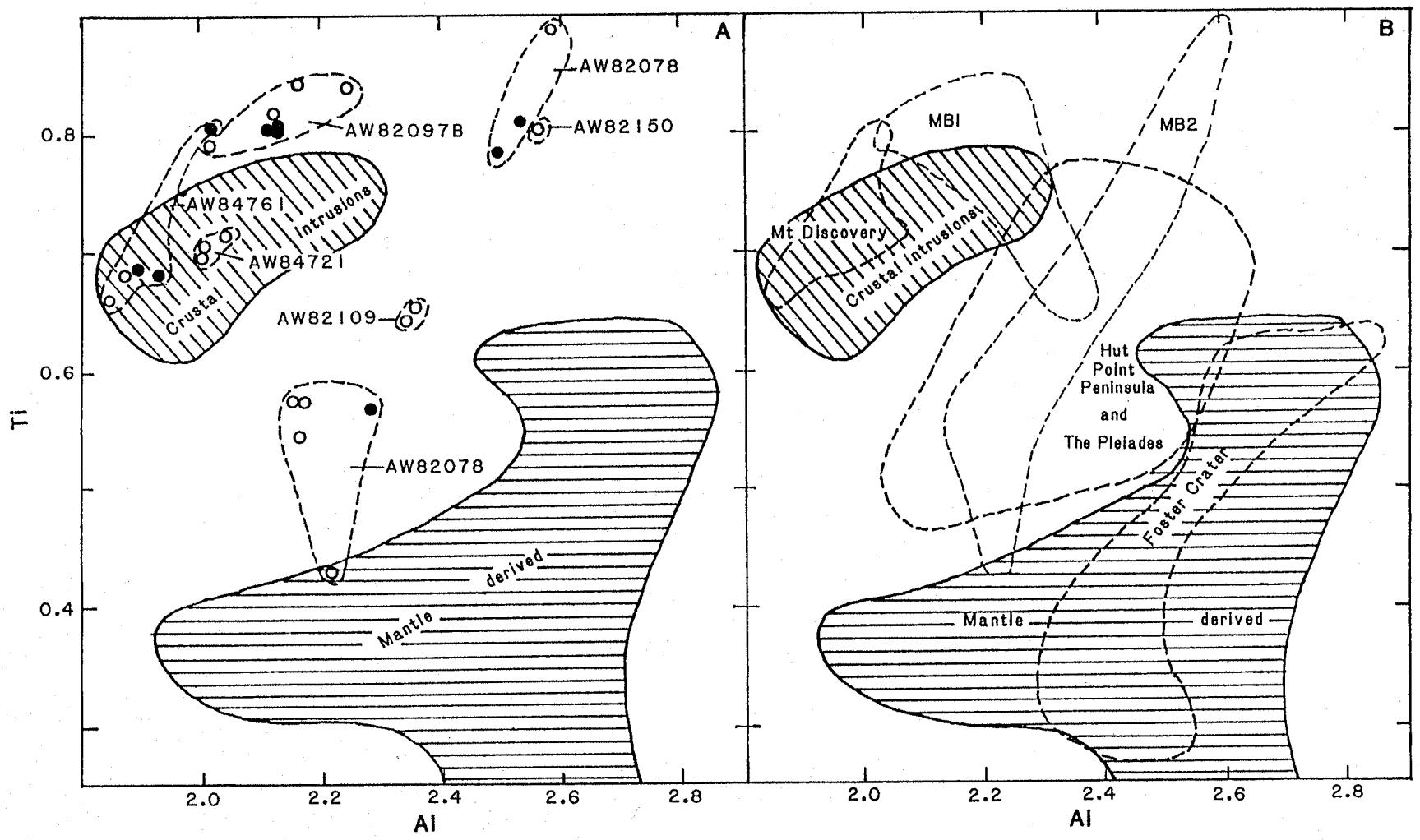

Figure 7.12 - A - Variation diagram of the Ti and Al content of kaersutites from Mt Discovery and Minna Bluff. Best's (1974) fields of shallow crustal and mantle-derived kaersutites are shown for comparison. B - Comparison of kaersutites from DVS rocks with those from elsewhere in the McMurdo Volcanic Group (Hut Point Peninsula (Kyle 1976; 1981c), The Pleiades (Kyle 1976; 1986), and Foster Crater (Kirsch, 1981). MB1 and MB2 refer to the lower and upper sequences, respectively, at Minna Bluff.

fied petrographically as arfvedsonite, but was not analysed.

Alkali amphibole is typically associated with peralkaline trachytes and syenites (Frisch, 1970). Experimental work indicates it is stable at lower pressures and oxygen fugacities than sodic pyroxene and aenigmatite (Ernst, 1972). Ernst's experiments also indicate that the stability field of alkali amphibole is expanded at higher fluid pressures. The total absence of arfvedsonite phenocrysts in Group I trachytes implies that these magmas evolved under low fluid pressures

7.7 BIOTITE

Pleochroic brown, Ti-rich biotite occurs as small microphenocrysts and as inclusions in feldspar in phonolite AW84741 at Mt Discovery (Figure 7.11). Analyses are low in SiO_2 (Table 7.6), but Si deficiencies in the Z site are more than compensated for by Al and Ti

AW84741 is a xenolith in tephrite, but the presence of biotite flakes as inclusions in feldspar phenocrysts and as slightly altered microphenocrysts suggests that it is a primary mineral, and not the product of contact metamorphism. It probably formed late in the magmatic history, perhaps as the result of a rise in P_{H2O}. Other rare occurrences of biotite are reported from MVG rocks, for instance, a K-trachyte sample from the Pleiades (Kyle, 1976; 1986).

7.8 FELDSPAR

7.8.1 Introduction

Feldspar was analysed in 19 samples (Figure 7.13). Representative analyses are given in Table 7.7. Cation formula are calculated on the basis of 32 oxygens. DVS feldspars have been analysed previously at

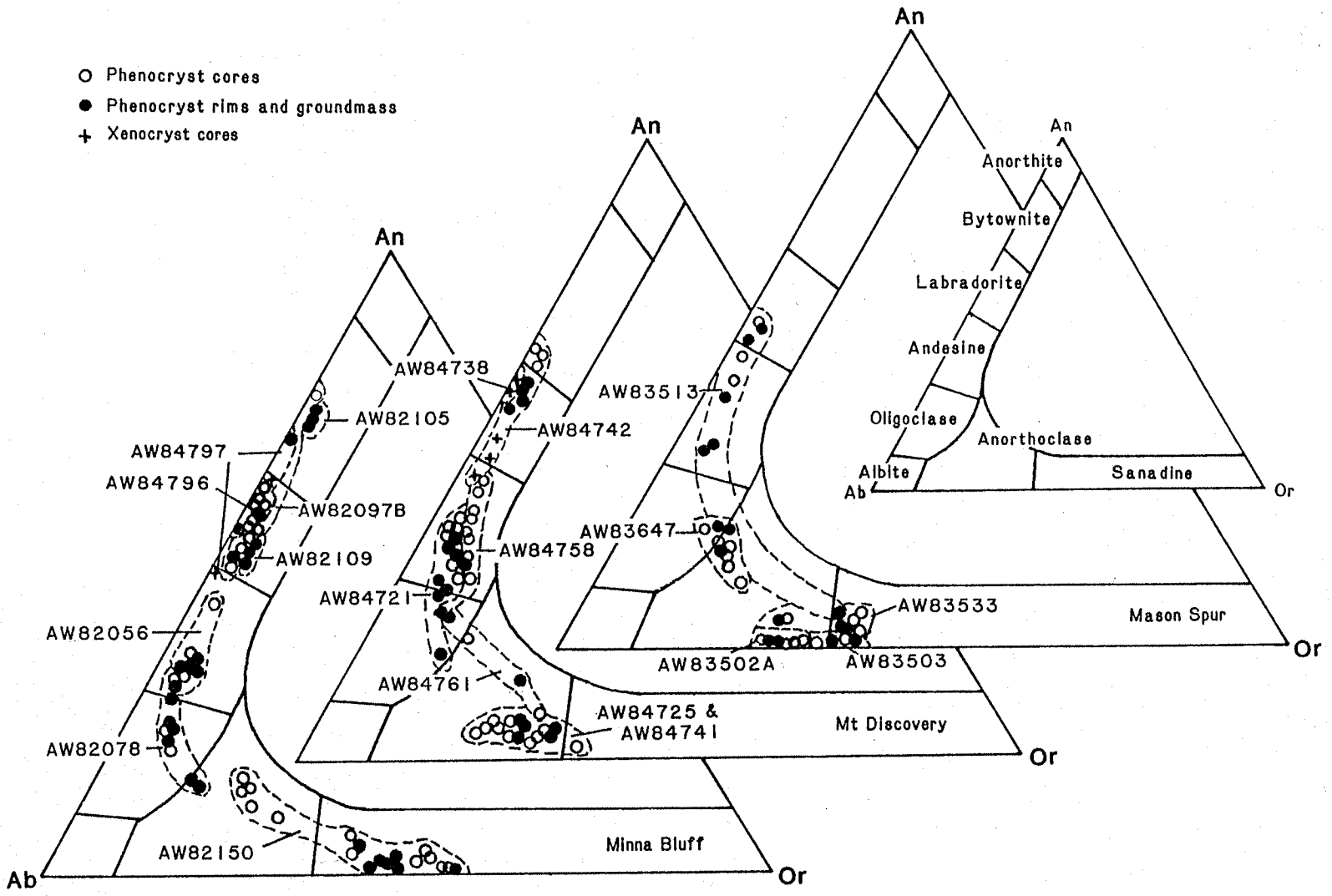

Figure 7.13 - Composition of feldspars from Minna Bluff, Mt Discovery, and Mason Spur. Feldspar nomenclature (Deer et al., 1966)is also shown.

Table 7.7 - Representative microprobe analyses of feldspar from the Discovery volcanic subprovince. Total iron was analysed as FeO*, but is given as Fe^{3+} in the cation formula. Feldspar compositions are expressed in terms of their end members: anorthite (An), albite (Ab), and orthoclase (Or).

Analysis No.	G1.C	S7.R	P1A.R	P2.R	P2B.C
SiO2	49.87	52.28	60.61	65.53	66.32
TiO2	0.14	0.17	<0.09	0.11	0.00
Al2O3	31.23	29.10	24.37	18.56	18.74
FeO*	0.61	0.53	0.32	0.60	<0.12
MgO	0.12	0.09	<0.04	<0.04	<0.04
CaO	15.69	12.65	5.96	0.16	0.15
Na2O	2.73	4.19	7.53	8.15	5.01
K2O	0.25	0.34	1.05	5.86	9.84
Total	100.64	99.35	99.84	98.97	100.11
Si	9.090	9.578	10.840	11.891	11.980
Ti	0.020	0.023	0.000	0.015	0.000
Al	6.750	6.283	5.160	3.969	4.020
Fe3+	0.091	0.081	0.056	0.091	0.000
Mg	0.030	0.025	0.000	0.000	0.000
Ca	3.070	2.483	1.140	0.031	0.030
Na	0.970	1.488	2.610	2.867	1.760
K	0.060	0.079	0.240	1.357	2.270
Total	20.081	20.041	20.046	20.248	20.060
An	74.9	61.3	28.6	0.3	0.7
Ab	23.9	36.7	65.4	68.6	43.3
Or	1.5	2.0	6.0	31.1	55.9

Sample Description:

G1.C Groundmass bytownite from basanite AW82105, MB1, Minna Bluff.

S7.R Labradorite microphenocryst rim from tephrite AW84742, MD2, Mt Discovery.

P1A.R Anorthoclase phenocryst rim from phonolite AW82078, MB2, Minna Bluff.

P2.R Anorthoclase phenocryst rim from peralkaline trachyte AW83502A, MS3, Mason Spur.

P2B.C Sanidine phenocryst core from phonolite AW82150, MB2, Minna Bluff.

Brandau Vent (McIver and Gevers, 1970) and Foster Crater (Kirsch, 1981). Feldspar nomenclature used is that of Deer et al., (1966).

7.8.2 Occurrence

Feldspar is a ubiquitous groundmass mineral, and forms phenocrysts in basic, intermediate, and acid hosts. Porphyritic plagioclase is also present in Group I basanites at Mason Spur (AW83545, AW83454) and Riviera Ridge (AW86036). Its abundance increases with the increasing SiO_2 content of the host. Feldspar composition ranges from bytownite to oligoclase to anorthoclase to sanidine. Porphyritic Group I samples suggest that the relative importance of plagioclase crystallization is greater in Group I than in Group II lavas. Plagioclase crystallization increases significantly in Group I benmoreites, and gives way to anorthoclase in the trachyte lavas. The transition from plagioclase to anorthoclase occurs at about the tephriphonolite - phonolite boundary in Group II lavas. Plagioclase phenocrysts are rare in phonolites, but do occur in phonolite AW82078 at Minna Bluff. AW82078 is also unusual because it crystallized groundmass kaersutite. Sanidine occurs as phenocrysts and in the groundmass of phonolite AW82150 from Minna Bluff, and in the peralkaline trachytes AW83533 and AW83503 at Mason Spur. Anorthoclase phenocrysts like those in the phonolites at Mt Erebus (Moore, 1986), are not present in DVS lavas.

Rounded and embayed plagioclase and alkali feldspar xenocrysts are present in many ultrabasic and basic Group II lavas. These xenocrysts are typically overgrown by a narrow feldspar rim of groundmass composition. Only a few of the plagioclase xenocrysts were analysed.

7.8.3 Chemical Composition

Feldspar compositions in Group II lavas range from bytownite ($An_{74.9}$) in the groundmass of basanite AW82105 to sanidine ($Or_{55.9}$) in phonolite AW82150. Feldspars were anlysed in benmoreites and trachytes from Group I. Compositions range from labradorite ($An_{52.3}$) in benmoreite AW83513 to sanidine ($Or_{39.6}$) in peralkaline trachyte AW83533. Feldspars in the more silicic peralkaline trachyte AW83502A, which also contains aegerine, are less potassic ($Or_{29.2-33.2}$).

Normal compositional zoning, especially in many plagioclase phenocrysts spans a considerable range, but was not studied.

The composition of feldspar xenocrysts is highly variable between samples and typically suggests derivation from more silicic magmas than their host.

7.8.4 Discussion

The distribution of feldspar indicates that plagioclase first crystallizes in Group II lavas of basic composition, but that it crystallized from some ultramafic lavas in Group I. Feldspar phenocrysts become increasingly abundant with increasing SiO_2 content of the host. The presence of plagioclase phenocrysts in ultrabasic and basic magmas suggests crystallization took place at pressures of <11 kb (Green 1970; Green and Ringwood, 1970).

Partitioning of Na and Ca between plagioclase and melt is strongly dependent on temperature and P_{H2O} (Yoder et al., 1957; Kudo and Weil, 1970; Drake 1976; Johannes, 1978), though Johannes has documented the problem of attaining equilibrium in experimental studies below 1000 °C. The effect of P_{H2O} is particularly marked, even for small

changes in P_{H2O} (Yoder et al., 1957). Higher P_{H2O} limits the solid solution of the An component into the alkali feldspar and forces feldspar compositional trends to veer more sharply towards the Ab apex on the An-Ab-Or diagram (Seck, 1971; Ribbe, 1975). The DVS feldspars do not exhibit separate compositional trends, which suggests Group I and II magmas evolved under similar P_{H2O} conditions.

The major element composition of plagioclase is essentially independent of melt composition, except perhaps for highly evolved melts (Keil et al., 1972; Drake, 1976). In the absence of H_2O, plagioclase composition is also independent of pressure to at least 10 kb (Drake, 1976). The normal compositional zoning evident in many DVS plagioclase phenocrysts is probably caused by crystallization under conditions of decreasing temperature.

7.9 NEPHELINE

Nepheline is a common normative mineral in DVS rocks, but is rarely identified modally. Tiny patches of interstitial nepheline may be present in the groundmass of some ultrabasic to intermediate Group II lavas. Microprobe analysis identified nepheline in coronas surrounding kaersutite in phonolite AW82150 (Table 7.8), and as a ground mass mineral in Group I trachyte (AW83533).

The stability of nepheline is sensitive to bulk composition, temperature and P_{H2O} (Gittins, 1979), in such a way that nepheline is stabilized over a greater compositional range under conditions of higher P_{H2O} and lower temperature. The presence of nepheline in some Group II lavas is probably controlled by the higher degree of undersaturation in these lavas. The only documented occurrence of nephelin in Group I lavas (trachyte AW83533) is from a stock. Perhaps the

Table 7.8 - Representative nepheline analyses from the Discovery volcanic subprovince. Total iron was analysed as Fe*. Cation formula are calculated on the basis of 32 oxygens.

Analysis No.	A4.C	G2.C	G5.C
SiO2	49.73	48.58	47.91
Al2O3	30.57	29.26	30.22
FeO*	1.42	2.07	1.75
MgO	0.25		
CaO	0.12		
Na2O	16.90	18.01	18.43
K2O	1.27	3.33	3.16
Total	100.10	101.25	101.47
Si	9.232	9.134	8.987
Al	6.686	6.484	6.681
Fe2+	0.221	0.325	0.275
Mg	0.069	-	-
Ca	0.023	-	-
Na	6.085	6.565	6.703
K	0.301	0.799	0.756
Total	22.617	23.307	23.402

Sample Description:

A4.C Nepheline from a multi-mineral corona surrounding a kaersutite phenocryst in phonolite AW82150, MB2, Minna Bluff.

G2.C Groundmass nepheline from peralkaline trachyte AW83533, MS3, Mason Spur.

G5.C Groundmass nepheline from peralkaline trachyte AW83533, MS3, Mason Spur.

slower cooling in the stock allowed the melt to reach sufficiently low temperatures for nepheline to crystallize, whereas other lavas have been quenched from higher temperatures.

7.10 OPAQUE OXIDES

7.10.1 Introduction

Opaque oxides were analysed in 18 samples, and range in composition from chromian spinel to titanomagnetite and ilmenite (Figures 7.14 and 7.15). Previous workers have analysed opaque oxides from Foster Crater (Kirsch, 1981) and Brandau Vent (McIver and Gevers, 1970). Representative analyses are given in Tables 7.9 and 7.10. Cation formula are calculated on the basis of 32 oxygens for the spinels, and 24 oxygens for the rhombohedral phase. Fe was analysed as FeO and estimates of Fe^{3+} and Fe^{2+} are calculated by charge balancing (Stormer, 1983). Some analytical totals are low (< 98.0 wt %) after charge balancing, probably as a result of oxidation to maghemite. Opaque oxide nomenclature is that of Haggerty (1976).

7.10.2 Occurrence

Opaque oxides occur in all DVS rocks except some Group I, aenigmatite-bearing trachytes at Mason Spur, Riviera Ridge and Gandalf Ridge. The vast majority of opaque oxides are titanomagnetites. They occur as a microphenocryst phase in basic and intermediate lavas, especially those in Group II, and as a groundmass phase. Titanomagnetite forms inclusions in ferromagnesian minerals, especially clinopyroxene. Kaersutite is often partially or totally replaced by titanomagnetite. Titanomagnetite is also an essential component in the

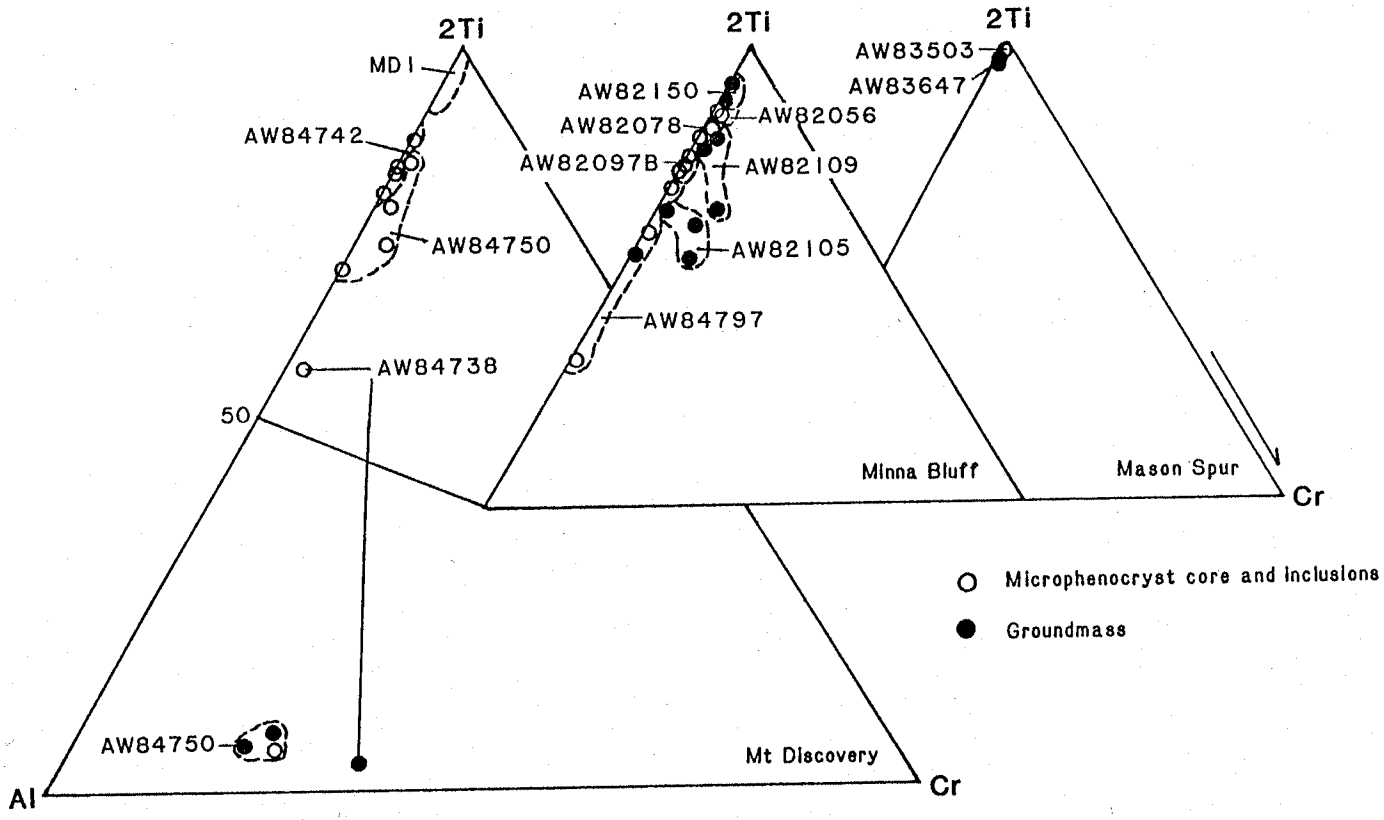

Figure 7.14 - Analyses of DVS spinels plotted on the Ti-Al-Cr face of the modified Johnson spinel prism (Haggerty, 1976). MD1 includes samples AW84758, AW84721, AW84741, and AW84725.

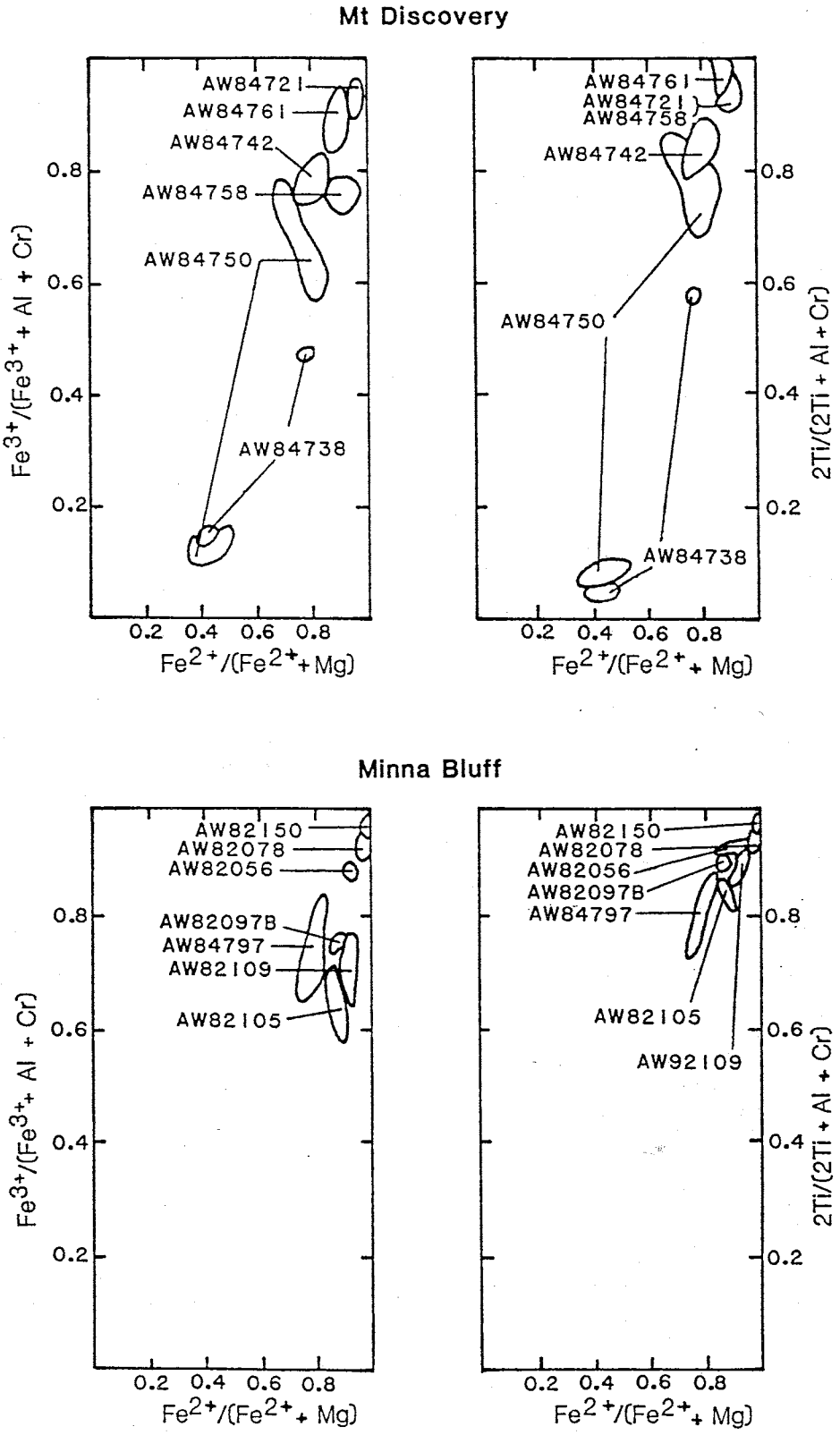

Figure 7.15 - Analyses of spinels from Mt Discovery and Minna Bluff, plotted on the Ti-Al and Fe3+-Al faces of the modified Johnson spinel prism (Haggerty, 1976).

Table 7.9 - Representative analyses of spinel series minerals from the Discovery Volcanic Subprovince. Total iron was analysed as FeO, and values of FeO and Fe_2O_3 were calculated by charge balancing after calculation of the cation formula on the basis of 32 oxygens. Ulvosinel (Usp) component was calculated by the method of Stormer (1983).

	I2.C	G2.C	S4.C	I3.C	G3.C	G1.C
SiO2	0.09	0.16	0.12	0.10	0.16	0.13
TiO2	27.06	25.79	21.19	20.50	2.77	13.50
Al2O3	3.09	2.94	2.34	3.82	34.42	1.18
Cr2O3	<0.16	0.24	0.00	0.00	16.94	<0.18
Fe2O3	14.06	15.60	26.86	27.31	12.55	41.32
FeO	51.92	51.07	47.13	41.67	20.49	42.33
MnO	1.07	0.93	1.08	0.82	0.20	1.55
MgO	2.46	2.22	2.19	5.38	12.57	0.06
CaO	<0.16	0.00	<0.20	0.00	0.19	<0.19
Total	99.75	98.95	100.43	99.61	100.29	100.05
Usp	82.4	79.8	61.8	59.4	58.4	39.6

Sample Description:

I2.C Titanomagnetite inclusion in feldspar, from tephriphonolite AW84758, MD1, Mt Discovery.
G2.C Groundmass titanomagnetite in tephrite AW82109, MB1, Minna Bluff.
S4.C Titanomagnetite microphenocryst in benmoreite AW82056, MB1, Minna Bluff.
I3.C Titanomagnetite inclusion in clinopyroxene from tephrite AW84742, MD2, Mt Discovery.
G3.C Chromian spinel microphenocryst in tephrite AW84750, MD2, Mt Discovery.
G1.C Groundmass titanomagnetite in phonolite AW82150, MB2, Minna Bluff.

Table 7.10 - Analyses of ilmenite and a coexisting titanomagnetite from xenolith AW84761 at Mt Discovery. Total iron was analysed as FeO. FeO and Fe_2O_3 are calculated by charge balancing after calculation of the cation formula based on 24 oxygens for ilmenite and 32 oxygens for titanomagnetite. The ilmenite (Il) and ulvospinel (Usp) components are calculated by the method of Stormer (1983).

	Ilmenite	Titanomagnetite
SiO2	0.05	0.07
TiO2	51.98	27.44
Al2O3	0.12	0.75
Cr2O3	0.00	<0.17
Fe2O3	4.90	15.86
FeO	37.97	50.58
MnO	1.56	1.47
MgO	4.07	2.87
CaO	<0.07	<0.08
Total	100.16	98.32
Usp		76.7
Il	95.0	

coronas that commonly surround kaersutite phenocrysts.

Chromian spinel occurs as inclusions in olivine in basanites and tephrites at Foster Crater (Kirsch, 1981) and Mt Discovery (AW84738, AW84750). Hercynite and chromian hercynite have been idenified by microprobe analysis in ultramafic xenoliths from Foster Crater (Kirsch, 1981). The bright green mineral in ultramafic nodules occurring elsewhere in the Foothills area and at Riviera Ridge is probably chronian spinel or hercynite.

Ilmenite occurs as exsolution lamellae in some titanomagnetites, and was identified as a primary mineral in the phonotephrite xenolith (AW84761) in phonolite at Mt Discovery. It is also reported in ultramafic inclusions at Foster Crater (Kirsch, 1981).

7.10.3 Chemical Composition

Titanomagnetite has a compositional range of $Usp_{83.1 - 37.6}$ in the Minna Bluff samples and $Usp_{82.4 - 55.6}$ in the samples from Mt Discovery (Figure 7.15). Within the modified Johnson spinel prism (Haggerty, 1976), analyses of titanomagnetite fall on or close to the Ti-Al and Fe^{3+}-Al faces reflecting their low Cr content. A marked gap separates titanomagnetite from the chromian spinel. There is a general increase in Ti and Fe^{3+} relative to Al and Cr, and in Fe^{2+} relative to Mg, which accompanies the progressive increase of SiO_2 in the melt. At Minna Bluff, there is a significant difference in the composition of titanomagnetites in the older MB1 benmoreite ($Usp_{73.8-59.4}$) and the younger MB2 phonolites ($Usp_{39.6-37.6}$), although these rocks have similar SiO_2 contents.

Titanomagnetite ($Usp_{59.2-64.4}$) was analysed from the groundmass of Group II trachyte AW83647 at Mason Spur. A microphenocryst of

titanomagnetite ($Usp_{75.9}$) in a Group I peralkaline trachyte (AW83503) at Mason Spur is in reaction relationship with aenigmatite.

Ilmenite ($Il_{95.0}$) coexists with titanomagnetite ($Usp_{76.7}$) as inclusions in a feldspar phenocryst in xenolith AW84761.

7.10.4 Discussion

The stability and composition of spinel series minerals are controlled by temperature, oxygen fugacity, type and composition of coexisting phases and melt composition (Hill and Roeder, 1974). The composition of chromian spinel is also sensitive to pressure (Basu an MacGregor, 1975; Haggerty, 1976), but interpretation has been ambiguous, because the Cr content of spinels is controlled by several factors.

General trends of Fe^{3+} and Ti enrichment, typical of spinel series minerals, are probably controlled by the changing melt composition and decreasing temperature (Haggerty, 1976). There is a significant difference in the ulvospinel content of titanomagnetite between MB1 benmoreite and MB2 phonolite at Minna Bluff. This may reflect higher temperatures of crystallization for the phonolite.

The stability and composition of ilmenite series minerals is als a function of bulk chemistry, temperature and f_{O2}.

The coexisting titanomagnetite - ilmenite pair in AW84761 was used to calculate an equilibrium temperature and oxygen fugacity for this lava using the method of Stormer (1983). Calculations suggest a crystallization temperature of 919 +/-75 ^{o}C and log f_{O2} of -13.50 +/- 0.98. These conditions are close to the QFM buffer curve.

7.11 AENIGMATITE

Aenigmatite occurs as a groundmass phase in most peralkaline, and a few non-peralkaline Group I trachytes. It also occurs in Group II trachytes from MB1 at Minna Bluff. Some samples contain resorbing opaque oxide minerals, which are in a late stage reaction relationship with aenigmatite. No electron microprobe analyses of aenigmatite were made.

Aenigmatite is common in peralkaline volcanic suites (Abbott, 1967; Deer et al., 1966; Marsh, 1975; Larsen, 1977) and the late stage formation of aenigmatite in DVS samples is consistent with their generally undersaturated nature (Larsen, 1977).

The composition and stability of aenigmatite is dependent on melt composition and has an inverse relationship to oxygen fugacity, temperature, and volatile pressure. Higher volatile pressures will favor the amphibole crystallization. The absence of alkali amphibole phenocrysts, coupled with the strong hedenbergite trend in clinopyroxene compositions suggests that magma evolution took place at relatively low f_{O2} and volatile pressures. Higher temperatures probably inhibited aenigmatite crystallization until after final emplacement or eruption.

7.12 APATITE

Apatite is an accessory mineral in many lavas of basic to intermediate composition. It is observed in the groundmass of a few samples, and as tiny inclusions in olivine and clinopyroxene. It generally forms larger inclusions in kaersutite. Apatite occurs as microphenocrysts in some MD1 tephriphonolites at Mt Discovery. Microprobe analyses of apatite were not made.

Apatite is a known sink for the trivalent REEs as well as being the only mineral containing appreciable amounts of P_2O_5. Partition coefficients are strongly dependent on temperature and melt composition (Watson, 1981), particularly in the more silicic lavas. Kyle (1976) noted high P_{2O5} in a kaersutite from the MVG and attributed it to apatite inclusions. The effect of apatite inclusions in kaersutite would enhance the ability of kaersutite fractionation in removing middle REEs. Apatite is, therefore, an important consideration in fractionation models.

7.13 SUMMARY

DVS lavas are composed of olivine, clinopyroxene, kaersutite, feldspar, opaque oxides and aenigmatite, with accessory nepheline, apatite, biotite, and alkali amphibole. Extensive solid solution series allow olivine, clinopyroxene, titanomagnetite, and feldspar to crystallize over a broad range of host compositions.

The main difference between lavas from Groups I and II is the prevalence of kaersutite in Group II lavas of basic and intermediate composition, and the presence of plagioclase phenocrysts in some Grou I ultrabasic lavas. Despite the earlier appearance of plagioclase phenocrysts in some Group I magmas, the changing feldspar composition in basic and intermediate lavas is similar for both Groups. This suggests that there were no major differences in temperature or PH2O conditions between Groups I and II.

Kaersutite crystallization in Group II magmas is probably controlled by bulk composition. However, the Ti and Al content of kaersu tites suggest that Group IIA magmas of tephrite to phonolite composi-

tion crystallized at greater depths than phonotephrite to phonolite magmas from Group IIB, perhaps in the vicinity of the mantle - crust boundary (Figure 7.12B). Kaersutites in Group IIB lavas forming the Mt Discovery volcano (MD1), and in a tephriphonolite from the lower sequence at Minna Bluff, suggest that these magmas probably crystallized at shallower crustal depths. Although crystallization of Al-clinopyroxene is dependent on melt composition, its presence is also consistent with crystallization of these magmas at higher pressures (Aoki and Shiba, 1973; Wass, 1979a; Duda and Schmincke, 1985) than Group I magmas.

The strong Fe^{2+} enrichment coupled with the lack of Fe^{3+} enrichment of clinopyroxenes in all but a few Group I rocks suggests that crystallization of most DVS magmas took place at oxygen fugacities below that controlled by the hematite - magnetite buffer reaction. However, it is likely that those Group I lavas crystallizing sodic pyroxene cystallized at higher f_{O2}. The restriction of arfevdsonite to the groundmass of Group I trachytes suggests f_{H2O} was also low throughout the crystallization of Group I magmas.

An ilmenite - titanomagnetite pair in phonotephrite from Mt Discovery suggests that log f_{O2} was between -12.5 and -14.5, and temperature was between 850 - 1000^{o} in this sample. These conditions are close to the QFM buffer curve and probably reflect the general temperature and oxygen fugacity conditions under which most DVS lavas crystallized. Variation in the ulvospinel content of titanomagnetites from lavas with a similar SiO_2 content at Minna Bluff suggests that the younger MB2 phonolite (AW82150) may have crystallized at higher temperatures than the older benmoreite (AW82056) and trachyte lavas.

Chapter 8

GEOCHEMISTRY

8.1 INTRODUCTION

Two hundred and ten new rock samples from the DVS were analysed for major and trace elements by X-ray fluorescence analysis (XRF). Loss on ignition determinations provided a combined assessment of volatile content and the effect of oxidation of FeO. Eighteen samples were subjected to wet chemical analysis to determine FeO content. Ninety-four samples were analysed for total iron as FeO (FeO*), Na_2O, and selected trace elements, including some rare earth elements, usin instrumental neutron activation analysis (INAA). Details of analytica procedures, data quality, and the tabulated results are presented in Appendix 5.

Prior to this study there were 73 analyses of lavas from the DVS area reported in several different sources (Table 8.1). Averaged analyses of samples from Black Island and White Island (Goldich et al., 1981) were not included in this study. Existing analyses from Gandalf Ridge, Castle Ridge, the Foothills area, Brown Peninsula, Black Island, and White Island are relied on heavily, because there are few, if any, new analyses from these areas.

8.2 FeO ANALYSIS

FeO was determined by back titration (Reichen and Fahey, 1962) o 18 samples which showed a range of SiO_2 concentrations and LOI value Results are presented in Table 8.2.

There is a weak inverse correlation ($r^2 = -0.67868$) between FeO/Fe_2O_3 ratio and SiO_2 content, which suggests that the FeO/Fe_2O_3

Table 8.1 - Distribution and density of existing and new analyses in the Discovery Volcanic Subprovince, listed by stratigraphic unit (RG - Riviera and Gandalf Ridges, MS - Mason Spur, MB - Minna Bluff, MD - Mt Discovery, BP - Brown Peninsula, BI - Black Island, WI - White Island, MM - Mt Morning).

Unit	Existing Analyses	Source	New XRF Analyses	New INAA Analyses
RG1	38	Muncy, 1979	8	4
RG2	0		12	5
RG3	0		7	1
MS1	0		7	1
MS2	0		3	2
MS3	0		29	9
MS5	0		17	3
MS7	0		10	3
MS8	0		3	3
MS9	0		13	3
MB1	0		22	19
MB2	2	Kyle, 1976 Goldich et al, 1975	10	8
MD1	4	Kyle, 1976 Goldich et al, 1975	26	14
MD2	1	Kyle, 1976	22	13
BP	11	Kyle et al, 1979 Goldich et al, 1975	0	0
BI1	2	Goldich et al, 1975	0	0
BI2	1	Goldich et al, 1975	0	0
WI	2	Goldich et al, 1975	0	0
MM1	0		6	3
MM2	3	Muncy, 1979 Goldich et al, 1975	11	3
F	10	Kirsch,1981 McIver & Gevers,1970 Keys et al, 1977 Goldich et al, 1975	4	0
Total	74		210	94

Table 8.2 - Analytical results of wet chemical FeO determinations on selected rock samples from the DVS, listed by increasing SiO_2 content SiO_2, XRF determination of total iron as Fe_2O_3 (Fe_2O_3*), FeO/Fe_2O_3, and loss on ignition (LOI) are also given.

Samle No.	SiO2	Fe2O3*	FeO	FeO/Fe2O3	LOI
AW83471	39.63	17.86	11.29	2.13	-0.91
AW83583	41.84	13.96	10.11	3.72	-0.32
AW83550	42.48	11.52	8.14	3.30	-0.52
AW83454	42.95	11.63	7.47	2.40	2.72
AW83413	46.00	12.38	7.85	2.14	-0.65
AW84753	48.66	10.87	7.68	3.30	-0.63
AW84758	52.46	7.52	0.50	0.07	0.01
AW83513	53.29	8.88	1.11	0.15	3.16
AW84756	56.08	7.15	4.41	1.96	-0.08
AW84744	59.70	4.99	1.83	0.62	0.39
AW83647	60.02	6.98	3.40	1.06	0.22
AW83431	60.72	6.20	0.29	0.05	2.11
AW83581	61.37	7.78	0.10	0.01	2.38
AW83653	61.60	8.75	2.78	0.49	1.41
AW83508	62.25	6.16	2.69	0.85	0.80
AW83569	63.43	6.50	0.00	0.00	1.46
AW83567	63.70	7.08	0.40	0.06	1.49
AW83411	66.82	2.57	0.04	0.02	0.54

ratio decreased with increasing differentiation. However, the oxidation state of iron may also have been modified by other processes such as:

1. exposure of hot lava to air during eruption.
2. chemical break down of primary mineral structures and glass in the presence of water and air during weathering.
3. heating during the analytical procedure.

Only the total iron determinations are quoted in the tables of analyses in Appendix 5, because of the uncertain petrologic significance of measured FeO content.

8.3 ROCK NOMENCLATURE

Rock samples are named according to the latest recommendations of the IUGS Subcommission on the Systematics of Igneous Rocks (Le Bas et al., 1986) using the total alkalis - silica (TAS) diagram (Figure 8.1). Further subdivision of these fields uses CIPW normative compositions. Since normative compositions depend on the iron oxidation state, and since this was not determined in most samples, a theoretical calculation of FeO/Fe_2O_3* was used. This particular procedure, based on an empirical comparison of the iron oxidation state relative to SiO_2 and total alkalis, was chosen, because it was the procedure adopted by Le Bas et al. (1986) in determining the fields on the

---

* Specific equations used (Le Maitre, 1976):

$$FeO = Fe_2O_3^* \, [0.93 - 0.0042 \, SiO_2 - 0.022 \, (Na_2O + K_2O)]$$

$$Fe_2O_3 = Fe_2O_3^* - 1.111 \, FeO$$

where all oxides are in weight per cent.

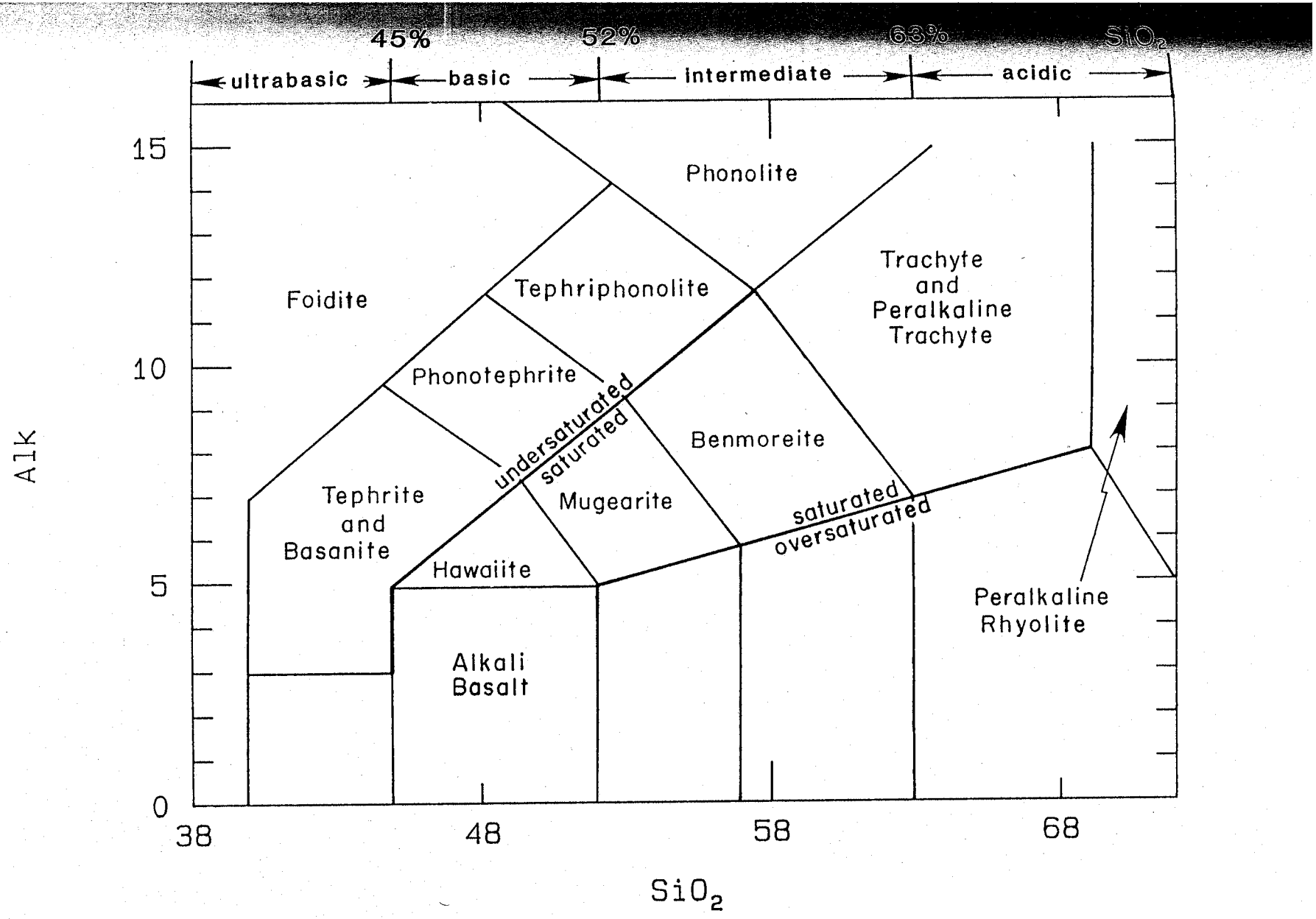

Figure 8.1 - Total alkalis (Alk) - silica diagram showing the IUGS recommended nomenclature for volcanic rocks (Le Bas et al., 1986). The division between basanite and tephrite is defined as greater than or less than 10 wt % normative nepheline, respectively. The prefix "peralkaline" is applied to rocks with an agpaitic index of one or greater. (Agpaitic index = $(Na_2O + K_2O)/Al_2O_3$ where elements are expressed in molecular proportions.) Fields of SiO_2 oversaturation, saturation, and undersaturation are given from

TAS diagram. A classification in which rock samples are divided into ultrabasic, basic, intermediate, and acidic is based on SiO_2 content (Le Bas et al., 1986), and is shown along the top of Figure 8.1.

8.4 SUBDIVISION OF DVS ROCKS BASED ON ALKALI ENRICHMENT TRENDS

Many DVS rock suites, each of which represents one of the stratigraphic units defined in Chapter 3, plot along smooth trends within the saturated to undersaturated compositional range of the alkali - SiO_2 diagram (Figure 8.2). Group I rock suites from the lower parts of the Mason and Gandalf volcanic complexes (MS1-5, RG1) exhibit trends of mild alkali enrichment, which may be followed by late stage alkali depletion (Figure 8.2A and B). The enrichment part of the trend is poorly constrained in both volcanic complexes, because of a scarcity of rocks less evolved than trachyte. In contrast, rock suites from the upper parts of these volcanic complexes (MS7,RG2) exhibit well defined trends. Group II rocks have higher alkali contents than Group I rocks (Figure 8.2G). Thus, there is a geochemical, as well as a chronological, difference between rocks in Groups I and II.

There is some variability in the alkali enrichment trends of individual Group II rock suites, although these trends merge in rocks with <52 wt % SiO_2. Intermediate rocks from Minna Bluff clearly define two alkali enrichment trends (Figure 8.2C), with the younger rocks (MB2) exhibiting stronger alkali enrichment than the older rocks (MB1). A similar relationship is suggested by rock suites at Mt Discovery (Figure 8.2D), although the evolved end of the younger MD2 trend is only controlled by a single sample. Older rocks from Mt Morning (MM1) exhibit a similar trend to those of MB1 and MD1 (Figure 8.2E), whereas the well-defined trend of strong alkali enrichment

Figure 8.2 - Variation of total alkali content (Alk) with SiO2 for DVS rock suites. Trends for individual rock suites are shown on diagrams A-F, and are all plotted on diagram G for comparison. Alkali and SiO2 concentrations are in oxide weight per cent.

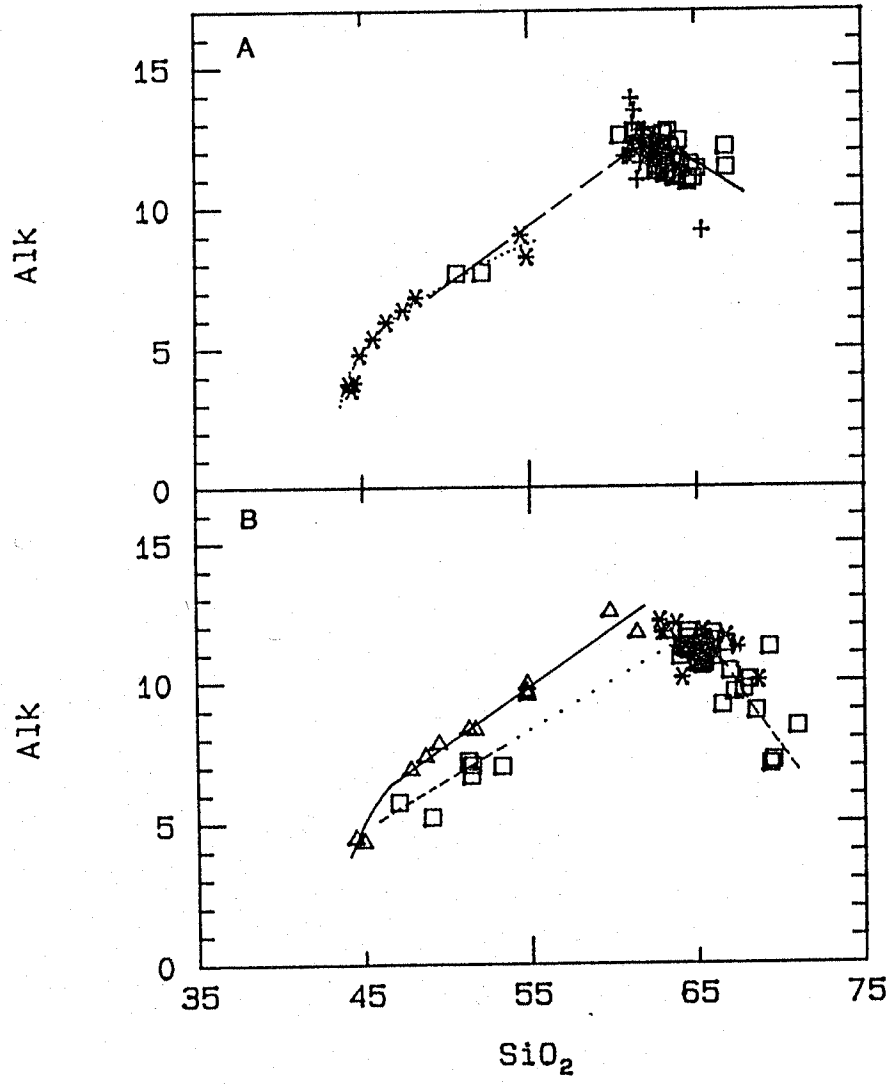

A - Group I rocks from Mason Spur

□ MS1 - MS3

\+ MS5

✳ MS7

—— MS1 - MS3 trend, dashed where inferred

····· MS7 trend

B - Group I rocks from Riviera and Gandalf Ridges

□ RG1 at Gandalf Ridge

✳ RG1 at Riviera Ridge

△ RG2

– – – RG1 trend, dotted where inferred

—— RG2 trend

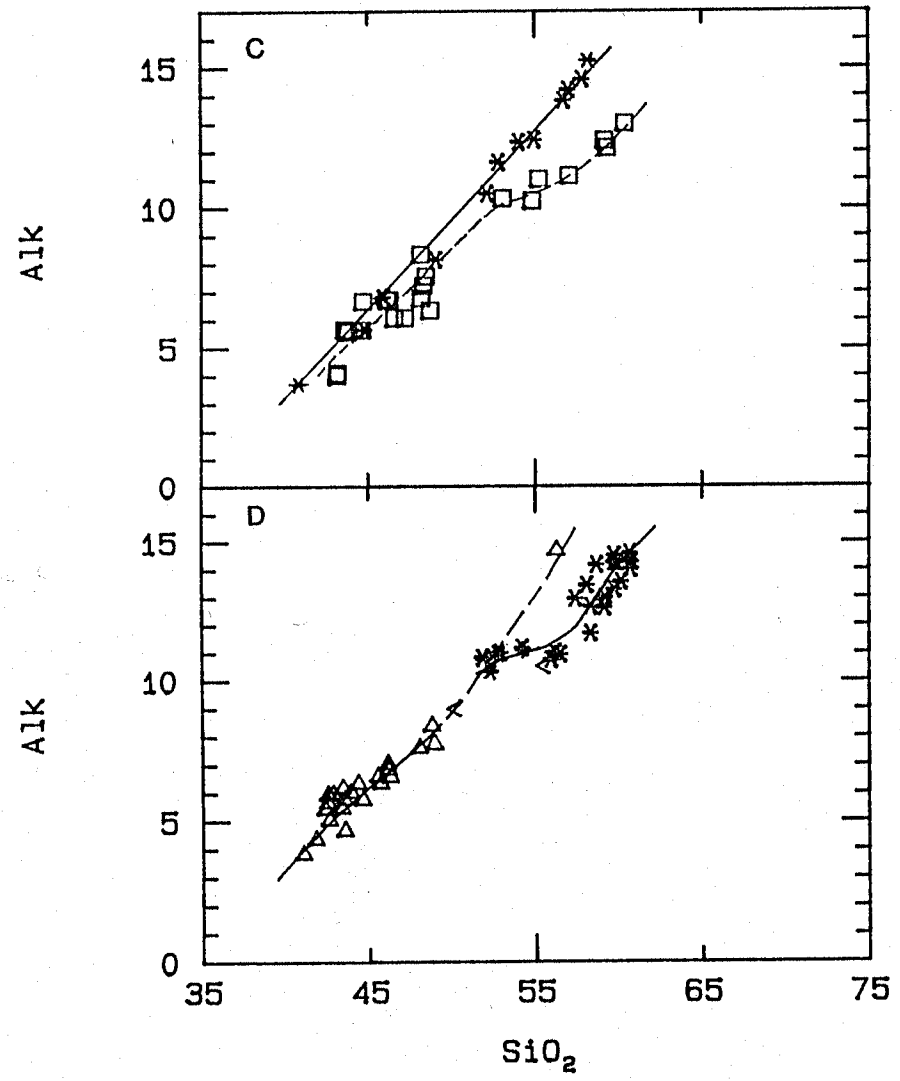

C - Group II samples from Minna Bluff

□ MB1

✳ MB2

----- MB1 trend

——— MB2 trend

D - Group II samples from Mt Discovery

✳ MD1

< Xenoliths in MD1

△ MD2

——— MD1 trend

—— — MD2 trend

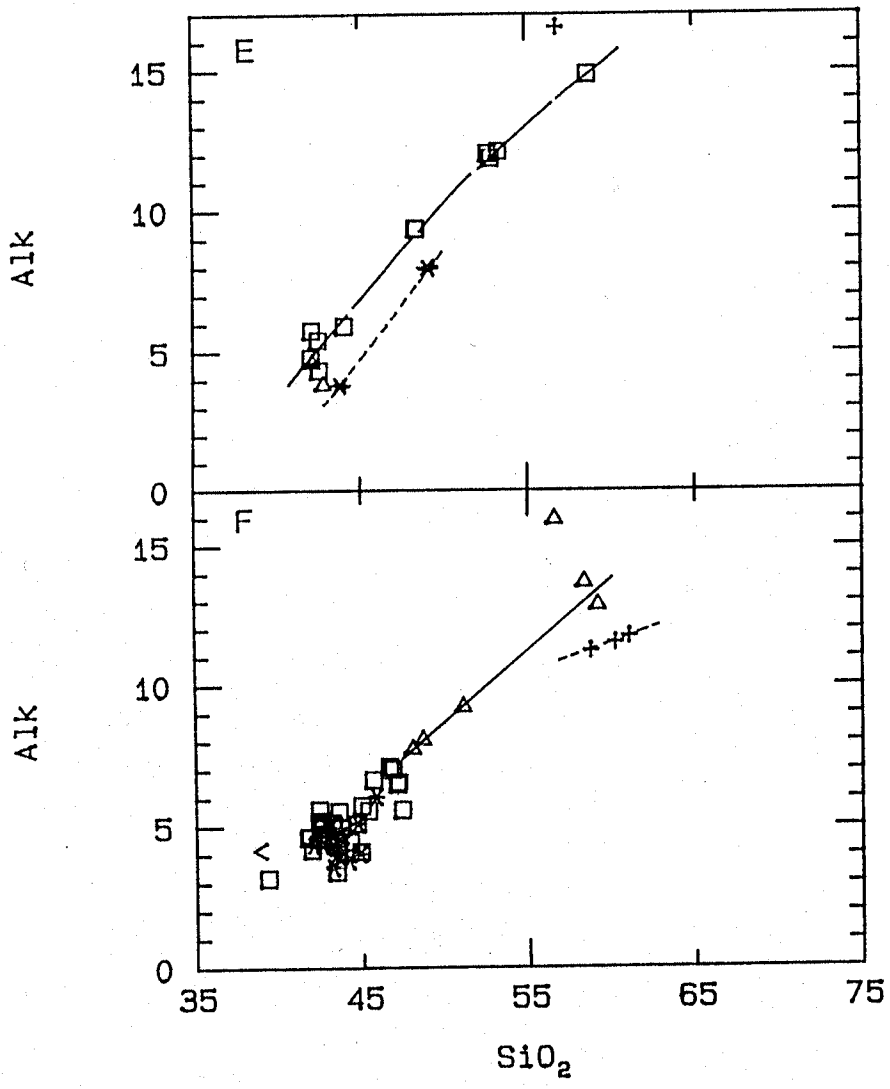

E - Group II samples from Brown Peninsula, Black Island, and White Island

□ BP

✳ BI1

\+ BI2

△ WI

——— BP trend

------ Possible BI1 trend

F - Group II samples from Mt Morning, Mason Spur (MS8 and MS9), Riviera Ridge (RG3), and the Foothills of Royal Society Range.

△ MM1

□ MM2, MS9, and RG3

\+ MS8

✳ F

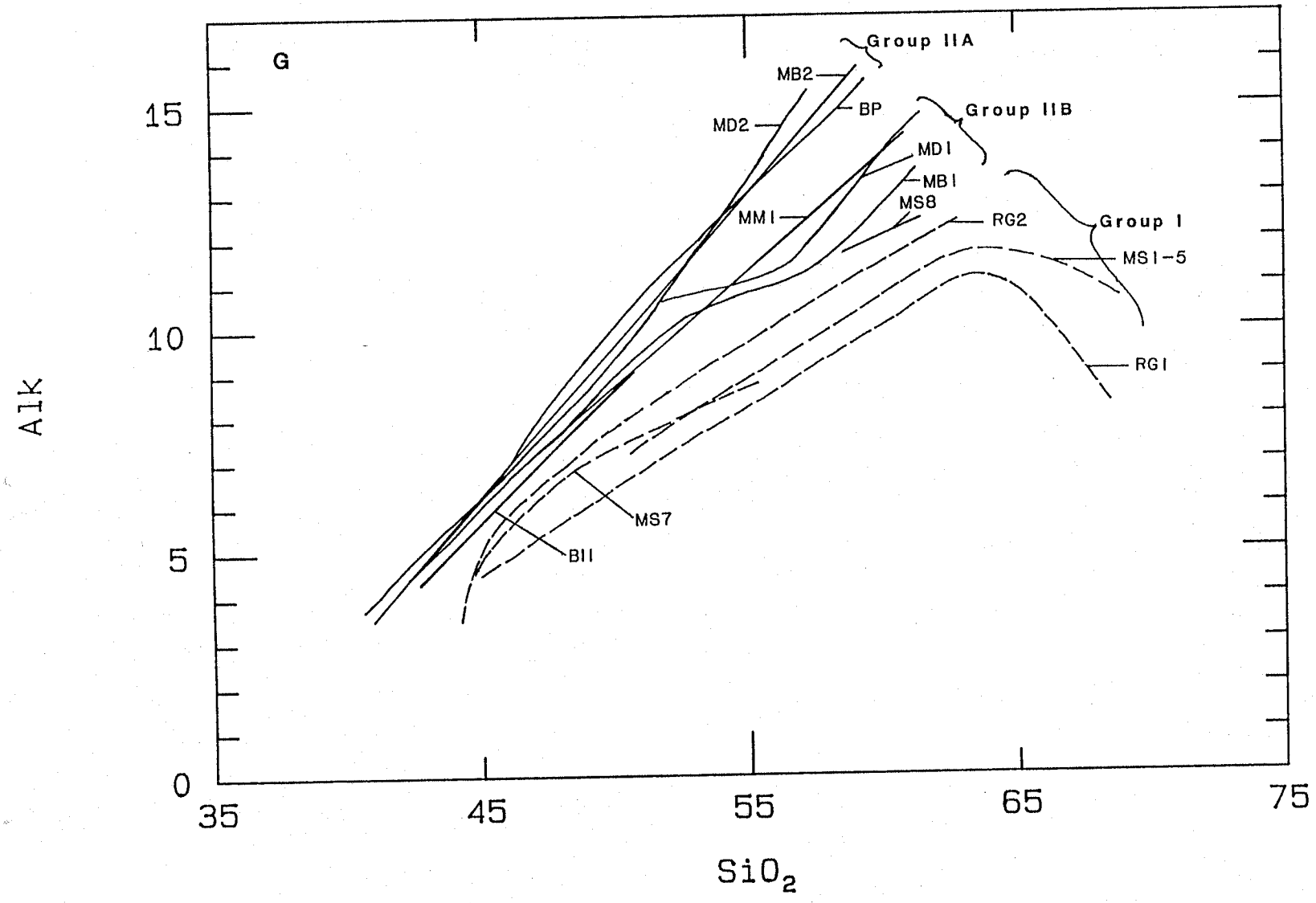

G - Compilation of alkali enrichment trends shown in Figures 8.2 A - F. Group I trends are dashed, whereas Group II trends are shown as solid lines.

exhibited by rocks from Brown Peninsula (Figure 8.2F) is similar to those of MB2 and MD2.

To facilitate data presentation and discussion, Group II rock suites are grouped into two suites on the basis of alkali enrichment trends (Figure 8.2G). The boundary between the suites is arbitrary. Those rock suites with stronger trends of alkali enrichment are designated as the "A" suite, and will be referred to as Group IIA. Group IIA comprises rocks from BP, MB2, and MD2. Group II rock suites with milder trends of alkali enrichment than Group IIA are designated as Group IIB. Group IIB comprises MB1, MD1, MM1 and MS8. Group II rock suites which do not contain rocks with >52 wt % SiO_2 (MM2, MS9, RG3, F, BI1 and WI) cannot be assigned in this subdivision. The decision to plot unassigned rock suites with Group IIA on geochemical diagrams is arbitary. A phonolite sample (AW86128) from MM1 lies well off the MM1 alkali enrichment trend, and is even atypical of other Group IIB rocks. Therefore, it has not been considered in determining the field of Group IIB rocks, but is plotted separately on variation diagrams comparing Group I, Group IIA, and Group IIB.

8.5 MAJOR ELEMENT CHEMISTRY

Major element chemistry is shown in variation diagrams (Figures 8.3 - 8.12).

Total iron (FeO*), MgO and CaO exhibit strong depletion trends in all DVS rock suites. Depletion is strongest for Group IIA and weakest for Group I rock suites. A similar, though less pronounced relationship is displayed by MgO and CaO. MnO remains fairly constant in Group II rocks, but exhibits a trend of mild enrichment, followed by strong depletion, in rocks from Group I.

Figure 8.3 - TiO_2 (wt %) plotted against SiO_2 (wt %).

Diagram	Group	Stratigraphic units
A	IIA	✳ BP, MB2, MD2, BI2, WI □ MM2, MS9, RG3, F < Amphibolite xenolith from RG3
B	IIB	□ MB1 ✳ MD1 △ MM1 + MS8 < Xenoliths in phonolite from MD1
C	I	+ MS1 - MS7 □ RG1 at Gandalf Ridge ✳ RG1 at Riviera Ridge △ RG2
D	composite diagram comprising fields drawn from the data in diagrams A to C, excluding xenolith analyses. The triangular symbol represents analyses of sample AW86128.	

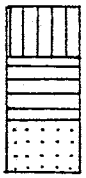

Group IIA

Group IIB

Group I

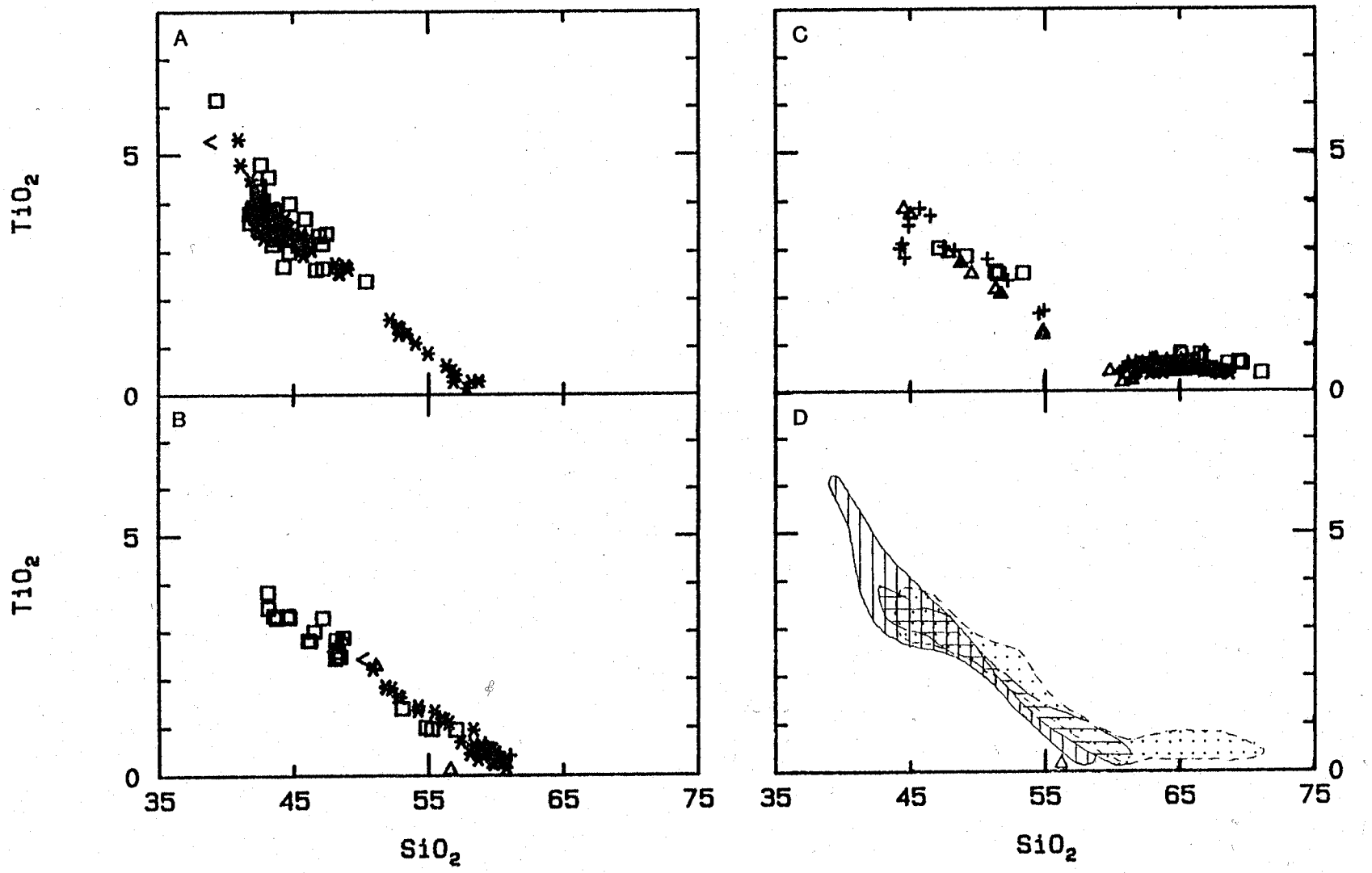
A
B
C
D
TiO_2
TiO_2
SiO_2
SiO_2
0
5
35
45
55
65
75

Figure 8.4 - Al_2O_3 (wt %) plotted against SiO_2 (wt %).

Diagram	Group	Stratigraphic units
A	IIA	✳ BP, MB2, MD2, BI2, WI □ MM2, MS9, RG3, F < Amphibolite xenolith from RG3
B	IIB	□ MB1 ✳ MD1 △ MM1 + MS8 < Xenoliths in phonolite from MD1
C	I	+ MS1 - MS7 □ RG1 at Gandalf Ridge ✳ RG1 at Riviera Ridge △ RG2
D	composite diagram comprising fields drawn from the data in diagrams A to C, excluding xenolith analyses. The triangular symbol represents analyses of sample AW86128.	

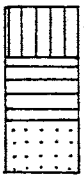

Group IIA

Group IIB

Group I

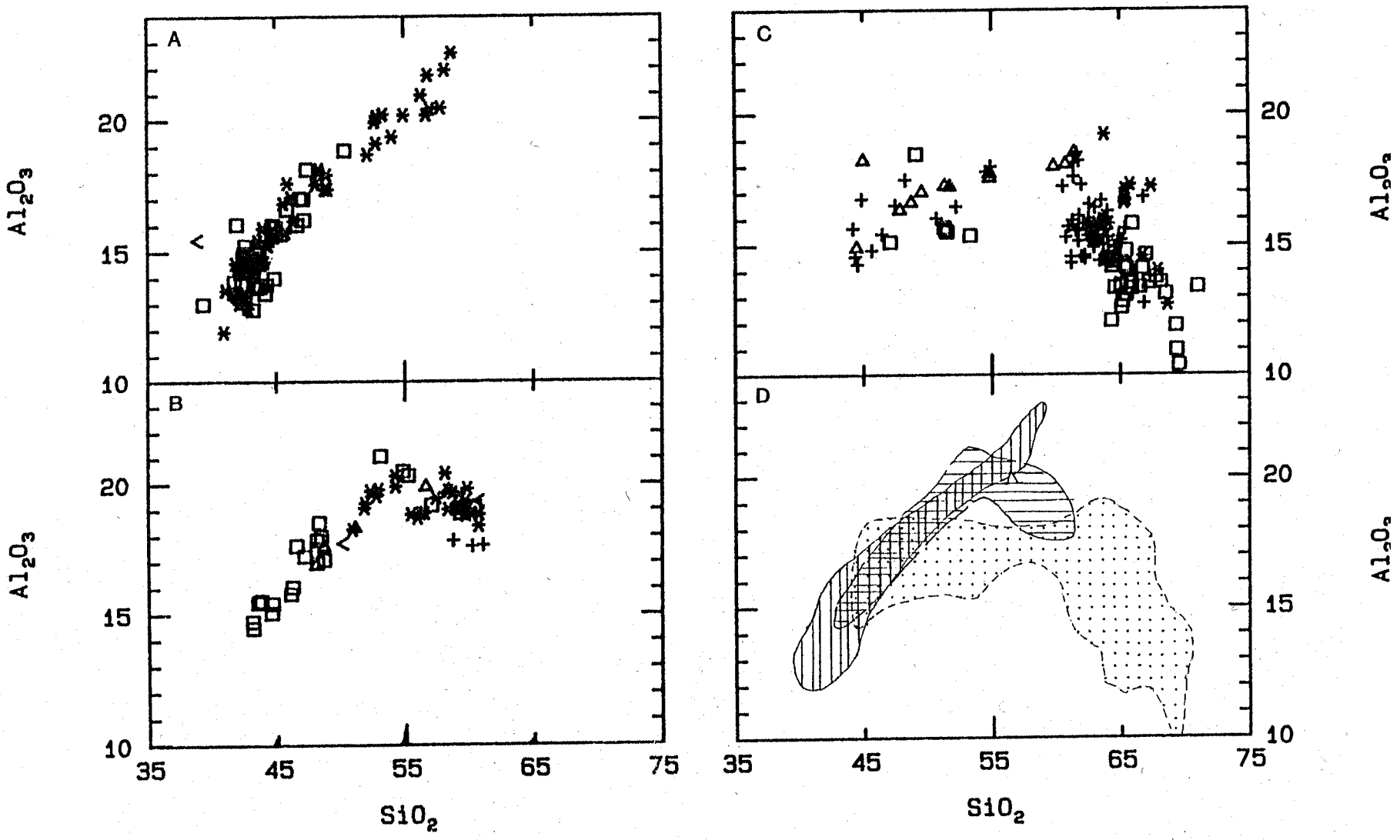
A
B
C
D
Al_2O_3
SiO_2
10
15
20
35
45
55
65
75

Figure 8.5 - FeO* (wt %) plotted against SiO_2 (wt %).

Diagram	Group	Stratigraphic units
A	IIA	✳ BP, MB2, MD2, BI2, WI □ MM2, MS9, RG3, F < Amphibolite xenolith from RG3
B	IIB	□ MB1 ✳ MD1 △ MM1 + MS8 < Xenoliths in phonolite from MD1
C	I	+ MS1 - MS7 □ RG1 at Gandalf Ridge ✳ RG1 at Riviera Ridge △ RG2
D	composite diagram comprising fields drawn from the data in diagrams A to C, excluding xenolith analyses. The triangular symbol represents analyses of sample AW86128.	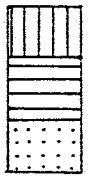 Group IIA Group IIB Group I

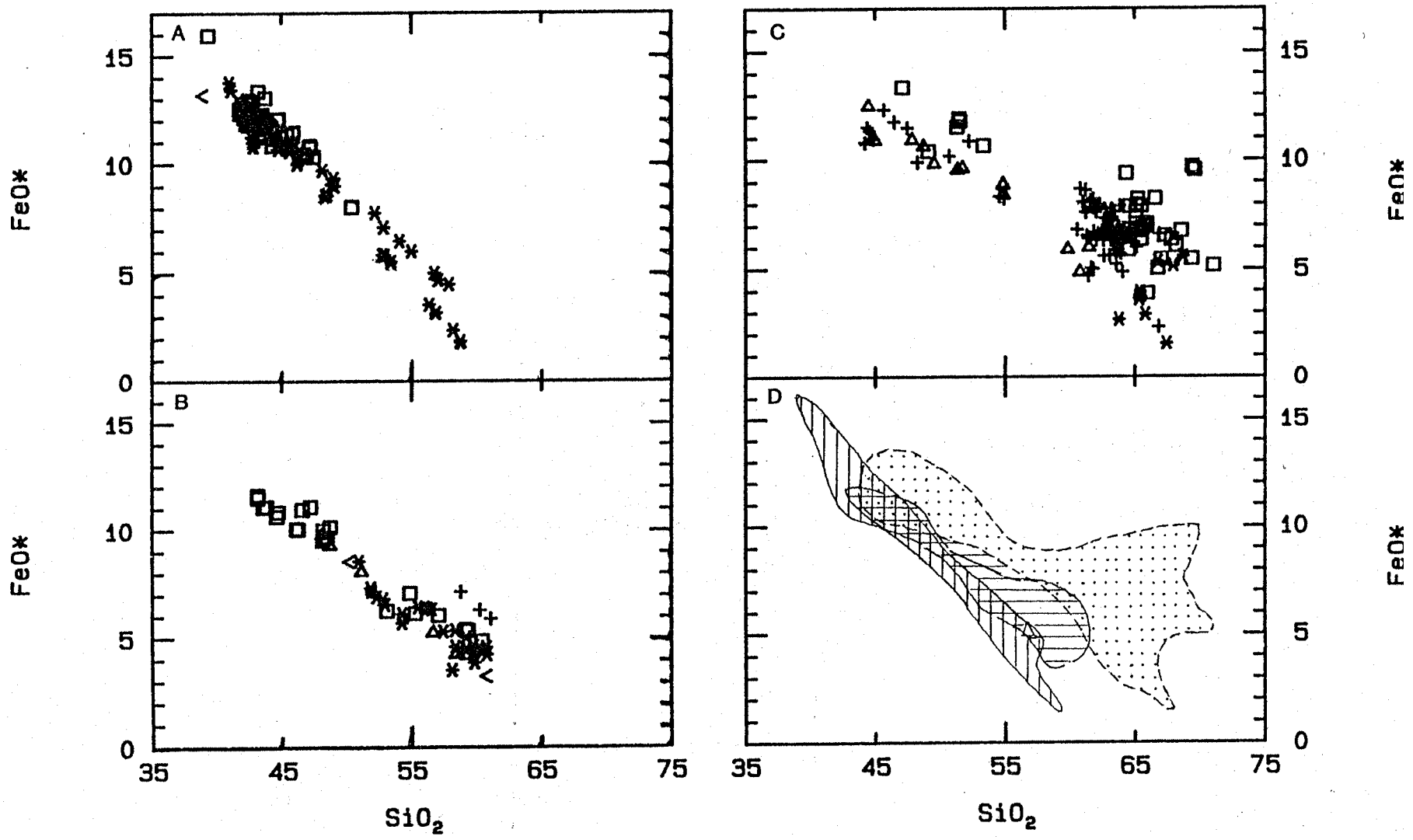
A
B
C
D
FeO*
FeO*
FeO*
FeO*
15
10
5
0
35
45
55
65
75
SiO2
SiO2

Figure 8.6 - MnO (wt %) plotted against SiO_2 (wt %).

Diagram	Group	Stratigraphic units
A	IIA	✳ BP, MB2, MD2, BI2, WI □ MM2, MS9, RG3, F < Amphibolite xenolith from RG3
B	IIB	□ MB1 ✳ MD1 △ MM1 + MS8 < Xenoliths in phonolite from MD1
C	I	+ MS1 - MS7 □ RG1 at Gandalf Ridge ✳ RG1 at Riviera Ridge △ RG2
D	composite diagram comprising fields drawn from the data in diagrams A to C, excluding xenolith analyses. The triangular symbol represents analyses of sample AW86128.	

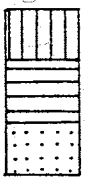

Group IIA

Group IIB

Group I

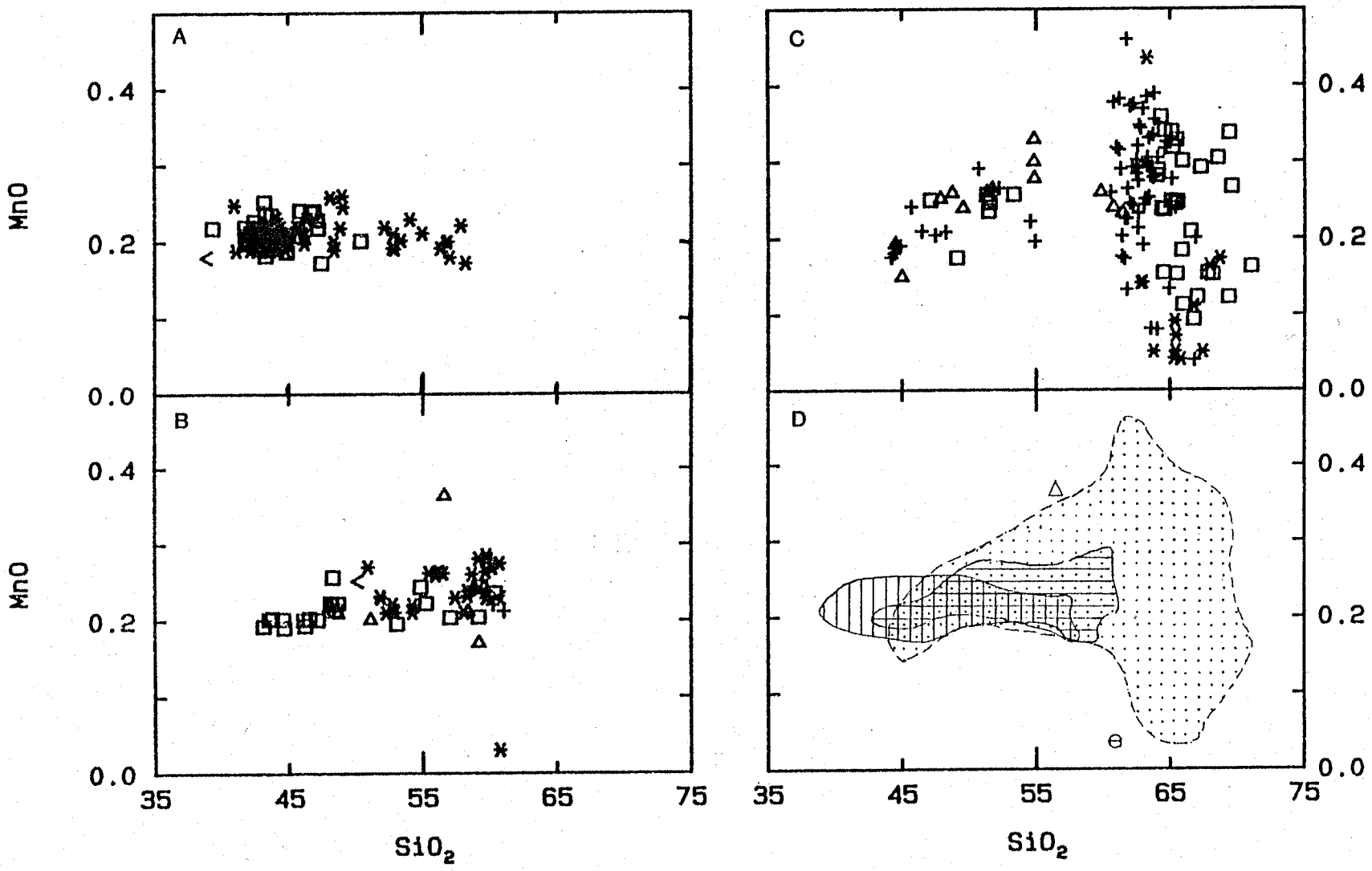
A
B
C
D
MnO
0.4
0.2
0.0
35
45
55
65
75
SiO2

Figure 8.7 - MgO (wt %) plotted against SiO_2 (wt %).

Diagram	Group	Stratigraphic units
A	IIA	✳ BP, MB2, MD2, BI2, WI □ MM2, MS9, RG3, F < Amphibolite xenolith from RG3
B	IIB	□ MB1 ✳ MD1 △ MM1 + MS8 < Xenoliths in phonolite from MD1
C	I	+ MS1 - MS7 □ RG1 at Gandalf Ridge ✳ RG1 at Riviera Ridge △ RG2
D	composite diagram comprising fields drawn from the data in diagrams A to C, excluding xenolith analyses. The triangular symbol represents analyses of sample AW86128.	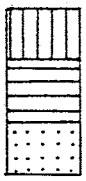 Group IIA Group IIB Group I

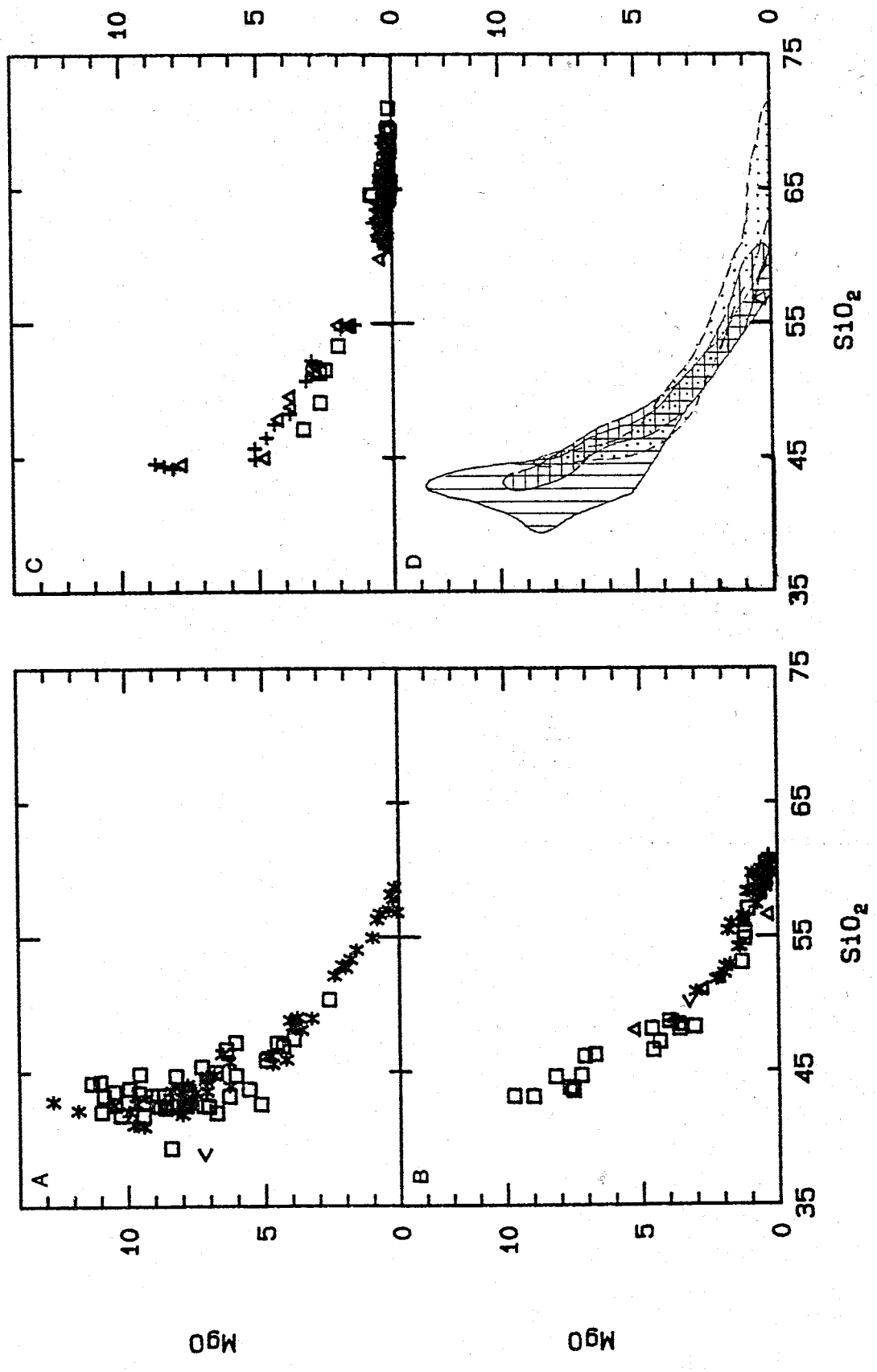
A
B
C
D
MgO
MgO
SiO_2
SiO_2
0
5
10
35
45
55
65
75

Figure 8.8 - CaO (wt %) plotted against SiO_2 (wt %).

Diagram	Group	Stratigraphic units
A	IIA	✳ BP, MB2, MD2, BI2, WI □ MM2, MS9, RG3, F < Amphibolite xenolith from RG3
B	IIB	□ MB1 ✳ MD1 △ MM1 + MS8 < Xenoliths in phonolite from MD1
C	I	+ MS1 - MS7 □ RG1 at Gandalf Ridge ✳ RG1 at Riviera Ridge △ RG2
D	composite diagram comprising fields drawn from the data in diagrams A to C, excluding xenolith analyses. The triangular symbol represents analyses of sample AW86128.	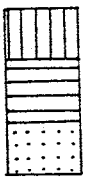 Group IIA Group IIB Group I

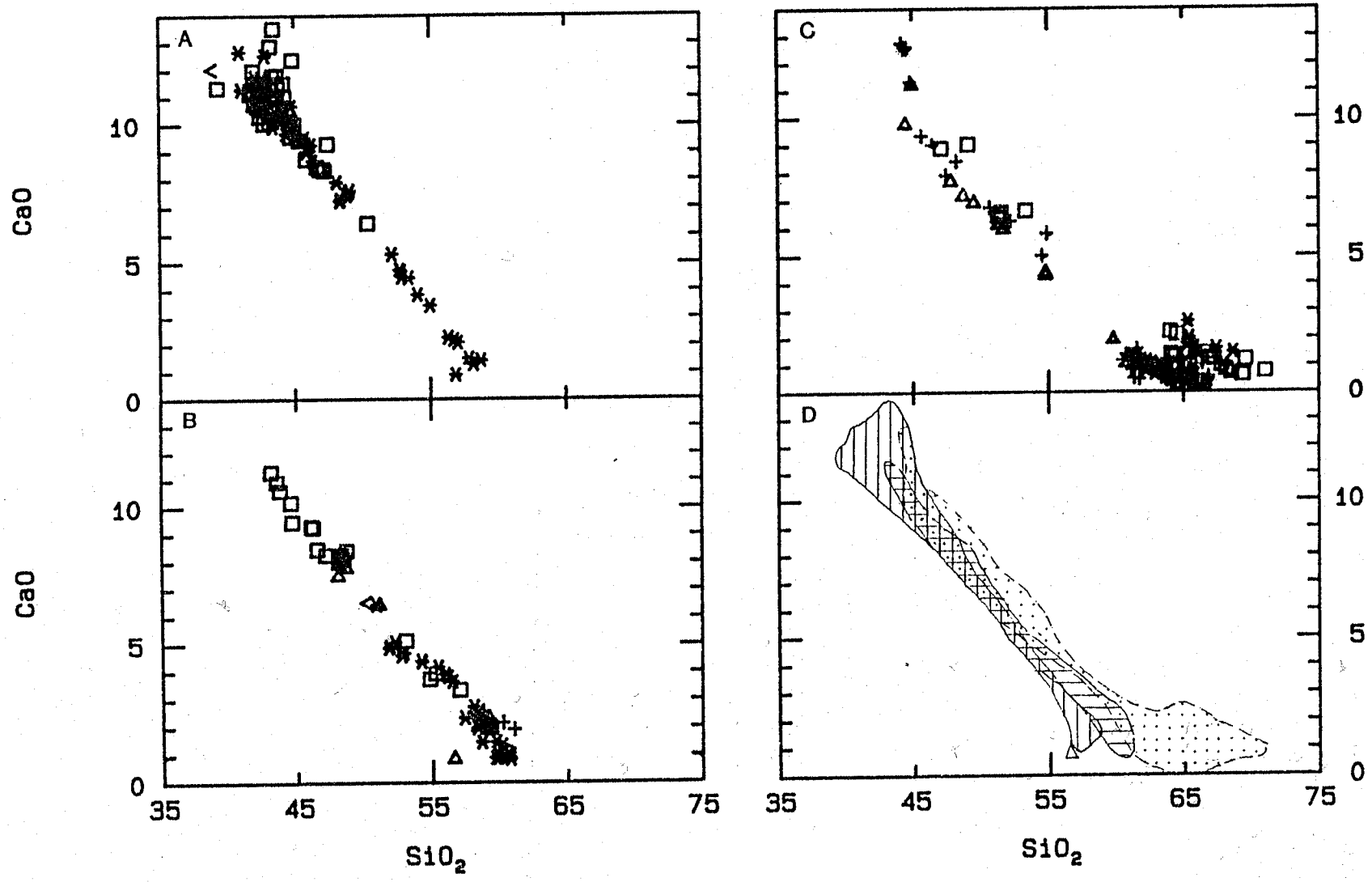
A
B
C
D
CaO
CaO
SiO_2
SiO_2
0
5
10
35
45
55
65
75

Figure 8.9 - Na_2O (wt %) plotted against SiO_2 (wt %).

Diagram	Group	Stratigraphic units
A	IIA	✳ BP, MB2, MD2, BI2, WI □ MM2, MS9, RG3, F < Amphibolite xenolith from RG3
B	IIB	□ MB1 ✳ MD1 △ MM1 + MS8 < Xenoliths in phonolite from MD1
C	I	+ MS1 - MS7 □ RG1 at Gandalf Ridge ✳ RG1 at Riviera Ridge △ RG2
D	composite diagram comprising fields drawn from the data in diagrams A to C, excluding xenolith analyses. The triangular symbol represents analyses of sample AW86128.	

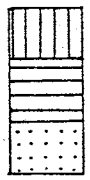

Group IIA

Group IIB

Group I

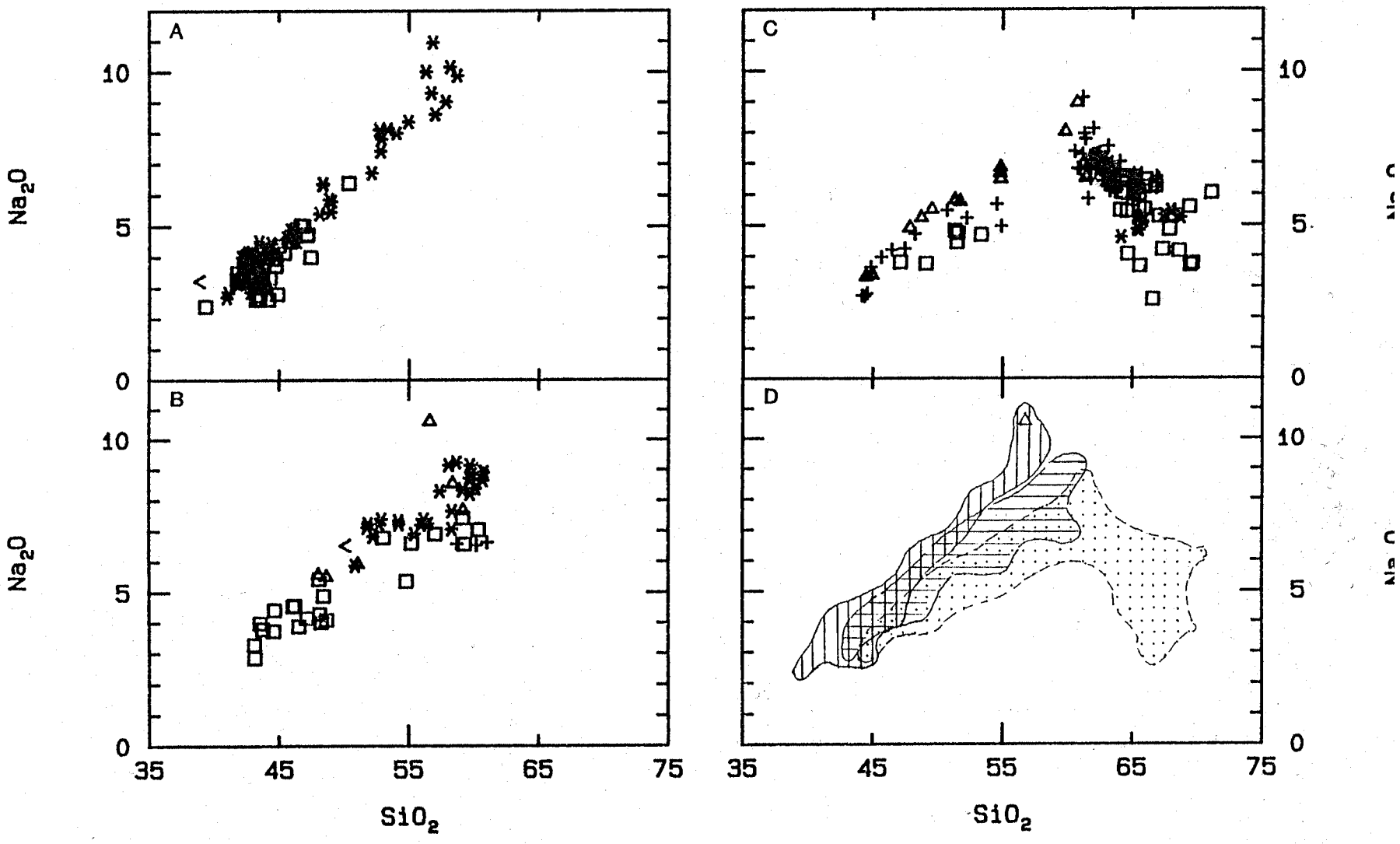
A
B
C
D
Na_2O
SiO_2
0
5
10
35
45
55
65
75

Figure 8.10 - K_2O (wt %) plotted against SiO_2 (wt %).

Diagram	Group	Stratigraphic units
A	IIA	✳ BP, MB2, MD2, BI2, WI □ MM2, MS9, RG3, F < Amphibolite xenolith from RG3
B	IIB	□ MB1 ✳ MD1 △ MM1 + MS8 < Xenoliths in phonolite from MD1
C	I	+ MS1 - MS7 □ RG1 at Gandalf Ridge ✳ RG1 at Riviera Ridge △ RG2
D	composite diagram comprising fields drawn from the data in diagrams A to C, excluding xenolith analyses. The triangular symbol represents analyses of sample AW86128.	

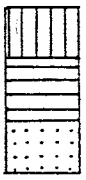

Group IIA

Group IIB

Group I

Figure 8.11 - P_2O_5 (wt %) plotted against SiO_2 (wt %).

Diagram	Group	Stratigraphic units
A	IIA	✳ BP, MB2, MD2, BI2, WI □ MM2, MS9, RG3, F < Amphibolite xenolith from RG3
B	IIB	□ MB1 ✳ MD1 △ MM1 + MS8 < Xenoliths in phonolite from MD1
C	I	+ MS1 - MS7 □ RG1 at Gandalf Ridge ✳ RG1 at Riviera Ridge △ RG2
D	composite diagram comprising fields drawn from the data in diagrams A to C, excluding xenolith analyses. The triangular symbol represents analyses of sample AW86128.	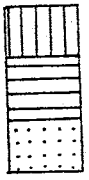 Group IIA Group IIB Group I

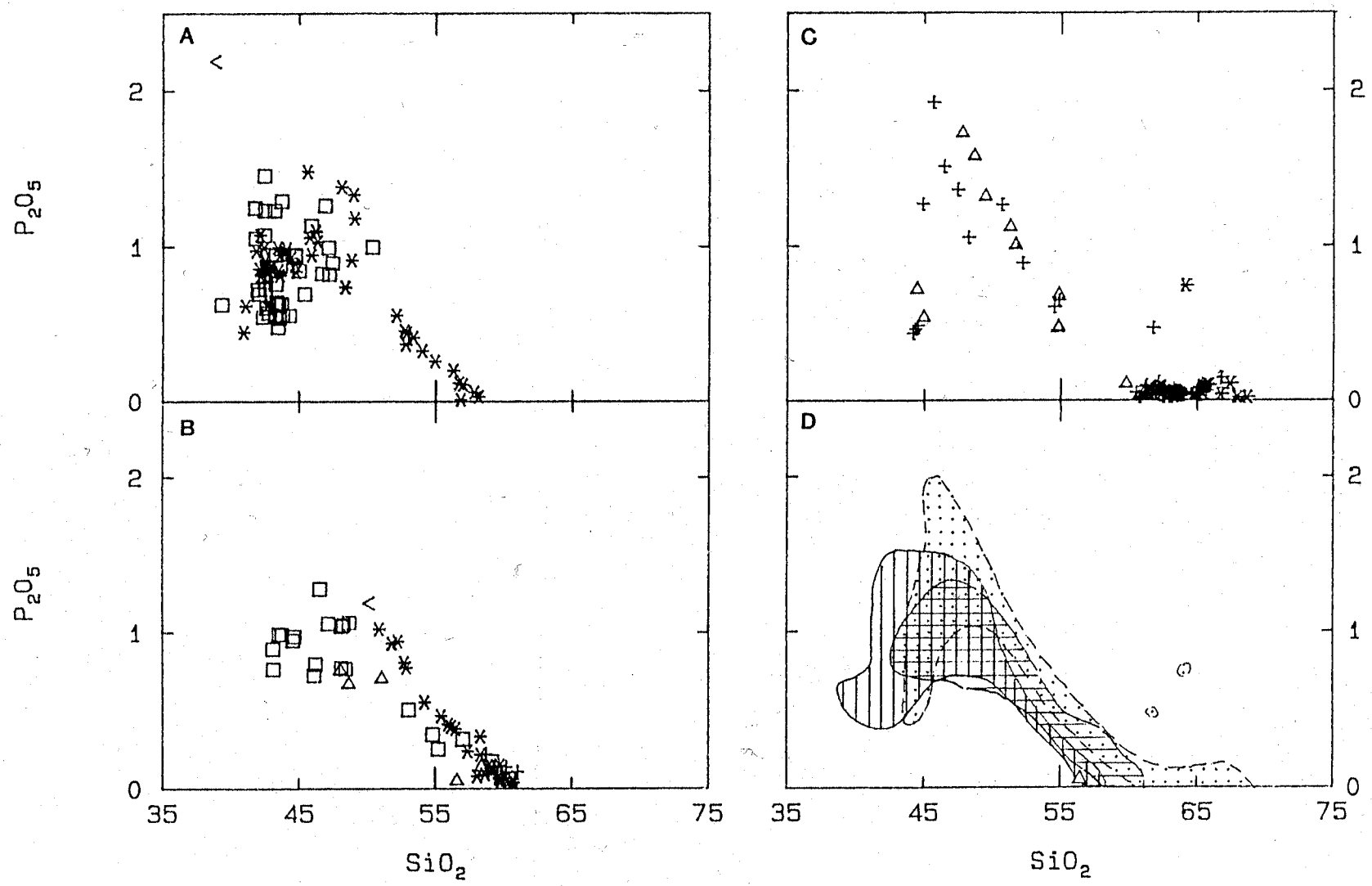
A
B
C
D
P_2O_5
SiO_2
0
1
2
35
45
55
65
75

Figure 8.12 - K_2O (wt %) plotted against Na_2O (wt %). The line $Na_2O/K_2O = 2$ divides MacDonald and Katsura's (1964) potassic and sodic fields.

Diagram	Group	Stratigraphic units
A	IIA	✳ BP, MB2, MD2, BI2, WI □ MM2, MS9, RG3, F < Amphibolite xenolith from RG3
B	IIB	□ MB1 ✳ MD1 △ MM1 + MS8 < Xenoliths in phonolite from MD1
C	I	+ MS1 - MS7 □ RG1 at Gandalf Ridge ✳ RG1 at Riviera Ridge △ RG2
D	composite diagram comprising fields drawn from the data in diagrams A to C, excluding xenolith analyses. The triangular symbol represents analyses of sample AW86128.	

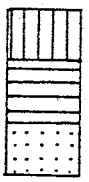

Group IIA

Group IIB

Group I

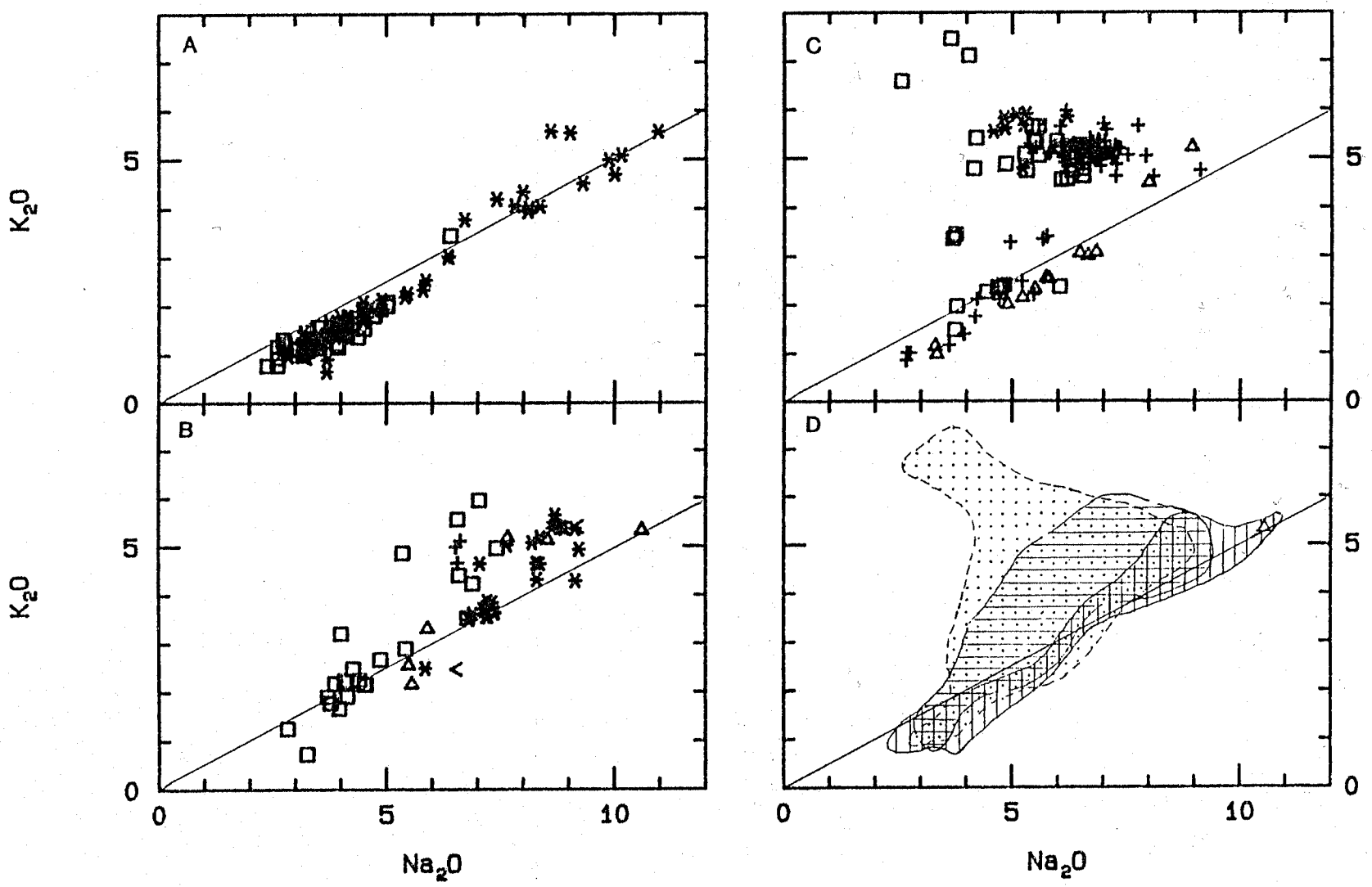
A
B
C
D
K_2O
K_2O
Na_2O
Na_2O
0
5
10

The behavior of Al_2O_3 varies considerably. Group IIA rock suites exhibit strong Al_2O_3 enrichment throughout differentiation, whereas those in Group IIB display strong Al_2O_3 enrichment in ultrabasic and basic rocks, followed by late stage depletion in rocks with >52 wt. % SiO_2. Early Al_2O_3 enrichment in basanites and tephrites from the Mason trend levels out in basic and intermediate rocks, and is followed by strong Al_2O_3 depletion in rocks with > 60 wt. % SiO_2.

DVS rocks are rich in alkalis. Sodium contents range from 2.41 to 10.95 wt. %, and potassium from 0.63 to 6.90 wt. %. Alkalis are enriched with differentiation, except for late stage depletion in some Group I trachytes. Na_2O enrichment is strongest for Group IIA and weakest for Group I. Although the K_2O enrichment trend is stronger in Group II rock suites, some Group I trachytes from Gandalf Ridge actually develop the highest K_2O contents of any DVS rocks. Group IIA straddles the line (Na_2O/K_2O = 2) MacDonald and Katsura (1964) used to divide sodic and potassic lineages (Figure 8.12). Group IIB and Group I samples plot to the potassic side of this line. Group I, Group IIB, and Group IIA suites broadly correlate with Kyle's (1976) potassic, transitional and sodic lineages descibed from The Pleiades in the Melbourne volcanic province.

8.6 TRACE ELEMENT CHEMISTRY

8.6.1 Incompatible Elements

Zr abundance ranges from 172 to 1985 ppm making it one of the most incompatible of the analysed trace elements. Therefore, Zr is used as a differentiation index in variation diagrams of SiO_2, and the trace elements (Figures 8.13 - 8.33). By comparing SiO_2 with Zr, it is

igure 8.13 - SiO_2 (wt %) plotted against Zr (ppm).

iagram	Group	Stratigraphic units
	IIA	✳ BP, MB2, MD2, BI2, WI □ MM2, MS9, RG3, F < Amphibolite xenolith from RG3
	IIB	□ MB1 ✳ MD1 △ MM1 + MS8 < Xenoliths in phonolite from MD1
:	I	+ MS1 - MS7 □ RG1 at Gandalf Ridge ✳ RG1 at Riviera Ridge △ RG2

) composite diagram comprising fields drawn from the data in diagrams A to C, excluding xenolith analyses. The triangular symbol represents analyses of sample AW86128.

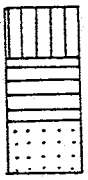

Group IIA

Group IIB

Group I

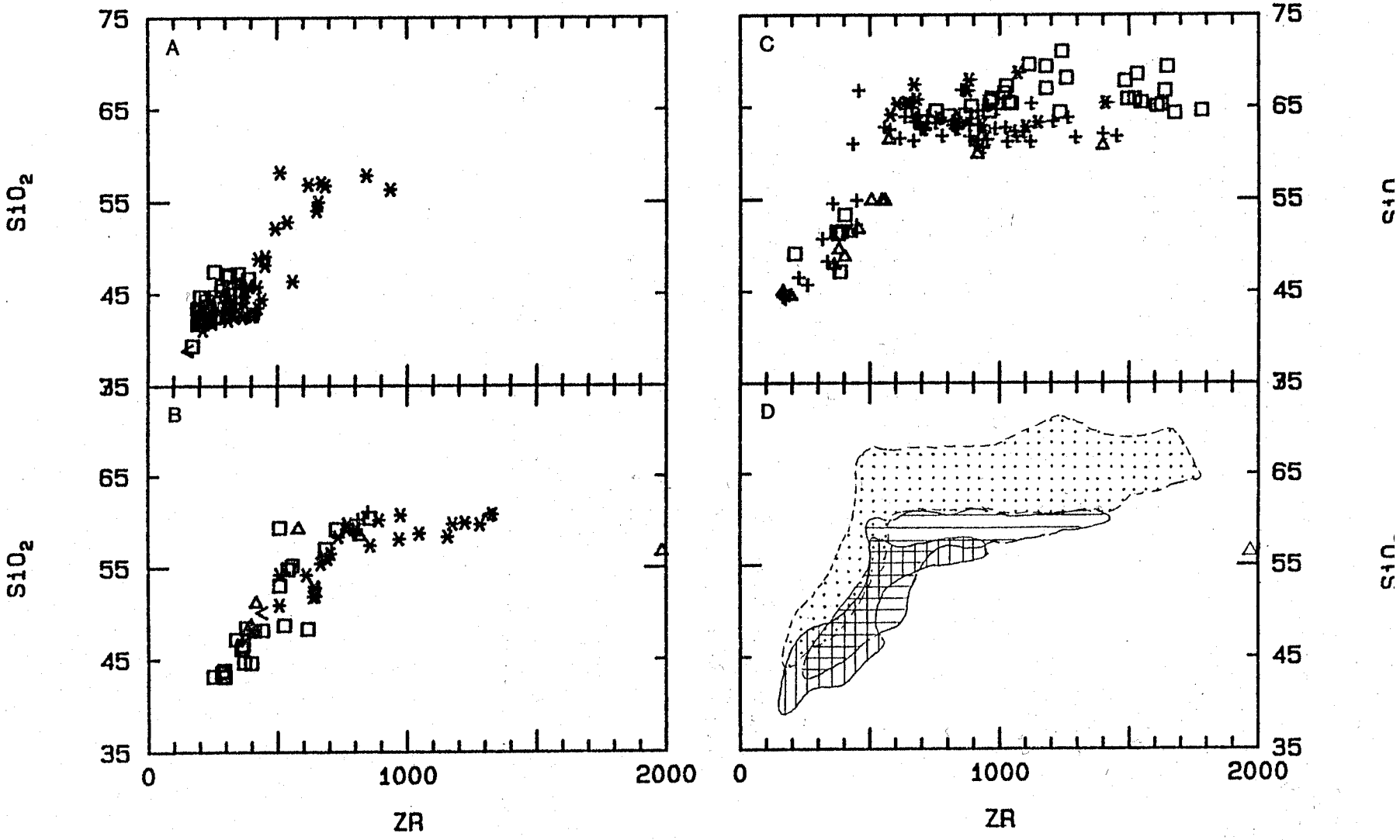
A
B
C
D
75
65
55
45
35
0
1000
2000
ZR
SiO2

Figure 8.14 - Nb (ppm) plotted against Zr (ppm).

Diagram	Group	Stratigraphic units
A	IIA	✳ BP, MB2, MD2, BI2, WI □ MM2, MS9, RG3, F < Amphibolite xenolith from RG3
B	IIB	□ MB1 ✳ MD1 △ MM1 + MS8 < Xenoliths in phonolite from MD1
C	I	+ MS1 - MS7 □ RG1 at Gandalf Ridge ✳ RG1 at Riviera Ridge △ RG2
D	composite diagram comprising fields drawn from the data in diagrams A to C, excluding xenolith analyses. The triangular symbol represents analyses of sample AW86128.	

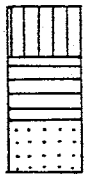

Group IIA

Group IIB

Group I

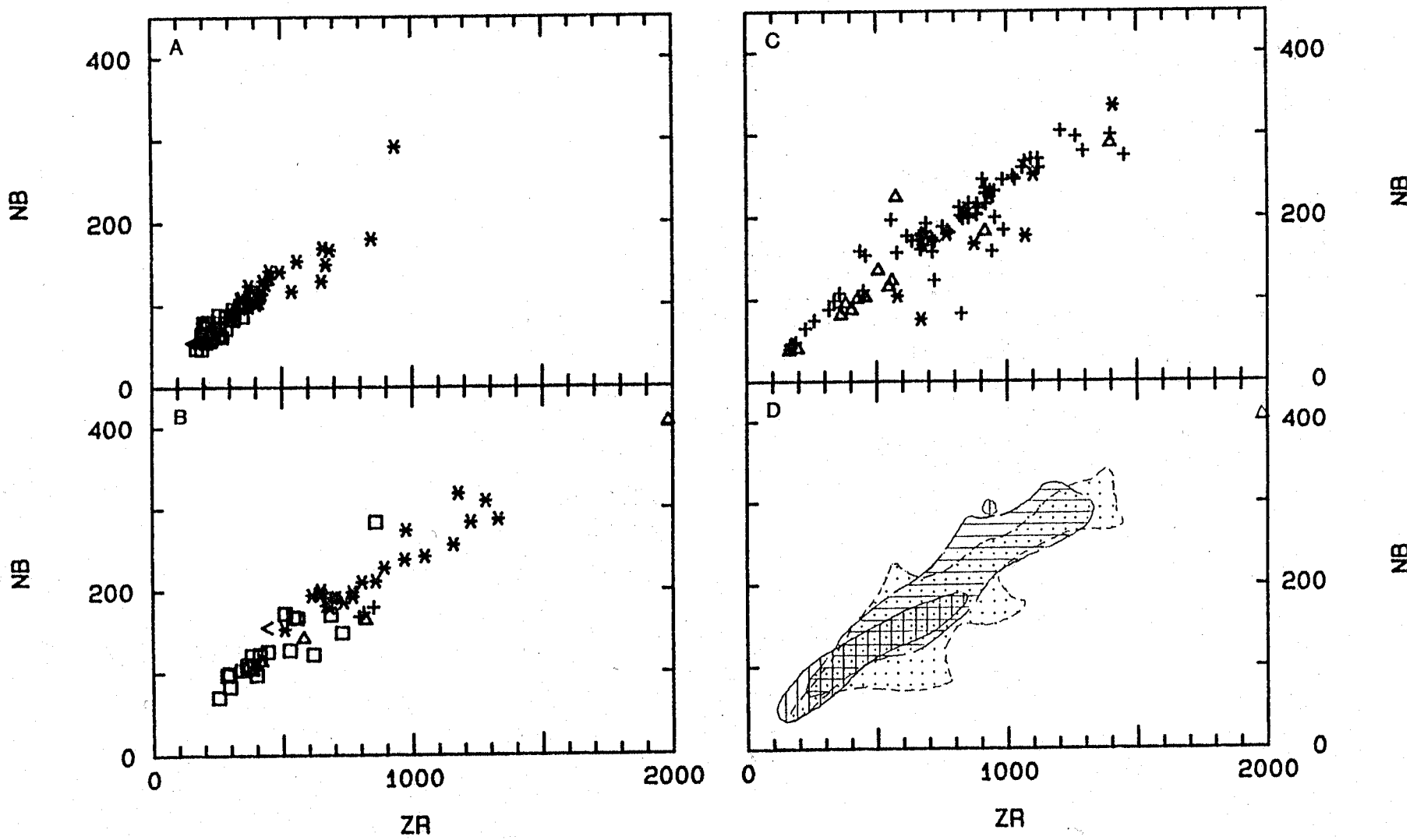
A
B
C
D
NB
ZR
0
200
400
1000
2000

Figure 8.15 - La (ppm) plotted against Zr (ppm).

Diagram	Group	Stratigraphic units
A	IIA	✳ BP, MB2, MD2, BI2, WI □ MM2, MS9, RG3, F < Amphibolite xenolith from RG3
B	IIB	□ MB1 ✳ MD1 △ MM1 + MS8 < Xenoliths in phonolite from MD1
C	I	+ MS1 - MS7 □ RG1 at Gandalf Ridge ✳ RG1 at Riviera Ridge △ RG2
D	composite diagram comprising fields drawn from the data in diagrams A to C, excluding xenolith analyses. The triangular symbol represents analyses of sample AW86128.	

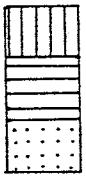

Group IIA

Group IIB

Group I

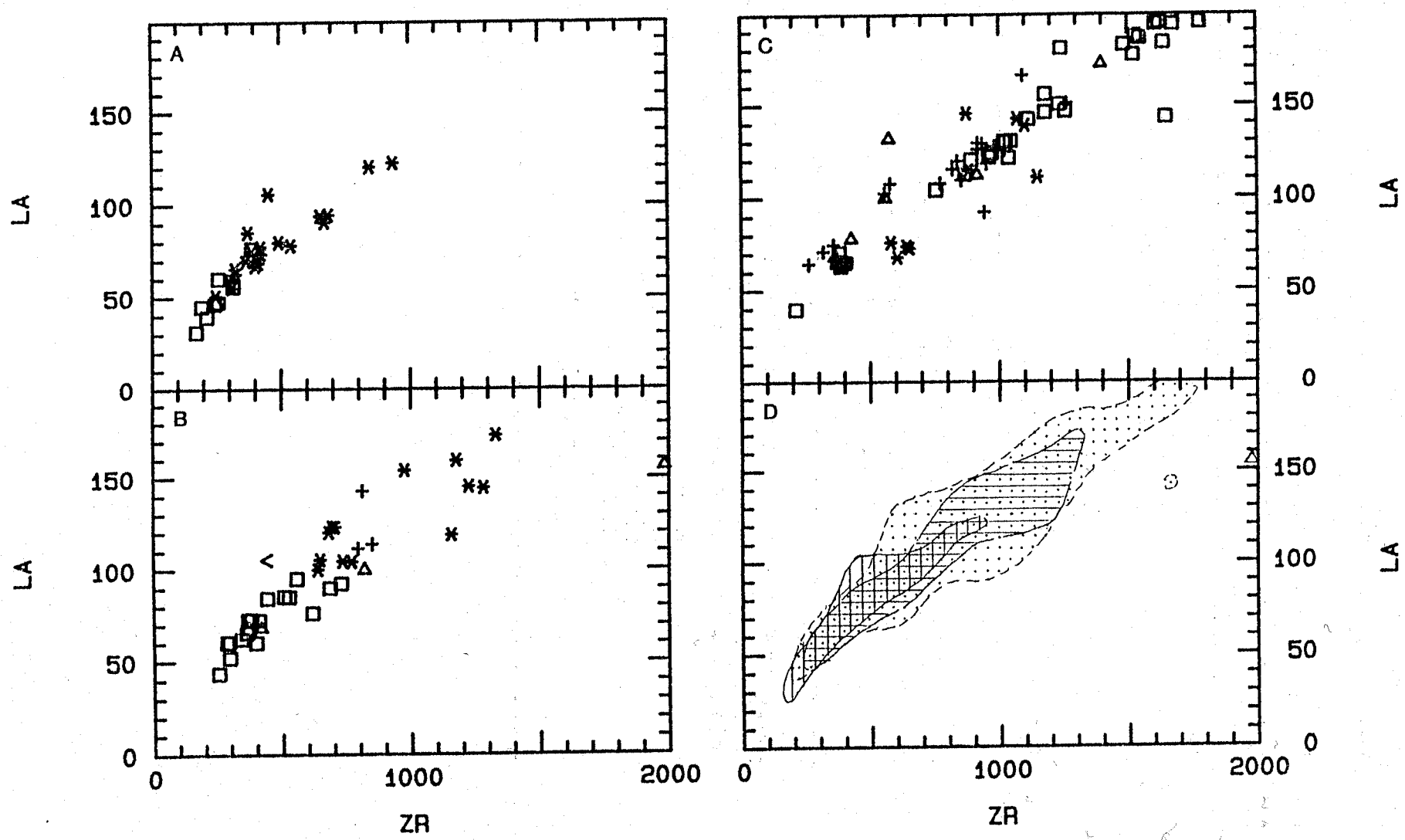
A
B
C
D
LA
ZR
0
50
100
150
1000
2000

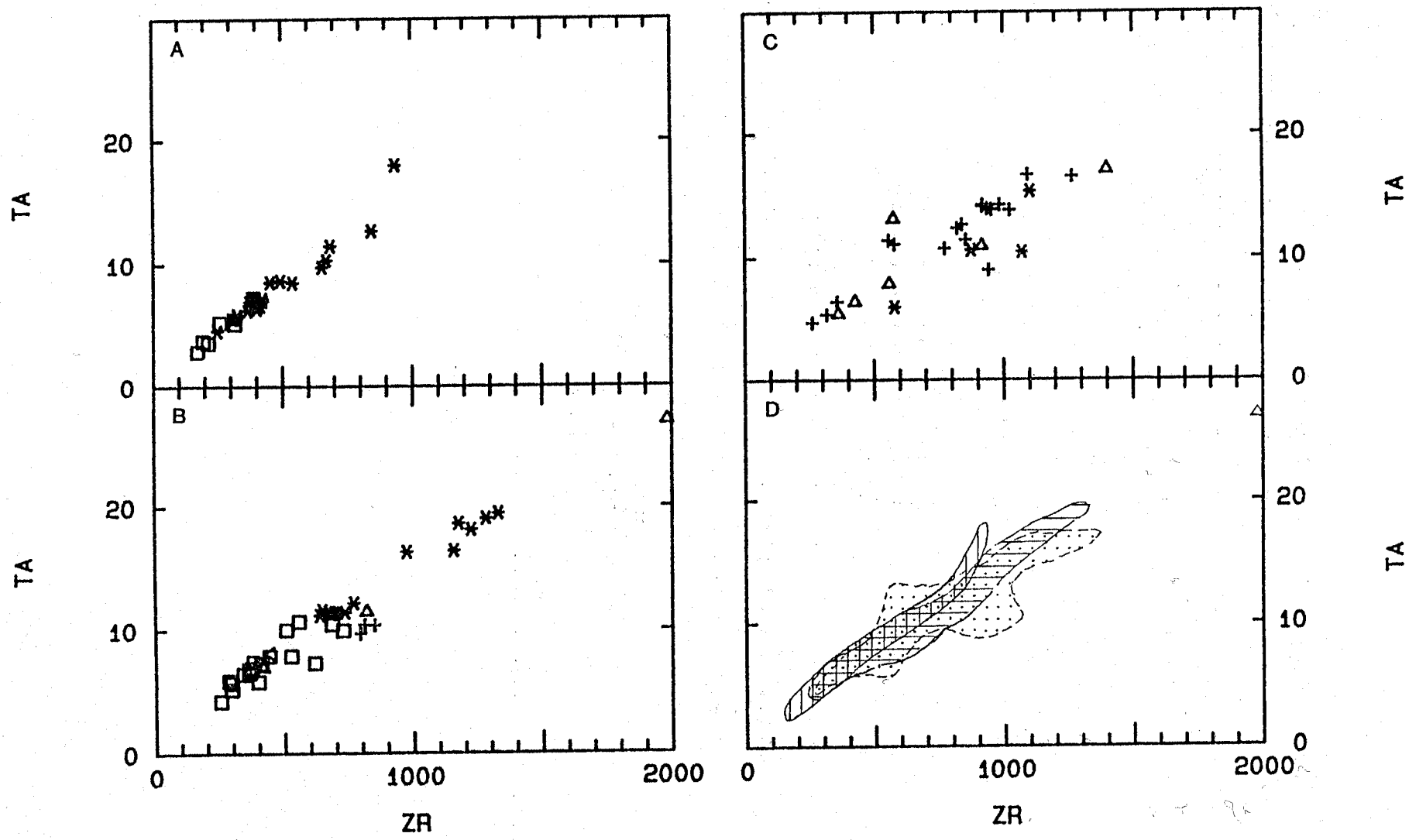
A
B
C
D
TA
TA
TA
TA
20
10
0
20
10
0
20
10
0
20
10
0
0
1000
2000
0
1000
2000
ZR
ZR

Figure 8.17 - Pb (ppm) plotted against Zr (ppm).

Diagram	Group	Stratigraphic units
A	IIA	✳ BP, MB2, MD2, BI2, WI □ MM2, MS9, RG3, F < Amphibolite xenolith from RG3
B	IIB	□ MB1 ✳ MD1 △ MM1 + MS8 < Xenoliths in phonolite from MD1
C	I	+ MS1 - MS7 □ RG1 at Gandalf Ridge ✳ RG1 at Riviera Ridge △ RG2
D	composite diagram comprising fields drawn from the data in diagrams A to C, excluding xenolith analyses. The triangular symbol represents analyses of sample AW86128.	

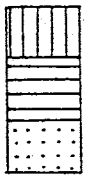

Group IIA

Group IIB

Group I

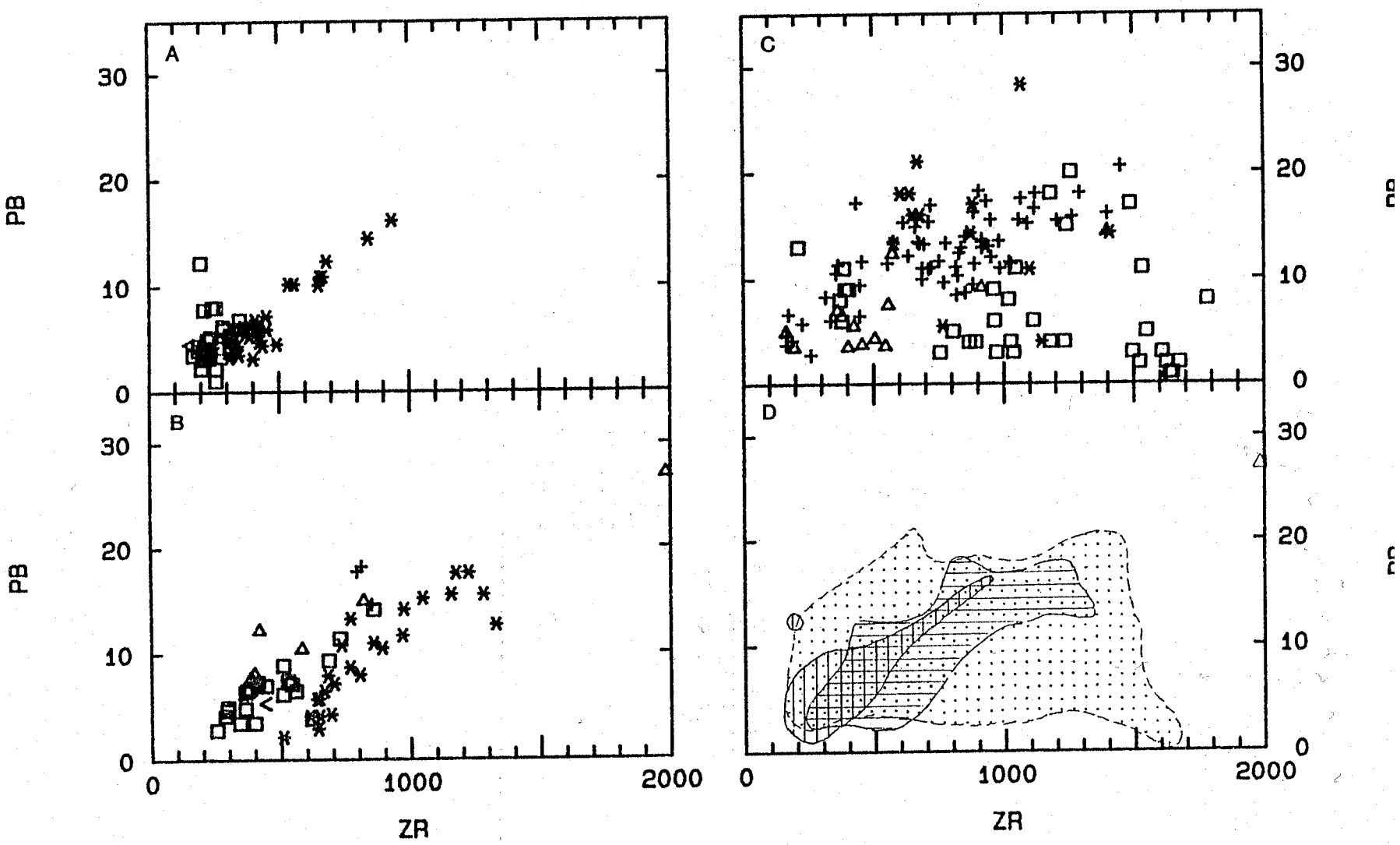
A
B
C
D
PB
PB
ZR
ZR
0
10
20
30
0
1000
2000

Figure 8.18 - U (ppm) plotted against Zr (ppm).

Diagram	Group	Stratigraphic units
A	IIA	✳ BP, MB2, MD2, BI2, WI □ MM2, MS9, RG3, F < Amphibolite xenolith from RG3
B	IIB	□ MB1 ✳ MD1 △ MM1 + MS8 < Xenoliths in phonolite from MD1
C	I	+ MS1 - MS7 □ RG1 at Gandalf Ridge ✳ RG1 at Riviera Ridge △ RG2
D	composite diagram comprising fields drawn from the data in diagrams A to C, excluding xenolith analyses. The triangular symbol represents analyses of sample AW86128.	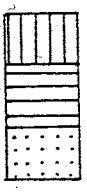 Group IIA Group IIB Group I

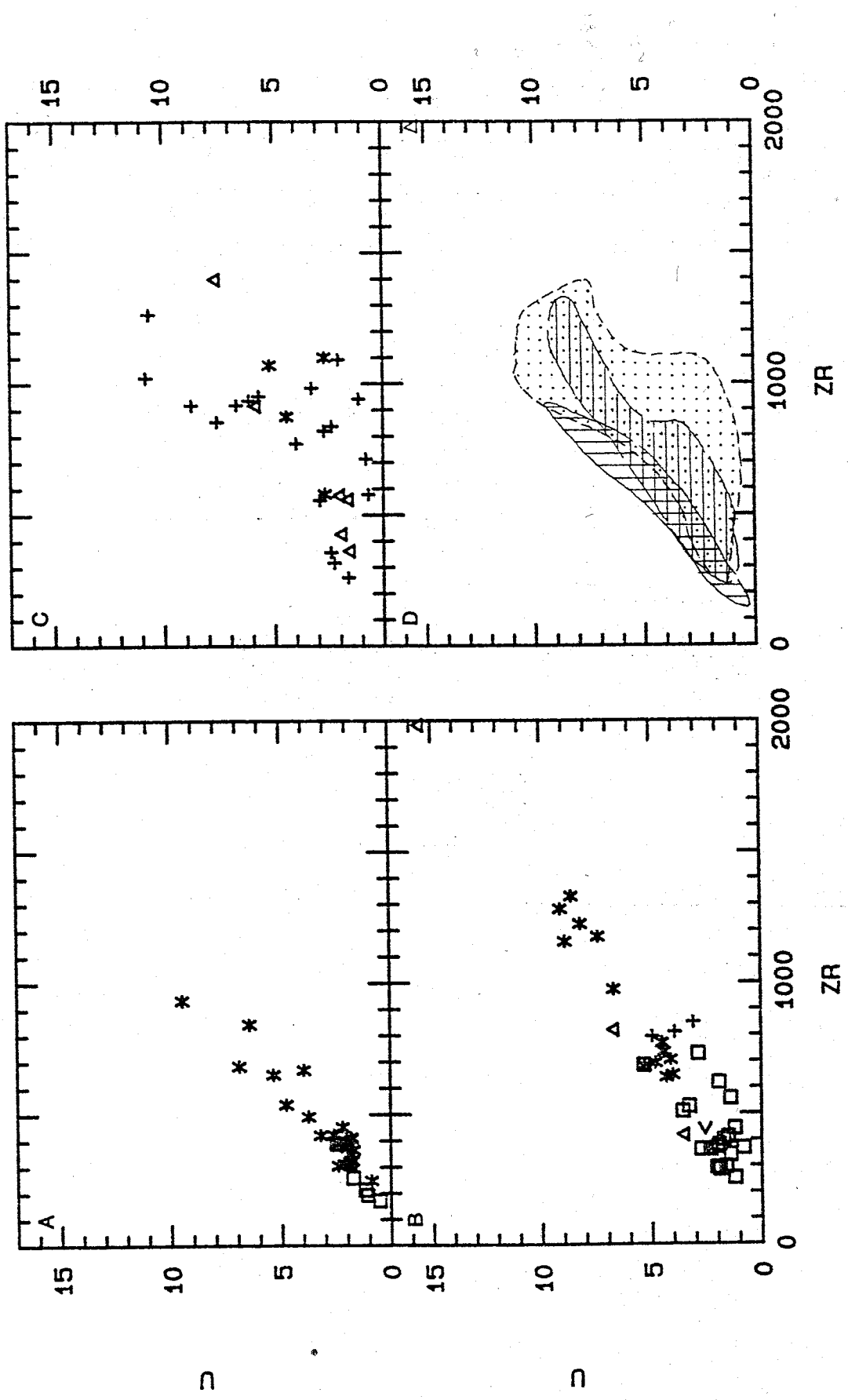
A
B
C
D
15
10
5
0
2000
1000
ZR

Figure 8.19 - Zn (ppm) plotted against Zr (ppm).

Diagram	Group	Stratigraphic units
A	IIA	✳ BP, MB2, MD2, BI2, WI □ MM2, MS9, RG3, F < Amphibolite xenolith from RG3
B	IIB	□ MB1 ✳ MD1 △ MM1 + MS8 < Xenoliths in phonolite from MD1
C	I	+ MS1 - MS7 □ RG1 at Gandalf Ridge ✳ RG1 at Riviera Ridge △ RG2
D	composite diagram comprising fields drawn from the data in diagrams A to C, excluding xenolith analyses. The triangular symbol represents analyses of sample AW86128.	

Group IIA

Group IIB

Group I

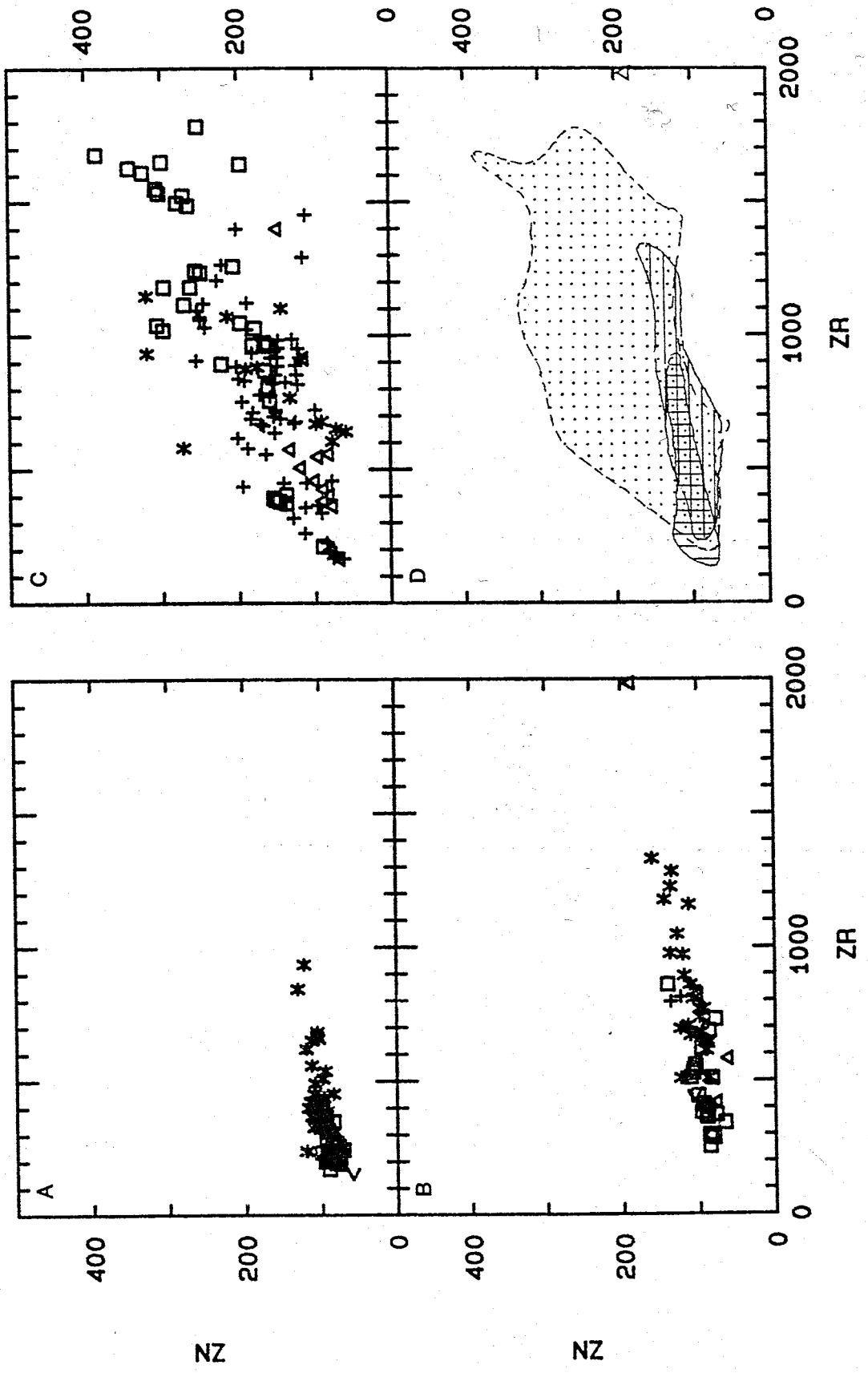
A
B
C
D
NZ
NZ
ZR
ZR
0
200
400
1000
2000

Figure 8.20 - Ga (ppm) plotted against Zr (ppm).

Diagram	Group	Stratigraphic units
A	IIA	✳ BP, MB2, MD2, BI2, WI □ MM2, MS9, RG3, F < Amphibolite xenolith from RG3
B	IIB	□ MB1 ✳ MD1 △ MM1 + MS8 < Xenoliths in phonolite from MD1
C	I	+ MS1 - MS7 □ RG1 at Gandalf Ridge ✳ RG1 at Riviera Ridge △ RG2
D	composite diagram comprising fields drawn from the data in diagrams A to C, excluding xenolith analyses. The triangular symbol represents analyses of sample AW86128.	

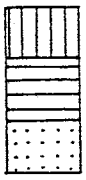

Group IIA

Group IIB

Group I

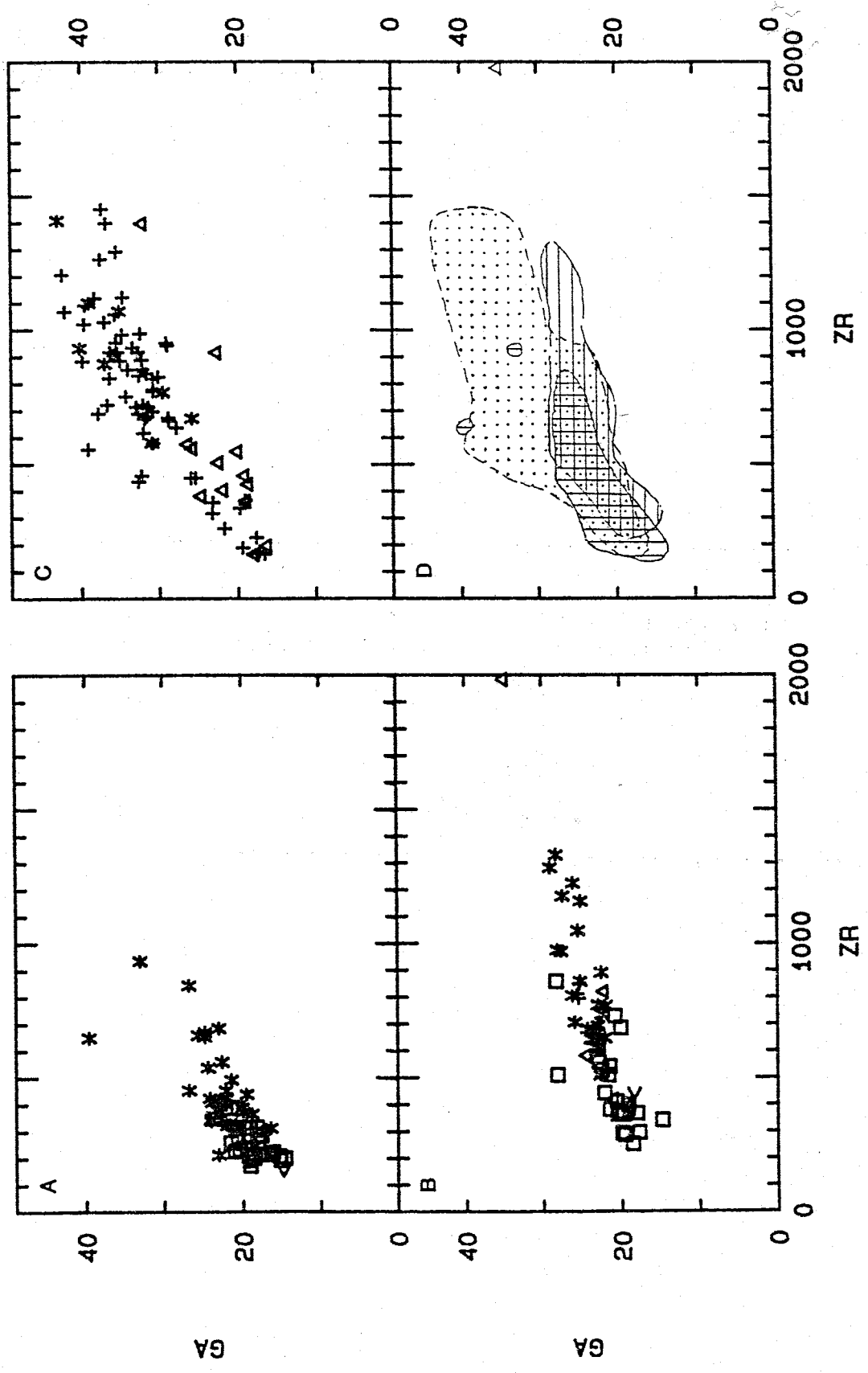
A
B
C
D
GA
GA
ZR
ZR
0
20
40
0
1000
2000

Figure 8.21 - Rb (ppm) plotted against Zr (ppm).

Diagram	Group	Stratigraphic units
A	IIA	✳ BP, MB2, MD2, BI2, WI □ MM2, MS9, RG3, F < Amphibolite xenolith from RG3
B	IIB	□ MB1 ✳ MD1 △ MM1 + MS8 < Xenoliths in phonolite from MD1
C	I	+ MS1 - MS7 □ RG1 at Gandalf Ridge ✳ RG1 at Riviera Ridge △ RG2
D	composite diagram comprising fields drawn from the data in diagrams A to C, excluding xenolith analyses. The triangular symbol represents analyses of sample AW86128.	

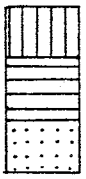

Group IIA

Group IIB

Group I

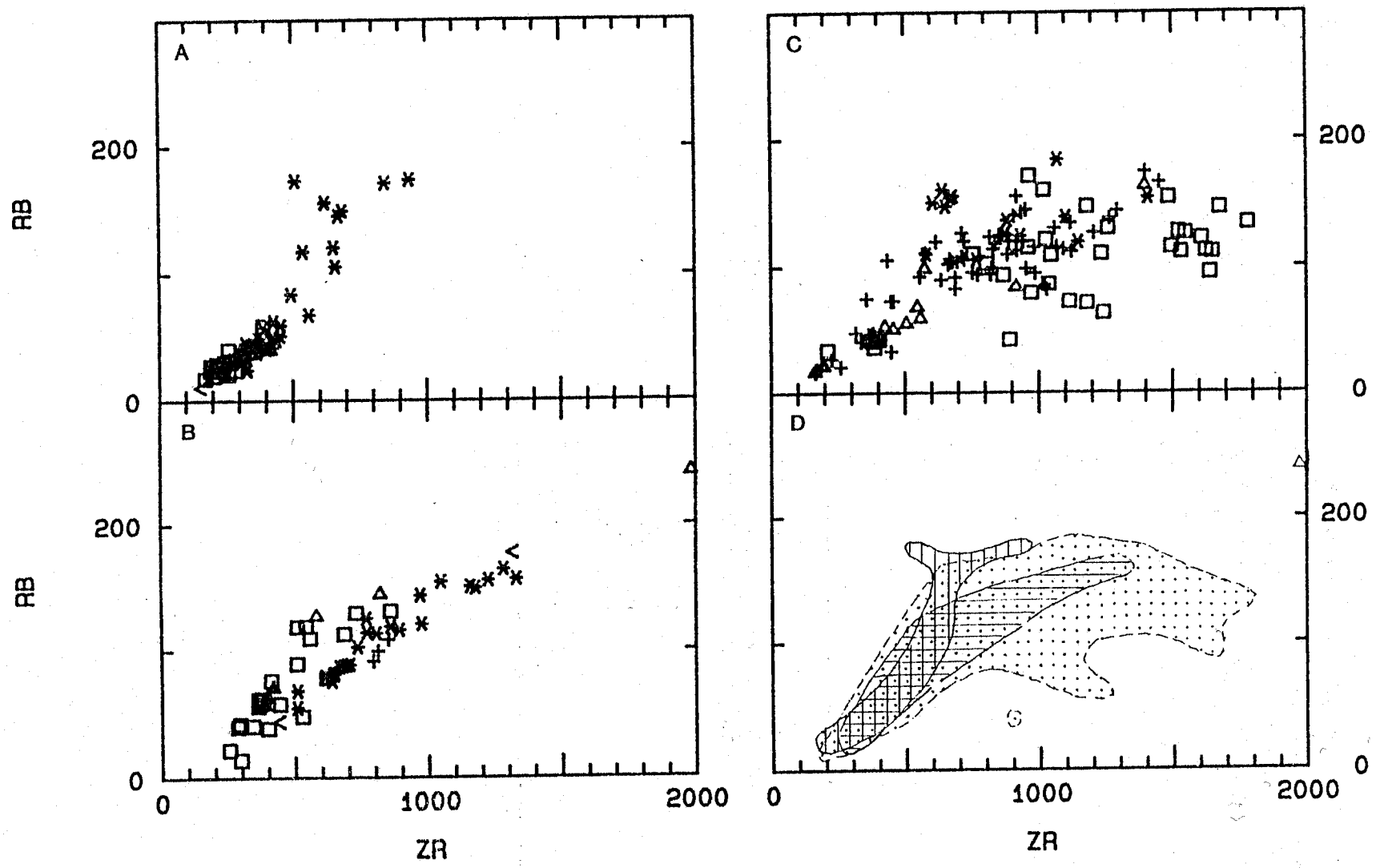
A
B
C
D
RB
RB
ZR
ZR
200
0
200
0
1000
2000
0
1000
2000
200
0
200
0

Figure 8.22 - Y (ppm) plotted against Zr (ppm).

Diagram	Group	Stratigraphic units
A	IIA	✳ BP, MB2, MD2, BI2, WI □ MM2, MS9, RG3, F < Amphibolite xenolith from RG3
B	IIB	□ MB1 ✳ MD1 △ MM1 + MS8 < Xenoliths in phonolite from MD1
C	I	+ MS1 - MS7 □ RG1 at Gandalf Ridge ✳ RG1 at Riviera Ridge △ RG2
D	composite diagram comprising fields drawn from the data in diagrams A to C, excluding xenolith analyses. The triangular symbol represents analyses of sample AW86128.	

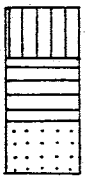

Group IIA

Group IIB

Group I

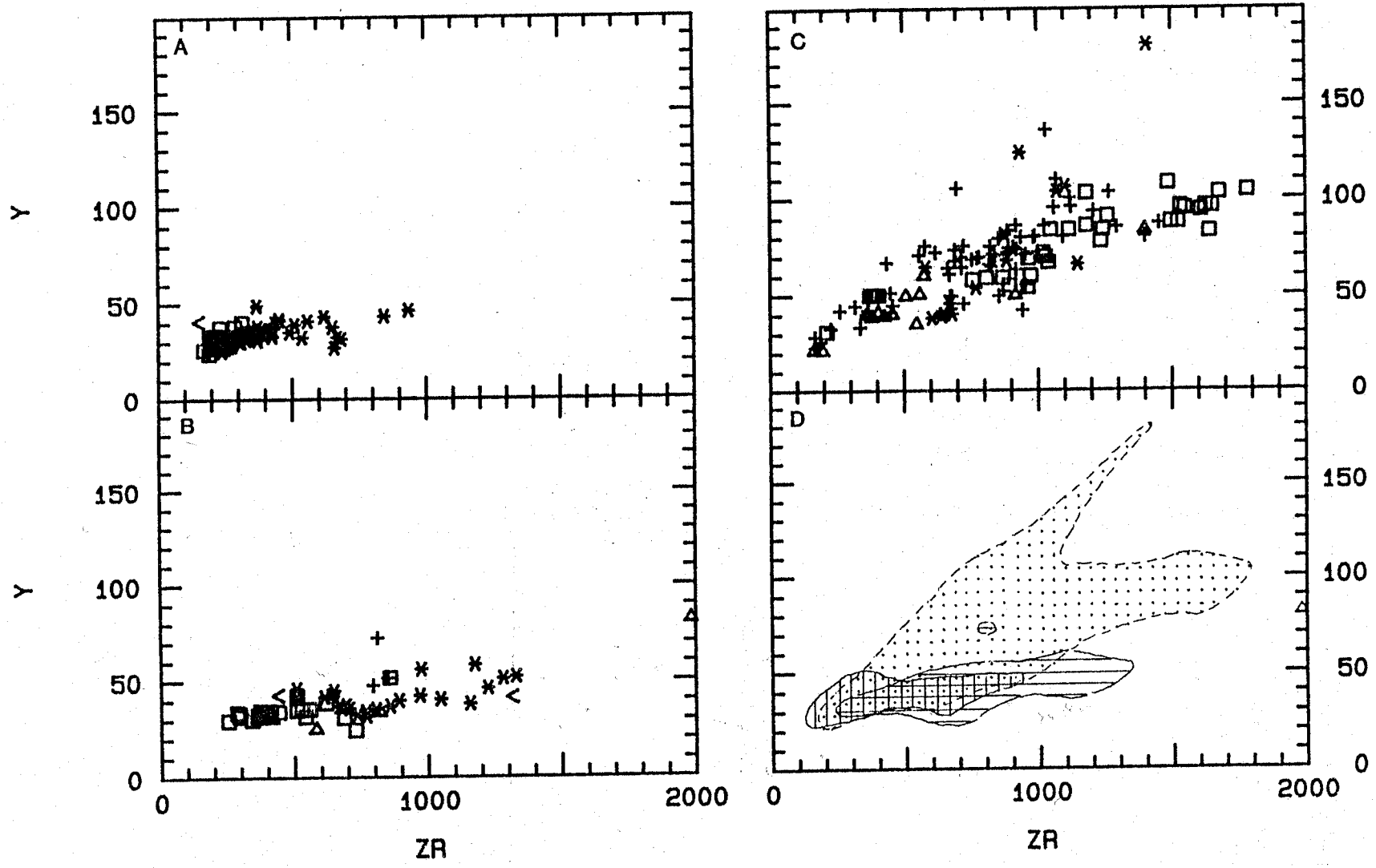
A
B
C
D
Y
Y
150
100
50
0
0
1000
2000
ZR
ZR

Figure 8.23 - Sb (ppm) plotted against Zr (ppm).

Diagram	Group	Stratigraphic units
A	IIA	✳ BP, MB2, MD2, BI2, WI □ MM2, MS9, RG3, F < Amphibolite xenolith from RG3
B	IIB	□ MB1 ✳ MD1 △ MM1 + MS8 < Xenoliths in phonolite from MD1
C	I	+ MS1 - MS7 □ RG1 at Gandalf Ridge ✳ RG1 at Riviera Ridge △ RG2
D	composite diagram comprising fields drawn from the data in diagrams A to C, excluding xenolith analyses. The triangular symbol represents analyses of sample AW86128.	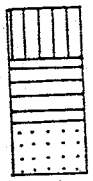 Group IIA Group IIB Group I

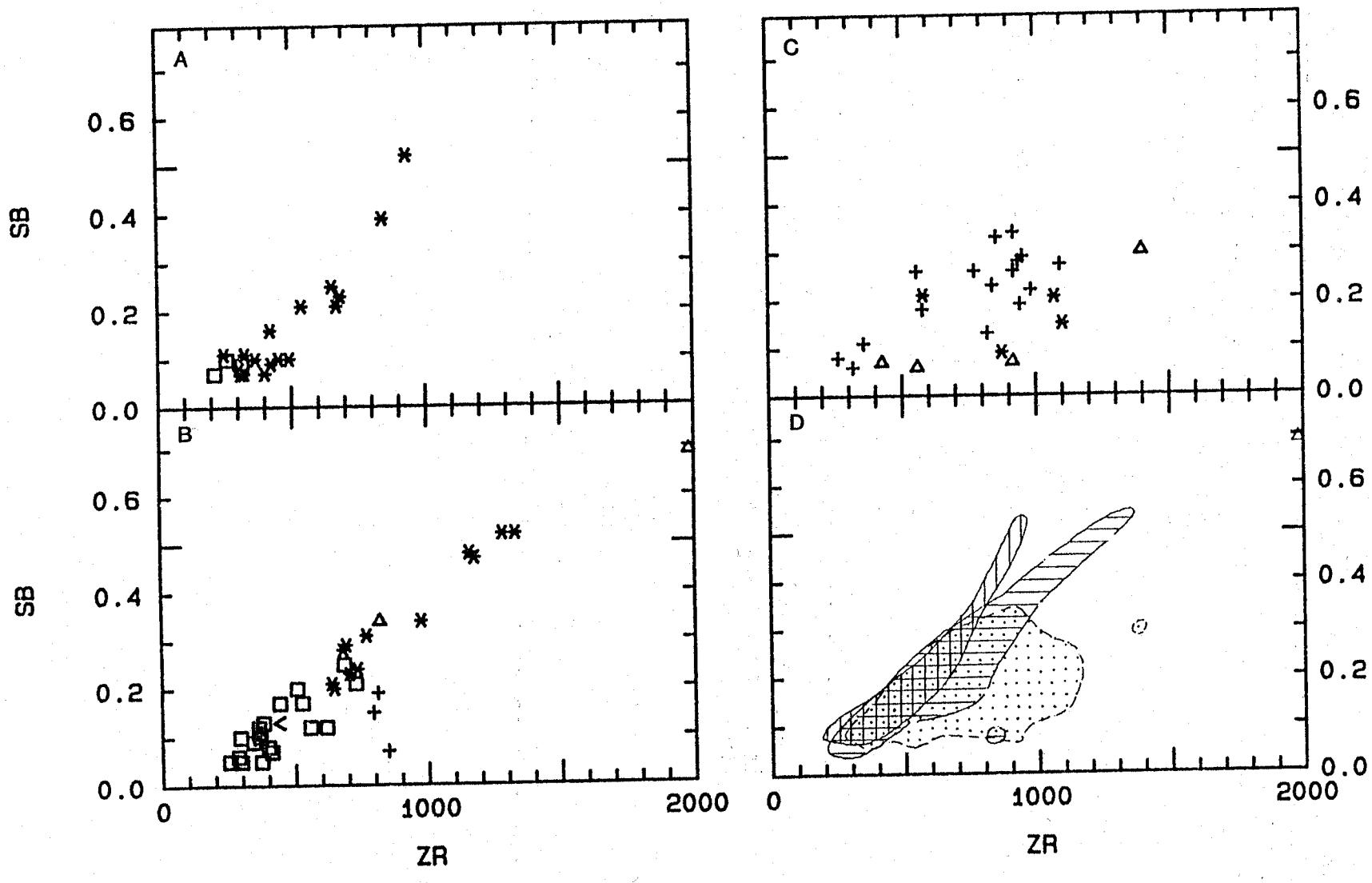
A
B
C
D
SB
SB
ZR
ZR
0.0
0.2
0.4
0.6
0
1000
2000

Figure 8.24 - Cs (ppm) plotted against Zr (ppm).

Diagram	Group	Stratigraphic units
A	IIA	✳ BP, MB2, MD2, BI2, WI □ MM2, MS9, RG3, F < Amphibolite xenolith from RG3
B	IIB	□ MB1 ✳ MD1 △ MM1 + MS8 < Xenoliths in phonolite from MD1
C	I	+ MS1 - MS7 □ RG1 at Gandalf Ridge ✳ RG1 at Riviera Ridge △ RG2
D	composite diagram comprising fields drawn from the data in diagrams A to C, excluding xenolith analyses. The triangular symbol represents analyses of sample AW86128.	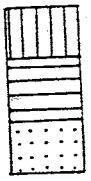 Group IIA Group IIB Group I

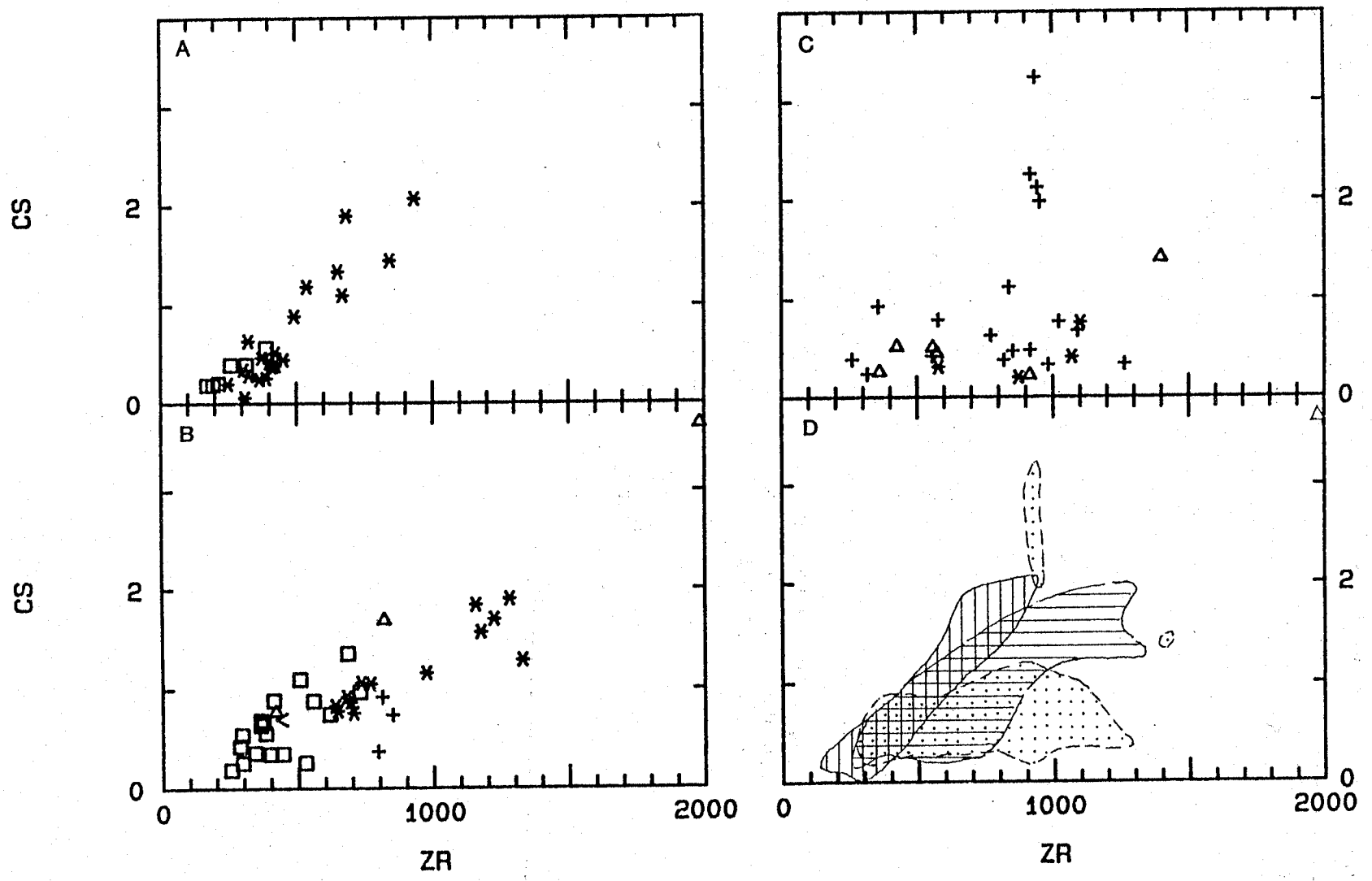
A
B
C
D
CS
CS
2
0
2
0
2
0
0
1000
2000
0
1000
2000
ZR
ZR

Figure 8.25 - Hf (ppm) plotted against Zr (ppm).

Diagram	Group	Stratigraphic units
A	IIA	✳ BP, MB2, MD2, BI2, WI □ MM2, MS9, RG3, F < Amphibolite xenolith from RG3
B	IIB	□ MB1 ✳ MD1 △ MM1 + MS8 < Xenoliths in phonolite from MD1
C	I	+ MS1 - MS7 □ RG1 at Gandalf Ridge ✳ RG1 at Riviera Ridge △ RG2
D	composite diagram comprising fields drawn from the data in diagrams A to C, excluding xenolith analyses. The triangular symbol represents analyses of sample AW86128.	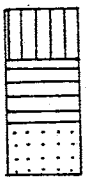 Group IIA Group IIB Group I

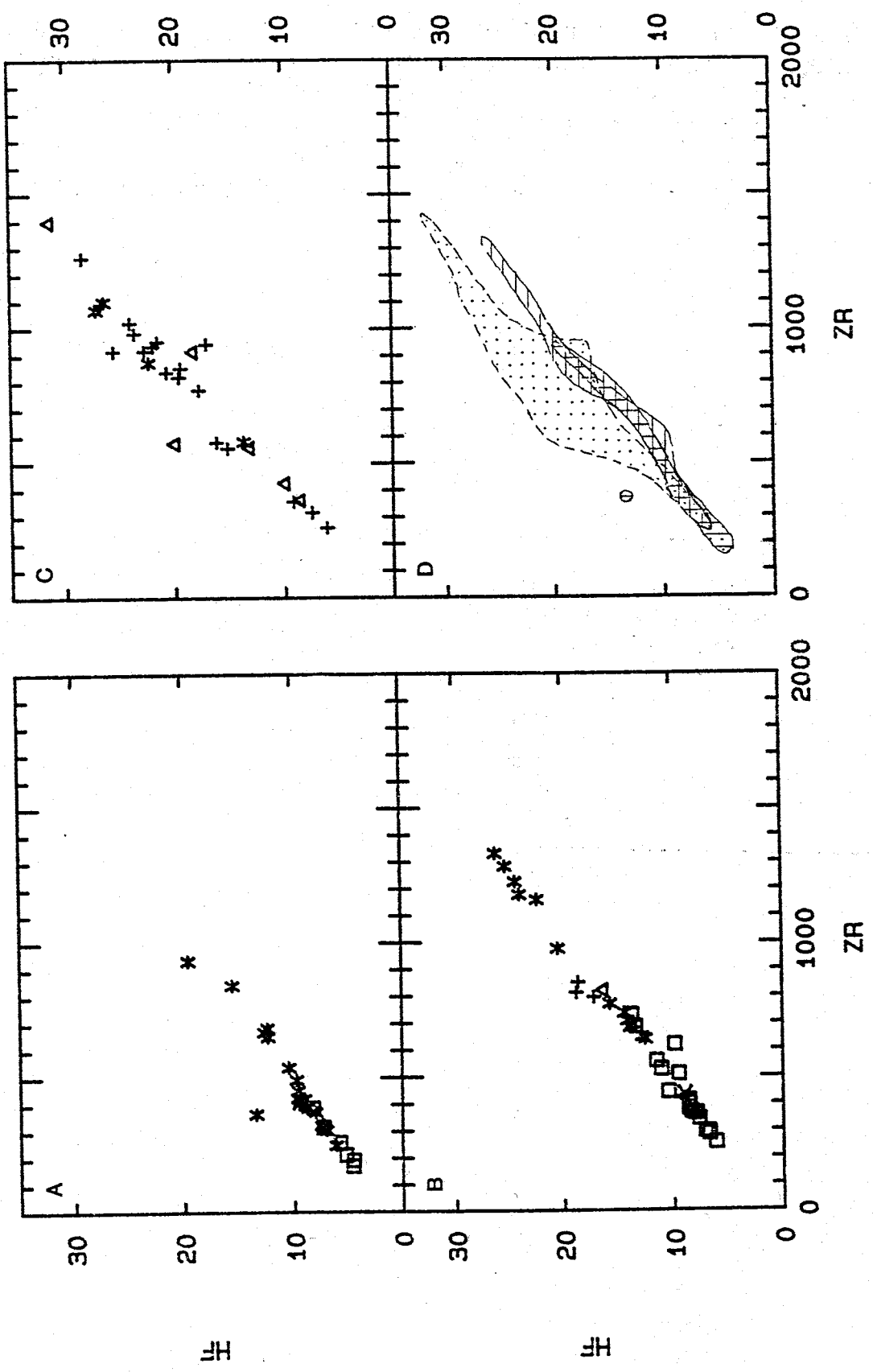
A
B
C
D
HF
ZR
0
10
20
30
1000
2000

Figure 8.26 - Th (ppm) plotted against Zr (ppm).

Diagram	Group	Stratigraphic units
A	IIA	✳ BP, MB2, MD2, BI2, WI □ MM2, MS9, RG3, F < Amphibolite xenolith from RG3
B	IIB	□ MB1 ✳ MD1 △ MM1 + MS8 < Xenoliths in phonolite from MD1
C	I	+ MS1 - MS7 □ RG1 at Gandalf Ridge ✳ RG1 at Riviera Ridge △ RG2
D	composite diagram comprising fields drawn from the data in diagrams A to C, excluding xenolith analyses. The triangular symbol represents analyses of sample AW86128.	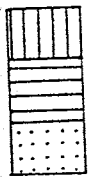 Group IIA Group IIB Group I

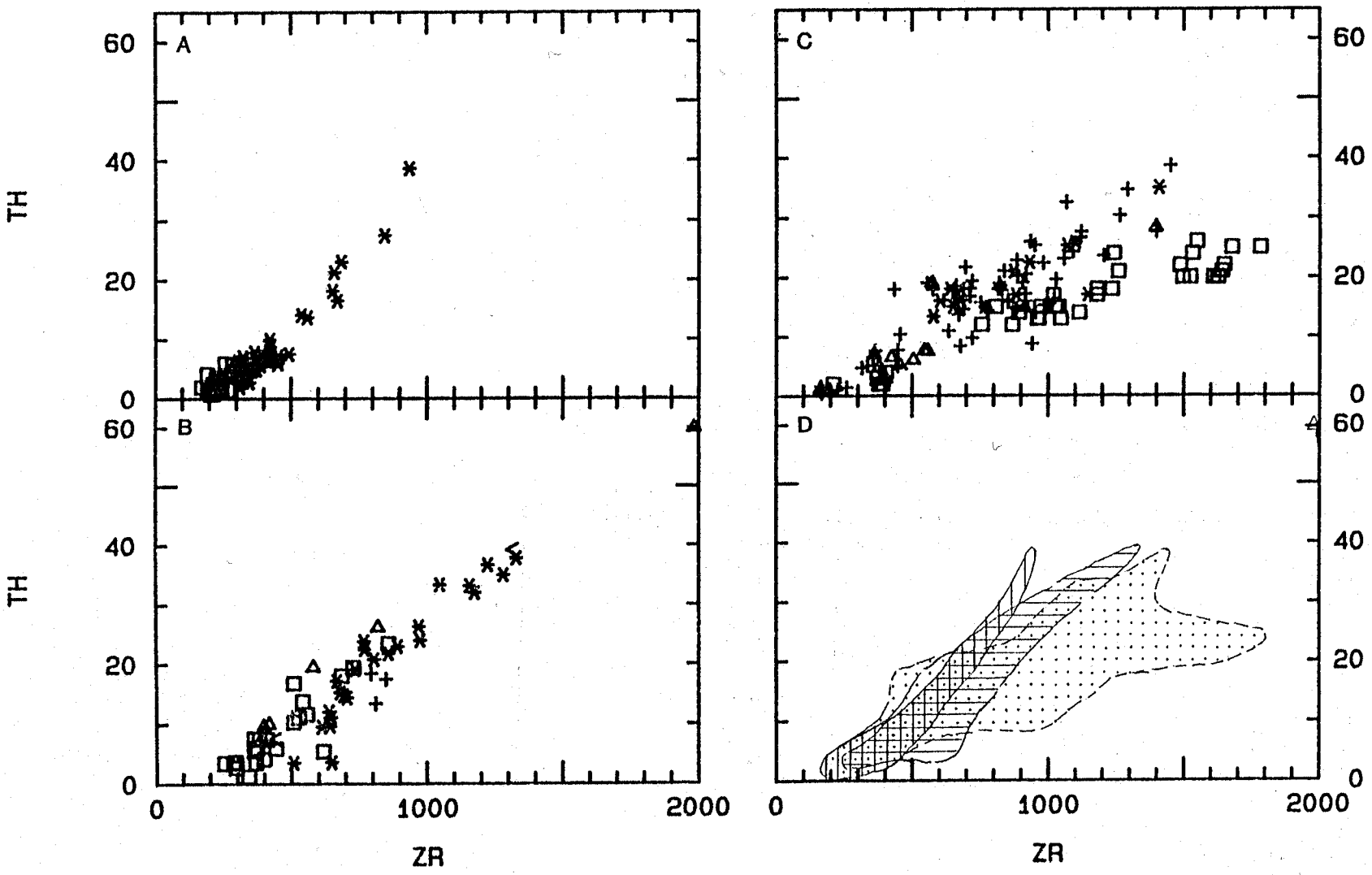
A
B
C
D
TH
TH
ZR
ZR
0
20
40
60
0
1000
2000

Figure 8.27 - Sr (ppm) plotted against Zr (ppm).

Diagram	Group	Stratigraphic units
A	IIA	✳ BP, MB2, MD2, BI2, WI □ MM2, MS9, RG3, F < Amphibolite xenolith from RG3
B	IIB	□ MB1 ✳ MD1 △ MM1 + MS8 < Xenoliths in phonolite from MD1
C	I	+ MS1 - MS7 □ RG1 at Gandalf Ridge ✳ RG1 at Riviera Ridge △ RG2
D	composite diagram comprising fields drawn from the data in diagrams A to C, excluding xenolith analyses. The triangular symbol represents analyses of sample AW86128.	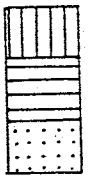 Group IIA Group IIB Group I

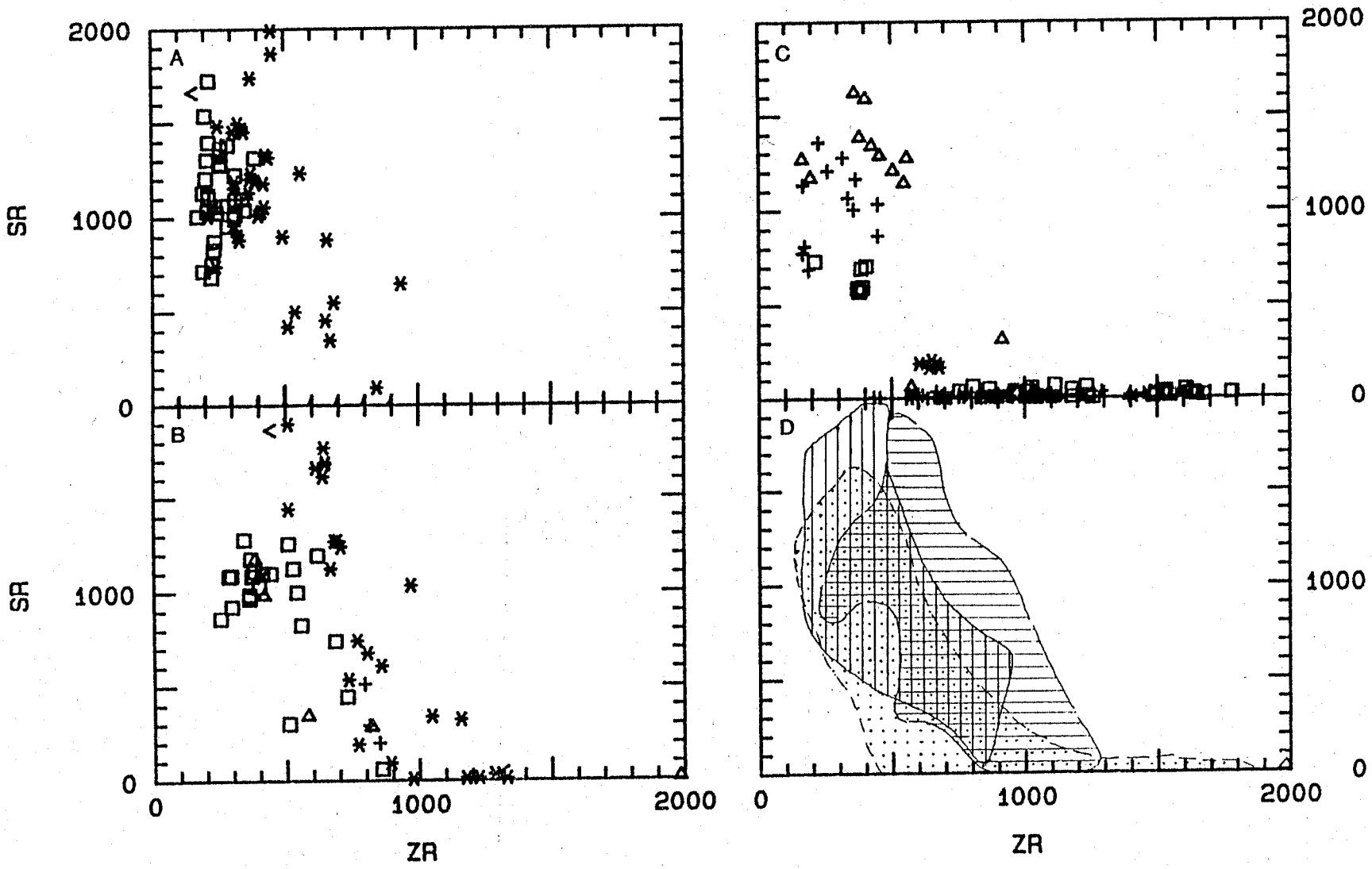
A
B
C
D
SR
SR
ZR
ZR
2000
1000
0
0
1000
2000

Figure 8.28 - Ba (ppm) plotted against Zr (ppm).

Diagram	Group	Stratigraphic units
A	IIA	✳ BP, MB2, MD2, BI2, WI □ MM2, MS9, RG3, F < Amphibolite xenolith from RG3
B	IIB	□ MB1 ✳ MD1 △ MM1 + MS8 < Xenoliths in phonolite from MD1
C	I	+ MS1 - MS7 □ RG1 at Gandalf Ridge ✳ RG1 at Riviera Ridge △ RG2
D	composite diagram comprising fields drawn from the data in diagrams A to C, excluding xenolith analyses. The triangular symbol represents analyses of sample AW86128.	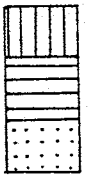 Group IIA Group IIB Group I

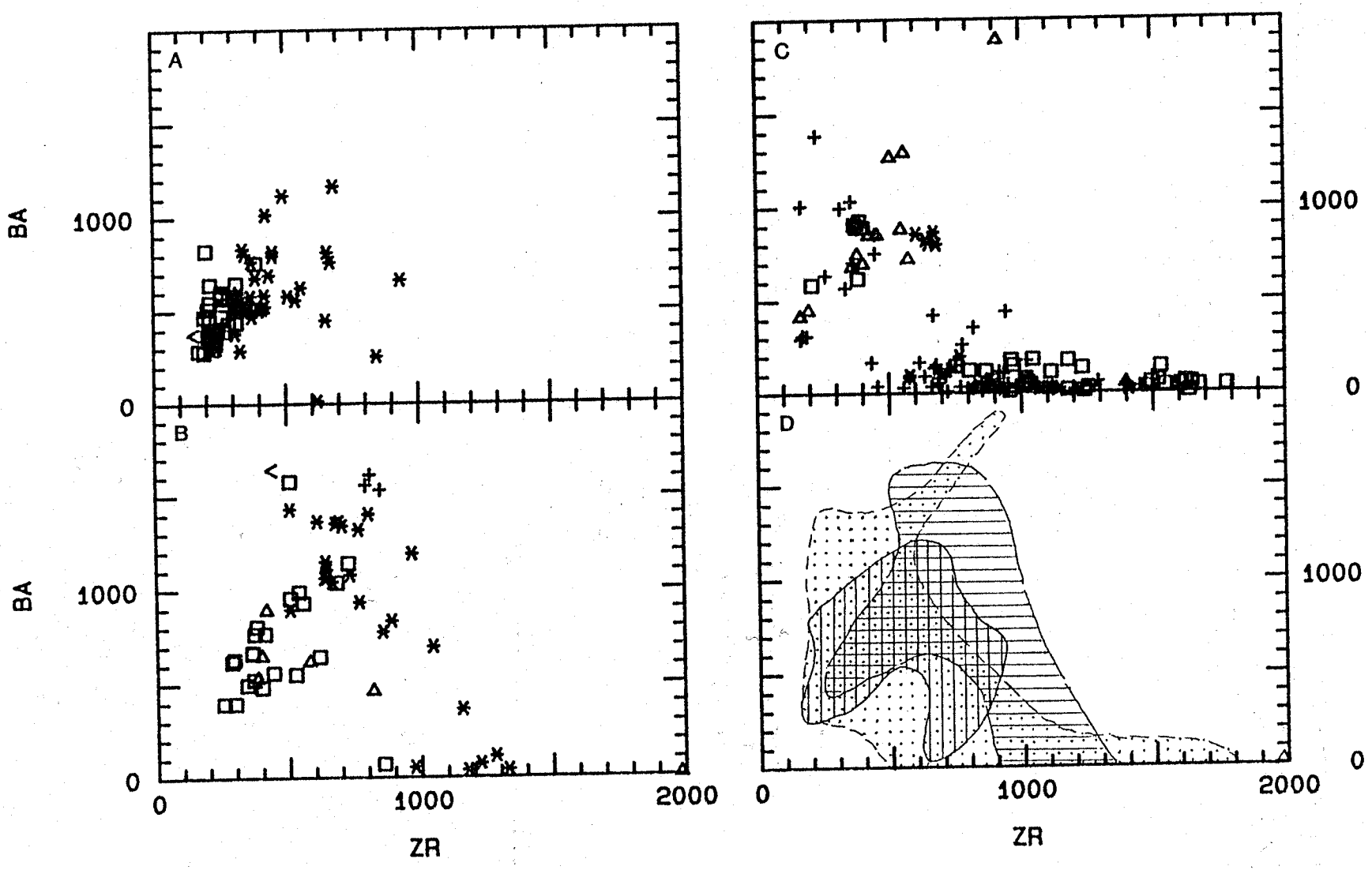
A
B
C
D
BA
BA
1000
0
1000
0
0
1000
2000
ZR
1000
0
1000
0
0
1000
2000
ZR

Figure 8.29 - Sc (ppm) plotted against Zr (ppm).

Diagram	Group	Stratigraphic units
A	IIA	✳ BP, MB2, MD2, BI2, WI □ MM2, MS9, RG3, F < Amphibolite xenolith from RG3
B	IIB	□ MB1 ✳ MD1 △ MM1 + MS8 < Xenoliths in phonolite from MD1
C	I	+ MS1 - MS7 □ RG1 at Gandalf Ridge ✳ RG1 at Riviera Ridge △ RG2
D	composite diagram comprising fields drawn from the data in diagrams A to C, excluding xenolith analyses. The triangular symbol represents analyses of sample AW86128.	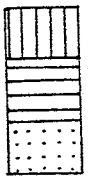 Group IIA Group IIB Group I

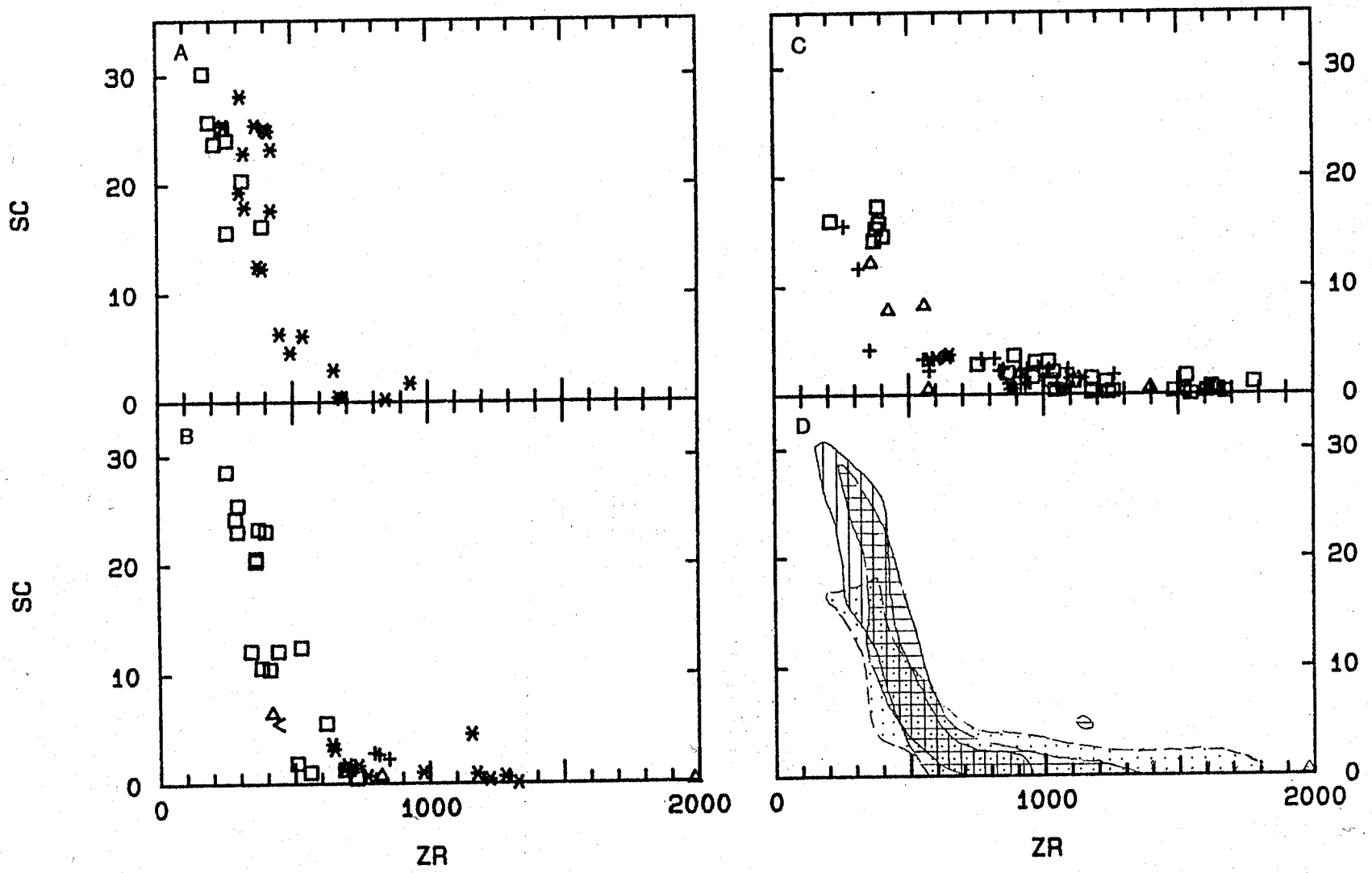
A
B
C
D
SC
SC
ZR
ZR
0
10
20
30
0
1000
2000

Figure 8.30 - V (ppm) plotted against Zr (ppm).

Diagram	Group	Stratigraphic units
A	IIA	✳ BP, MB2, MD2, BI2, WI □ MM2, MS9, RG3, F < Amphibolite xenolith from RG3
B	IIB	□ MB1 ✳ MD1 △ MM1 + MS8 < Xenoliths in phonolite from MD1
C	I	+ MS1 - MS7 □ RG1 at Gandalf Ridge ✳ RG1 at Riviera Ridge △ RG2
D	composite diagram comprising fields drawn from the data in diagrams A to C, excluding xenolith analyses. The triangular symbol represents analyses of sample AW86128.	

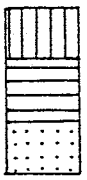

Group IIA

Group IIB

Group I

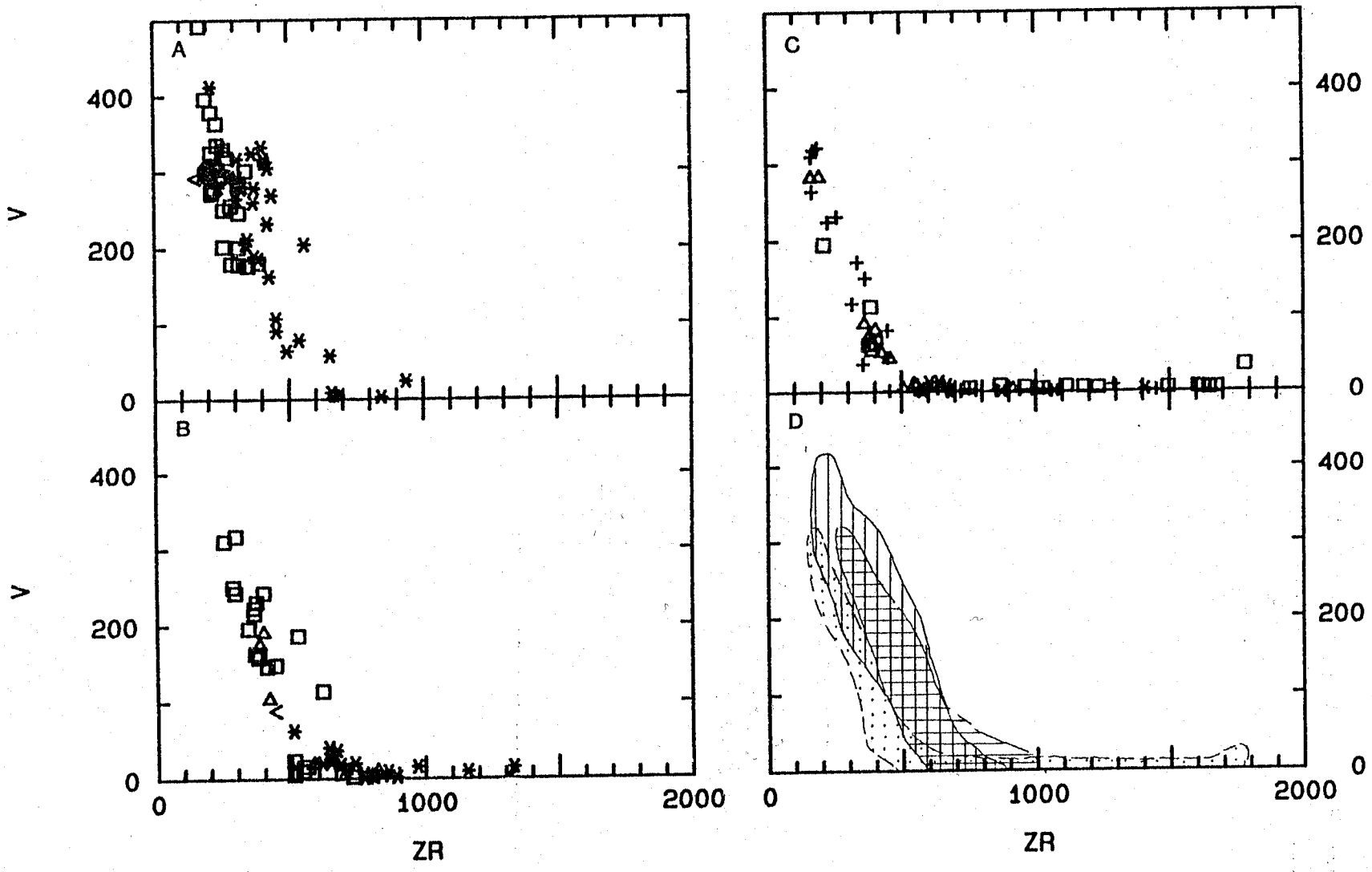
A
B
C
D
V
V
400
200
0
400
200
0
0
1000
2000
ZR
0
1000
2000
ZR

Figure 8.31 - Cr (ppm) plotted against Zr (ppm).

Diagram	Group	Stratigraphic units
A	IIA	✳ BP, MB2, MD2, BI2, WI □ MM2, MS9, RG3, F < Amphibolite xenolith from RG3
B	IIB	□ MB1 ✳ MD1 △ MM1 + MS8 < Xenoliths in phonolite from MD1
C	I	+ MS1 - MS7 □ RG1 at Gandalf Ridge ✳ RG1 at Riviera Ridge △ RG2
D	composite diagram comprising fields drawn from the data in diagrams A to C, excluding xenolith analyses. The triangular symbol represents analyses of sample AW86128.	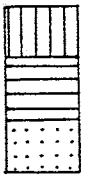 Group IIA Group IIB Group I

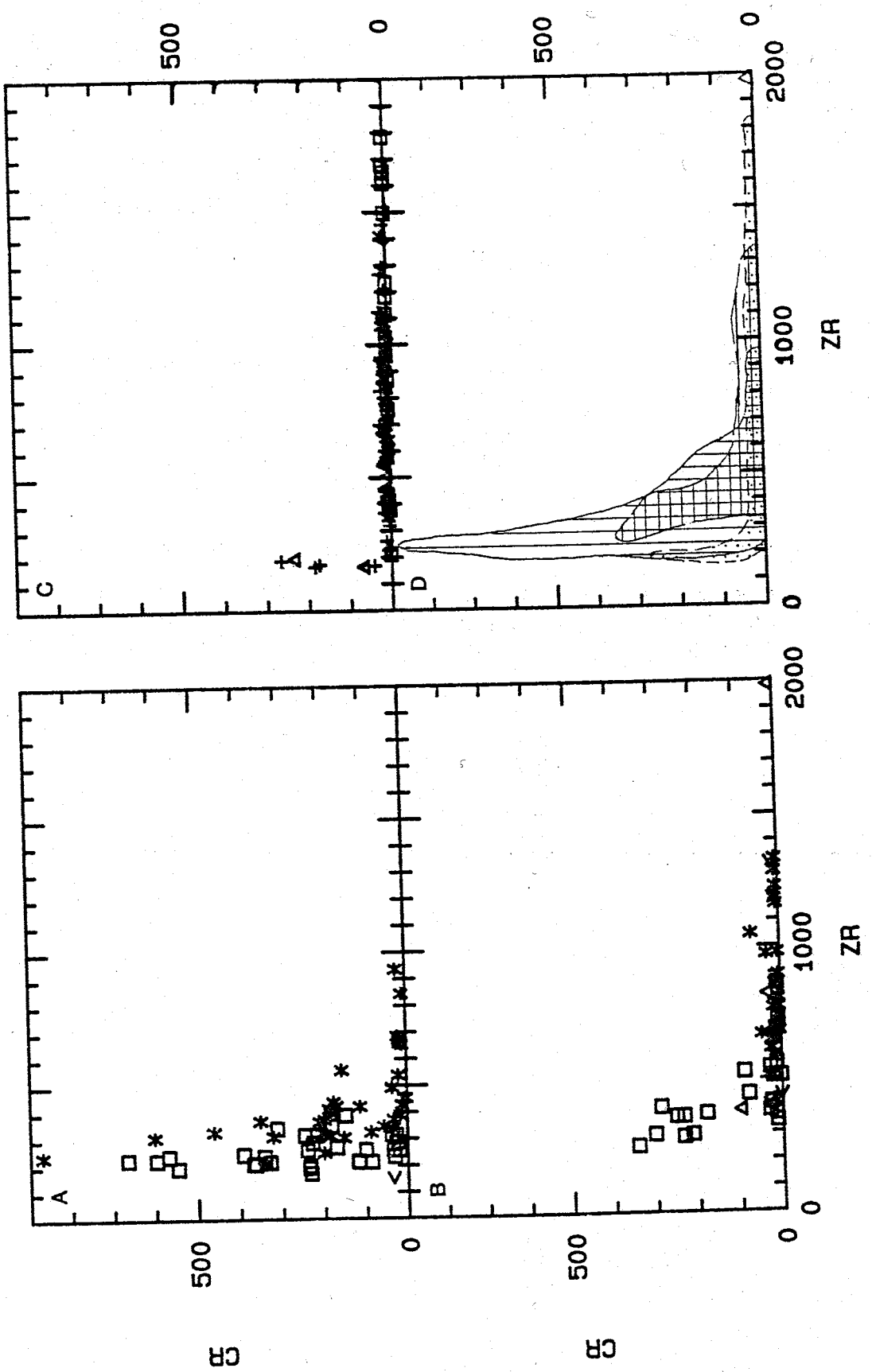
A
B
C
D
CR
CR
ZR
ZR
500
0
500
0
2000
1000
0
2000
1000
0

Figure 8.32 - Ni (ppm) plotted against Zr (ppm).

Diagram	Group	Stratigraphic units
A	IIA	✳ BP, MB2, MD2, BI2, WI □ MM2, MS9, RG3, F < Amphibolite xenolith from RG3
B	IIB	□ MB1 ✳ MD1 △ MM1 + MS8 < Xenoliths in phonolite from MD1
C	I	+ MS1 - MS7 □ RG1 at Gandalf Ridge ✳ RG1 at Riviera Ridge △ RG2
D	composite diagram comprising fields drawn from the data in diagrams A to C, excluding xenolith analyses. The triangular symbol represents analyses of sample AW86128.	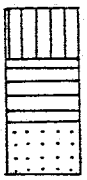 Group IIA Group IIB Group I

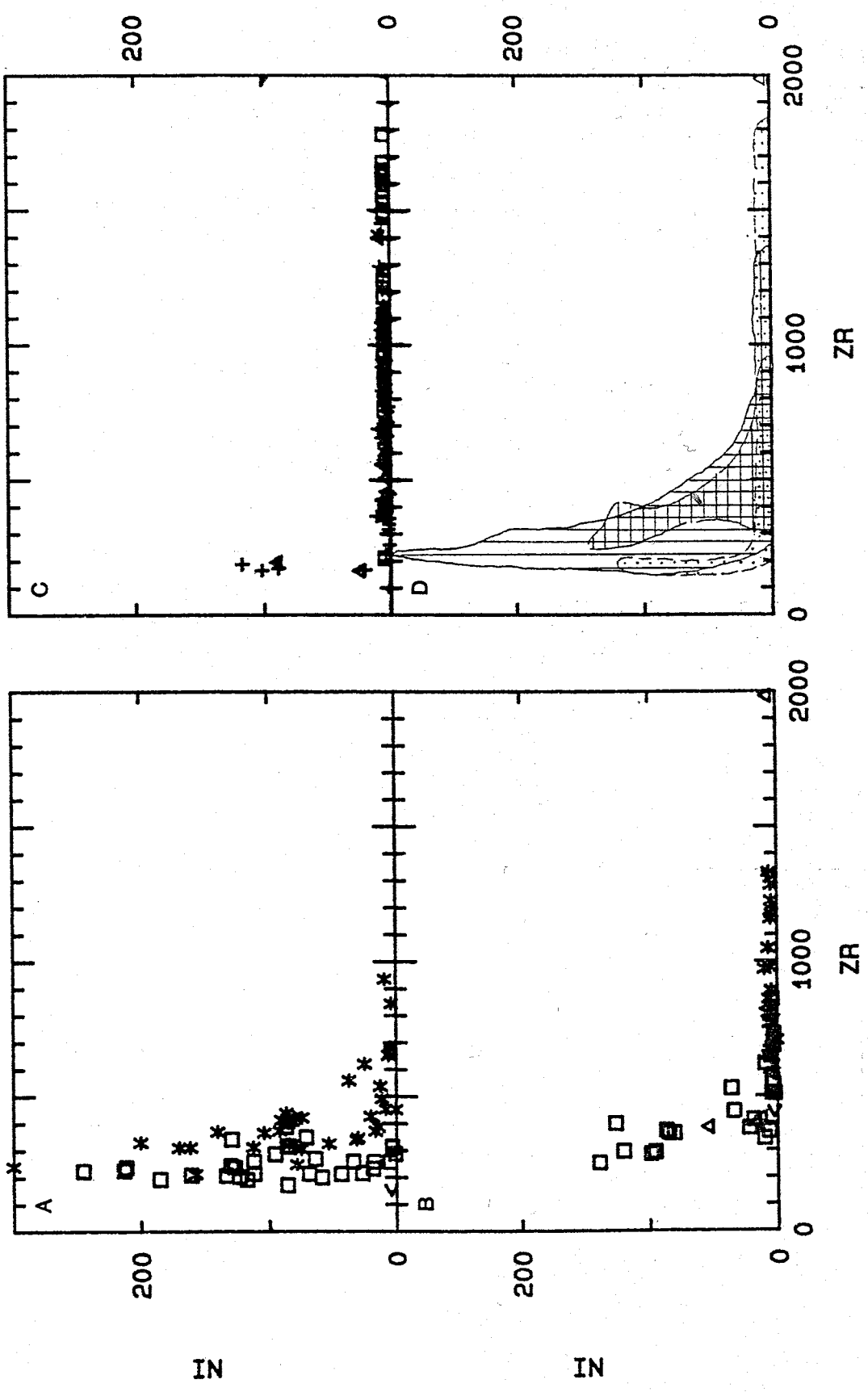
A
B
C
D
IN
IN
ZR
ZR
200
0
200
0
2000
1000
0
2000
1000
0

igure 8.33 - Cu (ppm) plotted against Zr (ppm).

iagram	Group	Stratigraphic units
	IIA	✳ BP, MB2, MD2, BI2, WI □ MM2, MS9, RG3, F < Amphibolite xenolith from RG3
3	IIB	□ MB1 ✳ MD1 △ MM1 + MS8 < Xenoliths in phonolite from MD1
C	I	+ MS1 - MS7 □ RG1 at Gandalf Ridge ✳ RG1 at Riviera Ridge △ RG2
D	composite diagram comprising fields drawn from the data in diagrams A to C, excluding xenolith analyses. The triangular symbol represents analyses of sample AW86128.	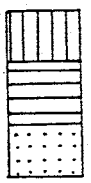 Group IIA Group IIB Group I

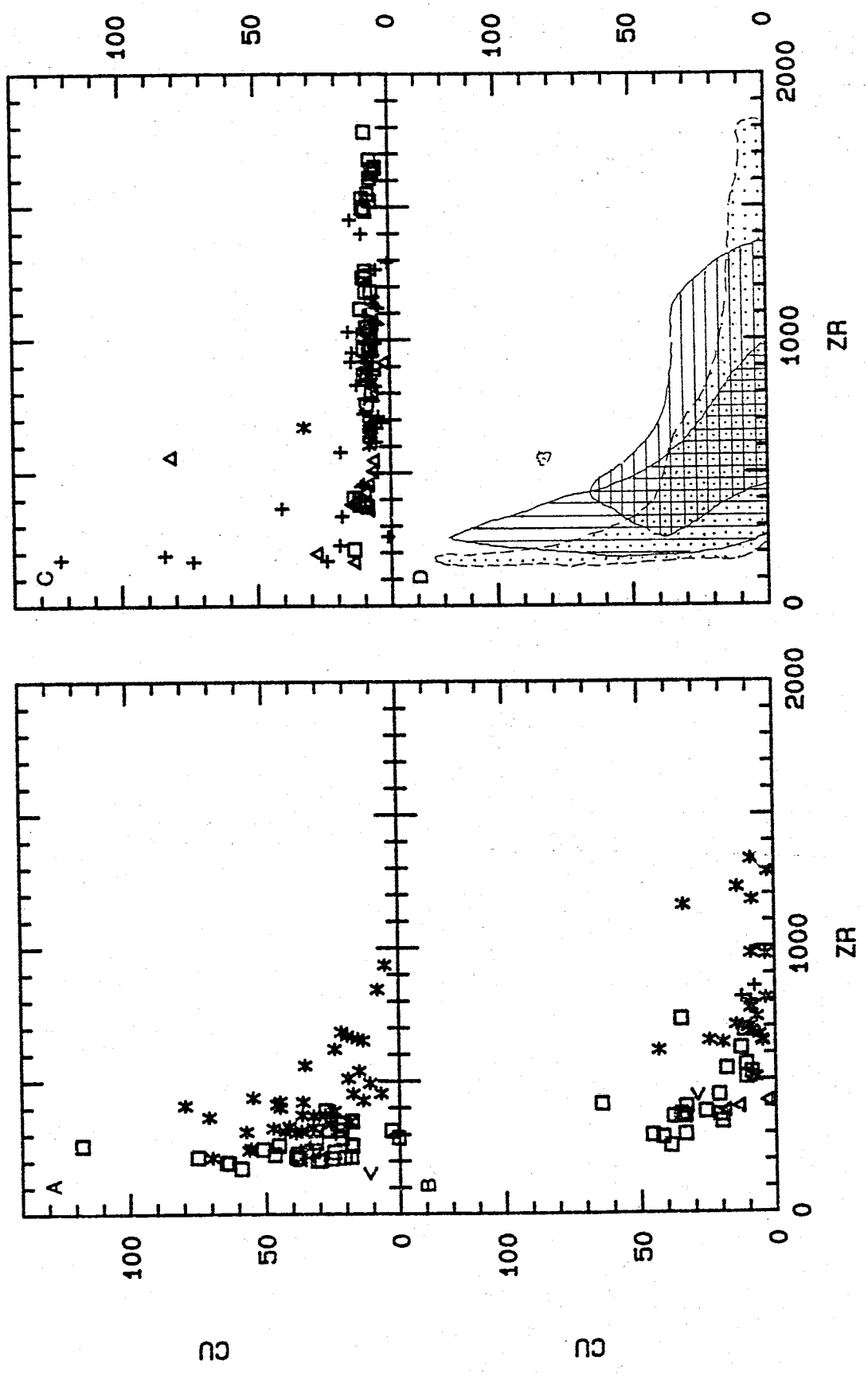
A
B
C
D
CU
CU
ZR
ZR
0
50
100
1000
2000

clear that differentiation proceeded beyond the trend of increasing SiO_2 in rock suits from all three geochemical subdivisions (Figure 8.13), but that this characteristic is most pronounced in Group I and least pronounced in the group IIA.

Nb, La, and Ta exhibit straight enrichment trends with Zr (Figures 8.14 - 8.16) that pass through the origin. Trends for Groups I, IIA and IIB generally overlap on variation diagrams. Pb and U also increases with Zr, although there is considerable scatter in data from Group I (Figures 8.17 and 8.18), and trends intersect the Zr axis at between 100 and 200 ppm Zr. The only exception is a broad scatter in Pb abundances in samples from Gandalf Ridge, for which it is impossible to define a trend.

A divergence of enrichment trends between Groups I and II is evident in the behaviour of other analysed incompatible elements, although there may also be considerable overlap between the two trends (Figures 8.19 - 8.26). In all cases element abundances in ultrabasic and basic rocks overlap completely, and Group II typically defines a more tightly constrained trend. Zn, Ga, Y and Hf tend to be more enriched in Group I samples relative to Group II, whereas Th tends to be depleted in Group I lavas, especially those from Gandalf Ridge. Th concentrations in samples from Gandalf Ridge are generally lower than in other DVS rocks, which suggests a separate trend of milder Th enrichment at Gandalf Ridge. Sb and Cs also tend to be more depleted in rocks from Group I relative to Group II, although Cs is anomalously high in four samples from the Mason volcanic complex.

The behavior of Rb tends to be distinctive for each stratigraphic unit, and does not relate coherently to the broad grouping of alkali enrichment trends. Rb enrichment is smallest in rocks from

Gandalf Ridge. Rocks from the Mason volcanic complex, the Gandalf volcanic complex at Riviera Ridge, and Mt Discovery (MD1 and MD2) exhibit slightly more pronounced enrichment trends. Samples from the BP, MB1 and MM1 rock suites have even more pronounced early enrichment trends which level out in the more differentiated rocks.

For Zn, Sb, Cs and Th the divergence of trends occurs throughout the differentiation process, but for Ga, Rb, Y and Hf the divergence is not discernable in samples with Zr concentrations less than about 400 ppm.

8.6.2 Elements with Mixed Incompatible - Compatible Behavior

Sr and Ba generally exhibit mixed incompatible - compatible behavior, and trends tend to be peculiar to individual rock suites. However, there is no evidence for early Sr enrichment in Group I (Figure 8.27). Sr depletion is most pronounced in rocks from the lower portion of the Mason and Gandalf volcanic complexes. Samples from RG2, MB1 and possibly MB2 exhibit trends suggestive of an early, mild Sr enrichment, followed by strong Sr depletion beginning when Zr reaches 400 - 500 ppm. The Sr content of rocks erupted since about 6 m.y. ago is difficult to interpret. These lavas are either characterized by much higher initial Sr than the older lavas, or an early trend of strong Sr enrichment until Zr reaches about 500 ppm. There is no question of the subsequent strong depletion of Sr. Because there is no similar variation in the initial concentration of other trace elements between rock suites it seems unlikely that Sr alone would be so enriched in parental magmas younger than 6 m.y.

Ba may behave as a purely compatible, or incompatible element in

some suites, but generally follows a trend of early enrichment followed by depletion. Compatible behavior is exhibited by samples from the Mason volcanic complex and Gandalf Ridge (Figure 8.28). Group I samples from Riviera Ridge exhibit two trends. RG1 and some RG2 samples follow a trend of initial Ba enrichment followed by strong depletion after Zr reaches about 500 to 600 ppm, but three RG2 samples lie along a trend of continued Ba enrichment. Group II rocks display considerable diversity in the behavior of Ba, especially in the rock suites from Minna Bluff, but all Group II suites are characterized by early incompatibility. Except for the MS8 trachytes in which Ba is incompatible, maximum Ba enrichment occurs at about 500 - 600 ppm Zr. The extent of this enrichment varies considerably, but is greatest in the MD1 lavas.

8.6.3 Compatible Elements

Strongly compatible behavior is exhibited by Sc, V, Cr, Ni and Cu (Figures 8.29 - 8.33). There is no discernable differences in the behavior of Sc between Group I and II rocks. V, Cr, and Ni depletion trends are generally slightly stronger for the Group I rocks, and most samples from F, MM2, MS9 and RG3 than for other Group II rocks. However, the most interesting feature of the compatible trace element chemistry is the tendency for basanites and tephrites from the western half of the DVS (MS7, MS9, RG2, RG3,MM2, RG2, F) to be displaced 100 - 200 ppm Zr less than similar rocks from the eastern half (MD2, MB2, BP, BI2,WI) of the area.

La is a strongly incompatible element (Figure 8.15), and increases systematically with magma evolution (Figures 8.34 and 8.35). Furthermore, there is an almost complete overlap in the La/Ce, La/Sm and La/Yb ratios of the least evolved lavas from Groups I and II (Table 8.3), despite differences in the magnitude of the SiO_2 and Zr content, which suggest that more differentiation has occurred in the least evolved Group I rocks. It is concluded that there has not been significant rare earth element (REE) fractionation during this early evolution, but there is a strong divergence in the REE patterns between the two groups with further differentiation (Figures 8.36, 8.37 and 8.38).

Unlike the Group I rocks, which are characterized by a lack of light REE (LREE) (La, Ce, Nd) fractionation with magma evolution (Figure 8.36), Group II lavas exhibit mild LREE depletion in rocks of intermediate composition. Two Group I samples from the Mason volcanic complex (AW85818, AW85860) have negative Ce anomalies, causing their La/Ce ratios to be even higher than is found in most Group II rocks. These particular samples also have abnormally small negative Eu anomalies compared to typical Mason volcanic complex lavas, which suggests they crystallized at higher oxygen fugacities than other DVS lavas, an interpretation that is corroborated by the presence of sodic pyroxene (e.g., AW83502A) (section 7.4.4).

Both Groups I and II exhibit middle REE (MREE)(Sm, Eu, Tb) depletion with increasing differentiation, but this trend is far more pronounced in Group II lavas (Figure 8.37). Most Group II lavas also exhibit a progressive heavy REE (HREE)(Yb, Lu) depletion (Figure 8.38), although this feature is less pronounced in intermediate

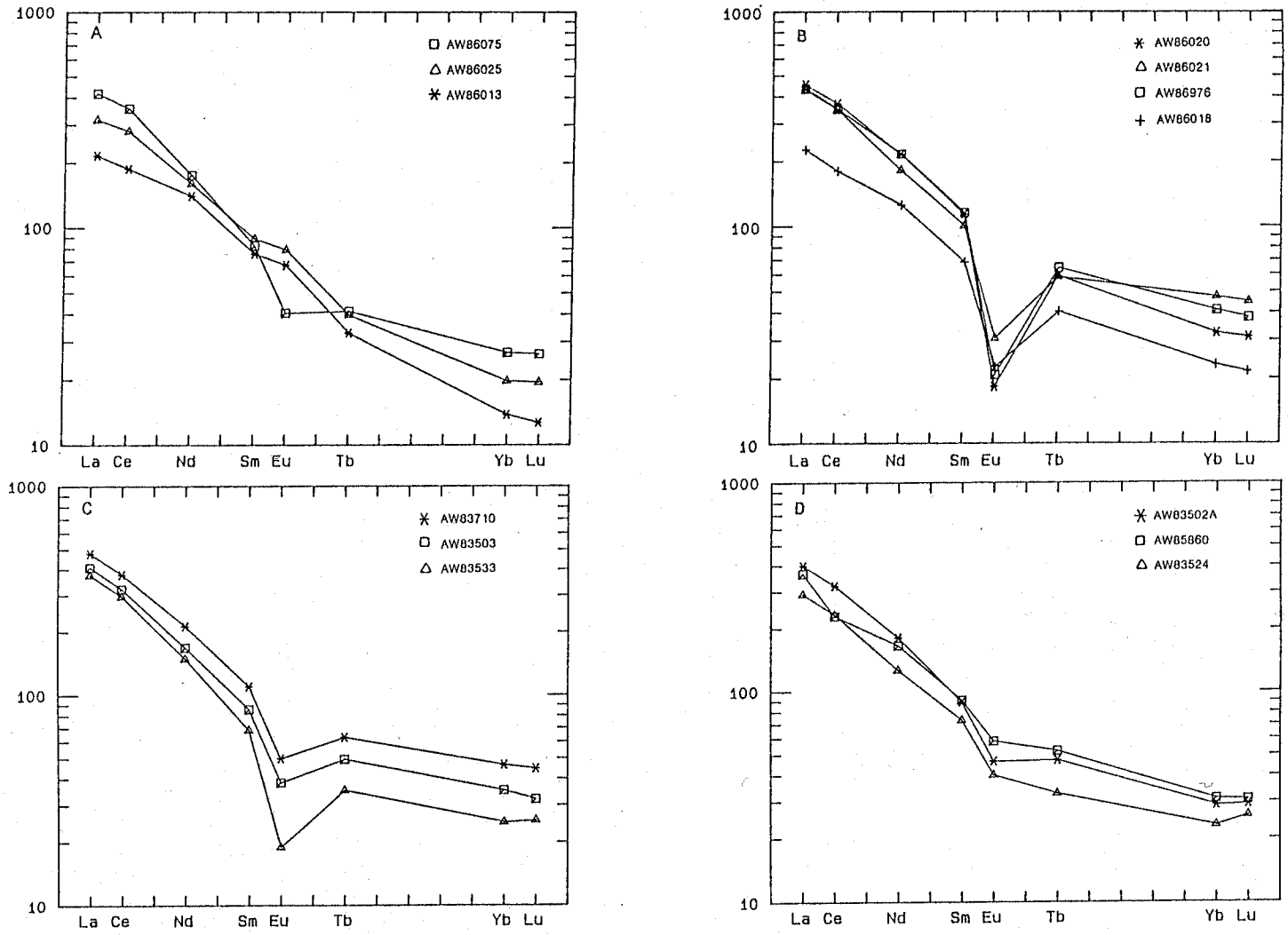

Figure 8.34 - Chondrite normalized rare earth element (REE) patterns for selected Group I samples: A - Samples from RG2 demonstrate a progressive increase in light and heavy REEs with increasing differentiation. A small, initially positive, Eu anomaly is preseved through the early development of a mild middle REE depletion trend, but is lost with the growth of a strong negative Eu anomaly in the more evolved lavas. B - Samples from RG1 at Castle Ridge exhibit mild middle REE depletion and a pronounced negative Eu anomaly. C - Samples from the Mason volcanic complex (MVC) exhibit similar middle REE depletion to the samples from RG1, but the negative Eu anomaly is typically less pronouced in the MVC samples. AW83533 and AW83710 are atypically extreme examples, whereas AW83503 is a typical

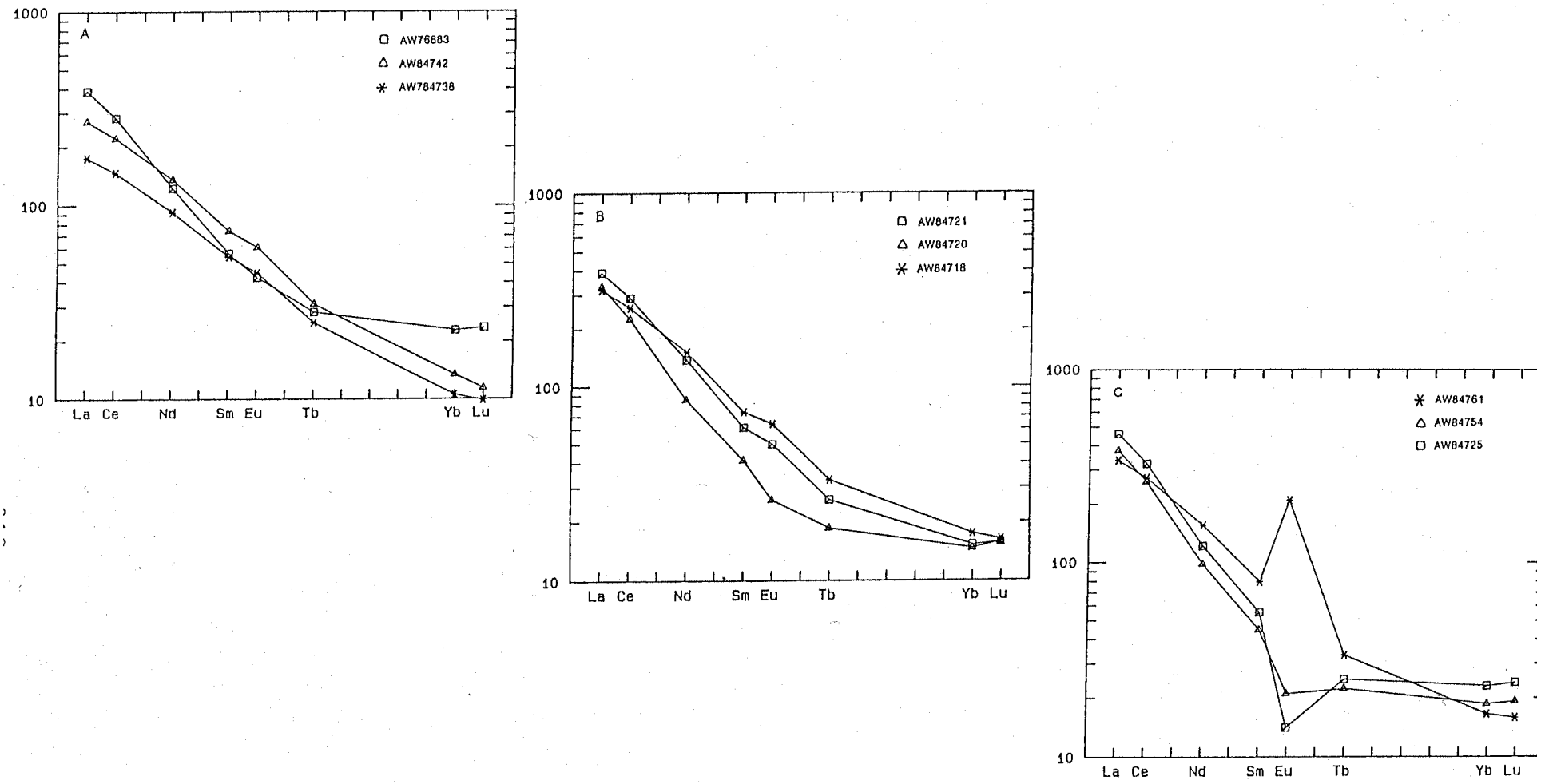

Figure 8.35 - Chondrite normalized rare earth element (REE) patterns for selected Group II samples. A - Less evolved samples from MD2 exhibit straight light REE enriched patterns with a small positive Eu anomaly, typical of Group II basanite and tephrites. The strongly depleted middle REE anomaly of AW86883 is also typical of the MS8 trachytes. B - Samples from MD1 show the progressive depletion of middle and heavy REE with differentiation from AW84718 (Zr=641 ppm) to AW84721 (Zr=707 ppm) to AW84720 (Zr=771 ppm). C - Samples from MD1 showing the development of a negative Eu anomaly superimposed on a middle REE depleted

Table 8.3 - Generalized summary of the rare earth element characteristics of lavas from the DVS. Concentration of La in chondrite standard is 0.315 ppm.

	Group I	Group II
Ultrabasic		
La enrichment		100 - 200 x chondrit
La/Ce		0.46 - 0.49
La/Sm		3.9 - 5.6
La/Yb		16.6 - 25.8
Basic		
La enrichment	200 - 250 x chondrite	200 - 300 x chondrit
La/Ce	0.45 - 0.47	0.47 - 0.50
La/Sm	4.4 - 5.8	5.4 - 7.8
La/Yb	20.9 - 23.7	21.9 - 29.4
Intermediate		
La enrichment	250 - 600 x chondrite	300 - 500 x chondrit
La/Ce	0.44 - 0.78	0.51 - 0.65
La/Sm	5.5 - 9.0	8.4 - 15.9
La/Yb	14.8 - 24.3	21.7 - 38.8
Acidic		
La enrichment	400 - 500 x chondrite	
La/Ce	0.47 - 0.48	
La/Sm	6.2 - 7.4	
La/Yb	16.0 - 21.2	

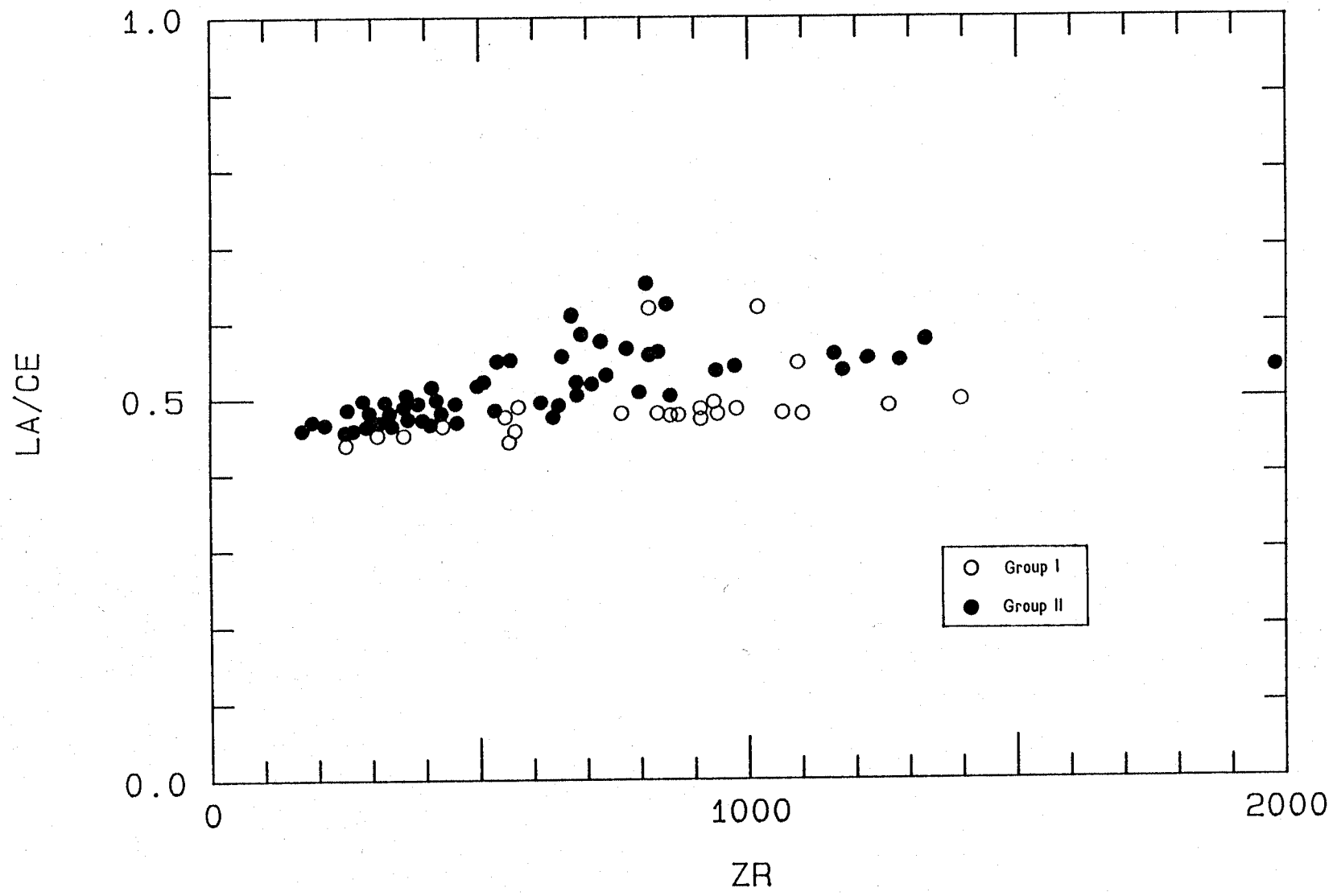

Figure 8.36 - Samples from Groups I and II showing the divergence in La/Ce ratios with magma evolution as indicated by Zr (ppm). Negative Ce anomalies in two Group I samples

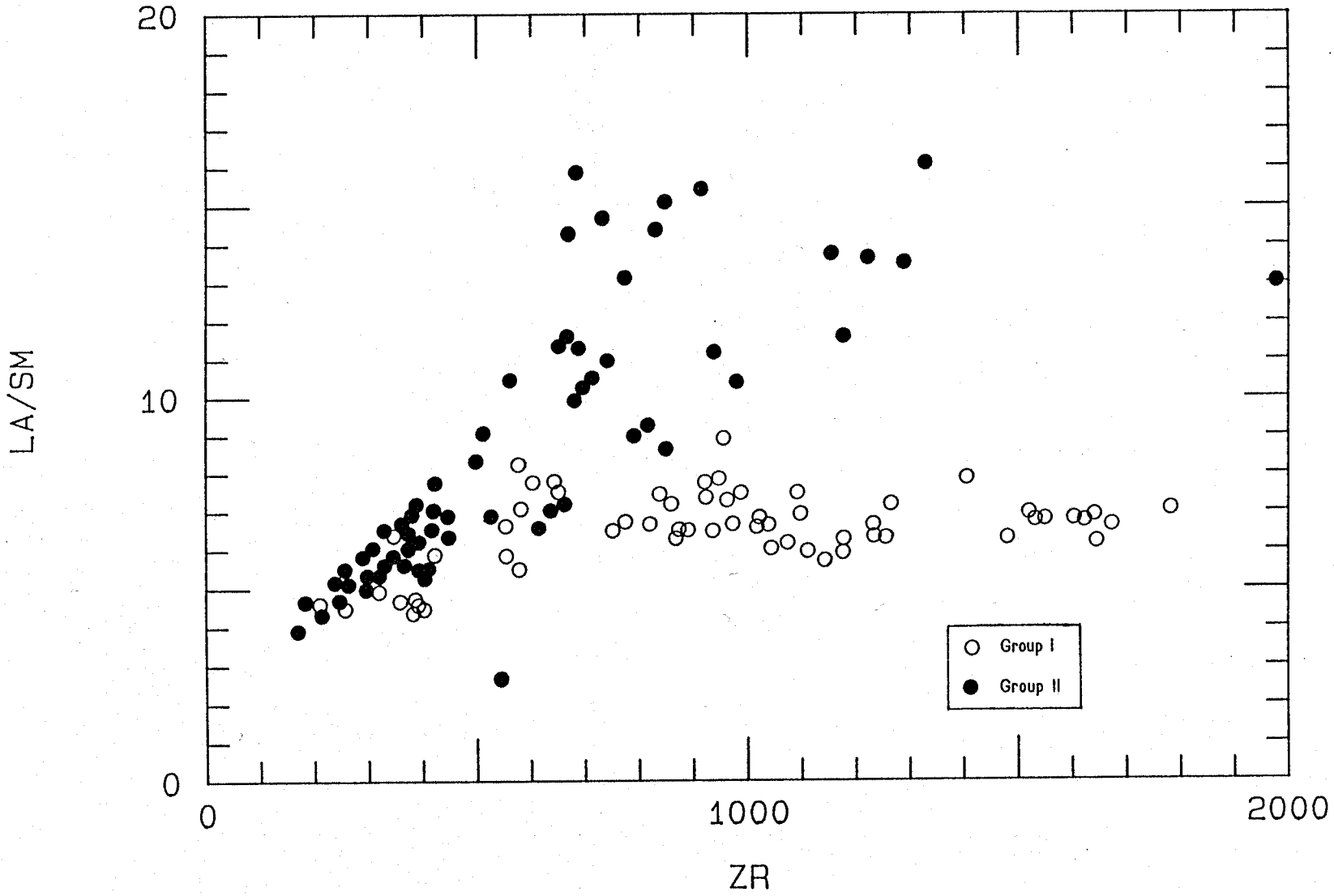

Figure 8.37 - Samples from Groups I and II show initial MREE depletion, but a marked divergence of trends in lavas more evolved than tephrite. Group I lavas exhibit no further

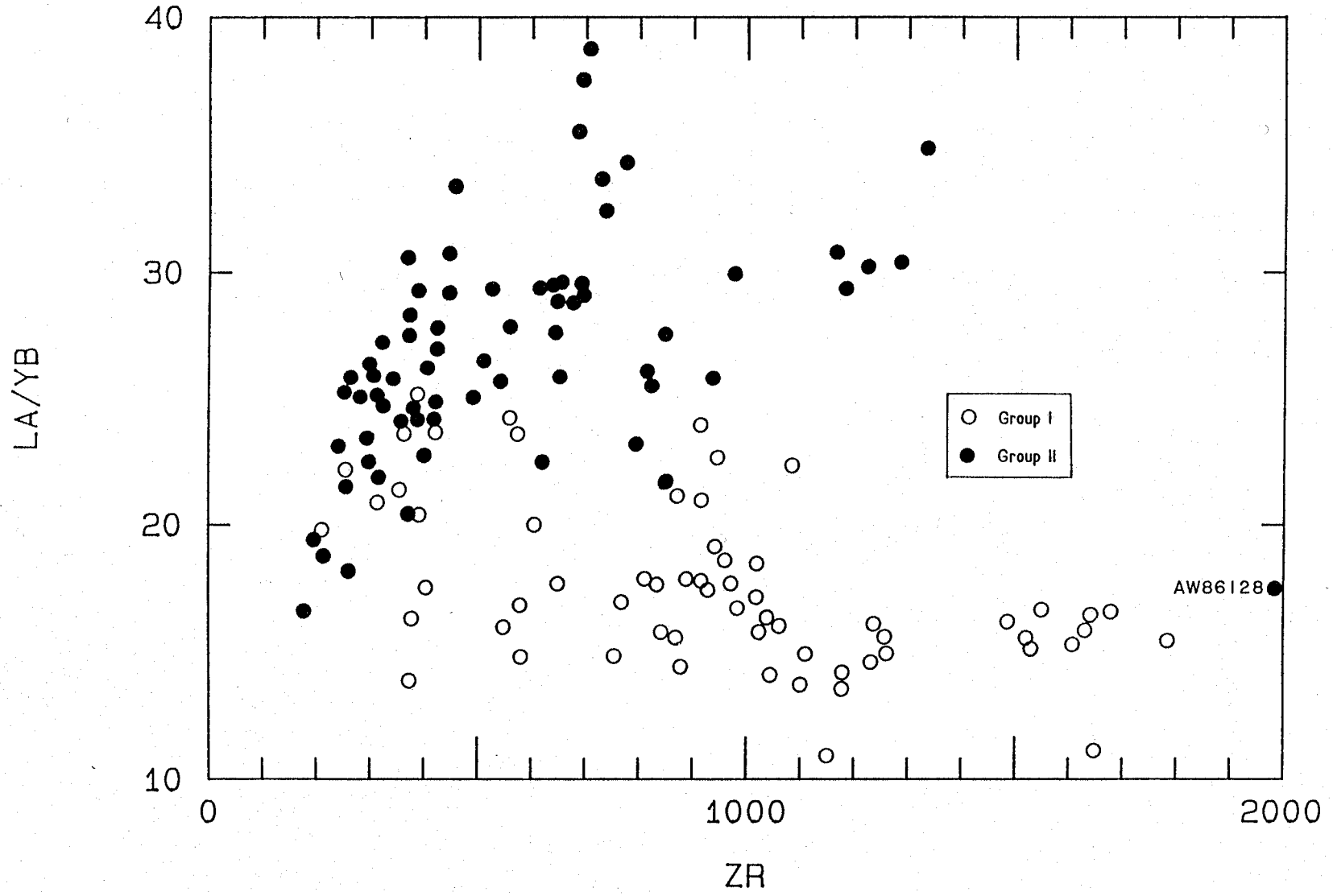

Figure 8.38 - Samples from Groups I and II exhibit a broad scatter in La/Yb ratios,

samples from MS8, MD2, and some from MD1 and MM1. Thus, two HREE fractionation trends are recognized in Group II. In contrast, after a small initial increase, Group I lavas have constant La/Sm ratios and decreasing La/Yb ratios throughout the rest of the differentiation trend. La/Yb ratios decrease most in the older, more peralkaline dominated parts of the Gandalf and Mason volcanic complexes.

Both positive and negative Eu anomalies may be superimposed on the various REE trends (Figures 8.34 and 8.35). Small positive anomalies are common in the ultrabasic, basic and some intermediate lavas with otherwise straight or mildly MREE depleted patterns. Small to pronounced negative Eu anomalies are characteristic of the trachytes and peralkaline trachytes of Group I, and a few Group II phonolites. The general magnitude of these negative Eu anomalies is higher in the Gandalf volcanic complex than the Mason volcanic complex, despite an otherwise strong similarity in the REE patterns and concentrations from both volcanic complexes. Mild to strong negative Eu anomalies are evident in a few MD1 and MB2 phonolites. The phonotephrite xenolith AW84761 from phonolite on Mt Discovery exhibits a strong positive Eu anomaly, but in other respects the REE pattern is almost identical to that of MD1 tephriphonolite (AW84718). This indicates that there is a cumulate feldspar component in xenolith AW84761. The lack of a significant Eu anomaly in the MD1 tephriphonolites indicates that the high plagioclase phenocryst content of these rocks is unlikely to be cumulus, and therefore, that the rock compositions represent real liquid compositions.

The chronologic division of DVS rocks into Groups I and II also has a strong geochemical basis (Table 8.4), which is most apparent in the strong divergence of middle (except Eu) and heavy REE depletion trends (Figures 8.37 and 8.38). There are also differences in the strength of enrichment or depletion trends for most major and trace elements. Na, La, Ta, U, and Pb exhibit similar incompatible behavior in both Groups.

The subdivision of Group II rock suites on the basis of differences in their alkali enrichment trends is supported by similar differences for most other major and some trace (Th, Cs, Sb, and possibl Rb and U) elements . There is always overlap between the fields of Group IIA and B on variation diagrams, but as Group IIA and B diverge Group IIB always lies closer to Group I than Group IIA does. Thus, Group I and Group IIA represent the extremes of a geochemical continuum in which the trends of individual rock suites become increasingly divergent with differentiation.

The phonolite AW86128 from Mt Morning exhibits an unusual geochemistry. Major element characteristics are most similar to those of Group IIA. However, most trace element characteristics lie on the probable extension of Group IIB trends. The behavior of Y, La, the La/Yb ratio are most similar to rocks from Group I.

Table 8.4 - Summary of age, stratigraphic units, rock types and geochemistry of Group I, Group IIA, and Group IIB.

	Group IIA	Group IIB	Group I
Age (m.y.)	2 - 9	1 - 11	11 - 19
Stratigraphic Units	BP MD2 MB2	MB1 MD1 MM1	MS1-7 RG1-2
Rock Types	Basanite to phonolite	Basanite to phonolite or tephrite	Basanite to trachyte or peralkaline trachyte
Alkali Enrichment	Strongest	Less strong	Weakest
SiO2	Strongly undersaturated	Less strongly undersaturated to saturated	Saturated to slightly oversaturated
FeO*	Strongest depletion	Less strongly depleted	Least strongly depleted
MgO, CaO, TiO2	Strongly depleted	Strongly depleted	Slightly less strongly depleted
Al2O3	Strongly enriched	Strongly enriched then mild depletion	Strongly enriched then strongly depleted
Na2O, K2O	Strongly enriched	Strongly enriched then less strongly enriched	Mild enrichment then strong depletion
Zr	Enriched	Stronger enrichment	Strongest enrichment
Nb, La, Ta U, Pb	Enriched	Enriched	Enriched
Zn, Ga, Y, Hf	Milder enrichment	Milder enrichment	Stronger enrichment
Th, Sb, Cs	Stronger enrichment	Stronger enrichment	Milder enrichment

Table 8.4 (continued)

	Group IIA	Group IIB	Group I
Rb	Variable enrichment	Variable enrichment	Variable enrichment
Sr	Strongest enrichment then depletion	Milder enrichment then depletion	Variable depletion
Ba	Variable enrichment then depletion	Variable enrichment then depletion	Variable enrichment and depletion
Sc, Cu, Ni, Cr, V	Strong depletion	Strong depletion	Strong depletion
La/Ce	Slight increase	Slight increase	Constant
La/Sm	Strong increase	Strong increase	Slight increase then constant
La/Yb	Very strong increase	Very strong increase	Mild decrease

Chapter 9

PETROGENESIS

9.1 INTRODUCTION

Lavas from the DVS span a broad compositional range from basanit to phonolite and peralkaline rhyolite. Possible mechanisms for this variation include:

1. Differences in the primary melt due to the mineralogical and geochemical composition of the source and the degree of partial melting.
2. Operation of open system processes such as magma mixing or contamination.
3. Operation of fractionation processes such as liquid immiscibility, volatile transfer, Soret diffusion, and fractional crystallizatior

This chapter discusses stratigraphic, chronologic, petrographic and geochemical evidence bearing on interpretations of the relative importance of each of these processes in creating the diversity of lavas found within the DVS.

9.2 DVS PARENTAL MAGMAS

Assuming that estimates of 2000 ppm Ni, and an olivine composition in the range of Fo_{92-88} are appropriate for mantle peridotite underlying the DVS, equilibrium partial melts will have Mg numbers (Mg/(Mg + 0.75 Fe*) of 0.68 - 0.77 and Ni contents of 300 - 400 ppm (Sun and Hanson, 1975; Green et al., 1974). Group II basanites have M numbers of 0.49 - 0.74, and Ni contents of 18 - 300 ppm Ni. Whereas M numbers suggest several Group II samples are essentially undifferentiated, primitive mantle melts, their Ni content is indicative of

small amounts of olivine fractionation. By analogy with basanites from Hut Point Peninsula, Ross Island, which have an average Mg number of 0.69 and Ni contents of 250 - 276 ppm (Kyle, 1981c), the least evolved Group IIA basanites have probably fractionated <10 % of olivine and clinopyroxene. Group I basanites have Mg numbers of 0.51 - 0.64 and Ni contents of 21 - 118 ppm suggesting that a greater degree of fractionation has occurred in these magmas prior to eruption.

No occurrences of alkali basalt were found in Group I rocks, whereas two localities are known for Group II rocks. These are at Black Island (BI1)(Cole and Ewart, 1968), and at Mason Spur (AW83662) AW83662 has a Mg number of 0.73 and a Ni content of 279 ppm, and is one of the more primitive lavas collected from the DVS. The Black Island alkali basalt has a Mg number of 0.67 and a Ni content of 150 ppm, and has obviously suffered some differentiation. These lavas are probably derived from an alkali basaltic primitive mantle melt. They are evidence that significant variation in the composition of primitive melts has probably occurred, at least in the last 11 m.y. However, the lack of alkali basalts in Group I and the presence of several Group I basanite occurrences, suggests that the Group I rocks may have evolved from a basanite rather than an alkali basalt parent.

There has been a substantial increase in the fequency with which near primitive melts reach the surface. Whereas older volcanic sequences are characterized by more differentiated rocks, lavas representing <10% fractionation have only been erupted over the last 5 m.y

Because of the variation in time and space of volcanic eruptions DVS lavas must be derived from many different batches of parental magma. Variations in minor and incompatible element abundances in

basanites probably reflect variations in the trace element content of various parental magmas, which is a product of their mantle source and degree of partial melting, as well as the effects of differentiation processes. The greater scatter of data points in Group II basanites probably reflects the more variable phenocryst and xenocryst content of these rocks. However, there is no clear correlation between phenocryst and xenocryst content and geochemistry.

9.3 ORIGIN OF ALKALINE BASALTIC MELTS

The compositional similarity of parental magmas for alkaline volcanic suites from oceanic islands and continental provinces necessitates that they be derived from the mantle, and that they undergo negligible interaction with the crustal rocks through which they ascend (Sorensen, 1974). Evidence from xenoliths, seismic velocities, and chondritic meteorites suggests that garnet peridotite is the most likely composition of the mantle (Bailey, 1982). LREE enrichment characteristics of alkaline volcanic rocks, including those from the DVS, require that garnet is a residual phase in the source. Experimental work shows that garnet will only be a residual phase at depths of >80 km (Green and Ringwood, 1967; Green 1970). Slight positive Eu anomalies in relatively undifferentiated DVS lavas suggest that oxyge fugacities in the source ranged from 10^{-6} to 10^{-9} atmospheres (Sun an Hanson, 1975).

Estimates for the degree of partial melting needed to generate alkaline basaltic liquids varies considerably depending on the approach taken (Green and Ringwood, 1967; Gast, 1968; Green, 1970; Ka and Gast, 1973; Sun and Hanson, 1975; Frey et al., 1978; Chauvel and Jahn, 1984). Trace element models of partial melting of probable

mantle compositions suggest that alkaline basaltic melts may be generated by about 1 - 2 % partial melting of a garnet peridotite source which was enriched in incompatible trace elements relative to chondrite (Gast, 1968; Kay and Gast, 1973). In contrast, experimental studies suggest that basanites and alkali basalts are generated by higher degrees of partial melting. Studies in southeastern Australia (Frey et al., 1978) concluded that basanite parental magmas were formed by 5 - 11% partial melting of an enriched garnet peridotite source, which contained 3 - 7 % H_2O and negligible CO_2. Alkali basalt resulted from a slightly greater degree of partial melting. These experimental models require a 6 - 9 times enrichment of the large ion lithophile and LREEs, and a 2 - 3 times enrichment of the high field strength and HREEs in the garnet peridotite source. Other studies also support the conclusion that CO_2 is not present in the mantle source for basanite and alkali basalt magams, but that it becomes increasing important in the generation of magmas more undersaturated than basanite (Brey and Green, 1975; Koster van Groos, 1975; Brey, 1976).

In contrast to the geochemical evidence indicating an enriched mantle source, isotopic studies clearly demonstrate that the mantle source regions for alkaline basaltic magmas typically have long-lived incompatible element depletion, including LREE depletion patterns (O'Nions et al., 1978; O'Nions et al., 1979). U/Pb and Rb/Sr isotopic studies within the Erebus volcanic province suggest that these lavas are derived from a mantle source depleted in incompatible elements about 1500 Ma ago (Sun and Hanson, 1975; Stuckless and Ericksen, 1976).

This anomaly can only be resolved if enrichment of the source

region is similar in age (within 100 m.y.) to the magmatic event (Carter et al., 1978; Menzies and Murthy, 1980; Hawksworth et al., 1987). There is now strong evidence indicating that enrichment of the source region occurs as a result of intrusion and metasomatic events associated with the alkaline magmatism (Windom and Boettcher, 1980; Wilshire, 1984; Wass and Rogers, 1980; Wass et al., 1980; Norry and Fitton, 1983; Hawkesworth et al., 1987). Textural, mineralogical, geochemical and isotopic studies of veined, mantle derived xenoliths provide particularly convincing evidence for a complex process of melting and subsequent intrusion at higher levels in the mantle, whic results in the upward transport and concentration of incompatible elements. There is also strong evidence for the presence of an immiscible volatile phase. The fluid phase is crucial to the mantle metasomatic process (Wass et al., 1980; Menzies and Hawkesworth, 1987), and is important in the upward transport of heat (Spera 1981, 1984, 1987).

It is concluded that DVS parental magmas probably formed by a small degree of partial melting of an enriched, hydrous garnet peridotite mantle source, with slightly higher degrees of partial melting being responsible for generating the alkali basalts. Enrichment of th source is attributed to ongoing magmatic and metasomatic events in th upper mantle, which explains why there has not been a depletion of incompatible elements with time. LREE enrichment evidence for the presence of garnet as a residual phase, suggests that partial melting took place at depths below about 80 km (Green, 1970). This is consistent with the inferred high H_2O/CO_2 ratios of basanite and alkali basalt source areas, a condition which probably occurs at depths of 7 - 120 km (Hawkesworth et al., 1987) beneath continental areas.

9.4 OPEN SYSTEM PROCESSES

Open system processes are those in which the magma interacts with materials that were not hitherto part of the magmatic system, and includes magma mixing and contamination processes. Three approaches to assessing the role of open system processes are:

1. an investigation of xenoliths and xenocrysts, and
2. isotopic studies of elements whose isotopic ratios are expected to differ between the parent magma and the contaminating source.
3. studies of trace element abundances and ratios.

9.4.1 Contamination

Xenoliths are rare in Group I lavas. Those that are found are small unconsolidated aggregates of feldspar and clinopyroxene crystal and are interpreted as cognate. In contrast, a wide diversity of xenoliths and related xenocrysts are present in many Group II lavas, though this material usually accounts for less than 5% of the rock. Lower crustal basic gneisses and granulites are the most widespread xenolith type, and are usually found in basanite and tephrite hosts. Oxidized xenoliths of probable Beacon sandstone also occur in a basanite at Mason Spur. These xenoliths are angular to subrounded, and exhibit variable degrees of disaggregation. Clearly, the opportunity for magma contamination by both lower and upper crustal rocks has been present for Group II magmas.

Ultramafic and mafic xenoliths are also common in Group II lavas especially basanites and tephrites. At Foster Crater they are inferred to have crystallized from earlier DVS magmas (Kirsch, 1981; Gamble and Kyle, 1987). Evidence of resorption and melting is common. Incorporation and assimilation of this material by the host may have caused

minor contamination of many lavas, and contributed to the scatter of compatible element data points in basanites and tephrites on variation diagrams.

Isotopic studies were not undertaken as part of this dissertation. Existing isotopic data for the DVS pertains only to Group II rocks, and includes Pb isotope determinations of a basanite from Mt Morning and a phonolite from Mt Discovery (Sun and Hanson, 1975); and Sr isotope determinations for eight other samples from the Foothills area, Mt Discovery, Minna Saddle, Brown Peninsula and Black Island (Jones and Walker, 1972; Stuckless and Ericksen, 1976). The Pb isotopic ratios are similar to the majority of rocks from Ross Island, which have been interpreted as being uncontaminated by crustal material (Sun and Hanson, 1975). $^{87}Sr/^{86}Sr$ ratios of DVS lavas fall in the range 0.7030 - 0.7041, and are well within the range of uncontaminated, mantle-derived basalts typical of oceanic islands (Peterman and Hedge, 1971). $^{87}Sr/^{86}Sr$ studies of crustal xenoliths in the Erebus volcanic province (Berg, 1984; Berg et al., 1985) shows that the xenoliths derived from the crust beneath McMurdo Sound have similar ratios to the host lavas, and therefore, could not be used to assess crustal contamination. Xenoliths derived from the crust beneath the Transantarctic Mountains to the west have ratios of 0.708 to 0.714 (Berg, et al., 1984). Since volcanoes in the Foothills area would be underlain by Transantarctic Mountains crust the lack of elevated Sr isotopic ratios in these lavas suggests that crustal contamination of Group II lavas has not been major.

9.4.2 Magma Mixing

DVS lava lineages typically exhibit some degree of enrichment followed by depletion of some or all of the following elements: Al_2O_3 Na_2O, K_2, P_2O_5, Sr and Ba. This geochemical configuration precludes derivation of the lava lineages by simple mixing of two end member compositions, such as silicic crustal melt and a basanite magma. This hypothesis is also unsupported by major element mixing models. Mixing models involving trace elements were not attempted.

Well rounded, porphyritic and vesicular xenoliths in some phonolites at Mt Discovery may be a second magma that became incorporated into the host at or about the time of eruption. The xenoliths are coarser grained than their hosts, have sharp boundaries, and typicall account for less than 2% of the total rock volume. They vary in size up to about 10 cm long, and are always oval in shape, and well rounded. Two xenoliths (AW84761, AW86895) were analysed for major an some trace elements. Both lie on the geochemical trends defined by other MDl lavas. In the only analyzed xenolith/host pair the xenolith was less evolved than the host. REEs were analysed in xenolith AW84761, which exhibits a pronounced positive Eu anomaly, indicating that accumulation of plagioclase has occurred in this sample. Pyroxen compositions are similar to pyroxenes precipitating from the phonolites, suggesting that they too may be accumulative. If the xenoliths were formed by the mixing of less evolved magmas with phonolite magma then the less evolved magma must have had a cumulative component.

The rounded green cores of clinopyroxenes in some Group II basanites and tephrites may have crystallized from a more evolved magma than the host, and have become incorporated into the host by magma mixing (Brookes and Printzlau, 1978; Duda and Schmincke, 1985). Such

mixing may also explain the presence of alkali feldspar xenoliths, which commonly occur in the same samples, and the compositional scatter exhibited by basanites and tephrites in many rock suites. By comparison with similar green-cored pyroxenes from the Massif Central France, and eastern Australia (Wass, 1979a; Duda and Schmincke, 1985 it is likely that such magma mixing took place at lower crustal or mantle depths.

9.5 FRACTIONATION PROCESSES

Fractionation processes are those which operate within a magma body, and do not involve the addition of external material. Assessmen of such processes include investigation of the changing mineralogy an geochemistry with time. Stratigraphic control of rock sequences is an important consideration, because it constrains the direction of geochemical trends with time.

9.5.1 Fractional Crystallization

Fractional crystallization takes place in the pressure/ temperature range between liquidus and solidus, and is the process whereby crystals are removed from a liquid, and thus cause a progressive change in the residual liquid composition. In crystal fractionation, crystallizing phases may be removed by the effect of gravity, by protective overgrowths or zoning of crystals, or simply by crystals attaching to the walls of a magma chamber or conduit. Liquid fractionation is a much faster process that produces similar geochemical trends in progressively more evolved magmas (Baker and McBirney, 1985). This is postulated to occur, because the more evolved and less

dense boundary layer, that has precipitated minerals along the walls of the magma chamber, flows upwards and collects at the top of the chamber, rather than remixing with the main body of magma. The proces of liquid fractionation necessarily produces a stratified magma chamber.

These processes produce a range of compositions characterized by magmas that become increasingly felsic with time and exhibit smooth curvilinear trends on elemental variation diagrams. Compatible elements decrease, whereas incompatible elements increase and maintain approximately constant ratios. "Normal" stratigraphic sequences are those in which older deposits are geochemically less evolved than the younger deposits. Such sequences can be erupted from either homogeneous or layered magma chambers, whereas "reverse" sequences can only be derived from the rapid and progressive downward emptying of a zoned magma chamber. For this reason, reverse geochemical zonation is typically associated with large explosive eruptions, for which there is no evidence in the DVS.

Fractional crystallization is commonly envoked to explain geochemical and mineralogical evolutionary trends in alkaline magmas (e.g., Coombs and Wilkinson, 1969; King, 1965; Le Roex, 1985; Le Roex and Erlank, 1982; Nash et al. 1969; Baker et al., 1977; Stuckless et al., 1981). Mass balance models calculated from major element analyse and supported by closely predicted estimates of trace element abundances in rocks from Ross Island and at Brown Peninsula (Kyle et al., 1979; Kyle 1981c; Moore, 1986), provide strong evidence that fractional crystallization is the dominant process controlling magma evolution in these volcanoes, and by analogy it is expected that the compositional spectrum of DVS lavas will have been similarly gen-

erated.

Some DVS rock suites display many geochemical characteristics typical of magmas which evolved by crystal fractionation. For instance, the tephriphonolite-phonolite rocks forming the central volcano of Mt Discovery (MD1), and the basanite-tephriphonolite volcanoes of Brown Peninsula. There is no stratigraphically constrained succession of increasingly more evolved lavas with time in the upper portions of the Gandalf and Mason volcanic complexes (RG2, MS7), and at Minna Bluff (MB1, MB2), but samples from the same stratigraphic unit lie along well defined geochemical trends (e.g., Figures 8.2A - 8.2C, which are consistent with evolution by liquid or crystal fractionation. This differentiation may have taken place in several, small discrete magma chambers undergoing similar differentation processes, which would account for the lack of stratigraphic evidence of progressive magma evolution. The compositions of rocks comprising the main body of evolved lavas in the Mason and Gandalf volcanic complexes (MS1-MS5, RG1) tend to cluster or exhibit limited compositional variation on variation diagrams (e.g., Figures 8.2A and 8.2B). They may not have evolved by simple fractional crystallization.

9.5.2 Qualitative Assessment of Fractional Crystallization

Even where clear stratigraphic evidence of progressive magma evolution is lacking, the petrographic and geochemical characteristics of DVS lavas are generally compatible with magma evolution by fractional crystallization. Trends of decreasing TiO_2, FeO*, MgO, CaO, Ni, Cr, Cu, Sc, and V are evidence for the fractionation of olivine, clinopyroxene and opaque oxides from ultrabasic and basic

lavas. MgO, Ni and Cr exhibit the strongest decreases, and are consistent with petrographic and mineralogical evidence for olivine and chromium spinel being the earliest crystallizing phases. Trends of increasing Al_2O_3 and P_2O_5 indicate that the crystallization of plagioclase, nepheline and apatite did not become important until later in the crystallization history. Plagioclase and nepheline precipitated from less evolved melt compositions in Group I as compared to Group II.

Fractionation of the MREEs (Sm, Eu Tb), first seen in rocks with compositions around the ultrabasic-basic boundary, is distinctly more pronounced in the Group II lavas, and is probably due to the fractionation of kaersutite. Additional evidence of kaersutite fractionation is seen in the cumulate amphibolite xenoliths (e.g., AW86999) that occur in some Group II lavas. Further evidence for kaersutite fractionation in Group IIA rocks, and to a lesser extent in rocks from Group IIB, is suggested by the behavior of the K/Rb ratio (Figure 9.1), which decreases with kaersutite fractionation. This feature arises because the distribution of Rb between kaersutite and clinopyroxene is similar, whereas the distribution of K into kaersutite is almost twice that of clinopyroxene (Kyle, 1981c). The K/Rb data suggests that kaersutite fractionation has been greatest in Group IIA magmas. The constant K/Rb ratios of Group I rocks imply that kaersutite has not been extracted from these magmas. The sharp, late stage decrease in the K/Rb ratio of Group I samples is attributed to fractionation of alkali feldspar.

Al_2O_3 and Na_2O trends display divergences between the three Groups, suggesting that differences in plagioclase and/or nepheline fractionation is a major factor contributing to the geochemical varia-

9.1 Variations of the K/Rb ratio of DVS lavas with SiO_2.

A - Group IIA
- ✳ BP, MD2, MB2, BI2, WI
- □ MS9, MM2, RG3, F2
- < Amphibolite xenolith from RG3

B - Group IIB
- ✳ MB1
- □ MD1
- △ MM1
- \+ MS8
- < Xenoliths in MD1 phonolites

C - Group I
- \+ MS1 - MS7
- ✳ RG1
- △ RG2

D - Summary of fields shown in A, B and C

Group IIA

Group IIB

Group I

Xenoliths compositions are not included in this summary plot. The sample AW86128 is shown as a triangle.

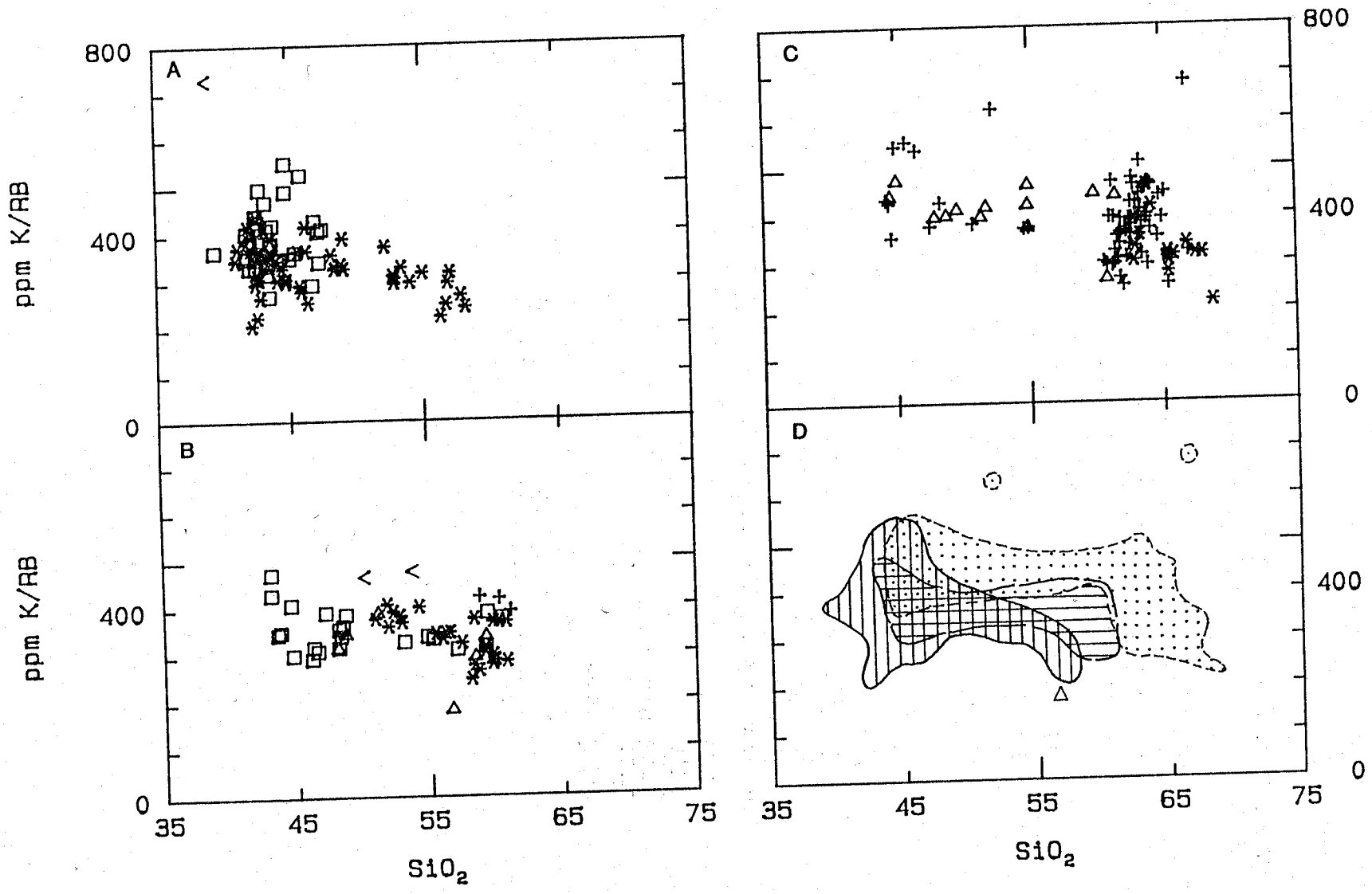
A
B
C
D
800
400
0
ppm K/RB
35
45
55
65
75
SiO2

tion of DVS lavas. Unlike the evolved rocks from Group II, there is a late stage decrease in K_2O relative to SiO_2 in Group I trachytes with >63 % SiO_2. The almost flat Al_2O_3/SiO_2 trends in Group I rocks, coupled with the lack of a similar trend for Na_2O/SiO_2 in lavas of ultrabasic and basic composition, suggests early calcic plagioclase fractionation. This is consistent with the generation of peralkalinity by the early fractionation of calcic plagioclase. Later depletion of Al_2O_3 and Na_2O in melts with >60 % SiO_2, indicates the fractionation of more sodic plagioclase. The late stage decrease in K_2O in some Group I samples suggests that alkali feldspar fractionated from Group I magmas with >63% SiO_2.

Sr and Ba exhibit broad trends that suggest either non-systematic variation in the amount of feldspar fractionation and/or variation in partitioning of these elements into feldspar, even within the same rock suite. Perhaps fractionation occurred in numerous small magma chambers. Alternatively fractionating magma may have been subjected to other magmatic or open system processes. The broad scatter of incompatible element ratios plotted against an index of increasing magma evolution (Figure 9.2) is further evidence to support the hypothesis that factors other than fractionation have been operative in the formation of evolved Group I lavas.

9.5.3 Quantitative Models of Fractional Crystallization

Modelling Procedure

Major element analyses of selected samples from rock suites representative of the three Groups were used to calculate least squares mass balance models (Bryan et al., 1969) in order to quantify

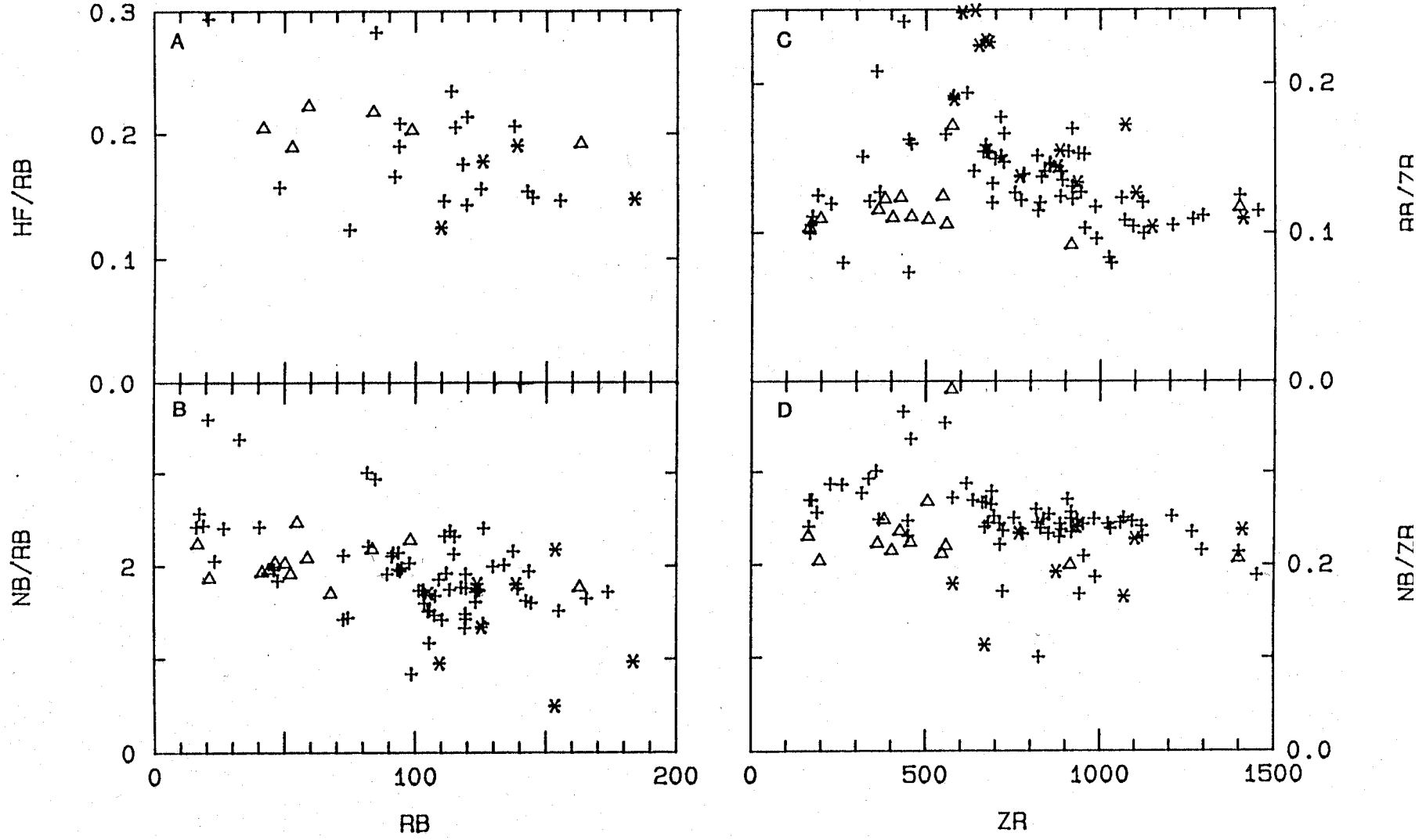

Figure 9.2 - A selection of trace element ratios in Group I lavas plotted against Zr or Rb (ppm). + MS1 - MS7, * RG1, Δ RG2. The trace elements chosen are normally incompatible in alkaline fractionation series, and as such would be expected to plot on a horizontal line if Group I lavas are related by simple fractional crystallization processes. The broad scatter in this data indicates that samples from the Mason and Gandalf volcanic

probable models of fractional crystallization. All analyses were normalized to 100% water-free, and total iron was calculated as FeO. Microprobe analyses of mineral phases (Table 9.1) from the selected rock samples were generally used, but occasionally it was necessary to use mineral analyses from closely related DVS rocks. Analyses of ilmenite, apatite, and nepheline were taken from other sources. Geologically and mineralogically reasonable solutions to the mass balance models were accepted if the calculated residual for each element was less than analytical uncertainty, and the sum of the residuals squared was less than or equal to 0.1.

Acceptable mass balance models were tested using the Rayleigh fractionation equation ($C_l = C_o F^{D-1}$) to predict the abundance of selected trace elements in the residual liquid (C_l) (Arth, 1976). C_o is the concentration of the trace element in the initial liquid, and F is the fraction of the residual liquid, as determined in the mass balance model. Measured mineral/melt partition coefficients (D) from compositionally similar rocks were taken from the literature (Table 9.2).

Group IIA

Group IIA rock suites crop out at Brown Peninsula (BP), and form the younger volcanic sequences at Mt Discovery (MD2), and Minna Bluff (MB2). The best sequence is reported from Brown Peninsula, where the geochemistry of a stratigraphically controlled basanite - tephriphonolite progression has been modelled previously using a method similar to that used here (Kyle et al., 1979). Kyle et al.'s mass balance models comprised two steps, and except for Sr, were supported by trace element data. The discordance between the predicted and observed Sr

Table 9.1 - Composition of minerals used for least squares mass balance modelling.

	OLIVINE		CLINOPYROXENE						KAERSUTITE
	Fo_{86}	Fo_{79}	En_{48}	En_{46}	En_{44}	En_{42}	En_{38}	En_{33}	K-1
SiO2	39.47	38.71	46.28	48.45	44.25	47.23	50.72	51.58	39.10
TiO2		0.09	2.45	2.02	3.55	2.10	1.67	0.36	5.80
Al2O3	0.08		7.76	6.63	9.94	5.84	3.84	1.46	13.35
FeO*	13.45	19.41	7.09	5.20	7.45	8.19	7.87	12.40	13.80
MnO	0.25	0.25	0.18		0.25	0.23	0.26	0.65	0.19
MgO	45.88	40.48	12.79	13.49	11.15	11.91	12.90	10.74	10.60
CaO	0.39	0.28	22.13	22.01	22.00	23.20	23.04	22.50	11.54
Na2O			0.64	0.45	0.69	0.65	0.67	0.67	2.77
K2O									1.07

	KAERSUTITE		TITANOMAGNETITE					
	K-2	K-3	Usp_{40}	$Usp_{61}A$	$Usp_{61}B$	$Usp_{61}C$	Usp_{62}	Usp_{76}
SiO2	40.58	40.36	0.13	0.07	0.11	0.10	0.11	0.11
TiO2	7.32	6.27	13.50	18.36	20.60	21.72	21.05	24.06
Al2O3	12.23	11.63	1.18	8.75	5.11	6.44	2.41	5.05
FeO*	12.19	14.51	79.49	62.45	65.01	62.91	70.85	63.93
MnO	0.19	0.44	1.55	0.41	0.35	0.54	1.04	0.55
MgO	11.07	9.98	0.06	7.15	6.42	5.81	2.20	4.45
CaO	12.07	11.43					0.09	
Na2O	2.70	3.24						
K2O	1.22	0.99						

Table 9.1 - (continued).

	TITANOMAGNETITE		ILMENITE[1]	FELDSPAR					
	Usp_{77}	Usp_{81}		An_{76}	An_{62}	An_{60}	An_{36}	An_{33}	An_{28}
SiO2	0.11	0.11	0.09	49.91	52.24	52.73	58.46	59.24	60.61
TiO2	24.91	26.89	49.48	0.09		0.14	0.07	0.13	
Al2O3	3.92	3.00	0.60	31.77	30.27	30.22	25.38	25.40	24.37
FeO*	64.12	65.58	40.46	0.33	0.37	0.43	0.22	0.19	0.32
MnO	0.79	1.11	0.72						
MgO	3.84	3.17	6.35	0.04	0.05	0.06			
CaO				15.69	12.75	12.27	7.26	6.87	5.96
Na2O				2.61	4.17	4.42	6.40	7.16	7.53
K2O				0.15	0.15	0.19	1.00	0.96	1.05

	NEPHELINE		APATITE[3]
	Ne-1[2]	Ne-2	
SiO2	44.65	49.73	0.18
TiO2			
Al2O3	32.03	30.57	
FeO*	0.53	1.42	0.34
MnO	0.13		
MgO	0.28	0.25	
CaO	0.71	0.12	53.69
Na2O	17.25	16.90	
K2O	3.66	1.27	
P2O5			41.54

1. Moore (1986)
2. Deer et al. (1966)
3. Kyle (unpublished)

Table 9.2 - Mineral/melt partition coefficients used in Rayleigh fractionation modelling of the MBl rock suite at Minna Bluff and the Group I rocks at Mason Spur. Values in parentheses are interpolated or extrapolated. The MBl model is divided into four steps: 1 - basanite to phonotephrite, 2 - phonotephrite to tephriphonolite, 3 - tephriphonolite to benmoreite, and 4 - benmoreite to trach The Group I model has two steps: 1 - basanite to tephrite, and 2 - tephrite to benmoreite. Within each step there is up to four separate geochemical models te

	Olivine					Clinopyroxene	
Step	MBl 1	MBl 2	MBl 3	Group I 1	Group I 2	MBl 1	MBl 2
Model	1,2	1-4	1	1,2	1	1,2	1-4
Rb	0.05	0.05	0.05	0.05	0.05	0.04	0.0
Sr	0.014	0.014	0.014	0.014	0.014	0.516	0.5
Zr	0.07	0.07	0.07	0.07	0.07	0.44	0.4
Ba	0.009	0.009	0.009		0.009	0.031	0.0
La	(0.009)	(0.009)	(0.009)		(0.009)	(0.30)	(0.3
Ce	0.009	0.009	0.009		0.009	0.359	0.3
Sm	0.011	0.011	0.011		0.011	0.98	0.5
Eu	0.010	0.010	0.010		0.010	0.85	0.8
Tb	(0.013)	(0.013)	(0.013)		(0.013)	(1.13)	(1.1
Yb	0.023	0.023	0.023		0.023	1.05	1.0
Source	1,2,15	1,2,15	1,2,15	2,15	1,2,15	3,4,15	3,4,1

	Clinopyroxene					Kaersutite	
Step	MBl 3	MBl 4	Group I 1	Group I 1	Group I 2	MBl 1	MBl 2
Model	1,2	2,3	1	2	1	2	1,3,4
Rb	0.04	0.04	0.04	0.01	0.01	0.11	0.11
Sr	0.516	0.516	0.516	0.516	0.516	0.58	0.58
Zr	0.44	1.02	0.44	0.01	0.44	0.41	0.41
Ba	0.031	0.131			0.031	0.62	0.62
La	(0.30)				0.10	0.31	0.31
Ce	0.359				0.18	0.49	0.49
Sm	0.98				0.56	1.07	1.07
Eu	0.85				0.58	1.09	1.09
Tb	(1.13)				0.73	(1.12)	(1.12
Yb	1.05				0.61	0.78	0.78
Source	6,15	6,15	6,15	5,6,12	6,12,15	4,6,15	5,6,1

Table 9.2 - (continued)

	Kaersutite		Titanomagnetite				
	MBl	MBl	MBl	MBl	MBl	MBl	Group I
Step	3	4	1	2	3	4	1
Model	2	1,2	1,2	1-4	1,2	1-3	1
Rb	0.11	0.2	0.01	0.01	0.01	0.14	0.1
Sr	0.61	3.1	0.01	0.01	0.01	0.01	0.1
Zr	o.41	0.72	0.94	0.2	0.2	0.24	3.6
Ba	0.62	0.86	0.01	0.01	0.01	0.31	
La	1.44		0.01	0.01	0.63		
Ce	1.98		0.01	0.01	0.9		
Sm	2.38		0.01	0.01	1.8		
Eu	2.70		0.01	0.01	1.7		
Tb	(3.44)		0.01	0.01	1.3		
Yb	2.02		0.01	0.01	0.75		
Source	6,11,15	2,11,15	13,15	9,13	7,9	7,15	13,15

	Titanomagnetite		Ilmenite	Feldspar			
	Group I	Group I	MBl	MBl	MBl	MBl	MBl
Step	1	2	1	1	2	3	4
Model	2	1	1	1,2	1-3	1,2	1,2
Rb	0.01	0.01	0.01	0.01	0.01	0.01	0.32
Sr	0.01	0.01	0.01	1.36	1.36	4.62	7
Zr	0.24	3.60	0.20	0.09	0.09	0.09	0.16
Ba		0.01	0.01	0.36	0.36	1.47	9
La		0.0173	0.01	0.280	0.280	0.280	
Ce		(0.0171)	0.01	0.215	0.215	0.215	
Sm		0.0165		0.170	0.170	0.170	
Eu		0.0162		1.10	1.10	1.10	
Tb		(0.019)		0.111	0.111	0.111	
Yb		(0.039)		0.062	0.062	0.062	
Source	13	12,13,15	13	2,6,14	2,6,14	1,6,15	8,11,14

Table 9.2 - (continued)

	Feldspar			Nepheline			
Step	Group I 1	Group I 1	Group I 2	MBl 2	MBl 3	MBl 4	Group I 1
Model	1	2	1	1,2	1,2	1-3	1
Rb	0.066	0.01	0.01	0.44	0.44	0.44	0.44
Sr	2.84	4.62	1.36	0.24	0.24	0.24	0.24
Zr	0.09	0.09	0.09	0.005	0.005	0.005	0.005
Ba			1.47	0.09	0.09	0.09	
La			0.31	0.01	0.12		
Ce			0.24	0.01	0.14		
Sm			0.17	0.02	0.22		
Eu			1.32	0.02	0.26		
Tb			0.16	0.03	0.33		
Yb			0.16	0.03	0.34		
Source	6,11,15	6,13,15	6,13,15	8,13	7,8	8	8

	Nepheline	Apatite					
Step	Group I 1	MBl 1	MBl 2	MBl 3	MBl 4	Group I 1	Group I 2
Model	2	1,2	1-4	1,2	1,2	2	1
Rb	0.01	0.01	0.01	0.01	0.01	0.01	0.01
Sr	0.24	5	5	5	5	5	5
Zr	0.005	0.01	0.01	0.01	0.01	0.01	0.01
Ba		0.10	0.10	0.10	0.10		0.10
La		10	10	(15)			15.2
Ce		12	12	18			16.6
Sm		20	20	29			20.7
Eu		16	16	21			14.7
Tb		18	18	25.6			19.8
Yb		8	8	13			9.4
Source	7,8	6,12	6,12	6,7,12	6,12	6,12	3,6,12

Sources

1. Philpotts and Schnetzler, 1970
2. Schnetzler and Philpotts, 1970
3. Nagasawa and Schnetzler, 1971
4. Nagasawa, 1973
5. Arth, 1976
6. Sun and Hanson, 1976
7. Cullers and Medaris, 1977
8. Larsen, 1979
9. Pearse and Norry, 1979
10. Le Roex and Erlank, 1982
11. Worner et al., 1983
12. Irving and Frey, 1984
13. Le Roex, 1985
14. Moore, 1986
15. Lemarchard et al., 1987

concentrations probably reflects the use of unrealistic partition coefficients for Sr.

The first step in Kyle et al.'s (1979) model from basanite to phonotephrite was achieved by the extraction of olivine, clinopyroxene, titanomagnetite, plagioclase (An_{60}), apatite and either ilmenite or kaersutite. The phonotephrite is a 42.1% to 41.1% residual liquid. The second step from phonotephrite to tephriphonolite leaves a 73.8% residual liquid, and requires the further extraction of clinopyroxene, kaersutite, plagioclase (An_{40}), and apatite.

Group IIB

Group IIB rock suites form the central volcanoes of Mt Discovery (MD1) and Mt Morning (MM1), the lower sequence at Minna Bluff (MB1). The geochemically most complete suite is the MB1 sequence. Although these lavas may not have evolved in a single magma chamber, their compositions can be related by acceptable fractional crystallization models, suggesting that they are at least derived from compositionally similar parental magmas which have evolved by fractional crystallization under similar physical conditions. The sequence is modelled in four steps: basanite - phonotephrite - tephriphonolite - benmoreite - trachyte.

Two acceptable mass balance models for the derivation of phonotephrite from basanite (Table 9.3) require the removal of clinopyroxene, plagioclase, olivine, titanomagnetite, apatite, and either ilmenite or kaersutite. The phonotephrite is a 41.1% to 43.1% residual liquid. With the exception of Rb, estimated trace element abundances agree well for both models, although the predicted REE abun-

Table 9.3 - Least squares mass balance models for the fractional crystallization of basanite AW82105 to form phonotephrite AW84796, in Group IIB lavas from Minna Bluff (step 1). Each mass balance model is generated by adding the composition of the fractionated minerals to that of the more evolved melt composition (in this case phonotephrite AW84796) to predict the initial melt composition (in this case basanite AW82105). The predicted value of each element is then compared to the measured value in the less evolved melt. The difference between predicted and measured value is squared, and the squared values summed to give the sum of the squared residuals (Sum R^2). This provides an overall indication of how well the model fits the data. The weight fraction of the residual liquid (F), and the weight fraction of the various minerals in each model are used to predict trace element concentrations (in ppm) in the more evolved melt, given the initial melt composition, and assuming Rayleigh fractionation, and partition coefficients given in Table 9.2.

Model	AW82105 (measured)	AW82105 (predicted) 1	AW82105 (predicted) 2	AW84796 (measured)
SiO2	43.75	43.52	43.46	48.69
TiO2	3.54	3.54	3.50	2.46
Al2O3	14.66	14.73	14.75	18.03
FeO*	11.64	11.63	11.64	18.03
MnO	0.20	0.16	0.16	0.23
MgO	9.85	9.88	9.89	3.65
CaO	11.45	11.50	11.51	8.10
Na2O	2.89	3.07	3.10	5.50
K2O	1.26	1.28	1.31	2.93
P2O5	0.77	0.71	0.69	0.78
F		0.431	0.411	
Olivine (Fo_{86})		0.185	0.164	
Clinopyroxene (En_{44})		0.466	0.404	
Kaersutite (K-1)		-	0.128	
Titanomagnetite (Usp_{61}^{A})		0.099	0.095	
Ilmenite		0.016	-	
Plagioclase (An_{62})		0.219	0.195	
Apatite		0.015	0.015	
Sum R^2		0.054	0.080	

	AW82105 (measured)	AW84796 (predicted) 1	AW84796 (predicted) 2	AW84796 (measured)
Rb	22	50	52	76
Sr	862	1190	1202	1102
Zr	254	445	453	413
Ba	359	767	754	747
La	43.6	75.1	76.5	72.6
Ce	95.1	158	158	141
Sm	9.14	10.8	10.3	10.2
Eu	2.80	3.10	2.95	3.02
Tb	1.10	1.29	1.21	1.21
Yb	2.02	2.75	2.75	2.99

dances are in closer agreement for the model in which kaersutite is extracted. The discordance between estimated and observed Rb abundances cannot be explained by the inappropriate choice of partition coefficients. The close agreement between INAA and XRF Rb determinations indicates that the discrepancy is not an analytical problem. Although the possibility of sample contamination cannot be ruled out, the discrepancy most probably results from variations in the initial Rb content of different primary melts.

Four acceptable mass balance models were generated for the derivation of tephriphonolite from phonotephrite (Table 9.4). These models extract clinopyroxene, titanomagnetite, olivine, apatite, and/or plagioclase, and/or kaersutite and/or nepheline. The tephriphonolite is a 74.6% to 76.1% residual liquid. The closest agreement between estimated and observed trace element abundances is obtained with the model in which plagioclase, kaersutite and nepheline are removed. The presence of kaersutite and feldspar phenocrysts in phonotephrites and tephriphonolites makes these minerals likely candidates for extraction, thereby rendering the models in which kaersutite and feldspar are not removed less probable.

Two acceptable mass balance models in which benmoreite is derived from tephriphonolite were generated (Table 9.5). Plagioclase, nepheline, titanomagnetite (different compositions), apatite, and either olivine and clinopyroxene, or kaersutite are extracted in these models. The benmoreite is a 74.7% to 73.8% residual liquid. Again it is the model in which kaersutite is extracted that provides the better estimated REE abundances.

Three acceptable mass balance models were generated for the derivation of the most evolved trachyte, from a benmoreite (Table

Table 9.4 - Least squares mass balance models for the fractional crystallization of phonotephrite (AW84796) to form tephriphonolite (AW92097B), in Group IIB lavas at Minna Bluff (step 2). A more detailed explanation of how the mass balance and trace element models are generated is given in the caption to Table 9.3.

Model	AW84796 (measured)	AW84796 (predicted) 1	2	3	4	AW82097B (measured)
SiO2	48.69	48.84	48.82	48.95	48.93	53.47
TiO2	2.46	2.52	2.45	2.57	2.54	1.40
Al2O3	18.03	17.90	17.95	17.85	17.93	21.22
FeO*	9.64	9.62	9.64	9.61	9.62	9.31
MnO	0.23	0.21	0.21	0.21	0.21	0.20
MgO	3.65	3.63	3.63	3.62	3.62	1.34
CaO	8.10	8.06	8.07	8.04	8.04	5.17
Na2O	5.50	5.54	5.53	5.44	5.41	6.84
K2O	2.93	2.74	2.72	2.77	2.75	3.56
P2O5	0.78	0.82	0.82	0.86	0.85	0.51
F		0.746	0.746	0.761	0.758	
Olivine (Fo_{79})		0.033	0.051	0.026	0.036	
Clinopyroxene (En_{42})		0.540	0.580	0.509	0.508	
Kaersutite (K-1)		0.123	-	0.238	0.187	
Titanomagnetite ($Usp_{61}B$)		0.188	0.206	0.182	0.188	
Plagioclase (An_{60})		0.021	0.056	-	0.036	
Nepheline (Ne-1)		0.054	0.066	-	-	
Apatite		0.041	0.040	0.045	0.045	
Sum R^2		0.055	0.054	0.072	0.068	

	AW84796 (measured)	AW82097B (predicted) 1	2	3	4	AW82097B (measured)
Rb	76	100	100	99	99	89
Sr	1102	1240	1241	1220	1214	1257
Zr	413	503	506	492	494	510
Ba	747	969	987	937	942	934
La	72.6	81.2	81.8	79.3	79.4	85.6
Ce	141	152	154	147	148	162
Sm	10.2	9.45	9.80	9.04	9.16	9.43
Eu	3.02	2.79	2.85	2.70	2.71	2.84
Tb	1.21	1.05	1.08	1.01	1.03	1.13
Yb	2.99	2.99	3.05	2.92	2.94	3.22

Table 9.5 - Least squares mass balance models for the fractional crystallization of tephriphonolite (AW82097B) to form benmoreite (AW82056), in Group IIB lavas at Minna Bluff (step 3). A more detailed explanation of how the mass balance and trace element models are generated is given in the caption to Table 9.3.

Model	AW82097B (measured)	AW82097B (predicted) 1	AW82097B (predicted) 2	AW82056 (measured)
SiO2	53.47	53.50	53.51	57.46
TiO2	1.40	1.35	1.38	0.95
Al2O3	21.22	21.17	21.38	19.30
FeO*	6.31	6.33	6.32	6.09
MnO	0.20	0.18	0.18	0.21
MgO	1.34	1.32	1.31	1.11
CaO	5.17	5.17	5.20	3.36
Na2O	6.84	6.86	6.89	6.95
K2O	3.56	3.48	3.50	4.26
P2O5	0.51	0.50	0.46	0.32
F		0.747	0.738	
Olivine (Fo_{79})		0.027	-	
Clinopyroxene (En_{38})		0.043	-	
Kaersutite (K-2)		-	0.153	
Titanomagnetite (Usp_{77})		0.090	-	
(Usp_{62})		-	0.066	
Plagioclase (An_{60})		0.513	0.465	
Nepheline (Ne-1)		0.303	0.295	
Apatite		0.024	0.020	
Sum R^2		0.011	0.017	

	AW82097B (measured)	AW82056 (predicted) 1	AW82056 (predicted) 2	AW82056 (measured)
Rb	89	114	115	113
Sr	1257	791	818	740
Zr	510	666	666	687
Ba	934	994	990	1071
La	85.6	96.0	93.0	90.1
Ce	162	178	169	173
Sm	9.43	9.28	8.86	7.97
Eu	2.84	2.57	2.42	2.41
Tb	1.13	1.15	1.04	0.87
Yb	3.22	3.37	3.21	3.08

9.6). In these models plagioclase, nepheline, titanomagnetite, apatite, and/or kaersutite, and/or clinopyroxene are removed. The trachyte is a 68.4% to 69.0% residual liquid. There are no REE data for the trachyte, so the trace element testing of these models is limited Models in which clinopyroxene is extracted exhibit the closest agreement between estimated and observed trace element abundances for Rb and Zr. None of the models allow reasonable predictions for the marke depletion of Sr and Ba in the trachyte. This suggests that the partitioning of these elements into feldspar is higher than allowed by the partition coefficients used. The trachyte represents an approximately 15% residual liquid of the basanite parent.

Group I

Older Group I lavas crop out at Mason Spur, Riviera Ridge and Gandalf Ridge, and were probably erupted from small to medium sized centers. Lavas less evolved than trachyte mostly occur towards the to of the Group I sequences at Mason Spur and Riviera Ridge. Group I basanites have Mg numbers of 0.51 to 0.64 and Ni contents of 21 to 11 ppm and have probably undergone considerable fractionation. An attemp was made to derive Group I tephrite AW83543 from a primitive Group II basanite AW83583 (both from Mason Spur), in order test whether Group rocks could be related by fractional crystallization to parental basanitic magmas similar to those from which the Group II rocks are derived. Tephrite AW83543 was chosen because it is the least evolved Group I rock for which there is full trace element data, including RE analyses. Acceptable mass balance models were not generated. However, successful mass balance models were generated in which the tephrite

Table 9.6 - Least squares mass balance models for the fractional crystallization of benmoreite (AW82056) to form trachyte (W84-2), in Group IIB lavas at Minna Bluff (step 4). A more detailed explanation of how the mass balance and trace element models are generated is given in the caption to Table 9.3.

Model	AW82056 (measured)	AW82056 (predicted) 1	2	3	W84-2 (measured
SiO2	57.46	57.24	57.35	57.29	60.74
TiO2	0.95	1.05	0.88	0.89	0.29
Al2O3	19.30	19.75	19.35	19.52	19.22
FeO*	6.09	6.07	6.11	6.10	4.88
MnO	0.21	0.21	0.23	0.22	0.24
MgO	1.11	1.10	1.02	1.12	0.43
CaO	3.36	3.34	3.43	3.40	1.06
Na2O	6.95	6.84	6.97	6.92	7.08
K2O	4.26	4.40	4.36	4.38	5.99
P2O5	0.32	0.34	0.22	0.26	0.06
F		0.684	0.690	0.686	
Clinopyroxene (En_{33})		-	0.193	0.093	
Kaersutite (K-2)		0.224	-	0.142	
Titanomagnetite (Usp_{33})		0.067	0.086	0.067	
Plagioclase (An_{33})		0.613	0.548	0.558	
Nepheline (Ne-2)		0.074	0.159	0.124	
Apatite		0.022	0.013	0.016	
Sum R^2		0.102	0.044	0.043	

	AW82056 (measured)	W84-2 (predicted) 1	2	3	W84-2 (measured
Rb	113	148	148	149	131
Sr	740	155	240	198	60
Zr	687	904	889	893	860
Ba	1039	172	236	214	70

AW83543 was derived from a more evolved Group II basanite, AW83614, also from Mason Spur (Table 9.7). In order to show that this model was not an isolated case, another similar model was generated in which tephrite AW83607 was also derived from basanite AW83614 (Table 9.7). Both models extract olivine, clinopyroxene, titanomagnetite, plagioclase, nepheline, and/or apatite, leaving a 52.6% to 55.6 residual liquid. With the exception of nepheline, the minerals extracted in the models are present in the rocks. Although modal nepheline has not been identified, it is a possible liquidus phase in melts of these compositions (Sack et al., 1987). Models involving the extraction of ilmenite or kaersutite were unacceptable. The correlation between observed and predicted abundances of Sr and Zr support the mass balance models. Predicted Rb abundances are variable, and probably reflect variable Rb contents in different batches of parental magma. The lack of REE and Ba analyses for AW83614 precluded a more rigorous testing of the mass balance models.

These models are consistent with the hypothesis that Group I lavas are derived from a parental basanite melt of similar composition to younger Group I basanites in the area. They do not preclude the qualitative model in which Group I trachytes are derived from an alkali basalt parent (Muncy, 1979), but they show that it is not necessary to have had a major change in the nature of DVS parental magmas about 11 m.y. ago.

The only acceptable mass balance model in which Group I benmoreite is derived from Group I tephrite requires the removal of plagioclase, clinopyroxene, titanomagnetite, olivine and apatite to leave a 35.3% residual liquid (Table 9.8). Models in which nepheline, kaersutite or ilmenite are extracted were not acceptable. With the

Table 9.7 - Least squares mass balance models for the hypothetical fractional crystallization of a Group II basanite (AW83614) to form Group I tephrites (AW83543, AW83607). This model was made in order to show that Group I lavas may be derived by fractional crystallization from a basanite parent that is similar in composition to Group II basanites. A more detailed explanation of how the mass balance and trace element models were generated in given in the caption to Table 9.3.

	AW83614 (measured)	AW83614 (predicted)	AW83543 (measured)	AW83614 (measured)	AW83614 (predicted)	AW8360 (measur
SiO2	45.27	45.19	46.32	45.27	45.16	48.09
TiO2	3.02	3.01	3.90	3.02	3.03	3.09
Al2O3	15.79	15.83	15.01	15.79	15.87	16.73
FeO*	10.97	10.97	12.47	10.97	10.97	11.60
MnO	0.21	0.17	0.24	0.21	0.18	0.21
MgO	8.32	8.33	5.21	8.32	8.34	4.47
CaO	10.28	10.30	9.47	10.28	10.31	8.02
Na2O	3.99	4.02	4.01	3.99	3.95	4.28
K2O	1.17	1.11	1.42	1.17	1.42	2.14
P2O5	0.96	1.08	1.95	0.96	0.93	1.38
F		0.553			0.526	
Olivine (Fo_{79})		0.190			-	
(Fo_{86})		-			0.151	
Clinopyroxene (En_{46})		0.300			-	
(En_{48})		-			0.407	
Titanomagnetite ($Usp_{61}C$)		0.056			-	
(Usp_{76})		-			0.079	
Plagioclase (An_{76})		0.269			0.191	
Nepheline (Ne-1)		0.184			0.077	
Apatite		-			0.010	
Sum R^2		0.023			0.070	

	AW83614 (measured)	AW83543 (predicted)	AW83543 (measured)	AW83614 (measured)	AW83607 (predicted)	AW83607 (measure
Rb	20	33	21	20	38	46
Sr	1203	1227	1207	1203	1085	1165
Zr	204	296	261	204	375	365

Table 9.8 - Least squares mass balance model for the fractional crystallization of Group I tephrite (AW83543) to form Group I benmoreite (AW85839) at Mason Spur. A more detailed explanation of ho the mass balance and trace element models were generated is given in the caption to Table 9.3.

	AW83543 (measured)	AW83543 (predicted)	AW85839 (measured)
SiO2	46.32	46.11	55.06
TiO2	3.90	3.79	1.66
Al2O3	15.01	15.03	17.94
FeO*	12.47	12.51	8.40
MnO	0.24	0.19	0.22
MgO	5.21	5.23	1.95
CaO	9.47	9.53	5.05
Na2O	4.01	4.21	5.72
K2O	1.42	1.48	3.38
P2O5	1.95	1.88	0.61
F		0.353	
Olivine (Fo_{79})		0.059	
Clinopyroxene (En_{48})		0.274	
Titanomagnetite (Usp_{76})		0.174	
Plagioclase (An_{28})		0.427	
Apatite		0.059	
Sum R^2		0.079	

	AW83543 (measured)	AW83543 (predicted)	AW86839 (measured
Rb	21	58	75
Sr	1207	1179	1004
Zr	261	322	358
Ba	636	920	1032
La	64.2	74.0	74.7
Ce	144	154	157
Sm	14.5	10.8	11.6
Eu	4.81	3.38	3.62
Tb	1.65	1.29	1.43
Yb	2.90	3.34	3.47

exception of Rb, reasonable agreement is seen between predicted and observed trace element abundances for the benmoreite. The discrepancy between predicted and observed Rb abundances cannot be explained by crystal fractionation, and requires either initial variations in the Rb content of parental magmas, or the operation of additional enrichment processes.

Evolution of the Group I trachytes from a parental benmoreite could not be modelled. Likewise, the derivation of evolved trachytes from less evolved trachytes in the same stratigraphic unit could not be modelled. It is concluded that the Group I trachytes are either not derived by simple fractionation processes, or the parent - daughter pairs are unknown. While the broad correlation between the incompatible elements suggests that fractional crystallization did occur, it is likely that other processes also operated to generate the observed geochemical variability.

9.5.4 Other Fractionation Processes

Other fractionation processes that have been proposed to explain elemental variations in alkaline lavas include magma immiscibility, Soret diffusion and volatile transfer. Immiscible magmas are only known to be associated with highly alkaline magmas rich in CO_2 and K_2O, and some very iron-rich tholeiites (McBirney, 1984). Since neither of these magma types occurs in the DVS, it is unlikely that liquid immiscibility contributes to the compositional diversity.

Diffusion across a thermal liquid/liquid boundary (Soret diffusion) typically causes concentration of the network-forming (Si, Na K) components on the hotter side, and the network modifiers (Fe, Mg,

Ca, Ti, and Mn) on the cooler side. Al can move either way depending on its coordination. This process has been proposed, in conjunction with convection, to explain minor and trace element enrichments and depletions in large stratified magma chambers (Hildreth, 1981; Walker and DeLong, 1982; Schott, 1983). Mass transport by Soret diffusion cannot normally develop significant compositional gradients in magmas bodies, because of the time restraints imposed by cooling and solidification of the magma (Schott, 1983; Baker and McBirney, 1985; Lesher, 1986). Therefore, it is unlikely that this process contributes to the chemical variation of the DVS lavas.

The process of volatile transfer is still poorly understood, but has been suggested as a mechanism for concentrating highly charged trace elements and halogens (Bailey and MacDonald, 1975; Hildreth, 1981; Taylor et al., 1981, Mahood and Hildreth, 1983). The lack of experimental data relevant to magmas, makes it impossible to rigorously evaluate the volatile transfer process (Baker and McBirney, 1985).

9.5.5 The Enigmatic Origin of Group I Trachytes

The lower sequences of the Gandalf and Mason volcanic complexes are predominantly composed of peralkaline trachyte, although small amounts of hawaiite to benmoreite, and trachyte lavas also occur. Qualitative evidence suggests fractional crystallization processes have contributed to the compositional variety of the trachyte lavas, but other lines of evidence indicate that other processes have also operated. Various lines of evidence include:

1. the scatter of data points on variation diagrams, and plots of incompetent trace element ratios against a differentiation index.

2. the lack of acceptable quantitative geochemical models supporting derivation of the trachytes from associated benmoreites, or more evolved trachyte from less evolved trachytes.

There is no clear evidence that other fractionation processes have operated, although the process of volatile transfer cannot be ruled out. Mass balance models in which the Mason Spur benmoreites and trachytes are contaminated with lower or upper crustal material to produce lavas with a more evolved composition are unacceptable.

Perhaps the lower sequences, dominated by trachyte are not derived by fractionation of a basic magma, but represent partial melting of crustal material. However, this hypothesis is not supported by non-modal batch melting models of lower and upper crustal material (Tables 9.9 and 9.11). Such models do not produce the spectrum of trace element abundances observed in the benmoreites or the trachytes at Mason Spur. In particular, melting of lower crustal basic granulite under the variety of conditions tested produced melts depleted in LREEs and Rb, and enriched in V, relative to the Mason Spur benmoreites and trachytes. Models in which upper crustal compositions were melted are too depleted in Zr and Nb, and too enriched in Rb to be realistic, even though the lowest reasonable mineral/melt partition coefficient was used for Zr in zircon.

The specific origin of the Group I trachytes has not been satisfactorily modelled. This may be because:

1. samples chosen for modelling have suffered post eruptive changes in chemistry due to alteration.
2. samples used in modelling calculations do not represent liquid compositions.
3. specific parent-daughter pairs of fractional crystallization have

Table 9.9 - Trace element models of non-modal batch melting of lower crustal basic granulite, and trace element abundances in Group I benmoreites (B), trachytes (T), and peralkaline trachytes (PT) from Mason Spur. The basic granulite analysis (except REE) (C_O) is typical of basic granulite xenoliths at Foster Crater and was supplied by J.H. Berg (pers. comm.). REE analyses are estimated values for the lower crust (Taylor and McClennan, 1985). The modal composition of the source is assumed to be 15% orthopyroxene, 15% clinopyroxene, 65% plagioclase, 3% titanomagnetite, 2% apatite. The models are calculated assuming a melt mode of 14% clinopyroxene, 85% plagioclase, and 1% titanomagnetite (K.C. Condie, pers. comm.). Several models are given in order to cover the probable range of degree of partial melting (given as the weight fraction of melt (F)) using both mafic and intermediate bulk distribution coefficients (K_D). These are calculated from mineral/melt partion coefficients given in Table 9.10. Element abundances are quoted in ppm.

	Observed compositional Ranges			Predicted Trace Element Abundances						C_o
				Mafic K_D			Intermediate K_D			
	B	T	PT	F= 0.1	0.2	0.3	0.1	0.2	0.3	
Sc	4		1-3	32	29	27	4.4	4.7	4.9	19.5
V	37	<3-9	<3-4	100	95	90	51	50	49	104
Zn	113	111-201	78-255	119	113	107				98
Rb	73-75	104-166	73-174	54	36	27	73	43	30	9.7
Sr	1004-1032	2-32	<1-41	537	567	601	368	401	440	723
Y	40-41	49-96	40-136	135	102	82	46	43	39	38
Zr	358-450	617-1451	458-1399	324	183	127	240	155	114	41
Nb	104-108	166-279	83-304	86	54	39	59	42	33	13.9
Ba	357-1032	<16-166	<16-438	1841	1392	1119	1305	1100	950	449
La	75		92-166	33	26	22	19	16	14	11
Ce	157		155-307	48	40	35	23	22	20	23
Nd	65		75-104	30	25	21	8.4	8.0	7.7	12.7
Sm	12		13-22	6.7	5.6	4.9	1.9	1.8	1.7	3.7
Eu	3.6		1.4-4.2	1.9	1.7	1.6	0.9	0.8	0.8	1.17
Tb	1.4		1.6-3.1	1.4	1.1	1.0	0.6	0.6	0.5	0.59
Yb	3.5		4.8-9.7	6.0	4.7	4.0	2.1	2.0	1.9	2.2
Lu	0.5		0.8-1.4	0.9	0.7	0.6	0.3	0.3	0.3	0.29

Table 9.10 - Distribution coefficients used in partial melting calculations given in Tables 9.9 and 9.11. Data is from an unpublished compilation by K.C. Condie (pers. comm.). Values in parentheses are less certain.

	Mafic					Intermediate				
	Plag	Cpx	Opx	Mag	Ap	Plag	Cpx	Opx	Mag	Ap
Sc	0.04	2.0	1.0	2.0	0.04	0.1	(22)	(64)	8	0
V	-	1.2	-	25	0	(0.01)	1.1	6.0	8	0
Zn	0.01	0.1	0.03	0.1	-					
Rb	0.13	0.02	0.02	0	0	0.05	0.03	0.003	0	0
Sr	2.0	0.10	0.02	0	5.0	3.0	0.52	0.01	0	0
Y	0.03	0.5	0.2	0.2	-	0.06	1.5	0.45	0.5	20
Zr	0.01	0.1	0.03	0.1	-	0.03	0.25	0.08	0.2	0.1
Nb	0.01	0.1	0.15	0.7	-	0.03	0.3	0.35	0.8	0.1
Ba	0.25	(0.005)	0.013	0	0	0.4	0.13	0.003	0	0
La	0.15	0.07	0.007	0	(7)	0.08	0.2	0.1	0	20
Ce	0.12	0.1	0.008	0	(15)	0.20	0.4	0.15	0	35
Nd	0.08	0.22	0.01	0	(12)	0.17	1.1	0.22	0	57
Sm	0.067	0.40	0.02	0	(14)	0.10	1.67	0.25	0	63
Eu	0.35	0.40	0.02	0	(13)	0.8	1.5	0.17	0	30
Tb	0.06	0.5	0.05	0	(11)	0.085	2.4	0.65	0.1	20
Yb	0.07	0.6	0.15	0	(7)	0.08	2.0	0.85	0.1	25
Lu	0.06	0.6	0.18	0	(5)	0.06	1.5	0.9	0.1	25

	Felsic								
	Plag	Orth	Qtz	Opx	Cpx	Bio	Mag	Zir	Ap
Sc	0.04	0.02	-	(7)	22	15	8	60	0
V	(0.01)	(0.01)	-	6.0	1.1	50	30	-	-
Rb	0.04	0.35	-	0.003	0.03	2.2	0	0	0
Sr	4.0	4.0	-	0.01	0.52	0.12	0.15	0	2.0
Y	0.1	(0.1)	-	1.0	4.0	0.03	2.0	60	40
Zr	0.1	0.1	-	0.2	0.6	2.0	0.8	1000	0.1
Nb	0.06	(0.05)	-	0.8	0.8	5.0	2.5	50	0.1
Ba	0.3	6.0	-	0.003	0.13	6.0	0	0	-
La	0.30	0.05	-	0.1	0.3	0.11	0	2.0	20
Ce	0.25	0.04	-	0.15	0.5	0.32	0	2.5	35
Nd	0.2	0.025	-	0.22	1.1	0.3	0	2.2	57
Sm	0.13	0.02	-	0.25	1.67	0.25	0	3.1	63
Eu	1.5	1.1	-	0.17	1.5	0.25	0	3.5	30
Tb	0.6	0.006	-	0.65	1.8	0.35	0.1	100	20
Yb	0.05	0.01	-	0.85	1.5	0.44	0.1	200	25
Lu	0.05	0.006	-	0.9	1.5	0.3	0.1	200	25
Pb	0.6	2.5	-	-	-	0.7	-	-	-

Table 9.11 - Trace element models of non-modal batch melting of a typical upper crustal composition (Taylor and McClennan, 1985), and observed trace element abundances in Group I benmoreites (B), trachytes (T), and peralkaline trachytes (PT). Models are generated using felsic bulk distribution coefficients (K_D) and assumed modal mineralogy for a tonalite and a granulite source (data from an unpublished compilation by K.C. Condie, pers. comm.). The bul distribution coefficient was calculated using partion coefficients given in Table 9.10. Severa models are given in order to cover variations in the degree of partial melting (given as the weight fraction of melt (F)). Trace element abundances are given in ppm.

	Observed compositional ranges			Tonalite			Granulite			C_o
	B	T	PT	F=0.05	0.1	0.2	0.05	0.1	0.2	
Sc	4		1-3	6.3	6.2	6.1	4.9	4.9	4.8	11
V	37	<3-9	<3-4	11	11	11	18	18	19	60
Rb	73-75	104-166	73-174	362	320	262	557	466	352	112
Sr	1004-1032	2-32	<1-41	137	142	151	136	141	150	350
Y	40-41	49-96	40-136	36	34	30	27	26	23	22
Zr	358-450	617-1451	458-1399	149	150	152	157	158	160	190
Nb	104-108	166-279	83-304	37	35	32	50	47	42	25
Ba	357-1032	<16-166	<16-438	458	485	552	606	656	784	550
La	75		92-166	70	63	54	68	62	52	30
Ce	157		155-307	112	104	91	110	102	90	64
Nd	65		75-104	34	32	29	32	31	28	26
Sm	12		13-22	5.8	5.5	5.0	5.3	5.1	4.6	4.5
Eu	3.6		1.4-4.2	0.69	0.69	0.68	0.66	0.66	0.65	0.88
Tb	1.4		1.6-3.1	0.90	0.86	0.79	0.80	0.77	0.71	0.64
Yb	3.5		4.8-9.7	3.9	3.7	3.25	3.4	3.2	2.9	2.2
Lu	0.5		0.8-1.4	0.58	0.55	0.48	0.50	0.47	0.43	0.32
Pb	9.11	13-21	8-21	33	33	33	35	35	35	20

Source:melt modes expressed as a percentage, are given below:

Tonalite - boitite (10:4), orthoclase (8:34), plagioclase (57:31), quartz (22:30), magnetite (2:
apatite (1:0.1), zircon (0.1:0.1)
Granulite - biotite (5:4), orthoclase (8:34), plagioclase (57:31), quartz (18:30), orthopyroxene
(5:0), clinopyroxene (4:0), magnetite (2:1), apatite (1:0.1), zircon (0.1:0.1)

not been recognized.

4. partition coefficients chosen for calculating models of fractional crystallization and partial melting are incorrect.
5. geochemical and/or modal crustal source compositions are incorrect.
6. actual processes are not approximated by fractional crystallization or non-modal batch melting, but are more complex.

9.6 PETROGENETIC SYNTHESIS

Evidence presented here suggests that rocks from Groups I, IIA, and IIB may all be derived from a basanite parental magma. There is no evidence to disprove the hypothesis that Group I lavas are derived from an alkali basalt parent (Muncy, 1979), but the presence of basanite and the lack of alkali basalts in Group I suggests that basanite is the more likely parent.

Except for Group I trachytes, geochemical differences associated with a particular rock suite can be explained by differences in the nature and composition of extracted mineral phases. The Ti and Al content of kaersutites from evolved Group IIA magmas suggest they underwent fractionation at greater depths than Group IIB magmas of similar composition (Best, 1974). Al-clinopyroxene in basanites and tephrites from southeastern Australia and the Massif Central, France, has been interpreted as having crystallized at mantle or perhaps lower crustal depths (Wass, 1979a; Duda and Schmincke, 1985). By analogy, it is suggested that the Al-clinopyroxenes in Group II lavas also crystallized at a similar depth. It is postulated that Group IIA and the basanites to phonotephrites of Group IIB crystallized in the vicinity of the mantle - crust boundary.

The greater amount of feldspar fractionated from models for the evolution of Group I magmas compared to those for Group II, and the earlier appearance of plagioclase as a phenocryst phase in Group I rocks, suggests that Group I magmas fractionated at lower pressures (Green, 1970; Green and Ringwood, 1970) than Group IIA magmas. The late stage fractionation of anorthoclase is likely to have occurred at upper crustal depths, because crystallization of hydrous magmas at pressures of >5 kb yields plagioclase and potassium feldspar (Tuttle and Bowen, 1958).

These observations suggest that a change in the depth of fractionating magma chambers may be the primary factor controlling differences in the geochemical and mineralogical evolution of DVS magmas. It is postulated that the chronological division of mineralogy and geochemistry reflects a systematic change in the depth of magma chambers, and that this is probably controlled by the tectonic regime. Prior to about 11 m.y. ago, near primary melts were injected into the crust, and perhaps to upper crustal levels, and proceeded to evolve by fractional crystallization under relatively low total pressure. Crystallization of ultrabasic and basic melts under these conditions promoted the fractionation of calcic plagioclase early in the differentiation history, and drove the residual liquid compositions towards peralkalinity. Although these conditions also provided the opportunity for crustal contamination, there is no geochemical evidence to suggest that contamination was involved in the evolution of the Group I magmas.

At about 11 m.y. primary melts began to cool and fractionate at greater depths and, therefore, at higher pressures. Conditions favored crystallization of kaersutite rather than plagioclase, which drove the

geochemistry of residual melts towards stronger alkali enrichment, and SiO_2 undersaturation. Magma either rose directly to the surface (Group IIA), or became trapped in crustal magma chambers (Group IIB), where fractionation continued to take place at lower pressure. Thus, the variety of individual evolutionary trends exhibited by DVS rock suites primarily reflects the variety of pressure conditions in different magma chambers.

Chapter 10

VOLCANIC EVOLUTION OF THE EREBUS VOLCANIC PROVINCE

10.1 INTRODUCTION

The Erebus volcanic province (EVP) comprises McMurdo Volcanic Group volcanism in the area from Franklin Island in the north to the DVS in the south. This volcanism is located in the Victoria Land rift basin and on the eastern flanks of the adjoining Transantarctic Mountains, and is an integral part of the extensional tectonic regime that gave rise to the major crustal structures (Kyle and Cole, 1974; Kyle, in press a). The Transantarctic Mountains in the southern EVP area have been subjected to some of the greatest uplift that has occurred along the entire mountain chain (Kyle, 1976). There is also a change in the axial trend of the mountains at this point. The EVP represents a major concentration of alkaline volcanic activity over the last 19 m.y., and this is the most extended period of volcanic activity in any area within the McMurdo Volcanic Group.

10.2 GEOLOGIC EVOLUTION OF THE EREBUS VOLCANIC PROVINCE

?19 - ~30 m.y. - Eruptions of peralkaline trachytes, which are not presently exposed, but which were a source area for sediments being deposited in McMurdo Sound (Barrett et al., 1986; Harwood, 1986).

11 - 19 m.y. - Eruption of small to medium sized volcanoes in the Mason Spur-Riviera Ridge-Gandalf Ridge area built up the the Mason and Gandalf volcanic complexes. Lithologies include lava flows, domes, subordinate breccias, and minor tuff and agglutinate. A trachytic hyaloclastite, and a deposit of massive basanite tuffs and pillow lavas at Mason Spur, may have formed by eruption beneath ice. In the

lower part of each volcanic complex aphyric to weakly feldspar-phyric peralkaline trachyte lavas predominate, but hawaiite, mugearite and trachyte also occur. The upper part of each complex comprises an aphyric to weakly porphyritic basanite to benmoreite or trachyte suite.

7 - 11 m.y. - Locus of activity shifted 50 km east to the Minna Bluff-Black Island area, perhaps due to a concentration of crustal extension along the eastern margin of the Victoria Land basin. Eruption of small to medium sized, overlapping, shield volcanoes, and small domes occurred. Lava flows predominated, but lobe hyaloclastites, and minor agglutinate also occur. Lavas are typically porphyritic and vesicular basanites to trachytes.

0 - 7 m.y. - Volcanic activity spread throughout the EVP area, except at Minna Bluff where activity had ceased. Activity in the DVS was probably related to activation of a northeast-trending transform aligned though the major volcanoes of Mt Discovery and Mt Morning. Eruptions formed small basanite to phonotephrite cinder cones and lava flows; small tephriphonolite to phonolite domes; small to large, basanite to tephriphonolite shield volcanoes; and the large basanite to phonolite stratovolcanoes. Lavas are generally porphyritic and vesicular. Crustal and mantle-derived xenoliths are associated with some basanite and tephrite centers.

The two-fold, geochronological division of DVS deposits is extended to include all EVP rocks. Rocks older than 11 m.y. comprise Group I: those younger than 11 m.y. comprise Group II. EVP rocks, other than the DVS, are younger than 5 m.y. and belong to Group II.

10.3 PETROLOGIC EVOLUTION OF THE EREBUS VOLCANIC PROVINCE

10.3.1 Introduction

Geochemical trends exhibited by EVP rocks comprise a spectrum of SiO_2 saturated and undersaturated compositions. Within the DVS the compositional spectrum has been divided into three groupings of alkal enrichment trends, namely Group I, Group IIA and Group IIB. The petrogenesis of the EVP is discussed within this framework.

10.3.2 Group IIA

Rock suites from Group II A exhibit the strongest trends of alkali and Al_2O_3 enrichment and FeO* depletion (Figures 10.1 - 10.3). These suites are comprised of a basanite-tephrite-phonotephrite-tephriphonolite-phonolite association that occurs in small to medium sized volcanoes at Brown Peninsula, Hut Point Peninsula, and the younger sequences at Mt Discovery, Black Island, and Minna Bluff. The widespread distribution of Group IIA rock suites in the EVP suggests that the conditions under which they are generated have become increasingly more prevalent in the EVP since they were first erupted at Minna Bluff between 8 and 9 m.y. ago.

Mass balance models are consistent with the derivation of Group IIA magmas by fractional crystallization of olivine, clinopyroxene, titanomagnetite, kaersutite, plagioclase, and apatite from a basanite parent (Kyle, 1981c; Kyle et al., 1979) (Figure 10.4). The small compositional range of ferromagnesian minerals suggests relatively constant temperature conditions prevailed throughout most of the crystallization history. A trend of increasing depletion of the middl REE, and mass balance models suggest significant amounts of kaersutit are extracted, and this is supported by the abundance of kaersutite

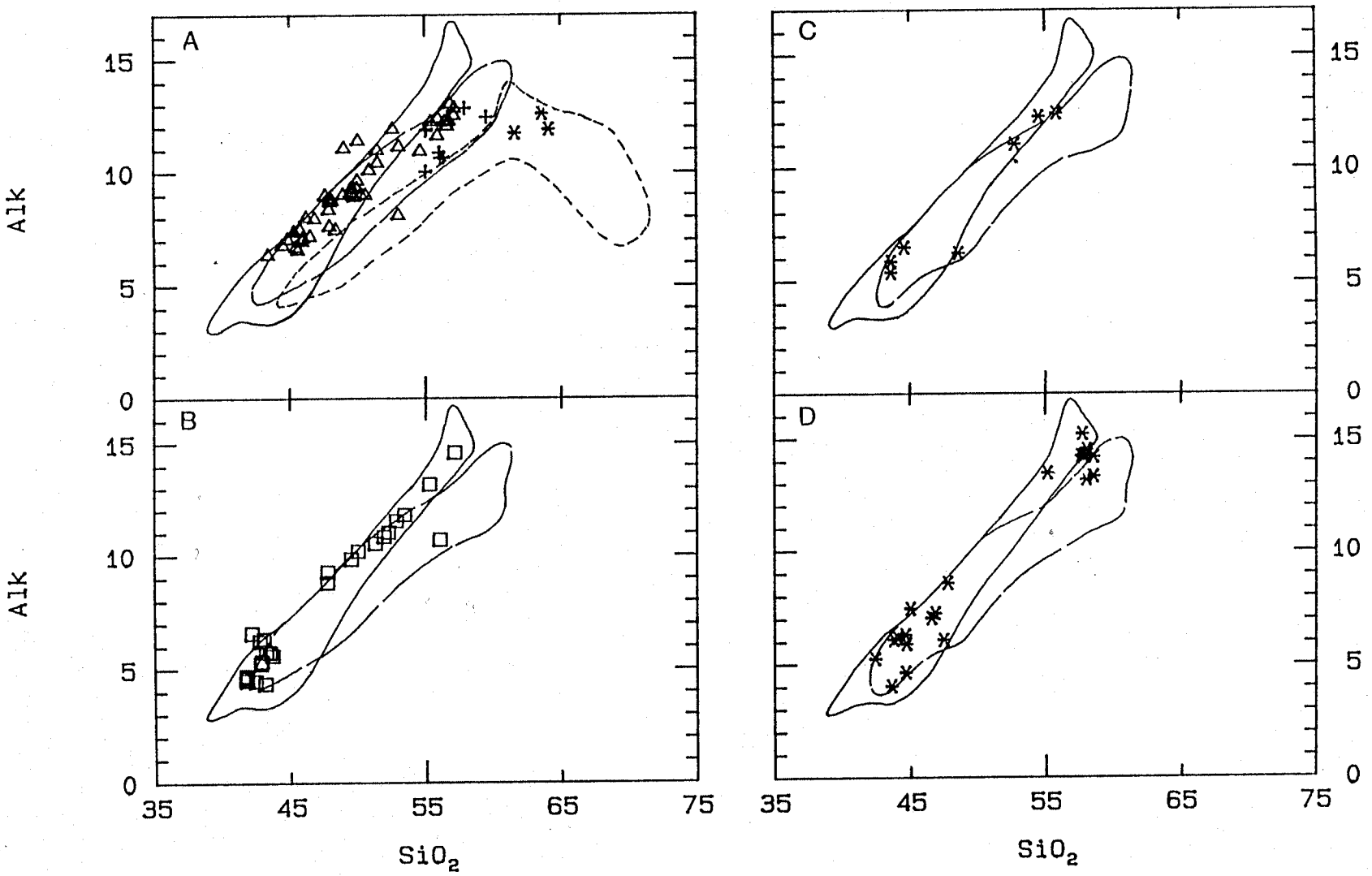

Figure 10.1 - Plot of alkalis (Alk) against SiO_2 (values in oxide wt. %) for samples from Ross Island, shown with respect to various geochemical trends exhibited by DVS rock suites ——— Group IIA, ———— Group IIB, --------- Group I. A - Mt Erebus samples (Moore, 1986 Erebus lineage; + benmoreites and kaersutite phonolites; * trachytes. B - DVDP lineage samples from Hut Point Peninsula (Kyle, 1981c). C - Mt Bird samples (cole and Ewart, 1968; Goldich et al., 1975; Jansen, 1916;). D - Cape Crozier samples (Kyle, 1976; Goldich et al., 1975; Prior, 1902, 1907)

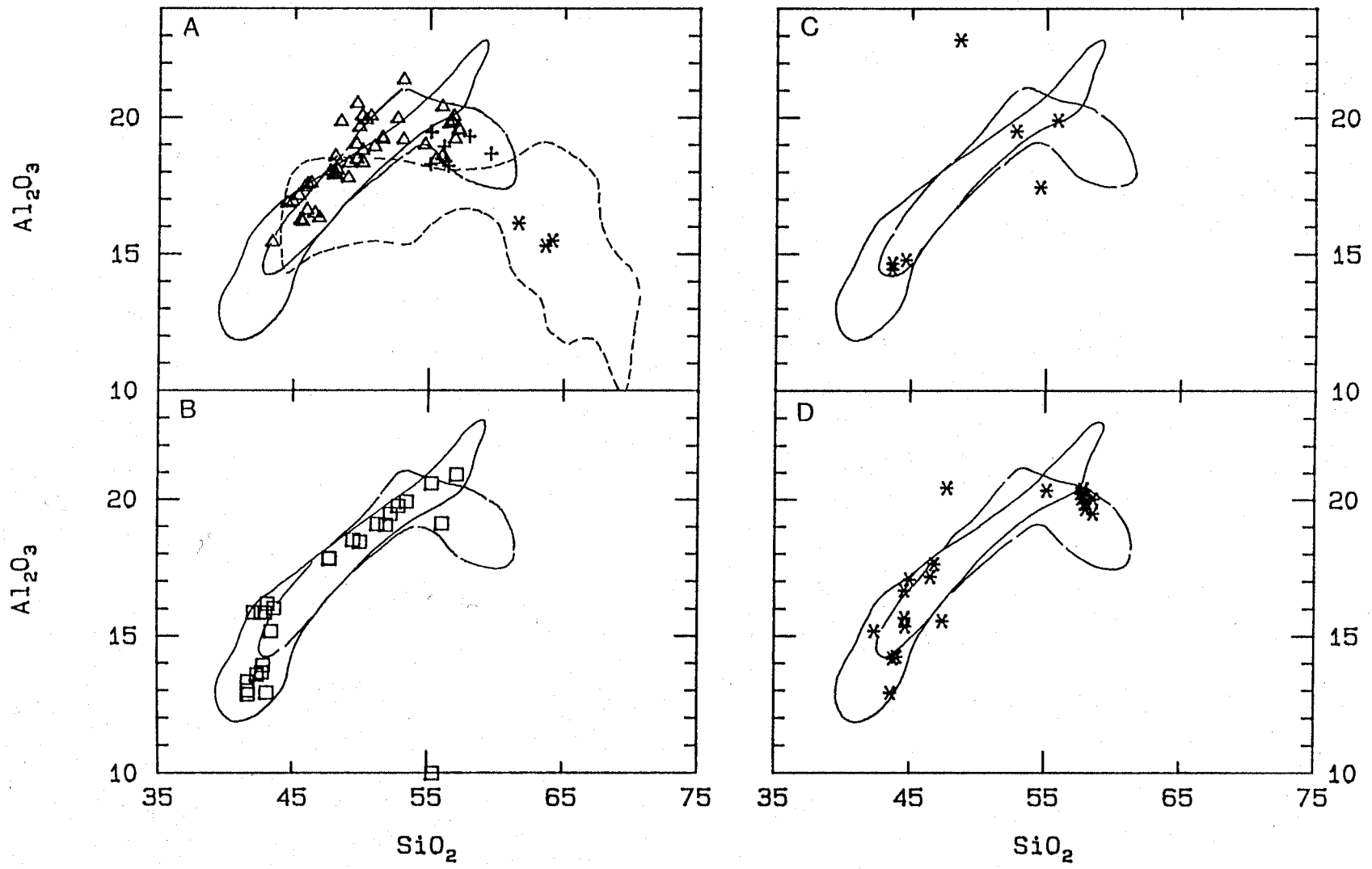

Figure 10.2 - Plot of Al_2O_3 against SiO_2 (values in oxide wt. %) for samples from Ross Island, shown with respect to various geochemical trends exhibited by DVS rock suites ———— Group IIA, ———— Group IIB, ---------- Group I. A - Mt Erebus samples (Moore, 1986): Δ Erebus lineage; + benmoreites and kaersutite phonolites; * trachytes. B - DVDP lineage samples from Hut Point Peninsula (Kyle, 1981c). C - Mt Bird samples (cole and Ewart, 1968; Goldich et al., 1975; Jansen, 1916;). D - Cape Crozier samples (Kyle, 1976; Goldich et al., 1975; Prior, 1902; 1907).

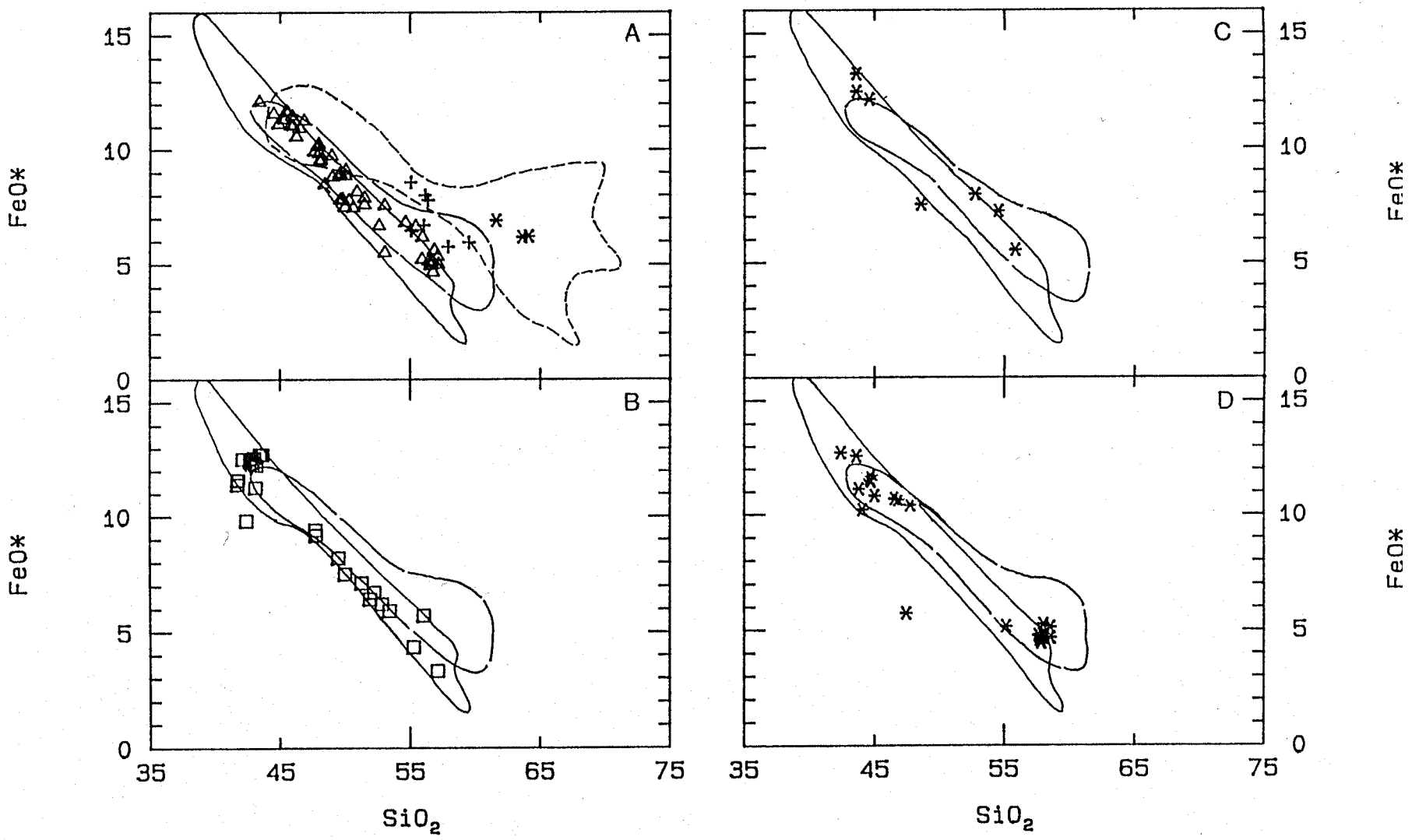

Figure 10.3 - Plot of FeO* (wt. %) against SiO_2 (wt. %) for samples from Ross Island, shown with respect to various geochemical trends exhibited by DVS rock suites ——— Group IIA, ——— ——— Group IIB, ---------- Group I. A - Mt Erebus samples (Moore, 1986): Δ Erebus lineage; + benmoreites and kaersutite phonolites;*trachytes. B - DVDP lineage samples from Hut Point Peninsula (Kyle, 1981c). C - Mt Bird samples (cole and Ewart, 1968; Goldich et al., 1975; Jansen, 1916;). D - Cape Crozier samples (Kyle, 1976; Goldich et al., 1975; Prior, 1902; 1907).

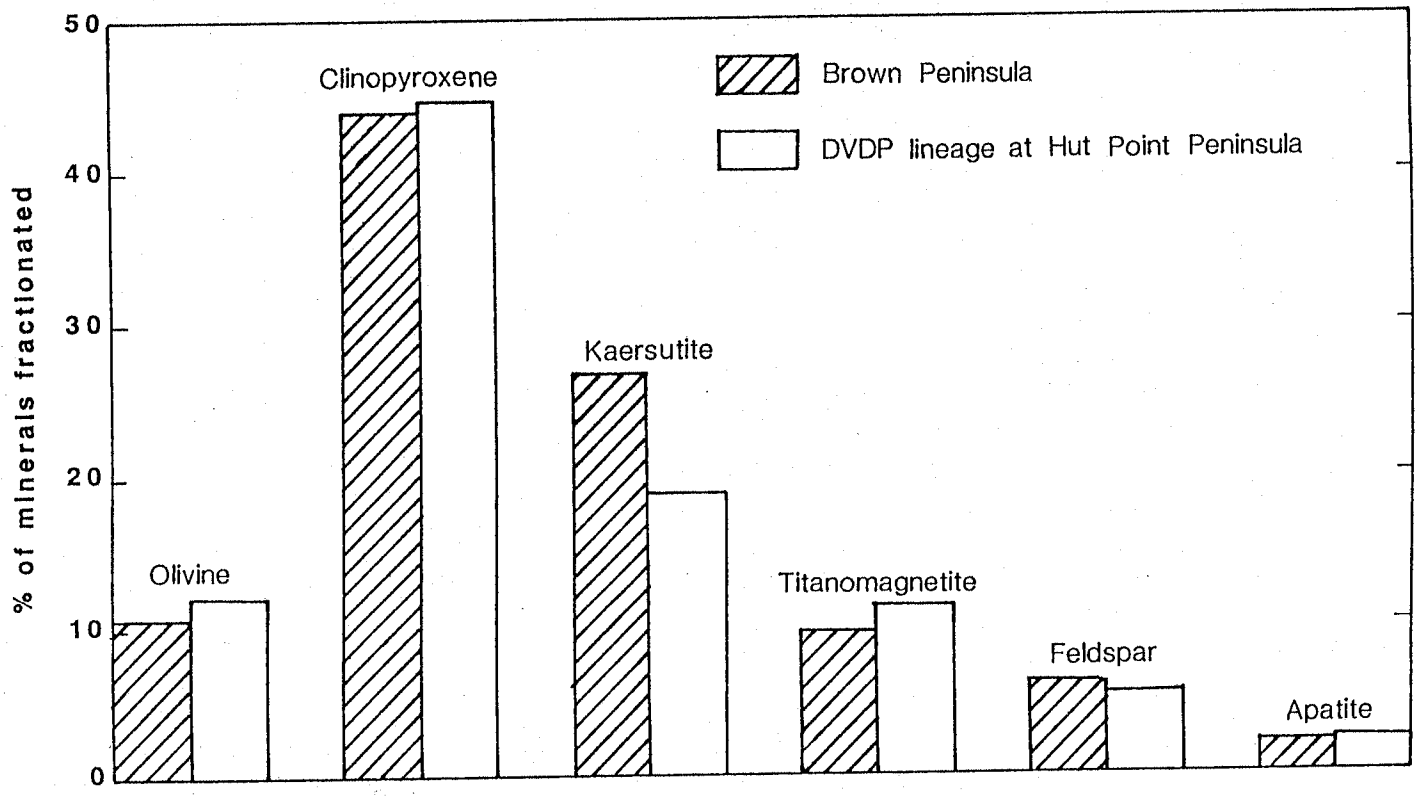

Figure 10.4 - Histogram comparing the amounts of various mineral phases extracted in preferred models of fractional crystallization of basanite to tephriphonolite for Group IIA rock suites at Brown Peninsula and Hut Point Peninsula (DVDP lineage). Data is from Kyle et al. (1979) and Kyle (1981c).

phenocrysts in rock samples. Except for the phonolites, feldspar is a minor phenocryst phase. It is the minor role of feldspar fractionatic that has allowed the strong enrichment of alkalis and Al_2O_3 relative to SiO_2 in residual liquids.

10.3.3 Group IIB

Group IIB rock suites exhibit similar alkali enrichment trends t Group IIA in rocks of basanite to tephriphonolite composition, but ir more evolved Group IIB lavas the alkalis increase at a slower rate than occurs in Group IIA. Group IIB rock suites form the large stratc volcanoes of Mt Erebus, Mt Discovery and Mt Morning, shield volcanoes in the lower sequence at Minna Bluff and small domes and flows on the flanks of Mt Erebus (Abbot Peak, Inaccessible Island). The lack of kaersutite in Erebus lineage lavas distinguishes this rock suite from other Group IIB suites. Major outcrops of kaersutite-bearing Group II rocks are only found to the west of McMurdo Sound.

Mass balance models for the Group IIB rocks at Minna Bluff are consistent with their derivation by fractional crystallization from a basanite. The petrogenetic model for the MB1 suite suggests the same minerals are fractionated as in the evolution of the Group IIA magmas but in different proportions (Figure 10.5). An ilmenite-magnetite pai at Mt Discovery suggests crystallization of phonotephrite liquids may have taken place at about 920oC and at f_{O2} controlled by the QFM buffer. Crystallization under these conditions involved the fractiona tion of greater amounts of plagioclase from tephriphonolites and benmoreites than occurred in the evolution of Group IIA magmas, and this has caused an increase in SiO_2 and a decrease in the Na/(Na+K)

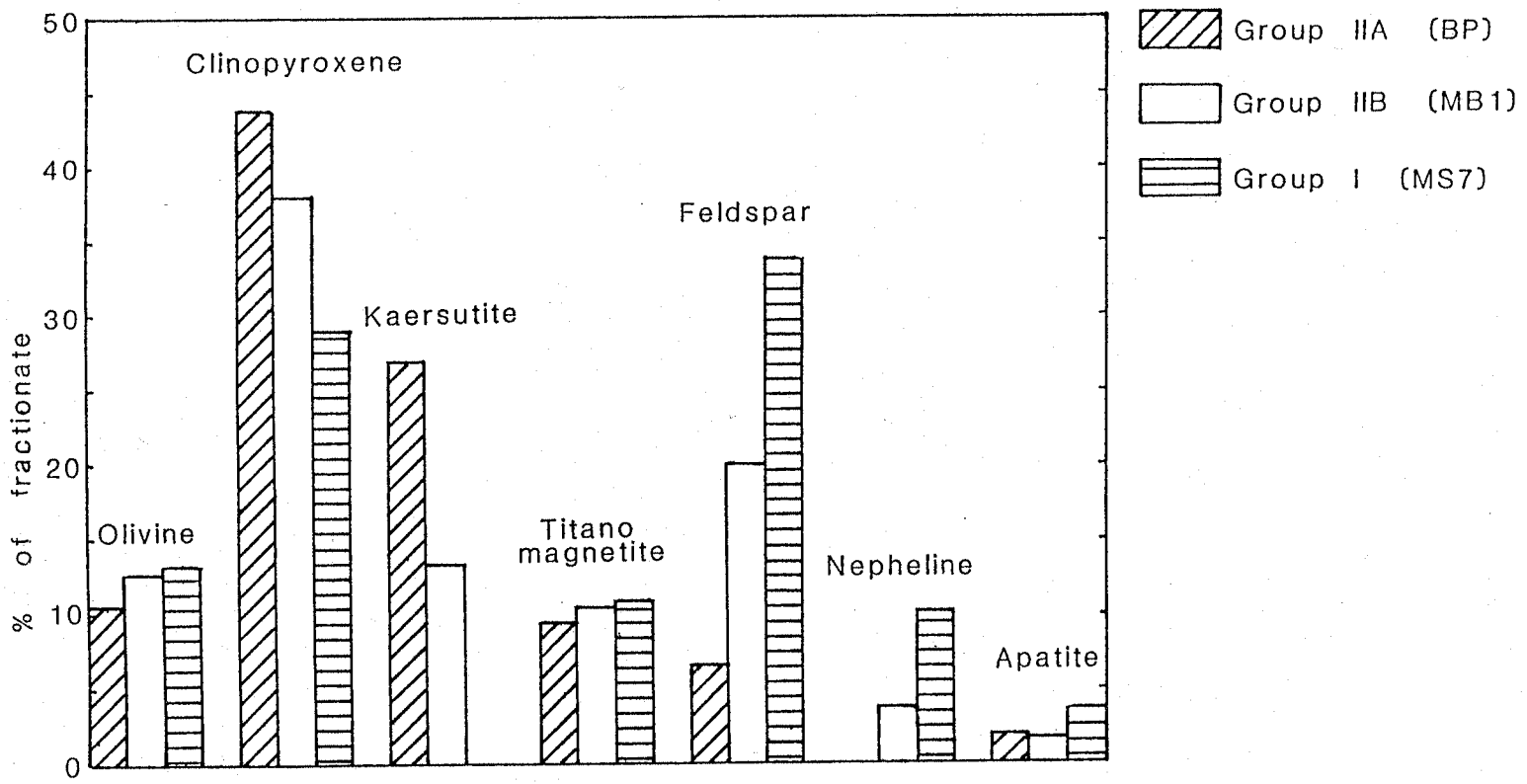

Figure 10.5 - Histogram comparing the amounts of various minerals extracted from preferred models of fractional crystallization of basanite to tephriphonolite or benmoreite, for

ratio, in residual liquids. The demise of kaersutite in Group IIB trachytes probably results from changing magma chemistry (Merrill Wyllie, 1975; Cawthorn, 1978a).

Lavas from Mt Erebus exhibit similar modified trends of alkal and Al_2O_3 enrichment and FeO* depletion to other Group IIB rock su (Figures 10.1 - 10.3), but have a markedly different mineralogy co pared to other Group IIB rocks. Mass balance models for the evolut of the Erebus lineage suggest it was generated by the extraction o clinopyroxene, olivine, Fe-Ti oxides, feldspar, nepheline and apat to leave a 24% residual phonolite liquid (Moore, 1986) (Figure 10. Much of the fractionation probably took place at mantle depths, bu fractionation of anorthoclase during the final stages of evolution probably took place at shallow crustal depths (Stuckless et al., 1981). The small variation in the composition of analysed ferromag-nesian minerals suggests crystallization took place at relatively constant temperatures. The absence of kaersutite in these lavas inc cates that crystallization temperatures were higher than for other Group IIB rock suites, probably in excess of 1100°C (Moore, 1986). Olivine and Fe-Ti oxides are present throughout the evolutionary sequence, which suggests that f_{O2} was probably controlled by the QF buffer reaction (Moore, 1986).

Rock suites from Mt Bird and Cape Crozier on Ross Island cannc be clearly related to either Groups I or II trends (Figures 10.1 - 10.3), and probably formed by fractional crystallization at interme iate depths. Samples from the Cape Crozier area exhibit a bimodal geochemistry, and trends are not recognized in the evolved lavas, perhaps because the lavas sampled were derived from several differe magma chambers.

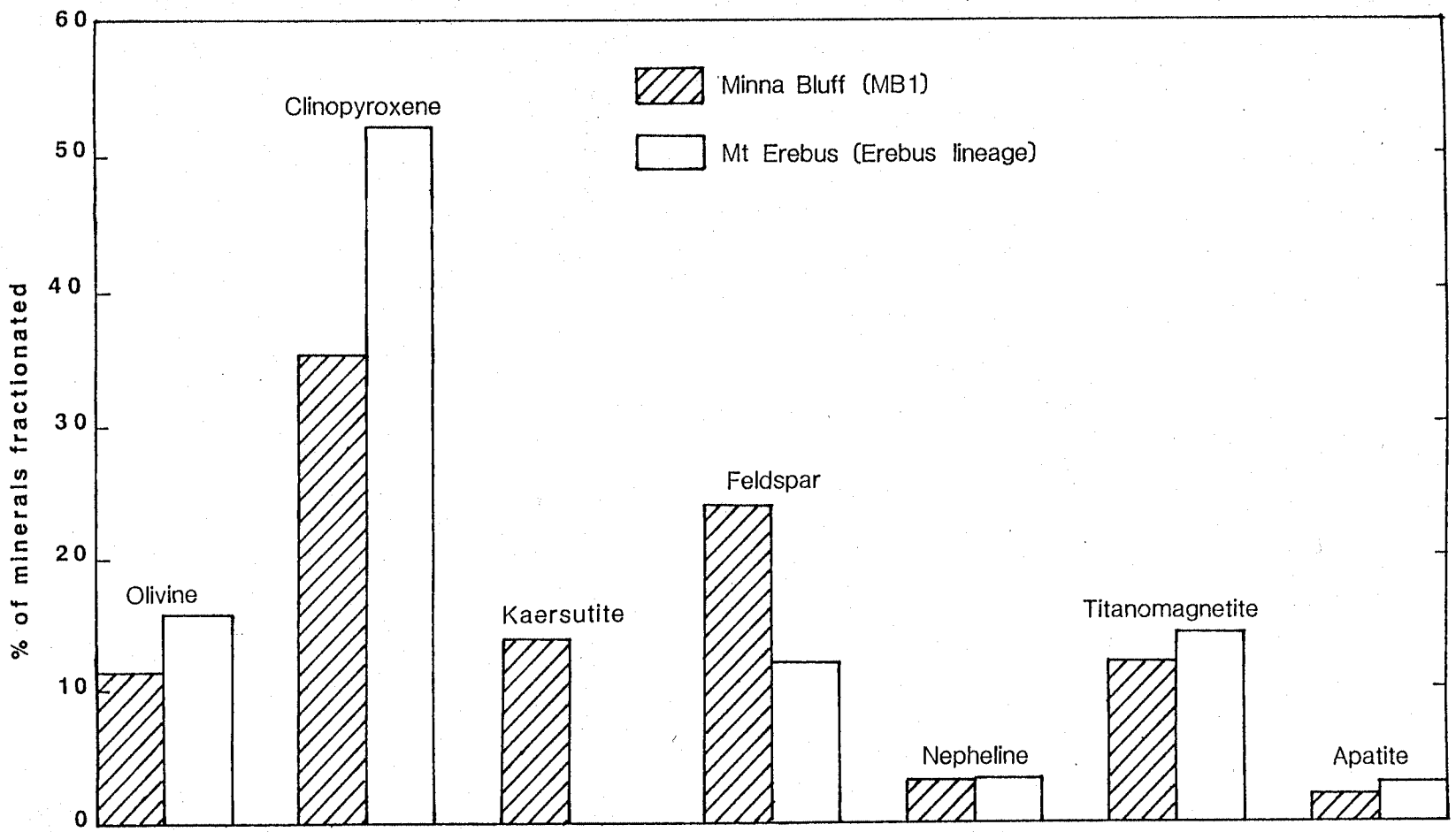

Figure 10.6 - Histogram contrasting the amounts of various mineral phases extracted by preferred models of fractional crystallization for Group IIB rock suites at Minna Bluff (MB1), and Mt Erebus (Erebus lineage). Models are for basanite to trachyte and basanite to phonolite, respectively, Data for the Erebus lineage is from Moore (1986).

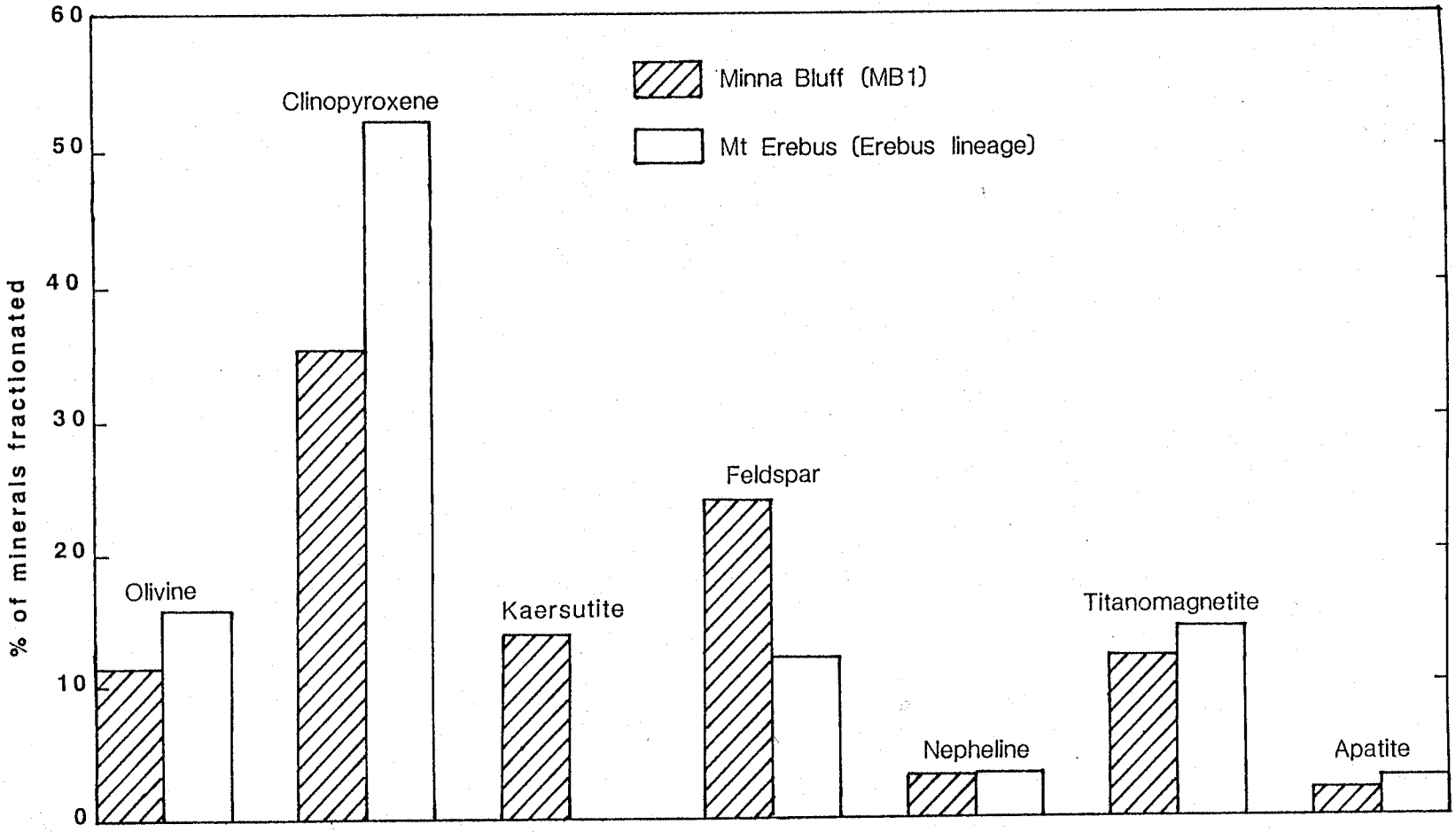

Figure 10.6 - Histogram contrasting the amounts of various mineral phases extracted by preferred models of fractional crystallization for Group IIB rock suites at Minna Bluff (MB1), and Mt Erebus (Erebus lineage). Models are for basanite to trachyte and basanite to phonolite, respectively, Data for the Erebus lineage is from Moore (1986).

10.3.4 Group I

Group I rock suites exhibit the least alkali and Al_2O_3 enrichment, which may be followed by late stage depletion, and the least depletion in FeO*. They comprise a basanite-tephrite-hawaiite-mugearite-benmoreite-trachyte-peralkaline trachyte-peralkaline rhyolite association, which only occurs in DVS rocks older than 11 m.y. From a qualitative assessment of mineralogy and geochemistry of Group I rocks at Riviera and Gandalf Ridges, Muncy (1979) suggested they were derived by fractional crystallization from an alkali basalt parent. However, the absence of alkali basalt in Group I, and the presence of basanite, suggest that basanite is the more likely parental magma. Small trachyte outcrops on the flanks of Mt Erebus (Bomb Peak, Aurora Cliffs, Mt Cis) are geochemically similar to non-peralkaline, Group I trachytes. The Mt Erebus trachytes have been called the enriched iron series by Moore (1986), and were postulated to have formed by fractional crystallization of an alkali basalt with some crustal contamination.

Mass balance modelling suggests that tephrites from Group I may be derived from a basanite parent, similar in composition to Group II basanites, by fractional crystallization of olivine, clinopyroxene, titanomagnetite, plagioclase, nepeline, and apatite. With the continued fractionation of these minerals it is possible to generate a Grou I benmoreite, although trace element data does not constrain these models as rigorously as it does for Group II models of fractional crystallization. The trachytes, peralkaline trachytes and peralkaline rhyolites appear to be part of this lineage on mineralogical and geochemical grounds, but cannot be quantitatively related to the less evolved lavas.

10.4 A MODEL FOR THE EVOLUTION OF THE EREBUS VOLCANIC PROVINCE

Any model for the volcano-tectonic evolution of the EVP must take into account the following observations:

1. Evidence that most lavas could have probably been derived from a basanite parental magma, and that there need not have been a change in parental magma composition with time.
2. The change in the geochemical evolution of magmas from a trend towards SiO_2 saturation to a general trend of SiO_2 undersaturati about 11 m.y. ago. The model must also allow for a late stage trend towards SiO_2 saturation in some rock suites younger than 1 m.y.
3. A general increase in the depth of magma chambers with time, as suggested by mineral chemistry.
4. An apparent increase in the areal distribution of activity with time.
5. An increase in the amount of less evolved lava reaching the surface with time, and the eruption of near parental melt compositions (<10% fractional crystallization) only in the last m.y.
6. A decrease in the crustal thickness from >40 km in the west to 2 in the east.

These features are accounted for by a model in which parental magmas are generated by small degrees of partial melting of an enriched garnet peridotite mantle source at depths of probably 80 120 km over the period of EVP volcanism (Figure 10.7). Small increa in the degree of partial melting have generated rare alkali basalt melts, but there has not been any significant change in the degree partial melting with time. This suggests that source area enrichmen

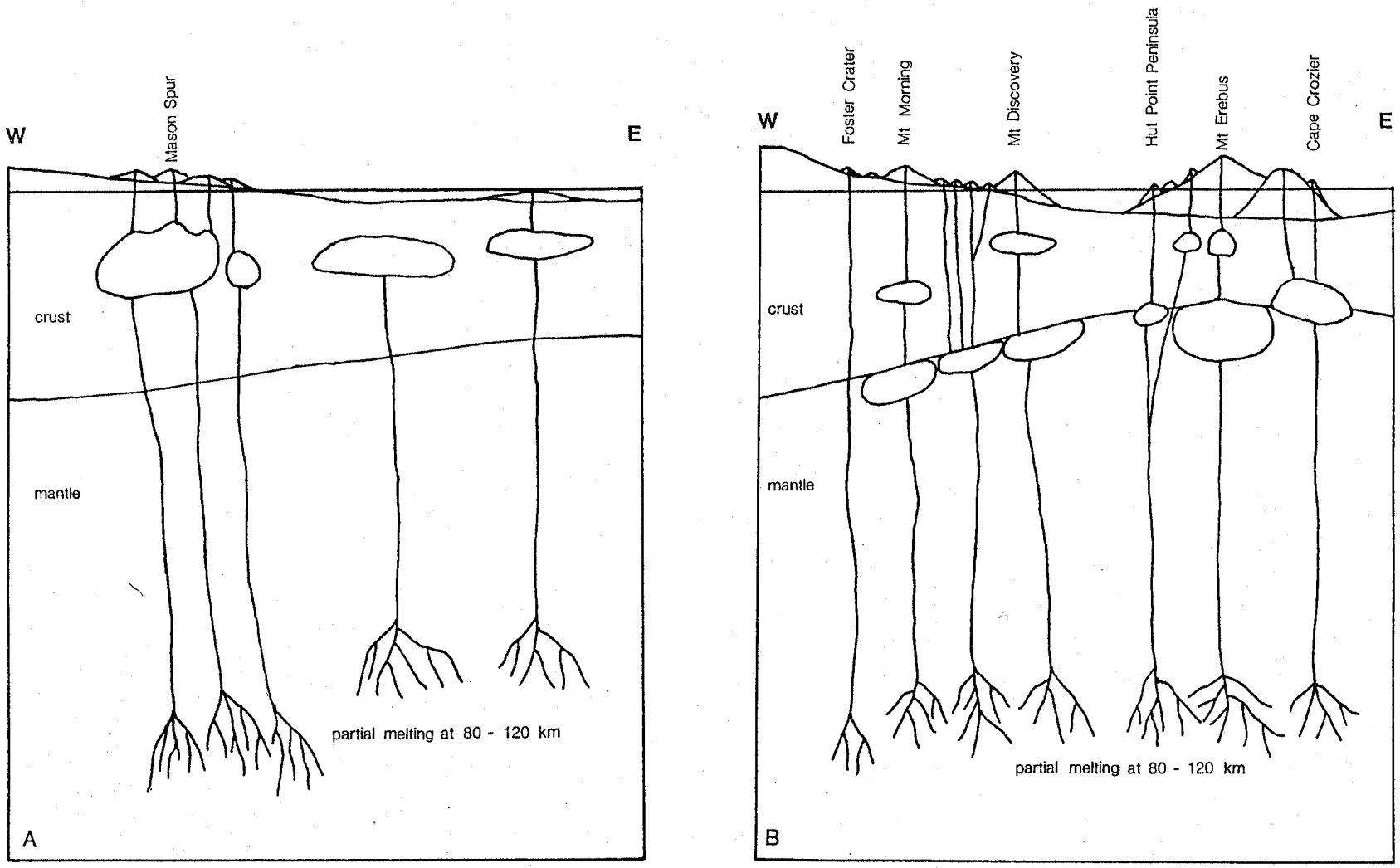

Figure 10.7 - Generalized model of the magmatic systems operating in the rebus volcanic province between 19 and 11 m.y. ago (A), and 11 m.y. ago and present (B). Small degrees of partial melting of an enriched garnet peridotite mantle at depths of 80 - 120 km has produced parental basanite magmas throughout. These differentiated in crustal magma chambers prior to 11 m.y. ago. Since 11 m.y. the basanite parental melts have fractionated in deeper magma chambers, perhaps in the vicinity of the crust - mantle boundary which is between 35 and 40 km deep. Some of these magmas escaped directly to the surface (forming

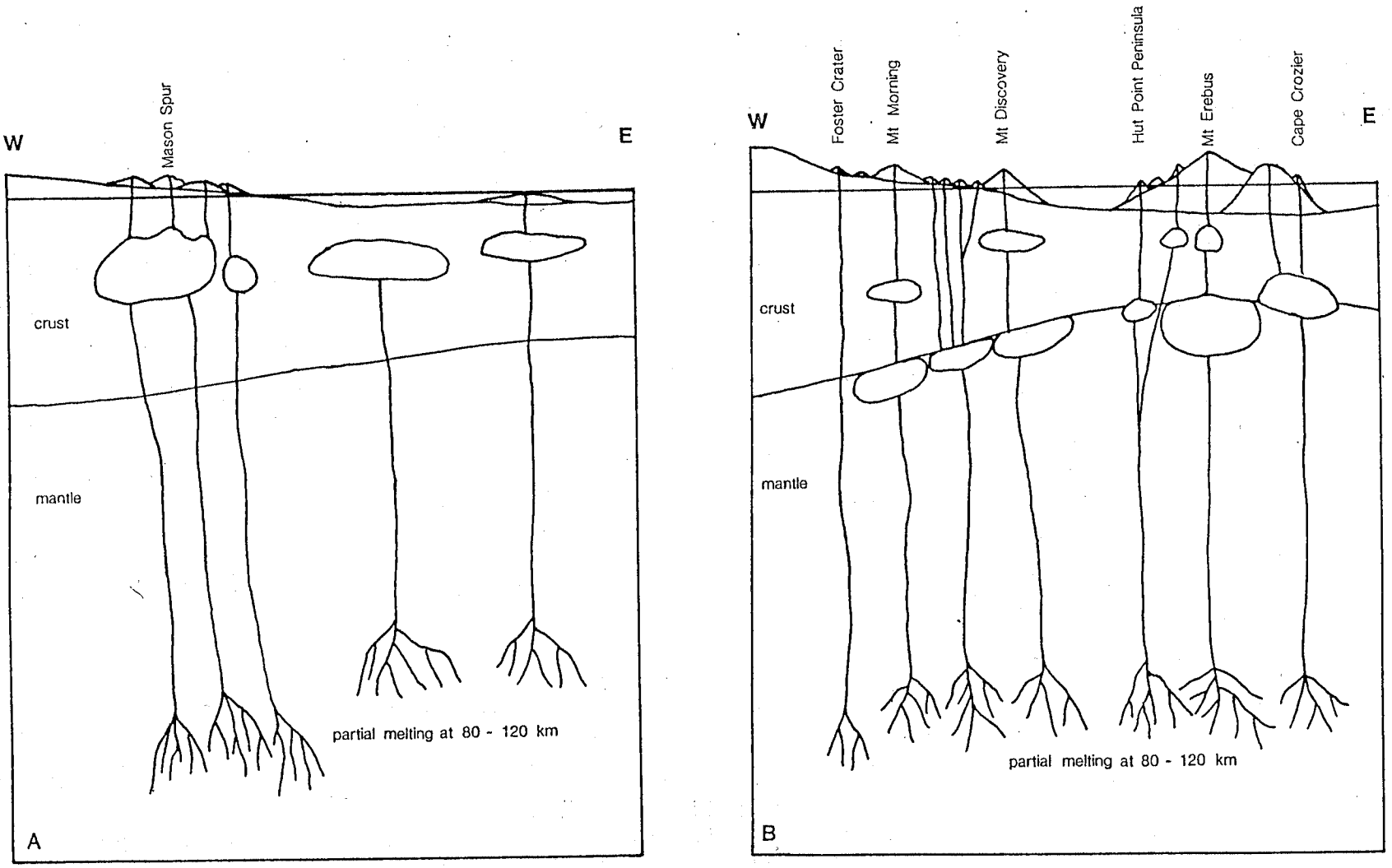

Figure 10.7 - Generalized model of the magmatic systems operating in the rebus volcanic province between 19 and 11 m.y. ago (A), and 11 m.y. ago and present (B). Small degrees of partial melting of an enriched garnet peridotite mantle at depths of 80 - 120 km has produced parental basanite magmas throughout. These differentiated in crustal magma chambers prior to 11 m.y. ago. Since 11 m.y. the basanite parental melts have fractionated in deeper magma chambers, perhaps in the vicinity of the crust - mantle boundary which is between 25 and 40 km deep. Some of these magmas escaped directly to the surface (forming

processes have remained relatively constant and should be viewed as dynamic and ongoing processes.

Parental basanite melts have been modified primarily by fractional crystallization. Prior to about 11 m.y. ago the parental melt probably underwent about 10% fractional crystallization at upper mantle depths before being injected into crustal level magma chambers. These magma chambers may have been small discrete magma bodies, or they may have been large, and had discrete cupolas in which late stag fractionation could evolve several closely spaced, but genetically unrelated evolved magma compositions. Magma chemistry evolved along a trend towards SiO_2 saturation, controlled by the fractionation of plagioclase and clinopyroxene. The fractionation of calcic plagioclas drove the composition of many residual liquids towards peralkalinity. Other processes besides fractional crystallization probably also operated, but have not been modelled.

An increase in the depth of fractionating magma chambers since about 11 m.y. ago, may account for the initiation of Group II geochemical trends. The composition of clinopyroxene and kaersutite, and the minor role of feldspar fractionation, as indicated by mass balanc models for Group IIA rock suites, suggests they may have been generated by fractional crystallization at a greater depth than those in Group I, perhaps in the vicinity of the mantle-crust boundary. The presence of kaersutite suggests crystallization took place at tempertures below about 1100 ^{o}C (Merrill and Wyllie, 1975). Injection of partially evolved magmas into crustal magma chambers and their contin ued fractionation under lower pressure and temperature conditions probably produced the geochemical variety of Group IIB rock suites.

The thicker crust in the western half of the EVP, and the probable existence of a transform, may have been important in determining the location of large volcanoes composed of kaersutite-bearing lavas. The distinctive Mt Erebus lavas are derived by fractional crystallization at temperatures above about 1100°C (Moore, 1986) and perhaps at lower volatile pressures than other Group IIB magmas.

The depth at which crustal magma chambers have formed probably reflects a balance between the boyancy of the magma, which will be a function of composition and temperature, and the confining pressure controlled by lithostatic loading and the tensional stress regime. The increase in the depth of magma chambers suggests that extensional tectonic effects have extended to greater depths with time. The increase in the volume of less evolved melts reaching the surface is probably a function of decreasing crustal thickness over the last 19 m.y., and perhaps an increase in fault density due to wrenching along a transform.

REFERENCES

Abbot, M.J. 1962: Aenigmatite from the groundmass of a peralkaline trachyte. American Mineralogist 52: 1895-1901.

Allen, J.C.; Boettcher, A.L. 1973: Phase relation and the stability o amphiboles in an olivine nephelinite at high pressure (Abstract) Transactions of the American Geophysical Union (EOS) 54: 481.

Aoki, K. 1970: Petrology of kaersutite-bearing ultramafic and mafic inclusions in Iki Island, Japan. Contributions to Mineralogy and Petrology 25: 270-283.

Aoki, K; Shiba, I. 1973: Pyroxenes from lherzolite inclusions of Itinome-gata, Japan. Lithos 6: 41-51.

Armstrong, R.L. 1978: K-Ar dating: Late Cenozoic McMurdo Volcanic Group and dry valley glacial history, Victoria Land, Antarctica. New Zealand Journal of Geology and Geophysics 21: 683-698.

Arth, J.G. 1976: Behaviour of trace elements during magmatic processes - A summary of the theoretical models and their applications. Journal of Research of the United States Geological Survey 4: 41-47.

Bailey, D.K. 1963: The stability of acmite. Carnegie Institute Washington Year Book 62: 131-133.

Bailey, D.K. 1969: The stability of acmite in the presence of H_2O. American Journal of Science 267A: 1-16.

Bailey, D.K. 1982: Mantle metasomatism. Continuing chemical changes within the earth. Nature 296: 525-560.

Bailey, D.K.; McDonald, R. 1975: Fluorine and chlorine in peralkaline liquidsandthe need for magma generation inanopensystem. Mineralogical Magazine 40: 405-414.

Baker, B.H.; Goles, G.G.; Leeman, W.P.; Lindstrom, M.M. 1977:

Geochemistry and petrogenesis of a basalt-benmoreite-trachyte suite from the southern part of the Gregory Rift, Kenya. Contributions to Mineralogy and Petrology 64: 303-332.

Baker,B.H.;McBirney,A.R.1985:Liquidfractionation PartII. Geochemistry ofzoned magmas and the compositionaleffects of liquid fractionation. Journal of Volcanology and Geothermal Research 24: 55-81.

Barrett, P.J. 1965: Geology of the area between the Axel Heiberg and Shackleton Glaciers, Queen Maud Range, Antarctica. Part 2 - Beacon Group. New Zealand Journal of Geology and Geophysics 8: 344-370.

Barrett, P.J. 1975: Textural characteristics of Cenozoic preglacial and glacial sediments at site 270, Ross Sea, Antarctica. Initial Reports of the Deep Sea Drilling Project 28: 757-767. U.S. Government Printing Office, Washington, D.C.

Barrett, P.J.; McKelvey, B.C. 1981: Cenozoic and tectonic history of the Transantarctic Mountains in the McMurdo Sound region: recent progress 1986: from drilling and related studies. Polar Research 20 543-548.

Barrett, P.J.; Grindley, G.W.; Webb, P.N. 1972: The Beacon Supergroup of East Antarctica. Pp 319-332 in Adie, R.J.(Ed.) Antarctic Geology and Geophysics. Oslo, Universitetsforlaget.

Barrett, P.J.; McKelvey, B.C. 1986: Stratigraphy. Pp 9-52 in Barrett, P.J. (Ed.) Antarctic Cenozoic history from the MSSTS-1 drillhole, McMurdo Sound. New Zealand DSIR Bulletin 237.

Barrett, P.J.; McKelvey, B.C.; Walker, B.C. 1986: Sand Provenance. Pp 137-144 in Barrett, P.J. (Ed.) Antarctic Cenozoic history from

the MSSTS-1 drillhole, McMurdo Sound. New Zealand DSIR Bulletin

Barton, M.; van Bergen, M.J. 1981: Green clinopyroxenes and associate phases in a potassium-rich lava from the Leucite Hills, Wyoming. Contributions to Mineralogy and Petrology 77: 101-114.

Barton, M.; Varekamp, J.C.; van Bergen, M.J. 1982: Complex zoning of clinopyroxenes in lavas of Vulsini, Latinum, Italy: evidence for magma mixing. Journal of Volcanology and Geothermal Research 14: 361-388.

Basu, A.R.; MacGregor, I.D. 1975: Chromite spinels from ultramafic xenoliths. Geochimica et Cosmochimica Acta 39: 937-945.

Bence, A.E.; Albee, A.L. 1968: Empirical correction factors for the electron microanalysis of silicates and oxides. Journal of Geology 76: 382-403.

Berg, J.H. 1984: Crustal inclusions from the Erebus Volcanic Province Antarctic Journal of the United States 19(5):27.

Berg, J.H.; Hank, R.A.; Kalamarides, R.I. 1985: Petrology and geochemistry of inclusions of lower crustal basic granulites fro the Erebus volcanic province, Antarctica. Antarctic Journal of the United States 19: 22-23.

Bennett, D.J.; Sissons, B.A. 1984: Gravity models across the Transantarctic Mountains front near New Harbour, McMurdo Sound, Antarctica. New Zealand Journal of Geology and Geophysics 27: 413-424.

Best, M.G. 1974: Mantle-derived amphibole within inclusions in alkali - basaltic lavas. Journal of Geophysical Research 79: 2107-2113.

Blank, H.R.; Cooper, R.A.; Wheeler, R.H.; Willis, I.A.G. 1963: Geolog of the Koettlitz - Blue Glacier region, Southern Victoria Land,

Antarctica. Journal of the Royal Society of New Zealand - Geology 2: 79-102.

Borg, S.G.; Stump, E.; Chappell, B.W.; McCulloch, H.T.; Wyborn, D.; Armstrong, R.L.; Holloway, J.R. 1987: Granitoids of northern Victoria Land: implications to regional crustal structure and tectonics. American Journal of Science 287: 127-169.

Borley, G.D.; Suddaby, P; Scott, P. 1971: Some xenoliths from the alkaline rocks of Tenerife, Canary Islands. Contributions to Mineralogy and Petrology 31: 102-114.

Brady, H.T. 1979: A diatom report of DVDP cores 3, 4A, 12, 14, 15, and other related surface sections. Pp 165-175 in Nagata, T. (Ed.) Proceedings of the Seminar III on Dry Valley Drilling Project, 1978. National Institute of Polar Reseach, Special Memoir No. 13.

Brady, H.T.; McKelvey, B.C. 1979: The interpretation of a Tertiary tillite at Mt Feather, Southern Victoria Land, Antarctica. Journal of Glaciology 22: 189-193.

Brey, G.P. 1976: CO_2 solubility and solubility mechanism in silicate melts at high pressures. Contributions to Mineralogy and Petrology 57: 215-221.

Brey, G.P.; Green, D.H. 1975: The role of CO_2 in the genesis of olivine melilite. Contributions to Mineralogy and Petrology 49: 93-103.

Brooks, C.K.; Printzlau, I. 1978: Magma mixing in mafic alkaline volcanic rocks: the evidence from relict phenocryst phases and other inclusions. Journal of Volcanological and Geothermal Research 4: 315-331.

Bryan, W.B.; Finger, L.W.; Chayes, F. 1969: Estimating proportions in petrographic mixing equations by least squares approximation.

Scince 163: 672-679.

Campbell, I.H.; Borley,G.D. 1974: The geochemistry of pyroxenes from the Lower Layered Series of the Jimberlana Intrusion, Western Australia. Contributions to Mineralogy and Petrology 47: 228-294

Carmichael, I.S.E.; Turner, F.J.; Verhoogen, J. 1974: Igneous Petrology. McGraw-Hill, 739p.

Carter, S.R.; Evensen, N.H.; Hamilton, P.J.; O'Nions, R.K. 1978: Continental volcanics derived from enriched and depleted source regions: Nd- and Sr-isotope evidence. Earth and Planetary Scienc Letters 37: 401-408.

Cawthorn, R.G. 1976a: Some chemical controls on igneous amphibole compositions. Geochimica et Cosmochemicia Acta 40: 1319-1328.

Cawthorn, R.G. 1976b: Melting relations in part of the system CaO - MgO - Al_2O_3 - SiO_2 - Na_2O - H_2O under 5 Kb pressure. Journal of Petrology 17: 44-72.

Chauvel, C.; Jahn, B.-M. 1984: Nd - Sr iostope and REE geochemistry c alakli basalts from the Massif Central, France. Geochimica et Cosmochimica Acta 48: 93-110.

Cole, J.W.; Ewart, A. 1968: Contributions to the volcanic geology of the Black Island, Brown Peninsula, and Cape Bird areas, McMurdo Sound, Antarctica. New Zealand Journal of Geology and Geophysics 11: 793-828.

Cole, J.W.; Kyle, P.R.; Neal, V.E. 1971: Contributions to the Quaternary geology of the Cape Crozier, White Island, and Hut Point Peninsula, McMurdo Sound region, Antarctica. New Zealand Journal of Geology and Geophysics 14: 528-546.

Coombs, D.S.; Wilkinson, J.F.G. 1969: Lineages and fractionation

trends in undersaturated volcanic rocks from East Otago volcanic province (New Zealand) and related rocks. Journal of Petrology 10: 440-501.

Cooper, A.K.; Davey, F.J. 1985: Episodic rifting of Phanerozoic rocks in the Victoria Land basin, western Ross Sea, Antarctica. Science 229: 1085-1087.

Craddock, C. 1971: Geologic map of Antarctica. 1:5,000,000. American Geophysical Society, New York.

Cullers, R.L.; Medaris, G. Jr. 1977: Rare earth elements in carbonatite and cogenetic alkaline rocks. Examples from Seabrook Lake and Callander Bay, Ontario. Contributions to Mineralogy and Petrology 65: 143-153.

Dalrymple, G.B. 1979: Critical tables for conversion of K-Ar ages from old to new constants. Geology 7: 558-560.

Dalrymple. G.B.; Lamphere, M.A. 1969: Potassium-argon dating. Freeman, San Francisco.

Davey, F.J. 1982: Geophysical studies in the Ross Sea region. Journal of the Royal Society of New Zealand 11: 465-479.

Davey, F.J.; Christoffel, D.A. 1984: The correlation of MSSTS-1 drillhole results with seismic reflection data from McMurdo Sound, Antarctica. New Zealand Journal of Geology and Geophysics 27: 405-412.

David, T.W.E.; Preistly, R.E. 1914: Glaciology, physiography, stratigraphy, and tectonic geology of south Victoria Land. Reports of Scientific Investigations, British Antarctic Expedition 1907-1909. Geology: 1-319.

Dawson, J.B.; Smith, J.V. 1982: Upper mantle amphiboles: a review. Mineralogical Magazine 45: 35-46.

Debenham, F. 1923: The physiography of the Ross Island Archipalego. British Antarctic ("Terra Nova") Expedition 1910-1913. London. Harrison.

Deer, W.A.; Howie, R.A.; Zussman, J. 1966: An introduction to the rock-forming minerals. London. Longmans.

Deer, W.A.; Howie, R.A.; Zussman, J. 1978: Rock forming minerals. Volume 2A (2nd ed.). Single-chain silicates. Wiley, New York. 667p.

Drake,M.J. 1976: Plagioclase - melt equilibria. Geochimica et Cosmochimia Acta 40: 457-465.

Duda, A.; Schmincke, H-U. 1985: Polybaric differentiation of alkali basaltic magmas: Evidence from green core clinopyroxenes (Eifel, FRG). Contributions to mineralogy and petrology 91: 340-353.

Duke, J.M. 1976: Distribution of the Period Four transition elements among olivine, calcic clinopyroxene, and mafic silicate liquids: experimental results. Journal of Petrology 17: 499-521.

Eaton, G.P. 1979: A plate-tectonic model for late Cenozoic crustal spreading in the western United States. Pp 7-32 in Riecker, R.E. (Ed.). The Rio Grande Rift: Tectonics and Magmatism. American Geophysical Union. Washington.

Egglston, T.L. 1987: Taylor Creek District, New Mexico: geology, petrology and tin deposits. PhD dissertation, New Mexico Institute of Mining and Technology, Socorro, New Mexico. 473 p.

Elston, D.P.; Bressler, S.L. 1981: Magnetic stratigraphy of DVDP dri cores and late Cenozoic histroy of Taylor Valley, Transantarcti Mountains, Antarctica.: 413-426.

Ernst, W.G. 1962: Synthesis, stability reations and occurrence of reibekite and reibekite-arfvedsonite solid solutions. Journal o

Geology 70: 689-.

Faure, G. 1977: Principles of Isotope Geology. Wiley, New York.

Ferrar, H.T. 1907: Report on the field-geology of the region explored during the "Discovery" Antarctic Expedition, 1901-4. National Antarctic Expedition 1901-4. Natural History 1: 1-100.

Findlay, R.H.; Skinner, D.N.B.; Craw, D. 1984: Lithostratigraphy and structure of the Koettlitz Group, McMurdo Sound, Antarctica. New Zealand Journal of Geology and Geophysics 27: 513-536.

Fitton, J.G.; Dunlop, H.M. 1985: The Cameroon line, West Africa, and its bearing on the origin of oceanic and continental alkali basalt. Earth and Planetary Science Letters 72: 23-38.

Fitzgerald, P.G.; Saniford, M.; Barrett, P.J.; Gleadow, A.J.W. 1986: Asymmetric extension associated with uplift and subsidence in the Transantarctic Mountains and Ross Embayment. Earth and Planetary Science Letters 81: 67-78.

Fleck, R.J.; Sutter, J.K.; Elliot, D.H. 1977: Interpretation of discordant $^{40}Ar/^{39}Ar$ age spectra of Mesozoic tholeiites from Antarctica. Geochimica et Cosmochemica Acta 41: 15-32.

Florensov, N.A. 1969: Rifts of the Baikal Mountain regions. Tectonophysics 8: 443-456.

Forbes, R.B.;Turner,D.L.; Carden, J.R. 1974: Age of trachyte from Ross Island, Antarctica. Geology 2: 297-298.

Frisch, T. 1970: Chemical variations among the amphiboles of Shefford Mountain, a monteregian intrusion in southern Quebec. Canadian Mineralogist 10: 553-570.

Frisch, T.; Schmincke, H-U. 1969: Petrology of clinopyroxene-amphibole inclusions from Roque Nublo volcanics, Gran Canaria,

Canary Islands. Bulletin Volcanologie 33: 1073-1088.

Frey, F.A.; Printz, M. 1978: Ultramafic inclusions fromSan Carbs, Arizona: petrological and geochemical data bearing on their petrogenesis. Earth and Planetary Science Letters 38: 129-176.

Frey, F.A.; Green, D.H.; Roy, S.D. 1978: Integrated models of basalt petrogenesis: A study of quartz tholeiites and olivine melilite from eastern Australia utilizing geochemical and experimental data. Journal of Petrology 19: 463-513.

Gamble, J.A.; Barrett, P.J.; Adams, C.J. 1986: Basaltic clasts from Unit 8. Antarctic Cenozoic history from the MSSTS-1 drillhole, western McMurdo Sound. New Zealand DSIR Miscellaneous Bulletin 237: 145-151.

Gamble, J.A.; Kyle, P.R. 1987: The origins of glass and amphibole in spinel-wehrlite xenoliths from Foster Crater, McMurdo Volcan Group, Antarctica. Journal of Petrology 28:

Gamble, J.A.; McGibbon, F.; Kirsch, I.; Kyle, P.R.; Menzies, M.A. in prep: Metasomatised xenoliths from Foster Crater, Antarctica: Implications for lithospheric structure and processes beneath the Transantarctic Mountain front.

Gast, P.W. 1968: Trace element fractionation and the origin of tholeiitic and alkaline magma types. Geochimica et Cosmochimica Acta 32: 1057-1086.

Gibb, F.G.F. 1973: The zoned clinopyroxenes of the Shiant Isles, Scotland. Journal of Petrology 14: 203-230.

Gittins, J. 1979: The feldspathoidal alkaline rocks. In Yoder, H.S. (Ed.) The evolution of the igneous rocks. Princeton University Press, Princeton. 351-390.

Gleadow, A.J.W.; Fitzgerald, P.G. 1984: Abstract of the Fourt

International Fission Track Dating Workshop. Troy, New York.

Gleadow, A.J.W.; McKelvey, B.C.; Ferguson, K.U. 1984: Uplift history of theTransantarcic Mountains in the Dry Valleys area, Southern Victoria Land, Antarctica, from apatite fission track ages. New Zealand Journal of Geology and Geophysics 27: 457-464.

Gleadow, A.J.W.; Fitzgerald, P.G. 1987: Uplift history and structure of the Transantarctic Mountains: new evidence from fission track dating of basement apatites in the Dry Valleys area, southern Victoria Land. Earth and Planetary Science Letters 82: 1-14.

Goldich, S.S.; Treves, S.B.; Suhr, N.H.; Stuckless, J.S. 1975: Geochemistry of the Cenozoic volcanic rocks of Ross Island and vicinity, Antarctica. Journal of Geology 83: 415-435.

Goldich, S.S.; Stuckless, J.S.; Suhr, N.H.; Bodkin, J.B.; Wamser, R.C 1981: Some trace element relationships in the Cenozoic volcanic rocks from Ross Island and vicinity, Antarctica. Dry Valley Drilling Project. Antarctic Research Series 33: 215-228.

Green, D.H. 1970: The origin of basaltic and nephelinitic magmas. Transactions of the Leister Literary and Philosophical Society 64: 28-54.

Green, D.H.; Ringwood, A.E. 1967: The genesis of basaltic magmas. Contributions to Mineralogy and Petrology 15: 103-190.

Green, D.H.; Hibberson, W. 1970: Experimental duplication of conditions of precipitation of high pressure phenocrysts in a basaltic magma. Physics of the Earth and Planetary Interiors 3: 247-254.

Green, D.H.; Ringwood, A.E. 1970: Mineralogy of peridotitic compositions under upper mantle conditions. Physics of the Earth

and Planetary Interiors 3: 359-371.

Green, D.H.; Edgar, A.D.; Beasley, P.; Kiss, E.; Ware, N.G. 1974: Upper mantle source for some hawaiites, mugearites, and benmoreites. Contributions to Mineralogy and Petrology 48: 33-4

Grindley, G.W. 1981: Precambrian rocks of the Ross Sea region. Journa of the Royal Society of New Zealand 11: 411-423.

Gunn, B.M.; Warren, G. 1972: The Geology of Victoria Land between the Mason and Mullock Glaciers, Ross Dependency, Antarctica. Geological Survey of New Zealand Bulletin 71.

Gupta, A.K.; Onuma, K.; Yagi, K.; Lidiak, E.G. 1973: Effect of silica concentration on the diopsidic pyroxenes in the system diopside-$CaTiAl_2O_6SiO_2$. Contributions to Mineralogy and Petrology 41: 33 344.

Gutmann, J.T. 1974: Tubular voids within labradorite phenocrysts from Sonora, Mexico. American Mineralogist 59: 666-672.

Haggerty, S.E. 1976: Opaque mineral oxides in the terrestrial igneous rocks. In Ribble, D. III (Ed.) Oxide Minerals. Mineralogical Society of America Short Course Notes 3: Hg101-Hg300.

Harrington, H.J. 1959: Narrative account ot the New Zealand Geologica Survey Antarctic Expedition, 1958-59. Unpublished report, NZDSIF

Harrison, T.M. 1983: Some observations on the interpretation of $^{40}Ar/^{39}Ar$ age spectra. Isotope Geology 1: 319-338.

Harwood, D.M. 1986: Diatoms. Pp 69-108 in Barrett, P.J. (Ed.) Antarctic Cenozoic history from the MSSTS-1 drillhole, McMurdo Sound. New Zealand DSIR Bulletin 237. Wellington.

Hawkesworth, C.J.; Van Calsteren, P; Roger, N.W.; Menzies, M.A. 1987: Isotope variations in recent volcanics. A trace-element perspective. Pp 365-385 in Menzies, M.A.; Hawkesworth, C.J. (Ed.

Mantle Metasomatism. Academic Press, Nantwich, UK.

Hayes, D.E.; Davey, F.J. 1975: A geophysical study of the Ross Sea. Initial Report of the Deep Sea Drlling Project 28: 887-907.

Hayes, D.E.; Frakes, L.E. 1975: Initial reports of the Deep Sea Drilling Project 28: 1017.

Hildreth, W. 1981: Gradients in silicic magma chambers: implications for lithospheric magmatism. Journal of Geophysical Research 86: 10153-10192.

Hill, R.; Roeder, P. 1974: The crystallization of spinel from basaltic liquids as a function of oxygen fugacity. Journal of Geology 82: 709-729.

Holloway, J.R. 1973: The system pargasite - H_2O - CO_2: a model for melting of a hydrous mineral with a mixed volatile fluid - I. Experimental results to 8 Kbar. Geochimica et Cosmochimica Acta 37: 651-666.

Holloway, J.R.; Ford, C.E. 1973: The effect of fluorine on hornblende fluid-absent melting of F - OH pargasite to 35 Kb (Abstract). Transactions of the American Geophysical Union (EOS) 54: 478.

Illies, J.H. 1969: An intracontinental belt of the world rift system. Tectonophysics 8: 5-29.

Illies, J.H. 1978: Rhinegraben: An extinct tensional rift valley reactivated by shear. International Symposium on the Rio Grande Rift. Program and Abstracts: 42-46.

Irvine, T.N. 1967: Chromian spinel as a petrogenetic indicator. Part 2. Petrologic applications. Canadian Journal of Earth Science 4: 71-103.

Irving, A.J. 1974: Geochemical and high pressure experimental studies

of garnet pyroxenite and pyroxene granulite xenoliths from the Delegate basaltic pipes, Australia. Jounal of Petrology 15: 1-40

Irving, A.J.; Frey, F.A. 1984: Trace element abundances in megacrysts and their host basanites: constraints on partition coefficients and megmacryst genesis. Geochimica et Cosmochimica Acta 48: 1201-1221.

Jensen, H.I. 1916: Report on the petrology of the alkaline rocks of M Erebus, Antarctica. Report of the British Antarctic Expedition 1907-1909. Geology 2: 93-128

Johannes, W. 1978: Melting of plagioclase in the system Ab-An-H_2O and Qz-Ab-An-H_2O at P_{H2O} = 5 Kb, an equilibrium problem. Contributions to Mineralogy and Petrology 66: 295-303.

Jones, L.; Walker, R.L. 1972: Geochemistry of the McMurdo volcanics, Victoria Land. Part I. Strontium isotope composition. Antarcic Journal of the United States 7: 142-144.

Jordan, H. 1981: Tectonic observations in the Hallett volcanic province, Antarctica. Geologisches Jahrbuch B41: 111-125.

Kay, R.; Gast, P.W. 1973: The rare earth content and origin of alkali-rich basalts. Journal of Geology 81: 653-682.

Keil, K.; Fodor, R.V.; Bunch, T.E. 1972: Contributions to the mineral chemistry of Hawaiian rocks. II. Feldspars and interstitial material in rocks from Haleakala and west Maui volvanicoes, Maui Hawaii. Contributions to Mineralogy and Petrology 37: 253-276.

Keys, J.R.; Anderton, P.W.; Kyle, P.R. 1977: Tephra and debris layers in the Skelton Neve and Kemp Glacier, South Victoria Land, Antarctica. New Zealand Journal of Geology and Geophysics 20:971-1002.

Keys, J.R.; McIntosh, W.C.; Kyle, P.R. 1983: Volcanic activity of Mount Melbourne, northern Victoria Land. Antarctic Journal of th United States 18: 10

King, B.C. 1965: Petrogenesis of the alkaline igneous rock suites of the volcanic and intrusive centers of eastern Uganda. Journal of Petrology 6: 67-100.

Kirsch, I.D. 1981: Evidence for mantle metasomatism in ultramafic inclusions from Foster Crater, Antarctica. MS thesis, Ohio State University. 164 p.

Kooster van Groos, A.F.; Wyllie, P.J. 1975: The effect of high CO_2 pressures on alkalic rocks and its bearing on the formation of a ultrabasic rocks and associated carbonates. American Journal of Science 275: 163-185.

Kyle, P.R. 1976: Geology, mineralogy, and geochemistry of the Late Cenozoic McMurdo Volcanic Group, Victoria Land, Antarctica. PhD dissertation, VictoriaUniversity of Wellington, New Zealand. 444 p.

Kyle, P.R. 1981 a: Glacial history of the McMurdo Sound area as indicated by the distribution and nature of McMurdo Volcanic Group rocks. Dry Valley Drilling Project. Antarctic Reseach Series 33: 403-412.

Kyle, P.R. 1981 b: Geological history of Hut Point Peninsula as inferred from DVDP 1, 2 and 3 drillholes and surface mapping. Dr Valley Drilling Project. Antarctic Reseach Series 33: 427-445.

Kyle, P.R. 1981 c: Evolution of a basanite - phonolite sequence, Hut Point Peninsula, Antarctica - Evidence from Dry Valley Drilling Project drillholes 1, 2 and 3. Journal of Petrology 22: 451-500.

Kyle, P.R. 1986: Mineral chemistry of Late Cenozoic McMurdo Volcanic

Group rocks from the Pleiades, northern Victoria Land. Geological Investigations of Northern Victoria Land Antarctic Research Series 46: 305-337. American Geophysical Union, Washington

Kyle, P.R. 1986: Volcanic activity of Mt Erebus: 1977-1984. International Volcanological Congress, 1986, Abstracts : 250.

Kyle, P.R. in press a: McMurdo Volcanic Group - Western Ross Embayment. Introduction. In Le Masurier, W.E.; Thomson, J.W. (Ed.) Late Cenozoic Volcanoes of Antarctica and the Subantarctic Islands.

Kyle, P.R. in press b: Melbourne Volcanic Province (Summary).In Le Masurier, W.E.; Thomson, J.W. (Ed.) Late Cenozoic volcanoes of Antarctica and the Subantarctic Islands.

Kyle, P.R.; Cole, J.W. 1974: Structural control of volcanism in the McMurdo Volcanic Group, Antarctica. Bulletin Volcanologique 38: 16-25.

Kyle, P.R.; Treves, S.B. 1974: Geology of Hut Point Peninsula, Ross Island Antarctica. Antarctic Journal of the United States 9: 127-129.

Kyle, P.R.; Muncy, H.L. 1978: Volcanic geology of the lower slopes of Mt Morning. Antarctic Journal of the United States 13: 34-36.

Kyle, P.R.; Adams, J.; Rankin, P.C. 1979: Geology and petrology of the McMurdo Volcanic Group at Rainbow Ridge, Brown Peninsula, Antarctica. Geological Society of America Bulletin 90: 676-688.

Kyle, P.R.; Elliott, D.H.; Sutter, J.F. 1980: Jurassic Ferrar Supergroup tholeiites from the Transantarctic Mountains, Antarctica, and their relationship to the initial fragmentation

of Gondwana. In Cresswell, M.M.; Vella, P. (Ed.) Proceedings of the Fifth International Gondwana Symposium, Victoria University of Wellington, New Zealand: 283-287.

Kyle, P.R.; Dibble, R.R.; Giggenbech, W.F.; Keyes, J. 1982: Volcanic activity associated with the anorthoclase phonolite lava lake, Mount Erebus, Antarctica. In Craddock, C. (Ed.) Antarctic Geosciences. University of Wisconsin Press.

Kyle, P.R.; Wright, A.; Kirsch, I. 1987: Ultramafic xenoliths in late Cenozoic McMurdo Volcanic Group, western Ross Sea embayment Antarctica. Pp 289-293 in Nixon, P.H. (Ed.) Mantle xenoliths. Wiley.

Kyle, P.R.; Muncy, H.L. in prep. Geochronlogy, petrogenesis and geological history of the McMurdo Volcanic Group on the northern slopes of Mt Morning, Antarctica.

Laird, M.G. 1981: Lower Paleozoic rocks of the Ross Sea area and thei significance in the Gondawana context. Journal of the Royal Society of New Zealand 11: 425-438.

Larsen, L.M. 1977: Aenigmatites from the Ilimaussaq intrusion, south Greenland: chemistry and petrological implications. Lithos 10: 257-270.

Larsen, L.M. 1979: Distribution of REE and other trace elements between phenocrysts and peralkaline undersaturated magmas, exemplified by rocks from the Gardar igneaous province, south Greenland. Lithos 12: 303-315.

Leake, B.E. 1978: Nomenclature of amphiboles. Mineralogical Magazine 42: 533-563.

Le Bas, M.J.; Le Maitre, R.W.; Streckeisen, A.; Zanettin, B. 1986 A chemical classification of volcanic rocks based on the Tota

Alkali - Silica Diagram. Journal of Perology 27: 745-750.

Leeman, W.P.; Scheidegger, K.F. 1977: Olivine/liquid distribution coefficients and a test for crystal - liquid equilibrium. Earth and Planetry Science Letters 35: 247-257.

Le Maitre, R.W. 1969: Kaersutite-bearing plutonic xenoliths from Tristan da Cunha, S. Atlantic. Mineral Magazine 37: 185-197.

Le Maitre, R.W. 1976: Some problems of the projection of chemical dat into mineralogical classifications. Contributions to Mineralogy and Petrology 56: 181-189.

Lemarchard, F.; Villemant, B.; Calas, G. 1987: Trace elemenet distribution coefficients in alkaline series. Geochemica et Cosmochimica Acta 51: 1071-1081.

Le Masurier, W.E.; Wade, F.A. 1976: Volcanic history of Marie Byrd Land: implications with regard to southern hemisphere tectonic reconstructions. In Gonzales-Ferran, O. (Ed.) Andean and Antarctic Volcanology. Chemistry of the Earth's Interior. 398-424.

Le Masurier, W.E.; Ellerman, P.J.; McIntosh, W.C.; Wright, A.C. 1983: USCGC Glacier cruise I, December 1982 - January 1983: Recconnaissance of hyaloclasities in the western Ross Sea regio Antarctic Journal of the United States 18: 60-61.

Le Roex, A.P. 1985: Geochemistry, mineralogy, and magmatic evolution of the basaltic and tracytic lavas from Gough Island, South Atlantic. Journal of Petrology 26: 149-186.

Le Roex, A.P.; Erlank, A.J. 1982: Qunatitative evolution of fractiona crystallization in Bouvet Island lavas. Journal of Volcanology and Geothermal Research 13: 309-338.

Lesher, C.E. 1986: Effects of silicate liquid composition on mineral-liquid element partioning from Soret diffusion studies. Journal of Geophysical Research 91: 6123-6141.

Lindsley, D.H. 1980: Phase Equiliria of pyroxenes at pressures >1 atmosphere. in Prewitt, C.T. (Ed.) Reviews in Mineralogy Vol. 7. Pyroxenes. Mineralogical Society of America. Washington D.C. 289-308.

Lloyd, F.E. 1981: Upper mantle metasomatism beneath a continental rift: clinopyroxenes in alkali mafic lavas and nodules from sout west Uganda. Mineralogical Magazine 44: 315-323.

Lyon, G.L. 1986: Stable isotope stratigraphy of ice cores and the age of the last eruption of Mount Melbourne, Antarctica (Note). New Zealand Journal of Geology and Geophysics 29: 135-138.

Manhood, G.A.; Hildreth, W. 1983: Large partition coefficients for trace elements in high silica rhyolites. Geochimica et Cosmochimica Acta 47: 11-30.

Marsh J.S. 1975: Aenigmatite stability in silica undersaturated rocks Contributions to Mineralogy and Petrology 50: 135-144.

Marsh, J.S. 1987: Evolution of a strongly differentiated suite of phonolites from the Klinghardt Mountains, Namibia. Lithos 20: 41-58.

MacDonald, R.; Katsura, T. 1964: Chemical composition of Hawaiian lavas. Journal of Petrology 5: 82-113.

McBirney, A.R. 1984: Igneous Petrology. Freeman, San Francisco.

McDowell, F.W. 1983: K-Ar dating: incomplete extraction of radiogenic argon from alkali feldspar. Isotope Geoscience 1: 119-126.

McGinnis, L.D.; Bowen, R.D.; Kreamer, J. 1983: Deep seismic soundings along the boundary between East and West Antarctica. Antarctic

Journal of the United States 18: 32-34.

McGinnis, L.D.; Bowen, R.H.; Erickson, J.M.; Allred, B.J.; Kreamer, J.L. 1985: East - west Antarctic boundary in McMurdo Sound. Tectonophysics 114: 341-356.

McIntosh, W.C.; Kyle, P.R. in press: Hallett Volcanic Province (Summary). In Le Masurier, W.E.; Thomson, J.W. (Ed.) Late Cenozoic volcanoes in Antarctica and the Subantarctic Islands.

McIntosh, W.C.; Gamble, J.A. in press: A subaerial eruptive environment for the Hallett Coast volcanoes. In Thompson, M.R.A. (Ed) Proceedings of the 5th International Symposium on Antarctic Earth Sciences, Cambridge.

McIver, J.R.; Gevers, T.W. 1970: Volcanic vents below the Royal Society Range, Central Victoria Land, Antarctica. Transactions o the Geological Society of South Africa 73: 65-88.

McKelvey, B.C. 1979: The Miocene - Pleistocene stratigraphy of easter Taylor Valley - an interpretation of DVDP cores 10 and 11. Pp 176-185 in Nagata, T. (Ed.) Proceedings of the Seminar III on Dr Valley Drilling Project, 1978. National Institute of Polar Reseach, Special Memoir No. 13.

Menzie, D. 1985: The extraction of magma from the crust and mantle. Earth and Planetary Science Letters 74: 81-91.

Menzies, M.A. 1983: Mantle ultramaftic xenoliths in alkaline magmas: evidence for mantle hetrogeneity modified by magmatic activity. Pp 92-110 in Hawkesworth, C.J.; Norry, M.J. (Ed.) Continental basalts and mantle xenoliths. Shiva, Nantwich, UK.

Menzies, M.A.; Murthy, V.R. 1980: Mantle metasomatism as a precursor to the genesis of alkaline magmas - isotopic evidence. American

Journal of Science 280A: 622-638.

Menzies, M.A.; Hawkesworth, C.J. (Ed.) 1987: Mantle Metasomatism. Academic Press, London. 472p.

Merril, R.B.; Wyllie, P.J. 1975: Kaersutite and kaersutite eclogite from Kakanui, New Zealand - water-excess and water-deficient melting to 30 kilobars. Geological Society of America Bulletin 8(555-570

Miagkov, S.M. 1975: The effect of the McMurdo Oasis glaciation on crustal movement. Dry Valley Drilling Project Bulletin 6: 19.

Molnar, P.; Atwater, T.; Mammericky, J.; Smith, 1975: Magnetic anomalies, bathimetry, and the tectonic evolution of the South Pacific since the Late Cretaceous. Geophysical Journal of the Royal Astronomical Society 40: 383-420.

Moore, J.A. 1986: Mineralogy, geochemistry and petrogenesis of the lavas of Mt. Erebus, Antarctica. MS thesis, Mew Mexico Institue of Mining and Technology, Socorro, New Mexico.

Moore, J.A.: Kyle, P.R. 1986: Mantle upwelling and evolution of phonolitic magmas at Ross Island (Abstract). International Volcanological Congress Abstracts. Royal Society of New Zealand: 188.

Moore, J.A.; Kyle, P.R. in press: Volcanic geology of Mt Erebus, Ross Island, Antarctica.

Muncy,H.L. 1979: Geologic history and petrogenesis ofalkaline volcanic rocks, Mt Morning,Antarctica. MS thesis, Ohio State University, Columbus, Ohio. 112 p.

Nagasawa, H. 1973: Rare earth element distribution in alkali rocks from Oki-Dogo Island, Japan. Contributions to Mineralogy and Petrology 39: 301-308.

Nagaswa, H.; Schnetzler, C.C. 1971: Partitioning of reare-earth, alkali and alkaline earth elements between phenocryst and acid igneous magma. Geological Society of America Bulletin 35: 953-968.

Nash, W.P.; Wilkinson, J.F.G. 1970: Shonkin Sag laccolith Montana. 1. Mafic minerals and estimates of temperature, pressure, and oxyge fugacity and silica activity. Contributions to Mineralogy and Petrology 25: 241-269.

Nathan, S.; Schulte, F. 1967: Recent thermal and volcanic activity on Mount Melbourne, northern Victoria Land, Antarctica. New Zealand Journal of Geology and Geophysics 10: 422-430.

Neumann, E.R. 1976: Two refinements for the calculation of structural formulae for pyroxenes and amphiboles. Norsk Geologisk Tidsskrif 56: 1-6.

Neilsen, T.F.D. 1979: The occurrence and formation of Ti-aegerines in peralkaline syentites. Contributions to Mineralogy and Petrology 69: 235-244.

Nishikawa, M.; Kurshiro, I.; Uyeda, S. 1971: Stability of natural hornblende at high water pressures: preliminary experiments. Japanese Journal of Geology and Geography XLI: 41-50.

Nitsan, U. 1974: Stability field of olivine with respect to oxidation and reduction. Journal of Geophysical Reseach 79: 706-711.

Norry, M.J.; Fitton, G. 1983: Compositional differences between oceanic and continental basic lavas and their significance. Pp 5 19 in Hawkesworth, C.J.; Norry, M.J. (Ed.) Continental Basalts and Mantle Xenoliths. Shiva, Cheshire.

Norrish, K.; Hutton, J.T. 1969: An accurate X-ray spectographic metho

for the analysis of a wide range of geochemical samples. Geochemica et Cosmochimca Acta 33: 431-453.

O'Nions, R.K.; Evensen, N.M.; Hamilton, P.J.; Carter, S.R. 1978: Melting of the mantle past and present: isotope and trace elemer evidence. Philosphical Transactions of the Royal Society of London A258: 547-559.

O'Nions, R.K.; Carter, S.R.; Evensen, N.M.; Hamilton, P.J. 1979: Geochemical and cosmochemical applications of Nd isotope analysis. Annual Review of Earth and Planetary Science 7: 11-38.

Papike, J.J.; Cameron, K.L.; Baldwin, K. 1974: Amphiboles and pyroxenes: characterization of other quadrilateral components an estimates of ferric iron from microprobe data. Abstract. Program of the Geological Society of America 6: 1053-1054.

Pearse, J.A.; Norry, M.J. 1979: Petrogenetic implicatins of Ti, Zr, Y and Nb variations in volcanic rocks. Contributions to Mineralogy and Petrology 34: 33-47.

Philpotts, A.R. 1974: The Monteregian province. Pp 293-310 in Sorenson, H. (Ed.) The Alkaline Rocks. Wiley.

Philpotts, J.A.; Schnetzler, C.C. 1970: Phenocryst-matrix partition coefficients for K, Rb, Sr, and Ba with applications to anorthosite and basalt genesis. Geochimica et Cosmochimica Acta 34: 307-322.

Polyakov, M.M.; Krylov, A.Ya.; Mazina, T.I. 1976: Quoted in Stuivier, M.; Braziunas, T.F. 1985: Compilation of isotopic dates from Antarctica. Radiocarbon, American Journal of Science: 161-164.

Priestly, R.E.; David, T.W.E. 1912: Geological notes of the British Antarctic Expedition, 1907-09. Internation Geological Congress XI,(Stockholm, 1910) 2: 767-811.

Prior, G.T. 1902: Report on the rock specimens collected by the Southern Cross Antarctic Expedition. Report of the Southern Cro collections (British Museum): 321-332

Prior, G.T. 1907: Report on the rock specimens collected during the "Discovery" Antarctic Expedition, 1901-1904. Natural History 1: 101-160.

Reichen, L.E.; Fahey, J.J. 1962: An improved method for the determination of FeO in rocks and minerals including garnet. U.S. Geological Survey Bulletin 1144-B: 1-5.

Ribbe, P.H. 1975: The chemistry, structure and nomenclature of feldspar. In Mineralogical Society of America. Short Course Notes. Feldspar mineralogy. vol. 2. Mineralogical Society of America, Washington D.C. R-1 - R-72.

Sack, R.O.; Walker, D.; Carmichael, I.S.E. 1987: Experimental petrology of alkaline lavas: constriants on cotectics of multip saturation in natural basic liquids. Contributions to Mineralog and Petrology 96: 1-23.

Schnetzler, C.C; Pholpotts, J.A. 1970: Partition coefficients of rar earth elements between igneous matrix material and rock-forming mineral phenocrysts II. Geochimica et Coasmochimica Acta 34: 33 340.

Schott, J. 1983: Thermal diffusion and magmatic differentiation: a ne look at an old problem. Mineralogical Bulletin 106: 247-262.

Seck, H.A. 1971: The effect of pressure on the composition of coexisting alkali feldspars and plagioclases in the system $NaAlSi_3O_8$-$KAlSi_3O_8$-$CaAl_2Si_2O_8$-H_2O. Contributions to Mineralogy and Petrology 31: 67-86.

Skinner, D.N.B.; Waterhouse, B.C.; Brehaut, G.; Sullivan, K. 1976: NZ Geological Survey Antarcic Expedition 1975/76. Skelton-Koettlitz Glaciers. New Zealand Geological Survey Report to Antarctic Division, DSIR. Christchurch, NZ. DS58.

Smellie, J.L. 1986: Geochemistry and tectonic setting of alkaline volcanic rocks in the Antarctic Peninsula. (Abstract) International Volcanological Congress, New Zealand. Royal Society of New Zealand. 208.

Smith, W.C. 1954: The volcanic rocks of the Ross Archipelago.British "Terra Nova" Expedition, 1910. Natural History Report. Geology 2 1-107.

Smith,R.L.;Bailey, R.A.;Russell, S.L. 1978: The volcanic evolution of the Jemez Mountains, and its relationship to the Rio Grande Rift (Abstract). In Olsen, K.H.; Chapin, C.E. (Ed.) International Symposium on the Rio Grande Rift. Santa Fe: 91.

Smithson, S.B. 1972: Gravity interpretation in the Transantarctic Mountains near McMurdo Sound. Geological Society of America Bulletin 83: 3437-3442.

Sorenson, H. 1970: Internal structures and geological setting of the three agpaitic intrusions - Khibina and Lovozero of the Kola Peninsula,and Ilimausaq, south Greenland. Canadian Mineralogist 10: 299-334.

Sorensen, H. 1974: The Alkaline Rocks. Wiley.

Spera, F.J. 1981: Carbon dioxide in igneous petrogenesis: II Fluid dynamics of mantle metasomatism. Contributions to Mineralogy and Petrology 77: 56-65.

Spera, F.J. 1984: Carbon dioxide in petrogenesis III: role of volatiles in the ascent of alkaline magma with special refernce to xenolith-bearing mafic lavas. Contributions to mineralogy and petrology 88: 217-232.

Spera, F.J. 1987: Dynamics of translithospheric migration of metasomatic fluid and alkaline magma. Pp 1-18 in Menzies, M.A.; Hawkesworth, C.J. (Ed.) Mantle Metasomatism. Academic Press, London.

Steiger, R.H.; Jager, E. 1977: Subcommission on geochemistry: convention on the use of decay constants in geo- and cosmochronology. Earth and Planetary Science Letters 36: 359-362

Stormer, J.C. 1973: Calcium zoning in olivine and its relationship to silica activity and pressure. Geochimica et Cosmochimia Acta 37: 1815-1821.

Stormer, J.C. 1983: The effects of recalculation on estimates of temperature and oxygen fugacity of multicomponent iron - titaniu oxides. American Mineralogist 68: 586-594.

Stuckless, J.S.; Ericksen, R.L. 1976: Strontium iostopic geochemistry of the volcanic rocks and associated megacrysts and inclusions from Ross Island and vicinity, Antarctica. Contributions to Mineralogy and Petrology 58: 111-126.

Stuckless, J.S.; Irving, A.J. 1976: Strontium isotope geochemistry o the megacrysts and host basalts from southeast Australia. Geochimica et Cosmochimica Acta 40: 209-213.

Stuckless, J.S.; Miesch, A.T.; Goldich, S.S.; Weiblen, P.W. 1981: A (mode factor model for the petrogenesis of the volcanic rocks fr Ross Island and vicinity, Antarctica. Dry Valley Driiling Project. Antarctic Research Series 33: 257-280.

Stump, E.; Sheridan, M.F.; Borg, S.G.; Sutter, J.F. 1980: Early Miocene subglacial basalts, the East Antarctic Ice Sheet, and uplift of the Transantarctic Mountains. Science 207: 757-758.

Stuvier, M.; Denton, G.H.; Hughes, T.J. 1981: Late Wurm and Holocene history of the marine ice sheet in West Antarctica: A working hypothesis. In Denton, G.H.; Hughes, T.J. (Ed.) The Last Great Ice Sheets. Wiley, New York.

Stuvier, M.; Braziunas, T.F. 1985: Compilation of isotopic dates from Antarctica. Radiocarbon, American Journal of Science.

Sun, S.S.; Hanson, G.N. 1975: Origin of Ross Island basanitoids and limitations upon the hetrogeneity of mantle sources for alkali basalts and nephelinites. Contribution to Minealogy and Petrology 52: 77-106.

Sun, S.S.; Hanson, G.N. 1976: Rare earth element evidence for differentiation of McMurdo Volcanics, Ross Island, Antarctica. Contributions to Mineralogy and Petrology 54: 139-155.

Taylor, R.P.; Strong, D.F.; Fryer, B.J. 1981: Volatile control of contrasting trace element distributions in peralkaline granitic and volcanic rocks. Contributions to Mineralogy and Petrology 77: 267-271.

Taylor, S.R.; McClennan, S.M. 1985: The Continental Crust: its composition and evolution: an examination of the geochemical record preserved in sedimentary rocks. Blackwell Scientific.

Thompson, R.H. 1974: Some high-pressure pyroxenes. Mineralogical Magazine 39: 768-787.

Thomson, J.A. 1916: Report on the inclusions of the volcanic rocks of the Ross Archipalego (with Appendix by F. Cohen). Report of the

British Antarctic Expedition 1907-9, Geology - 2: 129-51.

Treves, S.B. 1968: Volcanic rocks of the Ross Island area. Antarctic Journal of the US 3: 108.

Treves, S.B. 1970: Volcanic rocks of the Ross Island area. Antarctic Journal of the US 5: 103

Tuttle, O.F.; Bowen, N.L. 1958: Origin of granites in the light of experimental studies in the system $NaAlSi_3O_8$-$KAlSi_3O_8$- SiO_2-H_2O. Geological society of America Memoir 74: 153

Upton, B.G.J. 1974: The alkaline province of south-west Greenland. Pp 221-238 in Sorenson, H.(Ed.) The Alkaline Rocks. Wiley.

Vanney, J.R.; Falconer, R.K.H.; Johnson, G.L. 1981: Geomorphology of the Ross Sea and adjacent provinces. Marine Geology 41: 73-102.

Veiten, K. 1980: The minerals of the volcanic rock association of the Siebengebirge. I. Clinopyroxenes 2. Variation of chemical composition of the clinopyroxenes (salites) in the course of crystallization. Neues Jabrabuch Mineral Abhandelung 140: 54-88.

Vinx, R.; Jung, D. 1977: Pargasitic-kaersutitic amphibole from a basanitic diatreme at the Rosenberge, north of Kassel (north Germany). Contributions to Mineralogy and Petrology 65: 135-142.

Wass, S.Y. 1979a: Multiple origins of clinopyroxenes in alkali basaltic rocks. Lithos 12: 115-132.

Wass, S.Y. 1979b: Fractional crystallization in the mantle of late stage kimberlitic liquid - evidence in xenoliths from the Kiama area, NSW, Australia. In Boyd, F.R.; Meyer, H.O.A. (Ed). The Mantle Sample: Inclusions in kimberlites and other volcanics. American Geophysical Union, Washington D.C. 266-373.

Wass, S.Y.; Henderson, P.; Elliot, C.J. 1980: Chemical hetrogeneity and metasomatism in the upper mantle: evidence from rare earth

and other elements in apatite-rich xenoliths in basaltic rocks from eastern Australia. Philosophical Transactions of the Royal Society of London 297: 222-246.

Wass, S.Y.; Rogers, N.W. 1980: Mantle metasomatism - precursor to continental alkaline volcanism. Geochimica et Cosmochimica Acta 44: 1811-1823.

Walker, D.; De Long, S.E. 1982: Soret separation of mid-ocean ridge basalt magma. Contributions to Mineralogy and Petrology 79: 231-240.

Watson, E.B. 1977: Partioning of manganese between forsterite and silicate liquids. Geochimica et Cosmochimica Acta 41: 1363-1374.

Watson, E.B. 1981: Apatite/liquid partition coefficients for the rare earth elements and Sr. Earth and Planetary Science Letters 56: 405-421.

Webb, P.N. 1979: Palaeogeographic evolution of the Ross Sector during the Cenozoic. Pp 206-213 in Nagata, T. (Ed.) Proceedings of the Seminar III on

Webb, P.N.; Wrenn, J. 1982: Late Cenozoic micropalaeontology and biostratigraphy of eastern Taylor Valley, Antarctica. Pp 1117-1122 in Craddock, C. (Ed.) Antarctic Geoscience. Third Symposium on Antarctic Geology and Geophysics. Madison University of Wisconsin Press.

Wilkinson, J.F.C. 1961: Some aspects of the calciferous amphiboles, oxyhornblende, kaersutite and barkevikite. American Mineralogist 46: 340-354.

Wilkinson, J.F.G. 1956: Clinopyroxenes of alkali olivine-basalt magma. American Mineralogist 42: 724-743.

Wilkinson, J.F.G. 1975: Ultramafic inclusions and high pressure megacrysts from a nephelinite sill, Nandewar Mountains, northeastern New South Wales, and their bearing on the origin of certain ultramafic inclusions in alkaline volcanic rocks. Contributions to Mineralogy and Petrology 51: 235-262.

Wilkinson, J.F.G. 1977: Petrgenetic aspects of some alkali volcanic rocks. Journal of the Royal Society of New South Wales 10: 117-138.

Williams, G.P. 1983: Improper use of regression equations in earth sciences. Geology 11: 195-197.

Williams, H.; McBirney, A.R. 1979: Volcanology. Freeman-Cooper. San Francisco.

Wilshire, H.G. 1984: Mantle metasomatism; the REE story. Geology 12: 395-398.

Windom, K.E.; Boettcher, A.L. 1980: Mantle metasomatism and the kimberlitic and lamprophyre association: evidence from an ecolgite nodule from Roberts Victor Mine, South Africa. Journal of Geology 88: 705-712.

Worner, G.; Beusen, S.M.; Duchateau, N.; Gijibels, R.; Schminke, H.-U. 1983: Trace element abundances and mineral/melt distribution coefficients in phonlites from thr Laacher See volcano (Germany). Contributions to Mineralogy and Petrology 84: 152-173.

Worner, G.; Viereck, L. in press: A.10 Mt Melbourne.In Le Masurier, W.E.; Thomson, J.W. (Ed.) Late Cenozoic Volcanoes of Antarctica and the Subantarctic Islands.

Wrenn, J.; Webb, P.N. 1982: Phsiographic analysis and interpretation of the Ferrar Glacier - Victoria Valley area, Antarctica. Pp 1091-1099 in Craddock, C. (Ed.) Antarctic Geoscience. Third

Symposium on Antarctic Geology and Geophysics. Madison University of Wisconsin Press.

Wright, A.C. 1978: A reconnaissance study of the McMurdo Volcanics northwest of Koettlitz Glacier. New Zealand Antarcic Record 1(2): 10-15.

Wright, A.C. 1979a: McMurdo Volcanics on Chancellor Ridge, Southern Foothills of the Royal Society Range, Central Victoria Land, Antarctica. New Zealand Geological Survey internal report. 22 p.

Wright, A.C. 1979b: McMurdo Volcanics at Foster Crater, Southern Foothills of the Royal Society Range, Central Victoria Land, Antarctica. New Zealand Geological Survey internal report. 19 p.

Wright, A.C. 1979c: McMurdo Volcanics northwest of Koettlitz Glacier, Antarctica. New Zealand Geological Survey internal report. 41 p.

Wright, A.C. 1980: Landforms of the McMurdo Volcanic Group, Southern Foothills of Royal Society Range, Antarctica. New Zealand Journal of Geology and Geophysics 23: 605-613.

Wright, A.C.; McIntosh, W.; Ellerman, P. 1983: Volcanic geology of Turks Head, Tryggve Point, and Minna Bluff, Southern Victoria Land. Antarctic Journal of the US 18:35.

Wright, A.C.; Kyle, P.R.; McInosh, W.C.; Klich, I. 1984: Geological field investigations of volcanic rocks at Mount Discovery and Mason Spur, McMurdo Sound. Antarctic Journal of the US 19:20.

Wright, A. C.; Kyle, P.R.; Moore, J.A.; Meeker, K. in press 1986: Geological investigations of volcanic rocks at Mount Discovery, Mount Morning, and Mason Spur, McMurdo Sound. Antarctic Journal of the US.

Yagi, K. 1966: The system acmite-diopside and its bearing on the stability relations of natural pyroxenes of the acmite-

hedenbergite-diopside series. American Mineralogist 51: 976-100(

Yagi, K.; Onuma, K. 1967: The join $CaMgSi_2O_6$ - $CaTiAl_2O_6$ and its bearing on the titanaugites. Journal of the Facilty of Science, Hokkaido University. Series IV, 13, 117-138.

Yagi, K; Hariya, Y; Onuma, K. 1975: Stability relation of Kaersutite. Journal of the Faculty of Science, Hokkaido University. Series IV. 16: 331-342.

Yoder, H.S.; Stewart, D.B.; Smith, J.R. 1957: Ternary feldspars. Carnegie Institute, Washington, Yearbook 56: 206-214.

APPENDIX 1 - TABLE OF SAMPLE LOCATIONS

Samples are listed in alpha-numeric order. The column headed "map" gives figure numbers of the map on which the sample location is shown.

Sample	Latitude	Longitude	Map	Description of Location
AW82046	78° 40.2'S	167° 10'E	3.10	Columnar-jointed flow tongue near base of cliff.
AW82049	78° 40.0'S	167° 13'E	3.10	Platy dyke near base of cliff.
AW82056	78° 40.1'S	167° 12'E	3.10	Trachytic auto-breccia near base of cliff.
AW82059	78° 40.1'S	167° 12'E	3.10	Basanitic flow overlying trachytic auto-breccia.
AW82072	78° 41.1'S	166° 57'E	3.10	Greenish dyke part way up slope.
AW82077	78° 40.3'S	167° 02'E	3.10	Lava flow interbedded with agglutinate on ridge above AW82072.
AW82078	78° 40.6'S	167° 05'E	3.10	Flow capping area to the east of cinder cone
AW82097B	78° 38.5'S	167° 13'E	3.10	Lobe in hyaloclastite at base of cliff.
AW82103	78° 31.8'S	166° 09'E	3.10	Platy dyke cutting base of spur.
AW82105	78° 31.8'S	166° 09'E	3.10	Clast in hyaloclastite breccia at base of cliff.
AW82109	78° 31.7'S	166° 10'E	3.10	Xenocryst-bearing flow part way up spur.
AW82110	78° 31.6'S	166° 10'E	3.10	Flow above AW82109.
AW82113A	78° 31.6'S	166° 10'E	3.10	Flow above AW82110, and just below pocket of distinctive yellow palagonitized breccia.
AW82116	78° 34.0'S	166° 38'E	3.10	Platy dyke in gully on north side of spur.
AW82124	78° 34.0'S	166° 38'E	3.10	Thin flow on west side of spur.
AW82140	78° 33.5'S	167° 08'E	3.10	Uppermost basanite flow above the northern side of Middle Bay.
AW82141	78° 33.2'S	167° 04'E	3.10	Phonolite flow to the west of AW82140.
AW82149	78° 33.5'S	167° 00'E	3.10	Glaciated basanite flow overlying phonolite flows.
AW82150	78° 33.8'S	166° 59'E	3.10	Phonolite flow further up ridge from AW8214

Sample	Latitude	Longitude	Map	Description of Location
AW82156	78° 34.0′S	167° 00′E	3.10	Northwest side of phonolite dome.
AW82163	78° 33.3′S	166° 53′E	3.10	Basanite flow capping hill.
AW82165	78° 33.3′S	166° 53′E	3.10	Phonolite underlying AW82163 on south side of hill.
AW82296	78° 41.8′S	167° 09′E	3.10	Lava pod in hyaloclastite breccia about 10 m above the glacial unconformity.
AW83401	78° 35.3′S	164° 34′E	3.5	Western end of outcrop at the edge of the ice shelf.
AW83410	78° 32.8′S	164° 38′E	3.5	Vesicular basanite dyke intruding trachytes.
AW83411	78° 32.7′S	164° 37′E	3.5	Trachyte flow at the north end of Chalcedony Island.
AW83413	78° 37.2′S	164° 01′E	3.5	Easternmost debris cone.
AW83417	78° 38.0′S	164° 04′E	3.5	Dyke forming the most prominent black spine.
AW83422	78° 34.3′S	164° 24′E	3.7	Porphyritic trachyte from lowermost outcrop on ridge.
AW83430	78° 33.8′S	164° 24′E	3.7	Medium-grained trachyte where ridge meets base of bluffs.
AW83435	78° 24.1′S	164° 53′E	3.13	Bomb from cracked-boot crater.
AW83438	78° 25.0′S	164° 41′E	3.13	Remnant of phonolite flow.
AW83441	78° 33.6′S	164° 27′E	3.6	Massive lava on southwest side of Dads Thumb
AW83445	78° 33.6′S	164° 27′E	3.6	Green-gray trachytic dyke intruding upper Dads Thumb spur.
AW83453	78° 33.5′S	164° 25′E	3.6	Obsidian bombs in bomb tuff.
AW83454	78° 33.3′S	164° 25′E	3.6	Aphyric pillowed basanite at the base of small bluff.
AW83471	78° 33.1′S	164° 24′E	3.5	Basanite flows at top of slope.
AW83480	78° 37.8′S	164° 07′E	3.5	Thick flow or sill in south wall at head of Seal Canyon.
AW83484	78° 33.6′S	164° 27′E	3.6	Medium-grained trachyte dyke following trend of earlier dyke at the base of the western end of Birthday Bluffs.

Sample	Latitude	Longitude	Map	Description of Location
AW83485	78° 33.6′S	164° 27′E	3.6	Earlier trachyte dyke intruded by AW83484.
AW83491	78° 33.5′S	164° 27′E	3.6	Pale greenish-gray dyke intruding altered breccia at the base of the bluffs above Dads Thumb.
AW83496	78° 33.5′S	164° 27′E	3.6	Late phase trachyte dyke cutting up through bluff, to the east of AW83491.
AW83499	78° 33.5′S	164° 27′E	3.6	4-m-wide trachyte dyke intruding platy lava and breccia on southwest side of gully in th middle of Birthday Bluffs.
AW83502A	78° 33.5′S	164° 28′E	3.6	Late, 2 - 4 m wide dyke cutting base of bluf just west of Dads Nose.
AW83503	78° 33.4′S	164° 27′E	3.6	Late, 1-m-wide dyke cutting southwest side o gully in the middle of Birthday Bluffs.
AW83508	78° 33.4′S	164° 26′E	3.6	Platy trachyte flow exposed at base of secon spur up slope, west end Birthday Bluffs.
AW83510	78° 33.3′S	164° 27′E	3.6	Greenish trachyte dyke cut by later pinkish dyke.
AW83511	78° 33.3′S	164° 27′E	3.6	Homolithic, trachyte cinder breccia.
AW83513	78° 33.3′S	164° 26′E	3.6	Late, pinkish dyke following trend parallel to the front of the bluffs.
AW83515	78° 33.2′S	164° 26′E	3.6	Thick, green trachyte flow forming the base of the fourth spur up slope.
AW83516	78° 33.2′S	164° 26′E	3.6	Obsidian from breccia tuff overlying AW83515.
AW83517	78° 33.2′S	164° 26′E	3.6	Thick trachyte flow overlying AW83516.
AW83519	78° 33.1′S	164° 32′E	3.8	Obsidian from lobe hyaloclastite at base of east end of Windscoup Bluff.
AW83520	78° 33.0′S	164° 32′E	3.8	Trachyte flow overlying thin lapilli tuff layer above east end of Windscoup Bluff.
AW83522	78° 33.0′S	164° 32′E	3.8	Trachyte dyke intruding AW83520.
AW83524	78° 33.0′S	164° 32′E	3.8	Wide trachyte dyke just east of AW83520.
AW83532	78° 32.6′S	164° 34′E	3.5	Platy trachyte flow to west of Diamictite Saddle.

Sample	Latitude	Longitude	Map	Description of Location
AW83533	78° 32.9′S	164° 29′E	3.6	Circular, platy trachyte intrusion at the base of east end of Grassham Bluffs.
AW83534	78° 32.8′S	164° 29′E	3.8	Lowermost trachyte flow cropping out through scree slope.
AW83536	78° 32.7′S	164° 29′E	3.8	Lowermost basanite flow overlying AW83534.
AW83538	78° 32.6′S	164° 29′E	3.5	Basanite bomb from Surprise Cones.
AW83543	78° 32.4′S	164° 35′E	3.5	Glaciated, aphyric basanite flow east of Diamictite Saddle.
AW83545	78° 32.5′S	164° 38′E	3.5	Columnar-jointed flow remnant forming Snow Petrol Peak.
AW83550	78° 33.9′S	164° 23′E	3.7	Upper hawaiite flow in Anniversary Gully.
AW83554	78° 33.9′S	164° 23′E	3.7	Aphyric basanite flow overlying tuff beds above AW83550.
AW83558	78° 33.4′S	164° 24′E	3.5	Thick, porphyritic basanite flow overlying series of thin flows above AW83554.
AW83559	78° 33.0′S	164° 31′E	3.8	Thick, vertical trachyte body at western end of Windscoup Bluff.
AW83567	78° 33.4′S	164° 28′E	3.6	Green, lobate brecciating lava intruding breccia at the base of Dads Nose.
AW83569	78° 33.4′S	164° 28′E	3.6	Brecciating intrusive trachyte body just west of Dads Nose.
AW83580	78° 33.7′S	164° 22′E	3.7	Base of Anniversary Bluff.
AW83581	78° 33.9′S	164° 22′E	3.7	Funnel-shaped dyke at the base of Anniversar Bluff.
AW83583	78° 32.3′S	164° 29′E	3.5	Basanite flow underlying cinder on the east side of Surprise Cones.
AW83607	78° 29.4′S	164° 24′E	3.5	Flow beneath unconformity near base of bluff
AW83614	78° 29.4′S	164° 23′E	3.5	Thick, non-brecciating dyke intruding hyaloclastite sequence at base of bluff.
AW83618	78° 29.4′S	164° 23′E	3.5	Trachyte flow wedge below the unconformity.
AW83642	78° 33.2′S	164° 27′E	3.6	Small outcrop of uppermost trachyte flow of the older sequence, at the head of Chute Glacier.

Sample	Latitude	Longitude	Map	Description of Location
AW83645	78° 33.1′S	164° 27′E	3.6	Flow in the middle of upper trachyte flow sequence at the head of Chute Glacier.
AW83647	78° 32.7′S	164° 27′E	3.5	West side of trachyte dome near rim.
AW83650	78° 32.4′S	164° 25′E	3.5	Small spatter cone at northwestern end of fissure.
AW83653	78° 32.7′S	164° 25′E	3.5	Trachyte flow forming small bluff.
AW83662	78° 33.5′S	164° 19′E	3.5	Thin basanite flow on ridge to the west of Peking.
AW83677	78° 33.2′S	164° 22′E	3.6	Uppermost trachyte flow from the older sequence at the west end of Birthday Bluffs.
AW83678	78° 33.2′S	164° 22′E	3.76	Thick trachyte flow unconformably underlying AW83677.
AW83689	78° 32.2′S	164° 23′E	3.5	Bomb from glaciated cone at the northwest end of the Surprise Cones fissure.
AW83701	78° 33.2′S	164° 27′E	3.6	Uppermost trachyte flow in older sequence at head of Chute Glacier.
AW83706	78° 32.8′S	164° 13′E	3.5	Northern side of India cinder cone complex.
AW83707A	78° 34.2′S	164° 10′E	3.5	Ledge at top of thick trachyte flow.
AW83709	78° 33.1′S	164° 28′E	3.6	Block from scree at base of Grassham Bluffs.
AW83710	78° 33.1′S	164° 28′E	3.6	Early trachyte intrusive body at base of bluff.
AW83711	78° 33.1′S	164° 28′E	3.6	Block from scree at base of bluff.
AW83712	78° 33.1′S	164° 28′E	3.6	Lowermost trachyte flow at base of bluffs.
AW84714	78° 22.4′S	163° 42′E	3.3	Saddle west of the Survey Knob.
AW84715	78° 31.2′S	163° 42′E	3.18	Survey station on south side of the Mt Morning caldera.
AW84718	78° 21.9′S	164° 59′E	3.14	Feldspar-phyric flow remnant in center of valley.
AW84719	78° 21.9′S	164° 59′E	3.14	Phonolite flow forming ridge west of AW84718.
AW84720	78° 21.9′S	165° 00′E	3.14	Lower phonolite flow in ridge to east of AW84718.

Sample	Latitude	Longitude	Map	Description of Location
AW84721	78° 21.9′S	165° 00′E	3.14	Upper phonolite flow in ridge east of AW84718.
AW84722	78° 21.9′S	165° 00′E	3.14	Phonolite dyke intruding AW84721.
AW84723	78° 21.7′S	165° 01′E	3.14	Basanite flow.
AW84725	78° 21.8′S	165° 02′E	3.14	Phonolite flow above basanite cinder cone.
AW84728	78° 21.9′S	165° 02′E	3.14	Basanite flow.
AW84733	78° 20.5′S	165° 05′E	3.14	Glaciated basanite flow at point where ridge divides.
AW84735	78° 20.0′S	165° 04′E	3.14	Phonolite xenolith in basanite flow on weste ridge below where ridge divides.
AW84738	78° 19.9′S	165° 06′E	3.14	Basanite flow in cirque between eastern and western forks of the ridge.
AW84740	78° 19.8′S	165° 07′E	3.14	Flow interbedded with agglutinate to northeast of AW84738.
AW84741	78° 21.5′S	165° 03′E	3.14	Glaciated remnant of phonolitic dome.
AW84742	78° 21.5′S	165° 03′E	3.14	Basanite flow overlying AW84741.
AW84744	78° 21.5′S	165° 05′E	3.14	Lower, aphyric phonolite flow on slopes of main dome.
AW84745	78° 21.4′S	165° 05′E	3.14	Cavernously weathered phonolite dome to the north of AW84744.
AW84748	78° 21.1′S	165° 07′E	3.14	Thin basanite flow interbedded with agglutinate to the northeast of AW84745.
AW84749	78° 21.5′S	165° 09′E	3.14	Thick basanite sill or flow underlying cinder cone.
AW84750	78° 21.4′S	165° 07′E	3.14	Basanite dyke intruding phonolite to the east of AW84745.
AW84753	78° 22.1′S	165° 00′E	3.14	Aphyric hawaiite flow.
AW84754	78° 22.2′S	165° 00′E	3.14	Pumice lapilli in subcrop.
AW84756	78° 22.2′S	165° 02′E	3.14	Glaciated bomb and cinder deposit on rim of summit crater.
AW84758	78° 21.7′S	165° 01′E	3.14	Small outcrop of feldspar-phyric lava.

Sample	Latitude	Longitude	Map	Description of Location
AW84761	78° 21.9′S	165° 00′E	3.14	Inclusions in phonolite flow AW84720.
AW84763	78° 21.1′S	164° 59′E	3.14	Thick basanite flow on bench north of AW84720.
AW84768	78° 40.2′S	167° 13′E	3.10	Basanite flow underlying the unconformity a base of Southeast Cape section.
AW84777	78° 39.9′S	167° 11′E	3.10	Lowermost of the green phonolite flows near the middle of the Southeast Cape section.
AW84791	78° 40.7′S	167° 04′E	3.10	Platy trachyte dome below the unconformity.
AW84796	78° 40.2′S	167° 10′E	3.10	Flow lenses below the unconformity.
AW84797	78° 40.2′S	167° 10′E	3.10	Flow tongue embedded in palagonitized sediment associated with the unconformity.
AW85803	78° 33.5′S	164° 26′E	3.6	Early dyke truncated by local unconformity, near base of west end of Birthday Bluffs.
AW85809	78° 33.4′S	164° 27′E	3.6	Trachyte dyke cutting flow AW83508 at head embayment.
AW85818	78° 33.3′S	164° 26′E	3.6	Trachyte flow at base of third spur up on w of Birthday Bluffs.
AW85829	78° 33.1 S	164° 22′E	3.6	Massive trachyte flow on ridge at top of we of Birthday Bluffs.
AW85830	78° 33.1′S	164° 29′E	3.6	Trachyte dyke intruding trachytic agglutina at far eastern end of the base of Grassham Bluff.
AW85831	78° 33.1′S	164° 29′E	3.6	Thin trachyte flow interbedded with agglutinate.
AW85833	78° 33.1′S	164° 29′E	3.6	Thick green flow at base of east end of bluffs.
AW85837	78° 32.8′S	164° 28′E	3.6	Platy trachyte flow overlying trachyte agglutinate and tuff in the upper part of Grassham Bluffs.
AW85839	78° 32.8′S	164° 28′E	3.6	Aphyric basanite flow above the older trachyte sequence.
AW85847	78° 34.2′S	164° 23′E	3.7	Base of trachyte flow cascading south from Anniversary Bluff.
AW85850	78° 34.2′S	164° 23′E	3.7	Inclusion-bearing dyke cutting AW85847.

Sample	Latitude	Longitude	Map	Description of Location
AW85851	78° 34.1′S	164° 23′E	3.7	Late dyke intruded parallel to the front of Anniversary Bluff.
AW85860	78° 33.2′S	164° 25′E	3.6	Platy trachyte flow exposed on the eastern side of Green Island.
AW85861	78° 33.2′S	164° 25′E	3.6	Clast from breccia overlying AW86860.
AW85863	78° 33.2′S	164° 25′E	3.6	Aphyric lava flow east of dyke swarm.
AW85865	78° 33.4′S	164° 26′E	3.6	Flow forming second spur up at west end of Birthday Bluffs.
AW85869	78° 33.3′S	164° 28′E	3.6	Wide green trachyte dyke at tip of Dads Nose.
AW86881	78° 23.6′S	165° 29′E	3.13	Small phonolite dome.
AW86883	78° 21.5′S	165° 40′E	3.13	Phonolite dome.
AW86887	78° 26.1′S	165° 38′E	3.10	Cinder cone on ridge.
AW86889	78° 16.6′S	165° 08′E	3.13	Glaciated phonolite flow surface.
AW86891	78° 18.4′S	165° 09′E	3.13	Flow in crater of basanite cinder cone.
AW86895	78° 22.3′S	165° 14′E	3.13	Xenoliths from phonolite outcrop in glacier.
AW86898	78° 22.3′S	165° 07′E	3.14	Basanite flow derived from high up on the main dome.
AW86899	78° 22.4′S	165° 05′E	3.14	Benmoreite flow just below contact with overlying phonolite flow.
AW86901	78° 22.5′S	165° 06′E	3.14	Middle of the outcrop of hawaiite flows.
AW86909	78° 22.3′S	165° 09′E	3.14	Basanite flow forming bench.
AW86910	78° 22.3′S	165° 08′E	3.14	Tephrite flow cascading off higher slopes.
AW86922	78° 22.0′S	165° 05′E	3.14	Small ridge of hawaiite.
AW86943	78° 21.4′S	165° 19′E	3.14	Volcanic neck exposed by glacial erosion.
AW86944	78° 21.4′S	165° 17′E	3.14	Basanite flow infilling crater.
AW86947	78° 22.4′S	164° 50′E	3.14	5-m-thick, platy flow.
AW86950	78° 22.2′S	164° 55′E	3.14	Small ridge of feldspar-phyric tephriphonolite on northeast side of mounta

Sample	Latitude	Longitude	Map	Description of Location
AW86965A	78° 21.9′S	164° 51′E	3.14	Phonolite xenoliths from western side of phonolite flow
AW86970	78° 21.5′S	164° 56′E	3.14	Small phonolite dome.
AW86976	78° 22.6′S	163° 48′E	3.4	Thick, north-south trending dyke of porphyritic trachyte.
AW86978	78° 22.7′S	163° 48′E	3.4	Platy green trachyte dyke.
AW86986	78° 22.7′S	163° 47′E	3.4	4-m-wide trachyte dyke on south side of larg knob.
AW86988	78° 22.7′S	163° 47′E	3.4	Glassy dyke exposed in saddle behind large knob.
AW86999	78° 23.0′S	163° 45′E	3.3	Inclusion from flow at top of bluff.
AW86006	78° 22.6′S	163° 51′E	3.4	Relatively late phase green trachyte dyke cutting along southeast side of ridge.
AW86008	78° 22.6′S	163° 51′E	3.4	Massive, glomeroporphyritic trachyte predating dyke intrusion.
AW86012	78° 22.6′S	163° 46′E	3.3	Top of basanite flow sequence north of large knob.
AW86013	78° 22.7′S	163° 46′E	3.3	Bottom of basanite flow sequence north of large knob.
AW86016	78° 22.4′S	163° 47′E	3.3	Trachyandesite flow forming small bluff on south side of dome.
AW86018	78° 22.4′S	163° 49′E	3.4	Oldest dyke on lower end of Castle Ridge.
AW86020	78° 22.4′S	163° 49′E	3.4	Altered dyke on lower end of Castle Ridge.
AW86021	78° 22.4′S	163° 49′E	3.4	Platy green trachyte intrusion on lower end of Castle Ridge.
AW86025	78° 22.5′S	163° 47′E	3.3	East side of crater in trachyte dome.
AW86032	78° 22.8′S	163° 43′E	3.3	Platy flow exposed in gully floor.
AW86033	78° 22.3′S	163° 46′E	3.3	Basanite flow above trachyte dome.
AW86034	78° 22.4′S	163° 43′E	3.3	Southeast side of Survey Knob.
AW86035	78° 22.4′S	163° 42′E	3.3	South side of Survey Knob.
AW86036	78° 22.4′S	163° 42′E	3.3	Saddle on west side of Survey Knob.

Sample	Latitude	Longitude	Map	Description of Location
AW86037	78° 22.4'S	163° 41'E	3.3	Top of spur forming the west side of crater.
AW86041	78° 21.4'S	163° 46'E	3.3	Top of ridge.
AW86042	78° 21.1'S	163° 06'E	3.3	Eroded trachyte dome exposed in bluff.
AW86057	78° 23.5'S	164° 06'E	3.18	Lava flow fed by funnel-shaped dyke.
AW86058	78° 22.3'S	163° 59'E	3.18	Basanite cone in middle of glacier.
AW86059	78° 23.1'S	163° 53'E	3.18	Dyke on east side of cinder cone.
AW86061	78° 23.9'S	163° 51'E	3.3	Inclusion-rich flow.
AW86063	78° 23.9'S	163° 50'E	3.3	Basanite plug west of AW86061.
AW86070	78° 23.0'S	163° 50'E	3.3	Small dyke intruding agglutinate.
AW86072	78° 21.8'S	163° 46'E	3.3	Basanite flow at top of slope.
AW86075	78° 21.9'S	163° 46'E	3.3	Gray dyke part way up slope.
AW86088	78° 18.2'S	163° 26'E	3.20	Small dyke intruding hyaloclastite.
AW86089	78° 18.6'S	163° 30'E	3.20	Foot of aphyric flow cascading off ridge.
AW86094	78° 19.3'S	163° 24'E	3.20	Bomb from postglacial cinder cone.
AW86095	78° 19.7'S	164° 24'E	3.20	Flow to the north of AW86094.
AW86096	78° 28.9'S	164° 00'E	3.18	Flow in agglutinate atop small ridge.
AW86098	78° 27.0'S	163° 40'E	3.18	Aphyric tephrite flow.
AW86100	78° 19.9'S	165° 19'E	3.14	Phonolite flow.
AW86101	78° 19.3'S	165° 29'E	3.13	Basanite flow on southwest side of glaciated cinder cone.
AW86102	78° 20.9'S	165° 27'E	3.13	Basanite with numerous crustal xenoliths.
AW86119	78° 24.7'S	163° 45'E	3.18	Basanite shelf above Riviera Ridge.
AW86120	78° 27.1'S	163° 32'E	3.18	Basanite flow overlying phonolite.
AW86121	78° 27.1'S	163° 32'E	3.18	Phonolite flow from dome higher on mountain.
AW86122	78° 27.9'S	163° 26'E	3.18	Glassy ?phonolite overlying thick phonolite flow.
AW86123	78° 27.9'S	163° 26'E	3.18	Thick phonolite flow underlying AW86122.

Sample	Latitude	Longitude	Map	Description of Location
AW86124	78° 29.7′S	163° 23′E	3.18	Phonolite flow.
AW86127	78° 29.3′S	163° 34′E	3.18	Phonolite dome.
AW86128	78° 29.5′S	163° 49′E	3.18	Phonolite flow.
W84-2	78° 37.4′S	167° 12′E	3.10	Trachyte forming the Gumdrop.
W84-3	78° 34.5′S	167° 12′E	3.10	Thick green trachyte flow above glacial unconformity near the Gum Drop.
W8413-PM	78° 34.5′S	167° 09′E	3.10	Massive trachyte flow 100 m below unconformity at base of Middle Bay Section.

APPENDIX 2 - K-AR AGE DATING:

SAMPLE PREPARATION AND ANALYTICAL TECHNIQUES

Samples were chipped using a hammer and steel plate, then ground in a steel disc mill and sieved to give a 180 - 250 micron (60 - 80 mesh) size fraction.

Analyses were performed at the Ohio State University K-Ar dating laboratory under the supervision of Dr K. Foland, and at the University of Texas K-Ar dating laboratory under the supervision of Dr F. McDowell, as indicated in Table 4.1.

Analytical methods follow the procedure of Dalrymple and Lanphere (1969). K was analysed by flame photometer using a Li internal standard method and 200 mg sample aliquots. ^{40}Ar and ^{36}Ar were determined by isotope dilution using ^{38}Ar as a spike and 500 g sample aliquots. Unlike Dalrymple and Lamphere's method, the extraction line in the Ohio State University facility feed directly into the mass spectrometer, after providing for the division of the gas into three separate portions each of which was analsyed separately.

The method of age calculation is discussed in Dalrymple and Lamphere (1969) and Faure (1977). Average K values determined from multiple analyses on separate sample aliquots were used in the calculation of each age determination (Table 4.1). Uncertainties associated with determinations made at Ohio State University were estimated at the 68% confidence level for each $^{40}Ar^{*}$ measurement. The uncertainties associated with determinations made at the University of Texas were assigned for the average age determination only, and reflect not only the reproducibility of determinations made in this study, but also other reproducibility standards set by the laboratory.

The following constants were used in the age calculations (Steiger and Jager, 1977):

$\lambda(^{40}K_{\beta-}) = 4.962 \times 10^{-10} y^{-1}$

$\lambda(^{40}Ke) + \lambda'(^{40}Ke) = 0.581 \times 10^{-10} y^{-1}$

$^{39}K = 93.2581$ atom%

$^{40}K = 0.01167$ atom%

$^{41}K = 6.7302$ atom%

$^{40}Ar/^{36}Ar$ atmospheric = 295.5

With the exception of AW82097B and AW83653, samples were fresh and showed no obvious reasons why K-Ar ages should be erroneous. AW82097B and AW83653 both have minor growth of cryptocrystalline secondary minerals. Dates determined for these samples are considered to be minimum ages.

APPENDIX 3 - PETROGRAPHIC DESCRIPTIONS

The following petrographic descriptions are listed in alpha-numeric order. Phenocryst and groundmass minerals are described in decreasing order of abundance within each sample description.

AW82046

Seriate, euhedral - subhedral, zoned, pale brown augite (up to 1.4 mm across) may have salite cores which are commonly sieve-textured with inclusions of opaque minerals; microphenocrysts of augite are commonly glomeroporphyritic forming clots (up to 2.0 mm across) sometimes with olivine, which in one clot occupies the core area; seriate, euhedral - subhedral, partly iddingsitized, olivine (up to 1.2 mm across contains opaque inclusions; single subhedral kaersutite xenocryst (0.3 mm long) has wide opaque alteration rim; single plagioclase phenocryst (0.5 mm across) has sieve-textured core. Interstitial groundmass of plagioclase microlites, augite, iddingsitized olivine and opaque minerals.

AW82049

Euhedral to rounded, greenish brown kaersutite microphenocrysts (up to 0.3 mm across) rarely with altered augite core, in various stages of replacement by spongy opaque mineral aggregates which are preferentially developed along the kaersutite cleavage planes. Groundmass of trachytic-textured plagioclase microlites (up to 0.4 mm long), opaque minerals, iddingsitized olivine, and scattered fawn augite, with interstitial cryptocrystalline devitrified glass. Widespread calcite and later zeolite infilling of the numerous vesicles.

AW82056

Subhedral - anhedral kaersutite phenocrysts and pseudomorphs (0.2 - 1.2 mm across) rimmed and replaced by spongy aggregates of opaque minerals and iddingsitized olivine, with apatite inclusions preserved; rare subhedral pale green salite phenocrysts (0.1 - 0.7 mm across) may contain apatite inclusions; seriate, euhedral plagioclase (up to 1.2 mm across) contain large glass and devtrified glass inclusions in

the core zone; seriate, euhedral to skeletal opaque minerals (up to 0.3 mm across). Groundmass of trachytic-textured plagioclase to alkali feldspar microlites, scattered iddingsitized olivine and opaque minerals, and interstitial pale brown glass. Minor secondary calcite and zeolite.

AW82059

Seriate, euhedral - subhedral and embayed pale brown augite (up to 2.5 mm across) with opaque minerals, apatite and iddingsitized olivine inclusions especially in the core, typiacally intergrown with subordinate olivine and opaque minerals; seriate euhedral - subhedral olivine (up to 1.5 mm across) is commonly partly iddingsitized; irregular opaque phenocrysts (0.2 - 1.0 mm across); rare phenocrysts of kaersutite (0.2 - 1.0 mm across) have augite and olivine inclusions and are not in reaction relationship with opaque minerals; anhedral plagioclase phenocrysts (0.1 - 1.8 mm across) are sieve-textured with tiny clinopyroxene and cryptocrystalline inclusions and patchy calcite alteration, and may be intergrown with augite. Groundmass of plagioclase microlites, augite, partly iddingsitized olivine and opaque minerals, with interstitial dark brown glass containing strings of minute skeletal opaque minerals. Secondary calcite infills vesicles.

AW82072

Trachytic-textured, seriate and glomeroporphyritic, euhedral plagioclase (up to 0.8 mm across) with patchy opaque mineral and clinopyroxene inclusions in the cores of larger crystals; seriate, euhedral kaersutite (up to 1.2 mm across) contain opaque inclusions, are commonly twinned, may have a rounded core, and may be intergrown with plagioclase; scattered, seriate, zoned, pale brown to pale green pyroxene (up to 0.5 mm across); seriate skeletal opaque minerals (up to 0.3 mm across). Intergranular groundmass of plagioclase microlites, salite, kaersutite, and opaque minerals.

AW82077

Subhedral - anhedral pseudomorphs of kaersutite (0.1 - 0.2 mm across) with

kaersutite cores occasionally preserved, comprise aggregates of opaque minerals, clinopyroxene and feldspar, with large apatite inclusions preserved; subhedral to embayed plagioclase (0.3 - 1.0 mm across) and alkali feldspar (0.3 - 0.6 mm across) commonly rimmed by inclusion-rich alkali feldspar; rounded apatite microphenocrysts (0.1 - 0.2 mm across); euhedral, slightly iddingsitized olivine and pale brown augite microphenocrysts (up to 0.2 mm across). Groundmass of alkali feldspar microlites, iddingsitized olivine, granular salite and opaque minerals.

AW82078

Glomeroporphyritic clots (up to 2.0 mm across) and subhedral microphenocrysts (0.2 - 0.6 mm across) of alkali feldspar; euhedral -subhedral plagioclase microphenocrysts (0.2 - 0.6 mm across); scattered, seriate, subhedral kaersutite (up to 0.3 mm across) containing apatite inclusions, may form small clots. Tracytic-textured groundmass of plagioclase microlites with interstitial alkali feldspar enclosing opaque minerals. Minor patches of devitrified glass.

AW82097B

Euhedral plagioclase glomerocrysts (0.1 - 0.8 mm across) form clots (0.3 - 2.0 mm across) which rarely include minor salite and opaque minerals; euhedral - subhedral kaersutite glomerocrysts (0.1 - 0.8 mmacross) contain apatite and opaque inclusions and form separate clots (0.2 - 2.0 mm across) with minor opaque minerals and salite; rare subhedral pale brown augite to pale green clinopyroxene microphenocrysts (0.2 - 0.5 mm across) may be intergrown with opaque minerals; irregularly shaped opaque microphenocrysts (0.05 - 0.2 mm across). Groundmass of plagioclase microlites, iddingsitized olivine, opaque minerals and minor apatite in fawn glass enclosing a network of tiny pyroxene needles. Some brown staining along fractures in plagioclase glomerocrysts and minor calcite veining.

AW82103

Aphyric trachytic-textured plagioclase, skeletal opaque minerals, iddingsitized olivine, and occasional augite. Minor secondary calcite.

AW82105

Seriate, euhedral olivine (up to 0.5 mm across) partially iddingsitized with some serpentinization, may contain opaque inclusions especially near crystal margins; seriate, zoned, pale brown augite (up to 2.5 mm across) may have inclusions of rounded olivine and small opaque minerals. Intergranular groundmass of plagioclase microlites and partly iddingsitized olivine with tiny interstial augite and opaque minerals. Secondary calcite lines vesicles.

AW82109

Similar to AW82103, but contains anhedral and embayed kaersutite phenocrysts and pseudomorphs (0.2 - 1.0 mm across) rimmed or replaced by spongy aggregates of opaque minerals, iddingsitized olivine, and plagioclase; and seriate, euhedral pale brown augite (up to 1.0 mm across) which may contain olivine, opaque minerals and tiny fluid inclusions, and which are commonly intergrown in small clots that may include partially iddingsitized olivine.

AW82110

Seriate, subhedral, pale brown augite glomerocrysts and phenocrysts (up to 0.6 mm across) commonly intergrown in small clots (up to 1.0 mm across); single anhedral kaersutite (0.2 mm across) rimmed by an aggregate of opaque minerals and cryptocrystalline material; trachytic-textured microphenocrysts of euhedral plagioclase, partially iddingsitized olivine, and irregularly shaped opaque minerals. Fine grained to cryptocrystalline intergranular groundmass includes plagioclase microlites, tiny opaque minerals, iddingsitized olivine and clinopyroxene. Secondary calcite infills vesicles.

AW82113A

Seriate, larger rounded and embayed, to smaller euhedral, slightly iddingsitized olivine phenocrysts (up to 1.1 mm across); seriate, euhedral - subhedral pale brown augite phenocrysts (up to 0.7 mm across) occasionally have sieve-textured salite

cores; rare rounded anorthoclase xenocrysts (0.4 - 0.8 mm across). Intergranular groundmass of plagioclase microlites, granular augite, iddingsitized olivine and opaque minerals.

AW82116

Similar to AW82110, except for the lack of augite and kaersutite phenocrysts.

AW82124

Very similar to AW82105 except that serpentinization of olivine predominates over iddingsitization, and the groundmass is finer grained.

AW82140

Similar to AW82046 except for the lack of plagioclase phenocrysts, the greater variation in clinopyroxene from augite to pinkish brown titanaugite, the presence of anhedral opaque microphenocrysts (up to 0.2 mm across), and the non-trachytic groundmass.

AW82141

Subhedral - anhedral kaersutite phenocrysts (0.2 - 0.5 mm across) with rims of spongy opaque minerals (0.05 - 0.1 mm across) altered cores, and inclusions of opaque minerals, apatite, feldspar and augite; rare, suhedral to embayed augite phenocrysts, may be overgrown by rims of spongy salite and opaque minerals; rounded, sieve-textured plagioclase overgrown by euhedral alkali feldspar. Groundmass of trachytic-textured alkali feldspar microlites, with interstitial opaque oxides, salite, and amorphous areas of iron staining.

AW82149

Euhedral - subhedral pale brown augite phenocrysts (0.1 - 1.5 mm across) and glomerocrysts in clots (up to 0.5 mm across) with subordinate plagioclase and kaersutite, opaque inclusions are common especially in crystals with salite cores; subhedral kaersutite phenocrysts (0.2 - 0.8 mm across) rimmed by aggregates of opaque minerals, contain apatite and opaque inclusions , and may overgrow a core of rounded

or embayed augite; euhedral - subhedral plagioclase phenocrysts (0.2 - 1.2 mm across) may form glomeroporphyritic clots with kaersutite, have cores in various stages of alteration, and may be rimmed by alkali feldspar. Trachytic-textured groundmass of plagioclase microlites with interstitial alkali feldspar and pale brown glass enclosing iddingsitized olivine, tiny pyroxene needles and opaque minerals.

AW82150

Subhedral - anhedral anorthoclase and alkali feldspar phenocrysts (0.4 - 1.5 mm across) may be intergrown in monomineralic clots, contain large opaque and hedenbergite inclusions and a cloudiness due to crytocrystalline inclusions; rare, subhedral plagioclase phenocrysts (0.4 - 1.0 mm across) contain small hedenbergite and cryptocrystalline inclusions; euhedral - subhedral opaque pseudomorph of kaersutite (0.1 - 0.8 mm across) with occasional kaersutite cores preserved; rare, broken pale brown augite microphenocrysts (0.4 mm across) with green rims. Groundmass of alkali feldspar, hedenbergite and small opaque minerals.

AW82156

Rare, subhedral, partially iddingsitized olivine phenocrysts and glomerocrysts (0.2 - 0.4 mm across) may be intergrown with augite, and may be in reaction relationship with opaque minerals; euhedral pale brown augite phenocrysts (0.2 - 0.4 mm across) with salite cores; rare anhedral titanaugite phenocrysts (0.2 - 1.0 mm across) rimmed with opaque minerals; euhedral - subhedral kaersutite phenocrysts opaque pseudomorphs (0.2 - 2.0 mm across) may contain large feldspar inclusions, and are rimmed by opaque minerals; rare, euhedral plagioclase phenocryst with overgrowths of alkali feldspar, contain large inclusions of apatite and secondary opaque minerals. Trachytic-textured groundmass of plagioclase and salite microlites and interstitial alkali feldspar enclosing tiny sodic pyroxenes, iddingsitized olivine, and opaque minerals.

AW82163

Seriate, subhedral to rounded olivine phenocrysts (up to 4.0 mm across) with

opaque inclusions in rims; minor, seriate, euhedral - anhedral augite to titanaugite (up to 1.0 mm across); rare, euhedral - anhedral plagioclase phenocrysts (up to 1.0 mm across); anhedral opaque minerals (up to 0.2 mm across). Trachytic-textured groundmass of plagioclase microlites and partially iddingsitized olivine, with interstitial sodic pyroxene, opaque minerals, and alkali feldspar. Some incipient brown zeolite alteration in groundmass, which also partially infills vesicles.

AW82165

Euhedral - anhedral opaque to spongy opaque pseudomorphs of kaersutite phenocrysts (0.2 - 0.4 mm across). Trachytic-textured groundmass of sheaves of alkali feldspar enclosing opaque minerals, with interstitial crystals and crystal aggregates of hedenbergite.

AW82296

Seriate, euhedral to skeletal olivine (up to 2.5 mm across) with minor iddingsitization, and opaque inclusions near the margins; also augite overgrowths of rounded and deeply embayed olivine phenocrysts; seriate, euhedral - subhedral pale brown augite (up to 2.3 mm across) commonly intergrown in small clots with subordinate olivine and/or opaque minerals, larger crystals typically zoned; seriate, anhedral opaque minerals (up to 0.2 mm across). Groundmass of plagioclase microlites, augite, partially iddingsitized olivine and opaque minerals, with interstitial, unaltered brown glass. Secondary calcite and zeolites line vesicles.

AW83401

Seriate, subhedral - anhedral, pale brown augite (up to 2.3 mm across) commonly intergrown in clots, sometimes with olivine, contains opaque inclusions and cryptocrystalline inclusions that impart cloudiness; seriate, euhedral - subhedral olivine (up to 1 mm across) may form clots, contains opaque inclusions and cryptocrystalline inclusions that impart cloudiness, minor iddingsite alteration; seriate euhedral plagioclase (up to 0.5 mm across) may have rounded core zone. Single subhedral

plagioclase xenocryst (3 mm across) has rounded core outlined by sieve-textured cryptocrystalline zone, and overgrown by plagioclase. Very vesicular, dark groundmass of plagioclase, augite, olivine, opaque and cryptocrystalline minerals.

AW83410

Moderately coarse grained, subophitic, aphyric trachyte, comprising plagioclase, titanaugite, opaque minerals, and interstitial alkali feldspar. Secondary calcite infills vesicles, and a cryptocrystalline greenish brown ?zeolite and calcite are pervasive.

AW83411

Scattered euhedral alkali feldspar phenocrysts (0.7 - 1.0 mm across). Vesicular groundmass of dominantly alkali feldspar microlites, tiny interstitial aggregates of aegerine augite and irregular areas of late stage aenigmatite. Patches of incipient ?epidote alteration and fine grained epidote-calcite replaces areas of interstitial glass. Aggregates of a secondary, acicular opaque mineral (?pseudobrookite) always occurs in close proximity to aenigmatite.

AW83413

Seriate, subhedral to embayed olivine (up to 1.0 mm across) may contain small opaque inclusion; seriate, euhedral, pale brown augite phenocrysts and glomerocrysts (up to 0.4 mm across) may contain opaque inclusions and rarely have greenish cores packed with aggregates of opaque replacement minerals; rounded opaque phenocrysts (up to 0.4 mm across) may be kaersutite pseudomorphs; one broken crystal of kaersutite (0.5 mm across). Rounded and broken plagioclase xenocryst pseudomorphs (0.4 - 1.2 mm across) comprising augite and opaque mineral aggregates overgrown by fawn augite. Vesicular, fine grained to cryptocrystalline groundmass of plagioclase microlites, augite, opaque minerals and olivine.

AW83417

Strongly trachytic-textured, vesicular, aphyric basanite, with groundmass of plagioclase, titanaugite, opaque minerals and iddingsitized olivine. In one 1-cm-

thick flow band elongate titanaugite crystals (up to 0.5 mm long) have grown perpendicular to the trachytic texture as though they fill tension gashes.

AW83422

Alkali feldspar phenocrysts (0.4 - 0.8 mm across) are intergrown with opaque pseudomorphs of kaersutite, some of which still contain apatite inclusions. Trachytic-textured groundmass of alkali feldspar, small areas of tiny sodic pyroxene and aenigmatite, which appears to have been nucleated by earlier iron-rich mineral. Aenigmatite also fills vesicles and penetrates adjacent crystal boundaries. Later secondary calcite and fibrous zeolite infills central portions of vesicles. Patches of incipient secondary calcite are also present in the groundmass.

AW83430

Subhedral phenocrysts (0.8 - 1.2 mm across) and euhedral microphenocrysts (~0.2 mm across) of alkali feldspar. Coarse, trachytic-textured groundmass of alkali feldspar, with interstitial aenigmatite, aegerine augite, and rare arfvedsonite. Minor patches of secondary calcite.

AW83431

Rare, euhedral alkali feldspar phenocrysts (1.2 - 1.4 mm across) contain aenigmatite inclusions in rims. Groundmass of trachytic-textured sheaves of alkali feldspar microlites with interstitial aggregates of tiny aegerine-augite and cryptocrystalline material, scattered aenigmatite grains, and large patches of aenigmatite developed in vesicles and along partings.

AW83435

Very vesicular, aphyric basanite with euhedral microphenocrysts (up to 0.3 mm across) of plagioclase, olivine, augite and opaque minerals. Trachytic-textured groundmass of alkali feldspar, salite, opaque minerals, olivine, and interstitial ?nepheline.

AW83438

Seriate, euhedral alkali feldspar phenocrysts and glomerocrysts (up to 1.0 mm across) may contain small hedenbergite inclusions; anhedral kaersutite phenocrysts (up to 1.0 mm across) contain apatite inclusions and have dense opaque rims; euhedral - anhedral plagioclase phenocrysts (0.4 - 0.8 mm across) may contain numerous large kaersutite inclusions, and/or be rimmed by alkali feldspar. Groundmass of plagioclase and alkali feldspar microlites, hedenbergite and opaque minerals.

AW83445

Aphyric trachyte, comprising coarse, trachytic-textured sheaves of plagioclase, aegerine-augite, and rare arfvedsonite, with interstitial aenigmatite.

AW83454

Euhedral to rounded olivine phenocrysts (0.5 - 2.0 mm across) have variable iddingsitization; subhedral to embayed pale brown augite phenocrysts (0.3 - 1.0 mm across). Subhedral to rounded plagioclase and anorthoclase xenocrysts (up to 1.4 mm across) may be associated with intergrowths of euhedral plagioclase. Trachytic-textured groundmass of plagioclase microlites, with interstitial olivine, opaque minerals, and augite. Widespread development of greenish-brown zeolite, and secondary calcite infilling vesicles.

AW83471

Seriate, euhedral olivine (up to 1.6 mm across) commonly intergrown in monomineralic clots (typically 0.5 - 1.0 mm across) may contain opaque inclusions; two rounded pale brown augite xenocrysts (2.0 - 2.5 mm across) may have brown and opaque alteration minerals, especially along cleavage planes; one subhedral aegerine-augite xenocryst (1.0 mm across); seriate, opaque minerals (up to 0.4 mm across) may be dense or form spongy aggregates, one of which has a rounded core of a dark brown isotropic mineral. Fine grained groundmass of scattered plagioclase and alkali feldspar microlites, tiny opaque minerals, iddingsitized olivine and partly devitrified, interstitial brown glass.

AW83480

Similar to AW83454, except that the augite trends to pinkish titanaugite, no anorthoclase xenocrysts are present, and the groundmass is finer grained, and lacks the growth of secondary calcite.

AW83484

Rare, euhedral alkali feldspar phenocrysts (0.2 - 0.6 mm across). Medium to coarse grained groundmass of trachytic-textured plagioclase microlites with interstitial aenigmatite, minor aegerine-augite, and rare arfvedsonite. Aenigmatite and aegerine-augite may be intimately intergrown. Aenigmatite also lines vesicles, predating crystallization of a colorless fibrous zeolite.

AW83485

Rare, euhedral - subhedral alkali feldspar phenocrysts (0.3 - 0.4 mm across). Groundmass lacks arfvedsonite, has more aegerine-augite and is finer grained, but is otherwise similar to AW83484.

AW83491

Aphyric trachyte comprising a fine grained groundmass of felted alkali feldspar microlites, aegerine-augite and aenigmatite, with interstitial areas of alkali feldspar ophitically enclosing tiny aegerine-augite and aenigmatite grains. An opaque acicular mineral (?pseudobrookite) is commonly associated with aegerine-augite. Aenigmatite also occurs in veinlets, and in association with fine grained secondary calcite.

AW83496

Euhedral - subhedral plagioclase and alkali feldspar phenocrysts and glomerocrysts (0.2 - 0.7 mm across) commonly have narrow alkali feldspar rims containing aenigmatite inclusions. Groundmass comprises sheaves of alkali feldspar and aegerine-augite, with irregular shaped areas of predominantly interstitial aenigmatite. Aenigmatite also partially infills vesicles.

AW83499

Aphyric trachyte, comprising felted alkali feldspar and aegerine-augite microlites, and minute interstitial grains of aegerine-augite and interstitial aenigmatite in areas up to 0.2 mm across.

AW83502A

Subhedral - anhedral alkali feldspar phenocrysts and glomerocrysts (up to 1.2 mm across). Groundmass lacks arfvedsonite and is coarser grained that AW83441, but is otherwise similar.

AW83503

Euhedral - subhedral alkali feldspar phenocrysts (0.1 - 0.7 mm across) may have hazy plagioclase twinning, and small opaque and sodic pyroxene inclusions; euhedral salite microphenocrysts (0.05 - 0.15 mm across) may have opaque inclusions. Groundmass of alkali feldspar microlites, tiny sodic pyroxenes, and small areas of interstitial aenigmatite, with larger areas of dark, partially devitrified glass.

AW83508

Euhedral - subhedral alkali feldspar phenocrysts (0.2 - 0.7 mm across) ragged ends and inclusion packed rims common, occasionally intergrown with aegerine-augite phenocrysts; euhedral - subhedral aegerine-augite phenocrysts (0.15 - 0.3 mm across) may have salite cores. Trachytic-textured groundmass of alkali feldspar and aegerine-augite microlites with interstitial aenigmatite. Aegerine-augite crystals commonly extend into vesicles, which are rimmed with aenigmatite. Secondary clays form later deposits in vesicles.

AW83510

Aphyric trachyte comprising felted alkali feldspar microlites with minor interstitial devitrified glass and cryptocrystalline material. Aenigmatite does occur in interstitial areas, but more commonly infills vesicles. Secondary calcite occurs in partings and in the core zones of some amygdales.

AW83511

Euhedral - subhedral alkali feldspar phenocrysts and glomerocrysts (0.3 - 0.8 mm across) contain aenigmatite, aegerine-augite and numerous cryptocrystalline inclusions, and may be intergrown with minor opaque ?aenigmatite glomerocrysts. Felted groundmass of alkali feldspar, hedenbergite and aenigmatite, and ophitic interstitial alkali feldspar.

AW83513

Rare, subhedral plagioclase glomerocrysts (0.4 - 1.0 mm across) have narrow overgrowths of alkali feldspar, irregular areas of fine grained hematite inclusions, sieve-textured zones, and may be intergrown with pale brown augite glomerocrysts (0.2 - 0.8 mm across), mostly iddingsitized olivine glomerocrysts (0.2 - 0.5 mm across), and opaque subphenocrysts. Groundmass of plagioclase microlites, iddingsitized olivine, salite and opaque minerals. Secondary oxidation of opaque minerals is widespread, as is secondary calcite and opaque oxides which infill vesicles and fractures.

AW83515

Euhedral - anhedral alkali feldspar phenocrysts (0.4 - 1.3 mm across) typically display an overgrown rim with tiny inclusions of aegerine-augite and aenigmatite. Xenoliths (up to 0.5 mm by 2.0 cm) of alkali feldspar, aegerine-augite, aenigmatite, and devitrified glass may contain alkali feldspar phenocrysts, and have a radial texture outlined by tiny opaque grains, which may be a disequilibrium texture. Groundmass varies from fine to medium grained, trachytic-textured to felted alkali feldspar microlites, aegerine-augite and aenigmatite. Aenigmatite also lines vesicles. Vesicles and some interstitial areas filled with a fine grained, olive brown mineral, possibly a zeolite.

AW83517

Aphyric trachyte comprising alkali feldspar microlites, aegerine-augite, and

intergrowths of aenigmatite. Ophitic alkali feldspar occurs interstitially.

AW83520

Euhedral - anhedral alkali feldspar xenocrysts (0.2 - 1.6 mm across) may contain aegerine-augite inclusions and evidence of resorption and later overgrowth by sieve-textured rims. Subhedral microphenocrysts of sodic pyroxene (up to 0.2 mm across) and aenigmatite (up to 0.1 mm across). Flow banded, devitrified, spheriolitic groundmass of radiating, dusty alkali feldspar sheaves, aenigmatite and aegerine-augite, with patches of interstitial aenigmatite.

AW83522

Aphyric trachyte comprising sheaves of plagioclase and aegerine-augite, with scattered grains of aenigmatite. Interstitial cryptocrystalline material and aenigmatite. Vesicles typically free of aenigmatite and secondary minerals.

AW83524

Rare, ragged alkali feldspar phenocrysts (0.6 mm across) with overgrown, sieve-textured rims. Groundmass of felted alkali feldspar microlites, aenigmatite, aegerine-augite and rare arfvedsonite, with large olive green areas of altered interstitial glass.

AW83532

Subhedral - anhedral alkali feldspar phenocrysts (up to 0.5 mm across). Fine grained, intergranular to ophitic groundmass of alkali feldspar, aegerine-augite and aenigmatite. Aenigmatite also infills microfractures.

AW83533

Subhedral alkali feldspar phenocrysts (0.15 - 1.2 mm across) commonly contain inclusions of aenigmatite and aegerine-augite; rare, euhedral sodic pyroxene microphenocrysts (0.2 mm across). Coarse, trachytic-textured groundmass of sheaves of alkali feldspar, interstitial aegerine-augite, and small aenigmatite grains optically enclosed in other minerals as well as being interstitial. Widespread oxida-

tion of aegerine-augite, but aenigmatite and feldspar remain fresh.

AW83534

Subhedral - anhedral alkali feldspar phenocrysts and glomerocrysts (0.2 - 1.5 mm across) maycontain salite and opaqueinclusions.Euhedralsalite microphenocrysts (0.1 - 0.2 mm across) commonly intergrown with opaque microphenocrysts (up to 0.5 mm across). Groundmass of felted intergrowths of plagioclase microlites, aegerine-augite and aenigmatite, with interstitial alkali feldspar.

AW83536

Similar to AW83454, except that olivine and augite phenocrysts are considerably more common, augite trends to pinkish titanaugite, and may contain large plagioclase and smaller opaque inclusions. Anorthoclase xenocrysts are absent. Secondary alteration, other than iddingsitization of olivine is absent.

AW83538

Very similar to AW83401, except for the lack of plagioclase xenocrysts.

AW83543

Euhedral - subhedral plagioclase phenocrysts and glomerocrysts (0.1 - 0.5 mm across) commonly intergrown with pale greenish brown augite (0.8 - 1.2 mm across), that also occurs as scattered phenocrysts, and minor opaque minerals. Trachytic-textured groundmass of plagioclase microlites, slightly iddingsitized olivine, granular augite and opaque minerals.

AW83545

Seriate, partially iddingsitized, euhedral olivine (up to 0.5 mm across - and one crystal 2.1 mm across); subhedral pale brown augite glomerocryst (2.0 mm across) intergrown with olivine; euhedral augite subphenocrysts (up to 0.2 mm across). Groundmass of plagioclase microlites, augite, olivine and tiny opaque minerals varies from intergranular to cryptocrystalline in texture.

AW83550

Strongly glomeroporphyritic, subhedral - anhedral plagioclase (0.05 - 2.0 mm across) commonly zoned, some alteration, forms clots (up to 3.0 mm across) and may be complexly intergrown with subordinate olivine and augite; anhedral augite glomerocrysts and phenocrysts (0.4 - 3.0 mm across); anhedral, partially iddingsitized olivine glomerocrysts only preserved where they are enclosed within clots. Felted groundmass of plagioclase microlites with interstitial areas of intergranular opaque minerals and augite. Numerous spherical vesicles are infilled with secondary calcite and a greenish-brown zeolite.

AW83554

Rare, euhedral - subhedral plagioclase phenocrysts (0.2 - 0.8 mm across). Trachytic-textured groundmass of plagioclase microlites, iddingsitized olivine, augite, and opaque minerals. Secondary calcite and a greenish-brown zeolite pervasively replace irregular areas of probable glass.

AW83558

Similar to AW83401, except that phenocrysts are generally less cloudy, only the groundmass olivine is iddingsitized, and a single xenolith (1.0 mm across) is present comprising equigranular intergrowths of titanaugite, plagioclase, opaque minerals and alkali feldspar. There are no plagioclase xenocrysts.

AW83559

Anhedral remnants of kaersutite phenocrysts (0.2 - 0.4 mm across) are now mostly replaced by an opaque mineral resembling aenigmatite. Very vesicular groundmass comprises sheaves of alkali feldspar microlites, with granular aegerine-augite and aenigmatite, and interstitial alkali feldspar.

AW83567

Aphyric trachyte comprising trachytic-textured alkali feldspar microlites, intergranular aegerine-augite and acmite, and scattered aenigmatite grains and interstitial masses commonly infilling vesicles. A later zeolite also infills the central

portion of some vesicles, and a secondary opaque mineral with acicular habit (?pseudobrookite) is typically associated with areas of interstitial aenigmatite.

AW83569

Coarse-grained, aphyric trachyte similar to the groundmass of AW83484, except for the presence of considerably more arfvedsonite, and interstitial areas of devitrified glass.

AW83580

Similar to AW83441, except for the lack of plagioclase phenocrysts and arfvedsonite-bearing xenoliths. Secondary calcite is also absent.

AW83581

Occasional, euhedral - subhedral glomerocrysts (0.2 - 0.5 mm across) of alkali feldspar in clots (up to 1.0 mm across) associated with subordinate aenigmatite glomerocrysts. Trachytic-textured groundmass of alkali feldspar, aenigmatite, aegerine-augite and arfvedsonite, similar to, but finer-grained than, AW83484. Secondary calcite infills vesicles.

AW83583

Seriate, often skeletal, euhedral olivine (up to 1.5 mm across) with small opaque inclusions; scattered, subhedral - anhedral pale brown augite microphenocrysts and glomerocrysts (0.1 - 0.6 mm across) may contain opaque inclusions and rarely have poorly defined salite cores. Vesicular groundmass comprises flow bands of different degrees of crystallinity from cryptocrystalline to a fine grained, intergranular groundmass of augite, opaque minerals and opaque mineral aggregates, with minor plagioclase.

AW83607

Seriate, euhedral, partially iddingsitized olivine (up to 1.2 mm across) may be skeletal and contain opaque inclusions; seriate, euhedral plagioclase (up to 0.4 mm across) may be intergrown with opaque minerals and olivine; seriate, commonly skele-

tal opaque minerals (up to 0.4 mm across). Intergranular groundmass of plagioclase, iddingsitized olivine, opaque minerals and titanaugite.

AW83614

Seriate, euhedral olivine (up to 2.4 mm across) may contain small opaque inclusions; seriate, euhedral - subhedral colorless to pale brown augite (up to 2.4 mm across) with the larger crystals sometimes intergrown with olivine, may have opaque inclusions, and/or narrow titanaugite rims, and rarely salite cores; seriate, euhedral - anhedral and embayed plagioclase phenocrysts and glomerocrysts (up to 1.2 mm across) in clots (up to 8.0 mm across) have sieve-textured interiors. Intergranular groundmass of plagioclase, titanaugite, opaque minerals, and olivine, with minor dark brown intertitial glass.

AW83647

Seriate, euhedral to embayed olive green olivine microphenocrysts (up to 0.4 mm across) may contain opaque inclusions; seriate, euhedral - subhedral aegerine-augite (up to 0.15 mm across); seriate, euhedral - subhedral alkali feldspar (up to 0.4 mm across) occasionally displays anorthoclase twinning and contains numerous inclusions of aegerine-augite and opaque minerals. Trachytic-textured groundmass of alkali feldspar sheaves, enclosing aegerine-augite and opaque minerals, with interstitial areas of cryptocrystalline minerals, possibly devitried glass.

AW83650

Similar to AW83401, except that maximum phenocryst size is smaller (olivine - up to 0.4 mm across; augite - up to 0.9 mm across) and there is a lack of plagioclase xenocrysts.

AW83653

Aphyric trachyte comprising finely flow banded, felted to spheriolitic feldspar microlites, aegerine-augite, and aenigmatite. Small areas of incipient iron oxide staining, but no secondary alteration or mineralization associated with vesicles.

AW83662

Similar to AW83401, except that both olivine and augite phenocrysts are typically euhedral, less cloudy, and as large as 2.5 mm across; the presence of several olive green sodic pyroxene phenocrysts (0.4 - 1.8 mm across) with narrow augite rims; and the groundmass is more crystalline. There are no plagioclase xenocrysts.

AW83677

Aphyric, flow banded, trachyte comprising trachytic-textured to spheriolitic feldspar microlites, aenigmatite, and aegerine-augite, with minor interstitial alkali feldspar, and large areas of devitrified glass. No secondary mineralization associated with vesicles.

AW83678

Alkali feldspar phenocrysts and glomerocrysts (up to 1.0 mm across) intergrown with subordinate aenigmatite and minor aegerine-augite. Goundmass comprises sheaves of trachytic-textured alkali feldspar microlites with interstitial aegerine-augite, aenigmatite, and interstitial alkali feldspar. Widespread yellowish-brown areas of cryptocrystalline mineralization, probably represents areas of interstital devitrified glass.

AW83689

Similar to AW83401, except that large embayed augite phenocrysts have pinkish brown cores; the presence of scattered, anhedral kaersutite xenocrysts (0.2 - 1.2 mm across); the presence of seriate, irregular shaped opaque minerals (up to 2.0 mm across); the absence of plagioclase xenocrysts; and the lack of olivine iddingsitization.

AW83701

Euhedral - subhedral alkali feldspar phenocrysts (0.2 - 1.0 mm across). Felted groundmass of alkali feldspar microlites, sodic pyroxene, tiny grains of a fresh opaque mineral that occurs as inclusions and along grain boundaries, and large areas of cryptocrystalline material that probably represents altered glass. Iron oxide

deposits stain the margins of irregular shaped vesicles.

AW83706

Similar to AW83401, except that some augite phenocrysts contain apatite inclusions; augite is less common than olivine; larger olivine phenocrysts (>0.6 mm across) are embayed and sieve-textured with opaque and cryptocrystalline inclusions, plagioclase is present only as a groundmass phase. There are no plagioclase xenocrysts.

AW83707A

Aphyric trachyte comprising trachytic-textured alkali feldspar sheaves with aegerine-augite, aenigmatite and minor ?arfvedsonite. Some areas are less trachytic and contain more interstitial alkali feldspar. Considerable oxidization and development of cryptocrytalline secondary minerals.

AW84714

Microporphyritic plagioclase laths (up to 0.4 mm across), euhedral - subhedral olivine (up to 0.2 mm across); euhedral - skeletal opaque minerals (up to 0.3 mm across). Trachytic-textured groundmass of plagioclase microlites and tiny clinopyroxene, opaque minerals and olivine.

AW84715

Seriate, larger anhedral to smaller euhedral olivine (up to 1.0 mm across); euhedral augite microphenocrysts (up to 0.2 mm across); rare, subhedral to rounded augite xenocrysts (0.5 - 1.6 mm across), one large one of which is intergrown with kaersutite and contains kaersutite inclusions; anhedral plagioclase and alkali feldspar xenoliths and xenocrysts (up to 1.0 mm across); anhedral kaersutite xenocrysts (up to 1.2 mm across) with opaque reaction rims, and opaque kaersutite pseudomorphs; dark green aegerine-augite xenocrysts (0.1 - 0.2 mm across) typically being replaced by opaque mineral aggregates overgrown by augite . Very vesicular groundmass of plagioclase microlites, augite, olivine, opaque minerals, and cryptocrystalline interstitial areas.

AW84718

Scattered euhedral - subhedral plagioclase and alkali feldspar glomerocrysts and phenocrysts (0.05 - 5.0 mm across) contain inclusions of olivine, augite and opaque minerals; subhedral - anhedral olivine phenocrysts and glomerocrysts (0.2 - 1.0 mm across) contain numerous large apatite and opaque inclusions; subhedral - rounded pale brown augite to pale green salite phenocrysts and glomerocrysts (0.1 - 1.0 mm across) with large apatite and opaque inclusions; anhedral opaque phenocrysts (up to 0.4 mm across) contain large apatite inclusions; euhedral apatite microphenocrysts (up to 0.1 mm across). Fine grained groundmass of plagioclase microlites, opaque minerals and clinopyroxene, with minor olivine, apatite,and interstitial glass. Some secondary iron oxide staining.

AW84719

Seriate, euhedral - subhedral, zoned plagioclase (up to 0.8 mm across) with sieve-textured cores of glass and kaersutite inclusions common, and tiny acicular sodic pyroxene inclusions in some crystals; euhedral - subhedral alkali feldspar phenocrysts (up to 2.0 mm across) with inclusions of hedenbergite and opaque minerals; euhedral - subhedral kaersutite phenocrysts (0.1 - 0.6 mm across) and anhedral opaque phenocrysts (interpreted as kaersutite pseudomorphs) containing apatite inclusions. Rare, subhedral, pale green and fawn augite microphenocrysts (0.1 - 0.2 mm across) may contain kaersutite and opaque inclusions; rare, euhedral apatite microphenocrysts (up to 0.2 mm across). Rounded, intergranular, microcrystalline feldspar - clinopyroxene - opaque mineral xenoliths (up to 3.0 mm across). Groundmass of trachytic plagioclase microlites and alkali feldspar enclosing tiny green needles of sodic pyroxene and opaque minerals, with minor interstitial devitrified glass.

AW84720

Scattered, subhedral plagioclase phenocrysts (0.2 - 1.0 mm across) with numerous hedenbergite and associated ?aenigmatite inclusions, appear to be altering to alkali

feldspar; subhedral - anhedral opaque - sodic pyroxene areas (0.1 - 0.7 mm across) occasionally have remnant cores of kaersutite; rare, euhedral, pale green hedenbergite phenocrysts (0.2 - 0.6 mm across). Groundmass of fibrous sheaves of trachytic-textured alkali feldspar and hedenbergite.

AW84721

Similar to AW84719, except for the lack of alkali feldspar phenocrysts, although alkali feldspar does form a microphenocryst phase (up to 0.4 mm across). In places kaersutite appears to be in reaction relationship with hedenbergite as well as opaque minerals.

AW84722

Seriate, euhedral - subhedral, zoned alkali feldspar (up to 2.0 mm across) commonly with sieve-textured cores of salite and opaque inclusions; subhedral kaersutite pseudomorphs (0.1 - 0.5 mm across) of spongy opaque minerals and salite, may contain relict apatite inclusions; pale green sodic pyroxene microphenocrysts (up to 0.1 mm across). Groundmass of opaque minerals, sodic pyroxene and olive green ?olivine, ophitically to subophitically enclosed in alkali feldspar.

AW84723

Seriate, euhedral - subhedral olivine (up to 0.5 mm across) with minor iddingsitization; rare subhedral, pale brown augite microphenocrysts (up to 0.3 mm across) may have green salite cores; rare, euhedral plagioclase subphenocrysts (up to 0.3 mm across). Groundmass of plagioclase, olivine, opaque minerals, with interstitial glass and cryptocrystalline minerals.

AW84725

Euhedral - subhedral dusty plagioclase glomerocrysts (0.2 - 1.2 mm across) and alkali feldspar glomerocrysts (up to 2.0 mm across) form clots with minor hedenbergite and kaersutite; subhedral kaersutite phenocrysts (0.1 - 0.6 mm across) completely altered to opaque minerals; euhedral pale green salite microphenocrysts (0.1 - 0.4 mm across) commonly have large opaque inclusions. Groundmass of trachytic-textured

sheaves of alkali feldspar and hedenbergite and scattered opaque minerals. Patchy iron oxide staining associated with hedenbergite.

AW84728

Seriate, euhedral olivine (up to 1.0 mm across) commonly contains opaque inclusions; subhedral, zoned, pale brown augite to pinkish brown titanaugite glomerocrysts in clots (1.0 - 2.0 mm across) with minor olivine and opaque minerals. Rarely, augite crystals have sieve-textured, pale green salite cores. Rare, euhedral, zoned plagioclase microphenocrysts (0.5 - 0.1 mm across). Rare, anhedral, dusty feldspar xenocrysts. Intergranular groundmass of plagioclase, augite, olivine, and opaque minerals.

AW84733

Seriate, euhedral - subhedral olivine (up to 0.8 mm across) and pale brown augite (up to 1.2 mm across) contain numerous opaque inclusions; rare anhedral kaersutite mostly altered to opaque minerals. Plagioclase and alkali feldspar xenocrysts (1.0 - 2.0 mm across) characterized by a rounded core surrounded by sieve-textured zone and a thin vermicular rim. Groundmass of trachytic-textured plagioclase, with olivine, augite, opaque minerals and variable amounts of interstitial glass, cryptocrystalline material and ?nepheline.

AW84735

Aphyric trachyte comprising microphenocrysts of euhedral alkali feldspar (up to 0.3 mm across), and a groundmass of fibrous sheaves of trachytic-textured alkali feldspar and ?acmite, with clots of extremely fine opaque minerals.

AW84738

Seriate, euhedral - subhedral olivine (up to 0.3 mm across) with opaque inclusions and minor iddingsitization, may also occur as clots (up to 0.5 mm across); seriate, zoned pale brown to pinkish titanaugite (up to 2.0 mm across) may have pale green to olive green salite cores in some larger crystals, often with intergrowths of

?kaersutite along cleavage planes, opaque inclusions common; rare, rounded opaque phenocrysts with vermicular rims (0.8 mm across) may be altered kaersutite. Interstitial groundmass of plagioclase, olivine, titanaugite, and opaque minerals.

AW84740

Seriate, euhedral - subhedral olivine (up to 2.0 mm across); glomeroporphyritic, subhedral, zoned, pale brown augite (0.1 - 0.2 mm across) may be intergrown with minor olivine and opaque minerals. Flow banded, interstitial groundmass of felted plagioclase microlites, augite, olivine and opaque minerals.

AW84741

Similar to AW84725, except for the lack of alkali feldspar phenocrysts. Kaersutite is in variable stages of alteration (but not completely altered). Groundmass pyroxene is totally oxidized.

AW84742

Seriate, euhedral plagioclase (up to 1.2 mm across) with crystals >0.3 mm across typically having rounded sieve-textured cores containing augite, opaque and cryptocrystalline inclusions; seriate, euhedral, zoned fawn augite (up to 0.7 mm across) typically contains opaque, and minor plagioclase and olivine inclusions, and is commonly intergrown with these minerals in glomeroporphyritic clots. Euhedral - subhedral olivine microphenocrysts and glomerocrysts and skeletal opaque microphenocrysts commonly intergrown with augite. Intergranular groundmass of plagioclase, opaque minerals, augite, and interstitial alkali feldspar.

AW84744

Similar to AW84735, except that feldspar microphenocrysts are <0.5 mm across, and the groundmass pyroxene is hedenbergite and more abundant.

AW84745

Subhedral - anhedral alkali feldspar phenocrysts and glomerocrysts (0.1 - 1.5 mm across) may contain hedenbergite and opaque (possibly altered kaersutite) inclusions; scattered anhedral opaque microphenocrysts (0.1 - 0.2 mm across) probably kaersutite

pseudomorphs. Groundmass of fibrous sheaves of trachytic-textured alkali feldspar with scattered opaque minerals, and hedenbergite.

AW84748

Seriate, euhedral - subhedral olivine (up to 0.9 mm across) typically contains skeletal opaque inclusions; seriate, euhedral - subhedral, pale brown augite to pinkish brown titanaugite, some of which have salite cores that may be sieve-textured; rounded, spongy opaque aggregates interpreted as altered kaersutite. Euhedral plagioclase microphenocrysts (0.02 - 0.1 mm across). Rare anorthoclase xenocrysts with sieve-textured rims. Cryptocrystalline groundmass includes opauqe minerals.

AW84749

Seriate, euhedral to embayed olivine (up to 0.3 mm across) may contain opaque inclusions and has minor iddingsitization; seriate, subhedral, pale brown augite glomerocrysts (up to 0.4 mm across) may surround a core of olivine and also commonly contain tiny opaque inclusions. Trachytic-textured groundmass of plagioclase, augite, olivine, and opaque minerals, with interstitial alkali feldspar.

AW84750

Seriate, euhedral - subhedral augite to titanaugite phenocrysts (0.8 - 2.2 mm across) may have small kaersutite (only in the larger crystals) and opaque inclusions, remnant sieve-textured salite cores (only in the larger crystals), and crystals 0.1 - 0.2 mm across are commonly intergrown in clots with subordinate opaque minerals; seriate, euhedral - subhedral olivine phenocrysts (up to 2.3 mm across) may have skeletal opaque inclusions and occasionally be intergrown with clinopyroxene; skeletal opaque microphenocrysts (up to 0.2 mm across). Groundmass of plagioclase microlites, opaque minerals and olivine, with interstitial aggregates of tiny salite crystals and interstitial alkali feldspar.

AW84753

Aphyric hawaiite comprising intergranular, trachytic-textured plagioclase, pale

brown to pale green augite, skeletal opaque minerals, and minor olivine.

AW84754

Subhedral to broken alkali feldspar phenocrysts (0.1 - 0.7 mm across) rarely intergrown with plagioclase phenocrysts; subhedral to broken, pale green sodic pyroxene phenocrysts (0.1 - 0.5 mm across) commonly contain feldspar, apatite and large opaque inclusions, and may be intergrown with kaersutite; subhedral to broken kaersutite phenocrysts (0.1 - 0.5 mm across) may contain large inclusions (or alteration products) of opaque minerals and sodic pyroxene. Small xenoliths (0.2 - 1.0 mm across) of microcrystalline intergrowths of feldspar, sodic pyroxene and opaque minerals. Groundmass of broken shards of the phenocrysts phases, in an extremely vesiculated, colorless glass.

AW84756

Similar to AW84719, except for the lack of alkali feldspar phenocrysts.

AW84758

Scattered euhedral - subhedral plagioclase phenocrysts (0.5 - 2.0 mm across) contain inclusions of kaersutite and opaque alteration minerals; subhedral - anhedral, pale brown olivine phenocrysts and glomerocrysts (0.2 - 1.0 mm across) with numerous large inclusions of apatite and opaque minerals; rounded pale brown augite phenocrysts and glomerocrysts (0.1 - 1.0 mm across) with large opaque and apatite inclusions. Euhedral apatite microphenocrysts (up to 0.1 mm across) and anhedral opaque microphenocrysts (up to 0.2 mm across). Groundmass of plagioclase microlites, opaque minerals, clinopyroxene, minor olivine and apatite, with interstitial glass.

AW84761

Euhedral plagioclase and alkali feldspar phenocrysts (0.2 - 2.5 mm across) commonly contain mottled cores and ?hematite lamellae; euhedral - subhedral kaersutite phenocrysts (0.1 - 0.3 mm across) typically rimmed by spongy opaque mineral aggregates, may contain apatite inclusions; rare, subhedral olivine phenocrysts (0.2 - 0.4 mm across); rare, euhedral - subhedral salite microphenocrysts (0.2 - 0.4 mm

across). Coarse-grained groundmass of alkali feldspar enclosing kaersutite needles which have mostly altered to opaque minerals.

AW84763

Seriate, euhedral to embayed olivine (up to 0.8 mm across); seriate, euhedral pale brown augite to pinkish titanaugite (up to 0.2 mm across) may have sieve-textured salite cores. Both olivine and clinopyroxene also occur in glomeroporphyritic clots. Rounded felsic xenoliths (1.0 - 2.0 mm across) appear to be resorbing. Groundmass of titanaugite, plagioclase and opaque minerals with interstitial alkali feldspar, ?nepheline and cryptocrystalline material.

AW84768

Anhedral kaersutite phenocrysts (0.2 - 1.0 mm across) rimmed by spongy intergrowths of opaque minerals and iddingsitized olivine, contain apatite inclusions an may have anhedral augite cores; seriate, pale brown augite zoned to pinkish titanaugite (up to 1.0 mm across) typically intergrown with subordinate olivine, kaersutite and opaque minerals (and in one case, a 2-mm-across titanaugite crystal containing euhedral olivine inclusions), rarely have cores of salite or more common altered salite; seriate, euhedral apatite (up to 0.2 mm across); seriate, euhedral plagioclase (up to 0.8 mm across) commonly contain cores or zones of devitrified glass inclusions. Intergranular groundmass of augite, plagioclase, iddingsitized olivine, opaque minerals, apatite, and interstitial alkali feldspar and cryptocrystalline material.

AW84777

Euhedral plagioclase phenocrysts (up to 0.4 mm across); euhedral - subhedral kaersutite phenocrysts (up to 0.5 mm across) have apatite inclusions and opaque aggregate rims. Trachytic-textured groundmass of anorthoclase microlites and minute aegerine-augite and opaque minerals.

AW84791

Subhedral phenocrysts and glomerocrysts of alkali feldspar and plagioclase rimmed with alkali feldspar (0.6 - 1.5 mm across) have core packed with salite, iddingsitized olivine, opaque mineral, and cryptocrystalline inclusions; scattered anhedral aggregates of spongy salite and opaque microphenocrysts (0.4 mm across). Trachytic-textured groundmass of alkali feldspar, minor sodic pyroxene, and aenigmatite, with minor interstitial cryptocrystalline material.

AW84796

Similar to AW84768, except that clinopyroxene crystals may be as large as 6.0 across, and plagioclase forms glomeroporphyritic clots.

AW84797

Seriate, euhedral - subhedral augite to titanaugite phenocrysts and glomerocrysts (up to 3.0 mm across) commonly zoned and contain large inclusions of rounde olivine, opaque minerals, and in some crystals, patchy cryptocrystalline alteratio products probably replacing a salite core (salite cores are preserved rarely); euh ral to rounded olivine phenocrysts (0.3 - 1.0 mm across) with minor iddingsitizati that increases with decreasing crystal size; spongy aggregates of opaque minerals and ?iddingsitized olivine assumed to replace kaersutite phenocrysts; anhedral opa microphenocrysts (up to 0.3 mm across); subhedral - anhedral plagioclase and alkal feldspar phenocrysts (0.2 - 1.2mm across) have sieve-textured cores packed with gl and cryptocrystalline inclusions. Groundmass of plagioclase microlites, augite, partially iddingsitized olivine and opaque minerals. Widespread minor secondary calcite.

AW85802

Occasional euhedral alkali feldspar phenocrysts (0.2 - 0.4 mm across) with overgrowths of ?albite, in groundmass of spheriolitic ?albite masses 0.2 mm across and interstitial cryptocrystalline material, which, in places, is replaced by seco ary iron oxides.

AW85803

Occasional, euhedral alkali feldspar phenocrysts (0.2 - 0.5 mm across) in vesicular groundmass of trachytic-textured alkali feldspar microlites and interstitial dusty alkali feldspar and aenigmatite. Secondary calcite infills some vesicles.

AW85809

Aphyric trachyte comprising medium-grained, trachytic-textured alkali feldspar microlites, and minor aegerine-augite, with interstitial aenigmatite. Minor seconda calcite and later, radiating zeolite.

AW85830

Euhedral - subhedral alkali feldspar phenocrysts (up to 1.0 mm across) may be intergrown with rounded opaque phenocrysts (0.2 - 0.4 mm across). Coarse-grained, trachytic to felted groundmass of alkali feldspar microlites, subordinate aegerine-augite and arfvedsonite, intersitial aenigmatite and alkali feldspar. Minor seconda calcite and zeolite.

AW85831

Microporphyritic trachyte with phenocrysts of alkali feldspar (up to 0.2 mm long); scattered olive green sodic pyroxene and fawn augite phenocrysts (up to 0.05 mm across); opaque phenocrysts (up to 0.15 mm across). Trachytic-textured groundmas of alkali feldspar microlites with interstitial tiny salite and opaque minerals, varying to cryptocrystalline material.

AW85833

Occasional, euhedral alkali feldspar phenocrysts (0.2 - 0.5 mm across) in inte granular groundmass of alkali feldspar enclosing aegerine-augite and scattered anhe ral opaque minerals. Minor patches of secondary iron oxidation.

AW85837

One subhedral alkali feldspar phenocryst (0.3 mm across) with aegerine-augite inclusions. Felted to trachytic-textured groundmass of alkali feldspar microlites, aegerine-augite, and aenigmatite, with interstitial pale yellow glass.

AW85839

Microporphyritic basanite with phenocrysts of subhedral plagioclase and alkali feldspar (up to 0.2 mm across), and subhedral olivine phenocrysts (up to 0.1 mm across), in trachytic-textured groundmass of plagioclase microlites, mostly iddingsitized olivine, salite, and opaque minerals, with interstitial alkali feldspar and areas of secondary iron oxidation.

AW85847

Very similar to AW85830, except that the alkali feldspar phenocrysts are not intergrown with opaque phenocrysts.

AW85850

Very similar to AW85803, except for the addition of one rounded plutonic xenolith (2.0 mm across) of a plagioclase porphyritic lithology with a groundmass of pa brown to green pyroxene, opaque minerals, interstitial alkali feldspar, and an isotropic mineral. There is no secondary calcite.

AW85851

Very similar to AW85803, except for the lack of secondary calcite. Small pleochroic brown inclusions in feldspar may be kaersutite.

AW85860

Very similar to AW85837, except that alkali feldspar phenocrysts are up to 0.7 mm across and the groundmass is coarser grained.

AW85869

Very similar to AW85809, except for the presence of scattered euhedral alkali feldspar phenocrysts (up to 0.4 mm across), some of which have remnant plagioclase twining. No secondary zeolite.

AW86881

Microporphyritic phonolite, comprising seriate, euhedral alkali feldspar including anorthoclase (up to 0.4 mm across) which may be intergrown with or contai inclusions of aegerine-augite; seriate aegerine-augite (up to 0.8 mm across) common

intergrown in clots with subordinate kaersutite, larger crystals may be cored by anhedral colorless to pale brown augite; seriate hornblende (up to 0.6 mm across) ma be intergrown with opaque minerals in clots; seriate, scattered opaque minerals (up to 0.1 mm across). Trachytic-textured groundmass of alkali feldspar, aegerine-augit kaersuite and scattered opaque minerals, which are typically enclosed in the feldspar.

AW86883

Microporphyritic phonolite, comprising seriate kaersutite (up to 0.1 mm across mostly altered to spongy opaque mineral aggregates. Groundmass of felted alkali feldspar, hedenbergite, kaersutite and opaque minerals, with large, ophitic, interstitial alkali feldspars (typically 0.2 - 0.5 mm across).

AW86887

Rare, euhedral plagioclase phenocrysts (0.6 - 1.4 mm across). Coarse-grained intergranular groundmass of plagioclase, augite, opaque minerals and olivine.

AW86889

Seriate, subhedral alkali feldspar (up to 0.3 mm across) commonly with poorly defined inclusion-rich rims, and a glomerporphyritic clot of alkali feldspar (1.5 m across); occasional, seriate, anhedral opaque minerals (up to 0.3 mm across); rare, rounded olivine phenocrysts (0.5 mm across) with apatite inclusions. Trachytic-textured groundmass of alkali feldspar, hedenbergite, and opaque minerals.

AW86891

Euhedral - anhedral kaersutite phenocrysts and glomerocrysts (0.05 - 1.0 mm across) with rims of opaque mineral aggregates; seriate, euhedral - subhedral augit (up to 1.1 mm across) may be glomeroporphyritic, with opaque inclusions common, salite cores rarely preserved, and one clot with a 0.2 mm wide kaersutite overgrow

seriate, euhedral - subhedral olivine (up to 0.5 mm across) may have opaque inclusions, and one anhedral olivine phenocrysts (0.6 mm across) with a rim of spongy

opaque minerals suggesting an altered kaersutite overgrowth. Fine-grained, felted groundmass of plagioclase microlites, opaque minerals, pyroxene and olivine, with interstitial alkali feldspar.

AW86895

Euhedral - subhedral plagioclase phenocrysts (up to 1.4 mm across); euhedral kaersutite phenocrysts (up to 0.9 mm across) with apatite inclusions. Vesicular matrix of partially altered kaersutite needles enclosed in alkali feldspar.

AW86898

Seriate, euhedral to broken alkali feldspar (up to 1.0 mm across) and plagioclase (up to 1.3 mm across) with crystals >0.8 mm across commonly having sieve-textured cores; anhedral olivine (up to 0.6 mm across) may contain opaque inclusions euhedral - anhedral augite (up to 0.4 mm across) commonly intergrown and may contain opaque inclusions; seriate opaque minerals (up to 0.1 mm across). Fine grained groundmass of alkali feldspar microlites, opaque minerals, pyroxene and olivine, with interstitial alkali feldspar.

AW86899

Similar to AW84718, except that the feldspar phenocrysts are up to 5.5 mm across, there is a single subhedral kaersutite microphenocryst (0.1 mm across), and interstitial areas in the groundmass are filled by alkali feldspar rather than glass No secondary iron oxide staining.

AW86901

Similar to AW84718, except that the feldspar phenocrysts are up to 3.0 mm across and are typically glomeroporphyritic, with subordinate olivine, opaque, and apatite glomerocrysts. Groundmass is vesicular and comprises alkali feldspar microlites, olivine, salite and opaque minerals, in a brown glass.

AW86909

Euhedral - anhedral augite glomerocrysts (up to 0.7 mm across) in

clots (up to 0.8 mm across) intergrown with opaque minerals and minor olivine; euhedral - anhedral olivine phenocrysts and glomerocrysts (up to 0.5 mm across); seriate, euhedral plagioclase (up to 0.2 mm across). Euhedral opaque microphenocrysts commonly form inclusions in augite. Groundmass of plagioclase, augite, opaque minerals and olivine.

AW86910

Similar to AW86909 except that phenocrysts are larger: augite (up to 2.5 mm across) may have pale green core; olivine (up to 0.8 mm across); and plagioclase (up to 0.8 mm across).

AW86922

Subhedral - anhedral plagioclase and alkali feldspar phenocrysts (0.2 - 0.7 mm across) may be glomeroporphyritic and intergrown with minor kaersutite; anhedral kaersutite phenocrysts (0.2 - 0.7 mm across) may contain apatite and opaque inclusions, and are rimmed by opaque mineral aggregates, subhedral opaque phenocrysts and opaque mineral aggregates are pseudomorphic after kaersutite; rare, anhedral augite phenocrysts (0.3 - 0.5 mm across). Groundmass of plagioclase microlites, with interstitial areas of tiny salite and opaque minerals enclosed in alkali feldspar.

AW86943

Seriate, euhedral olivine (up to 0.2 mm across) and rare larger embayed olivine phenocrysts (up to 0.6 mm across) may contain apatite and occasional opaque inclusions; rare, anhedral augite glomerocryst (0.4 mm across) intergrown with kaersutite pseudomorphs; subhedral - anhedral opaque phenocrysts and opaque mineral aggregates (0.2 - 0.6 mm across) interpreted as kaersutite pseudomorphs; subhedral augite

microphenocrysts (up to 0.3 mm across) may have inclusion-rich salite cores preserved. Groundmass of olivine, plagioclase microlites, augite and opaque minerals, with interstitial alkali feldspar.

AW86944

Very similar to AW86943, except for the lack of kaersutite pseudomorphs, and the high vesicularity of the groundmass.

AW86947

Seriate, euhedral augite to titanaugite glomerocrysts (up to 1.4 mm across) may have pale green cores, in clots with opaque minerals (up to 3.0 mm across); subhedral - anhedral kaersutite phenocrysts and pseudomorphs (up to 0.6 mm across) have opaque alteration rims; scattered subhedral - anhedral plagioclase xenocrysts (up to 0.4 mm across) typically have sieve-textured and overgrown yellowish olivine phenocrysts (up to 1.0 mm across). Fine grained groundmass of plagioclase, opaque and cryptocrystalline minerals.

AW86950

Very similar to AW84718 except that feldspar phenocrysts reach a maximum of 2.1 mm across, and there is no secondary oxidation.

AW86965A

Seriate, euhedral alkali feldspar glomerocrysts and phenocrysts (up to 0.4 mm across); opaque microphenocrysts (up to 0.4 mm across). Trachyte-textured groundmass of sheaves of alkali feldspar and minor hedenbergite and opaque oxides.

AW86970

Euhedral - anhedral plagioclase and alkali feldspar phenocrysts (0.3 - 0.6 mm across) may contain sodic pyroxene inclusions; seriate, euhedral, mostly iddingsitized olivine (up to 0.2 mm across) commonly intergrown with opaque minerals; seriate, anhedral opaque minerals (up to 0.1 mm across). Trachytic-textured groundmass of alkali feldspar, salite, opaque minerals and olivine.

AW86976

Seriate, euhedral - subhedral alkali feldspar phenocrysts (up to 1.2 mm across) and glomerocrysts in clots (up to 2.5 mm across) may be intergrown with, or have alteration rims of, an opaque mineral; subhedral - anhedral brownish opaque mineral pseudomorphs (up to 0.5 mm across). Groundmass of interlocking, tabular alkali feldspar, arfvedsonite, and aegerine-augite. Secondary brownish opaque alteration mineral.

AW86978

Very vesicular, aphyric trachyte, comprising trachytic alkali feldspar microlites, and interstitial granular aggregates of aegerine-augite, with scattered opaque minerals. Secondary iron oxide mineralization in patches.

AW86986

Very similar to AW86978, except for scattered alkali feldspar phenocrysts (up to 0.4 mm across), and dusty to fibrous calcite infilling some vesicles.

AW86988

Seriate, euhedral opaque minerals (up to 0.4 mm across); seriate, euhedral - subhedral, partially iddingsitized olivine (up to 0.5 mm across) may contain opaque inclusions. Groundmass of strongly trachytic-textured plagioclase microlites, olivine, opaque minerals and interstitial salite.

AW86999

Anhedral kaersutite glomerocrysts (up to 1.4 mm across) with apatite inclusions, intergrown with subordinate plagioclase glomerocrysts (up to 1.3 mm across) with apatite inclusions, and sieve-textured rims common. Groundmass of broken to rounded kaersutite, plagioclase, alkali feldspar, apatite and augite crystals in a very vesicular opaque matrix. Minor secondary calcite in vesicles.

AW86006

Scattered, euhedral alkali feldspar phenocrysts and glomerocrysts (0.2 - 0.5 mm across) in small clots (up to 1.8 mm across). Trachytic-textured groundmass of alkali

feldspar microlites, with minute aegerine-augite, opaque minerals and rare arfvedsonite.

AW86008

Subhedral - anhedral plagioclase phenocrysts (1.0 - 3.0 mm across) typically overgrown by and altering to alkali feldspar; seriate, euhedral - subhedral alkali feldspar (up to 1.8 mm across). Groundmass of intergranular alkali feldspar, with minute opaque minerals and pyroxene. Secondary calcite and iron oxide minerals form anhedral areas.

AW86012

Very similar to AW86988, except for the presence of apatite in the groundmass.

AW86013

Similar to AW86988, except for the presence of subhedral plagioclase phenocrysts (up to 0.8 mm across) packed with salite, olivine and opaque inclusions, and a coarser groundmass in which apatite is present.

AW86016

Aphyric trachyte, comprising felted alkali feldspar microlites ophitically enclosing small opaque minerals, and granular aegerine-augite.

AW86018

Subhedral alkali feldspar phenocrysts (0.8 - 2.8 mm across) in vesicular groundmass of alkali feldspar microlites and interstitial aenigmatite.

AW86020

Very similar to AW86976.

AW86021

Similar to AW86978, except for the lack of vesicles, the presence of alkali feldspar microphenocrysts (up to 0.4 mm across), and the presence of more aegerine-augite and accessory arfvedsontie in the groundmass.

AW86025

Similar to AW86988, but much coarser grained. Minor secondary calcite.

AW86032

Rare, euhedral - anhedral alkali feldspar phenocrysts (0.4 - 0.6 mm across) may have plagioclase overgrowths; rare, anhedral pale brown augite phenocrysts (up to 0.5 mm across). Plagioclase and olivine microphenocrysts (up to 0.2 mm across), and euhedral - skeletal opaque microphenocrysts (up to 0.1 mm across). Fine grained groundmass of opaque minerals, augite, plagioclase and olivine , with interstitial alkali feldspar.

AW86033

Seriate, subhedral olivine (up to 1.2 mm across) may contain opaque inclusions; seriate, pale brown augite (up to 2.4 mm across) may be intergrown in clots, rarely with subordinate olivine; seriate plagioclase (up to 0.2 mm across). Groundmass of granular augite and opaque minerals, with trachytic-textured plagioclase microlites and scattered olivine.

AW86034

Very similar to AW86988, except for the presence of plagioclase microphenocrysts (up to 0.5 mm across) which contain olivine, opaque and augite inclusions; and apatite which is present as inclusions in opaque minerals, and in the groundmass. Partial iddingsitization of olivine.

AW86035

Similar to AW86988, except for abundant olivine and plagioclase microphenocrysts (up to 0.5 mm across) in a coarse-grained groundmass. Partial iddingsitization of olivine. Secondary calcite partially infills vesicles.

AW86036

Seriate, euhedral - anhedral plagioclase (up to 2.4 mm across) may be intergrown and commonly contain large inclusions of salite, olivine, and opaque minerals occasionally to the point of being sieve-textured. Seriate, euhedral - subhedral pale

brown augite (up to 1.7 mm across) may contain large opaque inclusions; seriate, partially iddingsitized olivine (up to 1.0 mm across) may contain large opaque inclusions in rims; seriate, anhedral opaque minerals (up to 0.9 mm across). Granular groundmass of plagioclase microlites, salite, iddingsitized olivine, and opaque minerals. Minor hematitzation along microfractures.

AW86037

Similar to, but finer grained than AW86033, with plagioclase only reaching a maximum size of 0.1 mm across.

AW86041

Seriate, subhedral plagioclase (up to 0.7 mm across); seriate, euhedral olivine (up to 0.5 mm across) may contain large apatite inclusions; seriate, subhedral pale green salite (up to 0.3 mm across) commonly contains large opaque inclusions; seriate, skeletal opaque minerals (up to 0.2 mm across) may contain small apatite inclusions. Coarse-grained groundmass of trachytic-textured plagioclase microlites, with salite, opaque minerals, and olivine.

AW86042

One anhedral alkali feldspar phenocryst (1.2 mm across) with tiny opaque inclusions in the overgrown rim. Groundmass of alkali feldspar microlites, with intersitial aegerine-augite and alkali feldspar enclosing opaque minerals.

AW86057

Euhedral - anhedral phenocrysts and glomerocrysts of pale brown augite (0.2 - 1.6 mm across) contain apatite, kaersutite, olivine and opaque inclusions, and may be intergrown with subordinate opaque minerals and occasionally plagioclase; subhedral - anhedral opaque phenocrysts (0.15 - 0.9 mm across) may have vermicular rims and be intergrown with subordinate olivine and/or augite; subhedral - anhedral plagioclase phenocrysts (0.2 - 0.8 mm across); seriate, euhedral - subhedral olivine (up to 0.5 mm across) may be intergrown with opaque minerals and/or augite. Groundmass of small

granular augite and opaque minerals, with scattered olivine and plagioclase, and interstitial ?nepheline.

AW86058

Seriate, euhedral olivine (up to 0.8 mm across) may have opaque inclusions and be intergrown in momomineralic clots; seriate, euhedral pale brown augite (up to 1.3 mm across) rarely has sieve-textured core zone. Vesicular groundmass of granular augite and opaque minerals, with scattered olivine and plagioclase, and interstitial ?alkali feldspar.

AW86059

Scattered, subhedral - anhedral and embayed olivine phenocrysts (0.4 - 1.4 mm across) rarely contain opaque inclusions; one rounded opaque phenocryst (0.9 mm across). Euhedral - subhedral olivine microphenocrysts (up to 0.2 mm across). Groundmass of plagioclase microlites, with scattered olivine and interstitial salite and opaque minerals.

AW86061

Similar to AW86059, except that euhedral olivine reaches 0.9 mm across, the absence of opaque phenocrysts and the presence of one rounded augite glomerocryst (1.4 mm across) with olivine inclusions.

AW86063

Similar to AW86032, except for the presence of one rounded opaque phenocryst (0.7 mm across) with apatite inclusions and vermicular rims, the absence of feldspar phenocrysts, and a coarser groundmass.

AW86070

Similar to AW86032, except for the presence of anhedral to embayed olivine phenocrysts (0.4 - 2.0 mm across) with opaque inclusions, the lack of feldspar phenocrysts, and a coarser groundmass.

AW86072

Very similar to AW86035, except for the lack of iddingsitization in olivine and

secondary calcite.

AW86075

Similar to AW86978, except for the presence of alkali feldspar microphenocrysts (up to 0.2 mm across), and a finer grained groundmass which lacks arfvedsonite and has considerable patchy oxidization of aegerine-augite.

AW86088

Seriate - subhedral plagioclase phenocrysts and glomerocrysts (up to 4 mm across) may be embayed with sieve-textured core; seriate, euhedral to skeletal olivine phenocrysts (up to 0.5 mm across) may have opaque inclusions; one anhedral augite phenocryst (1.1 mm across). Fine grained groundmass of tiny opaque minerals, pyroxene needles, scattered olivine and interstitial alkali feldspar.

AW86089

Microporphyritic, subhedral to anhedral alkali feldspar (up to 0.3 mm across) may be glomeroporphyritic; seriate, euhedral olivine (up to 0.15 mm across) may contain opaque minerals, olivine, and pyroxene needles, with interstitial alkali feldspar and ?nepheline. Minor secondary alteration and oxidation of groundmass minerals.

AW86094

Seriate, euhedral - subhedral olivine phenocrysts and glomerocrysts (up to 2.5 mm across) may have opaque inclusions; seriate, euhedral pale brown augite to pinkish brown titanaugite (up to 0.4 mm across) may be intergrown with olivine, and contain olivine and opaque inclusions. Interstitial groundmass of olivine, augite, plagioclase, opaque minerals, and interstitial alkali feldspar and ?nepheline.

AW86095

Seriate, euhedral - subhedral olivine (up to 1.0 mm across); seriate, euhedral, glomeroporphyritic, greenish brown augite (up to 0.6 mm across), intergrown in clots (up to 1.2 mm across) which may include olivine and smaller opaaque inlusions and

intergrowths. Very fine grained groundmass of plagioclase microlites, and cryptocrystalline minerals including tiny opaque minerals and pyroxenes.

AW86096

Subhedral - anhedral augite phenocrysts (up to 2.0 mm across) may contain rounded olivine inclusions; subhedral - anhedral olivine phenocrysts (up to 0.8 mm across); subhedral - anhedral plagioclase phenocrysts and glomerocrysts (0.4 - 1.1 mm across) may have sieve-textured zones and plagioclase overgrowths. Seriate euhedral olivine (up to 0.5 mm across). Groundmass of trachytic-textured plagioclase microlites, augite, and olivine with fine grained interstitial opaque minerals, clinopyroxene, and plagioclase. Minor iddingsitization of olivine.

AW86098

Scattered anhedral xenocrysts of alkali feldspar and anorthoclase (up to 2.0 mm across) may have plagioclase overgrowth and be sieve-textured. Rare euhedral olivine phenocrysts (up to 0.2 mm across) with opaque inclusions. Vesicular, trachytic-textured groundmass of plagioclase, opaque minerals, partially iddingsitized olivine, with interstitial alkali feldspar of nepheline, and cryptocrystalline material, at least some of which is secondary. Secondary calcite lines some vesicles.

AW86100

Rare, anhedral kaersutite phenocrysts (up to 2.0 mm across) with opaque margins. Trachytic-textured groundmass of alkali feldspar and mostly altered kaersutite microlites, with minor hedenbergite and interstitial glass.

AW86101

Seriate, euhedral olivine (up to 1 mm across) contains opaque inclusions at the crystal margins. Intergranular groundmass of plagioclase,opaque minerals, olivine, and clinopyroxene.

AW86102

Anhedral olivine xenocrysts (up to 3mm across); anhedral pale brown augite xenocrysts (up to 1.5 mm across) which may be intergrown with opaque minerals and

plagioclase, and commonly have reaction rims and lines of fluid inclusions. Seriate euhedral olivine (up to 0.2 mm across) and seriate euhedral augite (up to 0.1 mm across). Subophitic groundmass of plagioclase, opaque minerals, olivine and augite.

AW86119

Very similar to AW86033.

AW86120

Euhedral - subhedral olivine phenocrysts (0.2 - 0.6 mm across) may contain opaque inclusions; euhedral - subhedral augite phenocrysts and glomerocrysts (0.1 - 0.4 mm across); rare, anhedral salite phenocrysts (0.2 - 0.5 mm across) may contain occasional apatite inclusions and have augite rims. Very fine-grained, vesicular groundmass of olivine and plagioclase microlites in brown glass, with cryptocrystalline opaque minerals.

AW86121

Subhedral alkali feldspar phenocrysts (0.2 - 1.2 mm across) may have sieve-textured overgrowths; euhedral - anhedral kaersutite (0.2 - 0.8 mm across) with opaque mineral aggregates forming alteration rims, may contain apatite inclusions; euhedral - subhedral aggregates of opaque minerals, pyroxene and alkali feldspar (0.1 - 1.3 mm across) interpreted as kaersutite pseudomorphs; euhedral - anhedral augite phenocrysts and glomerocrysts (0.2 - 1.0 mm across) may have salite core packed with opaque inclusions; euhedral - subhedral cloudy apatite (0.05 - 0.4 mm across). Vesicular groundmass of alkali feldspar and plagioclase microlites, augite and opaque minerals, with interstitial alkali feldspar and ?nepheline.

AW86122

Subhedral - anhedral, very pleochroic kaersutite phenocrysts (0.08 - 0.6 mm across) with opaque rims and commonly twinned, may be intergrown with subordinate augite; anhedral plagioclase phenocrysts (0.1 - 1.0 mm across) may be sieve-textured; seriate, euhedral - subhedral augite (up to 0.6 mm across) commonly contain large

opaque inclusions, may be intergrown or rimmed by kaersutite. Subhedral opaque subphenocrysts (up to 0.2 mm across). Fine grained subophitic groundmass of alkali feldspar microlites, augite, and opaque minerals.

AW86123

Anhedral alkali feldspar phenocrysts (0.4 - 1.6 mm across); hedenbergite - opaque mineral pseudomorphs (0.2 - 0.3 mm across) rarely contain augite and apatite inclusions in remnant kaersutite cores; anhedral opaque subphenocrysts (0.1 - 0.4 mm across). Numerous rounded xenoliths (up to >3.0 mm across) contain euhedral kaersutite phenocrysts (up to 1.2 mm across) with apatite inclusions; subhedral alkali feldspar (1.4 mm across); opaque mineral, apatite and augite microphenocrysts (up to 0.15 mm across) in subophitic alkali feldspar, hedenbergite and opaque mineral groundmass. Anhedral olivine xenocrysts (up to 0.3 mm across) may be rimmed by augite overgrown by sodic pyroxene. Intergranular groundmass of alkali feldspar and hedenbergite intergrowths with interstitial ophitic alkali feldspar enclosing tiny opaque minerals.

AW86124

Rounded olivine phenocrysts and glomerocrysts (0.2 - 0.5 mm across) may be intergrown in clots (up to 1.4 mm across) contain apatite inclusions, and may have overgrowths of kaersutite; subhedral - anhedral kaersutite phenocrysts and glomerocrysts (0.05 - 0.2 mm across); anhedral plagioclase (0.2 - 2.7 mm across). Very vesicular, fine-grained groundmass of trachytic-textured alkali feldspar, augite, and opaque minerals.

AW86127

Subhedral anorthoclase phenocrysts and glomerocrysts (0.6 - 1.2 mm across); rare, euhedral augite phenocrysts (0.6 mm across) with salite rim and feldspar inclusions, may be rimmed by kaersutite overgrowths. Euhedral alkali feldspar subphenocrysts (up to 0.2 mm across); subhedral salite microphenocrysts (up to 0.3 mm across) have large opaque inclusions; anhedral kaersutite subphenocrysts (up to 0.4 mm

across) may be rimmed by salite and opaque overgrowths, one with an augite overgrowth is preserved in plagioclase - alkali feldspar xenolith. Trachytic-textured groundmass of albite microlites, salite and tiny opaque minerals.

AW86128

Euhedral - subhedral alkali feldspar phenocrysts (0.1 - 0.7 mm across) in vesicular devitrified glass.

W84-2

Euhedral - subhedral alkali feldspar phenocrysts (0.8 - 2.0 mm across) contain inclusions of sodic pyroxene needles and incorporate numerous tiny opaque inclusions near the phenocryst rims; subhedral aegerine-augite microphenocrysts (up to 0.4 mm across) may be intergrown with opaque microphenocrysts, which are irregular or hexagonal in outline and typically 0.2 mm across. The interstitial groundmass comprises aggregates of aegerine-augite, aenigmatite and interstitial alkali feldspar.

W84-3

Euhedral plagioclase glomerocrysts (0.1 - 0.4 mm across) may be intergrown with opaque microphenocrysts; rounded kaersutite phenocrysts (0.1 - 0.35 mm across) have narrow opaque rims, inclusions of apatite and opaque minerals, and may be intergrown with minor plagioclase and opaque microphenocrysts; subhedral - anhedral opaque subphenocrysts (up to 0.15 mm across); euhedral augite microphenocrysts (up to 0.15 mm across) typically intergrown with kaersutite and/or opaque microphenocrysts. Trachytic-textured groundmass of plagioclase microlites, aggregates of tiny sodic pyroxene, and ?aenigmatite.

W8413-PM

Rare, euhedral alkali feldspar phenocrysts (0.8 mm across); rare, kaersutite pseudomorphs (0.3 mm across) of aggregates of opaque minerals and pyroxene. Groundmass of alkali feldspar, aegerine-augite, and aenigmatite as enclosed grains and interstitial masses. Secondary calcite alteration is widespread.

APPENDIX 4 - ELECTRON MICROPROBE ANALYSIS

A4.1 Analytical Techniques

Electron microprobe analysis of carbon coated, polished thin sections was used to determine the composition of xenocryst, phenocryst, and groundmass minerals in representative samples from Minna Bluff (Tables A4.1.1 to A4.1.6), Mt Discovery (Tables A4.2.1 to A4.1.6), and Mason Spur (A4.3.1 to A4.3.6).

Analyses were made using the electron microprobe at Victoria University of Wellington, New Zealand, under the following operating conditions:

Accelerating voltage	15 kV
Beam current	1.2×10^{-8} A
Beam diameter (except feldspars)	1 microns
(feldspars)	10 microns

The broader beam used for feldspar analyses eliminated the problem of sodium volatilization. The empirical correction factors of Bence and Albee (1968) were used in data reduction. Synthetic oxides and wollastonite were used to calibrate the instrument, and three international mineral standards (Amelia Albite, Px-1 pyroxene,and Or-1 orthoclase) were run periodically as monitors. The instrument was very stable due to an automatic peak search routine that operated immediately prior to each analysis. Precision and accuracy data, determined on the mineral standards, is given in Table A4.4.

Table A4.1.1 - Microprobe Analyses of olivine from Minna Bluff. FeO* is total iron given as FeO. Detection limits are preceeded by a less than symbol where the analysis is below detection limit. Na_2O, K_2O, and Cr_2O_3 were analysed for, but are always below the detection limit, and have not been included in the table below. Cation formula are calculated on the basis of four oxygens. Iron is assumed to be present only as FeO.

	AW82105										
	P1A.C	P3.C	P4.C	P5.C	P1A.R	P3.R	P4.R	P5.R	G1.C	G2.C	G3.C
SiO2	39.17	40.30	39.41	40.28	39.17	39.46	39.60	39.50	40.10	39.45	39.63
TiO2	<0.09	<0.09	<0.09	0.00	<0.10	<0.09	<0.11	<0.09	0.09	<0.09	<0.10
Al2O3	0.04	0.04	0.06	0.06	0.04	0.05	<0.04	0.05	0.04	0.08	0.04
FeO*	22.02	12.93	17.11	14.71	18.14	17.35	17.41	19.11	17.51	17.83	17.34
MnO	0.34	<0.14	0.20	0.22	0.23	0.29	0.30	0.32	0.22	0.19	0.17
MgO	38.94	46.41	43.14	44.24	41.86	42.10	42.13	40.83	42.53	42.47	43.30
NiO	<0.14	0.24	0.19	0.18	<0.14	0.27	<0.18	<0.14	<0.15	<0.16	0.23
CaO	0.20	0.25	0.28	0.27	0.32	0.31	0.27	0.36	0.28	0.33	0.31
Total	100.71	100.17	100.21	99.96	99.76	99.83	99.71	100.17	100.77	100.35	101.02
Si	1.01	1.00	1.00	1.01	1.00	1.01	1.01	1.01	1.01	1.00	1.00
Ti	0.00	0.00	0.00	0.00	0.00	0.00	0.00	0.00	0.00	0.00	0.00
Al	0.00	0.00	0.00	0.00	0.00	0.00	0.00	0.00	0.00	0.00	0.00
Fe2+	0.47	0.27	0.36	0.31	0.39	0.37	0.37	0.41	0.37	0.38	0.37
Mn	0.01	0.00	0.02	0.02	0.00	0.01	0.01	0.01	0.00	0.00	0.00
Mg	1.49	1.72	1.63	1.65	1.59	1.60	1.60	1.55	1.60	1.60	1.63
Ni	0.00	0.01	0.00	0.00	0.00	0.01	0.00	0.00	0.00	0.00	0.01
Ca	0.01	0.01	0.01	0.01	0.01	0.01	0.01	0.01	0.01	0.01	0.01
	2.99	3.01	3.00	2.98	2.99	3.01	3.00	2.99	2.99	2.99	3.01
Fo	76.0	86.4	81.9	84.2	80.3	81.2	81.2	79.1	81.2	80.8	81.5
Fa	24.0	13.6	18.1	15.8	19.7	18.8	18.8	20.9	18.8	19.2	18.5

Appendix A4.1.1 (continued) - Microprobe analyses of olivine from Minna Bluff.

	AW84797						AW82109		
	P2A.C	P6B.C	P7.C	P2A.R	P6B.R	P7.R	G1.C	G2.C	G3.C
SiO2	38.96	38.71	39.47	38.91	38.21	39.72	36.37	37.08	36.31
TiO2	<0.10	0.09	<0.10	<0.10	<0.09	<0.09	<0.10	0.11	<0.10
Al2O3	<0.04	<0.04	0.08	<0.04	0.05	<0.04	0.05	<0.04	<0.04
FeO*	19.99	19.41	13.45	18.69	19.47	13.78	26.53	26.94	27.62
MnO	0.32	0.25	0.25	0.30	0.29	0.25	0.58	0.70	0.62
MgO	39.76	40.48	45.88	41.84	40.81	45.07	34.51	34.37	34.22
NiO	<0.17	<0.15	<0.17	0.24	0.17	0.22	<0.16	<0.17	<0.15
CaO	0.25	0.28	0.39	0.33	0.30	0.36	0.41	0.46	0.41
Total	99.28	99.22	99.52	100.31	99.30	99.40	98.45	99.66	99.18
Si	1.01	1.00	0.99	0.99	0.99	1.00	0.99	0.99	0.98
Ti	0.00	0.00	0.00	0.00	0.00	0.00	0.00	0.00	0.00
Al	0.00	0.00	0.00	0.00	0.00	0.00	0.00	0.00	0.00
Fe2+	0.43	0.42	0.28	0.40	0.42	0.29	0.60	0.60	0.63
Mn	0.01	0.01	0.01	0.01	0.01	0.01	0.01	0.02	0.01
Mg	1.53	1.56	1.72	1.59	1.58	1.69	1.40	1.37	1.38
Ni	0.00	0.00	0.00	0.01	0.00	0.00	0.00	0.00	0.00
Ca	0.01	0.01	0.01	0.01	0.01	0.01	0.01	0.01	0.01
	2.99	3.00	3.01	3.01	3.01	3.00	3.01	2.99	3.01
Fo	78.1	78.8	86.0	79.9	79.0	85.4	70.0	69.5	68.7
Fa	21.9	21.2	14.0	20.1	21.0	14.6	30.0	30.5	31.3

Table A4.1.2 - Microprobe analyses of pyroxenes from Minna Bluff. FeO* is total iron given as FeO. Detection limits are preceeded by a less than symbol where analysed values are below detection limit. NiO was analysed for, but is below detection limit in all samples and is not given in the table below. Cation formula are calculated on the basis of four cations, with Fe3+ being assessed by charge balancing. End members are asigned according to the method of Kyle (1976).

	AW82105								
	P1B.C	P1C.C	P2A.C	P2B.C	P6.C	P2A.R	P2B.R	P6.R	G1.C
SiO2	47.42	47.37	45.25	48.98	47.10	44.32	46.94	45.29	48.46
TiO2	2.39	2.96	3.37	1.85	2.65	4.85	2.67	3.03	2.01
Al2O3	7.79	7.59	9.19	6.58	8.56	8.65	8.80	9.45	6.18
Cr2O3	<0.14	0.24	0.21	0.57	<0.14	<0.13	0.57	<0.15	<0.13
FeO*	7.37	6.53	6.83	5.84	8.81	7.97	6.06	8.07	7.90
MnO	0.24	<0.14	0.12	<0.13	<0.15	0.16	<0.13	0.17	0.23
MgO	12.46	12.54	12.20	13.64	11.08	11.25	12.48	11.14	12.83
CaO	21.32	23.14	21.68	21.99	21.30	22.68	22.07	21.68	21.48
Na2O	0.84	0.43	0.77	0.61	0.99	0.59	0.51	0.87	0.76
K2O	<0.06	<0.05	<0.05	<0.06	<0.06	<0.06	<0.06	<0.06	<0.06
Total	99.83	100.56	99.41	100.06	100.49	100.47	100.10	99.70	99.85
Si	1.759	1.745	1.672	1.806	1.748	1.654	1.737	1.715	1.800
Ti	0.067	0.082	0.094	0.051	0.074	0.136	0.075	0.085	0.056
Al	0.341	0.331	0.400	0.286	0.374	0.381	0.384	0.421	0.271
Cr	0.000	0.007	0.032	0.017	0.000	0.000	0.017	0.000	0.000
Fe3+	0.068	0.038	0.091	0.029	0.054	0.082	0.013	0.095	0.071
Fe2+	0.161	0.164	0.121	0.152	0.219	0.167	0.175	0.108	0.174
Mn	0.008	0.000	0.004	0.000	0.000	0.005	0.000	0.005	0.007
Mg	0.689	0.689	0.672	0.749	0.613	0.626	0.688	0.624	0.711
Ca	0.848	0.914	0.858	0.867	0.847	0.907	0.867	0.877	0.855
Na	0.060	0.031	0.056	0.044	0.071	0.043	0.037	0.063	0.055
K	0.000	0.000	0.000	0.000	0.000	0.000	0.000	0.000	0.000
Ac	6.0	3.1	5.6	4.4	7.1	4.3	3.7	6.3	5.5
Ft	0.4	0.3	1.7	-	-	2.0	-	1.6	0.8
Tc	6.7	8.2	9.4	5.1	7.4	13.6	7.5	8.5	5.6
Ct	10.4	8.3	10.7	10.1	11.3	5.4	12.6	12.3	7.9
Wo	33.7	37.3	32.3	36.0	33.0	34.9	33.9	32.2	35.6
En	34.5	34.5	33.9	37.6	30.7	31.3	34.6	31.0	35.5
Fs	8.4	8.2	6.3	7.0	10.2	8.6	7.7	8.1	9.1
mg	75.1	77.4	76.1	80.6	69.2	71.5	78.6	75.4	74.4

Table A4.1.2 (continued) - Microprobe analyses of pyroxenes from Minna Bluff.

	AW84797								
	P1A.C	P3A.C	P8.C	P9.C	P1A.M	P3A.R	P3B.R	A4.C	A4.C
SiO2	48.45	44.25	48.44	50.37	48.88	42.90	43.24	43.96	44.33
TiO2	2.02	3.55	1.5	1.29	2.15	4.59	4.66	4.78	4.80
Al2O3	6.63	9.94	4.12	3.66	7.02	10.17	9.85	8.61	8.74
Cr2O3	0.28	<0.14	0.00	0.00	0.67	0.00	<0.14	<0.11	<0.12
FeO*	5.20	7.45	14.92	10.17	5.14	7.70	7.80	7.94	7.88
MnO	<0.16	<0.14	0.20	0.36	<0.14	<0.13	0.18	0.18	0.18
MgO	13.49	11.15	7.85	11.39	13.46	10.59	10.99	10.77	10.91
CaO	22.91	22.0	21.95	21.86	22.66	22.68	22.90	22.52	22.08
Na2O	0.45	0.69	0.93	0.91	0.50	0.64	0.62	0.75	0.75
K2O	0.00	<0.06	<0.05	<0.06	<0.06	<0.06	0.00	<0.06	0.07
Total	99.15	99.03	100.22	100.01	100.48	99.27	100.24	99.51	99.67
Si	1.798	1.662	1.857	1.890	1.804	1.617	1.614	1.657	1.667
Ti	0.056	0.100	0.043	0.036	0.060	0.130	0.131	0.135	0.136
Al	0.290	0.440	0.186	0.161	0.305	0.452	0.434	0.382	0.388
Cr	0.008	0.000	0.000	0.000	0.019	0.000	0.000	0.000	0.000
Fe3+	0.029	0.082	0.093	0.053	0.003	0.100	0.121	0.088	0.061
Fe2+	0.133	0.152	0.395	0.267	0.136	0.143	0.122	0.162	0.186
Mn	0.000	0.000	0.007	0.011	0.000	0.000	0.006	0.006	0.006
Mg	0.746	0.625	0.449	0.637	0.741	0.595	0.612	0.605	0.612
Ca	0.908	0.890	0.901	0.879	0.896	0.916	0.916	0.909	0.890
Na	0.032	0.050	0.069	0.066	0.036	0.047	0.045	0.055	0.055
K	0.000	0.000	0.000	0.000	0.000	0.000	0.000	0.000	0.000
Ac	3.2	5.0	6.9	6.6	3.6	4.7	4.5	5.5	5.5
Ft	-	1.6	0.7	-	-	2.7	3.8	1.7	0.3
Tc	5.6	10.0	4.3	3.6	6.0	13.0	13.1	13.5	13.6
Ct	9.3	12.0	5.0	4.5	10.2	9.6	8.6	5.6	5.8
Wo	38.0	32.5	40.1	39.9	36.7	33.2	33.0	35.1	34.6
En	37.4	31.2	22.4	31.9	37.1	29.8	30.6	30.3	30.6
Fs	6.5	7.6	20.6	12.8	6.3	7.1	6.4	8.4	9.6
mg	82.2	72.8	48.4	66.6	82.3	71.0	81.1	70.7	71.2

Table A4.1.2(continued) - Microprobe analyses of pyroxenes from Minna Bluff.

	AW82109									
	P2.C	P3.C	P4.C	P5.C	P5.C	P2.R	P2.R	P4.R	G1.C	G2.C
SiO2	48.87	47.30	44.44	48.54	49.01	46.28	48.90	49.57	47.90	48.65
TiO2	1.72	1.67	3.68	1.83	1.83	2.45	1.64	1.60	3.14	2.98
Al2O3	4.92	6.38	9.56	6.00	6.01	7.76	5.18	5.21	4.83	4.34
Cr2O3	<0.16	0.72	0.26	0.21	0.21	0.37	0.16	0.20	0.00	<0.14
FeO*	7.78	5.87	7.94	7.13	7.13	7.09	7.22	7.06	8.54	8.38
MnO	0.16	0.13	<0.13	0.17	0.16	0.18	0.15	0.15	0.21	0.27
MgO	14.36	13.70	11.76	13.86	13.87	12.79	13.63	14.45	11.93	12.47
CaO	21.05	22.07	21.32	21.97	21.95	22.13	21.43	21.45	22.87	22.49
Na2O	0.54	0.53	0.73	0.59	0.59	0.64	0.72	0.63	0.62	0.64
K2O	<0.06	0.00	0.00	<0.05	<0.05	<0.05	0.00	<0.05	<0.06	<0.07
Total	99.40	98.37	99.69	100.30	100.76	99.69	99.03	100.32	100.04	100.22
Si	1.817	1.772	1.663	1.790	1.800	1.724	1.827	1.819	1.795	1.816
Ti	0.048	0.047	0.100	0.051	0.051	0.069	0.046	0.044	0.088	0.084
Al	0.215	0.283	0.421	0.260	0.260	0.341	0.228	0.226	0.213	0.191
Cr	0.000	0.021	0.008	0.006	0.006	0.010	0.005	0.006	0.000	0.000
Fe3+	0.094	0.097	0.099	0.099	0.081	0.110	0.079	0.104	0.066	0.056
Fe2+	0.148	0.077	0.150	0.120	0.132	0.101	0.141	0.113	0.202	0.205
Mn	0.005	0.004	0.000	0.005	0.005	0.006	0.005	0.005	0.007	0.009
Mg	0.796	0.769	0.656	0.760	0.759	0.710	0.759	0.790	0.666	0.694
Ca	0.838	0.891	0.850	0.868	0.864	0.883	0.858	0.847	0.918	0.899
Na	0.039	0.039	0.053	0.042	0.042	0.046	0.052	0.045	0.045	0.046
K	0.000	0.000	0.000	0.000	0.000	0.000	0.000	0.000	0.000	0.000
Ac	3.9	3.9	5.3	4.2	4.2	4.6	5.2	5.4	4.5	4.6
Ft	2.8	2.9	2.3	2.8	1.9	3.7	1.3	2.5	1.0	0.5
Tc	4.8	4.7	10.4	5.1	5.1	6.9	4.6	4.4	8.8	8.4
Ct	6.0	9.4	10.7	8.0	8.0	10.2	6.8	6.8	1.8	1.2
Wo	35.1	36.0	31.1	35.5	35.7	33.8	36.5	35.5	40.1	39.9
En	39.8	38.5	32.8	38.1	38.0	35.5	38.0	39.5	33.3	34.7
Fs	7.6	4.6	7.5	6.3	7.2	5.3	7.6	5.9	10.4	10.7
mg	76.7	80.7	72.5	77.6	77.6	76.3	77.1	78.5	71.3	72.7

microphenocrysts (up to 0.3 mm across) may have inclusion-rich salite cores preserved. Groundmass of olivine, plagioclase microlites, augite and opaque minerals, with interstitial alkali feldspar.

AW86944

Very similar to AW86943, except for the lack of kaersutite pseudomorphs, and the high vesicularity of the groundmass.

AW86947

Seriate, euhedral augite to titanaugite glomerocrysts (up to 1.4 mm across) may have pale green cores, in clots with opaque minerals (up to 3.0 mm across); subhedral - anhedral kaersutite phenocrysts and pseudomorphs (up to 0.6 mm across) have opaque alteration rims; scattered subhedral - anhedral plagioclase xenocrysts (up to 0.4 mm across) typically have sieve-textured and overgrown yellowish olivine phenocrysts (up to 1.0 mm across). Fine grained groundmass of plagioclase, opaque and cryptocrystalline minerals.

AW86950

Very similar to AW84718 except that feldspar phenocrysts reach a maximum of 2.1 mm across, and there is no secondary oxidation.

AW86965A

Seriate, euhedral alkali feldspar glomerocrysts and phenocrysts (up to 0.4 mm across); opaque microphenocrysts (up to 0.4 mm across). Trachyte-textured groundmass of sheaves of alkali feldspar and minor hedenbergite and opaque oxides.

AW86970

Euhedral - anhedral plagioclase and alkali feldspar phenocrysts (0.3 - 0.6 mm across) may contain sodic pyroxene inclusions; seriate, euhedral, mostly iddingsitized olivine (up to 0.2 mm across) commonly intergrown with opaque minerals; seriate anhedral opaque minerals (up to 0.1 mm across). Trachytic-textured groundmass of alkali feldspar, salite, opaque minerals and olivine.

Table A4.1.2 (continued) - Microprobe analyses of pyroxenes from Minna Bluff.

	AW84796								
	P3.C	P3.C	P3.M	P3.R	P3.R	P1.C	P9B.C	P1.R	P9B.R
SiO2	47.21	47.06	42.75	47.33	47.23	49.14	50.03	42.63	47.78
TiO2	2.65	2.43	3.77	2.34	2.10	1.44	1.60	4.31	2.36
Al2O3	7.06	6.32	10.67	6.03	5.84	4.45	4.65	10.17	6.15
Cr2O3	<0.16	<0.15	<0.14	<0.15	<0.16	<0.15	<0.16	<0.13	<0.13
FeO*	7.86	7.62	7.07	8.07	8.19	10.31	9.14	7.70	7.81
MnO	0.17	0.00	0.00	0.19	0.25	0.42	0.34	0.15	0.23
MgO	11.76	11.83	11.35	12.15	11.91	11.45	12.33	10.93	12.65
CaO	22.97	23.17	22.93	23.15	23.20	22.39	22.13	22.80	22.92
Na2O	0.69	0.68	0.61	0.61	0.65	0.66	0.66	0.65	0.55
K2O	<0.05	<0.15	<0.56	<0.05	0.00	<0.05	<0.05	<0.05	<0.06
Total	100.37	99.11	99.15	99.88	99.37	100.26	100.88	99.34	100.45
Si	1.753	1.768	1.602	1.766	1.772	1.841	1.853	1.603	1.769
Ti	0.074	0.069	0.106	0.066	0.059	0.041	0.045	0.122	0.066
Al	0.309	0.280	0.471	0.265	0.258	0.196	0.203	0.450	0.269
Cr	0.000	0.000	0.000	0.000	0.000	0.000	0.000	0.000	0.000
Fe3+	0.087	0.097	0.157	0.117	0.127	0.089	0.050	0.148	0.101
Fe2+	0.157	0.142	0.065	0.135	0.130	0.234	0.233	0.094	0.141
Mn	0.005	0.000	0.000	0.006	0.008	0.013	0.011	0.005	0.007
Mg	0.651	0.662	0.634	0.676	0.666	0.639	0.681	0.613	0.698
Ca	0.914	0.932	0.921	0.925	0.932	0.899	0.878	0.918	0.909
Na	0.050	0.050	0.044	0.045	0.047	0.048	0.047	0.047	0.039
K	0.000	0.000	0.000	0.000	0.000	0.000	0.000	0.000	0.000
Ac	5.0	5.0	4.4	4.5	4.7	4.8	4.7	4.7	3.9
Ft	1.8	2.4	5.6	3.6	4.0	2.0	0.1	5.0	3.1
Tc	7.4	6.9	10.6	6.6	5.9	4.1	4.5	12.2	6.6
Ct	8.0	7.1	12.9	6.7	7.0	5.8	5.7	10.3	6.8
Wo	37.0	38.4	31.4	37.8	38.2	39.0	38.8	32.1	37.2
En	32.5	33.1	31.7	33.8	33.3	32.0	34.0	30.6	34.9
Fs	8.1	7.1	3.2	7.0	6.9	12.4	12.2	4.9	7.4
mg	72.7	73.5	74.1	72.8	72.2	66.4	70.6	71.7	74.3

Table A4.1.2 (continued) - Microprobe analyses of pyroxenes from Minna Bluff.

	AW82097B		AW82056						
	P1.C	P1.R	M3B.C	M3B.R	I1.C	I2.C	G1.C	G2.C	A4D.C
SiO2	50.72	50.21	49.24	50.58	50.52	49.32	49.48	51.58	49.77
TiO2	1.67	1.81	0.33	1.33	1.13	1.74	1.39	0.36	1.49
Al2O3	3.84	4.18	2.13	3.42	2.56	4.20	3.62	1.46	2.41
Cr2O3	0.00	0.00	<0.16	<0.15	<0.14	<0.14	0.00	<0.14	0.00
FeO*	7.87	7.24	19.16	10.11	8.75	9.15	11.97	12.40	10.50
MnO	0.23	0.24	1.09	0.34	0.33	0.29	0.59	0.65	0.40
MgO	12.90	12.53	5.96	11.49	13.26	12.04	10.80	10.74	11.39
CaO	23.04	22.83	20.80	22.22	22.60	22.69	21.73	22.50	21.71
Na2O	0.67	0.64	1.13	0.64	0.54	0.75	0.73	0.67	0.92
K2O	<0.05	<0.05	0.00	<0.06	<0.07	0.00	<0.05	<0.07	0.13
Total	100.94	99.68	99.84	100.13	99.69	100.18	100.31	100.36	99.59
Si	1.870	1.875	1.925	1.899	1.888	1.840	1.865	1.948	1.877
Ti	0.046	0.051	0.010	0.038	0.032	0.049	0.039	0.010	0.042
Al	0.167	0.184	0.098	0.152	0.113	0.185	0.161	0.065	0.146
Cr	0.000	0.000	0.000	0.000	0.000	0.000	0.000	0.000	0.000
Fe3+	0.048	0.012	0.118	0.022	0.086	0.091	0.083	0.067	0.089
Fe2+	0.194	0.215	0.509	0.296	0.187	0.195	0.295	0.324	0.242
Mn	0.007	0.008	0.036	0.011	0.010	0.009	0.019	0.021	0.013
Mg	0.709	0.697	0.347	0.643	0.739	0.670	0.607	0.605	0.640
Ca	0.910	0.913	0.871	0.894	0.905	0.907	0.878	0.910	0.877
Na	0.048	0.046	0.086	0.047	0.039	0.054	0.053	0.049	0.067
K	0.000	0.000	0.000	0.000	0.000	0.000	0.000	0.000	0.006
Ac	4.8	4.6	8.6	4.7	3.9	5.4	5.3	4.9	7.4
Ft	-	-	0.16	-	2.3	1.8	1.5	0.9	0.8
Tc	4.6	5.1	0.10	3.8	3.2	4.9	3.9	1.0	4.2
Ct	3.7	4.1	3.9	3.8	2.5	4.4	4.1	2.2	3.1
Wo	41.3	41.1	40.3	40.9	41.3	39.8	39.1	43.4	39.8
En	35.5	34.9	17.4	32.2	36.9	33.5	30.3	30.2	32.0
Fs	10.1	9.6	27.2	15.3	9.9	10.2	15.7	17.3	12.7
mg	74.6	75.4	35.6	66.9	73.0	70.1	61.6	69.7	65.9

Table A4.1.2 (continued) - Microprobe analyses of pyroxenes from Minna Bluff.

	AW82150								
	I2C.C	G1.C	G2.C	G3.C	G4.C	A4.C	A4.C	A4.C	A8.C
SiO2	49.16	48.60	48.28	48.45	48.46	45.06	48.32	48.44	46.17
TiO2	0.69	0.30	0.82	0.86	0.72	1.88	0.71	0.68	2.34
Al203	1.93	0.91	2.51	2.48	2.04	6.32	2.06	1.88	5.18
Cr203	<0.16	<0.15	<0.15	<0.14	<0.16	0.00	0.00	<0.14	0.00
FeO*	19.28	25.34	19.48	19.79	20.25	18.08	20.24	18.61	15.70
MnO	1.09	1.63	1.18	1.10	1.22	0.81	0.88	0.94	0.76
MgO	5.64	1.42	4.41	4.95	4.52	5.18	5.14	6.09	7.16
CaO	20.83	20.12	21.41	21.08	21.37	21.60	21.63	21.65	21.67
Na20	1.20	1.32	1.04	1.13	1.19	0.97	1.02	1.13	1.26
K20	0.06	<0.06	<0.06	0.10	<0.05	<0.06	<0.05	<0.06	<0.06
Total	99.88	99.64	99.13	99.94	100.02	99.90	100.00	99.42	100.24
Si	1.925	1.970	1.918	1.904	1.909	1.759	1.894	1.886	1.773
Ti	0.020	0.009	0.025	0.025	0.021	0.055	0.021	0.020	0.068
Al	0.089	0.043	0.118	0.115	0.095	0.291	0.101	0.100	0.235
Cr	0.000	0.000	0.000	0.000	0.000	0.000	0.000	0.000	0.000
Fe3+	0.114	0.103	0.077	0.117	0.135	0.155	0.142	0.159	0.177
Fe2+	0.518	0.756	0.570	0.533	0.541	0.436	0.523	0.451	0.327
Mn	0.036	0.056	0.040	0.037	0.041	0.027	0.029	0.031	0.025
Mg	0.329	0.086	0.261	0.290	0.265	0.301	0.301	0.356	0.410
Ca	0.874	0.874	0.911	0.888	0.902	0.903	0.911	0.910	0.892
Na	0.091	0.104	0.080	0.086	0.091	0.073	0.078	0.086	0.094
K	0.003	0.000	0.000	0.005	0.000	0.000	0.000	0.000	0.000
Ac	9.4	10.4	8.0	9.1	9.1	7.3	7.8	8.6	9.4
Ft	1.0	-	-	1.3	2.2	4.1	3.2	3.7	4.2
Tc	2.0	0.9	2.5	2.5	2.1	5.5	2.1	2.0	6.8
Ct	2.4	1.7	3.4	3.2	2.6	9.0	2.7	2.3	5.0
Wo	41.0	42.4	41.6	40.9	41.6	35.9	41.6	41.5	36.6
En	16.5	4.3	13.1	14.5	13.3	15.1	15.1	17.8	20.5
Fs	27.7	40.6	30.4	28.5	29.1	23.1	27.6	24.1	17.6
mg	34.2	9.1	28.7	30.9	28.2	33.7	31.2	36.9	44.9

Table A4.1.3 - Microprobe analyses of amphiboles from Minna Bluff. FeO* is total iron given as FeO. Detection limits are preceeded by a less than symbol and are given where the analysis is below detection limit. Cr_2O_3, NiO, and Cl were analysed, but are always below the detection limit and are not given in the table below. Cation formula are calculated on the basis of 23 oxygens. No attempt has been made to assess the Fe3+ content.

	AW82109			AW82097B						
	P1.C	P1.C	P1.R	P3.C	P5B.C	P5B.C	P6.C	P3.R	P5A.R	P5B.R
SiO2	39.10	38.44	39.00	40.45	39.41	39.94	40.62	40.50	40.58	40.60
TiO2	5.80	5.78	5.63	7.18	7.58	7.50	7.42	7.26	7.32	7.28
Al2O3	13.35	13.26	13.16	12.14	12.80	12.30	12.36	12.29	12.23	12.24
FeO*	13.80	13.41	13.73	12.49	12.20	12.30	12.18	12.11	12.19	12.26
MnO	0.26	0.21	0.00	0.29	0.22	0.17	0.19	0.18	0.19	0.22
MgO	10.60	10.65	10.34	11.11	10.94	11.28	11.44	11.04	11.07	11.15
CaO	11.54	11.62	11.50	12.28	12.13	12.08	11.99	12.11	12.07	12.17
Na2O	2.77	2.73	2.76	2.61	2.64	2.61	2.60	2.64	2.70	2.68
K2O	1.07	1.08	0.84	1.17	1.17	1.18	1.22	1.21	1.22	1.20
Total	98.29	97.18	96.96	99.72	99.09	99.36	100.02	99.34	99.57	99.80
Si	5.857	5.834	5.895	5.932	5.816	5.874	5.921	5.945	5.946	5.938
Ti	0.652	0.657	0.640	0.792	0.841	0.843	0.813	0.801	0.807	0.801
Al	2.353	2.364	2.344	2.098	2.226	2.132	2.123	2.126	2.112	2.110
Fe2+	1.726	1.696	1.736	1.532	1.506	1.513	1.485	1.487	1.494	1.500
Mn	0.033	0.027	0.000	0.036	0.028	0.021	0.024	0.022	0.024	0.027
Mg	2.363	2.401	2.330	2.429	2.407	2.473	2.486	2.416	2.418	2.431
Ca	1.849	1.883	1.862	1.929	1.918	1.904	1.873	1.905	1.895	1.907
Na	0.803	0.800	0.809	0.742	0.755	0.744	0.735	0.751	0.767	0.760
K	0.204	0.208	0.162	0.219	0.220	0.221	0.227	0.227	0.228	0.224
Total	15.829	15.851	15.778	15.708	15.717	15.713	15.685	15.680	15.689	15.698
mg	57.3	58.2	57.3	56.2	61.1	61.7	62.2	61.6	61.4	61.4

Table A4.1.3 (continued) - Microprobe analyses of amphiboles from Minna Bluff.

	AW82078								AW82150
	P1B.C	P2.C	P3.C	P8.C	P9.C	P2.R	G1.C	G2.C	P1A.C
SiO2	38.45	38.68	37.19	38.20	36.61	38.54	38.03	37.74	37.25
TiO2	4.64	4.89	3.51	4.86	7.94	4.88	7.01	7.29	7.20
Al203	11.82	11.51	11.59	11.71	14.76	12.31	14.26	14.59	14.61
FeO*	23.59	23.99	28.60	23.66	12.17	21.81	11.03	11.63	11.34
MnO	0.52	0.53	0.80	0.47	0.14	0.35	0.17	0.15	0.00
MgO	4.54	4.03	1.59	4.33	11.04	5.56	11.55	11.48	11.86
CaO	11.21	11.07	10.56	11.03	12.20	11.47	12.26	12.43	12.24
Na2O	2.78	2.51	2.69	2.64	2.45	2.65	2.53	2.52	2.86
K2O	1.35	1.47	1.81	1.42	1.33	1.45	1.15	1.16	1.08
Total	98.90	98.68	98.34	98.32	98.64	99.02	97.99	98.99	98.44
Si	6.005	6.060	6.016	6.004	5.457	5.958	5.653	5.575	5.531
Ti	0.545	0.576	0.427	0.574	0.890	0.567	0.784	0.810	0.804
Al	2.176	2.125	2.210	2.169	2.593	2.243	2.498	2.540	2.557
Fe2+	3.081	3.143	3.869	3.110	1.517	2.820	1.371	1.437	1.408
Mn	0.069	0.070	0.110	0.063	0.018	0.046	0.021	0.019	0.000
Mg	1.057	0.941	0.383	1.015	2.453	1.281	2.560	2.528	2.625
Ca	1.876	1.858	1.830	1.858	1.948	1.900	1.953	1.967	1.947
Na	0.842	0.762	0.844	0.804	0.708	0.794	0.729	0.722	0.823
K	0.269	0.294	0.374	0.285	0.253	0.286	0.218	0.219	0.205
Total	15.918	15.830	16.061	15.881	15.837	15.894	15.787	15.816	15.900
mg	25.1	22.7	8.8	24.2	61.8	31.3	65.1	63.5	56.2

Table A4.1.4 - Microprobe analyses of feldspars from Minna Bluff. FeO* is total iron given as FeO. Detection limits are preceeded by a less than symbol and indicate that the analysed value is below detection limit. MnO, NiO, and Cr_2O_3 were analysed for, but are always below detection limit and are not given in the table below. Cation formula are calculated on the basis of 32 oxygens.

	AW82105			AW84797			AW82109		
	G1.C	G2.C	G3.C	X1B.C	X1B.M	X1B.R	G1.C	G2.C	G3.C
SiO2	49.87	50.44	50.40	54.75	52.66	49.73	54.82	53.90	54.00
TiO2	0.14	0.00	0.14	0.09	0.18	<0.16	0.20	0.19	0.21
Al2O3	31.23	31.02	31.41	28.29	29.82	31.33	27.05	27.22	27.31
FeO*	0.61	0.55	0.54	0.38	0.60	0.57	0.89	0.40	0.64
MgO	0.12	0.11	0.13	<0.04	0.06	0.07	0.21	0.14	0.11
CaO	15.69	15.31	15.36	10.66	12.71	14.80	10.57	10.73	10.97
Na2O	2.73	3.01	2.78	5.68	4.30	3.30	5.16	5.11	5.09
K2O	0.25	0.24	0.23	0.36	0.34	0.19	0.67	0.55	0.59
Total	100.64	100.68	100.99	100.25	100.66	100.01	99.60	98.29	98.99
Si	9.09	9.18	9.14	9.89	9.52	9.11	9.99	9.94	9.91
Ti	0.02	0.00	0.02	0.01	0.02	0.00	0.03	0.03	0.03
Al	6.75	6.69	6.75	6.05	6.39	6.80	5.82	5.94	5.94
Fe2+	0.09	0.08	0.08	0.06	0.09	0.09	0.14	0.06	0.10
Mg	0.03	0.03	0.04	0.00	0.02	0.02	0.06	0.04	0.03
Ca	3.07	2.99	2.98	2.06	2.46	2.91	2.06	2.12	2.16
Na	0.97	1.06	0.98	1.99	1.51	1.17	1.83	1.83	1.81
K	0.06	0.06	0.05	0.08	0.08	0.04	0.16	0.13	0.14
	20.08	20.09	20.04	20.14	20.09	20.14	20.11	20.09	20.12
An	74.9	72.7	74.3	49.9	60.7	70.6	50.9	52.0	52.6
Ab	23.7	25.8	24.4	48.2	37.3	28.4	45.2	44.9	44.0
Or	1.5	1.5	1.2	1.9	2.0	1.0	4.0	3.2	3.4

Table A4.1.4 (continued) - Microprobe analyses of feldspars from Minna Bluff.

	AW84796								
	P5A.C	P6.C	M2.C	M3.C	M7A.C	P5A.R	P5B.R	P5B.R	P6.R
SiO2	53.26	52.78	52.24	53.58	52.73	52.88	51.99	51.75	53.49
TiO2	<0.09	0.11	<0.09	<0.10	0.14	<0.09	0.11	<0.09	0.16
Al2O3	29.04	29.27	30.27	29.04	30.22	29.22	29.57	29.29	29.07
FeO*	0.44	0.34	0.37	0.30	0.43	0.35	0.38	0.50	0.44
MgO	0.05	<0.04	0.05	0.05	0.06	0.05	0.04	0.06	0.06
CaO	11.80	12.31	12.75	11.42	12.27	12.13	12.51	12.19	11.37
Na2O	4.77	4.52	4.17	4.91	4.42	4.67	4.47	4.58	4.84
K2O	0.40	0.19	0.15	0.22	0.19	0.33	0.29	0.33	0.19
Total	99.76	99.52	100.00	99.52	100.46	99.63	99.36	98.70	99.62
Si	9.69	9.63	9.49	9.74	9.53	9.64	9.52	9.54	9.72
Ti02	0.00	0.02	0.00	0.00	0.02	0.00	0.02	0.00	0.02
Al	6.26	6.32	6.51	6.26	6.47	6.31	6.42	6.40	6.26
Fe2+	0.07	0.05	0.06	0.05	0.06	0.05	0.06	0.08	0.07
Mg	0.01	0.00	0.01	0.01	0.02	0.01	0.01	0.02	0.02
Ca	2.30	2.41	2.48	2.23	2.38	2.37	2.45	2.41	2.21
Na	1.68	1.60	1.47	1.73	1.55	1.65	1.59	1.64	1.71
K	0.09	0.04	0.03	0.05	0.04	0.08	0.07	0.08	0.04
	20.10	20.07	20.05	20.07	20.07	20.11	20.14	20.17	20.05
An	56.5	59.5	62.3	55.6	59.9	57.8	59.6	58.4	55.8
Ab	41.3	39.5	36.9	43.1	39.0	40.2	38.7	39.7	43.2
Or	2.2	1.0	0.8	1.2	1.0	2.0	1.7	1.9	1.0

Table A4.1.4 (continued) - Microprobe analyses of feldspars from Minna Bluff.

	AW82097B								
	P2.C	P4.C	P7.C	M1.C	M2.C	M3.C	P2.R	P4.R	P7.R
SiO2	55.73	55.98	49.91	54.95	55.76	54.90	54.59	56.25	53.98
TiO2	0.09	0.13	0.09	0.10	<0.09	0.10	0.10	0.13	0.10
Al203	26.73	27.55	31.77	27.80	27.79	28.37	26.83	27.48	29.01
FeO*	0.23	0.34	0.33	0.31	0.32	0.40	0.73	0.29	0.34
MgO	<0.04	0.04	0.04	<0.04	<0.04	0.09	0.29	0.05	0.04
CaO	10.31	10.32	15.69	11.16	11.03	11.66	10.97	10.65	12.19
Na20	5.08	5.51	2.61	4.95	5.19	4.78	4.84	5.19	4.59
K20	0.78	0.53	0.15	0.45	0.44	0.43	0.58	0.48	0.42
Total	98.95	100.40	100.59	99.72	100.56	100.73	98.93	100.52	100.63
Si	10.16	10.07	9.08	9.96	10.02	9.87	10.00	10.09	9.73
Ti	0.01	0.02	0.01	0.01	0.00	0.01	0.01	0.02	0.01
Al	5.77	7.87	6.85	5.97	5.92	6.04	5.82	5.84	6.20
Fe2+	0.04	0.05	0.05	0.05	0.05	0.06	0.11	0.04	0.05
Mg	0.00	0.01	0.01	0.00	0.01	0.02	0.08	0.01	0.00
Ca	2.01	1.99	3.06	2.17	2.12	2.25	2.15	2.05	2.36
Na	1.80	1.92	0.92	1.74	1.81	1.67	1.72	1.81	1.61
K	0.18	0.12	0.03	0.10	0.10	0.10	0.14	0.11	0.10
	19.97	20.05	20.01	20.00	20.03	20.02	20.03	19.97	20.06
An	50.4	49.4	76.3	54.1	52.6	56.0	53.6	51.6	58.0
Ab	45.1	47.6	22.9	43.4	44.9	41.5	42.9	45.6	39.6
Or	4.5	3.0	0.7	2.5	2.5	2.5	3.5	2.8	2.5

Table A4.1.4 (continued) - Microprobe analyses of feldspars from Minna Bluff.

	AW82056								
	P1A.C	P2.C	P4A.C	P1A.R	P2.R	P4A.R	G1.C	G2.C	G3.C
SiO2	56.30	58.72	59.24	59.59	59.42	59.20	58.87	58.95	59.38
TiO2	<0.09	0.09	0.13	<0.09	<0.10	0.13	<0.09	<0.09	0.09
Al203	26.93	25.52	25.40	24.78	24.81	25.67	25.42	24.98	25.26
FeO*	0.28	0.20	0.19	0.24	0.45	0.45	0.50	0.32	0.41
MgO	0.05	0.08	<0.04	0.00	<0.10	<0.12	0.09	<0.04	0.04
CaO	8.96	7.30	6.87	6.10	6.76	7.12	7.01	7.04	7.12
Na20	5.97	6.76	7.16	7.31	6.92	6.84	7.03	7.05	6.74
K20	0.59	0.88	0.96	0.88	1.22	0.89	0.87	0.94	1.06
Total	99.08	99.55	99.95	98.90	99.58	100.30	100.58	99.28	100.10
Si	10.22	10.56	10.61	10.75	10.69	10.57	10.51	10.64	10.63
Ti	0.00	0.01	0.02	0.00	0.00	0.02	0.00	0.00	0.01
Al	5.79	5.44	5.39	5.30	5.29	5.43	5.37	5.34	5.36
Fe2+	0.04	0.03	0.03	0.04	0.07	0.07	0.07	0.05	0.06
Mg	0.01	0.02	0.00	0.00	0.00	0.00	0.23	0.00	0.00
Ca	1.74	1.41	1.32	1.18	1.30	1.36	1.34	1.36	1.37
Na	2.10	2.36	2.49	2.56	2.42	2.37	2.44	2.47	2.34
K	0.14	0.20	0.22	0.20	0.28	0.20	0.20	0.22	0.24
	20.04	20.03	20.08	20.03	20.05	20.02	20.16	20.08	20.02
An	43.7	35.5	32.8	29.9	32.5	34.6	33.7	33.6	34.7
Ab	52.8	59.4	61.8	65.0	60.5	60.3	61.3	61.0	59.2
Or	3.5	5.0	5.5	5.1	7.0	5.1	5.0	5.4	6.1

Table A4.1.1 (continued) - Microprobe analyses of feldspars from Minna Bluff.

	AW82078								
	P1A.C	P4.C	P6.C	P1A.R	P4.R	P6.R	G1.C	G2.C	G3.C
SiO2	59.93	62.23	62.31	60.61	62.88	63.07	61.08	61.36	60.98
TiO2	<0.09	<0.08	<0.09	<0.09	<0.09	0.09	<0.09	<0.09	<0.09
Al2O3	25.09	23.70	23.42	24.37	22.28	21.91	23.30	23.04	23.81
FeO*	0.30	0.23	0.23	0.32	0.29	0.37	0.40	0.47	0.43
MgO	<0.04	<0.04	<0.04	<0.04	0.00	<0.04	<0.04	<0.04	<0.04
CaO	6.55	4.81	4.21	5.96	3.39	2.97	4.85	4.51	4.98
Na2O	7.35	7.94	8.11	7.53	8.13	7.82	7.76	7.99	7.76
K2O	0.90	1.30	1.47	1.05	2.36	2.60	1.35	1.42	1.27
Total	100.12	100.21	99.75	99.84	99.33	98.83	98.74	98.79	99.23
Si	10.70	11.05	11.11	10.84	11.28	11.35	11.02	11.07	10.96
Ti	0.00	0.00	0.00	0.00	0.00	0.01	0.00	0.00	0.00
Al	5.31	4.99	4.95	5.16	4.73	4.67	4.98	4.93	5.07
Fe2+	0.04	0.03	0.03	0.05	0.04	0.06	0.06	0.07	0.06
Mg	0.00	0.00	0.00	0.00	0.00	0.00	0.00	0.00	0.00
Ca	1.25	0.91	0.80	1.14	0.65	0.57	0.94	0.87	0.96
Na	2.55	2.74	2.81	2.61	2.83	2.73	2.72	2.80	2.71
K	0.21	0.29	0.33	0.24	0.54	0.60	0.31	0.33	0.29
	20.06	20.01	20.03	20.04	20.07	19.99	20.03	20.07	20.05
An	31.2	23.1	20.3	28.6	16.2	14.6	23.7	21.8	24.2
Ab	63.6	69.5	71.3	65.4	70.4	70.0	68.5	70.0	68.4
Or	5.2	7.4	8.4	6.0	13.4	15.4	7.8	8.3	7.3

Table A4.1.1 (continued) - Microprobe analyses of feldspars from Minna Bluff.

	AW82150									
	P2A.C	P2B.C	P3.C	P3.C	P3.C	P2A.M	P2B.M	P3.M	P2A.R	P2B.R
SiO2	64.23	66.32	64.25	64.37	65.00	65.79	65.02	63.01	64.60	66.42
TiO2	0.11	0.00	<0.09	0.00	<0.09	<0.09	<0.09	<0.09	<0.09	0.00
Al2O3	22.25	18.79	19.91	19.80	19.60	20.00	21.15	21.78	21.48	19.94
FeO*	<0.13	<0.12	<0.13	<0.14	<0.13	<0.12	0.12	0.16	0.19	0.15
MgO	<0.04	<0.04	<0.04	0.00	<0.04	<0.04	0.00	0.00	0.00	0.00
CaO	3.29	0.15	0.84	0.77	0.62	1.02	2.01	3.03	2.44	0.82
Na2O	7.42	5.01	5.80	5.91	5.77	6.13	7.10	7.41	7.59	6.32
K2O	3.61	9.84	7.72	7.83	7.99	7.23	4.87	3.74	4.21	7.41
Total	100.91	100.11	98.52	98.68	98.98	100.17	100.27	99.13	100.51	101.06
Si	11.36	11.98	11.74	11.75	11.82	11.79	11.58	11.36	11.48	11.81
Ti	0.01	0.00	0.00	0.00	0.00	0.00	0.00	0.00	0.00	0.00
Al	4.66	4.02	4.31	4.28	4.22	4.25	4.46	4.65	4.52	4.20
Fe2+	0.00	0.00	0.00	0.00	0.00	0.00	0.02	0.02	0.03	0.02
Mg	0.00	0.00	0.00	0.00	0.00	0.00	0.00	0.00	0.00	0.00
Ca	0.62	0.03	0.16	0.15	0.12	0.20	0.38	0.59	0.46	0.16
Na	2.55	1.76	2.06	2.09	2.04	2.13	2.45	2.59	0.46	0.16
K	0.81	2.27	1.80	1.82	1.85	1.65	1.11	0.86	0.95	1.68
	20.01	20.06	20.07	20.09	20.05	20.02	20.00	20.07	20.06	20.05
An	15.6	0.7	4.0	3.7	3.0	5.0	9.6	14.6	11.4	4.0
Ab	64.1	43.3	51.2	51.5	50.9	53.5	62.2	64.1	65.0	54.2
Or	20.4	55.9	44.8	44.8	46.1	41.5	28.2	21.3	23.6	41.8

Table A4.1.4 (continued) - Microprobe analyses of feldspars from Minna Bluff.

	AW82150					
	P3.R	S5B.C	G1.C	G2.C	G3.C	G5.C
SiO2	65.08	63.82	65.33	65.14	64.64	66.14
TiO2	<0.09	<0.09	<0.09	<0.09	<0.08	<0.09
Al2O3	19.69	21.47	19.32	19.51	18.95	19.35
FeO*	0.14	0.15	0.30	0.36	0.28	0.37
MgO	0.00	0.00	0.00	<0.04	0.00	0.00
CaO	0.70	2.83	0.46	0.59	0.11	0.35
Na2O	5.66	7.40	5.96	5.87	4.71	5.70
K2O	8.21	3.61	7.91	8.36	9.52	8.42
Total	99.48	99.28	99.28	99.83	98.21	100.33
Si	11.79	11.46	11.85	11.79	11.90	11.88
Ti	0.00	0.00	0.00	0.00	0.00	0.00
Al	4.23	4.57	4.15	4.19	4.13	4.12
Fe2+	0.02	0.02	0.05	0.05	0.04	0.06
Mg	0.00	0.00	0.00	0.00	0.00	0.00
Ca	0.14	0.54	0.09	0.11	0.02	0.07
Na	1.99	2.58	2.10	2.06	1.68	1.99
K	1.90	0.83	1.83	1.93	2.24	1.93
	20.07	20.00	20.07	20.13	20.01	20.05
An	3.5	13.7	2.2	2.7	0.5	1.8
Ab	49.4	65.3	52.2	50.2	42.6	49.9
Or	47.1	21.0	45.5	47.1	56.9	48.4

Table A4.1.5 - Microprobe analyses of opaque oxides from Minna Bluff. Detection limits are preceeded by a less than symbol and indicate that the analysed value is below detection limit. Na_2O, and K_2O were analysed for, but are always below detection limit and are not given in the table below. Iron was analysed as FeO*, and Fe_2O_3 and FeO asigned by charge balancing of the cation formula calculated on the basis of 32 oxygen. Stormer's (1983) method was used to calculate the ulvospinel component.

	AW82105			AW84797				AW82109		
	G1.C	G2.C	G3.C	I3B.C	I6D.C	G1.C	G10.C	G1.C	G2.C	G3.C
SiO2	0.12	0.11	0.13	0.11	0.07	0.10	0.06	0.15	0.16	0.14
TiO2	23.67	24.06	24.31	20.60	18.36	21.72	19.76	23.31	25.79	26.81
Al203	5.25	5.05	4.69	5.11	8.75	6.44	3.68	3.81	2.94	2.83
Cr203	2.28	<0.17	1.70	<0.18	0.00	<0.18	0.00	2.06	0.24	0.27
Fe203	15.45	18.76	15.41	26.59	26.86	22.20	28.94	17.44	15.60	13.56
FeO	47.54	47.05	47.96	41.08	38.28	42.93	41.84	47.42	51.07	52.26
MnO	0.55	0.55	0.48	0.35	0.41	0.54	0.41	0.80	0.93	0.96
MgO	3.64	4.45	3.72	6.42	7.15	5.81	5.07	3.12	2.22	1.99
NiO	<0.19	<0.18	0.00	<0.19	<0.19	<0.17	<0.18	<0.19	0.00	<0.18
CaO	<0.08	<0.08	0.15	<0.08	<0.08	<0.08	<0.08	<0.08	0.10	0.10
Total	98.50	100.03	98.39	100.26	99.88	99.74	99.76	98.11	98.95	98.82
Si	0.001	0.001	0.002	0.001	0.001	0.001	0.001	0.002	0.002	0.002
Ti	0.214	0.214	0.220	0.180	0.158	0.190	0.177	0.214	0.237	0.247
Al	0.074	0.070	0.067	0.070	0.118	0.089	0.052	0.055	0.042	0.041
Cr	0.022	0.000	0.016	0.000	0.000	0.000	0.000	0.020	0.002	0.003
Fe3+	0.140	0.167	0.140	0.233	0.231	0.195	0.259	0.160	0.144	0.125
Fe2+	0.478	0.464	0.484	0.400	0.366	0.419	0.417	0.484	0.522	0.536
Mn	0.006	0.005	0.005	0.003	0.004	0.005	0.004	0.008	0.010	0.010
Mg	0.065	0.078	0.067	0.111	0.122	0.101	0.090	0.057	0.040	0.036
Ni	0.000	0.000	0.000	0.000	0.000	0.000	0.000	0.000	0.000	0.000
Ca	0.000	0.000	0.001	0.000	0.000	0.000	0.000	0.000	0.001	0.001
Usp	81.8	75.5	81.4	61.0	60.6	69.4	57.2	77.5	79.8	83.1

Table A4.1.5 (continued) - Microprobe analyses of opaque oxides from Minna Bluff.

	AW82097B			AW82056				AW82078		
	M4.C	M8.C	M8.C	M2.C	M4.C	M4.C	A4D.C	P5.C	P5.R	G1.
SiO2	0.07	0.08	0.11	0.11	0.12	0.11	0.14	0.15	0.14	0.
TiO2	25.16	24.63	24.91	21.05	21.19	19.76	24.72	18.08	19.94	13.
Al2O3	3.81	4.03	3.92	2.41	2.34	2.26	2.99	1.54	1.70	1.
Cr2O3	0.00	<0.16	0.00	<0.17	0.00	<0.17	<0.16	<0.19	0.00	<0.
Fe2O3	18.20	19.13	17.73	26.76	26.86	27.45	18.32	31.86	28.21	39.
FeO	48.39	48.00	48.16	46.77	47.13	44.82	45.86	46.78	47.73	40.
MnO	0.92	0.90	0.79	1.04	1.08	1.12	1.00	1.20	1.27	1.
MgO	3.91	3.94	3.84	2.20	2.19	2.13	4.39	0.17	0.60	0.
NiO	0.00	<0.17	<0.18	<0.17	<0.20	<0.19	0.00	<0.18	<0.19	<0.
CaO	<0.08	<0.07	<0.07	0.09	<0.08	<0.08	0.33	0.00	<0.08	0.
Total	100.46	100.72	99.47	100.43	100.91	97.65	97.78	99.78	99.60	98.
Si	0.001	0.001	0.001	0.001	0.001	0.001	0.002	0.002	0.002	0.
Ti	0.225	0.219	0.224	0.192	0.193	0.186	0.226	0.170	0.187	0.
Al	0.053	0.056	0.055	0.035	0.033	0.033	0.043	0.023	0.025	0.
Cr	0.000	0.000	0.000	0.000	0.000	0.000	0.000	0.000	0.000	0.
Fe3+	0.163	0.170	0.160	0.245	0.245	0.259	0.168	0.300	0.265	0.
Fe2+	0.480	0.475	0.482	0.475	0.477	0.469	0.467	0.489	0.497	0.
Mn	0.009	0.009	0.008	0.011	0.011	0.012	0.010	0.013	0.013	0.
Mg	0.069	0.069	0.069	0.040	0.040	0.040	0.080	0.003	0.011	0.
Ni	0.000	0.000	0.000	0.000	0.000	0.000	0.000	0.000	0.000	0.
Ca	0.000	0.000	0.000	0.001	0.000	0.000	0.004	0.000	0.000	0.
Usp	75.9	74.6	76.5	61.8	61.8	59.4	73.8	54.2	59.6	40.

Table A4.1.5 (continued) - Microprobe analyses of opaque oxides from Minna Bluff.

	AW82150	
	G1.C	G2.C
SiO2	0.13	0.25
TiO2	13.50	12.60
Al2O3	1.18	0.66
Cr2O3	<0.18	<0.18
Fe2O3	41.30	41.42
FeO	42.33	40.87
MnO	1.55	1.47
MgO	0.06	0.00
NiO	<0.19	<0.17
CaO	<0.09	<0.08
Total	100.05	97.27
Si	0.002	0.003
Ti	0.128	0.123
Al	0.017	0.010
Cr	0.000	0.000
Fe3+	0.391	0.404
Fe2+	0.445	0.443
Mn	0.017	0.016
Mg	0.001	0.000
Ni	0.000	0.000
Ca	0.000	0.000
Usp	39.6	37.6

Table A4.1.6 - Microprobe analysis of probable nepheline from Minna Bluff. FeO* is total iron given as FeO. Cation formula is calculated on the basis of 32 oxygens.

	AW82150
	A4.C
SiO2	49.73
TiO2	0.00
Al2O3	30.57
FeO*	1.42
MnO	0.00
MgO	0.25
CaO	0.12
Na2O	16.90
K2O	1.27
Total	100.10
Si	9.231
Al	6.688
Fe2+	0.220
Mg	0.069
Ca	0.024
Na	6.083
K	0.301
Total	22.616

Table A4.2.1 - Microprobe analyses of olivine from Mt Discovery. FeO* is total iron given as FeO. Detection limits are preceeded by a less than symbol where the analysed value is below detection limit. Na_2O, K_2O, and Cr_2O_3 were analysed for, but are below detection limit in all samples and are not included in the table below. Cation formula are calculated on the basis of four oxygens. Iron is assumed to be present only as FeO.

	AW84738								
	P.C	P5.C	P3.C	P3.C	P6.C	P.R	P5.R	P3.R	P6.R
SiO2	38.98	39.31	39.40	40.40	41.46	39.25	40.51	39.51	40.41
TiO2	0.00	<0.09	<0.09	<0.08	<0.09	0.00	<0.09	0.00	0.00
Al2O3	0.00	<0.43	0.00	0.00	<0.44	0.00	0.00	0.00	0.00
FeO*	18.73	23.07	11.41	11.58	12.41	15.96	15.89	14.14	15.50
MnO	0.15	<0.33	<0.13	0.20	0.14	0.18	0.20	0.16	0.16
MgO	41.91	38.55	48.29	48.63	48.60	45.29	44.94	45.81	44.63
NiO	<0.16	<0.16	0.27	0.37	0.31	0.00	0.22	0.21	<0.17
CaO	0.15	0.16	0.19	0.23	0.24	0.20	0.33	0.28	0.31
Total	99.92	101.09	99.56	101.41	102.71	100.88	101.87	99.90	101.01
Si	0.997	1.009	0.980	0.987	0.997	0.983	1.000	0.989	1.005
Ti	0.000	0.000	0.000	0.000	0.000	0.000	0.000	0.000	0.000
Al	0.000	0.000	0.000	0.000	0.000	0.000	0.000	0.000	0.000
Fe2+	0.401	0.495	0.237	0.237	0.250	0.334	0.328	0.296	0.322
Mn	0.003	0.007	0.000	0.004	0.000	0.004	0.004	0.003	0.003
Mg	1.598	1.475	1.791	1.772	1.743	1.691	1.654	1.710	1.655
Ni	0.000	0.000	0.005	0.007	0.006	0.000	0.004	0.004	0.000
Ca	0.004	0.004	0.005	0.006	0.006	0.005	0.009	0.008	0.008
	3.003	2.991	3.020	3.013	3.003	3.017	3.000	3.011	2.995
Fo	79.8	74.6	88.3	88.0	87.5	83.3	83.3	85.1	83.6
Fa	20.2	25.4	11.7	12.0	12.5	16.7	16.7	14.9	16.4

Table A4.2.1 (continued) - Microprobe analyses of olivines from Mt Discovery.

	AW84750							AW84742		
	P1.C	P2.C	P3.C	P5A.C	P2.R	P3.R	P5A.R	P6.C	P6.R	G1.C
SiO2	38.33	38.48	39.29	38.60	39.04	38.57	37.71	38.01	37.77	37.90
TiO2	<0.09	<0.09	0.00	<0.10	<0.09	<0.10	<0.09	<0.09	<0.10	0.22
Al2O3	<0.04	<0.05	<0.05	<0.04	<0.05	0.05	<0.05	<0.04	<0.04	0.04
FeO*	18.83	18.08	15.33	19.64	17.70	18.55	19.00	20.25	22.66	23.14
MnO	0.00	0.31	0.15	0.29	0.25	0.23	0.32	0.42	0.54	0.54
MgO	42.03	42.28	44.36	41.40	42.67	41.81	41.61	40.54	37.64	37.29
NiO	0.00	<0.15	0.22	0.20	<0.17	<0.16	<0.15	<0.17	0.00	<0.16
CaO	0.28	0.26	0.26	0.15	0.30	0.28	0.31	0.31	0.33	0.31
Total	99.47	99.41	99.61	100.28	99.96	99.49	98.95	99.53	98.94	99.44
Si	0.979	0.989	0.994	0.990	0.994	0.992	0.980	0.987	0.998	0.998
Ti	0.000	0.000	0.000	0.000	0.000	0.000	0.000	0.000	0.000	0.004
Al	0.000	0.000	0.000	0.000	0.000	0.000	0.000	0.000	0.000	0.000
Fe2+	0.402	0.389	0.324	0.421	0.377	0.399	0.413	0.440	0.501	0.501
Mn	0.000	0.007	0.003	0.006	0.005	0.005	0.007	0.009	0.012	0.012
Mg	1.601	1.620	1.673	1.583	1.620	1.604	1.612	1.569	1.482	1.464
Ni	0.000	0.000	0.004	0.004	0.000	0.000	0.000	0.000	0.000	0.000
Ca	0.008	0.007	0.007	0.004	0.008	0.008	0.009	0.009	0.009	0.009
	2.990	3.027	3.006	3.010	3.006	3.008	3.020	3.013	3.002	2.997
Fo	79.9	80.4	83.6	78.7	80.9	79.9	79.3	77.8	74.3	73.7
Fa	20.1	19.6	16.4	21.3	19.1	20.1	20.7	22.2	25.7	26.3

Table A4.2.1 (continued) - Microprobe analyses of olivines from Mt Discovery.

	AW84758			
	P1.C	P2.C	P6.C	I4.C
SiO2	35.55	35.81	35.67	35.36
TiO2	<0.10	<0.10	<0.10	<0.10
Al2O3	<0.06	<0.06	<0.07	<0.07
FeO*	34.97	35.94	35.02	35.52
MnO	1.11	1.19	1.07	1.08
MgO	27.45	26.57	27.26	26.76
NiO	<0.16	0.00	0.00	<0.15
CaO	0.43	0.39	0.39	0.45
Total	99.51	99.90	99.41	99.17
Si	0.997	1.004	1.001	0.998
Ti	0.000	0.000	0.000	0.000
Al	0.000	0.000	0.000	0.000
Fe2+	0.820	0.842	0.822	0.838
Mn	0.026	0.028	0.025	0.026
Mg	1.146	1.110	1.140	1.126
Ni	0.000	0.000	0.000	0.000
Ca	0.013	0.012	0.012	0.014
	3.003	2.996	2.999	3.002
Fo	57.5	56.0	57.4	56.6
Fa	42.5	44.0	42.6	43.4

Table A4.2.2 - Microprobe analysesof pyroxenes fromMt Discovery. FeO* is total iron given as FeO. Detection limits are preceeded by a less than symbol where analysed values are below detecion limit. NiO was analysed for, but is always below detection limit and is not given in the table below. Cation formula are calculated on the basis of four cations, with Fe3+ being assessed by charge balancing. End members are assigned according to the method of Kyle (1976).

	AW84738								
	P4.C	P4.C	M1.C	M2A.C	M2B.C	M2C.C	P4.M	P4.R	M1.R
SiO2	44.61	45.77	45.22	43.66	45.75	44.68	45.2	47.49	49.14
TiO2	3.33	3.37	2.44	3.66	3.15	3.24	3.45	3.96	1.97
Al2O3	10.89	9.73	7.46	9.46	8.19	8.59	10.11	6.39	5.14
Cr2O3	<0.15	<0.15	<0.13	<0.15	0.54	<0.18	<0.16	<0.14	0.47
FeO*	7.71	7.60	9.64	7.53	6.29	6.79	7.48	7.11	5.74
MnO	<0.12	0.15	0.20	<0.12	0.14	<0.13	<0.12	<0.15	0.13
MgO	10.86	11.12	11.63	12.72	12.69	13.07	11.75	13.05	14.49
CaO	22.01	21.72	21.28	21.60	22.04	21.07	21.88	23.37	21.69
Na2O	<1.29	1.57	1.24	<1.13	<1.18	<0.84	<1.26	<1.21	<0.95
K2O	<0.05	<0.06	<0.06	<0.05	<0.06	0.08	0.00	<0.06	<0.05
Total	99.41	101.03	99.11	98.63	98.79	97.52	99.87	101.37	98.77
Si	1.681	1.677	1.696	1.648	1.725	1.701	1.691	1.752	1.855
Ti	0.094	0.093	0.069	0.104	0.089	0.093	0.097	0.110	0.056
Al	0.483	0.421	0.330	0.421	0.364	0.385	0.446	0.278	0.229
Cr	0.000	0.000	0.000	0.000	0.016	0.000	0.000	0.000	0.014
Fe3+	0.000	0.151	0.230	0.075	0.000	0.031	0.000	0.000	0.000
Fe2+	0.243	0.082	0.073	0.163	0.198	0.185	0.234	0.219	0.150
Mn	0.000	0.005	0.006	0.000	0.004	0.000	0.000	0.000	0.004
Mg	0.610	0.608	0.650	0.716	0.713	0.742	0.655	0.718	0.815
Ca	0.888	0.853	0.855	0.874	0.890	0.859	0.877	0.924	0.877
Na	0.000	0.112	0.090	0.000	0.000	0.000	0.000	0.000	0.000
K	0.000	0.000	0.000	0.000	0.000	0.004	0.000	0.000	0.000
Ac	-	11.2	9.0	-	-	-	-	-	-
Ft	-	2.0	7.0	3.8	-	1.4	-	-	-
Tc	9.4	9.3	6.9	10.4	8.9	9.3	9.7	11.0	5.6
Ct	14.7	11.7	9.6	10.7	10.1	10.0	12.6	2.9	6.5
Wo	32.3	31.2	31.0	31.3	35.0	32.6	32.7	39.2	37.8
En	30.5	30.4	32.5	35.8	35.7	37.1	32.8	35.9	40.8
Fs	12.1	4.3	4.0	8.1	10.1	9.2	11.7	11.0	7.7

Table A4.2.2 (continued) - Microprobe analyses of pyroxenes from Mt Discovery.

	AW84750							
	P1.C	P4B.C	P5B.C	P1.R	P4B.R	P4C.R	P5B.R	I2.R
SiO2	44.81	45.13	44.08	43.75	41.33	42.89	43.48	41.93
TiO2	3.11	3.50	3.77	3.78	5.98	4.19	4.67	4.87
Al2O3	8.76	8.72	7.79	9.13	10.29	9.61	8.87	9.67
Cr2O3	<0.15	<0.15	<0.15	<0.15	<0.13	<0.26	<0.12	<0.14
FeO*	7.00	7.19	13.03	7.27	7.91	7.27	7.41	7.65
MnO	<0.15	<0.13	0.51	0.14	0.17	<0.13	<0.14	<0.15
MgO	11.97	11.87	7.67	11.88	10.44	11.41	11.68	11.00
CaO	22.71	22.67	22.24	22.85	22.35	22.96	22.80	23.04
Na2O	0.46	0.74	1.00	0.66	0.70	0.42	0.56	0.59
K2O	<0.06	<0.05	<0.06	<0.06	<0.06	0.05	<0.06	<0.05
Total	98.82	99.82	100.09	99.46	99.17	98.80	99.47	98.75
Si	1.685	1.680	1.685	1.635	1.566	1.619	1.632	1.588
Ti	0.088	0.098	0.108	0.106	0.170	0.119	0.132	0.139
Al	0.388	0.382	0.351	0.402	0.459	0.428	0.392	0.432
Cr	0.000	0.000	0.000	0.000	0.000	0.000	0.000	0.000
Fe3+	0.100	0.116	0.136	0.163	0.120	0.129	0.121	0.158
Fe2+	0.120	0.108	0.281	0.064	0.131	0.101	0.112	0.084
Mn	0.000	0.000	0.017	0.004	0.005	0.000	0.000	0.000
Mg	0.671	0.659	0.437	0.662	0.590	0.642	0.654	0.621
Ca	0.915	0.904	0.911	0.915	0.907	0.929	0.917	0.935
Na	0.034	0.053	0.074	0.048	0.051	0.031	0.041	0.043
K	0.000	0.000	0.000	0.000	0.000	0.002	0.000	0.000
Ac	3.4	5.3	7.4	4.8	5.1	3.3	4.1	4.3
Ft	3.3	3.1	3.1	5.8	3.4	4.8	4.0	5.7
Tc	8.8	9.8	10.8	10.6	17.6	11.9	13.2	13.9
Ct	10.6	9.3	6.7	9.5	5.9	9.5	6.4	7.7
Wo	34.4	34.1	35.6	32.8	32.2	33.4	34.0	33.1
En	33.5	32.9	21.9	33.1	29.5	32.1	32.7	31.1
Fs	6.0	5.4	14.9	3.4	6.8	5.1	5.6	4.2
mg	75.3	74.6	51.2	74.5	70.2	73.6	73.7	72.0

Table A4.2.2 (continued) - Microprobe analyses of pyroxenes from Mt Discovery.

	AW84742					AW84761		
	P2.C	P3.C	P4.C	P2.R	P3.R	P5.C	P5.R	I7.C
SiO2	48.70	44.13	45.56	45.49	45.30	51.90	51.22	51.66
TiO2	2.35	3.80	3.40	3.30	3.42	0.56	0.62	0.80
Al2O3	5.10	7.57	8.48	7.08	7.28	1.45	1.26	1.61
Cr2O3	<0.14	<0.14	<0.13	0.00	0.00	<0.13	0.00	0.00
FeO*	6.70	7.67	7.23	7.59	7.36	12.33	11.80	9.24
MnO	0.14	<0.14	<0.13	0.18	0.17	0.89	0.82	0.63
MgO	13.40	11.47	12.14	12.12	12.04	10.72	11.18	12.93
CaO	23.08	22.93	23.05	22.73	22.85	22.11	22.36	22.08
Na2O	0.50	0.63	0.58	0.56	0.60	0.63	0.66	0.62
K2O	<0.05	<0.06	<0.05	<0.05	<0.06	<0.05	<0.05	<0.05
Total	99.97	99.11	99.53	99.05	99.02	100.59	99.92	99.57
Si	1.806	1.661	1.703	1.711	1.704	1.959	1.935	1.939
Ti	0.066	0.108	0.096	0.093	0.097	0.016	0.018	0.023
Al	0.223	0.376	0.334	0.314	0.323	0.064	0.061	0.072
Cr	0.000	0.000	0.000	0.000	0.000	0.000	0.000	0.000
Fe3+	0.070	0.133	0.111	0.117	0.120	0.032	0.078	0.050
Fe2+	0.137	0.108	0.115	0.121	0.112	0.357	0.296	0.240
Mn	0.004	0.000	0.000	0.006	0.005	0.028	0.026	0.020
Mg	0.741	0.644	0.677	0.680	0.675	0.603	0.631	0.724
Ca	0.917	0.925	0.923	0.916	0.921	0.894	0.907	0.888
Na	0.036	0.046	0.042	0.041	0.044	0.046	0.048	0.045
K	0.000	0.000	0.000	0.000	0.000	0.000	0.000	0.000
Ac	3.6	4.6	4.2	4.1	4.4	4.6	4.8	4.5
Ft	1.7	4.4	3.5	3.8	3.8	-	1.5	0.3
Tc	6.6	10.8	9.6	9.3	9.7	1.6	1.8	2.3
Ct	4.6	8.1	7.1	6.4	6.5	1.6	1.0	1.3
Wo	39.4	34.6	36.1	36.0	36.1	43.1	43.2	42.5
En	37.0	32.2	33.8	34.0	33.8	30.2	31.6	36.2
Fs	7.1	5.4	5.7	6.4	5.9	18.6	16.1	13.0
mg	78.2	72.8	75.0	74.1	74.4	60.8	62.8	71.4

Table A4.2.2 (continued) - Microprobe analyses of pyroxenes from Mt Discovery.

	AW84758					AW84721		
	P7.C	M1.C	M2.C	P7.R	M2.R	M1.C	M2.C	M5.C
SiO2	50.68	49.24	49.43	49.63	49.14	51.54	51.35	50.83
TiO2	1.72	1.54	1.85	2.29	1.69	0.80	0.79	0.89
Al2O3	3.15	4.00	3.94	4.03	3.79	2.06	2.12	2.84
Cr2O3	<0.15	<0.13	<0.15	<0.15	<0.15	0.00	<0.16	<0.14
FeO*	8.22	8.81	9.05	8.22	9.13	10.67	9.87	11.02
MnO	0.27	0.37	0.34	0.31	0.35	0.74	0.58	0.80
MgO	12.72	12.41	11.92	12.14	11.89	11.64	11.73	10.34
CaO	22.26	21.60	21.62	22.36	21.52	22.27	21.78	21.71
Na2O	0.73	0.95	1.15	0.71	1.04	0.76	0.67	1.08
K2O	<0.05	<0.06	<0.05	<0.06	<0.06	<0.05	<0.05	0.00
Total	99.75	98.92	99.30	100.40	98.55	100.48	98.86	99.51
Si	1.894	1.853	1.857	1.851	1.861	1.930	1.951	1.927
Ti	0.048	0.044	0.052	0.064	0.048	0.023	0.023	0.025
Al	0.139	0.178	0.174	0.177	0.169	0.091	0.095	0.127
Cr	0.000	0.000	0.000	0.000	0.000	0.000	0.000	0.000
Fe3+	0.029	0.098	0.091	0.044	0.088	0.059	0.007	0.048
Fe2+	0.228	0.179	0.193	0.234	0.201	0.275	0.305	0.302
Mn	0.009	0.012	0.011	0.010	0.011	0.023	0.019	0.026
Mg	0.709	0.696	0.668	0.675	0.671	0.650	0.664	0.584
Ca	0.891	0.871	0.870	0.893	0.873	0.894	0.887	0.882
Na	0.053	0.069	0.084	0.051	0.076	0.055	0.049	0.079
K	0.000	0.000	0.000	0.000	0.000	0.000	0.000	0.000
Ac	5.3	6.9	8.4	5.1	7.6	5.5	4.9	7.9
Ft	-	1.4	0.4	-	0.6	0.2	-	-
Tc	4.8	4.4	5.2	6.4	4.8	2.3	2.3	2.5
Ct	2.2	4.5	3.5	2.5	3.6	2.3	2.5	3.9
Wo	41.1	38.4	39.0	40.2	39.1	42.3	42.0	40.9
En	35.5	34.8	33.4	33.7	33.6	32.5	33.2	29.2
Fs	10.8	9.5	10.2	11.4	10.6	14.9	14.3	15.0
mg	73.4	71.5	70.2	70.8	69.9	66.1	68.0	62.5

Table A4.2.2 (continued) - Microprobe analyses of pyroxenes from Mt Discovery.

	AW84741			AW84725		
	M.C	M3.C	I2.C	M4.C	G1.C	G2.C
SiO2	50.47	50.15	49.96	50.38	49.38	49.12
TiO2	0.25	0.42	0.48	0.40	0.35	0.52
Al2O3	0.90	1.36	1.32	0.96	1.37	1.34
Cr2O3	0.00	<0.14	<0.14	<0.16	<0.14	0.00
FeO*	16.06	15.78	15.65	15.54	20.01	20.75
MnO	1.25	1.12	1.12	1.58	1.51	1.58
MgO	7.67	8.29	8.09	5.88	4.85	4.55
CaO	22.06	21.72	21.92	24.55	20.43	20.33
Na2O	0.83	0.88	0.88	0.89	1.00	1.06
K2O	<0.06	<0.06	0.00	0.00	<0.06	<0.06
Total	99.49	99.72	99.42	100.18	98.90	99.25
Si	1.962	1.936	1.934	1.958	1.969	1.957
Ti	0.007	0.012	0.014	0.012	0.010	0.016
Al	0.041	0.063	0.063	0.044	0.064	0.063
Cr	0.000	0.000	0.000	0.000	0.000	0.000
Fe3+	0.082	0.105	0.104	0.084	0.054	0.074
Fe2+	0.440	0.405	0.404	0.421	0.613	0.617
Mn	0.041	0.037	0.037	0.052	0.051	0.053
Mg	0.445	0.447	0.468	0.341	0.288	0.270
Ca	0.919	0.899	0.911	1.022	0.873	0.868
Na	0.063	0.066	0.066	0.067	0.077	0.082
K	0.000	0.000	0.000	0.000	0.000	0.000
Ac	6.3	6.6	6.6	6.7	7.7	7.7
Ft	1.0	2.0	1.9	0.9	-	-
Tc	0.7	1.2	1.4	1.2	1.0	1.6
Ct	1.3	1.9	1.6	1.0	2.2	1.6
Wo	44.4	42.4	43.1	49.6	42.1	41.8
En	22.2	23.9	23.4	17.0	14.4	13.5
Fs	24.0	22.1	22.0	23.6	32.2	33.2
mg	46.0	46.7	48.0	40.3	30.2	28.1

Table A4.2.3 - Microprobe analyses of amphiboles from Mt Discovery. FeO* is total iron given as FeO. Detection limits are preceeded by a less than symbol and are given where the analysed values is below detection limit. Cr_2O_3, NiO, and Cl were analysed for, but are always below detection limit and are not given in the table below. Cation formula are calculated on the basis of 23 oxygens. No attempt has been made to assess the Fe^{3+} content.

	AW84761					AW84721			
	P1.C	P2.C	P1.R	P2.R	G1.C	P4.C	P4.C	P6A.C	P6B.C
SiO2	40.89	40.51	40.91	40.78	38.55	40.39	40.36	38.35	39.92
TiO2	6.08	5.80	5.87	6.08	7.19	6.21	6.27	6.40	6.26
Al2O3	10.67	10.38	10.99	10.70	12.94	11.73	11.63	14.02	11.96
FeO*	12.40	14.67	13.66	12.60	10.41	14.62	14.51	11.67	12.94
MnO	0.41	0.51	0.51	0.36	0.14	0.51	0.44	0.20	0.31
MgO	12.19	10.76	11.11	11.36	12.56	9.78	9.98	11.36	10.47
CaO	11.29	11.13	11.40	11.42	12.48	11.35	11.43	11.79	11.47
Na2O	2.95	3.16	2.90	2.88	2.84	3.19	3.24	3.00	3.34
K2O	0.97	1.01	1.05	1.03	0.78	1.03	0.99	0.88	1.03
Total	97.85	97.93	98.40	97.21	97.89	98.81	98.85	97.67	97.70
Si	6.097	6.111	6.102	6.127	5.723	6.032	6.023	5.725	5.990
Ti	0.682	0.658	0.659	0.687	0.803	0.697	0.704	0.719	0.706
Al	1.875	1.846	1.932	1.895	2.264	2.065	2.046	2.467	2.115
Fe2+	1.546	1.851	1.704	1.583	1.292	1.826	1.811	1.457	1.624
Mn	0.052	0.065	0.064	0.046	0.018	0.065	0.056	0.025	0.039
Mg	2.710	2.420	2.471	2.545	2.779	2.177	2.220	2.528	2.342
Ca	1.804	1.799	1.822	1.838	1.985	1.816	1.828	1.886	1.844
Na	0.853	0.924	0.839	0.839	0.817	0.924	0.937	0.868	0.972
K	0.185	0.194	0.200	0.197	0.148	0.196	0.189	0.168	0.197
Total	15.802	15.868	15.792	15.757	15.826	15.798	15.813	15.841	15.830
mg	62.9	55.0	58.3	61.0	68.0	53.5	54.3	63.0	58.5

Table A4.2.4 - Microprobe analyses of biotite from Mt Discovery. FeO* is total iron given as FeO. Detection limits are preceeded by a less than symbol and are given where the analysed value is below detection limit. Cr_2O_3, NiO and Cl were analysed, but are always below detection limit and are not given in the table below. Cation formula are calculated on the basis of 22 oxygens. No attempt has been made to assess the Fe^{3+} or volatile content.

	AW84741			
	M2.C	I2.C	I2.C	I5.C
SiO2	35.16	34.40	32.85	34.57
TiO2	5.87	6.24	5.67	5.48
Al2O3	13.22	13.04	12.43	13.24
FeO*	25.43	25.11	26.62	25.18
MnO	0.64	0.62	0.70	0.71
MgO	7.41	7.14	7.13	7.43
CaO	<0.07	<0.07	<0.07	0.00
Na2O	1.28	0.95	1.30	1.06
K2O	8.72	8.76	8.25	8.70
Total	97.73	96.26	94.95	96.37
Si	5.437	5.410	5.304	5.431
Ti	0.679	0.737	0.689	0.647
Al	2.417	2.419	2.366	2.453
Fe2+	3.290	3.298	3.597	3.303
Mn	0.084	0.085	0.097	0.094
Mg	1.710	1.673	1.716	1.736
Ca	0.000	0.000	0.000	0.000
Na	0.390	0.284	0.408	0.320
K	1.728	1.758	1.706	1.736
Total	15.735	15.664	15.883	15.720
mg	33.6	33.1	31.7	33.8

Table A4.2.5 - Microprobe analysesof feldspars fromMt Discovery. FeO* is total iron given as FeO. Detection limits are preceeded by a less than symbol and indicate the analysed value is below detection limit. MnO, NiO, and Cr_2O_3 were analysed for, but are always below detection limit and are not given in the table below. Cation formula are calculated on the basis of 32 oxygens.

	AW84738		AW84742							
	X7.C	X7.R	X1B.C	X9.C	X9.M	M1.C	M7.C	M8.C	X1A.R	X1B.R
SiO2	53.36	53.28	56.53	55.73	54.49	49.72	50.24	50.50	52.28	52.64
TiO2	<0.09	<0.09	<0.09	<0.09	0.27	<0.09	0.13	0.12	0.15	0.21
Al2O3	30.16	29.49	26.67	26.70	26.87	31.21	30.38	30.59	28.93	28.59
FeO*	<0.12	0.16	0.33	0.28	0.88	0.56	0.36	0.50	0.45	0.66
MgO	<0.53	0.59	0.06	<0.12	0.00	0.08	0.07	0.07	0.07	0.08
CaO	12.02	13.35	8.98	9.47	10.66	14.45	14.30	14.59	12.40	11.68
Na2O	3.71	4.77	6.14	5.82	5.14	3.27	3.39	3.36	4.22	4.65
K2O	0.25	0.21	0.55	0.52	0.47	0.23	0.21	0.24	0.51	0.42
Total	99.50	101.85	99.26	98.52	98.88	99.52	99.08	99.97	99.01	98.93
Si	9.665	9.537	10.249	10.190	9.994	9.144	9.265	9.244	9.609	9.675
Ti	0.000	0.000	0.000	0.000	0.037	0.000	0.018	0.017	0.021	0.029
Al	6.438	6.221	5.699	5.754	5.808	6.765	6.603	6.599	6.267	6.193
Fe2+	0.000	0.024	0.050	0.043	0.135	0.086	0.056	0.077	0.069	0.101
Mg	0.000	0.157	0.016	0.000	0.027	0.022	0.019	0.019	0.019	0.022
Ca	2.333	2.560	1.744	1.855	2.095	2.847	2.825	2.861	2.442	2.300
Na	1.303	1.655	2.158	2.063	1.828	1.166	1.212	1.192	1.504	1.657
K	0.058	0.048	0.127	0.121	0.110	0.054	0.049	0.056	0.120	0.098
	19.796	20.204	20.044	20.026	20.034	20.084	20.065	20.065	20.049	20.077
An	63.2	60.0	43.3	45.9	51.9	70.0	69.1	69.6	60.1	56.7
Ab	35.3	38.8	53.6	51.1	45.3	28.7	29.7	29.0	37.0	40.9
Or	1.6	1.1	3.2	3.0	2.7	1.3	1.2	1.4	2.9	2.4

Table A4.2.5 (continued) - Microprobe analyses of feldspars from Mt Discovery.

	AW84742			AW84761					
	M1.R	M7.R	G2.C	P1.C	P4.C	P3.C	P3.C	P1.R	P4.R
SiO2	52.22	52.28	50.39	61.07	63.98	59.04	59.15	58.50	60.65
TiO2	0.16	0.17	0.17	0.14	0.10	<0.09	0.10	0.10	0.10
Al2O3	29.76	29.10	30.26	22.49	20.04	23.97	24.14	24.97	22.97
FeO*	0.62	0.53	0.51	0.25	0.27	0.28	0.26	0.31	0.20
MgO	0.08	0.09	0.09	<0.05	0.00	<0.04	<0.04	<0.04	0.00
CaO	12.91	12.65	13.57	4.11	1.57	6.59	6.44	7.66	4.81
Na2O	4.18	4.19	3.76	7.60	6.99	6.96	7.08	6.59	7.66
K2O	0.34	0.34	0.24	2.45	5.17	1.00	1.19	0.74	1.60
Total	100.27	99.35	98.99	98.17	98.12	97.93	98.44	98.90	98.07
Si	9.493	9.578	9.298	11.126	11.665	10.788	10.763	10.599	11.038
Ti	0.022	0.023	0.024	0.019	0.014	0.000	0.014	0.014	0.014
Al	6.376	6.283	6.580	4.829	4.306	5.162	5.177	5.332	4.927
Fe2+	0.094	0.081	0.079	0.038	0.041	0.043	0.040	0.047	0.030
Mg	0.022	0.025	0.025	0.000	0.000	0.000	0.000	0.000	0.000
Ca	2.514	2.483	2.683	0.802	0.307	1.290	1.255	1.487	0.938
Na	1.473	1.488	1.345	2.684	2.471	2.466	2.498	2.315	2.703
K	0.079	0.079	0.056	0.569	1.202	0.233	0.276	0.171	0.371
	20.073	20.041	20.089	20.068	20.005	19.981	20.022	19.964	20.022
An	61.8	61.3	65.7	19.8	7.7	32.3	31.2	37.4	23.4
Ab	36.2	36.7	32.9	66.2	62.1	61.8	62.0	58.3	67.4
Or	1.9	2.0	1.4	14.0	30.2	5.8	6.9	4.3	9.3

Table A4.2.5 (continued) - Microprobe analyses of feldspars from Mt Discovery.

	AW84761				AW84758			
	P.R	P4.R	G1.C	G2.C	P3.C	P4.C	P4.C	P5.C
SiO2	60.70	60.52	58.89	63.46	56.06	56.92	57.18	58.35
TiO2	0.10	<0.09	0.13	<0.10	0.14	0.15	0.14	0.13
Al2O3	23.32	23.25	24.35	20.87	27.14	27.76	26.65	25.11
FeO*	0.20	0.31	0.51	0.35	0.22	0.18	0.19	0.24
MgO	<0.05	<0.04	<0.04	<0.04	<0.15	<0.13	<0.11	0.00
CaO	5.49	5.51	6.55	2.68	9.44	9.08	8.11	6.18
Na2O	7.41	7.56	6.97	7.16	5.80	6.00	6.37	7.34
K2O	1.34	1.28	1.01	4.38	0.71	0.80	0.99	1.16
Total	98.63	98.63	98.46	99.05	99.51	100.89	99.63	99.91
Si	10.982	10.955	10.715	11.492	10.153	10.156	10.318	10.660
Ti	0.014	0.014	0.014	0.018	0.019	0.020	0.019	0.018
Al	4.973	4.981	5.222	4.454	5.793	5.838	5.668	5.312
Fe2+	0.030	0.047	0.078	0.053	0.033	0.027	0.029	0.036
Mg	0.000	0.000	0.000	0.000	0.000	0.000	0.000	0.000
Ca	1.064	1.069	1.277	0.520	1.832	1.736	1.568	1.189
Na	2.599	2.653	2.459	2.514	2.037	2.076	2.229	2.554
K	0.309	0.296	0.234	1.012	0.164	0.182	0.228	0.348
	19.972	20.029	20.003	20.044	20.031	20.034	20.058	20.117
An	26.8	26.6	32.2	12.9	45.4	43.5	39.0	29.1
Ab	65.4	66.0	61.9	62.1	50.5	52.0	55.4	62.4
Or	7.8	7.4	5.9	25.0	4.1	4.6	5.7	8.5

Table A4.2.5 (continued) - Microprobe analyses of feldspars from Mt Discovery.

	AW84758							AW84721	
	M1.C	M2.C	M3.C	P3.M	P3.R	P4.R	P5.R	P1.C	P1.C
SiO2	57.53	58.55	58.46	58.35	59.67	59.66	60.22	58.61	58.28
TiO2	0.13	0.14	0.07	0.13	0.14	0.16	0.22	<0.08	<0.09
Al2O3	26.62	24.73	25.38	25.61	25.20	25.08	23.59	25.85	25.85
FeO*	0.18	0.28	0.22	0.23	0.21	0.23	0.70	0.34	0.24
MgO	<0.08	<0.08	<0.08	<0.07	<0.08	<0.08	0.12	<0.04	<0.04
CaO	8.47	6.69	7.26	7.11	6.50	6.68	4.95	7.83	8.02
Na2O	6.25	6.73	6.40	6.45	6.78	6.93	8.08	7.22	7.17
K2O	0.91	1.30	1.00	1.16	1.38	1.26	1.53	0.83	0.74
Total	100.09	98.42	98.79	99.04	99.88	100.00	99.41	100.69	100.40
Si	10.332	10.658	10.587	10.551	10.686	10.679	10.866	10.470	10.444
Ti	0.018	0.019	0.010	0.018	0.019	0.022	0.030	0.000	0.000
Al	5.634	5.306	5.417	5.458	5.319	5.291	5.016	5.443	5.460
Fe2+	0.027	0.043	0.033	0.035	0.031	0.034	0.106	0.052	0.051
Mg	0.000	0.000	0.000	0.000	0.000	0.000	0.032	0.000	0.000
Ca	1.630	1.305	1.409	1.377	1.247	1.281	0.957	1.499	1.540
Na	2.176	2.375	2.247	2.261	2.354	2.405	2.827	2.501	2.491
K	0.208	0.302	0.231	0.268	0.315	0.288	0.352	0.189	0.169
	20.026	20.008	19.934	19.967	19.971	20.000	20.186	20.154	20.156
An	40.6	32.8	36.2	35.3	31.8	32.2	23.1	35.8	36.7
Ab	54.2	59.7	57.8	57.9	60.1	60.5	68.3	59.7	59.3
Or	5.2	7.6	5.9	6.9	8.0	7.2	8.5	4.5	4.0

Table A4.2.5 (continued) - Microprobe analyses of feldspars from Mt Discovery.

	AW84721							
	P2.C	P3.C	M1.C	M2.C	P1.R	P2.R	P3.R	P3.R
SiO2	58.41	58.62	58.16	58.07	60.85	59.60	58.91	61.00
TiO2	<0.09	<0.09	0.10	0.13	0.13	<0.09	<0.09	<0.09
Al2O3	25.25	26.18	25.67	26.24	24.18	25.27	25.75	22.71
FeO*	0.23	0.30	0.27	0.31	0.40	0.33	0.27	0.63
MgO	<0.04	<0.04	<0.04	0.04	<0.04	<0.04	<0.04	<0.04
CaO	7.98	8.06	7.69	8.33	6.06	7.45	7.94	3.85
Na2O	6.86	6.93	7.11	6.90	7.57	7.33	7.09	9.15
K2O	0.78	0.62	0.74	0.64	1.09	0.81	0.64	2.43
Total	99.51	100.71	99.74	100.66	100.28	100.79	100.60	99.77
Si	10.539	10.449	10.474	10.377	10.848	10.610	10.510	11.015
Ti	0.000	0.000	0.014	0.017	0.017	0.000	0.000	0.000
Al	5.370	5.500	5.449	5.527	5.080	5.302	5.415	4.833
Fe2+	0.035	0.045	0.041	0.046	0.060	0.049	0.040	0.095
Mg	0.000	0.000	0.000	0.011	0.000	0.000	0.000	0.000
Ca	1.543	1.539	1.484	1.595	1.157	1.421	1.518	0.745
Na	2.400	2.395	2.483	2.391	2.616	2.530	2.453	3.203
K	0.180	0.141	0.170	0.146	0.248	0.184	0.146	0.560
	20.066	20.069	20.114	20.110	20.027	20.096	20.081	20.451
An	37.4	37.8	35.9	38.6	28.8	34.4	36.9	16.5
Ab	28.2	28.8	60.0	57.9	65.1	61.2	59.6	71.1
Or	4.4	3.5	4.1	3.5	6.2	4.4	3.5	12.4

Table A4.2.6 - Microprobe analyses of opaque oxides from Mt Discovery. Detection limits are preceeded by a less than symbol and indicate that the analysed values is below detection limit. K_2O was analysed for, but is always below detection limit and is not given in the table below. Iron was analysed as FeO, and Fe_2O_3 and FeO calculated by charge balancing the cation formula calculated on the basis of 32 oxygens. Stormer's (1983) method was used to calculate the ulvospinel (Usp) or ilmenite (Il) component.

	AW84738		AW84750						
	I3.C	I4.C	M1.C	I3.C	I4C.C	I5B1.C	I3.R	G2.C	G3.C
SiO2	<0.35	0.00	0.09	0.11	0.11	0.12	0.08	0.16	0.16
TiO2	1.22	16.64	20.92	2.21	17.44	22.24	20.44	2.24	2.77
Al2O3	31.01	15.48	4.82	36.42	9.52	7.43	8.29	39.14	34.42
Cr2O3	25.76	0.79	<0.18	18.12	<0.18	0.46	1.97	15.37	16.94
Fe2O3	9.36	21.83	26.68	11.00	26.35	18.95	20.77	11.17	12.55
FeO	11.39	39.05	41.79	19.62	38.96	45.60	42.91	17.55	20.49
MnO	<0.15	0.41	0.43	<0.15	0.71	0.44	0.48	0.14	0.20
MgO	16.30	6.49	6.18	13.34	5.90	4.61	5.43	14.80	12.57
NiO	<0.19	<0.19	<0.19	<0.18	<0.19	<0.20	<0.19	0.23	0.19
CaO	<0.07	<0.08	<0.08	<0.07	<0.08	<0.08	<0.08	0.00	<0.07
Na2O	1.17	0.00	0.00	<0.12	0.00	0.00	0.00	0.00	<0.09
Total	96.21	100.70	100.91	100.81	98.99	99.85	100.37	100.80	100.29
Si	0.000	0.000	0.001	0.001	0.001	0.001	0.001	0.002	0.002
Ti	0.009	0.138	0.183	0.016	0.152	0.195	0.177	0.016	0.020
Al	0.370	0.202	0.066	0.414	0.130	0.102	0.113	0.437	0.398
Cr	0.206	0.007	0.000	0.138	0.000	0.004	0.018	0.115	0.131
Fe3+	0.071	0.182	0.233	0.080	0.230	0.167	0.180	0.080	0.093
Fe2+	0.097	0.361	0.406	0.158	0.378	0.446	0.413	0.139	0.168
Mn	0.000	0.004	0.004	0.000	0.007	0.004	0.005	0.001	0.002
Mg	0.246	0.107	0.107	0.192	0.102	0.080	0.093	0.209	0.184
Ni	0.000	0.000	0.000	0.000	0.000	0.000	0.000	0.002	0.002
Ca	0.000	0.000	0.000	0.000	0.000	0.000	0.000	0.000	0.000
Na	0.009	0.000	0.000	0.000	0.000	0.000	0.000	0.000	0.000
Usp	40.0	71.5	61.2	59.0	61.7	76.4	73.3	55.8	58.4

Table A4.2.6 (continued) - Microprobe analyses of opaque oxides from Mt Discovery.

	AW84742				AW84761				
	M1.C	I3.C	I4.C	I6.C	M.C	I3.C	I3.C	I7.C	G1.C
SiO2	0.13	0.10	0.09	0.09	0.09	0.07	0.05	0.11	0.07
TiO2	20.57	20.50	18.05	20.35	21.86	27.44	51.98	22.39	22.05
Al2O3	5.02	3.82	6.03	4.77	2.48	0.75	0.12	2.08	2.41
Cr2O3	0.00	0.00	<0.17	0.50	<0.15	<0.17	0.00	0.00	<0.17
Fe2O3	25.72	27.31	28.87	26.13	24.27	15.86	4.90	24.57	24.42
FeO	42.78	41.67	37.71	40.88	45.37	50.58	37.97	46.20	45.75
MnO	0.79	0.82	0.50	0.85	1.15	1.47	1.56	1.38	1.24
MgO	4.96	5.38	6.50	5.85	3.18	2.87	4.07	3.06	3.09
NiO	0.00	0.00	<0.18	<0.18	<0.20	0.00	<0.18	<0.18	<0.19
CaO	0.00	<0.08	0.09	0.00	0.00	<0.08	<0.07	0.00	<0.08
Na2O	0.00	<0.07	0.09	<0.07	0.10	0.09	0.00	0.00	<0.08
Total	99.97	99.61	97.84	99.42	98.40	99.04	100.65	99.79	99.03
Si	0.002	0.001	0.001	0.001	0.001	0.001	0.001	0.001	0.001
Ti	0.183	0.183	0.161	0.181	0.202	0.254	0.473	0.205	0.203
Al	0.070	0.054	0.084	0.066	0.036	0.011	0.002	0.030	0.035
Cr	0.000	0.000	0.000	0.005	0.000	0.000	0.000	0.000	0.000
Fe3+	0.228	0.244	0.258	0.232	0.224	0.147	0.039	0.225	0.225
Fe2+	0.422	0.414	0.374	0.404	0.466	0.520	0.390	0.470	0.468
Mn	0.008	0.008	0.005	0.009	0.012	0.015	0.016	0.014	0.013
Mg	0.087	0.095	0.115	0.103	0.058	0.053	0.073	0.055	0.056
Ni	0.000	0.000	0.000	0.000	0.000	0.000	0.000	0.000	0.000
Ca	0.000	0.000	0.000	0.000	0.000	0.000	0.000	0.000	0.000
Na	0.000	0.000	0.001	0.000	0.001	0.001	0.000	0.000	0.000
Usp	63.0	59.4	55.6	61.4	64.5	76.7		64.2	64.5
Il							95.0		

Table A4.2.6 (continued) - Microprobe analyses of opaque oxides from Mt Discovery.

	AW84758				AW84721	
	M1.C	M2.C	I2.C	I7.C	M1.C	I2.C
SiO2	0.11	0.13	0.09	<0.08	0.07	0.13
TiO2	26.89	26.06	27.06	26.83	19.48	20.25
Al2O3	3.00	2.98	3.09	3.02	1.57	1.92
Cr2O3	0.00	<0.16	<0.16	<0.17	0.00	<0.19
Fe2O3	15.03	15.10	14.06	15.50	30.03	28.74
FeO	50.73	49.85	51.92	50.94	45.51	46.11
MnO	1.11	1.01	1.07	0.83	1.61	1.86
MgO	3.17	2.92	2.46	3.13	1.50	1.71
NiO	0.00	<0.16	<0.16	<0.17	<0.21	<0.19
CaO	<0.08	<0.08	0.00	<0.08	<0.08	<0.08
Na2O	<0.16	<0.16	<0.16	<0.16	0.00	<0.09
Total	100.04	98.05	99.75	100.24	99.77	100.75
Si	0.001	0.002	0.001	0.000	0.001	0.002
Ti	0.243	0.240	0.246	0.242	0.181	0.186
Al	0.042	0.043	0.044	0.042	0.023	0.028
Cr	0.000	0.000	0.000	0.000	0.000	0.000
Fe3+	0.136	0.139	0.128	0.140	0.280	0.264
Fe2+	0.509	0.511	0.525	0.511	0.471	0.470
Mn	0.011	0.010	0.011	0.008	0.017	0.019
Mg	0.057	0.053	0.044	0.060	0.028	0.031
Ni	0.000	0.000	0.000	0.000	0.000	0.000
Ca	0.000	0.000	0.000	0.000	0.000	0.000
Na	0.000	0.000	0.000	0.000	0.000	0.000
Usp	80.6	80.1	82.4	80.0	56.2	58.5

Table A4.3.1 - Microprobe analyses of olivine from Mason Spur. FeO* is total iron given as FeO. Detection limits are preceeded by a less than symbol where the analysis is below detection limit. TiO_2, Al_2O_3, Na_2O, K_2O, Cr_2O_3, and NiO were analysed for, but were always below detection limit, and have not been included in the table below. Cation formula are calculated on the basis of four oxygens. Iron is assumed to be present only as FeO.

	AW83647		
	I1.C	I2.C	M1.C
SiO2	31.97	31.96	31.75
FeO	56.30	56.00	55.46
MnO	2.38	2.43	2.36
MgO	7.86	7.93	8.02
CaO	0.98	0.94	0.85
Total	99.12	99.34	100.05
Si	1.016	1.018	1.018
Fe2+	1.497	1.491	1.487
Mn	0.064	0.066	0.064
Mg	0.373	0.376	0.383
Ca	0.033	0.032	0.029
Total	2.984	2.981	2.982
Fo	19.9	20.2	20.5
Fa	80.1	79.8	79.5

Table A4.3.2 - Microprobe analyses of pyroxenes from Mason Spur. FeO* is total iron given as FeO. Detection limits are preceeded by a less than symbol where analyses are below detection limit. NiO, and Cr_2O_3 were also analysed for, but are below detection limit in all samples and are not given in the table below. Cation formula are calculated on the basis of four cations, with Fe^{3+} being assessed by charge balancing. End members are assigned according to the method of Kyle (1976).

	AW83502A				AW83503				AW83533	AW83513
	P4.C	P2.R	P2.R	P4.R	P4.C	M1.C	M3.C	M3.C	G1.C	G1.C
SiO2	50.74	50.76	51.04	50.86	50.48	49.50	50.20	49.16	54.80	49.56
TiO2	0.45	0.50	<0.15	0.58	0.80	0.84	0.89	0.90	0.24	1.93
Al2O3	0.31	0.45	0.32	0.32	0.94	0.94	1.02	0.89	0.60	3.28
FeO*	28.26	28.62	28.95	27.18	22.48	23.35	23.06	22.81	2.83	10.53
MnO	0.47	0.24	0.40	0.36	0.87	1.01	1.02	0.94	<0.13	0.28
MgO	0.76	0.59	0.68	0.77	4.13	3.55	3.83	3.73	16.51	11.62
CaO	5.75	5.40	6.79	6.70	20.39	20.05	20.01	20.03	25.11	21.63
Na2O	10.79	11.38	10.70	10.85	0.98	1.08	1.01	1.09	0.24	0.57
Total	97.53	97.94	98.88	97.62	101.07	100.32	101.04	99.55	100.33	99.40
Si	1.956	1.945	1.944	1.956	1.987	1.970	1.982	1.960	1.992	1.879
Ti	0.014	0.014	0.000	0.016	0.024	0.025	0.026	0.027	0.007	0.055
Al	0.014	0.018	0.014	0.014	0.043	0.044	0.047	0.042	0.026	0.146
Fe3+	0.852	0.907	0.914	0.859	0.010	0.048	0.014	0.051	0.000	0.028
Fe2+	0.059	0.009	0.009	0.015	0.730	0.729	0.748	0.721	0.086	0.306
Mn	0.016	0.007	0.014	0.011	0.029	0.034	0.034	0.032	0.000	0.009
Mg	0.044	0.035	0.039	0.044	0.242	0.211	0.225	0.223	0.895	0.657
Ca	0.239	0.221	0.277	0.275	0.860	0.855	0.846	0.859	0.970	0.878
Na	0.807	0.845	0.790	0.809	0.075	0.083	0.077	0.085	0.017	0.042
Tc	0.7	0.9	-	0.7	2.2	2.2	2.5	2.6	0.7	5.5
NT	1.4	1.0	-	1.8	0.4	0.6	1.2	-	-	-
Ac	79.2	83.5	79.0	80.9	7.2	7.7	5.5	8.1	1.7	4.2
Ft	2.3	3.6	6.2	2.5	-	-	-	-	-	-
Ct	-	-	0.7	-	-	-	-	0.8	0.6	1.8
Wo	9.3	8.8	10.4	11.6	42.4	41.9	42.6	40.5	48.2	40.4
En	2.2	1.8	2.0	2.2	12.2	10.7	11.7	10.6	45.1	33.0
Fs	3.4	0.6	1.2	0.9	35.5	36.9	36.4	37.4	3.6	15.1
mg	4.6	3.7	4.1	4.8	2.5	2.1	2.3	2.2	91.2	66.3

Table A4.3.3 - Microprobe analyses of feldspars from Mason Spur. FeO* is total iron given as FeO. Detection limits are preceeded by a less than symbol and indicate the analysed value is below detection limit. MnO, NiO, and Cr_2O_3 were analysed for, but are below detection limit in all samples and are not given in the table below. Cation formula are calculated on the basis of 32 oxygens.

	AW83502A							
	P2.C	P2.C	P3.C	P2.R	P2.R	P3.R	G1.C	G2.C
SiO2	66.22	65.93	66.25	66.67	65.53	66.02	66.93	66.95
TiO2	<0.10	<0.09	0.11	<0.09	0.11	<0.09	0.00	<0.10
Al2O3	18.62	18.75	18.87	18.85	18.56	18.21	18.53	18.63
FeO*	0.24	0.27	0.42	0.41	0.60	0.43	0.34	0.28
MgO	0.04	<0.04	0.00	<0.04	<0.04	<0.04	<0.04	<0.04
CaO	0.07	<0.08	0.21	0.20	0.16	0.07	0.13	0.14
Na2O	8.03	8.15	8.50	8.33	8.15	8.45	8.33	8.58
K2O	6.09	6.15	5.39	6.13	5.86	5.82	5.61	5.61
Total	99.31	99.25	99.75	100.59	98.97	99.00	99.87	100.14
Si	11.948	11.916	11.891	11.905	11.891	11.965	11.985	11.964
Ti	0.000	0.000	0.015	0.000	0.015	0.000	0.000	0.000
Al	3.959	3.994	3.992	3.967	3.969	3.890	3.911	3.924
Fe2+	0.036	0.041	0.063	0.061	0.091	0.065	0.051	0.042
Mg	0.011	0.000	0.000	0.000	0.000	0.000	0.000	0.000
Ca	0.014	0.000	0.040	0.038	0.031	0.014	0.025	0.027
Na	2.809	2.856	2.958	2.884	2.867	2.969	2.892	2.955
K	1.402	1.418	1.234	1.396	1.357	1.346	1.282	1.279
Total	20.178	20.224	20.194	20.252	20.221	20.248	20.146	20.191
An	0.3	-	1.0	0.9	0.7	0.3	0.6	0.6
Ab	66.5	66.8	69.9	66.8	67.4	68.6	68.9	69.4
Or	33.2	33.2	29.2	32.3	31.9	31.1	30.5	30.0

Table A4.3.3 (continued) - Microprobe analyses of feldspars from Mason Spur.

	AW83503					AW83533			
	P1.C	P2.C	P3.C	P2.R	P3.R	P1.C	P1.C	P1.C	P1.R
SiO2	68.46	67.04	67.43	67.74	66.84	66.33	66.94	67.40	66.93
TiO2	<0.09	<0.09	<0.09	<0.09	<0.09	<0.09	<0.08	<0.08	<0.09
Al2O3	18.55	18.55	18.17	18.82	18.18	19.25	18.90	19.61	19.18
FeO*	0.19	0.12	<0.72	0.21	0.65	0.16	0.16	0.15	<0.14
MgO	<0.04	<0.04	<0.04	<0.04	<0.04	<0.04	<0.04	<0.04	<0.04
CaO	0.21	0.25	<0.28	0.34	0.34	0.60	0.45	1.08	0.82
Na2O	7.01	7.21	7.58	7.53	6.80	7.11	6.87	8.15	7.22
K2O	7.04	6.54	5.84	6.91	7.26	7.23	7.47	5.16	6.98
Total	101.46	99.71	99.02	101.55	100.07	100.68	100.79	101.55	101.13
Si	12.078	12.025	12.118	11.976	12.020	11.860	11.945	11.854	11.892
Ti	0.000	0.000	0.000	0.000	0.000	0.000	0.000	0.000	0.000
Al	3.857	3.921	3.849	3.921	3.853	4.057	3.975	4.065	4.017
Fe2+	0.028	0.018	0.000	0.031	0.098	0.024	0.024	0.022	0.000
Mg	0.000	0.000	0.000	0.000	0.000	0.000	0.000	0.000	0.000
Ca	0.040	0.048	0.000	0.064	0.066	0.115	0.086	0.204	0.156
Na	2.398	2.507	2.641	2.581	2.371	2.465	2.377	2.779	2.487
K	1.584	1.497	1.339	1.559	1.666	1.649	1.700	1.158	1.582
Total	19.985	20.016	19.947	20.133	20.072	20.169	20.107	20.082	20.134
An	1.0	1.2	-	1.5	1.6	2.7	2.1	4.9	3.7
Ab	59.6	61.9	66.4	61.4	57.8	58.3	57.1	67.1	58.9
Or	39.4	36.9	33.6	37.1	40.6	39.0	40.8	28.0	37.4

Table A4.3.3 (continued) - Microprobe analyses of feldspars from Mason Spur.

	AW83533			AW83513					
	G3.C	G4.C	G.C	P1.C	P2.C	P3.C	P1.R	P2.R	P3.R
SiO2	66.59	65.62	67.28	57.23	54.45	55.45	54.94	57.26	54.14
TiO2	<0.10	<0.08	0.00	<0.08	<0.09	0.09	<0.09	0.11	0.11
Al2O3	18.81	18.69	19.44	26.82	28.68	27.71	28.12	26.27	27.71
FeO*0	0.26	0.30	0.25	0.24	0.24	0.23	0.28	0.23	<0.14
MgO	<0.04	<0.04	<0.04	<0.04	0.04	0.04	0.05	<0.04	0.05
CaO	0.34	0.22	0.85	9.34	11.10	10.12	11.07	8.63	10.12
Na2O	7.20	7.25	8.19	6.32	5.36	5.95	5.32	6.52	5.41
K2O	7.37	6.88	5.29	0.56	0.36	0.45	0.39	0.56	0.35
Total	100.57	98.96	101.29	100.51	100.23	100.04	100.17	99.58	97.89
Si	11.925	11.918	11.872	10.256	9.834	10.015	9.923	10.338	9.967
Ti	0.000	0.000	0.000	0.000	0.000	0.012	0.000	0.015	0.015
Al	3.970	4.001	4.043	5.665	6.105	5.899	5.986	5.590	6.012
Fe2+	0.039	0.046	0.037	0.036	0.036	0.035	0.042	0.035	0.000
Mg	0.000	0.000	0.000	0.000	0.011	0.011	0.013	0.000	0.014
Ca	0.065	0.043	0.159	1.793	2.148	1.958	2.142	1.669	1.996
Na	2.500	2.553	2.802	2.196	1.877	2.084	1.863	2.282	1.931
K	1.684	1.594	1.191	0.128	0.083	0.104	0.090	0.129	0.082
Total	20.182	20.155	20.103	20.074	20.094	20.117	20.060	20.058	20.018
An	1.5	1.0	3.8	43.6	52.3	47.2	52.2	40.9	49.8
Ab	58.8	60.9	67.5	53.3	45.7	50.3	45.5	55.9	48.2
Or	39.6	38.0	28.7	3.1	2.0	2.5	2.2	3.2	2.1

Table A4.3.3 (continued) - Microprobe analyses of feldspars from Mason Spur.

	AW83513			AW83647							
	G1.C	G2.C	G3.C	P1.C	P1.C	P2.C	P1.R	P1.R	P2.R	G1.C	G2.C
SiO2	60.27	66.33	59.43	64.02	63.70	63.53	64.61	63.23	63.34	62.49	65.0
TiO2	0.12	0.14	0.18	0.11	<0.09	<0.09	<0.10	<0.09	<0.09	<0.09	<0.0
Al2O3	24.71	19.59	24.97	21.06	21.50	22.12	21.12	21.82	22.59	22.26	21.4
FeO*	0.25	0.30	0.36	0.00	0.22	0.19	0.56	0.30	0.21	0.26	0.3
MgO	<0.04	<0.04	0.05	<0.04	<0.04	<0.04	0.00	0.00	<0.04	<0.04	<0.0
CaO	6.92	1.09	7.12	2.24	3.18	3.83	3.02	3.52	4.13	4.26	3.3
Na2O	7.56	7.00	7.31	8.09	7.94	8.02	8.44	7.91	8.32	7.97	8.1
K2O	0.89	6.76	0.97	3.60	2.80	2.36	3.12	2.83	1.99	2.30	2.8
Total	100.72	101.21	100.39	99.12	99.34	100.05	100.87	99.61	100.58	99.54	101.2
Si	10.719	11.791	10.625	11.511	11.421	11.313	11.459	11.333	11.226	11.215	11.5(
Ti	0.016	0.019	0.024	0.015	0.000	0.000	0.000	0.000	0.000	0.000	0.0(
Al	5.180	4.104	5.262	4.463	4.543	4.642	4.415	4.609	4.719	4.708	4.4
Fe2+	0.037	0.045	0.054	0.000	0.033	0.028	0.083	0.045	0.031	0.039	0.0
Mg	0.000	0.000	0.013	0.000	0.000	0.000	0.000	0.000	0.000	0.000	0.0(
Ca	1.319	0.208	1.364	0.432	0.611	0.731	0.574	0.676	0.784	0.819	0.6
Na	2.607	2.413	2.534	2.820	2.760	2.769	2.902	2.749	2.859	2.773	2.7
K	0.202	1.533	0.221	0.826	0.640	0.536	0.706	0.647	0.450	0.527	0.6
Total	20.079	20.111	20.097	20.066	20.008	20.019	20.138	20.060	20.069	20.081	19.98
An	31.9	5.0	33.1	10.6	15.2	18.1	13.7	16.6	19.2	19.9	15.7
Ab	63.2	58.1	61.5	69.2	68.8	68.6	69.4	67.5	69.8	67.3	68.7
Or	4.9	36.9	5.4	20.3	16.0	13.3	16.9	15.9	11.0	12.8	15.6

Table A4.3.4 - Microprobe analyses of opaque minerals from Mason Spur. FeO* is total iron as FeO. Detection limits are preceeded by a less than symbol and indicate that the analysed value is below detection limit. Na_2O, K_2O, NiO and Cr_2O_3 were analysed for, but are below detection limit in all samples and are not given in the table below. Fe_2O_3 is calculated by charge balancing, and the ulvospinel fraction is calculated by the method of Stormer (1983).

	AW83503	AW83647	
	M3.C	G1.C	G2.C
SiO2	0.14	0.16	0.12
TiO2	25.67	21.62	20.09
Al2O3	0.65	1.65	1.48
Fe2O3	16.42	25.18	28.65
FeO	51.50	49.40	48.23
MnO	2.39	1.01	0.95
MgO	0.24	0.75	0.65
CaO	0.00	<0.08	<0.08
Total	97.02	99.76	100.17
Si	0.002	0.002	0.001
Ti	0.247	0.202	0.187
Al	0.010	0.024	0.021
Fe3+	0.160	0.235	0.267
Fe2+	0.552	0.513	0.500
Mn	0.026	0.011	0.010
Mg	0.001	0.014	0.012
Ca	0.000	0.000	0.000
Usp	0.759	0.644	0.592

Table A4.3.5 - Microprobe analyses of nephelines from Mason Spur. FeO* is total iron given as FeO. Cation formula are calculated on the basis of 32 oxygens.

	AW83533		
	G1.C	G2.C	G5.C
SiO2	48.98	48.58	47.91
Al2O3	29.75	29.26	30.22
FeO*	1.78	2.07	1.75
Na2O	18.61	18.01	18.43
K2O	2.97	3.33	3.16
Total	102.09	101.25	101.47
Si	9.114	9.134	8.987
Al	6.524	6.484	6.681
Fe2+	0.277	0.325	0.275
Na	6.714	6.565	6.703
K	0.705	0.799	0.756
Total	23.334	23.307	23.402

Table A4.4 - Precision, accuracy, and statistical parameters of microprobe analyses, as determir for standard minerals (unpublished data supplied by staff of the electron microprobe facility, Victoria University of Wellington).

Wt.%	Mean	Var.	Std. Dev.	Rel. Dev.%	Std. Error	Skew	Kurt.	Max.	Min.	Range	N	Rec.	
SiO_2	53.98	.376	.613	1.14	.134	-1.51	5.45	54.85	52.12	2.73	21	53.94	Px-1 Pyroxene
Al_2O_3	.61	.002	.049	8.06	.011	1.86	6.92	.78	.56	.21		.66	
TiO_2	.23	.001	.033	14.12	.007	.92	3.28	.32	.19	.13		.26	
FeO	2.90	.072	.268	9.24	.584	1.86	6.90	3.79	2.56	1.23		2.93	
MnO	.08	.002	.046	58.31	.010	-.24	1.85	.14	.00	.14		.07	
MgO	16.80	.034	.185	1.10	.040	2.33	9.27	17.47	16.56	.91		16.93	
CaO	24.70	.077	.277	1.12	.061	-.57	2.31	25.07	24.14	.93		24.55	
Na_2O	.22	.001	.033	15.04	.007	.61	2.19	.29	.18	.11		.24	
Cr_2O_3	.23	.002	.041	18.14	.009	.69	3.45	.34	.16	.18		.21	
SiO_2	64.63	.075	.275	.43	.065	-.17	2.54	65.05	64.04	1.01	18	64.39	Or-1 Orthoclase
Al_2O_3	18.53	.025	.159	.86	.037	-.65	2.05	18.73	18.24	.49		18.58	
Na_2O	1.05	.003	.053	4.99	.012	.87	2.83	1.17	.99	.18		1.14	
K_2O	14.90	.098	.312	2.10	.074	-1.72	5.52	15.19	13.96	1.23		14.92	
BaO	.91	.036	.189	20.92	.045	.11	2.24	1.28	.61	.67		.82	
SiO_2	40.19	.087	.295	.74	.066	1.40	4.24	41.00	39.86	1.14	20	40.81	San Carlos Olivine
Al_2O_3	.04	<.001	.011	28.50	.002	.37	2.29	.06	.02	.04		-	
FeO	9.58	.043	.207	2.16	.046	-.83	3.76	9.95	9.09	.86		9.55	
MnO	.16	.001	.033	20.99	.007	.11	2.38	.23	.10	.13		.14	
MgO	49.61	.086	.293	.59	.066	.27	2.51	50.29	49.13	1.16		49.42	
CaO	.09	.001	.027	29.41	.006	-1.86	7.90	.13	.00	.13		<.05	
NiO	.37	.004	.066	17.73	.015	-1.63	6.14	.47	.17	.30		.37	
SiO_2	38.98	.043	.209	.54	.046	-1.31	4.53	39.23	38.38	.85	21	38.95	Springwater Olivine
FeO	16.82	.048	.218	1.30	.048	.11	2.25	17.26	16.47	.79		16.62	
MnO	.34	.001	.034	10.00	.007	-.36	3.22	.41	.26	.15		.30	
MgO	43.76	.109	.331	.76	.072	-.07	2.32	44.33	43.16	1.17		43.58	
SiO_2	55.31	.085	.292	.53	.061	-.18	1.87	55.71	54.77	.94	23	55.36	63-1827 Diopside
MgO	18.59	.018	.133	.72	.028	-.13	2.54	18.85	18.30	.55		18.77	
CaO	26.07	.060	.245	.94	.051	-.54	2.34	26.41	25.60	.81		25.70	
SiO_2	50.44	.122	.350	.69	.049	-.75	-138.62	50.95	49.42	1.53	50	50.73	Kakanui Augite
TiO_2	.77	.002	.047	6.10	.007	.11	2.71	.88	.67	.21		.74	
Al_2O_3	8.18	.031	.177	2.16	.025	-.52	2.08	8.53	7.56	.97		8.73*	7.86 (original value)
FeO	6.34	.087	.296	4.67	.042	-1.50	5.46	6.85	5.37	1.48		6.34	
MnO	.19	.001	.035	18.42	.005	-.02	2.69	.20	.04	.16		.13	
MgO	16.07	.034	.185	1.15	.026	-.32	-83.19	16.53	15.49	1.04		16.65	
CaO	15.86	.127	.356	2.24	.050	-2.08	3.03	16.31	14.28	2.03		15.82	
Na_2O	1.32	.003	.051	3.86	.007	-.93	6.03	1.42	1.13	.29		1.27	
Cr_2O_3	.14	.001	.027	19.29	.004	-.14	1.97	.19	.09	.10		-	

Std.Error = Std. Dev. / $\sqrt{N}$

A4.2 Explanation of Tabulated Analyses

Samples are listed below. For more detailed sample descriptions see Appendix 3.

AW82056 - benmoreite, Minna Bluff (MB1)

AW82078 - phonolite, Minna Bluff (MB2)

AW82097B- benmoreite, Minna Bluff (MB1)

AW82105 - basanite, Minna Bluff (MB1)

AW82109 - tephrite, Minna Bluff (MB1)

AW82150 - phonolite, Minna Bluff (MB2)

AW83502A- peralkaline trachyte, Mason Spur (MS3)

AW83503 - peralkaline trachyte, Mason Spur (MS3)

AW83513 - benmoreite, Mason Spur (MS7)

AW83533 - peralkaline trachyte, Mason Spur (MS5)

AW83647 - trachyte, Mason Spur (MS8)

AW84721 - tephriphonolite, Mt Discovery (MD1)

AW84725 - phonolite, Mt Discovery (MD1)

AW84738 - basanite, Mt Discovery (MD2)

AW84741 - phonolite inclusion (MD1) in AW84742 (MD2), Mt Discovery

AW84742 - tephrite, Mt Discovery (MD2)

AW84750 - tephrite, Mt Discovery (MD2)

AW84758 - tephriphonolite, Mt Discovery (MD1)

AW84796 - phonotephrite, Minna Bluff (MB1)

AW84797 - Tephrite, Minna Bluff (MB1)

Individual analysis numbers are interpreted as follows:

First letter: X - xenocryst, P - phenocryst, M - microphenocryst, G - groundmass, I - inclusion in another mineral, A - alteration product in corona surrounding kaersutite.

Next number (and letter): arbitrary number defining areas of the thin section. If more than one crystal is analysed from an area individual crystals are denoted by a subsequent letter.

Letter after the period: C - core, M - mantle, R - rim.

For example, analysis P2A.C is of the core of phenocryst A in area 2.

Calculation of cation proportions and assignment of theoretical end member compositions is described in the table captions. The following abbreviations are used to denote mineral end members:

Fo - forsterite, Fa - fayalite, Ac - acmite, Ft - ferritschermak, Tc - Ti-Ca-Tschermak, Ct - Ca-tschermak, Wo - wollastonite, En - enstatite, Fs - ferrisilite, NT - Na-Ti-tschermak, An - anorthit Ab - albite, Or - orthoclase, Usp - ulvospinel, Il - ilmenite.

A magnesium index number (mg) is calculated for pyroxene, amphibole and biotite analyses as follows: $mg = 100Mg/(Mg + Fe^*)$, where Mg and Fe* are atomic proportions of magnesium and total iron, respectively.

APPENDIX 5 - GEOCHEMICAL ANALYSIS

A5.1 Sample Preparation

Between 100 and 700 g (depending on grain size) of each sample was reduced to 1 - 3 cm chips using a rock hammer and steel plate. Chips were hand picked to remove visible secondary mineralization.

Samples were then ground to a powder (approximately 10 microns) in a high-speed TEMA mill with a tungsten-carbide head. Approximately 100 g of sample was ground at a time, which took 30 - 60 seconds, and then the whole sample was thoroughly remixed.

A5.2 X-ray Fluorescence Analysis

Major elements and some trace elements (V, Cr, Ni, Cu, Zn, Ga, Rb, Sr, Y, Zr, Nb, Ba, Pb, Th) were analysed using a Rh tube in the Rigaku XRF spectrometer at New Mexico Institute of Mining and Technology. Samples for major element analysis were prepared by weighing out approximately 0.5 g of powdered sample, mixing it with a Li tetraborate-Li carbonate-La oxide flux, and a little NH_4NO_3 to oxidize FeO to Fe_2O_3, then fusing it in a Pt-Au crucible, and pressing it to form a glass disc. Analytical and data reduction procedures are those of Norrish and Hutton (1969). Analyses were made during five separate runs, each of which was independently calibrated using a large suite of international rock standards. Determinations of analytical precision are given in Table A5.1. Lower detection limits for major elements are about 0.01 weight %.

Trace element analyses were determined on pressed powder pellets made by mixing 6 - 8 g of powdered sample with a few drops of a binder solution (2% PVA solution) and pressing at 10 tons for 30 seconds. For most elements mass absorption corrections were calculated from counts

Table A5.1 - Major element precision estimates for rock standards NMR (rhyolite) and CZB (alkali basalt) as determined by Eggelston (1987).

NMR1 internal standard.

SAMPLE	SIO2	TIO2	AL2O3	FE2O3	MNO	MGO	CAO	NA2O	K2O	P2O5
NMR1-8	72.72	0.44	14.32	2.55	0.06	0.43	1.60	3.16	4.83	0.13
40	0.18	0.01	0.03	0.01	0.003	0.019	0.007	0.029	0.009	0.002
	0.24	1.30	0.20	0.40	4.90	4.40	0.46	0.90	0.20	1.22
NMR1-9	72.75	0.43	14.33	2.67	0.05	0.47	1.60	3.12	4.83	0.13
40	0.17	0.01	0.03	0.01	0.003	0.018	0.008	0.037	0.016	0.002
	0.24	1.34	0.17	0.42	5.05	3.86	0.52	0.52	0.33	1.57
NMR1-10	72.39	0.43	14.26	2.64	0.06	0.42	1.60	3.13	4.78	0.14
40	0.20	0.01	0.03	0.01	0.003	0.018	0.011	0.038	0.017	0.003
	0.28	1.45	0.24	0.48	5.7	3.86	0.66	1.22	0.35	1.83
NMR1-11	72.43	0.43	14.29	2.66	0.06	0.42	1.60	3.13	4.78	0.14
40	0.21	0.01	0.02	0.01	0.003	0.018	0.008	0.025	0.02	0.002
	0.29	1.36	0.28	0.47	5.48	4.92	0.49	0.80	0.41	1.36
NMR1-12	72.76	0.43	14.34	2.69	0.06	0.45	1.60	3.14	4.83	0.13
40	0.19	0.01	0.04	0.01	0.002	0.023	0.008	0.027	0.017	0.002
	0.26	1.38	0.26	0.45	4.26	5.26	0.57	0.87	0.36	1.53
TOTALS	72.61	0.43	14.31	2.64	0.06	0.44	1.60	3.14	4.82	0.13
5	0.19	0.01	0.03	0.05	0.004	0.022	0.008	0.015	0.022	0.002
CV=	0.25	1.00	0.23	2.06	7.47	4.95	0.52	0.47	0.45	1.74

CZB internal standard.

SAMPLE	SIO2	TIO2	AL2O3	FE2O3	MNO	MGO	CAO	NA2O	K2O	P2O5
CZB-1	58.56	0.98	16.39	9.52	0.23	0.98	3.61	6.03	3.87	0.29
15	0.12	0.01	0.08	0.01	0.005	0.068	0.007	0.131	0.008	0.007
	0.21	0.61	0.46	0.10	2.00	6.92	0.21	2.17	0.21	2.55
CZB-2	59.63	0.98	16.37	9.42	0.23	1.07	3.61	6.10	3.89	0.29
15	0.08	0.01	0.04	0.023	0.005	0.067	0.012	0.139	0.009	0.005
	0.14	0.75	0.25	0.25	2.01	6.22	0.34	2.29	0.23	1.79
CZB-3	58.52	0.98	16.30	9.62	0.23	0.91	3.63	6.06	3.90	0.29
5	0.05	0.002	0.06	0.025	0.003	0.077	0.011	0.097	0.007	0.004
	0.09	0.19	0.10	0.26	1.20	8.40	0.30	1.59	0.18	0.19
TOTALS	58.57	0.98	16.35	9.52	0.23	0.99	3.62	6.06	3.89	0.29
3	0.06	0.002	0.05	0.10	0.002	0.080	0.012	0.035	0.015	0.001
CV=	0.10	0.24	0.29	1.05	0.67	8.13	0.32	0.58	0.39	0.20

on the Rh K alpha compton peak. However, for Cr, V, and Ba major element compositions were used to calculate mass absorption coefficients. Calibration curves were generated using international rock standards. Because of some doubt as to the consistency of calibrations on different analytical runs, a set of 10 internal standards was analysed for each calibration. In order to maximize internal consistency of trace element data, individual analyses have been recalculated relative to average values for the set of internal standards, using linear regression (Williams, 1983). Lower detection limits and estimates of analytical precision are given in Table A5.2.

A5.3 Instrumental Neutron Activation Analysis

Total iron as FeO*, Na_2O and trace elements (Sc, Cr, Rb, Sb, Cs, Ba, La, Ce, Nd, Sm, Tb, Yb, Lu, Th, U) were determined by INAA. Analyses were performed on approximately 100 mg of powdered sample sealed inside a ultrapure quartz vial. Vials were irradiated for about 40 hr at a flux of 2.2×10^{13} $n.cm^{-2}.sec^{-1}$, at the University of Missouri Research Reactor. Each sample was counted for about 3 hr, approximately 7 days and 40 days after irradiation. BCR-1 and NBS 1633A were used as standards. Lower detection limits were calculated for individual analyses as part of the data reduction process, and are based on peak height relative to background at the peak. There is minor Ta contamination from the tungsen-carbide head used to grind samples.

Table A5.2 - Calculated lower detection limits (LLD)* (Egglston, 1987) and empirical precision data for XRF trace element analysis.

Element	LLD (ppm)	Precision (variance at given concentration)
V	3	5% (20 ppm) - 1% (500 ppm)
Cr	10	8% (12 ppm) - 0.4% (500 ppm)
Ni	5	2% (100 ppm) - 1% (200 ppm)
Cu	15	20% (40 ppm) - 10% (100 ppm)
Zn	4	2% (80 ppm) - 1% (110 ppm)
Ga	3	10% (15 ppm) - 5% (30 ppm)
Rb	1	7% (15 ppm) - 0.5% (150 ppm)
Sr	1	5% (25 ppm) - 0.3% (1500 ppm)
Y	1	4% (30 ppm) - 1% (60 ppm)
Zr	2	1% (200 ppm) - 0.2% (1000 ppm)
Nb	1	1% (60 ppm) - 0.5% (200 ppm)
Ba	16	10% (50 ppm) - 0.5% (200 ppm)
Pb	3	10% (10 ppm) - 5% (20 ppm)
Th	3	10% (8 ppm) - 3% (35 ppm)

* Formula used to calculate LLD:

$$LLD = 3/M * (R_b/T_b)^{1/2}$$

M = counts/second/ppm
R_b = background counts/second
T_b = count time on background

A5.4 Loss on Ignition

The volatile component and oxidation of FeO were jointly assesse by fusing 1 - 2 g of powdered sample for 2 hr at 1000°C, and measurir the weight difference. Negative LOI determinations are presumed to reflect weight gain due to oxidation of FeO in the sample.

A5.5 Ferrous Ion Analysis

FeO was determined in 18 samples using the back-titration metho of Reichen and Fahey (1962). Between 0.5 g and 1.0 g of powdered sample was dissolved in HF acid and mixed with a standard potassium dichromate solution to oxidize all Fe^{2+} in the sample solution. Remaining dichromate was then measured by titrating first with standard ferrous ammonium sulphate solution, then back-titrating with standard dichromate solution.

APPENDIX 6 - TABLES OF GEOCHEMICAL ANALYSES

New geochemical analyses of DVS rocks are given in Tables A6.1 - A6.6. Within each of the geographic areas, samples are listed first by stratigraphic unit and then in order of increasing SiO_2 content. Rock names are listed at the end of each table.

Major elements are given in oxide weight per cent and are listed on a dry basis (i.e. after drying at 100°C). Trace elements are given in parts per million. For those analyses below detection limit, the detection limit, prefixed by a less-than symbol, is given. V, Ni, Cu, Zn, Ga, Sr, Y, Zr, Nb, Pb were determined by XRF analysis: Sc, As, Sb Cs, La, Ce, Nd, Sm, Eu, Tb, Yb, Lu, Hf, Ta, U by INAA. FeO*, Na_2O, Cr Rb, Ba, and Th were analysed by both methods; the element symbol for the INAA analyses are prefixed by "I".

Table A6.1 - Geochemical analyses of samples from Riviera Ridge.

	RG1							
	AW86978	AW86021	AW86006	AW86018	AW86986	AW86020	AW86008	AW869
SiO2	62.11	62.42	62.73	62.97	64.26	66.25	66.46	67.4
TiO2	0.40	0.38	0.38	0.49	0.44	0.42	0.47	0.3
Al2O3	15.02	15.64	18.88	15.52	16.81	14.45	16.98	12.4
FeO*	7.64	6.69	2.61	6.48	3.85	5.29	1.53	5.4
MnO	0.14	0.14	0.05	0.78	0.05	0.11	0.05	0.1
MgO	0.26	0.28	0.58	0.22	0.33	0.19	0.16	0.3
CaO	0.66	1.01	0.94	0.38	0.45	0.40	1.58	1.4
Na2O	6.70	7.06	6.10	4.51	6.51	6.42	5.23	5.1
K2O	4.91	5.04	5.76	5.44	5.09	5.09	5.82	4.7
P2O5	0.04	0.02	0.06	0.73	0.05	0.04	0.11	0.0
LOI	1.42	0.94	2.20	2.18	1.96	0.69	1.23	2.6
Total	99.30	99.62	100.29	99.70	99.80	99.35	99.62	100.1
IFeO*	-	6.77	-	6.63	-	5.45	-	5.5
INa2O	-	-	-	-	-	-	-	-
Sc	-	1.46	-	3.29	-	0.98	-	0.4
V	<3	<3	<3	<3	<3	<3	9	<3
Cr	<10	11	<10	<10	11	12	11	13
ICr	-	<1	-	<1	-	<1	-	2.4
Ni	6	5	5	5	9	5	7	7
Cu	<15	<15	<15	<15	<15	<15	32	<15
Zn	319	144	132	272	538	190	99	214
Ga	40	39	29	31	43	37	26	35
Rb	124	139	105	110	154	126	154	184
IRb	-	132	-	103	-	119	-	173
Sr	4	5	16	21	5	7	184	15
Y	124	106	54	65	180	81	46	104
Zr	933	1101	768	580	1409	874	671	1070
Nb	224	251	179	104	334	168	76	177
Sb	-	0.15	-	0.21	-	0.09	-	0.2
Cs	-	0.76	-	0.31	-	0.20	-	0.4
Ba	<16	23	196	94	<16	<16	865	21
IBa	-	<16	-	121	-	13.3	-	46.4
La	-	139	-	75.7	-	145	-	142
Ce	-	290	-	155	-	306	-	296
Nd	-	111	-	79.1	-	131	-	134
Sm	-	19.8	-	13.9	-	22.2	-	23.1
Eu	-	2.27	-	1.74	-	1.35	-	1.5
Tb	-	2.94	-	2.10	-	2.94	-	3.2
Yb	-	10.1	-	5.12	-	6.85	-	8.8
Lu	-	1.49	-	0.74	-	1.02	-	1.2
Hf	-	26.4	-	13.7	-	22.3	-	27.1
Ta	-	15.3	-	5.93	-	10.6	-	10.4
Pb	13	11	6	13	14	14	21	28
Th	22	26	15	13	35	21	17	25
ITh	-	20.6	-	10.3	-	18.0	-	19.5
U	-	2.68	-	2.68	-	4.42	-	5.2

Table A6.1 - Geochemical analyses of samples from Riviera Ridge.

	RG2							
	AW86035	AW86036	AW86013	AW86012	AW86072	AW84714	AW86034	AW86
SiO2	43.91	45.26	47.53	48.95	49.68	50.90	51.25	53.
TiO2	3.78	3.74	2.89	2.72	2.48	2.02	2.14	1.
Al2O3	14.70	18.33	16.23	16.70	17.06	16.95	17.23	17.
FeO*	12.30	10.95	10.83	10.65	9.83	9.46	9.52	8.
MnO	0.19	0.15	0.25	0.26	0.24	0.26	0.26	0.
MgO	7.65	4.77	4.21	3.81	3.81	2.75	2.84	1.
CaO	9.64	11.28	7.64	7.20	6.94	5.86	6.11	4.
Na2O	3.28	3.38	4.87	5.25	5.51	5.66	5.80	6.
K2O	1.13	0.98	1.99	2.15	2.33	2.51	2.52	2.
P2O5	0.71	0.54	1.71	1.58	1.32	0.99	1.12	0.
LOI	1.21	0.11	0.43	-0.34	-0.57	0.96	-0.10	2.
Total	98.50	99.49	98.58	99.27	99.20	98.32	98.79	98.
IFeO*	-	-	11.06	-	-	-	9.77	-
INa2O	-	-	-	-	-	-	-	-
Sc	-	-	12.2	-	-	-	7.82	-
V	283	282	91	83	73	44	52	1
Cr	232	66	<10	14	<10	12	<10	1
ICr	-	-	<1	-	-	-	<1	-
Ni	90	25	<5	<5	5	<5	6	<
Cu	27	<15	<15	<15	15	<15	<15	<1
Zn	81	65	77	81	90	101	89	9
Ga	16	18	19	22	25	19	19	2
Rb	22	17	42	44	47	51	53	6
IRb	-	-	43	-	-	-	-	-
Sr	1171	1268	1624	1591	1386	1288	1341	114
Y	21	21	40	41	39	40	39	3
Zr	197	165	362	404	381	458	427	54
Nb	40	38	81	87	95	102	101	11
Sb	-	-	<0.01	-	-	-	0.07	-
Cs	-	-	0.26	-	-	-	0.52	-
Ba	447	415	680	696	746	851	849	88
IBa	-	-	580	-	-	-	1597	-
La	-	-	68.2	-	-	-	77.8	-
Ce	-	-	152	-	-	-	167	-
Nd	-	-	83.6	-	-	-	79.0	-
Sm	-	-	14.6	-	-	-	13.5	-
Eu	-	-	4.86	-	-	-	4.77	-
Tb	-	-	1.61	-	-	-	1.55	-
Yb	-	-	2.88	-	-	-	3.28	-
Lu	-	-	0.41	-	-	-	0.47	-
Hf	-	-	8.53	-	-	-	9.94	-
Ta	-	-	5.38	-	-	-	6.37	-
Pb	9	<3	7	4	6	4	6	4
Th	<3	<3	5	<3	5	5	7	8
ITh	-	-	5.98	-	-	-	7.79	-
U	-	-	1.52	-	-	-	1.89	-

Table A6.1 (continued) - Geochemical analyses of samples from Riviera Ridge.

	RG2					RG3		
	AW86025	AW86041	AW86016	AW86075	AW86042	AW86999	AW86033	AW860
SiO2	54.95	55.07	59.88	60.74	60.84	38.86	42.86	43.3
TiO2	1.20	1.20	0.42	0.22	0.18	5.28	4.40	4.1
Al2O3	17.74	17.62	17.99	18.29	18.07	15.46	15.08	14.7
FeO*	8.85	8.92	5.90	5.33	4.85	13.19	12.53	12.5
MnO	0.30	0.33	0.26	0.23	0.24	0.18	0.20	0.2
MgO	1.64	1.53	0.44	0.47	0.17	7.20	7.93	9.5
CaO	4.40	4.30	1.93	1.34	1.06	12.05	10.86	10.1
Na2O	6.68	6.87	8.01	6.44	8.96	3.22	3.44	3.5
K2O	3.01	3.09	4.50	5.16	5.22	0.94	1.34	1.2
P2O5	0.47	0.48	0.11	0.06	0.03	2.19	0.78	0.5
LOI	0.41	-0.21	0.24	1.76	0.33	-0.17	-0.53	-0.8
Total	99.65	99.41	99.68	100.04	99.95	98.57	99.42	99.9
IFeO*	9.12	-	6.13	5.34	4.96	-	-	-
INa2O	-	-	-	-	-	-	-	-
Sc	8.25	-	1.91	0.52	0.58	-	-	-
V	8	5	3	<3	<3	292	319	305
Cr	10	<10	<10	<10	<10	34	170	368
ICr	<1	-	<1	1.00	0.06	-	-	-
Ni	7	<5	<5	<5	8	<5	64	161
Cu	81	<15	<15	<15	<15	<15	31	26
Zn	82	119	114	133	148	59	81	81
Ga	26	22	23	26	32	15	21	19
Rb	59	55	84	98	163	11	30	20
IRb	60	-	83	95	152	-	-	-
Sr	1273	1207	314	63	7	1664	1064	1032
Y	50	50	50	60	84	41	28	31
Zr	559	506	916	575	1399	152	269	209
Nb	123	136	182	224	288	55	62	56
Sb	0.06	-	0.07	<0.01	0.30	-	-	-
Cs	0.51	-	0.22	0.45	1.41	-	-	-
Ba	1291	1266	1887	721	50	375	392	373
IBa	1287	-	1918	679	<70	-	-	-
La	99.7	-	112	132	172	-	-	-
Ce	228	-	238	289	347	-	-	-
Nd	95.3	-	94.6	105	126	-	-	-
Sm	17.1	-	7.29	15.9	21.9	-	-	-
Eu	5.72	-	4.32	2.92	2.13	-	-	-
Tb	1.94	-	1.82	2.02	2.76	-	-	-
Yb	4.11	-	4.66	5.56	7.70	-	-	-
Lu	0.63	-	0.71	0.85	1.18	-	-	-
Hf	13.1	-	18.3	20.0	31.3	-	-	-
Ta	7.85	-	10.9	13.1	17.0	-	-	-
Pb	8	4	9	12	14	5	4	4
Th	8	6	15	19	28	<3	<3	<3
ITh	9.54	-	12.4	15.6	23.0	-	-	-
U	1.58	-	5.80	1.98	7.6	-	-	-

Table A6.1 (continued) - Geochemical analyses of samples from Riviera Ridge.

	RG3			
	AW86061	AW86037	AW86032	AW86063
SiO2	44.63	45.28	47.36	47.61
TiO2	2.71	3.31	3.18	2.67
Al2O3	13.85	16.02	17.09	16.36
FeO*	10.91	11.01	10.87	10.82
MnO	0.20	0.21	0.23	0.22
MgO	11.10	6.83	4.55	6.10
CaO	11.12	10.09	8.40	8.40
Na2O	3.36	4.40	4.74	4.79
K2O	1.13	1.37	1.80	1.83
P2O5	0.56	0.85	1.00	0.83
LOI	-0.27	-0.61	-0.35	-0.85
Total	99.57	99.37	99.22	99.63
IFeO*	-	11.32	-	-
INa2O	-	-	-	-
Sc	-	20.3	-	-
V	278	247	201	176
Cr	597	217	27	181
ICr	-	207	-	-
Ni	245	86	<5	71
Cu	47	23	<15	18
Zn	77	94	92	85
Ga	16	18	19	24
Rb	27	32	37	44
IRb	-	30	-	-
Sr	684	1095	1014	1040
Y	27	34	34	35
Zr	225	316	314	349
Nb	60	85	83	87
Sb	-	0.09	-	-
Cs	-	0.40	-	-
Ba	359	438	523	536
IBa	-	467	-	-
La	-	55.7	-	-
Ce	-	119	-	-
Nd	-	53.8	-	-
Sm	-	10.3	-	-
Eu	-	3.13	-	-
Tb	-	1.17	-	-
Yb	-	2.54	-	-
Lu	-	0.38	-	-
Hf	-	7.25	-	-
Ta	-	5.13	-	-
Pb	4	5	5	7
Th	3	4	6	5
ITh	-	5.85	-	-
U	-	1.89	-	-

Sample descriptions

RG1

AW86978	trachyte
AW86021	peralkaline trachyte
AW86006	trachyte
AW86018	trachyte
AW86986	trachyte
AW86020	peralkaline trachyte
AW86008	trachyte
AW86976	peralkaline trachyte

RG2

AW86035	basanite
AW86036	basanite
AW86013	tephrite
AW86012	phonotephrite
AW86072	phonotephrite
AW84714	mugearite
AW86034	phonotephrite
AW86988	benmoreite
AW86025	benmoreite
AW86041	benmoreite
AW86016	trachyte
AW86075	trachyte
AW86042	phonolite

RG3

AW86999	clinopyroxene amphibolite xenolith
AW86033	basanite
AW86070	basanite
AW86061	basanite
AW86037	tephrite
AW86032	tephrite
AW86063	tephrite

Table A6.2 - Geochemical analyses of samples from the Mason Spur area.

	MS1							M
	AW83581	AW83422	AW83441	AW83508	AW85865	AW85803	AW83569	AW85
SiO2	61.37	61.40	61.42	62.25	62.39	62.48	63.43	50.
TiO2	0.59	0.59	0.68	0.49	0.51	0.70	0.66	2.
Al2O3	14.70	13.93	14.54	16.21	16.49	15.16	14.79	15.
FeO*	7.00	7.38	7.16	5.54	5.57	7.26	5.85	10.
MnO	0.29	0.32	0.36	0.24	0.29	0.38	0.27	0.
MgO	0.35	0.50	0.42	0.32	0.54	0.26	0.16	3.
CaO	0.64	0.97	0.97	0.96	1.01	0.71	0.52	6.
Na2O	6.17	6.24	6.10	6.82	6.86	6.02	5.93	5.
K2O	5.14	4.66	5.06	5.26	5.35	5.02	5.14	2.
P2O5	0.04	0.05	0.06	0.05	0.05	0.03	0.03	1.
LOI	2.38	2.06	1.96	0.80	0.35	0.99	1.46	1.
Total	98.67	98.10	98.73	98.94	99.41	99.01	98.24	99.
IFeO*	-	-	-	-	5.65	-	-	10.
INa2O	-	-	-	-	-	-	-	-
Sc	-	-	-	-	2.56	-	-	11.
V	<3	<3	<3	<3	<3	<3	<3	11
Cr	<10	<10	<10	<10	<10	<10	<10	<1
ICr	-	-	-	-	<1	-	-	<
Ni	5	6	5	5	<5	<5	<5	<
Cu	<15	<15	<15	<15	<15	<15	<15	<1
Zn	151	228	202	149	148	195	148	12
Ga	34	42	40	33	35	34	35	2
Rb	123	126	109	112	115	95	98	4
IRb	-	-	-	-	109	-	-	4
Sr	9	6	2	7	6	5	3	127
Y	79	93	72	74	80	69	71	4
Zr	853	1206	884	919	983	753	954	31
Nb	199	304	203	216	245	188	199	8
Sb	-	-	-	-	0.22	-	-	0.
Cs	-	-	-	-	0.33	-	-	0.
Ba	44	18	63	44	36	150	24	99
IBa	-	-	-	-	27.3	-	-	98
La	-	-	-	-	127	-	-	71.
Ce	-	-	-	-	261	-	-	15
Nd	-	-	-	-	99.1	-	-	72.
Sm	-	-	-	-	17.0	-	-	14.
Eu	-	-	-	-	2.62	-	-	5.
Tb	-	-	-	-	2.49	-	-	1.
Yb	-	-	-	-	7.57	-	-	3.
Lu	-	-	-	-	1.15	-	-	0.
Hf	-	-	-	-	23.6	-	-	7.
Ta	-	-	-	-	14.2	-	-	5.
Pb	14	15	9	13	14	12	12	
Th	16	24	15	21	22	16	14	
ITh	-	-	-	-	18.6	-	-	6.
U	-	-	-	-	3.27	-	-	2.

Table A6.2 (continued) - Geochemical analyses of samples from the Mason Spur area.

	MS2		MS3					
	AW85831	AW83511	AW83503	AW83496	AW85851	AW85850	AW83711	AW8343
SiO2	51.17	61.71	58.37	59.29	60.17	60.31	60.41	60.72
TiO2	2.29	0.57	0.39	0.39	0.39	0.29	0.61	0.37
Al2O3	16.14	15.15	16.61	16.99	18.05	17.76	14.82	16.93
FeO*	9.56	6.66	6.56	6.19	4.91	4.87	8.04	5.58
MnO	0.26	0.28	0.25	0.17	0.22	0.22	0.45	0.24
MgO	2.96	0.40	0.24	0.16	0.38	0.42	0.16	0.37
CaO	6.13	0.82	1.13	0.49	1.01	0.91	0.46	0.82
Na2O	5.11	7.24	7.10	6.82	6.72	6.69	7.05	7.11
K2O	2.43	5.14	5.00	5.39	5.20	5.20	4.92	5.15
P2O5	0.87	0.07	0.05	0.05	0.06	0.05	0.04	0.05
LOI	1.71	0.64	2.70	2.60	2.99	3.07	1.32	2.11
Total	98.63	98.68	98.40	98.54	100.10	99.79	98.28	99.45
IFeO*	-	6.77	6.66	6.31	-	-	-	-
INa2O	-	-	-	-	-	-	-	-
Sc	-	2.22	0.89	0.90	-	-	-	-
V	82	3	<3	<3	9	<3	<3	<3
Cr	<10	<10	12	<10	<10	<10	<10	<10
ICr	-	<1	<1	<1	-	-	-	-
Ni	<5	5	5	6	8	7	5	7
Cu	<15	19	<15	<15	<15	15	<15	<15
Zn	142	188	182	120	115	111	250	202
Ga	26	31	33	36	35	37	42	37
Rb	33	111	143	155	144	166	115	174
IRb	-	106	133	151	-	-	-	-
Sr	865	1	7	6	32	20	2	12
Y	51	76	80	86	85	87	110	81
Zr	449	578	935	917	1293	1451	1068	1399
Nb	111	157	232	235	279	273	267	299
Sb	-	0.18	0.28	0.34	-	-	-	-
Cs	-	0.79	3.24	2.25	-	-	-	-
Ba	754	85	104	114	59	33	25	43
IBa	-	21.4	106	154	-	-	-	-
La	-	107	129	129	-	-	-	-
Ce	-	220	261	266	-	-	-	-
Nd	-	88.5	100	104	-	-	-	-
Sm	-	15.3	16.5	16.7	-	-	-	-
Eu	-	3.16	2.77	2.90	-	-	-	-
Tb	-	2.28	2.43	2.51	-	-	-	-
Yb	-	6.39	7.32	7.25	-	-	-	-
Lu	-	0.89	1.03	1.03	-	-	-	-
Hf	-	16.2	21.9	22.7	-	-	-	-
Ta	-	11.1	14.0	14.2	-	-	-	-
Pb	6	13	17	13	18	21	18	16
Th	5	18	26	16	35	39	33	28
ITh	-	15.8	20.6	16.9	-	-	-	-
U	-	0.69	6.15	6.73	-	-	-	-

Table A6.2 (continued) - Geochemical analyses of samples from the Mason Spur area.

	MS3							
	AW85818	AW83445	AW83678	AW83499	AW83515	AW85847	AW83484	AW858
SiO2	61.50	61.57	61.71	61.72	62.11	62.19	62.28	62.3
TiO2	0.57	0.53	0.56	0.48	0.52	0.66	0.58	0.5
Al2O3	15.10	15.56	15.79	15.43	15.45	15.05	15.18	15.5
FeO*	7.17	6.45	6.23	5.69	6.64	6.80	6.74	6.4
MnO	0.34	0.27	0.21	0.27	0.30	0.34	0.38	0.3
MgO	0.51	0.28	0.3	0.34	0.71	0.59	0.34	0.3
CaO	1.00	0.95	1.14	0.97	1.08	1.01	0.51	0.8
Na2O	6.27	6.92	6.64	5.86	6.71	6.56	5.97	6.3
K2O	4.78	5.09	5.25	5.47	5.09	5.07	4.89	5.0
P2O5	0.05	0.04	0.09	0.05	0.06	0.04	0.03	0.0
LOI	1.51	0.75	1.18	1.99	0.74	0.85	2.16	1.7
Total	98.80	98.41	99.12	98.27	99.41	99.16	99.06	99.5
IFeO*	8.82	-	-	-	-	6.89	-	-
INa2O	-	-	-	-	-	-	-	-
Sc	2.32	-	-	-	-	3.28	-	-
V	<3	<3	<3	<3	<3	<3	3	<3
Cr	<10	<10	22	<10	<10	<10	<10	13
ICr	162	-	-	-	-	<0.4	-	-
Ni	5	7	7	5	<5	<5	<5	<5
Cu	<15	<15	<15	<15	<15	<15	<15	<15
Zn	189	192	154	125	181	165	126	127
Ga	40	33	31	32	31	39	31	29
Rb	85	113	104	120	126	92	104	103
IRb	73	-	-	-	-	87	-	-
Sr	10	1	4	2	5	1	2	2
Y	86	71	105	74	70	71	49	50
Zr	1023	830	697	889	713	556	679	673
Nb	249	198	175	211	174	196	166	180
Sb	<0.01	-	-	-	-	0.23	-	-
Cs	0.77	-	-	-	-	0.42	-	-
Ba	172	35	109	32	91	30	153	134
IBa	231	-	-	-	-	37.8	-	-
La	125	-	-	-	-	102	-	-
Ce	202	-	-	-	-	214	-	-
Nd	94.4	-	-	-	-	77.3	-	-
Sm	18.9	-	-	-	-	15.4	-	-
Eu	3.91	-	-	-	-	3.09	-	-
Tb	2.74	-	-	-	-	2.33	-	-
Yb	6.77	-	-	-	-	6.38	-	-
Lu	0.95	-	-	-	-	0.93	-	-
Hf	24.0	-	-	-	-	15.2	-	-
Ta	13.8	-	-	-	-	11.4	-	-
Pb	12	12	13	11	15	11	13	13
Th	16	18	22	20	18	19	8	14
ITh	12.5	-	-	-	-	17.1	-	-
U	10.8	-	-	-	-	2.93	-	-

Table A6.2 (continued) - Geochemical analyses of samples from the Mason Spur area.

	MS3							
	AW85837	AW85860	AW83491	AW83580	AW83709	AW83710	AW85833	AW8583
SiO2	62.56	62.59	62.62	62.82	62.86	62.95	62.96	63.14
TiO2	0.53	0.58	0.49	0.60	0.56	0.60	0.59	0.66
Al2O3	15.81	14.84	15.75	14.79	16.51	14.25	15.07	15.07
FeO*	6.47	7.13	5.78	6.86	5.16	7.79	6.29	6.25
MnO	0.32	0.19	0.25	0.33	0.08	0.35	0.22	0.30
MgO	0.36	0.50	0.17	0.33	0.27	0.19	0.42	0.28
CaO	1.02	1.07	0.51	0.46	0.92	0.74	0.87	0.71
Na2O	7.06	6.89	6.91	6.51	6.63	6.07	7.51	6.43
K2O	5.08	4.80	5.63	5.11	5.34	4.83	5.04	5.02
P2O5	0.05	0.05	0.04	0.06	0.05	0.04	0.04	0.04
LOI	-0.27	1.07	1.26	1.53	0.67	1.19	0.44	1.47
Total	99.26	99.71	99.41	99.40	99.05	99.00	99.48	99.37
IFeO*	6.53	7.14	-	6.89	-	8.02	-	-
INa2O	-	-	-	-	-	-	-	-
Sc	2.20	3.34	-	3.29	-	1.80	-	-
V	<3	<3	<3	<3	<3	<3	<3	<3
Cr	<10	<10	<10	<10	19	15	<10	14
ICr	<1	<0.8	-	<1	-	<1	-	-
Ni	5	<5	5	<5	<5	5	<5	6
Cu	<15	<15	<15	<15	<15	<15	<15	<15
Zn	200	156	122	159	138	221	152	145
Ga	32	36	31	31	30	38	37	38
Rb	118	94	123	94	99	138	106	91
IRb	111	94	-	95	-	130	-	-
Sr	<1	5	1	4	<1	1	1	14
Y	70	75	66	69	65	103	76	74
Zr	839	820	817	772	825	1264	721	690
Nb	208	201	212	184	83	297	123	192
Sb	0.23	0.13	-	0.26	-	2.10	-	-
Cs	1.12	0.38	-	0.63	-	0.34	-	-
Ba	32	353	23	32	39	27	<16	52
IBa	54.4	334	-	37.0	-	75.9	-	-
La	119	115	-	107	-	151	-	-
Ce	246	187	-	223	-	307	-	-
Nd	91.3	98.7	-	94.5	-	127	-	-
Sm	16.1	17.4	-	16.2	-	21.1	-	-
Eu	2.97	4.19	-	3.01	-	3.61	-	-
Tb	2.29	2.55	-	2.21	-	3.09	-	-
Yb	6.76	6.42	-	6.27	-	9.66	-	-
Lu	1.04	0.99	-	0.96	-	1.44	-	-
Hf	20.7	19.6	-	17.8	-	28.4	-	-
Ta	12.7	12.4	-	10.7	-	16.5	-	-
Pb	13	8	11	10	10	16	17	11
Th	21	19	18	15	18	30	19	18
ITh	17.0	14.9	-	14.9	-	22.9	-	-
U	2.36	2.72	-	3.99	-	10.7	-	-

Table A6.2 (continued) Geochemical analyses of samples from the Mason Spur area.

	MS3							MS5
	AW83502A	AW85869	AW83510	AW83567	AW83485	AW83712	AW83411	AW858
SiO2	63.20	63.29	63.32	63.70	64.18	66.68	66.82	59.4
TiO2	0.62	0.57	0.51	0.61	0.63	0.53	0.84	0.5
Al2O3	14.61	15.86	14.96	14.66	16.32	12.72	16.82	15.3
FeO*	6.94	5.63	6.08	6.37	4.87	6.59	2.31	7.8
MnO	0.31	0.28	0.13	0.32	0.08	0.20	0.04	0.3
MgO	0.23	0.38	0.32	0.19	0.53	0.32	0.17	0.3
CaO	0.50	0.75	0.78	0.49	0.66	0.56	0.46	1.3
Na2O	5.68	6.68	6.06	6.41	7.04	6.53	6.18	6.6
K2O	4.98	4.99	4.70	4.93	5.35	4.84	5.97	4.8
P2O5	0.04	0.03	0.04	0.05	0.04	0.04	0.15	0.0
LOI	1.99	1.48	1.78	1.49	0.54	0.67	0.54	2.3
Total	99.10	99.94	98.68	99.22	100.24	99.68	100.30	98.9
IFeO*	7.09	-	-	-	-	6.71	-	-
INa2O	-	-	-	-	-	-	-	-
Sc	2.29	-	-	-	-	2.37	-	-
V	<3	4	<3	<3	<3	<3	<3	<3
Cr	10	<10	16	<10	<10	13	<10	<10
ICr	<1	-	-	-	-	<1	-	-
Ni	5	5	<5	5	5	<5	<5	<5
Cu	15	<15	<15	<15	<15	<15	<15	<15
Zn	158	153	168	129	99	124	78	195
Ga	35	28	29	32	32	32	32	33
Rb	120	90	102	95	120	125	73	105
IRb	116	-	-	-	-	122	-	-
Sr	4	1	5	3	3	2	6	8
Y	63	40	64	81	46	50	45	67
Zr	917	636	663	987	722	854	458	435
Nb	228	171	177	184	171	217	154	159
Sb	0.26	-	-	-	-	0.33	-	-
Cs	0.48	-	-	-	-	0.47	-	-
Ba	52	92	35	26	129	<16	38	168
IBa	71	-	-	-	-	42	-	-
La	126	-	-	-	-	109	-	-
Ce	260	-	-	-	-	227	-	-
Nd	108	-	-	-	-	91.0	-	-
Sm	17.1	-	-	-	-	15.3	-	-
Eu	3.36	-	-	-	-	2.19	-	-
Tb	2.31	-	-	-	-	1.81	-	-
Yb	5.97	-	-	-	-	6.95	-	-
Lu	0.94	-	-	-	-	1.12	-	-
Hf	25.6	-	-	-	-	19.4	-	-
Ta	14.1	-	-	-	-	11.4	-	-
Pb	14	12	15	11	11	9	12	17
Th	17	11	19	15	10	16	10	18
ITh	14.8	-	-	-	-	12.8	-	-
U	8.75	-	-	-	-	7.6	-	-

Table A6.2 (continued) Geochemical analyses of samples from the Mason Spur area.

	MS5							
	AW83701	AW83532	AW83516	AW83453	AW83707A	AW83522	AW83533	AW83
SiO2	59.14	59.52	59.90	60.00	60.19	60.47	60.52	60.
TiO2	0.42	0.47	0.58	0.59	0.60	0.52	0.27	0.
Al2O3	17.54	14.98	14.05	14.34	14.31	15.26	17.86	15.
FeO*	6.91	8.49	7.37	6.34	8.48	7.98	4.62	7.
MnO	0.14	0.37	0.36	0.22	0.31	0.17	0.20	0.
MgO	0.15	0.25	0.32	0.40	0.51	0.55	0.22	0.
CaO	0.76	1.36	0.86	0.69	1.32	1.56	1.12	1.
Na2O	5.21	6.67	7.82	5.29	7.15	5.73	7.65	6.
K2O	5.16	4.88	4.46	3.12	4.55	5.03	5.58	4.
P2O5	0.05	0.02	0.09	0.10	0.05	0.07	0.05	0.
LOI	3.20	2.18	2.04	7.82	1.74	1.70	1.05	2.
Total	98.68	99.19	97.85	98.91	99.21	99.04	99.14	99.
IFeO*	-	-	-	-	-	-	4.61	-
INa2O	-	-	-	-	-	-	-	-
Sc	-	-	-	-	-	-	1.06	-
V	<3	<3	-	<3	3	<3	<3	<
Cr	<10	<10	-	19	<10	<10	16	<1
ICr	-	-	-	-	-	-	0.50	-
Ni	<5	<5	-	6	6	<5	<5	<
Cu	<15	<15	-	<15	16	<15	<15	<1
Zn	174	255	-	189	244	201	122	14
Ga	32	36	-	35	37	32	29	3
Rb	120	139	-	112	82	119	145	12
IRb	-	-	-	-	-	-	133	-
Sr	10	7	-	8	17	16	6	1
Y	62	75	-	96	136	72	55	8
Zr	903	907	-	1122	1030	617	952	88
Nb	232	245	-	259	246	177	231	21
Sb	-	-	-	-	-	-	0.29	-
Cs	-	-	-	-	-	-	1.98	-
Ba	149	43	-	<16	55	166	44	6
IBa	-	-	-	-	-	-	36.0	-
La	-	-	-	-	-	-	118	-
Ce	-	-	-	-	-	-	240	-
Nd	-	-	-	-	-	-	88.8	-
Sm	-	-	-	-	-	-	13.1	-
Eu	-	-	-	-	-	-	1.37	-
Tb	-	-	-	-	-	-	1.73	-
Yb	-	-	-	-	-	-	5.18	-
Lu	-	-	-	-	-	-	0.82	-
HF	-	-	-	-	-	-	21.5	-
Ta	-	-	-	-	-	-	13.9	-
Pb	16	18	-	18	11	15	16	16
Th	25	19	-	28	20	16	25	2
ITh	-	-	-	-	-	-	20.3	-
U	-	-	-	-	-	-	5.70	-

Table A6.2 (continued) - Geochemical analyses of samples from the Mason Spur area.

	MS5							
	AW83520	AW83642	AW83519	AW83677	AW83653	AW83524	AW83517	AW835
SiO2	60.76	60.85	61.30	61.40	61.60	61.72	61.96	62.5
TiO2	0.52	0.59	0.56	0.59	0.61	0.55	0.58	0.6
Al2O3	15.84	14.22	15.93	14.28	14.44	15.68	15.56	15.0
FeO*	6.60	7.56	6.53	7.75	7.88	6.58	6.51	6.2
MnO	0.26	0.38	0.29	0.37	0.24	0.29	0.23	0.2
MgO	0.41	0.29	0.33	0.45	0.35	0.43	0.39	0.4
CaO	1.28	0.85	1.30	0.88	0.89	1.19	1.01	0.8
Na2O	6.84	9.07	7.93	7.18	7.12	6.72	6.92	6.8
K2O	5.00	4.71	5.04	4.80	4.93	5.29	5.03	5.0
P2O5	0.08	0.09	0.10	0.07	0.03	0.12	0.06	0.0
LOI	1.32	-0.37	-0.54	1.36	1.41	1.05	0.75	1.0
Total	98.91	98.61	99.31	99.13	99.50	99.64	99.00	99.1
IFeO*	-	-	-	-	7.91	6.65	-	-
INa2O	-	-	-	-	-	-	-	-
Sc	-	-	-	-	2.34	2.36	-	-
V	<3	<3	<3	<3	<3	<3	<3	<3
Cr	<10	13	17	<10	<10	17	<10	<10
ICr	-	-	-	-	<1	<1	-	-
Ni	5	6	6	5	6	<5	<5	10
Cu	<15	<15	<15	<15	<15	<15	<15	<15
Zn	172	245	171	250	254	153	151	184
Ga	31	38	32	36	39	29	33	33
Rb	108	134	106	130	114	119	108	82
IRb	-	-	-	-	112	118	-	-
Sr	32	3	37	3	6	41	5	6
Y	70	100	61	95	80	42	64	68
Zr	779	1119	670	1058	1092	942	714	689
Nb	181	270	161	259	269	159	158	182
Sb	-	-	-	-	0.27	0.19	-	-
Cs	-	-	-	-	0.68	2.12	-	-
Ba	261	28	420	24	21	438	91	80
IBa	-	-	-	-	30.0	444	-	-
La	-	-	-	-	166	92.0	-	-
Ce	-	-	-	-	303	189	-	-
Nd	-	-	-	-	126	75.2	-	-
Sm	-	-	-	-	22.3	14.0	-	-
Eu	-	-	-	-	3.73	2.89	-	-
Tb	-	-	-	-	2.95	1.60	-	-
Yb	-	-	-	-	7.40	4.79	-	-
Lu	-	-	-	-	1.15	0.83	-	-
Hf	-	-	-	-	26.7	17.0	-	-
Ta	-	-	-	-	16.6	8.96	-	-
Pb	13	17	16	15	15	13	11	10
Th	14	27	16	23	24	9	17	15
ITh	-	-	-	-	22.5	6.13	-	-
U	-	-	-	-	2.06	1.12	-	-

Table A6.2 (continued) Geochemical analyses of samples from the Mason Spur area.

	MS7							
	AW83550	AW83454	AW83545	AW83536	AW83554	AW83543	AW83410	AW836
SiO2	42.48	42.95	44.27	44.32	44.46	45.43	46.31	46.5
TiO2	3.30	2.92	2.80	3.10	3.53	3.82	2.85	2.9
Al2O3	15.87	15.20	14.16	14.53	14.76	14.72	16.78	16.1
FeO*	10.37	10.47	11.23	11.45	11.23	12.23	9.48	11.2
MnO	0.18	0.17	0.19	0.18	0.20	0.24	0.20	0.2
MgO	4.86	7.88	8.69	8.41	4.50	5.11	3.67	4.3
CaO	10.73	12.39	12.50	12.58	8.61	9.29	8.08	7.7
Na2O	3.43	2.63	2.75	2.68	4.01	3.93	4.52	4.1
K2O	1.10	0.98	1.00	0.85	1.68	1.39	2.02	2.0
P2O5	1.20	0.42	0.48	0.46	1.44	1.91	1.01	1.3
LOI	5.23	2.73	0.14	-0.34	3.53	1.02	3.92	1.9
Total	98.75	98.73	98.21	98.56	97.95	99.09	98.84	98.6
IFeO*	-	-	-	-	-	12.25	-	-
INa2O	-	-	-	-	-	-	-	-
Sc	-	-	-	-	-	15.6	-	-
V	265	319	321	310	225	232	172	151
Cr	42	174	267	185	<10	11	<10	15
ICr	-	-	-	-	-	<2	-	-
Ni	21	89	118	102	<5	<5	<5	12
Cu	24	123	84	74	19	<15	19	41
Zn	77	75	74	63	85	114	92	97
Ga	18	17	19	17	18	22	20	19
Rb	18	19	24	17	27	21	41	46
IRb	-	-	-	-	-	19	-	-
Sr	1135	812	688	775	1358	1207	1065	1165
Y	28	23	26	23	33	42	33	42
Zr	168	174	187	166	227	261	337	365
Nb	45	47	48	40	65	75	98	91
Sb	-	-	-	-	-	0.08	-	-
Cs	-	-	-	-	-	0.39	-	-
Ba	1008	313	311	295	1383	636	569	704
IBa	-	-	-	-	-	641	-	-
La	-	-	-	-	-	64.2	-	-
Ce	-	-	-	-	-	144	-	-
Nd	-	-	-	-	-	75.7	-	-
Sm	-	-	-	-	-	14.5	-	-
Eu	-	-	-	-	-	4.81	-	-
Tb	-	-	-	-	-	1.65	-	-
Yb	-	-	-	-	-	2.90	-	-
Lu	-	-	-	-	-	0.45	-	-
Hf	-	-	-	-	-	6.11	-	-
Ta	-	-	-	-	-	4.67	-	-
Pb	5	7	4	4	6	3	6	11
Th	<3	<3	<3	<3	<3	<3	5	8
ITh	-	-	-	-	-	5.08	-	-
U	-	-	-	-	-	1.64	-	-

Table 6.2 (continued) - Geochemical analyses of samples from the Mason Spur area.

	MS7		MS8			MS9		
	AW83513	AW85839	AW83618	AW83647	AW83645	AW83471	AW83583	AW835
SiO2	53.29	54.07	57.76	60.02	60.41	39.63	41.84	42.1
TiO2	1.65	1.63	0.59	0.47	0.41	6.19	3.79	3.6
Al2O3	17.45	17.62	17.51	17.54	17.45	13.09	13.88	13.5
FeO*	7.99	8.25	7.03	6.28	5.83	16.07	12.56	12.4
MnO	0.19	0.22	0.24	0.22	0.21	0.22	0.22	0.2
MgO	1.36	1.91	0.58	0.62	0.33	8.47	9.43	10.3
CaO	5.64	4.96	2.53	2.15	1.90	11.44	11.15	11.3
Na2O	4.81	5.62	6.46	6.51	6.56	2.41	3.29	3.5
K2O	3.19	3.32	4.57	4.97	5.06	0.78	1.34	1.1
P2O5	0.63	0.60	0.22	0.14	0.11	0.63	1.25	1.0
LOI	3.16	0.77	0.81	0.22	0.27	-0.91	-0.32	-0.7
Total	99.36	98.97	98.30	99.14	98.54	98.93	98.75	99.3
IFeO*	-	8.48	7.22	6.18	6.02	16.38	12.15	-
INa2O	-	-	-	-	-	-	-	-
Sc	-	4.18	2.79	2.67	2.25	30.2	25.7	-
V	46	37	<3	4	5	492	299	295
Cr	14	<10	15	<10	<10	231	546	363
ICr	-	<1	<1	<1	1.00	234	495	-
Ni	<5	<5	<5	6	6	86	185	133
Cu	<15	<15	<15	<15	<15	59	64	37
Zn	112	113	137	124	106	90	82	92
Ga	25	23	25	26	25	19	15	15
Rb	73	75	91	99	108	18	28	27
IRb	-	74	86	93	102	17	30	-
Sr	1032	1004	513	294	200	1006	1131	1303
Y	41	40	48	73	51	26	33	33
Zr	450	358	796	813	851	172	194	208
Nb	104	108	168	173	180	48	66	73
Sb	-	0.11	0.15	0.19	0.07	<0.04	<0.01	-
Cs	-	0.93	0.37	0.92	0.74	0.19	0.19	-
Ba	357	1032	1557	1613	1532	288	471	513
IBa	-	1066	1626	1434	1565	279	508	-
La	-	74.7	111	143	114	31.1	44.9	-
Ce	-	157	219	219	227	67.7	95.6	-
Nd	-	65.4	79.3	91.0	82.1	40.9	57.5	-
Sm	-	11.6	12.3	15.4	13.1	8.04	9.61	-
Eu	-	3.62	3.28	3.49	2.83	2.72	3.04	-
Tb	-	1.43	1.47	2.02	1.56	0.80	1.02	-
Yb	-	3.47	4.79	5.50	5.23	1.87	2.31	-
Lu	-	0.53	0.75	0.85	0.82	0.24	0.32	-
Hf	-	9.18	17.2	18.8	18.6	4.58	4.51	-
Ta	-	6.38	9.69	10.4	10.4	2.88	3.74	-
Pb	9	11	18	18	15	3	4	3
Th	8	7	18	13	17	<3	<3	<3
ITh	-	9.29	16.1	7.40	15.1	2.51	3.59	-
U	-	2.44	4.95	3.91	3.06	0.51	1.07	-

Table 6.2 (continued) - Geochemical analyses of samples from the Mason Spur area.

	MS9							
	AW83417	AW83480	AW83689	AW83650	AW83558	AW83401	AW83706	AW8361
SiO2	42.50	42.66	42.72	42.73	42.76	42.80	42.97	44.77
TiO2	4.78	3.69	3.49	3.96	3.54	4.50	4.14	2.99
Al2O3	15.19	14.57	14.68	14.82	14.42	14.29	14.99	15.62
FeO*	12.89	12.74	11.86	12.89	11.93	13.24	13.12	10.85
MnO	0.21	0.23	0.21	0.21	0.21	0.25	0.23	0.21
MgO	5.12	5.43	8.65	7.25	8.87	6.23	7.13	8.23
CaO	11.58	10.72	10.97	11.48	11.15	9.97	10.42	10.17
Na2O	3.56	3.58	4.02	3.59	3.95	3.68	3.80	3.95
K2O	1.57	1.26	1.62	1.39	1.24	1.41	1.45	1.16
P2O5	0.87	1.26	1.08	0.73	1.24	1.22	1.47	0.95
LOI	-0.19	1.98	-0.41	-0.70	-0.67	0.16	-0.47	0.26
Total	98.27	98.12	99.30	99.05	99.31	97.75	99.72	99.16
IFeO*	-	-	12.10	-	-	-	-	-
INa2O	-	-	-	-	-	-	-	-
Sc	-	-	24.0	-	-	-	-	-
V	330	364	295	325	274	302	272	-
Cr	34	31	239	117	329	234	118	-
ICr	-	-	250	-	-	-	-	-
Ni	18	19	112	69	112	59	27	124
Cu	45	24	118	39	75	31	18	29
Zn	86	101	82	93	85	96	91	78
Ga	22	20	18	19	17	15	16	19
Rb	31	26	41	28	29	25	27	20
IRb	-	-	36	-	-	-	-	-
Sr	1327	828	1283	1103	1396	1539	1725	1203
Y	32	38	33	29	33	33	34	27
Zr	259	233	260	214	215	201	217	204
Nb	80	68	88	67	74	79	80	60
Sb	-	-	0.10	-	-	-	-	-
Cs	-	-	0.40	-	-	-	-	-
Ba	583	351	604	452	548	824	644	-
IBa	-	-	607	-	-	-	-	-
La	-	-	60.21	-	-	-	-	-
Ce	-	-	124	-	-	-	-	-
Nd	-	-	56.3	-	-	-	-	-
Sm	-	-	10.8	-	-	-	-	-
Eu	-	-	3.22	-	-	-	-	-
Tb	-	-	1.11	-	-	-	-	-
Yb	-	-	2.33	-	-	-	-	-
Lu	-	-	0.38	-	-	-	-	-
Hf	-	-	5.76	-	-	-	-	-
Ta	-	-	5.26	-	-	-	-	-
Pb	<3	3	<3	8	3	12	4	<3
Th	<3	<3	4	<3	<3	<3	<3	<3
ITh	-	-	5.81	-	-	-	-	-
U	-	-	1.73	-	-	-	-	-

Table 6.2 (continued) - Geochemical analyses of samples from the Mason Spur area.

	MS9	
	AW83662	AW83413
SiO2	45.43	46.00
TiO2	2.34	2.89
Al2O3	12.94	15.60
FeO*	11.01	11.14
MnO	0.19	0.23
MgO	12.45	6.49
CaO	10.96	9.49
Na2O	2.98	4.61
K2O	1.17	2.10
P2O5	0.42	0.84
LOI	-0.51	-0.65
Total	99.89	99.39
IFeO*	-	10.95
INa2O	-	-
Sc	-	17.7
V	259	191
Cr	700	285
ICr	-	262
Ni	279	90
Cu	93	27
Zn	80	94
Ga	17	17
Rb	27	39
IRb	-	43
Sr	580	1810
Y	26	32
Zr	222	303
Nb	57	109
Sb	-	<0.01
Cs	-	0.42
Ba	304	934
IBa	-	447
La	-	67.4
Ce	-	142
Nd	-	78.3
Sm	-	11.1
Eu	-	3.62
Tb	-	1.23
Yb	-	2.58
Lu	-	0.39
Hf	-	6.87
Ta	-	6.10
Pb	7	<3
Th	5	<3
ITh	-	5.43
U	-	1.74

Sample description

MS1

AW83581	peralkaline trachyte
AW83422	peralkaline trachyte
AW83441	peralkaline trachyte
AW83508	peralkaline trachyte
AW85865	peralkaline trachyte
AW85803	peralkaline trachyte
AW83569	peralkaline trachyte

MS2

AW85863	mugearite
AW85831	mugearite
AW83511	peralkaline trachyte

MS3

AW83503	peralkaline trachyte
AW83496	peralkaline trachyte
AW85851	trachyte
AW85850	trachyte
AW83711	peralkaline trachyte
AW83430	peralkaline trachyte
AW85818	peralkaline trachyte
AW83445	peralkaline trachyte
AW83678	peralkaline trachyte
AW83499	peralkaline trachyte
AW83515	peralkaline trachyte
AW85847	peralkaline trachyte
AW83484	trachyte
AW85809	peralkaline trachyte
AW85837	peralkaline trachyte
AW85860	peralkaline trachyte
AW83491	peralkaline trachyte
AW83580	peralkaline trachyte
AW83709	peralkaline trachyte
AW83710	peralkaline trachyte
AW85833	peralkaline trachyte
AW85830	peralkaline trachyte
AW83502A	peralkaline trachyte
AW85869	peralkaline trachyte
AW83510	peralkaline trachyte
AW83567	peralkaline trachyte
AW83485	peralkaline trachyte
AW83712	peralkaline trachyte
AW83411	peralkaline trachyte

MS5

AW85829	peralkaline trachyte
AW83701	trachyte
AW83532	peralkaline trachyte
AW83516	peralkaline trachyte obsidian
AW83453	trachyte
AW83707A	peralkaline trachyte
AW83522	trachyte
AW83533	peralkaline trachyte
AW83559	peralkaline trachyte

MS5 (continued)

AW83520	peralkaline trachyte
AW83642	peralkaline trachyte
AW83519	peralkaline trachyte obsidian
AW83677	peralkaline trachyte
AW83653	peralkaline trachyte
AW83524	peralkaline trachyte
AW83517	peralkaline trachyte
AW83534	peralkaline trachyte

MS7

AW83550	basanite
AW83454	basanite
AW83545	basanite
AW83536	basanite
AW82554	tephrite
AW83543	tephrite
AW83410	tephrite
AW83607	tephrite
AW83513	benmoreite
AW85839	benmoreite

MS8

AW83618	trachyte
AW83647	trachyte
AW83645	trachyte

MS9

AW83471	basanite
AW83583	basanite
AW83538	basanite
AW83417	basanite
AW83480	basanite
AW83689	basanite
AW83650	basanite
AW83558	basanite
AW83401	basanite
AW83706	basanite
AW83614	basanite
AW83662	alkali basalt
AW83413	tephrite

Table A6.3 - Geochemical analyses of samples from Minna Bluff.

	MB1							
	AW82105	AW82124	AW84797	AW82059	AW82113A	AW82140	AW82296	AW821
SiO2	42.60	42.61	43.13	43.23	44.28	44.63	45.51	45.8
TiO2	3.45	3.78	3.24	3.31	3.32	3.29	2.76	2.9
Al2O3	14.27	14.52	15.27	15.33	14.94	15.38	15.78	17.3
FeO*	11.33	11.48	10.92	10.97	10.55	10.81	9.86	10.7
MnO	0.19	0.19	0.20	0.20	0.20	0.19	0.19	0.2
MgO	9.59	8.89	7.54	7.47	8.12	7.23	6.63	4.5
CaO	11.15	11.14	10.44	10.84	10.09	9.43	9.10	8.3
Na2O	2.81	3.23	3.73	3.95	3.70	4.41	4.49	3.8
K2O	1.23	0.72	1.75	1.65	1.89	2.24	2.12	2.1
P2O5	0.75	0.88	0.97	0.98	0.94	0.97	0.78	1.2
LOI	0.76	1.91	1.57	1.64	0.21	0.57	1.75	2.3
Total	99.13	99.35	98.76	99.57	99.24	99.15	98.97	99.6
IFeO*	11.70	11.52	11.16	11.19	11.08	10.84	10.15	10.8
INa2O	2.25	3.07	3.76	3.70	3.50	4.33	4.22	3.6
Sc	28.6	25.4	23.0	24.2	23.1	23.2	20.3	9.8
V	310	317	243	250	243	231	223	163
Cr	343	303	213	234	288	179	251	15
ICr	324	277	217	223	257	176	216	2.0
Ni	139	121	95	99	127	87	81	6
Cu	39	33	46	42	33	35	38	21
Zn	86	87	84	81	89	78	90	91
Ga	19	18	20	20	19	20	21	18
Rb	22	14	42	40	39	62	56	58
IRb	25	20	42	42	42	57	55	61
Sr	862	925	1088	1086	1030	1086	989	1178
Y	30	32	34	34	34	35	32	32
Zr	254	297	296	288	401	374	365	370
Nb	70	83	99	97	97	110	108	110
Sb	0.05	0.05	0.10	0.06	0.08	0.05	0.11	0.1
Cs	0.19	0.26	0.54	0.43	0.35	0.68	0.64	0.6
Ba	395	397	632	621	484	770	670	524
IBa	359	402	571	548	462	712	635	525
La	43.6	52.2	60.7	60.5	60.3	68.6	65.6	72.9
Ce	95.1	112	124	121	127	137	130	150
Nd	49.7	54.8	53.2	58.3	63.2	56.6	48.1	62.1
Sm	9.14	10.4	10.5	10.4	11.1	10.8	9.64	11.4
Eu	2.80	3.05	3.17	3.13	3.25	3.26	2.88	3.2
Tb	1.10	1.16	1.25	1.16	1.22	1.24	1.16	1.2
Yb	2.02	2.23	2.68	2.41	2.64	3.35	2.75	2.5
Lu	0.29	0.33	0.41	0.40	0.41	0.42	0.41	0.4
Hf	6.11	7.05	6.77	6.73	8.53	8.40	8.05	8.3
Ta	4.20	5.15	5.68	5.88	5.79	6.91	6.51	6.6
Pb	3	5	5	4	3	7	5	6
Th	3	3	4	3	4	6	8	4
ITh	4.57	5.08	3.83	6.21	5.91	8.55	8.93	7.8
U	1.20	1.60	2.03	1.90	1.70	2.00	2.73	0.8

Table A6.3 (continued) - Geochemical analyses of samples from Minna Bluff.

	MB1							
	AW82046	AW82116	AW82049	AW84796	AW84768	AW82109	AW82110	AW8209
SiO2	45.94	46.91	47.02	47.49	47.58	47.81	48.15	51.5
TiO2	2.81	3.27	2.50	2.40	2.43	2.80	2.84	1.3
Al2O3	15.71	17.12	18.01	17.59	17.65	16.85	16.89	20.4
FeO*	10.03	11.02	9.39	9.40	9.50	9.94	10.04	6.0
MnO	0.20	0.20	0.25	0.22	0.21	0.22	0.22	0.1
MgO	7.08	4.32	2.98	3.56	3.58	4.61	3.94	1.2
CaO	9.25	8.20	8.02	7.90	7.95	8.13	8.31	4.9
Na2O	4.52	4.13	3.91	5.36	4.79	4.25	4.05	6.5
K2O	2.15	1.90	3.12	2.86	2.62	2.46	2.21	3.4
P2O5	0.72	1.05	1.02	0.76	0.75	1.03	1.05	0.4
LOI	1.15	1.16	3.20	1.69	1.62	1.42	0.96	3.5
Total	99.56	99.28	99.42	99.23	98.68	99.52	98.66	99.8
IFeO*	10.12	11.13	9.35	9.40	9.61	10.14	10.32	6.0
INa2O	4.39	3.98	3.92	5.05	4.89	4.11	3.94	6.3
Sc	20.6	12.1	5.53	10.5	10.6	12.1	12.5	1.8
V	216	196	114	146	158	148	186	24
Cr	234	13	16	25	30	79	89	22
ICr	226	13.2	<0.9	31.1	29.4	87.0	89.9	<1.3
Ni	85	10	10	19	22	34	36	<5
Cu	34	20	<15	64	26	21	<15	<15
Zn	89	66	97	94	97	101	108	83
Ga	20	15	23	21	21	22	22	22
Rb	61	41	78	76	61	58	48	89
IRb	63	43	75	74	63	58	49	86
Sr	969	1280	1195	1102	1112	1100	1126	1257
Y	33	30	39	35	34	34	36	35
Zr	364	344	621	413	382	444	529	510
Nb	109	104	122	122	121	126	127	172
Sb	0.12	0.09	0.12	0.07	0.13	0.17	0.17	0.2
Cs	0.69	0.36	0.75	0.89	0.56	0.35	0.26	1.1
Ba	666	497	645	770	809	560	552	957
IBa	654	976	658	747	796	553	563	934
La	65.7	62.4	76.4	72.6	73.2	84.5	85.2	85.6
Ce	129	132	155	141	145	173	175	162
Nd	54.8	58.6	64.2	60.4	52.2	65.3	73.6	57.4
Sm	9.64	10.7	11.6	10.2	10.4	12.4	12.4	9.4
Eu	2.94	3.22	3.33	3.02	3.14	3.48	3.57	2.8
Tb	1.12	1.17	1.35	1.21	1.22	1.37	1.37	1.1
Yb	2.75	2.42	3.40	2.99	2.98	2.89	2.90	3.2
Lu	0.41	0.37	0.53	0.47	0.48	0.43	0.46	0.5
Hf	7.87	7.63	9.83	8.57	8.58	10.4	11.0	9.4
Ta	6.79	6.42	7.29	7.24	7.38	7.85	7.85	10.0
Pb	6	3	4	7	7	7	7	6
Th	5	<3	5	7	7	6	11	10
ITh	8.99	6.62	9.25	9.33	9.66	9.07	9.94	13.4
U	2.33	1.41	1.92	1.52	1.93	1.20	3.27	3.5

Table A6.3 (continued) - Geochemical analyses of samples from Minna Bluff.

	MB1						MB2	
	W84-3	AW82072	AW82056	AW84791	W8413-PM	W84-2	AW82163	AW82(
SiO2	53.87	54.54	55.98	57.83	58.18	58.84	44.84	46.(
TiO2	0.98	0.95	0.93	0.46	0.54	0.28	3.31	3.1
Al2O3	20.12	20.05	18.80	18.60	18.49	18.62	15.89	17.6
FeO*	6.96	6.07	5.93	5.27	5.24	4.73	10.69	11.(
MnO	0.24	0.22	0.20	0.20	0.24	0.23	0.19	0.2
MgO	1.22	1.19	1.08	0.44	0.83	0.42	6.85	4.2
CaO	3.66	3.88	3.27	2.02	1.93	1.03	10.70	9.(
Na2O	5.27	6.52	6.77	7.26	6.44	6.86	3.98	4.8
K2O	4.78	4.35	4.15	4.85	5.45	5.80	1.67	1.9
P2O5	0.34	0.25	0.31	0.17	0.13	0.06	0.84	0.9
LOI	1.97	0.49	2.53	1.57	2.24	2.21	-0.11	0.1
Total	99.41	~~99~~ 98.51	99.95	98.67	99.71	99.08	98.96	99.2
IFeO*	-	6.34	5.93	5.37	-	-	10.83	11.1
INa2O	-	7.32	6.58	7.24	-	-	4.06	4.8
Sc	-	1.06	1.26	0.48	-	-	22.9	12.3
V	10	16	7	3	6	<3	286	186
Cr	27	12	13	<10	<10	<10	205	16
ICr	-	<1.7	<0.9	<0.3	-	-	190	6.6
Ni	<5	<5	<5	<5	5	<5	84	14
Cu	18	<15	<15	35	<15	<15	47	24
Zn	107	105	87	79	112	141	98	92
Ga	21	23	20	21	28	28	22	20
Rb	119	110	113	130	119	131	45	57
IRb	-	111	109	126	-	-	49	56
Sr	1001	827	740	445	303	60	903	1191
Y	32	35	31	25	42	52	33	37
Zr	543	559	687	731	511	860	323	388
Nb	168	167	171	148	173	283	91	117
Sb	-	0.12	0.25	0.21	-	-	0.07	<0.(
Cs	-	0.88	1.36	0.97	-	-	0.64	0.2
Ba	988	932	1039	1141	1579	70	526	679
IBa	-	954	1071	1160	-	-	511	630
La	-	95.2	90.1	92.4	-	-	65.5	74.6
Ce	-	172	173	160	-	-	132	150
Nd	-	56.8	54.3	45.8	-	-	59.4	69.6
Sm	-	9.00	7.97	6.30	-	-	10.1	11.8
Eu	-	2.53	2.41	1.83	-	-	3.06	3.5
Tb	-	1.05	0.87	0.74	-	-	1.21	1.3
Yb	-	3.41	3.08	2.74	-	-	2.40	3.(
Lu	-	0.56	0.53	0.48	-	-	0.38	0.4
Hf	-	11.5	13.4	13.8	-	-	7.42	8.7
Ta	-	10.7	9.33	9.93	-	-	5.62	7.3
Pb	7	6	9	11	9	14	5	5
Th	14	12	18	19	17	23	7	6
ITh	-	16.3	18.0	18.3	-	-	6.76	8.5
U	-	1.40	5.34	2.86	-	-	1.80	2.5

Table A6.3 (continued) - Geochemical analyses of samples from Minna Bluff.

	MB2							
	AW86887	AW82149	AW82156	AW82141	AW84777	AW82078	AW82150	AW821(
SiO2	49.86	52.36	52.77	54.15	54.60	57.03	57.03	57.5
TiO2	2.68	1.58	1.27	1.09	0.86	0.50	0.41	0.1
Al2O3	17.65	18.76	19.09	19.40	20.06	20.30	20.43	20.3(
FeO*	9.14	7.81	7.10	6.51	5.98	5.03	4.69	4.4(
MnO	0.25	0.22	0.21	0.23	0.21	0.20	0.18	0.2
MgO	3.85	2.41	2.02	1.59	0.98	0.71	0.38	0.2
CaO	7.72	5.33	4.07	3.84	3.41	2.19	2.08	1.4
Na2O	5.90	6.74	7.41	8.01	8.31	9.36	8.61	8.9(
K2O	2.37	3.79	4.19	4.34	4.02	4.53	5.58	5.5
P2O5	1.20	0.56	0.37	0.33	0.26	0.12	0.11	0.0(
LOI	0.00	0.29	0.18	0.16	0.10	0.42	0.17	0.5
Total	100.62	99.85	99.31	99.65	98.79	100.39	99.67	99.54
IFeO*	-	7.96	7.14	6.55	-	5.07	4.62	4.5(
INa2O	-	6.49	7.16	8.11	-	9.14	8.39	8.9
Sc	-	4.59	6.11	2.98	-	0.32	0.45	0.1
V	91	64	79	58	9	5	5	3
Cr	<10	35	20	11	16	20	17	10
ICr	-	12.7	15.5	<4.4	-	<0.7	<1.3	<0.8
Ni	8	11	13	6	5	5	<5	<5
Cu	<15	<15	15	<15	15	21	19	<15
Zn	84	109	95	113	104	105	106	131
Ga	27	21	24	25	26	23	25	27
Rb	59	84	118	121	106	150	146	171
IRb	-	86	110	115	-	141	140	166
Sr	1868	899	499	453	880	548	348	95
Y	41	35	32	38	27	31	32	43
Zr	454	492	538	653	659	685	670	844
Nb	133	141	117	129	169	167	150	180
Sb	-	0.10	0.21	0.25	-	0.23	0.21	0.39
Cs	-	0.89	1.19	1.34	-	1.90	1.10	1.45
Ba	818	1118	559	449	815	1166	761	254
IBa	-	1109	553	459	-	1129	798	287
La	-	79.8	78.1	93.8	-	94.3	90.5	120
Ce	-	154	141	168	-	160	148	192
Nd	-	53.4	46.8	51.1	-	43.0	44.0	56.6
Sm	-	9.53	30.3	8.16	-	5.94	6.34	7.96
Eu	-	3.00	2.00	1.98	-	1.85	1.66	1.25
Tb	-	1.14	0.94	1.01	-	0.74	0.79	1.02
Yb	-	3.18	3.04	3.62	-	3.20	3.13	4.36
Lu	-	0.50	0.49	0.60	-	0.54	0.53	0.71
Hf	-	9.68	10.4	12.3	-	12.3	12.6	15.5
Ta	-	8.63	8.48	9.74	-	11.5	10.3	12.7
PB/b	6	5	10	10	11	12	11	14
Th	7	8	14	18	21	23	16	27
ITh	-	11.4	14.6	18.2	-	22.3	16.2	24.0
U	-	3.74	4.76	5.34	-	6.90	3.95	6.42

Sample descriptions

MB1

AW82105	basanite
AW82124	basanite
AW84797	tephrite
AW82059	basanite
AW82113A	basanite
AW82140	tephrite
AW82296	tephrite
AW82103	tephrite
AW82046	tephrite
AW82116	tephrite
AW82049	tephrite
AW84796	phonotephrite
AW84768	phonotephrite
AW82109	tephrite
AW82110	hawaiite
AW82097B	tephriphonolite
W84-3	tephriphonolite
AW82072	tephriphonolite
AW82056	benmoreite
AW84791	trachyte
W8413-PM	trachyte
W84-2	trachyte

MB2

AW82163	tephrite
AW82077	tephrite
AW86887	phonotephrite
AW82149	tephriphonolite
AW82156	tephriphonolite
AW82141	tephriphonolite
AW84777	tephriphonolite
AW82078	phonolite
AW82150	phonolite
AW82165	phonolite

Table A6.4 - Geochemical analyses of samples from the Mt Discovery area.

	MD1							
	AW84761	AW84718	AW86899	AW48758	AW86950	AW86901	AW86895	AW847
SiO2	49.72	51.46	51.92	52.46	52.78	54.06	54.97	55.4
TiO2	2.40	1.83	1.83	1.63	1.61	1.35	1.31	1.1
Al2O3	17.58	18.92	19.25	19.41	19.71	20.23	18.65	18.5
FeO*	8.49	7.26	7.19	6.77	6.53	5.69	6.38	6.2
MnO	0.25	0.23	0.23	0.22	0.21	0.21	0.26	0.2
MgO	3.23	2.25	2.19	1.91	1.75	1.44	1.81	1.2
CaO	6.48	4.83	4.92	4.55	4.66	4.38	4.14	3.7
Na2O	6.48	7.07	7.24	7.18	7.36	7.30	6.84	7.2
K2O	2.45	3.68	3.55	3.72	3.61	3.83	3.58	3.5
P2O5	1.18	0.92	0.93	0.80	0.77	0.55	0.46	0.3
LOI	0.17	0.10	-0.22	0.01	0.30	0.00	1.20	0.1
Total	98.43	98.55	99.03	98.66	99.29	99.04	99.60	98.9 97.9
IFeO*	8.65	6.93	-	6.80	-	-	-	6.2
INa2O	6.51	7.01	-	7.04	-	-	-	7.1
Sc	5.49	3.61	-	3.19	-	-	-	1.3
V	89	41	32	23	22	20	37	18
Cr	<10	<10	21	15	23	24	45	<10
ICr	2.00	1.10	-	<0.05	-	-	-	<0.9
Ni	<5	5	7	<5	5	<5	6	<5
Cu	29	19	<15	24	<15	43	<15	<15
Zn	107	89	89	91	92	91	111	96
Ga	18	24	89	22	24	23	23	24
Rb	44	76	82	81	81	79	87	88
IRb	42	75	-	76	-	-	-	83
Sr	1867	1614	1689	1681	1769	1661	1124	1268
Y	43	43	45	45	43	42	37	36
Zr	440	641	649	649	644	614	669	682
Nb	155	197	196	200	196	194	182	179
Sb	0.13	0.21	-	0.20	-	-	-	0.2
Cs	0.70	0.83	-	0.78	-	-	-	0.9
Ba	1642	1063	1067	1107	1148	1364	1043	1354
IBa	1666	972	-	1184	-	-	-	1331
La	105	100	-	105	-	-	-	120
Ce	222	210	-	215	-	-	-	238
Nd	92.7	90.4	-	83.5	-	-	-	84.3
Sm	15.3	14.1	-	14.6	-	-	-	11.8
Eu	15.1	4.58	-	4.78	-	-	-	3.6
Tb	1.62	1.60	-	1.63	-	-	-	1.2
Yb	3.43	3.62	-	3.65	-	-	-	3.3
Lu	0.51	0.53	-	0.55	-	-	-	0.5
Hf	8.92	12.5	-	12.8	-	-	-	13.9
Ta	8.10	11.2	-	11.6	-	-	-	11.3
Pb	5	6	4	6	3	4	6	8
Th	8	12	4	11	10	10	17	15
ITh	11.7	13.6	-	14.3	-	-	-	16.2
U	2.57	4.30	-	4.00	-	-	-	5.3

Table A6.4 (continued) - Geochemical analyses of samples from the Mt Discovery area

	MDl							
	AW84756	AW84721	AW84754	AW86922	AW84719	AW86881	AW86100	AW84
SiO2	56.08	56.12	56.25	57.43	57.81	58.03	58.55	58.
TiO2	1.18	1.09	0.61	0.70	0.94	0.45	0.34	0.
Al2O3	18.72	18.73	19.00	19.44	18.83	20.38	19.60	18.
FeO*	6.44	6.29	4.42	5.30	5.30	3.52	4.37	4.
MnO	0.26	0.26	0.23	0.23	0.23	0.21	0.26	0.
MgO	1.71	1.26	1.08	0.80	1.04	0.68	0.46	0.
CaO	3.91	3.62	1.90	2.33	2.42	2.72	1.45	0.
Na2O	7.21	7.18	7.37	8.30	6.99	9.14	9.21	8.
K2O	3.56	3.68	4.84	4.65	4.60	4.28	4.92	5.
P2O5	0.41	0.38	0.21	0.24	0.33	0.08	0.09	0.
LOI	-0.08	0.30	4.01	0.46	0.65	0.29	0.22	0.
Total	99.48	98.91	99.92	~~100.00~~ 99.88	99.14	99.78	99.47	98.
IFeO*	6.44	6.26	6.95	-	5.22	-	-	4.
INa2O	7.19	6.96	7.54	-	6.61	-	-	8.
Sc	1.70	1.30	4.50	-	1.63	-	-	0.
V	12	14	9	9	20	15	<3	<
Cr	<10	<10	<10	12	<10	31	67	<1
ICr	<0.8	<0.6	<1.6	-	<0.5	-	-	0.
Ni	<5	<5	5	7	<5	10	7	<
Cu	<15	<15	34	<15	<15	<15	<15	<1
Zn	124	114	112	111	98	120	128	14
Ga	23	26	25	25	23	28	25	2
Rb	88	89	150	119	103	144	154	14
IRb	85	88	144	-	102	-	-	14
Sr	1271	1238	323	608	536	1034	340	1
Y	37	36	38	37	33	42	40	5
Zr	694	707	1158	860	737	970	1048	117
Nb	191	191	255	211	186	237	241	31
Sb	0.29	.23	0.48	-	0.24	-	-	0
Cs	0.87	0.76	1.84	-	1.06	-	-	1.
Ba	1362	1340	363	777	1078	1190	697	3
IBa	1310	1343	491	-	1102	-	-	<8
La	123	123	119	-	105	-	-	15
Ce	235	235	212	-	197	-	-	29
Nd	89.0	82.2	58.5	-	68.2	-	-	99.
Sm	11.9	11.7	8.60	-	9.49	-	-	13.
Eu	3.70	3.60	1.52	-	2.63	-	-	1.
Tb	1.31	1.27	1.09	-	1.06	-	-	1.
Yb	3.26	3.17	3.87	-	3.23	-	-	5.
Lu	0.54	0.51	0.62	-	0.51	-	-	0.
Hf	13.7	14.1	22.3	-	14.4	-	-	23.
Ta	11.4	11.4	16.4	-	11.4	-	-	18.
Pb	4	7	16	11	11	12	15	1
Th	15	14	33	22	19	26	33	3
ITh	15.9	15.8	29.1	-	17.8	-	-	26.
U	4.80	4.10	8.90	-	4.40	-	-	7.

Table A6.4 (continued) - Geochemical analyses of samples from the Mt Discovery area.

	MD1							
	AW83438	AW84741	AW86970	AW84744	AW84725	AW84720	AW84735	AW868
SiO2	58.81	58.92	59.00	59.70	59.81	59.81	59.91	60.5
TiO2	0.44	0.28	0.53	0.32	0.24	0.54	0.16	0.3
Al2O3	19.47	19.06	18.97	18.07	18.99	18.92	18.54	18.9
FeO*	4.48	4.25	5.02	4.49	4.41	4.30	4.18	4.5
MnO	0.24	0.26	0.28	0.27	0.28	0.23	0.23	0.2
MgO	0.41	0.44	0.63	0.25	0.45	0.93	0.34	0.4
CaO	1.96	0.87	1.99	0.87	0.97	1.46	0.83	1.3
Na2O	8.31	8.61	8.29	8.50	8.84	8.21	8.79	8.4
K2O	4.60	5.46	4.30	5.28	5.39	5.08	5.29	5.2
P2O5	0.11	0.07	0.14	0.06	0.05	0.15	0.04	0.0
LOI	0.73	0.84	0.27	0.39	0.41	0.09	0.38	0.5
Total	99.56	99.03	99.42	99.20	99.89	99.72	99.15	100.6
IFeO*	-	4.22	-	4.56	4.36	4.29	4.23	-
INa2O	-	7.50	-	8.46	8.71	8.07	9.05	-
Sc	-	0.63	-	1.02	0.36	0.70	0.05	-
V	7	<3	<3	<3	<3	<3	15	<3
Cr	17	<10	<10	<10	<10	<10	<10	<10
ICr	-	<0.9	-	<0.7	0.90	0.80	<0.70	-
Ni	6	5	7	6	<5	5	6	<5
Cu	<15	<15	<15	<15	<15	<15	<15	<15
Zn	99	135	107	137	136	94	160	119
Ga	22	29	26	28	26	23	28	23
Rb	125	164	114	121	155	114	156	116
IRb	-	157	-	115	150	110	153	-
Sr	742	32	676	8	13	192	11	92
Y	34	51	35	56	46	32	52	40
Zr	769	1282	807	976	1225	771	1330	893
Nb	198	309	210	273	283	193	286	228
Sb	-	0.52	-	0.34	<0.01	0.31	0.52	-
Cs	-	1.90	-	1.16	1.70	1.05	1.29	-
Ba	1319	112	1400	55	72	935	38	835
IBa	-	<160	-	<100	171	932	<47	-
La	-	144	-	154	145	104	173	-
Ce	-	260	-	285	262	184	300	-
Nd	-	75.9	-	104	72.6	50.9	76.2	-
Sm	-	10.7	-	14.8	10.6	7.90	10.7	-
Eu	-	1.07	-	1.50	1.02	1.87	1.07	-
Tb	-	1.35	-	1.90	1.22	0.91	1.29	-
Yb	-	4.73	-	5.14	4.78	3.04	4.97	-
Lu	-	0.75	-	0.82	0.77	0.51	0.80	-
Hf	-	25.2	-	20.4	24.3	15.7	26.1	-
Ta	-	19.0	-	16.3	18.1	12.2	19.4	-
Pb	9	16	8	14	18	13	13	10
TH	24	35	21	24	37	22	38	23
ITh	-	30.6	-	21.1	30.1	19.1	31.4	-
U	-	9.10	-	6.70	8.20	4.50	8.60	-

Table A6.4 (continued) - Geochemical analyses of samples from the Mt Discovery area

	MD1	MD2					
	AW86965A	AW86101	AW84733	AW84723	AW84740	AW84738	AW84728	AW8472
SiO2	60.64	41.34	42.16	42.55	42.82	42.93	42.94	43.0
TiO2	0.31	4.81	4.53	3.98	3.96	3.92	3.96	3.9
Al2O3	19.31	13.61	14.67	14.15	14.32	14.38	14.28	14.3
FeO*	3.25	13.50	12.85	12.58	12.07	11.29	12.65	12.2
MnO	0.23	0.19	0.20	0.21	0.21	0.19	0.22	0.2
MgO	0.21	9.81	8.05	7.93	8.73	9.74	7.81	7.7
CaO	1.00	11.36	11.50	10.64	11.00	11.05	10.63	10.6
Na2O	9.18	2.85	3.15	4.09	4.10	3.71	4.18	4.2
K2O	5.40	1.00	1.23	1.56	1.37	1.36	1.81	1.7
P2O5	0.04	0.62	0.98	0.87	1.00	0.78	0.89	0.8
LOI	0.31	-0.63	-0.50	0.09	-0.48	-0.47	-0.60	-0.6
Total	99.88	99.09	99.32	98.65	99.58	99.35	99.37	98.9
IFeO*	-	-	13.01	12.85	12.27	11.44	12.90	-
INa2O	-	-	3.08	3.61	3.79	3.29	3.96	-
Sc	-	-	25.4	25.1	25.4	28.1	24.9	-
V	<3	412	333	332	324	317	316	312
Cr	16	339	199	184	210	321	181	187
ICr	-	-	202	196	211	355	186	-
Ni	6	157	78	85	104	162	82	90
Cu	<15	70	55	44	72	43	79	45
Zn	118	84	90	117	97	84	108	107
Ga	24	23	18	22	19	20	24	23
Rb	177	22	24	41	38	37	42	42
IRb	-	-	25	46	36	36	38	-
Sr	40	1005	1484	1011	1129	1153	1025	1031
Y	41	27	30	34	36	30	36	36
Zr	1314	212	248	402	366	311	409	413
Nb	280	58	74	101	103	87	104	103
Sb	-	-	0.11	0.07	0.10	0.07	<0.01	-
Cs	-	-	0.20	0.42	0.25	0.06	0.38	-
Ba	186	372	411	504	509	513	517	51
IBa	-	-	424	527	497	516	497	-
La	-	-	50.8	67.0	69.4	55.1	68.4	-
Ce	-	-	111	142	146	119	144	-
Nd	-	-	57.3	72.0	73.4	55.1	66.9	-
Sm	-	-	10.7	12.1	12.3	10.4	12.4	-
Eu	-	-	3.30	3.63	3.59	3.23	3.55	-
Tb	-	-	1.80	1.37	1.37	1.22	1.38	-
Yb	-	-	2.01	2.66	2.51	2.19	2.61	-
Lu	-	-	0.32	0.37	0.44	0.32	0.36	-
Hf	-	-	6.10	9.45	13.4	7.13	9.37	-
Ta	-	-	4.55	6.36	6.21	5.52	6.59	-
Pb	18	4	4	3	6	5	7	
Th	39	<3	3	7	8	5	7	
ITh	-	-	4.69	7.63	7.20	6.10	7.75	-
U	-	-	0.89	2.10	1.70	2.10	1.80	-

Table A6.4 (continued) - Geochemical analyses of samples from the Mt Discovery area.

	MD2							
	AW86944	AW84763	AW84750	AW86102	AW84748	AW86943	AW86909	AW8474
SiO2	43.75	43.76	43.82	43.93	44.24	44.53	44.93	45.67
TiO2	3.93	3.74	3.88	3.87	3.88	3.68	3.50	3.36
Al2O3	14.74	14.62	15.49	14.80	16.00	15.28	15.72	16.87
FeO*	12.29	12.01	11.65	12.10	11.48	11.16	10.91	10.58
MnO	0.20	0.22	0.21	0.21	0.21	0.22	0.21	0.22
MgO	7.98	7.56	7.14	8.44	6.30	7.16	7.16	4.71
CaO	9.99	10.32	10.28	10.55	10.18	9.68	10.22	9.45
Na2O	3.92	4.53	4.11	3.22	4.36	4.46	4.17	4.64
K2O	1.57	1.69	1.69	1.48	1.70	1.90	1.61	1.98
P2O5	1.00	0.85	0.95	0.82	0.97	0.93	0.89	1.48
LOI	-0.77	-0.51	-0.68	-0.18	-0.39	-0.51	-0.21	-0.25
Total	99.37	99.30	99.22	99.42	99.32	99.00	99.37 not LOI	98.96
IFeO*	-	12.28	11.79	-	11.62	-	-	10.55
INa2O	-	3.90	3.80	-	4.20	-	-	4.55
Sc	-	23.2	19.3	-	17.9	-	-	12.5
V	292	305	265	324	278	269	279	189
Cr	184	168	151	283	87	175	198	32
ICr	-	168	161	-	89.0	-	-	22.0
Ni	113	80	75	101	53	86	92	16
Cu	37	44	39	33	32	54	28	36
Zn	87	115	89	88	92	97	93	96
Ga	16	24	18	17	22	19	23	20
Rb	36	42	36	34	41	48	44	45
IRb	-	45	35	-	39	-	-	44
Sr	1187	1053	1452	1126	1496	1314	1227	1739
Y	33	37	30	31	34	40	31	38
Zr	312	424	305	308	325	439	373	373
Nb	85	113	92	80	96	126	98	124
Sb	-	0.09	0.08	-	0.11	-	-	<0.0
Cs	-	0.39	0.35	-	0.29	-	-	0.4
Ba	505	525	587	427	603	693	471	766
IBa	-	510	583	-	579	-	-	737
La	-	73.5	59.6	-	62.6	-	-	85.1
Ce	-	150	127	-	134	-	-	180
Nd	-	73.0	63.9	-	63.8	-	-	80.7
Sm	-	12.7	11.0	-	11.3	-	-	14.2
Eu	-	3.65	3.44	-	3.52	-	-	4.3
Tb	-	1.45	1.21	-	1.28	-	-	1.5
Yb	-	2.64	2.29	-	2.53	-	-	2.7
Lu	-	0.37	0.34	-	0.37	-	-	0.3
Hf	-	9.60	6.96	-	7.20	-	-	7.9
Ta	-	7.00	5.53	-	5.85	-	-	6.9
Pb	3	5	5	4	4	4	6	6
Th	<3	9	4	<3	3	6	6	5
ITh	-	8.24	5.99	-	6.47	-	-	7.9
U	-	2.60	2.40	-	1.74	-	-	2.0

Table A6.4 (continued) - Geochemical analyses of samples from the Mt Discovery are

	MD2							
	AW86891	AW84749	AW86910	AW86898	AW84753	AW86947	AW83435	AW86
SiO2	46.32	46.33	46.46	46.54	48.46	49.25	50.88	55.
TiO2	3.03	2.96	3.31	3.30	2.76	2.72	2.22	0.
Al2O3	16.16	15.93	17.12	17.19	17.69	17.52	18.22	20.
FeO*	10.22	11.05	10.11	10.07	9.78	9.14	8.56	3.
MnO	0.23	0.22	0.21	0.20	0.26	0.22	0.27	0.
MgO	6.53	6.38	4.89	4.81	3.66	4.08	3.00	0.
CaO	8.67	9.62	9.30	9.32	7.96	7.50	6.44	2.
Na2O	4.49	4.63	4.94	4.94	5.45	5.91	5.86	9.
K2O	2.08	1.80	1.93	2.15	2.21	2.55	2.48	4.
P2O5	1.03	1.07	1.10	1.11	1.39	0.92	1.02	0.
LOI	0.32	-0.64	-0.24	-0.48	-0.63	-1.02	0.09	0.
Total	99.08	99.99	99.13	99.15	99.62	98.79	99.04	99.
IFeO*	-	11.12	-	-	9.89	-	-	3.
INa2O	-	4.45	-	-	5.47	-	-	-
Sc	-	17.6	-	-	6.29	-	-	1.
V	205	232	206	212	107	163	63	2
Cr	155	113	35	56	<10	12	24	2
ICr	-	119	-	-	1.70	-	-	6.
Ni	37	74	31	30	<5	20	<5	
Cu	35	36	26	19	17	<15	<15	<1
Zn	113	114	94	92	110	98	123	12
Ga	23	22	24	24	22	22	23	3
Rb	68	51	44	43	51	63	55	17
IRb	-	50	-	-	49	-	-	16
Sr	1230	1177	1469	1451	1990	1325	1898	64
Y	41	34	33	37	42	33	41	4
Zr	559	422	340	347	453	428	509	93
Nb	153	114	108	109	142	130	153	29
Sb	-	0.16	-	-	0.10	-	-	0.
Cs	-	0.52	-	-	0.45	-	-	2.
Ba	624	585	832	807	797	1018	897	66
IBa	-	554	-	-	776	-	-	70
La	-	77.2	-	-	106	-	-	12
Ce	-	159	-	-	223	-	-	22
Nd	-	71.2	-	-	98.7	-	-	72.
Sm	-	11.7	-	-	16.7	-	-	10.
Eu	-	3.49	-	-	4.95	-	-	3.
Tb	-	1.30	-	-	1.65	-	-	1.
Yb	-	2.85	-	-	3.17	-	-	4.
Lu	-	0.42	-	-	0.48	-	-	0.
Hf	-	8.93	-	-	9.53	-	-	19.
Ta	-	7.20	-	-	8.53	-	-	18.
Pb	10	6	4	4	7	5	<3	1
Th	14	10	4	3	6	6	3	3
ITh	-	9.26	-	-	9.75	-	-	34.
U	-	3.20	-	-	2.20	-	-	9.

Sample Descriptions

MD1	
AW84761	phonotephrite xenolith in phonolite
AW84718	tephriphonolite
AW86899	tephriphonolite
AW84758	trphriphonolite
AW86950	tephriphonolite
AW86901	tephriphonolite
AW86895	tephriphonolite xenolith in phonolite
AW84722	tephriphonolite
AW84756	tephriphonolite
AW84721	benmorite
AW84754	phonolite
AW86922	phonolite
AW84719	trachyte
AW86881	phonolite
AW86100	phonolite
AW84745	phonolite
AW83438	phonolite
AW84741	phonolite
AW86970	phonolite
AW84744	phonolite
AW84725	phonolite
AW84720	phonolite
AW84735	phonolite
AW86889	phonolite
AW86965A	phonolite

MD2	
AW86101	basanite
AW84733	basanite
AW84723	basanite
AW84740	basanite
AW84738	basanite
AW84728	tephrite
AW84728A	tephrite
AW86944	basanite
AW84763	tephrite
AW84750	tephrite
AW86102	basanite
AW84748	tephrite
AW86943	tephrite
AW86909	tephrite
AW86742	tephrite
AW86891	tephrite
AW84749	tephrite
AW86910	tephrite
AW86898	tephrite
AW84753	phonotephrite
AW86947	phonotephrite
AW83435	phonotephrite
AW86883	phonolite

Table A6.5 - Geochemical analyses from the Mt Morning area.

	MM1						MM2	
	AW86124	AW86122	AW86121	AW86128	AW86127	AW86123	AW86057	AW86096
SiO2	48.38	48.90	50.89	56.03	57.97	59.14	42.37	43.50
TiO2	2.68	2.83	2.27	0.11	0.50	0.63	3.92	3.15
Al2O3	16.98	17.64	18.21	19.67	19.58	19.34	16.21	13.74
FeO*	9.86	9.33	8.04	5.19	4.23	4.18	12.94	11.23
MnO	0.22	0.21	0.20	0.36	0.21	0.17	0.20	0.19
MgO	5.28	3.85	2.71	0.33	0.57	0.65	6.82	9.59
CaO	7.53	7.82	6.40	0.84	2.00	2.31	12.10	13.53
Na2O	5.61	5.53	5.89	10.50	8.48	7.66	3.21	2.62
K2O	2.17	2.56	3.29	5.27	5.09	5.17	1.00	0.78
P2O5	0.76	0.67	0.70	0.05	0.14	0.14	0.73	0.48
LOI	-0.41	-0.44	0.32	0.64	0.26	-0.05	-0.52	-0.06
Total	99.47	99.34	98.92	98.99	99.03	99.39	99.50	98.81
IFeO*	-	-	7.99	5.32	4.38	-	13.23	-
INa2O	-	-	-	-	-	-	-	-
Sc	-	-	6.42	0.19	0.69	-	23.7	-
V	174	191	104	<3	10	19	379	396
Cr	96	28	26	10	29	<10	86	235
ICr	-	-	19.9	<1.00	0.48	-	70.4	-
Ni	54	17	12	7	8	5	44	117
Cu	18	<15	<15	<15	<15	<15	21	64
Zn	86	88	77	187	101	62	81	76
Ga	19	19	21	35	22	24	19	19
Rb	57	62	71	242	145	127	25	24
IRb	-	-	73	229	136	-	20	-
Sr	1175	1084	984	14	287	345	1117	717
Y	31	32	31	82	34	25	29	24
Zr	385	400	420	1985	822	583	214	192
Nb	102	108	114	406	164	141	59	47
Sb	-	-	<0.01	0.69	0.34	-	0.07	-
Cs	-	-	0.77	3.68	1.69	-	0.21	-
Ba	531	649	894	<16	462	619	401	278
IBa	-	-	812	<54	486	-	388	-
La	-	-	68.3	156	99.8	-	39.3	-
Ce	-	-	136	288	178	-	83.7	-
Nd	-	-	55.0	81.6	47.9	-	42.9	-
Sm	-	-	8.78	11.9	6.92	-	8.67	-
Eu	-	-	2.96	0.85	1.57	-	2.70	-
Tb	-	-	1.04	1.97	0.91	-	1.01	-
Yb	-	-	2.75	8.95	3.92	-	2.09	-
Lu	-	-	0.44	1.46	0.63	-	0.31	-
Hf	-	-	9.00	42.2	16.3	-	5.22	-
Ta	-	-	6.91	27.0	11.5	-	3.56	-
Pb	8	8	12	27	15	10	4	4
Th	7	10	10	60	26	19	3	4
ITh	-	-	10.3	48.6	22.1	-	3.64	-
U	-	-	3.48	15.5	6.67	-	1.18	-

Table A6.5 (continued) - Geochemical analyses from the Mt Morning area.

	MM2					
	AW86058	AW86119	AW86120	AW86059	AW86098	AW84715
SiO2	43.51	43.87	44.06	45.81	46.78	46.85
TiO2	3.62	3.29	3.45	3.16	3.32	2.63
Al2O3	14.39	13.72	15.38	15.82	17.00	16.09
FeO*	11.45	11.70	11.48	11.43	10.34	10.48
MnO	0.24	0.20	0.22	0.21	0.24	0.24
MgO	8.94	10.58	7.87	7.36	4.30	6.42
CaO	11.06	11.17	10.77	9.51	8.35	8.49
Na2O	3.52	3.24	4.02	4.17	5.01	5.05
K2O	1.58	1.09	1.57	1.44	2.00	2.10
P2O5	0.95	0.54	0.88	0.70	1.26	0.83
LOI	-0.92	-0.79	-0.79	-0.58	0.06	0.14
Total	99.26	99.40	99.70	99.61	98.66	99.32
IFeO	-	-	-	-	-	10.50
INa2O	-	-	-	-	-	-
Sc	-	-	-	-	-	16.2
V	301	309	283	256	179	181
Cr	312	665	245	227	38	148
ICr	-	-	-	-	-	151
Ni	129	213	84	95	<5	87
Cu	22	38	27	22	<15	28
Zn	95	84	93	87	95	100
Ga	22	21	21	19	21	21
Rb	39	24	34	33	38	59
IRb	-	-	-	-	-	56
Sr	1099	753	1065	954	1223	1312
Y	35	29	34	33	40	35
Zr	341	227	315	286	315	389
Nb	99	58	87	72	95	117
Sb	-	-	-	-	-	<0.01
Cs	-	-	-	-	-	0.57
Ba	522	299	438	435	649	759
IBa	-	-	-	-	-	661
La	-	-	-	-	-	76.5
Ce	-	-	-	-	-	154
Nd	-	-	-	-	-	62.0
Sm	-	-	-	-	-	10.6
Eu	-	-	-	-	-	3.38
Tb	-	-	-	-	-	1.11
Yb	-	-	-	-	-	2.61
Lu	-	-	-	-	-	0.40
Hf	-	-	-	-	-	8.20
Ta	-	-	-	-	-	7.26
Pb	6	5	5	6	4	6
Th	5	4	5	6	4	7
ITh	-	-	-	-	-	8.23
U	-	-	-	-	-	2.48

Sample descriptions

MM1

AW86124 - phonotephrite
AW86122 - phonotephrite
AW86121 - phonotephrite
AW86128 - phonolite
AW86127 - phonolite
AW86123 - phonolite

MM2

AW86057 - basanite
AW86096 - basanite
AW86058 - basanite
AW86119 - basanite
AW86120 - basanite
AW86059 - basanite
AW86098 - tephrite
AW84715 - tephrite

Table A6.6 - Geochemical analyses of new samples from the Foothills of Royal Society Range.

	F			
	AW86094	AW86095	AW86088	AW86089
SiO2	42.40	43.50	44.66	45.66
TiO2	3.96	3.67	3.98	3.66
Al2O3	13.46	14.51	15.99	16.54
FeO*	12.38	11.92	12.03	11.39
MnO	0.21	0.20	0.20	0.24
MgO	11.06	8.69	6.03	4.91
CaO	10.86	11.55	9.53	8.69
Na2O	3.25	3.23	3.71	4.49
K2O	1.13	1.23	1.39	1.53
P2O5	0.70	0.63	0.94	1.13
LOI	-0.82	-0.77	0.21	0.72
Total	99.41	99.13	98.67	98.96
V	303	335	250	180
Cr	568	341	100	23
Ni	211	127	34	<5
Cu	32	35	18	<15
Zn	82	94	85	94
Ga	19	19	18	18
Rb	24	25	21	24
Sr	1058	873	1365	1381
Y	30	32	29	38
Zr	239	237	260	288
Nb	62	62	65	87
Ba	363	324	475	575
Pb	5	4	<3	6
Th	<3	3	<3	5

Sample	descriptions
AW86094	basanite
AW86095	basanite
AW86088	basanite
AW86089	tephrite